



Core-collapse Supernova Progenitors in the Era of Untargeted Transient Searches

Citation

Sanders, Nathan Edward. 2014. Core-collapse Supernova Progenitors in the Era of Untargeted Transient Searches. Doctoral dissertation, Harvard University.

Permanent link

<http://nrs.harvard.edu/urn-3:HUL.InstRepos:12271795>

Terms of Use

This article was downloaded from Harvard University's DASH repository, and is made available under the terms and conditions applicable to Other Posted Material, as set forth at <http://nrs.harvard.edu/urn-3:HUL.InstRepos:dash.current.terms-of-use#LAA>

Share Your Story

The Harvard community has made this article openly available.
Please share how this access benefits you. [Submit a story](#).

[Accessibility](#)

**Core-collapse Supernova Progenitors
in the Era of Untargeted Transient Searches**

A dissertation presented

by

Nathan Edward Sanders

to

The Department of Astronomy

in partial fulfillment of the requirements

for the degree of

Doctor of Philosophy

in the subject of

Astronomy and Astrophysics

Harvard University

Cambridge, Massachusetts

April 2014

© 2014 — Nathan Edward Sanders

All rights reserved.

Core-collapse Supernova Progenitors in the Era of Untargeted Transient Searches

Abstract

Core-collapse supernovae (SNe) are the highly energetic explosions of massive stars ($\gtrsim 8 M_{\odot}$) that are pervasive in their influence throughout astrophysics. They are the phenomenon with primary responsibility for enriching the universe with many of the heavy elements (like carbon and oxygen) that are needed for life, provide a critical feedback pressure which helps to shape the galaxies that host them, and are the likely formation mechanism for stellar mass black holes. In the past decade, the study of these explosions has been revolutionized by the advent of wide field, untargeted transient searches like Pan-STARRS1 (PS1). These new searches permit the discovery of SNe at unprecedented rates, and absent of many of the selection effects that have enforced biases on past, targeted transient searches. This thesis presents a broad survey of core-collapse SN phenomenology exhibited in the discoveries of untargeted searches, and statistically quantifies population properties of these explosions that link them to distinct classes of progenitor stars. Through studies of the host galaxy and explosion properties of extreme PS1-discovered events, and controlled samples of specific classes of core-collapse objects, we constrain the effect of progenitor star chemical composition (metallicity) on their eventual death states. We provide a new observational, photometric tool which lowers the cost of precisely and accurately

measuring the metallicities of distant galaxies and supernova host environments. Moreover, we develop and apply a novel, multi-level Bayesian model for optical transient light curves which we apply to simultaneously interpret more than 20,000 PS1 images. This study illustrates how population-level modeling of data from large photometric surveys can yield improved physical inference on their progenitor stars through comparison to physical models. In the coming era, as next-generation facilities like the Large Synoptic Survey Telescope come online, the supernova discovery rate will accelerate, far outpacing the community's capacity for detailed individual observational follow-up. New observational and statistical tools like those presented here will be critical to enable the next generation of studies in supernova astrophysics.

Contents

Abstract	iii
Acknowledgments	xiii
1 Introduction	1
1.1 The role of metallicity in core-collapse supernovae	5
1.2 Characterizing the limits of the core-collapse mechanism	7
1.3 21st century tools for supernova studies	8
1.4 Tools for the 21st century scientist	10
2 SN 2010ay is a Luminous and Broad-lined Type Ic Supernova within a Low-metallicity Host Galaxy	11
2.1 INTRODUCTION	13
2.2 OBSERVATIONS	16
2.2.1 Discovery by CRTS	16
2.2.2 Pre-Discovery Detection With Pan-STARRS1 3π	17
2.2.3 Optical observations	19
2.2.4 Radio Observations	26
2.3 Initial Constraints	28
2.3.1 Light Curve Modeling	28
2.3.2 Large Nickel Mass for SN 2010ay	31
2.3.3 Unusually high velocity	32

CONTENTS

2.3.4	Ejecta Mass and Energy	36
2.4	Constraints on Relativistic Ejecta	40
2.4.1	Freely-expanding shockwave	42
2.4.2	Relativistic Ejecta	44
2.5	Constraints on an associated GRB	46
2.6	Sub-solar Host Environment Metallicity	52
2.6.1	Blue Compact Galaxy Host	54
2.6.2	Comparison to SNe Ic-BL and GRB-SNe Host Galaxies . . .	56
2.7	Discussion	61
2.8	CONCLUSIONS	65
3	The Metallicity Profile of M31 from Spectroscopy of Hundreds of HII Regions and PNe	68
3.1	INTRODUCTION	69
3.2	OBSERVATIONS	74
3.2.1	Data collection	74
3.2.2	Classification	79
3.2.3	Galactocentric distance	82
3.2.4	Emission line fluxes	83
3.2.5	Extinction	86
3.2.6	Direct abundance estimation	88
3.2.7	Strong line diagnostics	90
3.3	DISCUSSION	95
3.3.1	Extinction	97
3.3.2	Radial oxygen abundance gradient	100
3.3.3	Intrinsic scatter	104
3.3.4	Dependence on HII region properties	111

3.3.5	Time-variation in the abundance gradient	115
3.3.6	HII region nitrogen abundance gradient	117
3.3.7	Comparison to previous observations of M31	119
3.4	CONCLUSIONS	122
4	A Spectroscopic Study of Type Ibc Supernova Host Galaxies from Untargeted Surveys	124
4.1	INTRODUCTION	125
4.2	SAMPLE CONSTRUCTION	130
4.2.1	SN sample	130
4.2.2	Spectroscopic Observations	136
4.2.3	Spectroscopic analysis	140
4.3	HOST ENVIRONMENT PROPERTIES	142
4.3.1	Dust extinction	142
4.3.2	Metallicity Estimation	146
4.3.3	Metallicity Distribution of SN Ibc Progenitor Environments	152
4.3.4	Statistical tests on metallicity distributions	161
4.3.5	Young stellar population ages	163
4.3.6	Wolf-Rayet star populations	165
4.4	Combined SN Ibc Dataset	167
4.4.1	Criteria of the Combined SN Ibc dataset	167
4.4.2	SN Ib vs. Ic metallicities	170
4.4.3	SN Ic vs. Ic-BL metallicities	177
4.4.4	SN I Ib vs. Ibc metallicities	179
4.4.5	Type Ic supernovae from dwarf host galaxies	180
4.5	Systematic Effects	182
4.5.1	Targeted vs. Untargeted SN Searches	182

4.5.2	Isolating the SN Explosion Site	185
4.5.3	Uncertainties in SN classification	191
4.5.4	Selection effects in spectroscopic follow-up	193
4.5.5	Depth limits for host galaxy spectroscopy	195
4.6	DISCUSSION	196
4.6.1	SN Ib and Ic progenitor models	196
4.6.2	Comparison to nearby GRB-SNe	199
4.6.3	Studies of SN Ibc in the LSST era	201
4.7	CONCLUSIONS	203
5	Using Colors to Improve Photometric Metallicity Estimates for Galaxies	208
5.1	INTRODUCTION	209
5.2	GALAXY SAMPLE	211
5.3	LUMINOSITY-METALLICITY-COLOR RELATION	214
5.4	CAVEATS	222
5.5	APPLICATIONS	224
6	PS1-12sk is a Peculiar Supernova From a He-rich Progenitor System in a Brightest Cluster Galaxy Environment	229
6.1	INTRODUCTION	231
6.2	OBSERVATIONS	233
6.2.1	Optical Photometry	233
6.2.2	Optical spectroscopy	237
6.2.3	NIR imaging	239
6.2.4	Radio Observations	241
6.2.5	X-ray Observations	242
6.3	Comparison to Past Type Ibn Supernovae	243

6.3.1	Light curve evolution	243
6.3.2	Spectroscopic evolution	247
6.4	Host environment properties	252
6.5	Discussion	258
6.5.1	Basic Physical Constraints	259
6.5.2	Radioactive Decay	261
6.5.3	Host Environment	265
6.6	Progenitor Scenarios	268
6.6.1	Core Collapse Progenitor Models	268
6.6.2	A Degenerate Progenitor?	271
6.7	CONCLUSIONS	277
7	Towards Characterization of the Type IIP Supernova Progenitor Population: a Statistical Sample of Light Curves from Pan-STARRS1	281
7.1	INTRODUCTION	282
7.2	OBSERVATIONS	285
7.2.1	Pan-STARRS1 imaging	285
7.2.2	Optical spectroscopy	287
7.2.3	<i>K</i> -corrections	291
7.3	LIGHT CURVE MODELING	292
7.3.1	Parameterized light curve model	292
7.3.2	Fitting methodology	298
7.3.3	Fitting validation	302
7.3.4	Type II SN sub-classification	304
7.4	RESULTS	309
7.4.1	SN IIP Light Curve Template	309
7.4.2	Search for an SN IIL sub-population	310

7.4.3	Plateau duration distribution	314
7.4.4	Line of sight extinction	317
7.4.5	Peak magnitude distribution	319
7.4.6	Decline rate–peak magnitude relation	322
7.5	Progenitor Modeling	329
7.5.1	Bolometric luminosity	329
7.5.2	Ejected Ni mass	329
7.5.3	Comparison to hydrodynamic models	333
7.5.4	Progenitor initial mass inference	334
7.5.5	Implications for the Red Supergiant Problem	336
7.6	CONCLUSIONS	339
7.7	Appendix A: Individual Light Curve Stan Model	341
8	Unsupervised Transient Light Curve Analysis Via Hierarchical Bayesian Inference	365
8.1	INTRODUCTION	366
8.2	MODEL DESIGN	369
8.2.1	Light curve model	370
8.2.2	Hierarchical structure	370
8.2.3	Stan implementation	373
8.3	SAMPLE DATA	378
8.3.1	Pan-STARSS1 Optical Observations	378
8.3.2	Posterior Probability Convergence	379
8.4	RESULTS	380
8.4.1	Sampling Characteristics and Fit Convergence	380
8.4.2	Posterior Predictive Check Comparison	383
8.4.3	Population Parameter Distribution Characteristics	391

8.5	DISCUSSION	392
8.6	CONCLUSIONS	396
8.7	Appendix A: Hierarchical Light Curve Stan Model	397
9	Conclusions and Future Directions	405
9.1	Supernova progenitor insights from trailblazing wide field transient searches	406
9.1.1	The role of metallicity in core-collapse supernovae	406
9.1.2	Characterizing the limits of the core-collapse mechanism	408
9.1.3	21st century tools for supernova studies	409
9.2	Future directions	412
A	Supplemental Tables for Chapter 3	416
B	Preparing Undergraduates for Research Careers	481
B.1	Introduction	482
B.2	Describing Astrobites	483
B.3	Astrobites in the Classroom	486
B.3.1	Past uses of Astrobites	486
B.3.2	Suggested uses of Astrobites	487
B.4	Conclusions	489
C	Interactive Modules for Science Education	490
C.1	Introduction	491
C.2	Technologies for Module Development	494
C.2.1	WorldWide Telescope	494
C.2.2	Javascript / d3	497
C.2.3	Wolfram Computable Documents	498
C.2.4	Python	499

CONTENTS

C.3	Examples of Student Modules	500
C.3.1	Simulating the Lyman Alpha Forest (Yuan-Sen Ting)	502
C.3.2	Landmarks of the Interstellar Medium (Meredith MacGregor)	503
C.3.3	The Effects of Clumpiness in Giant Molecular Clouds (George Miller)	504
C.3.4	Magnetohydrodynamic Shocks (Philip Mocz)	505
C.4	Recommendations for Instructors	506
C.5	Evaluation and Reuse of Modules in cMOOC Environments	509
D	Public Awareness, Policy, & Science: A Mystic River Case Study	515
D.1	An Act Promoting Awareness of Safe Recreation in Public Waterways	520
	References	524

Acknowledgments

I could not express my gratitude to anyone before I thank my advisor, Alicia Soderberg, for her abundance of wisdom and guidance. Her strong leadership, brilliant scientific insight, and sagacious teaching has set the standard that all the scientists in her group strive to follow. I thank her for teaching me the technical skills of the trade, modeling the professional and entrepreneurial behavior of a modern scientist, and for constructing in me the ability and confidence to lead my own way forward. The true demonstration of my success as her student will not be this thesis, but will be whether or not I can ever serve the same formative role in someone else's career that she has in mine.

I thank all the other faculty on my thesis and research exam committees for their generosity of spirit, encouragement, and feedback. Edo Berger has been a constant font of level-headed genius, as well as a fantastic collaborator. Ramesh Narayan, Daniel Eisenstein, Josh Grindlay, and Doug Finkbeiner have guided my work in ways, I suspect, both conscious and unconscious. Alyssa Goodman has shown me the way that both science, and the education of scientists, should be done. Alyssa, Bob Kirshner, and Alessandro Massarotti taught me how to teach. John Johnson managed to be a mentor to me, and so many of us, before he even came to Harvard. This university is blessed to have Michael Brenner and Andrew Gelman so frequently at the head of its classrooms.

For both their contributions to this work and their mentoring and friendship, I thank all the collaborators who joined me in these projects. I thank Raffaella Margutti and Dan Milisavljevic for all they have taught me, and for making

CONTENTS

every day at the Center for Astrophysics a little brighter. I only regret that this may be the first time I ever spelled either of their names correctly. I thank Michael Betancourt, Kaisey Mandel, Emily Levesque, Ryan Foley, and Ryan Chornock for their extensive tutelage—I promise to pass the favor along to others. I thank Nelson Caldwell, Jonathan McDowell, Ashley Zauderer, Laura Chomiuk, Atish Kamble, and Sayan Chakraborti, and also too many members of the Pan-STARRS1 consortium to name, for many stimulating discussions and collaborations.

There have been no greater influences on me at the Center for Astrophysics than my fellow graduate students. I thank my fellow ComSciCon organizers, Courtney Dressing, Maria Drout, Chris Faesi, Kara Manke, Shannon Morey, Elisabeth Newton, and Sukrit Ranjan. I thank Ian Czekala, Courtney, Elisabeth, Katherine Rosenfeld, and Josh Suresh for leaping with me to found Astrobites. I am so grateful to have embarked on these projects with this phenomenal group, which has made these projects a thoroughly rewarding and enjoyable experience. I thank Tanmoy Laskar for so many great observing nights. Jason Dittman, Raginhild Lunnan, Tony Pan, and Andrew Friedman made supernova research at Harvard a blast. I thank Wen-fai Fong and Anjali Tripathi, who are mentors to all of us.

I give my insufficient thanks to Peg Herlihy, Robb Scholten, and Donna Adams. None of us could make it through without them, and I know I caused them more trouble than most.

I would like to give special thanks to John Huchra, whose exceptional interest

CONTENTS

in, and generosity with, students made a deep impression on me in the short time I knew him. Losing him so soon after I started my Ph.D. was a terrible shock, but his presence persists as a role model and an inspiration.

I thank Senator Pat Jehlen, Tim Snyder, Dan Smith, and all her staff, and Representative Denise Provost, Mark Kennedy, and Pooja Phaltankar for the most enlightening and stimulating fellowship experience possible. I did not think it was possible to learn so much, of so great value, in so short a time. I thank Margot Gill and Erin Driver-Linn for their support of and contributions to ComSciCon. I learned some of my most valuable lessons through these past four years from them.

I thank all my family and, most of all, I thank Shannon Morey, my wife, whose love and support has made all my work possible, and all my work worthwhile.

Chapter 1

Introduction

Investigations over the past decade have revealed that core-collapse supernovae (SNe), explosions triggered by the gravitational collapse of stars more massive than about $8 M_{\odot}$, exhibit a range of properties far more diverse than previously recognized. The photometric and spectroscopic properties of these supernovae depend not only on the kinetic energy of the explosion and the mass of ^{56}Ni and other radioactive material ejected during the event, but also depend sensitively on the mass and composition of the stellar envelope at the time of the progenitor star's death and the star's eruptive mass loss history in its final years. All these parameters, in turn, may be strong functions of the progenitor's initial mass, metallicity, and rate of rotation. Looming over all of these effects, which the potential to profoundly influence each one, is the multiplicity of the stellar system and the potential for binary interaction between stellar companions.

Throughout the universe, this broad range of initial conditions yields a variety of core-collapse supernova phenomena traditionally classified by the

features in their optical spectra (Filippenko 1997). Type II supernovae, rich in hydrogen, are thought to originate from the least massive stars which undergo core-collapse ($\sim 8 - 20 M_{\odot}$). A close spectroscopic cousin, Type IIn supernovae, have narrow hydrogen features that suggest a violent history of eruptions by the stellar progenitor immediately preceding its explosive death. Type I supernovae exhibit no hydrogen features, and the Type Ibc designation is given to many different hydrogen-poor subclasses that evidently originate from stars undergoing core-collapse. SNe Ibc are united in that some process must have ejected most of their progenitor star's atmospheric envelopes before explosion, but the nature of this process—be it continuum radiation pressure from the luminous stellar core, metal line-driven winds, binary interaction, or some combination of these—may differ between sub-classes. While some of these SNe Ibc retain some fraction of their helium envelopes, as is visible in their optical spectra (SNe Ib), explosions completely devoid of either hydrogen or helium (SNe Ic) are much more common. A transitional class (SNe IIb) exhibits some transient hydrogen features. Perhaps the rarest of these classes, Type Ibn supernovae, have optical features suggesting episodic eruptions from a helium-rich progenitor star, not predicted to occur during any well-characterized phase of stellar evolution. Finally, the most energetic of these explosion classes, SNe Ic-BL, exhibit broad-lined absorption features reflecting photospheric velocities in the relativistic regime.

It is integral to improve our understanding of each class in this menagerie of explosions as, together, they have a pervasive influence throughout astrophysics. First and foremost, as the markers of the end states of the lives of massive stars, core-collapse SNe are fundamental boundary conditions for models of stellar

evolution. The discovery of an increasing number of exotic core-collapse explosion types has driven our increasingly complex and sophisticated understanding of stellar evolution. Moreover, core-collapse SNe enrich the interstellar media of galaxies with critical heavy elements like carbon and oxygen that are needed for planet formation and life; they provide a significant component of the hydrodynamic pressure that mediates the equilibrium structure and evolution of galaxies; they serve as the formation mechanism for compact remnants like neutron stars and stellar mass black holes; and, being capable of sterilizing life from surrounding planets, they are arguably the greatest antagonist to life in the universe.

Over the past decade, wide field surveys have emerged as a key tool for astronomers to explore this menagerie, study each species of supernova explosion, and, through this research, strengthen our understanding of the paths that stars take to the final stages of their lives. Modern wide field surveys build on the pioneering CCD imaging surveys of the 1990's to scan large swaths of the sky with deep imaging to detect transients from distant galaxies, a fast cadence to discover explosions as soon as possible after their emergence, and long durations to monitor explosions as they expand and evolve. Critically, transient searches are increasingly being conducted with an untargeted survey strategy, meaning that the search is not limited to a list of nearby and pre-selected host galaxies. This has proved crucial for 1) enabling discovery of extreme, previously unknown explosion classes from rare and low-luminosity host environments and 2) freeing studies of supernova populations and host environments from biases inherent to traditional, targeted transient search methodologies. Our collaboration has

used the Medium Deep Survey of the Pan-STARRS1 (PS1; Kaiser et al. 2002) telescope in Hawaii, an exemplar of the current generation of untargeted wide field transient searches, to discover and characterize hundreds of supernovae over the past four years.

The chapters in this thesis combine to contribute to our understanding of three critical aspects of core-collapse supernova phenomena. In particular, they illuminate the role of a fundamental stellar property, metallicity, in the explosions of core-collapse SNe, through studies of their host galaxy properties (Section 1.1); test the limits of the core-collapse mechanism, through the study of some of the most extreme examples of core-collapse phenomenology yet discovered in the universe (Section 1.2); and suggest a path forward for many aspects of supernova research for the twenty-first century, as new facilities and technological change continue to revolutionize the field (Section 1.3).

A common theme throughout these works is the use of novel, primarily Bayesian statistical methods to extract information from astrophysical observations rooted in the low signal-to-noise regime. These techniques have allowed us to derive physical inferences based on samples of objects that are more complete, more representative, and less biased than past studies of their kind, while accounting appropriately for observational uncertainty.

1.1 The role of metallicity in core-collapse supernovae

For about two decades, metal line-driven winds have served as a neat and persuasive theoretical mechanism for stripping the atmospheric H and He envelopes from the progenitor stars of Type Ibc SNe (see e.g. Woosley et al. 1995). This theory has the benefit of providing a strong prediction that can be tested observationally: SNe which exhibit highly-stripped progenitor star atmospheres (e.g. SNe Ic) should have higher metallicity progenitors than those whose optical spectra suggest less highly-stripped progenitor stars (SNe Ib and II).

In just the past few years, this theory has been confronted with observations for the first time, through several concurrent spectroscopic studies of the host environments of core-collapse SNe. These host environment studies have measured the metallicity of the star forming regions which produced the short-lived progenitor stars of these explosions as a proxy for the chemical composition of the progenitors themselves. The first studies of this type were in conflict, including both detections and non-detections of metallicity differences between Type Ib and Ic progenitor environments.

Our study (Chapter 4) aimed to resolve this conflict by overcoming a crucial source of bias in metallicity estimation: galaxy targeting. Traditional transient searches, in targeting specific, nearby, highly luminous galaxies, introduce a recognized bias towards high-metallicity host environments. We have performed the first spectroscopic study of SNe exclusively discovered by untargeted transient

searches, more than doubling the number of host environment metallicity measurements of SNe from untargeted searches to date. Through analysis of our new dataset and a synthesis of past studies, we test for differences between the observed metallicity distributions of Type Ibc SN sub-classes, and examine the evidence for metal line-driven winds as a mechanism for stripping of SN Ibc progenitor stars.

Crucial to this SN metallicity study is a firm understanding of the limits of host environment spectroscopy as a proxy for the chemical composition of individual progenitor stars. Prominent among these limitations is the variation in the metallicity of star formations within individual galaxies, which can be significantly larger than the observational uncertainty attributed to spectroscopic metallicity measurements. Our study of emission nebulae in the nearby galaxy M31 (Chapter 3) provides perhaps the most comprehensive dataset for assessing this variation, both deterministically as a function of galaxy radius (metallicity gradients; Zaritsky et al. 1994) and stochastically among neighboring star forming regions (metallicity variance). In Chapter 4, we use this and other studies to statistically evaluate the likelihood that host environment chemical variance and other confounding factors may influence our progenitor metallicity distribution inferences.

1.2 Characterizing the limits of the core-collapse mechanism

This thesis examines two particular transients discovered by PS1 whose nature challenges our understanding of core-collapse SN progenitor theory.

In Chapter 2, we report on the Type Ic-BL SN 2010ay, one of the most energetic Type Ibc SNe discovered to date. The discovery of this extreme SN by PS1 prompted comparison to SN 2010bh, a contemporaneous event from the rare class of Gamma Ray Burst (GRB)-associated SNe. We explore remarkable similarities between these two events among a variety of explosion and host environment factors. We use these two twin SNe to test a key prediction of the long-established paradigm for GRB-SN production, that low-metallicity progenitor stars should support relativistic outflow formation via conservation of angular momentum (see e.g. MacFadyen & Woosley 1999). To this end, we study gamma-ray and radio observations to search for evidence of a relativistic outflow, and host galaxy observations to measure the metallicity of the progenitor star.

In Chapter 6, we report on the SN PS1-12sk, just the sixth known member of the Type Ibn sub-class. Type Ibn SNe, exemplified by SN 2006jc, are thought to be produced by some of the most massive stellar progenitors of the modern universe. While no known stellar evolution mechanism predicts the episodic ejection of significant quantities of He by a SN progenitor star immediately before core-collapse, the He-rich nature of the circumstellar environments of SNe Ibn seems to demand this behavior. Our multi-wavelength study of PS1-12sk and

its host galaxy reveals a progenitor environment absolutely unique among not only among SNe Ibn, but core-collapse SNe generally, and offers unprecedented photometry of the rising phase of an SN Ibn light curve. We use these unique properties to explore the possibility that these exotic transients may not originate from a core-collapse explosion mechanism.

1.3 21st century tools for supernova studies

The final components of this thesis look forward to the coming era, when many of the techniques applied in the previous sections, and relied upon for much of the discovery potential in supernova astrophysics today, will no longer apply. This remarkable, modern period of expansion in our understanding of the diversity of stellar explosions heralded by the recent discoveries and recognition of GRB-SNe, ultraluminous supernovae, SNe Ibn, Ca-rich SNe, and other extreme classes is not sustainable. Ever-more prolific transient searches, like the upcoming Large Synoptic Survey Telescope (LSST), and new observational regimes like gravitational wave detection, promise to reveal yet more rare and exotic transient classes and unexpected stellar death behaviors. But new tools are needed to successfully plumb these enormous data sources for unique events. Perhaps even more importantly, new tools are needed to cohesively synthesize the wealth of data that next generation wide field surveys will provide to synthesize insights on already-recognized supernova classes.

First, to facilitate next-generation studies of the kind presented in Chapter 4, we develop a new methodology (Chapter 5) for measuring the metallicity of

distant galaxies. This method, the Luminosity-Metallicity-Color (LZC) relation, is meant to allow for host galaxy metallicity to be measured concurrently with supernova discovery through wide field, multi-band transient searches like PS1 and LSST. We calibrate the LZC and compare it to past photometric metallicity measurement techniques. We test particularly for a reduction in the observational bias associated with metallicity estimation of low-luminosity host galaxies, like those characteristically hosting exotic transients like SNe Ic-BL. We advocate for the LZC as a method for metallicity estimation applicable to a substantial fraction of galaxies in the nearby universe, without the need for expensive spectroscopic followup.

Finally, we turn our attention to the photometric light curve data amassed by wide field transient searches. The availability of light curve data will grow rapidly as new searches come online, with the quality of data captured for individual objects varying greatly as untargeted surveys reach both far and wide. In Chapter 7, we discuss the unprecedented Type IIP SN light curve dataset collected over 4 years of observations with PS1. Applying Bayesian modeling to the SN light curves and comparing to theoretical hydrodynamic light curve models, we extract physically relevant explosion parameters for the SNe in the PS1 sample. The results from this first study of a large, homogeneously observed population of SNe IIP challenge a number of past claims about the nature and diversity of the progenitor stars producing this class of transient, the most common end state of massive stars in the universe. In Chapter 8, we present a multi-level Bayesian framework for population-level modeling of transient light curves. We demonstrate the effectiveness of this method by applying it to the

PS1 SN IIP sample, improving posterior constraints on key parameters versus our non-hierarchical light curve modeling. We discuss how this approach will allow studies of the kind presented in Chapter 7 to be improved and generalized to other surveys and transient classes.

1.4 Tools for the 21st century scientist

Finally, in the appendices of this thesis, we discuss several novel methods, resources, and applications we have developed in the fields of scientific outreach, education, and evidence-based public policy. We view these tools as sharing an equal importance and relevance as the preceding research results. While we hope the work discussed in Section 1.3 has enriched the scientific literature over these past several years, the work described in Appendices B, C, and D serve to enrich the twenty-first century scientist, and our communities more broadly.

Chapter 2

SN 2010ay is a Luminous and Broad-lined Type Ic Supernova within a Low-metallicity Host Galaxy

N. E. Sanders, A. M. Soderberg, S. Valenti, R. J. Foley, R. Chornock, L. Chomiuk, E. Berger, S. Smartt, K. Hurley, S. D. Barthelmy, E. M. Levesque, G. Narayan, M. T. Botticella, M. S. Briggs, V. Connaughton, Y. Terada, N. Gehrels, S. Golenetskii, E. Mazets, T. Cline, A. von Kienlin, W. Boynton, K. C. Chambers, T. Grav, J. N. Heasley, K. W. Hodapp, R. Jedicke, N. Kaiser, R. P. Kirshner, R.-P. Kudritzki, G. A. Luppino, R. H. Lupton, E. A. Magnier, D. G. Monet, J. S. Morgan, P. M. Onaka, P. A. Price, C. W. Stubbs, J. L. Tonry, R. J. Wainscoat, & M. F. Watson 2012, *The Astrophysical Journal*, Vol. 756, 184

Abstract

We report on our serendipitous pre-discovery detection and follow-up observations of the broad-lined Type Ic supernova (SN) 2010ay at $z = 0.067$ imaged by the Pan-STARRS1 3π survey just ~ 4 days after explosion. The SN had a peak luminosity, $M_R \approx -20.2$ mag, significantly more luminous than known GRB-SNe and one of the most luminous SNe Ib/c ever discovered. The absorption velocity of SN 2010ay is $v_{\text{Si}} \approx 19 \times 10^3 \text{ km s}^{-1}$ at ~ 40 days after explosion, 2 – 5 times higher than other broad-lined SNe and similar to the GRB-SN 2010bh at comparable epochs. Moreover, the velocity declines ~ 2 times slower than other SNe Ic-BL and GRB-SNe. Assuming that the optical emission is powered by radioactive decay, the peak magnitude implies the synthesis of an unusually large mass of ^{56}Ni , $M_{\text{Ni}} = 0.9 M_{\odot}$. Applying scaling relations to the light-curve, we estimate a total ejecta mass, $M_{\text{ej}} \approx 4.7 M_{\odot}$, and total kinetic energy, $E_K \approx 11 \text{ times } 10^{51} \text{ ergs}$. The ratio of M_{Ni} to M_{ej} is ~ 2 times as large for SN 2010ay as typical GRB-SNe and may suggest an additional energy reservoir. The metallicity ($\log(\text{O}/\text{H})_{\text{PP04}} + 12 = 8.19$) of the explosion site within the host galaxy places SN 2010ay in the low-metallicity regime populated by GRB-SNe, and $\sim 0.5(0.2)$ dex lower than that typically measured for the host environments of normal (broad-lined) Ic supernovae. We constrain any gamma-ray emission with $E_{\gamma} \lesssim 6 \times 10^{48} \text{ erg}$ (25-150 keV) and our deep radio follow-up observations with the Expanded Very Large Array rule out relativistic ejecta with energy, $E \gtrsim 10^{48} \text{ erg}$. We therefore rule out the association of a relativistic outflow like those which accompanied SN 1998bw and traditional long-duration GRBs,

but place less-stringent constraints on a weak afterglow like that seen from XRF 060218. If this SN did not harbor a GRB, these observations challenge the importance of progenitor metallicity for the production of relativistic ejecta, and suggest that other parameters also play a key role.

2.1 INTRODUCTION

Recent observations have shown that long-duration gamma-ray bursts are accompanied by Type Ic supernovae (SNe) with broad absorption features (hereafter, “broad-lined,” BL), indicative of high photospheric expansion velocities (see Woosley & Bloom 2006, for a review). This GRB-SN connection is popularly explained by the favored “collapsar model” (MacFadyen et al. 2001) in which the gravitational collapse of a massive ($M \gtrsim 20 M_{\odot}$) progenitor star gives birth to a central engine – a rapidly rotating and accreting compact object – that powers a relativistic outflow. At the same time, not all SNe Ic-BL show evidence for a central engine. Radio observations constrain the fraction of SNe Ic-BL harboring relativistic outflows to be less than a third (Soderberg et al. 2006a, 2010).

The physical parameter(s) that distinguish the progenitors of GRB-associated SNe from other SNe Ic-BL remains debated, while theoretical considerations indicate that progenitor metallicity may play a key role (Woosley & Heger 2006). In the collapsar scenario, massive progenitor stars with metallicity above a threshold, $Z \gtrsim 0.3 Z_{\odot}$, lose angular momentum to metal line-driven winds, preventing the formation of a rapidly rotating compact remnant, and in turn, a

relativistic outflow. At the same time, the hydrogen-free spectra of SNe Ic-BL indicate that their stellar envelopes have been stripped prior to explosion, requiring higher metallicities (e.g., $Z \approx Z_{\odot}$) if due to radiation driven-winds (Woosley et al. 1995). Alternatively, short-period (~ 0.1 days) binary interaction may be invoked to spin up stars via tidal forces as well as cause mass loss via Roche lobe overflow (Podsiadlowski et al. 2004; Fryer & Heger 2005). However, even in the binary scenario, GRB formation is predicted to occur at higher rates in lower-metallicity environments, where the radius and mass loss rates of stars should be smaller (Izzard et al. 2004).

Observationally, *most* GRB-SNe are discovered within dwarf star-forming galaxies (Fruchter et al. 2006) characterized by sub-solar metallicities, $Z \lesssim 0.5 Z_{\odot}$ (Levesque et al. 2010a). This has been interpreted as observational support for the metallicity-dependent collapsar model (Stanek et al. 2006). Meanwhile, it was noted early on that SNe Ic-BL without associated GRBs have been found in more enriched environments (e.g., Modjaz et al. 2008; Prieto et al. 2008), motivating the suggestion of an observationally determined cut-off metallicity above which GRB-SNe do not form (Kocevski et al. 2009). This metallicity difference may be partly attributable to the different survey strategies: SNe have been primarily discovered by galaxy-targeted surveys biased towards more luminous (and therefore higher metallicity) environments, while GRB host galaxies are found in an untargeted manner through their gamma-ray emission (Stanek et al. 2006).

Against this backdrop of progress, recent observations have begun to call into question some aspects of this scenario. First, there are two reported long-duration GRBs in solar or super-solar metallicity environments (GRB 020819; Levesque

et al. 2010c, GRB 051022; Graham et al. 2009). Similarly, the luminous radio emission seen from SN Ic-BL 2009bb pointed unequivocally to the production of copious relativistic ejecta resembling a GRB afterglow (Soderberg et al. 2010) while the explosion environment was characterized by a super-solar metallicity, $Z \sim 1 - 2 Z_{\odot}$ (Levesque et al. 2010d). Together with the growing lack of evidence for massive progenitor stars for SNe Ic in pre-explosion *Hubble Space Telescope* images (Smartt 2009), a lower mass ($M \sim 10 - 20 M_{\odot}$) binary progenitor system model (with a gentler metallicity dependence) is gaining increasing popularity (Yoon et al. 2010). Multi-wavelength studies of SNe Ic-BL in metal-poor environments may shed further light on the role of metallicity in the nature of the progenitor and the explosion properties, including the production of relativistic ejecta.

Fortunately, with the recent advent of wide-field optical transient surveys (e.g., Catalina Real-time Transient Survey (CRTS); Drake et al. 2009a, Panchromatic Survey Telescope and Rapid Response System; (Pan-STARRS1, abbreviated PS1) Kaiser et al. 2002, Palomar Transient Factory; Law et al. 2009) SNe Ic-BL are now being discovered in metal-poor environments, $Z \sim 0.5 Z_{\odot}$ thanks to an unbiased search technique (see e.g. Stanek et al. 2006; Modjaz et al. 2008, 2011a; Young et al. 2008; Arcavi et al. 2010; Leloudas et al. 2011; Kelly & Kirshner 2012; Sanders et al. 2012c; Stoll et al. 2012). In this paper, we present pre-discovery Pan-STARRS1 imaging and multi-wavelength follow-up observations for the broad-lined Type Ic SN 2010ay discovered by CRTS (Drake et al. 2010). In §2.2, we report our optical (Pan-STARRS1, Gemini, William Herschel Telescope) and radio (Expanded Very Large Array; EVLA) observations.

In §2.3, we model the optical light-curve and analyze the spectra to derive the explosion properties of SN 2010ay. In §2.4, we use our observations of SN 2010ay with the EVLA to place strict limits on the presence of relativistic outflow. In §2.5, we draw from gamma-ray satellite coverage to rule out a *detected* gamma-ray burst in association with SN 2010ay. In §2.6, we derive the explosion site metallicity and find it to be significantly sub-solar and typical of most GRB-SNe host environments. In §2.7, we discuss the implications of these findings in the context of the explosion and progenitor properties and conclude in §2.8.

2.2 OBSERVATIONS

2.2.1 Discovery by CRTS

SN 2010ay was discovered by the Catalina Real-time Transient Survey (Drake et al. 2009a) on 2010 March 17.38 UT (Drake et al. 2010) and designated CSS100317:123527+270403, with an unfiltered magnitude of $m \approx 17.5$ mag and located $\lesssim 1''$ of the center of a compact galaxy, SDSS J123527.19+270402.7 at $z = 0.067$ (Table 2.1). We adopt a distance, $D_L = 297.9$ Mpc, to the host galaxy¹, and note that the Galactic extinction toward this galaxy is $E(B - V) = 0.017$ (Schlegel et al. 1998). Pre-discovery unfiltered images from CRTS revealed an earlier detection of the SN on Mar 5.45 UT at $m \approx 18.2$ mag and a non-detection from Feb 17.45 UT at $m \gtrsim 18.3$ mag (Drake et al. 2010).

¹We assume $H_0 = 71$ km s⁻¹ Mpc⁻¹, $\Omega_\Lambda = 0.73$, $\Omega_M = 0.27$

A spectrum obtained on Mar 22 UT revealed the SN to be of Type Ic with broad features, similar to the GRB-associated SN 1998bw spectrum obtained near maximum light (Filippenko et al. 2010). This classification was confirmed by Prieto (2010) who additionally reported photometry for the SN (see Table 2.2). After numerically subtracting the host galaxy emission, they estimate an unusually luminous absolute magnitude of $V \approx -19.4$ mag.

2.2.2 Pre-Discovery Detection With Pan-STARRS1 3π

The field of SN 2010ay was serendipitously observed with the PS1 3π survey in the weeks preceding its discovery. Pan-STARRS1 is a wide-field imaging system at Haleakala, Hawaii dedicated to survey observations (Kaiser et al. 2002). The PS1 optical design (Hodapp et al. 2004) uses a 1.8 meter diameter $f/4.4$ primary mirror, and a 0.9 m secondary. The telescope illuminates a diameter of 3.3 degrees. The Pan-STARRS1 imager (Tonry & Onaka 2009) comprises a total of 60 4800×4800 pixel detectors, with $10 \mu\text{m}$ pixels that subtend 0.258 arcsec. The PS1 observations are obtained through a set of five broadband filters designated as g_{P1} , r_{P1} , i_{P1} , z_{P1} , and y_{P1} . These filters are similar to those used in previous surveys, such as SDSS (Fukugita et al. 1996). However, The g_{P1} filter extends 20 nm redward of g' , the z_{P1} filter is cut off at 930 nm, and SDSS has no corresponding y_{P1} filter (Stubbs et al. 2010).

The field of SN 2010ay was observed on 2010 February 21st (r_{P1} -band) and February 25th (i_{P1} -band, Figure 2.1). On each night, four exposures were collected following the strategy of the PS1-3pi survey (Chambers et al., in preparation).

Table 2.1. SN 2010ay host galaxy SDSS J123527.19+270402.7

Parameter	Value
RA	12 ^h 35 ^m 27 ^s .19 (J2000)
DEC	+27°04′02.7″ (J2000)
Redshift (<i>z</i>)	0.0671
Petrosian radius	1.355″
Photometry ^a	
<i>u</i> '	19.56 ± 0.03 mag
<i>g</i> '	19.02 ± 0.01 mag
<i>r</i> '	19.02 ± 0.01 mag
<i>i</i> '	18.69 ± 0.01 mag
<i>z</i> '	18.87 ± 0.04 mag
<i>U</i>	19.50 ± 0.06 mag
<i>B</i>	19.02 ± 0.05 mag
<i>V</i>	19.13 ± 0.05 mag
<i>R</i>	18.94 ± 0.05 mag
<i>I</i>	18.90 ± 0.06 mag
Extinction	
E(B-V) _{MW} ^b	0.017 mag
E(B-V) _{host} ^c	0.2 mag

Note. — SDSS host galaxy properties and *ugriz* photometry.

^aSDSS DR8 model magnitudes (Aihara et al. 2011). Photometry has not been corrected for extinction. Filter transformation performed following Blanton & Roweis (2007).

^bThe Milky Way extinction as determined by Schlegel et al. (1998), assuming $R_V = 3.1$.

^cThe host galaxy extinction determined from the SDSS spectrum via the Balmer decrement (§2.2.3).

Following the CRTS discovery and announcement of SN 2010ay, we geometrically registered SDSS pre-explosion images to the PS1 images and performed digital image subtraction using the *ISIS* package (Alard 2000). Photometric calibration was performed using many field stars in the SDSS catalog with magnitudes $r \approx 13 - 19$ mag. No residual flux was found in the difference r_{P1} -band image from 2010 February 21 with an upper limit of $r > 22.0$ mag. However, we detect residual flux at the position of SN 2010ay in the i_{P1} -band residual image from 2010 February 25 with a magnitude of $i = 21.1 \pm 0.3$ mag.

The field was again observed in the i_{P1} band on 2011 March 25 and the r_{P1} -band on 2011 March 29, but no residual flux was detected in the subtractions at the SN position to limits of $i' \gtrsim 22.2$ and $r' \gtrsim 21.9$.

In Table 2.2 and Figure 2.2, we compile photometry from the PS1 detections, our optical observations, and the circulars to construct a light-curve for SN 2010ay.

2.2.3 Optical observations

We obtained an optical spectrum ($\sim 3000 - 11000 \text{ \AA}$) of SN 2010ay on April 1 UT, from the *ISIS* blue arm instrument of the 4.2 m William Herschel Telescope (WHT) at the Roque de Los Muchachos Observatory. The spectrum was taken at the parallactic angle and the exposure time was 1800 sec. We obtained a second 1800 sec optical spectrum ($\sim 3600 - 9600 \text{ \AA}$) using the Gemini Multi-Object Spectrograph (GMOS) on the 8.1 m Gemini North telescope on 2010 April 11.4 UT. We employed standard two-dimensional long-slit image reduction

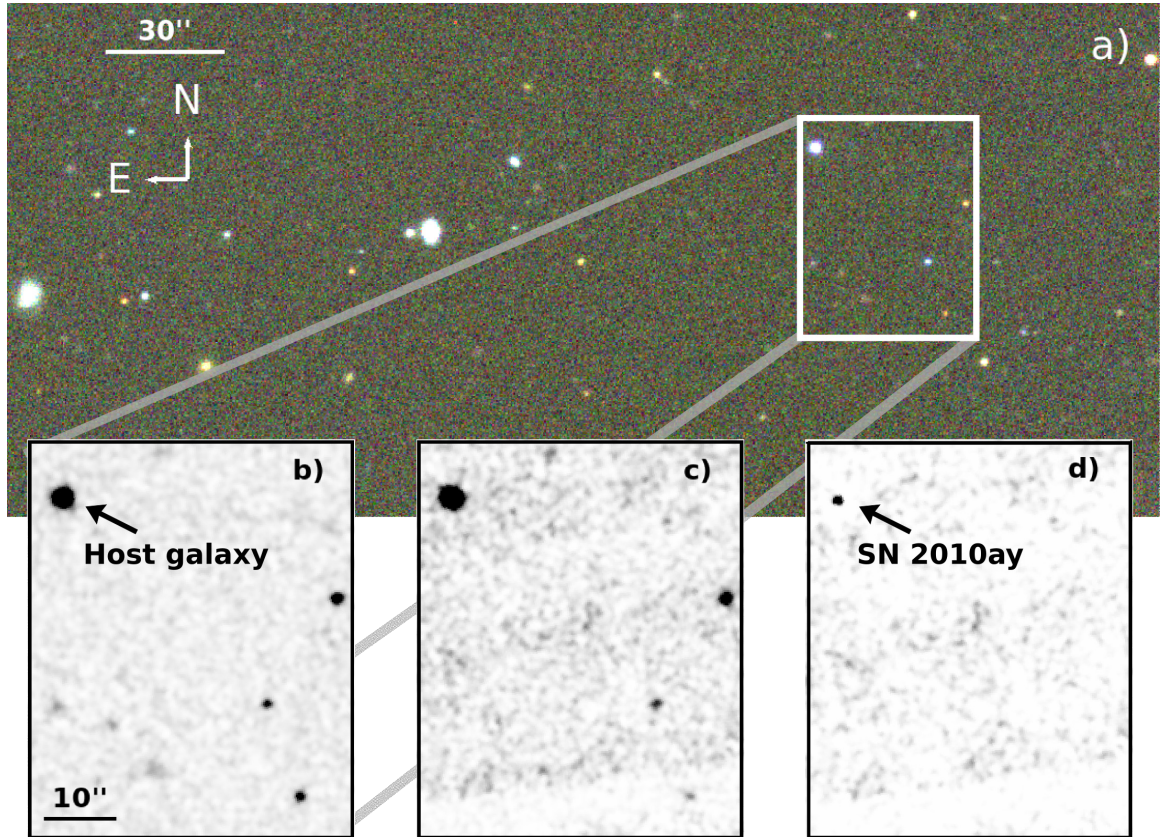


Figure 2.1.— Images illustrating the Pan-STARRS1 pre-discovery detection of SN 2010ay and the surrounding field. a) Pre-explosion *gri*-composite image from the SDSS DR7 (Abazajian et al. 2009), observed 2004 December 21, b) SDSS *i*-band image geometrically registered to the PS1 image frames and zoomed in to the host galaxy of SN 2010ay, c) *i*_{P1}-band image from the 3π survey of PS1, observed 2010 February 25, d) the difference of the SDSS *i*' and PS1 *i*_{P1} images. The transient emission can be seen in the NE corner of the last panel. Nearby stars are included in the zoomed-in frames to illustrate the efficiency of subtraction.

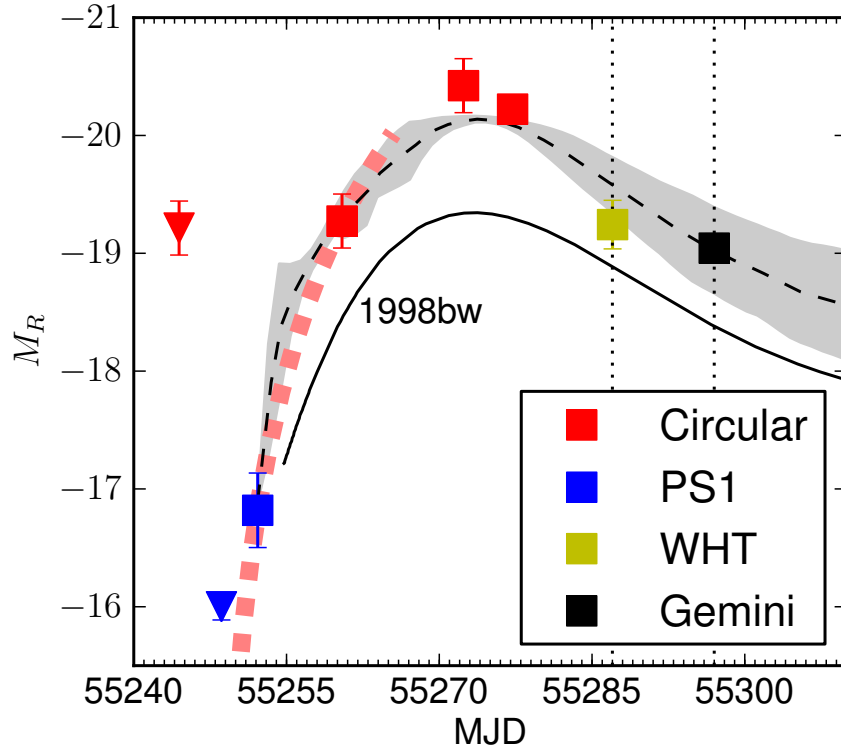


Figure 2.2.— The optical R-band light curve of SN 2010ay, as compiled in Table 2.2 from CBET 2224 (red squares), the PS1 3π survey (blue), our Gemini images (black), and synthetic photometry (§2.2.3) based on our WHT spectrum (gold). Triangles denote upper limits. The thick dashed line represents the luminosity of an expanding fireball fit to our early-time photometry (§2.3.1). The thin dashed line is the SN Ib/c light-curve template of Drout et al. (2011) and the gray field represents the standard deviation among its constituent photometry. The template is stretched by $(1+z) = 1.067$ with the best fit parameters $t_{\text{Rpeak}} = \text{March}18 \pm 2$ (MJD 55273 ± 2), $M_{\text{Rpeak}} = -20.2 \pm 0.2$ mag. The solid line is the light-curve of the GRB-SN 1998bw (Galama et al. 1998), redshifted to match SN 2010ay. The vertical dotted lines mark the epochs of our Gemini and WHT spectroscopy.

Table 2.2. SN 2010ay light-curve photometry

UT date	MJD	t_{peak}^a	Filter	m^b	M_R^c	Source
733820.4	55244.4	-29	...	< 18.3	$< -19.2 \pm 0.2$	d
733824.6	55248.6	-25	r_{P1}	$< 22.0 \pm 0.1$	$< -16.0 \pm 0.1$	e
733828.2	55252.2	-21	i_{P1}	21.1 ± 0.3	-16.8 ± 0.3	e
733836.4	55260.4	-13	...	18.2	-19.3 ± 0.2	d
733848.4	55272.4	-1	...	17.5	-20.4 ± 0.2	d
733853.2	55277.2	4	B	18.39 ± 0.05	...	f
733853.2	55277.2	4	V	17.61 ± 0.05	...	f
733853.2	55277.2	4	R	17.44 ± 0.05	-20.22 ± 0.07	f
733863.0	55287.0	14	R	18.2 ± 0.2	-19.2 ± 0.2	g
733873.0	55297.0	24	g	18.9 ± 0.1	...	h
733873.0	55297.0	24	r	18.3 ± 0.1	-19.0 ± 0.1	h
733873.0	55297.0	24	i	18.0 ± 0.1	...	h
734221.0	55645.0	372	i_{P1}	$< 22.2 \pm 0.2$	$< -16.22 \pm 0.10$	e
734225.0	55649.0	376	r_{P1}	$< 21.9 \pm 0.1$	$< -15.7 \pm 0.1$	e

^aTime since peak in days, relative to the fitted value: 2010 March 18.5 ± 0.2 .

^bThe measured apparent magnitude of the source, in the filter noted and without extinction correction. For the Pan-STARRS1 photometry, a template image was subtracted; for the other points, the host galaxy flux has not been subtracted.

^cThe absolute R magnitude of the SN. Filter conversion, host flux subtraction, and extinction correction have been performed as described in §2.3.1.

^dDrake et al. (2010), unfiltered (synthetic V-band).

^ePhotometry from the Pan-STARRS1 3π survey.

^fPrieto (2010).

^gSynthetic photometry obtained from our WHT spectrum as described in §2.2.3.

^hPhotometry from our Gemini/GMOS observations described in §2.2.2.

and spectral extraction routines in IRAF². We do not apply a correction for atmospheric differential refraction, because the displacement should be $\lesssim 0.5''$ at the airmass of the observations, ≈ 1.0 .

In both our Gemini and WHT spectra, broad absorption features associated with the SN are clearly detected in addition to narrow emission lines typical of star forming galaxies. We distinguish the host galaxy emission from the continuum dominated by the highly broadened SN emission by subtracting a high-order spline fit to the continuum. Both SN and host galaxy spectral components are shown in Figure 2.3. As illustrated in the Figure, the broad, highly-blended spectral features of SN 2010ay resemble those of the Type Ic-BL SN 2010bh (associated with GRB100316D) at a similar similar epoch (Chornock et al. 2010). In particular, the broadening and blueshift of the feature near 6355 Å are similar for SN 2010ay and SN 2010bh, and are broader and more blueshifted than in SN 1998bw at a comparable epoch. We discuss the comparison between these two SN further in §2.3.3 and §2.6.2.

Additionally, we obtained 60 s *gri*-band images of SN 2010ay on 2010 April 11.4 UT using GMOS. The data were reduced using the `gemini` package in IRAF, and photometry was performed using the standard GMOS zero-points³. We measure that $[g, r, i] = [18.90, 18.32, 18.04] \pm 0.1$ mag.

²IRAF is distributed by the National Optical Astronomy Observatory, which is operated by the Association of Universities for Research in Astronomy (AURA) under cooperative agreement with the National Science Foundation.

³<http://www.gemini.edu/?q=node/10445>

Imaging photometry is not available at the epoch of our WHT spectrum. However, the spectrum was flux-calibrated against observations of the standard star Feige34, which was observed the same night and at approximately the same low airmass as the supernova. For the observations of both the standard star and supernova, the slit was placed at the parallactic angle. We perform synthetic photometry on the spectrum to extract the flux at the central frequency of the R-band (6527 Å) and find $R = 18.2 \pm 0.2$ mag. We then subtract the host galaxy flux numerically.

Host galaxy features

We measure fluxes of the narrow emission lines from the host galaxy in our Gemini spectrum, as reported in Table 2.3. We fit a Gaussian profile to each narrow emission line; for nearby lines such as [N II] and $H\alpha$, we fit multiple Gaussians simultaneously. We model the local continuum with a linear fit to 20 Å regions on either side of each line. We estimate uncertainties in quantities derived from the line fluxes by Monte Carlo propagation of the uncertainties in the flux measurement.

The host galaxy is significantly reddened as evidenced by the flux ratio of $H\alpha$ to $H\beta$, $\approx 3.45 \pm 0.02$. We infer $E(B - V) = 0.2$ mag ($A_V = 0.6$ mag), as measured from the Balmer decrement in our Gemini spectrum, assuming $R_V = 3.1$, Case B recombination (Osterbrock & Ferland 2006), and the reddening law of Cardelli et al. (1989). This is similar to the value derived from the SDSS DR8 nuclear fiber spectroscopy line fluxes for the host galaxy ($E(B - V) = 0.2$ mag). The

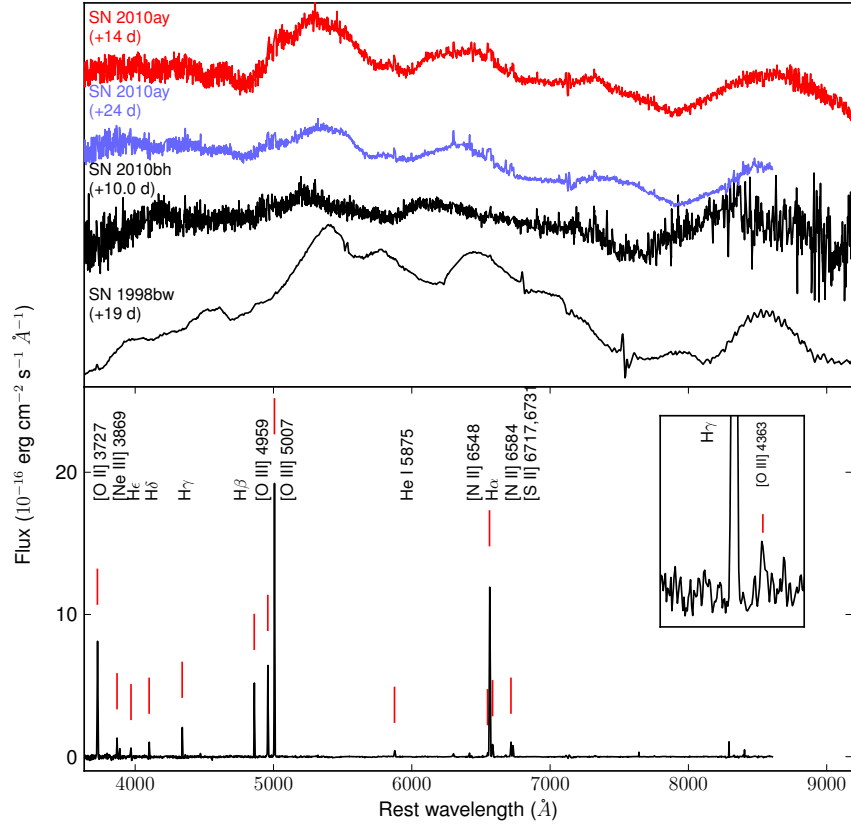


Figure 2.3.— Optical spectra of SN 2010ay from Gemini (24 days after R-band peak) and the WHT (14 days). The spectrum is plotted decomposed into SN (above, with narrow lines clipped) and host galaxy (below, from Gemini, with spline-fit subtracted) components for clarity. The spectrum of SN 2010bh from Chornock et al. (2010) is given in black for comparison, at 21.2 days after the GRB 100316D trigger (~ 10.0 days after R-band peak, Cano et al. 2011a). The spectrum of SN 1998bw at +19 days from Patat et al. (2001) is also plotted. Both are transformed to the redshift of SN 2010ay. The SNe are shifted in flux for clarity. In the lower plot, relevant host galaxy emission lines are marked with a red line and labeled.

value reported in Modjaz et al. (2010) was also similar: $E(B-V) = 0.3$ mag. Furthermore, we note that the color ($B - V = 0.78 \pm 0.07$ mag) as reported by Prieto (2010) at 4 d after R -band peak is significantly redder than SN Ib/c color curve templates Drout et al. (2011), further supporting a non-negligible host galaxy extinction.

2.2.4 Radio Observations

We observed SN 2010ay with the EVLA (Perley et al. 2009) on three epochs, 2010 March 26, 2010 April 29, and 2011 May 7. All EVLA observations were obtained with a bandwidth of 256 MHz centered at 4.9 GHz. We used calibrator J1221+2813 to monitor the phase and 3C286 for flux calibration. Data were reduced using the standard packages of the Astronomical Image Processing System (AIPS). We do not detect a radio counterpart to SN 2010ay in these observations and place upper limits of $F_\nu \lesssim 46, 42, 30 \mu\text{Jy}$ (3σ) for each epoch respectively corresponding to upper limits on the spectral luminosity spanning $L_\nu \lesssim (3.6 - 5.5) \times 10^{27} \text{ erg cm}^{-2} \text{ s}^{-1}$.

As shown in Figure 2.4, these limits are comparable to the peak luminosities observed for ordinary SNe Ib/c (Berger et al. 2003a; Soderberg 2007; Chevalier & Fransson 2006; Soderberg et al. 2010 and references within) and a factor of 10^2 to 10^3 less luminous than the radio afterglows associated with GRBs 020903, 030329, and 031203 at early epochs (Berger et al. 2003b; Soderberg et al. 2004a,b; Frail et al. 2005). In comparison with the radio luminosities observed for the relativistic SNe 1998bw (Kulkarni et al. 1998) and 2009bb (Soderberg et al. 2010),

Table 2.3. Emission line fluxes measured for the host galaxy of SN 2010ay

Emission Line	Flux ($10^{-16}\text{erg s}^{-1}\text{cm}^{-2}$)
[O II] λ 3726, 3729	52 ± 1
H δ	4.5 ± 0.2
H γ	9.9 ± 0.1
[O III] λ 4363	0.7 ± 0.1
H β	24.5 ± 0.1
[O III] λ 4959	30.4 ± 0.1
[O III] λ 5007	90.1 ± 0.2
[N II] λ 6548	2.2 ± 0.1
H α	84.5 ± 0.1
[N II] λ 6584	6.33 ± 0.06
[S II] λ 6717	7.46 ± 0.06
[S II] λ 6731	5.59 ± 0.06

Note. — All fluxes have been measured from our Gemini spectrum. No reddening correction has been applied. There is an additional systematic uncertainty in the flux measurements of $\sim 10\%$ due to flux calibration.

SN 2010ay is a factor of $\gtrsim 10$ less luminous. The peak radio luminosity observed for GRB 100316D was a factor of a few higher than the first EVLA non-detection of SN 2010ay (Margutti in preparation). The only relativistic explosion with detected radio emission below our EVLA limits is the weak and fast fading XRF 060218 (Soderberg et al. 2006a).

2.3 Initial Constraints

2.3.1 Light Curve Modeling

We construct an R-band lightcurve for SN 2010ay using the observations described in §2.2.3 (Table 2.2). We convert the i_{P1} and r' band data points to the R -band using the fiducial lightcurve method of Soderberg et al. (2006b), assuming the unextincted $i' - R$ and $r' - R$ colors observed for the Type Ic-BL SN 1998bw at the appropriate epoch (Galama et al. 1998). Photometry for the unfiltered CRTS images was reported by Drake et al. (2010) after transformation to the synthetic V-band (A.J. Drake, private communication); we therefore convert to the R -band assuming the $V - R$ color of SN 1998bw at the appropriate epoch. For the Pan-STARRS1 photometry, the host galaxy flux was subtracted using a template image. For all other photometry, we have subtracted the flux of the host galaxy numerically assuming the magnitude reported in Table 2.1. A total (Galactic + host) reddening of $E(B-V) = 0.2$ mag has been assumed (see §2.2.3).

To estimate the explosion date of SN 2010ay we have fit an expanding fireball model to the optical light curve (Figure 2.2), following Conley et al. (2006). In

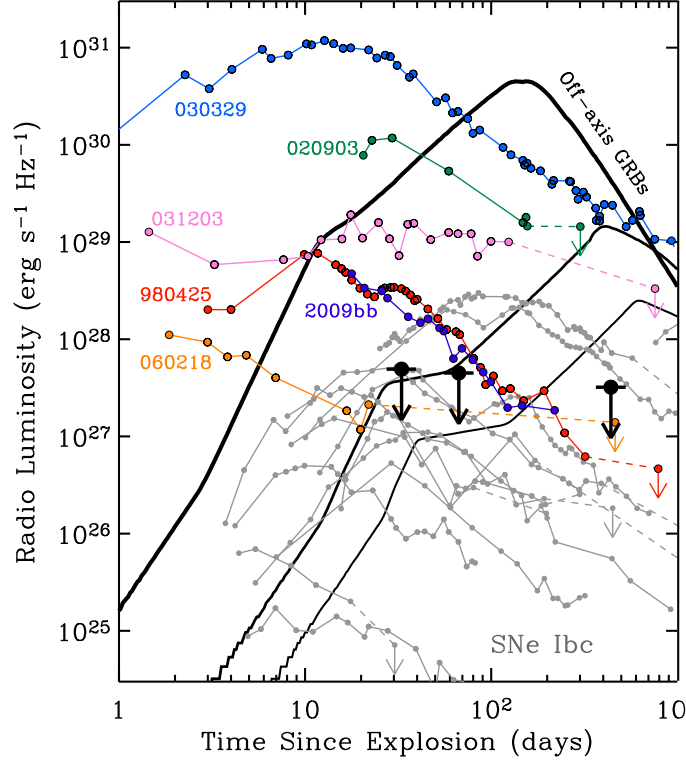


Figure 2.4.— EVLA upper limits for SN 2010ay (black arrows) are compared with off-axis GRB afterglow light curve models (black curves; standard parameters: $E_K \approx 10^{51}$ erg, $A_* = 1$, $\epsilon_e = \epsilon_B = 0.1$, $\theta_j = 5^\circ$, viewing angles of 30, 60, 90°) and the observed radio light-curves for ordinary SNe Ib/c (grey; Soderberg 2007 and references within) and the radio afterglows of all GRB-SNe within $z \leq 0.25$. SN 2010ay is a factor of 10^2 to 10^3 less luminous than XRF 020903 (orange; Soderberg et al. 2004a), GRB 030329 (blue; Berger et al. 2003b; Frail et al. 2005), and GRB 031203 (Soderberg et al. 2004b). Relativistic, engine-driven SNe 1998bw (red; Kulkarni et al. 1998) and 2009bb (dark blue; Soderberg et al. 2010) are a factor of 10 more luminous than the SN 2010ay limits on a comparable timescale, while XRF 060218 lies a factor of a few below the limits. We constrain the radio counterpart to be no more luminous than XRF 060218 and comparable to the peak luminosities of ordinary SNe Ib/c.

this model, the luminosity increases as

$$L \propto \left(\frac{t - t_0}{1 + z} \right)^n \quad (2.1)$$

We derive an explosion date t_0 of 2010 February 21.3±1.3. Here we have assumed an index $n = 2$. This suggests that the PS1 3π i_{P1} band pre-discovery detection image of SN 2010ay was taken ~ 4 days after the explosion. Observations by the PS1 survey have therefore provided a valuable datapoint for estimating the explosion date and also for constraining the rise-time of SN 2010ay, as well as other nearby SNe (e.g. SN 2011bm Valenti et al. 2012).

In Figure 2.2, we compare the light curve of SN 2010ay to the SN Ib/c light-curve template of Drout et al. (2011) after stretching by a factor of $(1 + z)$. The template provides a reasonable fit to the optical evolution of SN 2010ay. Fitting the template to our photometry we derive (reduced $\chi^2 = 0.3$) a date of R-band peak of 2010 March 18 ± 2 UT (MJD 55273 ± 2) and a R-band peak magnitude of $M_R \approx -19.7$ mag before extinction correction. As discussed in §2.2.3, based on the Balmer decrement observed for the host galaxy emission lines, we assume an extinction of $E(B - V) = 0.2$ mag. Applying this correction, the peak absolute magnitude is $M_R \approx -20.2 \pm 0.2$ mag. We note that this fitted value is ≈ 0.2 mag fainter than that estimated from the data point near peak. Here, the uncertainty is dominated by the template fitting.

Regardless of the extinction correction, SN 2010ay is more luminous than all the 25 SNe Ib/c in the sample of Drout et al. (2011), except for SN 2007D ($M_R \approx -20.65$ mag, which was also significantly extinguished: $A_V \sim 1.0$ mag).

Assuming an intrinsic V-R color of zero at peak (e.g. 1998bw: Galama et al. 1998; Patat et al. 2001), SN 2010ay is also more luminous than any of the 22 GRB and XRF-producing SNe in the compilation of Cano et al. (2011b), all corrected for extinction, and is 1.5 standard deviations from the mean luminosity. The peak magnitude is only ~ 1 mag below that of the Type Ic SN 2007bi ($M_R = -21.3 \pm 0.1$ mag), which Gal-Yam et al. (2009) report as a candidate pair-instability supernova.

2.3.2 Large Nickel Mass for SN 2010ay

We use the available photometry for SN 2010ay discussed above to derive the mass of ^{56}Ni required to power the optical light-curve under the assumption that the emission is powered by radioactive decay. Using the relation between M_{Ni} and M_R found by Drout et al. (2011), $\log(M_{\text{Ni}}) = (-0.41 M_R - 8.3) M_{\odot}$, we estimate that SN 2010ay synthesized a nickel mass of $M_{\text{Ni}} = 0.9_{-0.1}^{+0.1} M_{\odot}$. We have estimated the uncertainty in the M_{Ni} estimate by propagation of the uncertainty in the template fitted peak magnitude — systematic uncertainties are not included. If we instead adopt the most luminous individual data point in the light curve as the peak value, rather than the smaller peak value from template fitting, we find $M_{\text{Ni}} \approx 1.2 M_{\odot}$.

The M_{Ni} estimate for SN 2010ay is larger than that of all but one (SN 2007D) of the 25 SNe Ib/c in the Drout et al. (2011) compilation and significantly larger than the estimate for GRB-SN 2010bh, $M_{\text{Ni}} = 0.12 \pm 0.01 M_{\odot}$ (Cano et al. 2011a). On the other hand, M_{Ni} of SN 2010ay is at least $3\times$ smaller than for SN 2007bi

($M_{\text{Ni}} \approx 3.5 - 4.5 M_{\odot}$, Young et al. 2010). A pair instability supernova should produce $M_{\text{Ni}} \gtrsim 3 M_{\odot}$ (Gal-Yam et al. 2009).

2.3.3 Unusually high velocity

As illustrated in Figure 2.3, the broad, highly-blended spectral features of SN 2010ay at the time of the WHT observations (14 days after R-band peak, see §2.3.1) resemble those of SN 2010bh at a similar time (10.0 d after peak, Chornock et al. 2010). In particular, the blueshift of the feature near 6355 Å is larger than in SN 1998bw and more similar to SN 2010bh. This feature is commonly associated with Si II $\lambda 6355\text{\AA}$ (e.g. Patat et al. 2001). However, this feature has two clearly-detectable absorption minima in SN 2010ay, but not in SN 2010bh. This could be due to increased blending in SN 2010bh or the absence of contaminating lines. The red ends of the SN 2010ay and SN 2010bh spectra (rest wavelength $> 7500\text{\AA}$) have similar P-Cygni features, but the emission and absorption components in SN 2010bh are each blueshifted by $\sim 200\text{\AA}$ more than in the spectrum of SN 2010ay. Chornock et al. (2010) attribute this feature to the Ca II NIR triplet, with a gf -weighted line centroid of 8479 Å, and find a velocity that is high, but consistent with the early-time velocity of Si II $\lambda 6355\text{\AA}$ ($30 - 35 \times 10^3\text{ km s}^{-1}$).

We measure the absorption velocity from the minimum of the Si II $\lambda 6355\text{\AA}$ absorption feature (v_{Si}). We smooth the spectrum using an inverse-variance-weighted Gaussian filter (Blondin et al. 2006a, with $d\lambda/\lambda = 0.005$) and measure the minimum position of the redmost component of the absorption profile. The

blue component of the absorption profile shifts blueward over time, suggesting that it is produced by a combination of ions separated by several 10^3 km s^{-1} , such as He I $\lambda 5876\text{\AA}$ and Na I D, whose relative optical depth changes with time.

The absorption velocity inferred from the Si II $\lambda 6355\text{\AA}$ feature is $\sim 2\times$ faster than that of SN 1998bw at similar times, and more similar to that of SN 2010bh (Figure 3). For SN 1998bw, Patat et al. (2001) measured $\sim 10 \times 10^3 \text{ km s}^{-1}$ at +13 days. For SN 2010bh, Chornock et al. (2010) measured $v_{\text{Si}} \approx 26 \times 10^3 \text{ km s}^{-1}$ at +10.0 days after explosion. Prieto (2010) reported a velocity of $v_{\text{Si}} \approx 22.6 \times 10^3 \text{ km s}^{-1}$ from the Si II $\lambda 6355\text{\AA}$ feature in a spectrum of SN 2010ay taken at +4 days; Prieto (2010) do not discuss the details of their methodology for the velocity measurement. From our [WHT,Gemini] spectra taken [+14, +24] days after R-band peak (see §2.3.1), we estimate $v_{\text{Si}} \approx [19.2, 18.3] \times 10^3 \text{ km s}^{-1}$.

In addition to the broadening of the spectral features and the blueshift of the Si II $\lambda 6355\text{\AA}$ line, additional lines of evidence suggest a high photospheric expansion velocity for SN 2010ay. We measure $v_{\text{Si}} \approx [21.7, 20.1] \times 10^3 \text{ km s}^{-1}$ from the Ca II NIR triplet on the smoothed [WHT,Gemini] spectra, relative to a line center at 8479 \AA . This is within a few 10^3 km s^{-1} of the v_{Si} we measure from Si II $\lambda 6355\text{\AA}$ at these epochs. Furthermore, we do not detect the broad emission “bump” near 4500 \AA in either of our spectra. This feature was also absent in SN 2010bh, but was identified in SN 2003dh, SN2006aj, and several Ic-BLs not associated with GRBs and normal SNe Ic; Chornock et al. (2010) suggest that the absence of this feature indicates a high expansion velocity if it is due to blending of the iron lines to the blue and red of 4500 \AA .

We compare the late-time expansion velocity of SN 2010ay to other SNe Ic-BL and GRB-SNe with detailed, multi-epoch velocity measurements from the literature in Figure 2.5. We note that the velocities for SNe 1997ef, 2003dh, 2003lw plotted in the figure were estimated by Mazzali et al. (2006) via spectral modeling, rather than measured directly from the minimum of the Si II $\lambda 6355\text{\AA}$ absorption feature; however, these velocities should be equivalent to within a few 10^3 km s^{-1} , as the minimum of the Si II feature is typically well-fit by the photospheric velocity of the spectral models (see e.g. Mazzali et al. 2000; Kinugasa et al. 2002). In this figure, we also fit power-law gradients to the time-evolution of the velocity of these SNe with the form $v_{\text{Si}} = v_{\text{Si}}^{30}(t/30)^\alpha$, where t is the time since explosion in days and v_{Si}^{30} is the velocity at 30 days in units of 10^3 km s^{-1} . These parameters are listed in Table 2.4. Figure 2.5 illustrates that most SNe are well described by a single power law.⁴ However, due to lack of late-time spectroscopy, the v_{Si}^{30} measurement amounts to an extrapolation for some objects (particularly 2006aj), and contamination from different ions or detached features will add uncertainty to velocities measured from the Si II $\lambda 6355\text{\AA}$ feature.

SN 2010ay and 2010bh share high characteristic velocities at 30 days after explosion and velocity gradients that are low relative to other broad-lined Ic SNe with and without associated GRBs. For SN 2010ay, $v_{\text{Si}}^{30} = 21 \pm 2$ is $2 - 4\times$ larger than for other SNe Ic-BL without associated GRBs ($v_{\text{Si}}^{30} = 6 \pm 2$ for 1997ef, 5 ± 2 for 2002ap, 10 ± 1 for 2003jd, 9 ± 2 for 2007bg, and 10.3 ± 0.7 for 2007ru) and is similar to the GRB-SN 2010bh ($v_{\text{Si}}^{30} = 24 \pm 3$). No other GRB-SN or SN Ic-BL has

⁴A break at $\sim 2 \times 10^4 \text{ km s}^{-1}$ appears to exist for SN 1998bw at ~ 16 days, as noted by Kinugasa et al. (2002).

Table 2.4. Velocity Evolution of SNe Ic-BL

SN	v_{Si}^{30}	α
SNe Ic-BL		
1997ef	6 ± 2	-0.8 ± 0.4
2002ap	5 ± 2	-1.5 ± 0.7
2003jd	10 ± 1	-0.5 ± 0.2
2007bg	9 ± 2	-0.3 ± 0.2
2007ru	10.3 ± 0.7	-0.5 ± 0.1
2010ay	21 ± 2	-0.4 ± 0.3
Engine-driven SNe Ic-BL		
1998bw	10.3 ± 0.7	-0.86 ± 0.08
2003dh	12.0 ± 0.9	-0.9 ± 0.1
2003lw	10 ± 1	-0.8 ± 0.2
2006aj	15 ± 3	-0.3 ± 0.2
2009bb	10.7 ± 0.4	-0.84 ± 0.08
2010bh	24 ± 3	-0.22 ± 0.07

Note. — To the velocity measurements for each SN, we have fit a power law of the form $v_{\text{Si}} = v_{\text{Si}}^{30} (t/30)^\alpha$, where t is the time since explosion in days and v_{Si}^{30} is the velocity at 30 days in units of 10^3 km s^{-1} . These power law fits are illustrated in Figure 2.5. We adopt a conservative error of 10% on individual velocity measurements in order to compare the allowable range of fitted parameters for different SNe and note that this uncertainty is likely dominated by systematic effects. Uncertainties in the explosion date for SNe without detected GRBs vary due to availability of early-time photometry; we adopt the following conservative uncertainties: 7 d (1997ef, Hu et al. 1997), 7 d (2002ap, Gal-Yam et al. 2002b), 6 d (2003jd, Valenti et al. 2008), 14 d (2007bg), 3 d (2007ru, Sahu et al. 2009), 1 d (2009bb, Pignata et al. 2011), 2 d (2010ay; this paper).

$v_{\text{Si}}^{30} > 15$. The SNe Ic-BL and GRB-SNe with the most shallow velocity gradients among these twelve objects have $\alpha < -0.5$; they are SN 2006aj ($\alpha = -0.3 \pm 0.2$), SN 2007bg ($\alpha = -0.3 \pm 0.2$), SN 2010ay ($\alpha = -0.4 \pm 0.3$), and SN 2010bh ($\alpha = -0.22 \pm 0.07$). This places SN 2010ay in the company of two GRB-SNe in having a slowly-evolving absorption velocity, and SN 2007bg (whose unusually-fast decline rate distinguishes it from other SNe Ic-BL, Young et al. 2010). The velocities of SNe 2010ay and 2010bh, respectively, decline about 2 and 4 \times more slowly than the other SNe Ic-BL (mean and standard deviation: $\alpha = -0.8 \pm 0.4$) and about 1.5 and 3 \times more slowly the other GRB-SNe ($\alpha = -0.7 \pm 0.2$). The slow Si II $\lambda 6355\text{\AA}$ absorption velocity evolution of SN 2010ay at late times resembles the slow evolution of the Fe II lines of the spectroscopically-normal Type Ic SNe 2007gr and 2011bm at late times (Valenti et al. 2012).

Given the high peak luminosity of SN 2010ay (§2.3.1), we also consider the velocity of the candidate pair-instability SN 2007bi. Velocity measurements for SN 2007bi are only available at late times (> 50 d, Young et al. 2010). Fitting to these late-time Si II $\lambda 6355\text{\AA}$ velocity measurements, we find that SN 2007bi has a characteristic velocity $\sim 3\times$ smaller than 2010ay: $v_{\text{Si}}^{30} = 8 \pm 2$ and the late-time velocity gradient is $\sim 2\times$ more shallow: $\alpha = -0.2 \pm 0.2$.

2.3.4 Ejecta Mass and Energy

We use the scaling relations provided by Drout et al. (2011), based on the original formalism of Arnett (1982) and modified by Valenti et al. (2008), to derive the total mass of the ejecta and the kinetic energy.

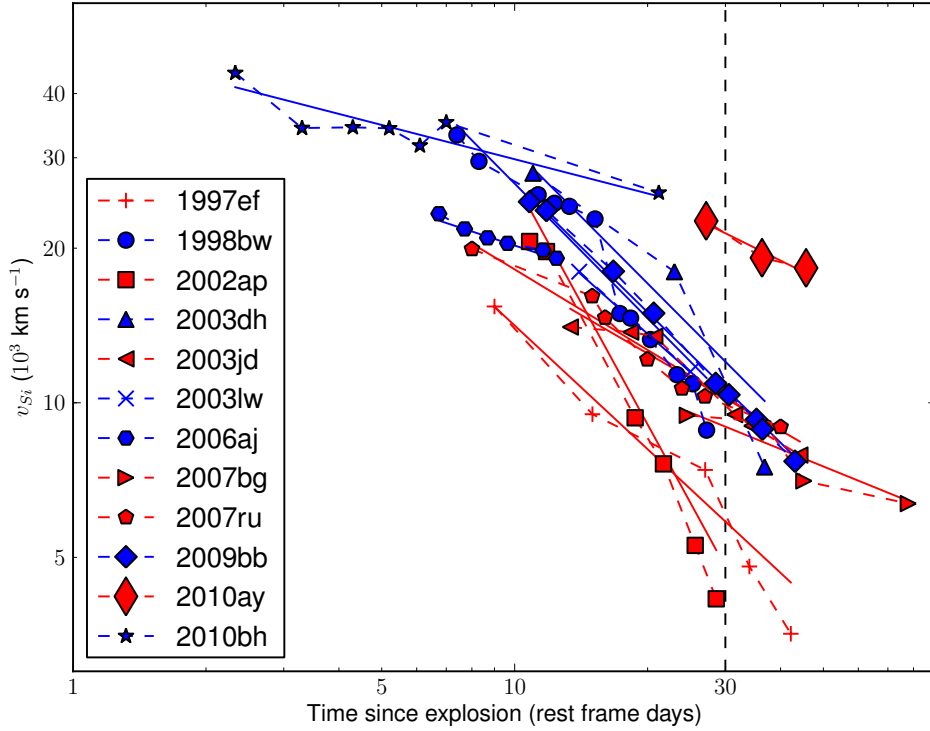


Figure 2.5.— A comparison of the time-evolving absorption velocity of SN 2010ay and other SNe Ic-BL (red) and engine-driven explosions (blue) from the literature. For each SN, we fit a power law of the form $v_{Si} = v_{Si}^{30}(t/30)^\alpha$, where t is the time in days, v_{Si}^{30} is the velocity at 30 days after explosion (dashed vertical line), and α is the velocity gradient. The velocities for SNe 1997ef, 2003dh, 2003lw are from Mazzali et al. (2006), as determined by spectral modeling. The velocities for all other SNe are measured from the Si II $\lambda 6355\text{\AA}$ feature as follows: SN 2007ru are from Sahu et al. (2009); SNe 1998bw, 2006aj, and 2010bh are from Chornock et al. (2010), from spectra in references therein; SN 2007bg are from Young et al. (2010); SNe 2002ap, 2009bb, and 2003jd are from Pignata et al. (2011) and references therein; SN 2010ay is from Prieto (2010) and this paper. See Table 2.4 for uncertainties.

$$M_{\text{ej}} = 0.8 \left(\frac{\tau_c}{8\text{d}} \right)^2 \left(\frac{v_{\text{Si}}}{10,000 \text{ km s}^{-1}} \right) M_{\odot} \quad (2.2)$$

$$E_K = 0.5 \left(\frac{\tau_c}{8\text{d}} \right)^2 \left(\frac{v_{\text{Si}}}{10,000 \text{ km s}^{-1}} \right)^3 \times 10^{51} \text{ erg} \quad (2.3)$$

We assume the fitted peak magnitude for SN 2010ay ($M_R = -20.2 \pm 0.2$, §2.3.1), the absorption velocity we measure from our WHT spectrum at 14 days after maximum light ($v_{\text{Si}} = 19.2 \times 10^3 \text{ km s}^{-1}$, §2.3.3), and a characteristic time (light-curve width) consistent with the data and the mean value from the Drout et al. (2011) sample of SNe Ic-BL ($\tau_c = 14 \text{ d}$).

Using these values, the total mass ejected was $M_{\text{ej}} \approx 4.7 M_{\odot}$, and the total kinetic energy of the explosion was $E_K \approx 10.8 \times 10^{51} \text{ ergs}$. Hereafter we refer to the definition $E_{K,51} = E_K/10^{51} \text{ ergs}$.

The systematic uncertainties associated with this modeling dominate the statistical uncertainties. In particular, the models rely on the assumptions of homologous expansion, spherical symmetry, all ^{56}Ni centralized at the center of the ejecta, optically thick ejecta and constant opacity.

We note that an earlier measurement of the absorption velocity is preferred for optical modeling. Since we have argued that SN 2010ay and SN 2010bh have similar characteristic velocities (v_{Si}^{30}), if we instead adopt a higher velocity of $25,000 \text{ km s}^{-1}$ as measured for SN 2010bh by Cano et al. (2011a), we estimate $M_{\text{ej}} \approx 6.1 M_{\odot}$ and $E_{K,51} \approx 23.9$ for SN 2010ay.

The M_{ej} and $E_{K,51}$ of SN 2010ay are consistent with the mean for SNe Ic-BL in the Drout et al. (2011) sample ($4.7^{+2.3}_{-1.8} M_{\odot}$ and 11^{+6}_{-4} , respectively), because the

authors assumed a velocity ($v_{\text{Si}} = 2 \times 10^4 \text{ km s}^{-1}$) similar to the late-time velocity we measure. For comparison, SN 2010bh had a total ejecta mass of $\sim 2 M_{\odot}$ and a total kinetic energy of $E_{K,51} \approx 13$ (Cano et al. 2011a).

The ratio of Ni to total ejecta mass is ~ 0.2 for SN 2010ay, significantly higher than the values typical of SNe Ic-BL and GRB-SNe. For comparison, the ratio is just ~ 0.05 for SN 2010bh. Adopting the values derived from bolometric light curve modeling by Cano et al. (2011a), the M_{Ni} and $M_{\text{Ni}}/M_{\text{ej}}$ ratios for other GRB-SNe are: $\sim 0.5 M_{\odot}$ and $\sim 0.06 - 0.22$ (1998bw), $\sim 0.4 M_{\odot}$ and ~ 0.08 (2003dh), $\sim 0.15 M_{\odot}$ and $\sim 0.07 - 0.1$ (2006aj), and $\sim 0.2 M_{\odot}$ and ~ 0.06 (2009bb). This ratio for SN 2010ay is larger than that of all but 4 of the 25 SNe of Drout et al. (2011): the Type Ic SNe 2004ge ($M_{\text{Ni}}/M_{\text{ej}} \sim 0.4$) and 2005eo ($M_{\text{Ni}}/M_{\text{ej}} \sim 0.2$), the Type Ib SN 2005hg (~ 0.4), and the Type Ic-BL SN 2007D (~ 0.6).

The large value of M_{Ni} we estimate for SN 2010ay raises the question of whether a process other than Ni decay may be powering its light-curve (e.g. Chatzopoulos et al. 2009). An independent test of the physical process powering the light-curve is the decay rate of the late-time light curve which should be $\approx 0.01 \text{ mag day}^{-1}$ for SNe powered by radioactive decay of ^{56}Co . For SN 2007bi, Gal-Yam et al. (2009) derive $M_{\text{Ni}} = 3.5 M_{\odot}$ from the measured peak magnitude and find that the late-time light curve is consistent with the decay rate of ^{56}Co . While the Pan-STARRS1 3π survey also observed the field in 2011 March, the SN was not detected in our subtracted images and the limits are not constraining in the context of ^{56}Co decay (see §2.2.2 and Table 2.2). Another possible process is a radiation-dominated shock that emerges due to interaction with an opaque

circumstellar medium, as has recently been proposed by Chevalier & Irwin (2011) for the ultra-luminous SNe 2006gy and 2010gx (Pastorello et al. 2010; Quimby et al. 2011). However, while this class of ultra-luminous objects shares some spectroscopic similarities to SNe Ic (Pastorello et al. 2010), they show peak luminosities $\sim 4 - 100\times$ higher than SN2010ay (Chomiuk et al. 2011; Quimby et al. 2011).

2.4 Constraints on Relativistic Ejecta

We use our EVLA upper limits for SN2010ay spanning $\Delta t \approx 29 - 433$ days to constrain the properties of the shockwave and those of the local circumstellar environment. The radio emission from SNe Ib/c and GRBs is produced by the dynamical interaction of the fastest ejecta with the surrounding material (Chevalier 1982). The kinetic energy of the ejecta is converted, in part, to internal energy of the shocked material which itself is partitioned between relativistic electrons (ϵ_e) and amplified magnetic fields (ϵ_B). Following the breakout of the shockwave from the stellar surface, electrons in the environment of the explosion are shock-accelerated to relativistic velocities with Lorentz factor, γ_e and distributed in a power-law distribution characterized by $N(\gamma_e) \propto \gamma_e^{-p}$. Here, p characterizes the electron energy index. The particles gyrate in amplified magnetic fields and give rise to non-thermal synchrotron emission that peaks in the radio and mm-bands in the days to weeks following explosion with observed spectral index, $F_\nu \propto \nu^{-(p-1)/2}$. At lower frequencies the emission is suppressed due to synchrotron self-absorption which defines a spectral peak, ν_p (Chevalier

1998).

The dynamics of the shockwave determine the evolution of the synchrotron spectrum, and in turn, the properties of the observed radio light-curves. In the case of SNe Ib/c, there are three primary scenarios for the dynamical regime of the ejecta depending on the shock velocity, $v = \beta c$ (associated Lorentz factor, Γ): (i) non-relativistic ($v \approx 0.2c$) free-expansion as in the case of ordinary SNe Ib/c (Chevalier 1998), (ii) a decoupled and relativistic ($\Gamma \sim 10$) shell of ejecta that evolves according to the Blandford-McKee solution for several months (Sari et al. 1998) before transitioning to the Sedov-Taylor regime (Frail et al. 2000). This is the standard scenario for typical GRBs. And (iii) a sub-energetic GRB with trans-relativistic velocity ($\beta\Gamma \lesssim 3$) that bridges the free-expansion and Blandford McKee dynamical regimes (e.g. SN 1998bw; Kulkarni et al. 1998, Li & Chevalier 1999).

We consider our EVLA upper limits in the context of these three models below. For shock velocities of $v \gtrsim 0.2c$, $\epsilon_e \approx 0.1$ is reasonable (Soderberg et al. 2005; Chevalier & Fransson 2006). We further assume equipartition, $\epsilon_e = \epsilon_B = 0.1$. We adopt a free expansion model for both the non-relativistic ordinary SN Ib/c case and the sub-energetic, trans-relativistic GRB scenario. As shown by Li & Chevalier (1999) a free-expansion model is still reasonable in the trans-relativistic regime (cases iii, see above).

2.4.1 Freely-expanding shockwave

In the free-expansion scenario, a shock discontinuity separates the forward and reverse shocks, located at the outer edge of the stellar envelope. The bulk ejecta is in free expansion while the thin layer of post shock material is slightly decelerated, $R \propto t^{0.9}$ (Chevalier & Fransson 2006). At a given frequency, the bell-shaped light-curves of the SN synchrotron emission may be described as (Chevalier 1998)

$$L_\nu \approx 1.582 \times L_{\nu,p} \left(\frac{\Delta t}{t_p} \right)^a \left[1 - e^{-(\Delta t/t_p)^{-(a+b)}} \right] \quad (2.4)$$

where $L_{\nu,p}$ is the flux density at the spectral peak at epoch, t_p . Assuming an electron index of $p \approx 3$, consistent with radio spectra of SNe Ib/c (Chevalier & Fransson 2006), the exponents are $a \approx 2.3$ and $b \approx 1.3$. The time averaged shockwave velocity is $\bar{v} \approx R/\Delta t$ where R is the shockwave radius defined as

$$R \approx 2.9 \times 10^{16} \left(\frac{\epsilon_e}{\epsilon_B} \right)^{-1/19} \left(\frac{L_{\nu,p}}{10^{28} \text{ erg s}^{-1} \text{ Hz}^{-1}} \right)^{9/19} \times \left(\frac{\nu_p}{5 \text{ GHz}} \right)^{-1} \text{ cm}. \quad (2.5)$$

Here we make the assumption that the radio emitting region is half of the total volume enclosed by a spherical blastwave. Next, we estimate the internal energy, E , of the radio emitting material from the post-shock magnetic energy density, $E \approx B^2 R^3 / 12 \epsilon_B$ where we maintain the assumption of equipartition. As shown by Chevalier (1998), the amplified magnetic field at peak luminosity is also directly determined from the observed radio properties,

$$\begin{aligned}
 B \approx & 0.43 \left(\frac{\epsilon_e}{\epsilon_B} \right)^{-4/19} \left(\frac{L_{\nu,p}}{10^{28} \text{ erg s}^{-1} \text{ Hz}^{-1}} \right)^{-2/19} \\
 & \times \left(\frac{\nu_p}{5 \text{ GHz}} \right) \text{ G.}
 \end{aligned} \tag{2.6}$$

Finally, the mass loss rate of the progenitor star, \dot{M} , may be derived from the number density of emitting electrons. Here we normalize the wind profile according to $\rho \propto Ar^{-2}$ and $A_* = A/5 \times 10^{11} \text{ g cm}^{-3}$. This normalization of A_* implies that an A_* of 1 corresponds to typical Wolf-Rayet progenitor wind properties of $\dot{M} = 10^{-5} M_\odot \text{ yr}^{-1}$ and a progenitor wind velocity of $v_w = 10^3 \text{ km s}^{-1}$.

$$\begin{aligned}
 A_* \approx & 0.15 \left(\frac{\epsilon_B}{0.1} \right)^{-1} \left(\frac{\epsilon_e}{\epsilon_B} \right)^{-8/19} \left(\frac{L_{\nu,p}}{10^{28} \text{ erg s}^{-1} \text{ Hz}^{-1}} \right)^{-4/19} \\
 & \times \left(\frac{\nu_p}{5 \text{ GHz}} \right)^2 \left(\frac{\Delta t}{10 \text{ days}} \right)^2 \text{ cm}^{-1}
 \end{aligned} \tag{2.7}$$

where we assume a shock compression factor of ~ 4 and an nucleon-to-electron ratio of two.

We built a two-dimensional grid of fiducial radio light-curves according to Eqn. 2.4 in which we vary the parameters $L_{\nu,p}$ and ν_p over a reasonable range of parameter space, bounded by $t_p \approx [1, 3000]$ days and $F_{\nu,p} \approx 0.04 - 1000 \text{ mJy}$. We identify the fiducial light-curves associated with a radio luminosity *higher* than the EVLA upper limits for SN 2010ay at each epoch as these are excluded by our observations. We extract the physical parameters associated with these excluded light-curves (R , B , E , A_*) to define the parameter space excluded by our radio

observations. The parameter space for ν_p and $F_{\nu,p}$ are bounded by the respective values for which the model exceeds relativistic velocities, $\beta\Gamma \sim \text{few}$.

As shown in Figure 2.6, our deep EVLA limits enable us to rule out a scenario in which there is copious energy, $E \gtrsim 10^{48}$ erg, coupled to a relativistic outflow, in this two-dimensional $E - v$ parameter space. The excluded region includes GRB-SNe 1998bw and 060218 as well as the relativistic SN 2009bb. It does not exclude the standard scenario in which a small percent of the energy is coupled to fast moving material within the homologous outflow, as is typically observed for ordinary SNe Ib/c ($E \approx 10^{47}$ and $v \approx 0.2c$; Soderberg et al. 2010).

Next we consider the effects of circumstellar density since lower mass loss rates produce fainter radio counterparts. As shown in Figure 2.7, the EVLA limits for SN 2010ay exclude the region of parameter space populated by SNe 1998bw and 2009bb with mass loss rates of $A_* \sim 0.1$, however, the low density environment of GRB 060218 lies outside of our excluded region due to its lower CSM density, $A_* \sim 0.01$ that gives rise to a lower luminosity radio counterpart.

2.4.2 Relativistic Ejecta

In the case of relativistic deceleration the ejecta are confined to a thin jet and are physically separated from the homologous SN component. Deceleration of the jet occurs on a timescale of $\Delta t \approx (E_{51}/A_*)$ years in a wind-stratified medium (Waxman 2004). On this same timescale, any ejecta components that were originally off-axis spread sideways into the observer's line-of-sight. While the early EVLA limits constrain the properties of the on-axis ejecta according to the

free-expansion model described above, the late time EVLA upper limits constrain any radio emission from a GRB jet originally pointed away from our line-of-sight.

For this scenario, we adopt the semi-analytic model of Soderberg et al. (2006c) for off-axis GRB jets. In Figure 2.4 we compare the radio upper limits for SN 2010ay with the predictions for an off axis jet with standard parameters ($E_K \approx 10^{51}$ erg, $A_* = 1$, $\epsilon_e = \epsilon_B = 0.1$, $\theta_j = 5^\circ$) and assuming a viewing angle of $\theta_{\text{oa}} = 30, 60$, or 90 degrees. Our EVLA upper limits rule out all three of these model light-curves. We derive the two-dimensional parameter space (energy and CSM density) that is excluded based on our EVLA upper limit at $\Delta t \approx 1.2$ years. We note that this model accommodates the full transition from relativistic to non-relativistic evolution. We built a collection of model light-curves spanning parameter range, $A_* \approx [0.01 - 100]$ and $E \approx [10^{49} - 10^{52}]$ erg, maintaining the assumption of $p = 3$ and $\epsilon_e = \epsilon_B = 0.1$. Here we adopted a jet opening angle of $\theta_j = 5^\circ$ and an off-axis viewing angle of $\theta_{\text{oa}} = 90^\circ$ (the most conservative scenario). We note that van Eerten & MacFadyen (2011) have developed off-axis GRB afterglow lightcurve models based on hydrodynamic simulations that reproduce the semi-analytic models presented here to within factors of a few (see also van Eerten et al. 2010).

As shown in Figure 2.8, we are able to exclude the parameter space associated with typical GRBs, i.e. $E \approx 10^{51}$ erg (beaming corrected) and $A_* \approx 1$. GRBs with lower energies and densities are better constrained using the trans-relativistic formalism above. In conclusion, our radio follow-up of SN 2010ay reveals no evidence for a relativistic outflow similar to those observed in conjunction with the nearest GRB-SNe, however a weak afterglow like that seen from XRF 060218

cannot be excluded.

2.5 Constraints on an associated GRB

Given the estimate of the explosion date we have derived (§2.3.1), we have searched for gamma-ray emission that may have been detected by satellites. No GRBs consistent with SN 2010ay were reported in the circulars of the Gamma-ray Coordinates Network Circulars, but it is possible that bursts were detected below the instrument triggering thresholds.

We next consulted the sub-threshold bursts from the Swift Burst Alert Telescope (BAT; Gehrels et al. 2004; Barthelmy et al. 2005) detected within the 6 days surrounding the explosion date estimate. We find that no gamma-ray emission was detected within 0.5 degrees of the position of SN 2010ay by the BAT during this period. Given the sensitivity of the BAT, this corresponds to an upper limit on the gamma-ray flux of $\sim 10^{-8}$ erg s $^{-1}$ cm $^{-2}$ (15-150 keV). However, the field of SN 2010ay was in the field of view of the instrument for only 106 ksec during these 6 days, or $\sim 20\%$ of the duration.

For complete temporal coverage, we have searched the records of the interplanetary network (IPN), which is sensitive to bursts with fluences down to $\sim 6 \times 10^{-7}$ erg cm $^{-2}$ (25-150 keV) (50% efficiency limit, Hurley et al. 2010), and observes the entire sky

with a temporal duty cycle close to 100%. An undetected,

sub-threshold burst should have a fluence below this limit. Between 2010

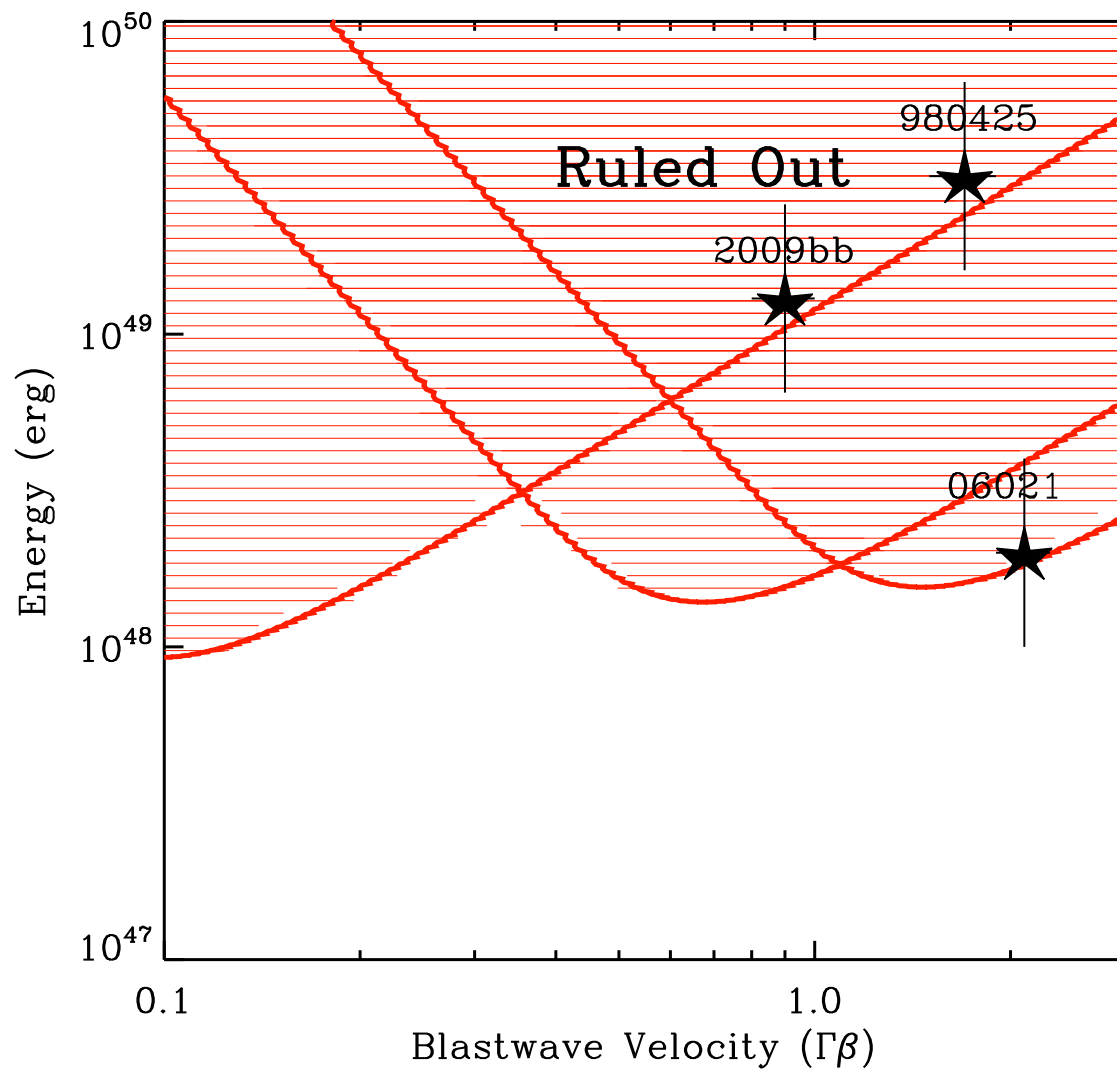


Figure 2.6.— The region of energy-velocity space ruled out (red) by our EVLA observations for on-axis ejecta under the assumption of a free-expansion model.

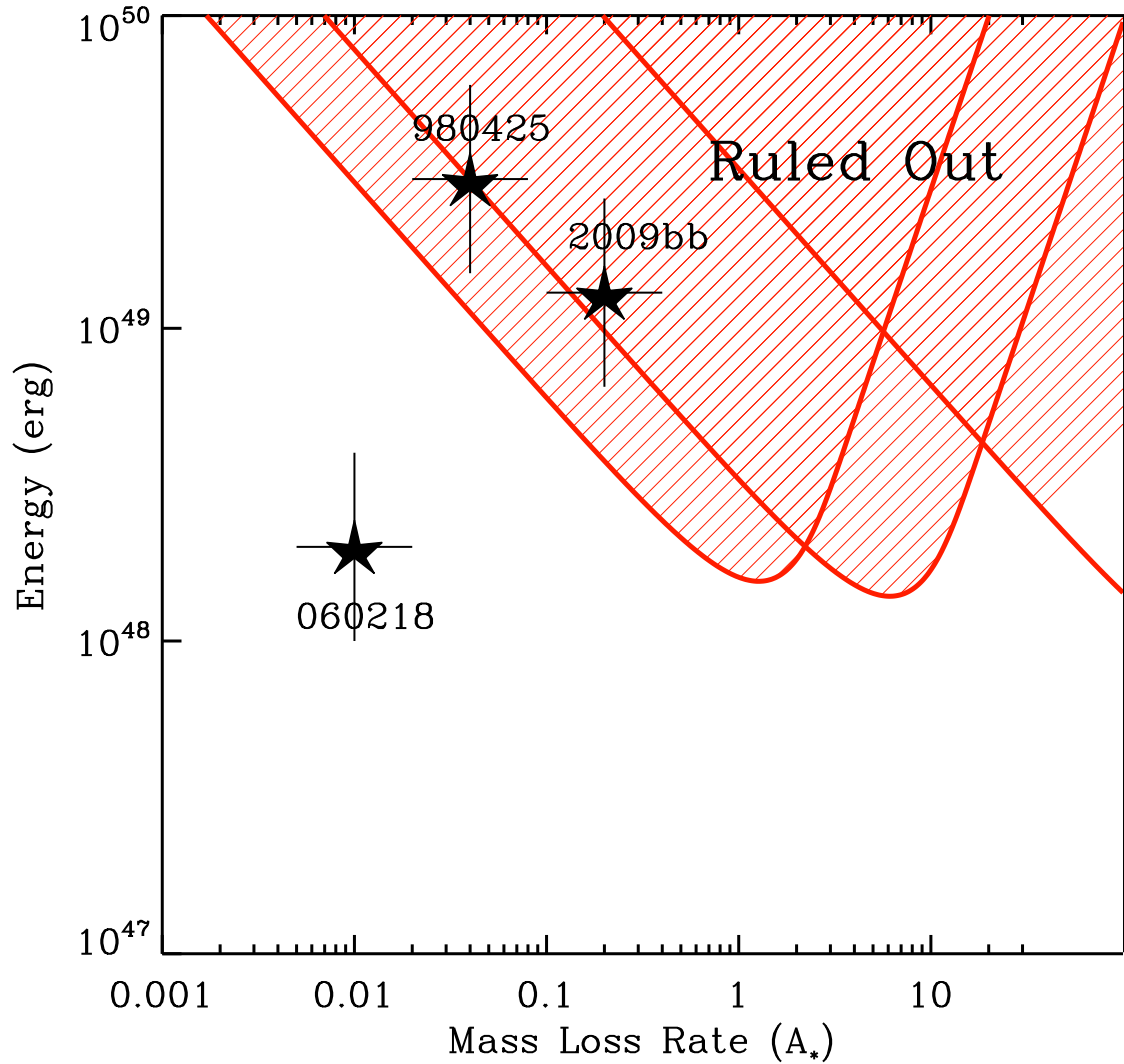


Figure 2.7.— The region of energy-mass loss space ruled out (red) by our EVLA observations for on-axis ejecta under the assumption of a free-expansion model.

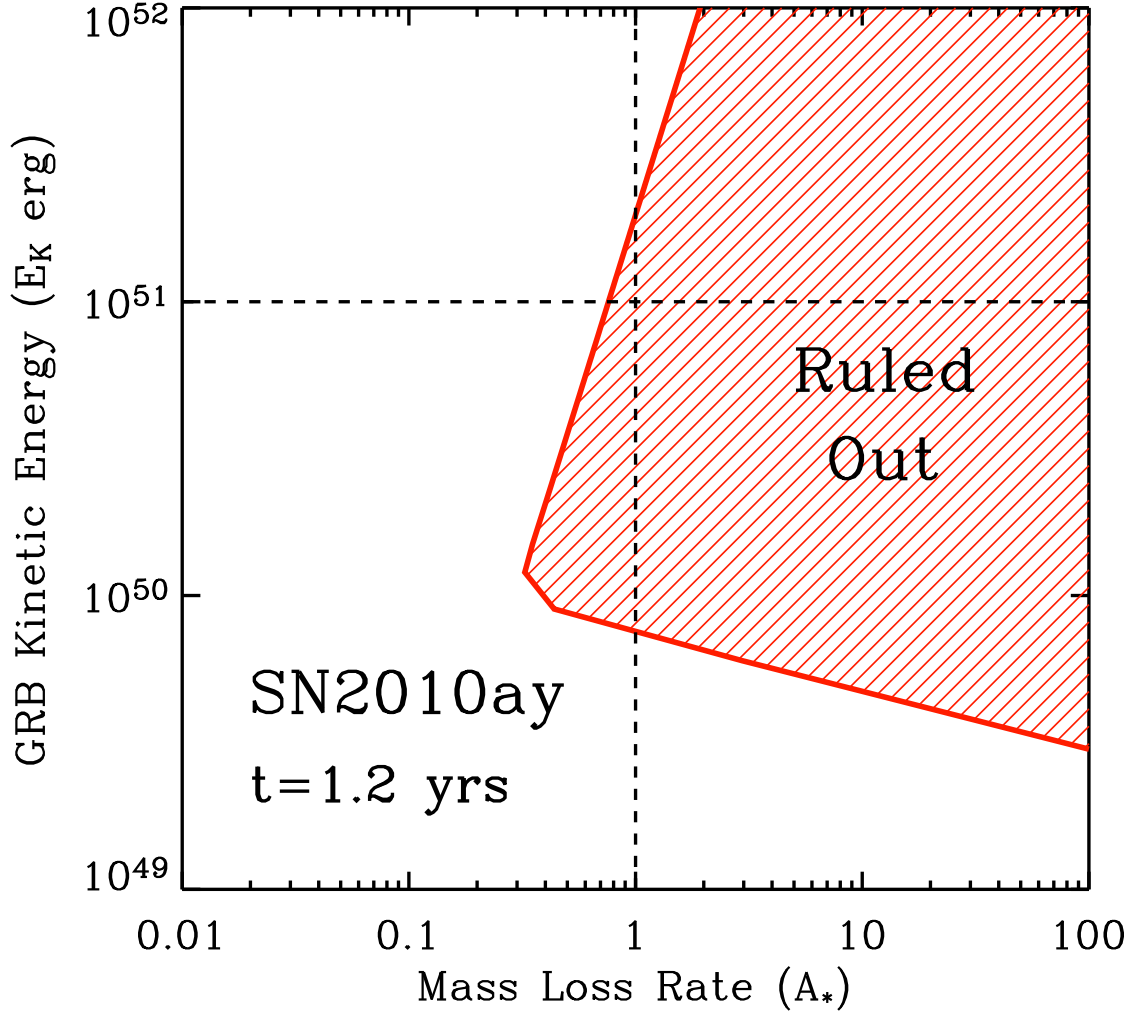


Figure 2.8.— Our EVLA observations at $\Delta t \approx 1.2$ years after explosion constrain the properties of a possibly associated off-axis GRB jet. Using our semi-analytic model as described in §2.4.2, we assume partition fractions of $\epsilon_e = \epsilon_B = 0.1$, $\theta_j = 5$ degrees, $p = 2.5$, and an off-axis viewing angle of $\theta_{oa} = 90$ degrees. We are able to exclude the region of $E_K - A_*$ parameter space (red) associated with typical GRBs, i.e. $E_K = 10^{51}$ erg and $A_* = 1$ (dashed black lines).

February 21 and 25, inclusive, a total of 12 bursts were detected by the spacecraft of the IPN (Mars Odyssey, Konus-Wind, RHESSI, INTEGRAL (SPI-ACS), Swift-BAT, Suzaku, AGILE, MESSENGER, and Fermi (GBM)). Ten of them are confirmed bursts; they were observed by more than one instrument on one or more spacecraft, and could be localized. Two of them are unconfirmed bursts; they were observed by one instrument on one spacecraft (Suzaku). The total area of the localizations of the 10 confirmed bursts is $\sim 0.58 \times 4\pi$ sr. This implies that about 0.58 bursts can be expected to have positions that are consistent with any given point on the sky simply by chance (i.e. within the 3σ error region), and indeed *none* of the bursts in this sample has a position consistent with the SN position.

These non-detections imply upper-limits to the gamma-ray energy (E_γ) of a burst that may have been associated with SN 2010ay. The IPN non-detection indicates $E_\gamma \lesssim 6 \times 10^{48}$ erg (25-150 keV), while the BAT non-detection indicates that the peak energy of the burst was $\lesssim 1 \times 10^{47}$ erg s⁻¹ (15-150 keV) if the burst occurred while in the field of view of the instrument.

We consider whether or not a hypothetical GRB associated with SN 2010ay would have been detected by BAT or the IPN if it had characteristics similar to well-studied SN-associated GRBs. The isotropic prompt energy release of long GRBs is typically $E_{\gamma,\text{iso}} \sim 10^{52}$ erg, however the prompt emission of the sub-energetic class of GRB-SNe can be several orders of magnitude fainter (Soderberg et al. 2006a). GRB 980425/SN 1998bw had a peak gamma-ray luminosity of $\sim 5 \times 10^{46}$ erg s⁻¹ (24-1820 keV Galama et al. 1998), which is a factor of 2 below our BAT limit, and $E_{\gamma,\text{iso}} \sim 5 \times 10^{47}$ erg (Pian et al. 2000), more

than a factor of five below our limit. Neither satellite should have detected such a burst. In contrast, GRB 031203/SN 2003lw had a peak gamma-ray luminosity of $\sim 1 \times 10^{49}$ erg s⁻¹ (20-200 keV) and a total isotropic equivalent energy of $E_{\gamma,\text{iso}} = (4 \pm 1) \times 10^{49}$ erg (Sazonov et al. 2004), about two orders of magnitude above the sensitivity of the BAT and twice the threshold of the IPN, respectively. GRB 030329/2003dh was even more luminous, with $E_{\gamma,\text{iso}} \sim 7 \times 10^{49}$ erg (Hjorth et al. 2003). A burst like GRB 031203 or 030329 should certainly have been detected by IPN, or the BAT if it occurred while the field of SN 2010ay was in the field of view of the instrument. XRF 060218/SN 2006aj, an extremely long-duration ($\Delta t \approx 2000$ s) event, had a peak luminosity observed by BAT of $\sim 10^{-8}$ erg cm⁻² s⁻¹ (15-150 keV), corresponding to a peak emission of $\approx 2.4 \times 10^{46}$ erg s⁻¹ given the redshift of the burst ($z = 0.033$), and a total isotropic equivalent energy of $E_{\gamma,\text{iso}} = (6.2 \pm 0.3) \times 10^{49}$ erg (Campana et al. 2006). If such a burst was associated with SN 2010ay, its peak emission may have been a factor of four below the BAT sensitivity limit, although its total isotropic energy emission is an order of magnitude larger than our IPN limit for SN 2010ay. Finally, the event whose host galaxy and supernova properties seem most similar to SN 2010ay, GRB 100316D/SN 2010bh had $E_{\gamma,\text{iso}} \geq (5.9 \pm 0.5) \times 10^{49}$ erg Starling et al. (2011) — a full order of magnitude above our IPN limit.

Another possibility is that prompt emission associated with SN 2010ay may have been too soft to be detected by the BAT or IPN. For example, the spectrum of XRF 060218 rose to a peak at 0.3 – 10 keV at ~ 985 s after triggering, then softened significantly thereafter. Even though the the total emission of this burst is well above our IPN limit, it may have escaped detection if it was similarly soft.

2.6 Sub-solar Host Environment Metallicity

We estimate the oxygen abundance of the host environment of SN 2010ay from the strong nebular emission line fluxes measured from our Gemini spectrum (Table 2.3). At the distance of the host galaxy, the 1" Gemini slit width corresponds to a physical size of 1.3 kpc. The properties we infer for the explosion site of SN 2010ay represent a luminosity-weighted average over this radius.

We employ several different oxygen abundance diagnostics in order to determine the metallicity of the host galaxy from its optical spectrum (e.g. Modjaz et al. 2011a). From the O3N2 diagnostic of Pettini & Pagel (2004) (PP04), we derive a metallicity of $\log(\text{O}/\text{H}) = 8.19$, or $Z \sim 0.3 Z_{\odot}$, adopting the solar metallicity $\log(\text{O}/\text{H})_{\odot} + 12 = 8.69$ from Asplund et al. (2005). Using the N2 diagnostic of PP04, we find $\log(\text{O}/\text{H}) + 12 = 8.26$. Using the abundance diagnostic, $R_{23} = \log([\text{O II}]\lambda 3727 + [\text{O III}]\lambda\lambda 4959, 5007)/\text{H}\beta$, we find $\log(\text{O}/\text{H})+12_{Z94} = 8.49$ (Smartt 2009) and $\log(\text{O}/\text{H})+12_{\text{KD02}} = 8.50$ (Kewley & Dopita 2002). However, these R_{23} -based estimates are more sensitive to flux-calibration and reddening-correction. Moreover, there is a well-known bi-valued relationship between R_{23} and oxygen abundance. The value $R_{23} = 0.873 \pm 0.006$ measured at the explosion site places it near the turnover point, but we assume that it lies on the upper branch based on its $[\text{N II}]/[\text{O II}]$ ratio, following Kewley & Ellison (2008). The metallicity values we derive using the PP04 and KD02 diagnostics are approximately equivalent given the offset that exists between these two diagnostics Kewley & Ellison (2008). These measurements are similar to the values reported by Modjaz et al. (2010) ($\log(\text{O}/\text{H})+12$ [PP04,KD02]= [8.2, 8.4])

for the SN 2010ay host galaxy. The statistical errors in our strong line metallicity estimates are small (< 0.01 dex), as determined by propagating the errors in the line flux measurement through the abundance calculation. However, for example the representative systematic error for the PP04 O3N2 abundance diagnostic is ~ 0.07 dex, as determined by Kewley & Ellison (2008) via comparison to other strong line abundance indicators.

Fortunately, our detection of the weak [O III] $\lambda 4363$ auroral line ($S/N \sim 6$; Figure 3) allows us to derive an oxygen abundance via the “direct,” T_e method. We employ a methodology similar to that used by, for example, Levesque et al. (2010a). We first derive the electron temperature ($T_e = 1.09 \pm 0.06 \times 10^4$ K) and density ($n_e = 80 \pm 20 \text{ cm}^{-3}$) from the [O III] and [S II] line ratios using the `temden` task of the IRAF package `nebular` (Shaw & Dufour 1994), derive the O^+ temperature using the calibration of Garnett (1992), and finally estimate the O^+ and O^{++} abundances following Shi et al. (2006). The direct abundance, $\log(O/H)+12 = 8.24 \pm 0.08$, is in good agreement with the PP04 O3N2 value. The stated uncertainty reflects the propagation of the uncertainties for the line flux measurements. Indeed, the offset between these two diagnostics should be very small at this metallicity Kewley & Ellison (2008).

We estimate the star formation rate (SFR) of the host galaxy using the $H\alpha$ relation of Kennicutt (1998). After correcting for host galaxy extinction, we measure the $H\alpha$ luminosity from our Gemini spectrum (Table 2.3) and estimate $SFR = 1.1 M_\odot \text{ yr}^{-1}$.

2.6.1 Blue Compact Galaxy Host

We compare the host galaxy of SN 2010ay to the nearby galaxy population of the SDSS spectroscopic survey. The physical properties of the host galaxy, SDSS J123527.19+270402.7, are estimated in the MPA/JHU catalog⁵. The total (photometric) galaxy stellar mass (M_*) is given as $3.6_{-1.3}^{+2.9} \times 10^8 M_\odot$, the aperture-corrected SFR is $1.0_{-0.2}^{+0.3} M_\odot \text{ yr}^{-1}$, and the nuclear (fiber) oxygen abundance (O/H_o) is $\log(\text{O}/\text{H})+12 = 8.58_{-0.03}^{+0.02}$ on the scale of Tremonti et al. (2004) (Tremonti04). The specific star formation rate (SSFR) of the host galaxy is then $\approx 2.8_{-0.4}^{+0.9} \text{ Gyr}^{-1}$. For consistency, we consider these values of M_* , the oxygen abundance, and the SFR for the host galaxy of SN 2010ay when comparing to other galaxies in the MPA/JHU catalog.

The oxygen abundance and SFR of the host galaxy of SN 2010ay listed in the MPA/JHU catalog are consistent with the values we derive in this paper (see also Kelly & Kirshner 2012). The MPA/JHU catalog lists metallicities on the Tremonti04 scale. Using the Kewley & Ellison (2008) conversion to the PP04 scale, the Tremonti04 metallicity estimate corresponds to a metallicity of $\log(\text{O}/\text{H})+12 = 8.38$, which is ~ 0.2 dex higher than the one we measure ($\log(\text{O}/\text{H})+12 = 8.19$). However, there is a large (~ 0.2 dex) rms scatter between the PP04 O3N2 and Tremonti04 diagnostics at the regime of $\log(\text{O}/\text{H})+12_{\text{PP04}} \sim 8.2$ (Kewley & Ellison 2008). The SFR in the MPA/JHU catalog is also in good agreement with the value we estimate from the $\text{H}\alpha$

⁵<http://www.mpa-garching.mpg.de/SDSS> (described in Kauffmann et al. 2003a; Tremonti et al. 2004; Brinchmann et al. 2004; Salim et al. 2007, and updated for SDSS DR7)

luminosity. Although our estimate does not include an aperture correction, the size of the Gemini slit (1") should encompass most of the star formation in the galaxy (Petrosian $r = 1.355''$; Table 2.1).

The mass to light ratio of the host galaxy of SN 2010ay is low compared to typical star-forming galaxies. To compare the host galaxy to the general galaxy population, we select a subset of the MPA/JHU catalog by requiring that estimates of M_* , SFR, and O/H_o be available and we remove AGN according to Kauffmann et al. (2003a). We consider 167,837 starbursting galaxies following these constraints. The host galaxy ranks in the [4th,38th,11th] percentile in $[M_*,\text{SFR},O/H_o]$ among these galaxies. Among the selected galaxies with a stellar mass as low as the host galaxy⁶, the median and standard deviation of the B-band⁷ absolute magnitude is -15.8 ± 1.3 mag. With $M_B = -18.35 \pm 0.05$ mag, the host of SN 2010ay is more luminous than other galaxies with a similar mass at the 2σ level. The discrepancy is due to the blue color of the SN 2010ay host galaxy, which indicates a stellar population that is very young and therefore has a low stellar mass to light ratio. Among the 1,184 galaxies in the MPA/JHU catalog that meet the constraints above and have a color similar to the host of SN 2010ay ($0.47 < u - r < 0.67$, from SDSS fiber magnitudes), the host galaxy has typical properties, with $[M_*,\text{SFR},O/H_o]$ in the [46th,49th,54th] percentile.

⁶This subset is selected such that the host galaxy of SN 2010ay has the median mass: $1.39 < M_* < 5.62 \times 10^8 M_\odot$, $N_{\text{sim}} = 6,978$.

⁷We obtain B-band magnitudes by converting the k -corrected gri magnitudes given in the MPA/JHU catalog to BVR magnitudes using the transformation of Blanton & Roweis (2007).

Based on these properties, we classify the host galaxy of SN 2010ay as a luminous Blue Compact Galaxy (BCG). BCGs span a large range in luminosity ($-21 < M_B < -12$, where luminous BCGs have $M_B < -17$), but are distinguished by their blue colors ($B - V < 0.45$), high SFR ($1 < \text{SFR} < 20 M_\odot \text{ yr}^{-1}$), and low metallicity ($Z_\odot/50 < Z < Z_\odot/2$; Kunth & Östlin 2000; Kong & Cheng 2002). The host galaxy of SN 2010ay has a luminosity ($M_B = -18.35 \pm 0.05$), color ($B - V = 0.11 \pm 0.07$), SFR ($1.0_{-0.2}^{+0.3} M_\odot \text{ yr}^{-1}$), and metallicity ($Z \sim 0.3 Z_\odot$) consistent with all these ranges.⁸

2.6.2 Comparison to SNe Ic-BL and GRB-SNe Host Galaxies

Our measurement of the metallicity from the Gemini spectrum indicates that the explosion site of SN 2010ay is ~ 0.5 (0.2) dex lower in metallicity than the median SNe Ic (Ic-BL) in the sample of Modjaz et al. (2011a). In that sample, the median PP04 O3N2 metallicity measured at the explosion site of SNe Ic is $\log(\text{O}/\text{H})+12 \approx 8.7$ and for Ic-BL is ≈ 8.4 dex, for 12 and 13 objects, respectively. If instead the KD02 metallicity is used, the median of the sample is ≈ 8.9 dex for SNe Ic (13 objects) and ≈ 8.7 dex for Ic-BL (15 objects), so the abundance of the SN 2010ay host galaxy is similarly low compared to the median.

The metallicity of the environment of SN 2010ay is more similar to

⁸We note that a large fraction of luminous BCGs show evidence for disturbed morphologies or interaction with close companions (Garland et al. 2004; López-Sánchez et al. 2006), but we do not see evidence for a companion at the depth of SDSS images of the host galaxy of SN 2010ay.

previously-studied nearby GRB-SN progenitors. A metallicity identical to our measurement was measured at the explosion site of SN 2010bh (Levesque et al. 2011): $\log(\text{O}/\text{H})+12 = 8.2$. In the survey of Levesque et al. (2010a), and adding the measurement for SN 2010bh, the GRB-SNe host galaxies have an average and standard deviation PP04 O3N2 metallicity of $\log(\text{O}/\text{H})+12 = 8.1 \pm 0.1$ on the PP04 scale, which is consistent with the SN 2010ay environment. Among the 17 LGRB host galaxies surveyed in Savaglio et al. (2009) the average metallicity is somewhat lower, $1/6 Z_{\odot}$ or $\log(\text{O}/\text{H})+12 \sim 7.9$, but these are at an average redshift of $z \sim 0.5$ that is much higher than SN 2010ay.

This evidence suggests that the host galaxy of SN 2010ay has chemical properties more consistent with LGRBs/GRB-SNe than SNe Ic-BL without associated GRBs; however, selection effects may mitigate this discrepancy. SNe found in targeted surveys of luminous galaxies have host galaxy properties biased towards higher metallicities, due to the luminosity-metallicity ($L - Z$) relation (Tremonti et al. 2004). LGRBs are found in an untargeted manner through their gamma-ray emission and therefore are not biased by this relation.

SN 2010ay joins a growing list of SNe Ic-BL that have been discovered in low metallicity host galaxies. Given the systematic uncertainty in strong line oxygen abundance diagnostics (~ 0.07 dex), we will consider host galaxies with metallicity $\log(\text{O}/\text{H})_{\text{PP04}} + 12 < 8.3$ ($Z \lesssim 0.4Z_{\odot}$) to be in the low-metallicity regime of SN 2010ay. Among the 15 SNe Ic-BL (9 discovered by untargeted searches) in the surveys of Modjaz et al. (2008) and Modjaz et al. (2011a), 4 were found in low metallicity environments: SN [2007eb,2007qw,2005kr,2006nx] at $\log(\text{O}/\text{H})_{\text{PP04}} + 12 = [8.26, 8.19, 8.24, 8.24]$. All of these SNe were discovered

by untargeted searches. Young et al. (2010) measure the metallicity of the host galaxy of the broad-lined Ic SN 2007bg to be $\log(\text{O}/\text{H})_{\text{PP04}} + 12 = 8.18$, although this SN has lightcurve and spectral properties that distinguish it from normal SNe Ic-BL (§2.3.3). Furthermore, Arcavi et al. (2010) find that SNe Ic-BL are more common in dwarf ($M_r \geq -18$) host galaxies, which the authors attribute to a preference for lower metallicities.

The star formation properties of the host galaxy of SN 2010ay also resemble the host galaxies of LGRBs. If we consider those galaxies in the MPA/JHU catalog with masses similar to the host galaxy of SN 2010ay (as defined above), then the median SFR and O/H_o of these galaxies is $0.13 M_\odot \text{ yr}^{-1}$ and $\log(\text{O}/\text{H}_o) + 12 = 8.36$, respectively. The host galaxy of SN 2010ay is in the [96th,77th] percentile for [SFR, O/H_o] among these galaxies. This indicates that, while the host galaxy of SN 2010ay falls within 1σ of the mass-metallicity ($M - Z$) relation for star-forming galaxies, its SFR is extreme for its mass. The 39 LGRB host galaxies in the survey of Savaglio et al. (2009) are similarly low in mass and have high star formation rates, with an average stellar mass of $M_* \sim 10^9 M_\odot$ and $\text{SSFR} \sim 3.5 \text{ Gyr}^{-1}$.

The host galaxy of SN 2010ay falls below the $L - Z$ relation for nearby star-forming galaxies, as illustrated by Figure 2.9. We have transformed the k -corrected *gri* magnitudes from the MPA/JHU catalog to B-band (Blanton & Roweis 2007). At the luminosity of the host galaxy of SN 2010ay, the median metallicity and standard deviation of the SDSS galaxies on the Tremonti04 scale is $\log(\text{O}/\text{H}) + 12 = 8.93 \pm 0.17$; the host galaxy of SN 2010ay falls in the 3rd percentile. In other words, the host galaxy of SN 2010ay is a 2σ outlier from the

$L - Z$ relation. Similarly, Levesque et al. (2010a) and Han et al. (2010) suggest that the host galaxies of LGRBs fall below the $L - Z$ relation as defined by normal star-forming galaxies, BCGs, and the host galaxies of Type Ic SNe.

Mannucci et al. (2011) have explained the offset of LGRB host galaxies from the $M - Z$ relation as a preference for LGRBs to occur in host galaxies with high SFR, as characterized by the Fundamental Metallicity Relation (FMR) of Mannucci et al. (2010) (see also Lara-López et al. 2010). Using the extended FMR for low mass galaxies from (Mannucci et al. 2011), the host galaxy of SN 2010ay should have a metallicity of $\log(\text{O}/\text{H})+12 = 8.20$ given its stellar mass and SFR. The FMR is calibrated to the Nagao et al. (2006) metallicity scale, which is similar to that of PP04 at this metallicity. Given the intrinsic scatter in the extended FMR on the order of ~ 0.05 dex, this value is consistent with the PP04 value we measure from our Gemini spectrum: $\log(\text{O}/\text{H})+12 = 8.19$. Kocevski & West (2011) similarly explain the offset of LGRB host-galaxies from the $M - Z$ relation as a SFR effect, but suggest that the long GRB host galaxies have even higher SFR than would be implied by the FMR.

SN 2010ay is an example of a SN Ic-BL where the host galaxy is consistent with the $M - Z$ relation for star-forming galaxies, but deviates from the $L - Z$ relation due to its low stellar mass to light ratio (§2.6.1). Its 2σ discrepancy from the $L - Z$ relation would be hard to explain as a SFR rate effect alone because among galaxies in the MPA/JHU catalog without AGN (as defined above) and with M_B within 0.1 mag of the host galaxy of SN 2010ay, the host galaxy has a SFR in the 26th percentile ($< 1\sigma$ discrepancy).

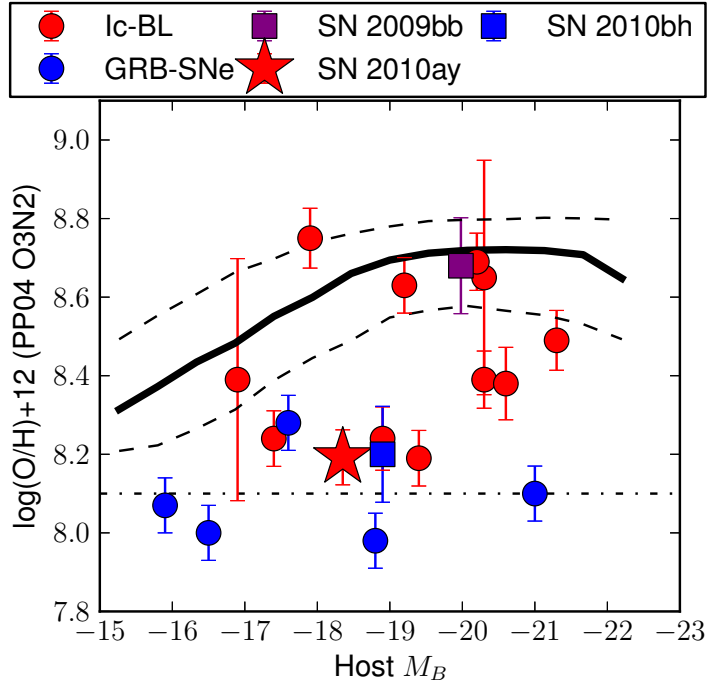


Figure 2.9.— Host galaxy metallicity versus brightness for SNe Ic-BL (red) and engine-driven explosions (blue). The solid line is the L-Z relation of nearby star-forming galaxies, with the 15th and 85th percentile boundaries of the galaxy distribution (dashed lines). Here we have transformed the k -corrected gri magnitudes from the MPA/JHU catalog to B-band (Blanton & Roweis 2007) and converted the Tremonti04 metallicity values to the PP04 scale (Kewley & Ellison 2008), for the purpose of comparing it to metallicity measurements for SN host galaxies in the literature. The dot-dashed horizontal line is the divider between GRB-SNe and SNe Ic-BL host environments suggested by Modjaz et al. (2008). The host galaxy properties of GRB/SNe other than 2010ay are from the following references: Starling et al. 2011; Cano et al. 2011a (2010bh), Modjaz et al. 2011a (Ic-BL), Levesque et al. 2010d (2009bb), and Levesque et al. 2010a (other GRB-SNe). Error bars illustrate measurement uncertainty, when published, plus a 0.07 dex systematic uncertainty.

2.7 Discussion

SN 2010ay has all the hallmark features associated with GRB-SNe, and yet we find no evidence of a relativistic explosion to sensitive limits. We are able to place constraints on the energy, density, velocity, progenitor mass-loss rate, and gamma-ray flux of any GRB that may have been associated with it. In particular, we may rule out the association of a GRB that looks similar to any spectroscopically confirmed GRB-SN to date, except for XRF 060218.

The low metallicity of the host environment of SN 2010ay may be suitable for GRB jet formation in the “collapsar” model, but our observations strongly constrain any relativistic outflow (§2.4 & 2.5). In MacFadyen & Woosley (1999), a high rate of rotation in the core of the progenitor is required to power a relativistic jet. A low metallicity is prescribed to suppress the line driven winds that would deprive the core of angular momentum. Apparently supporting this model, Stanek et al. (2006) found that the isotropic prompt energy release of the GRB-SNe decreases steeply with metallicity, and other surveys have found observational evidence for the preferential occurrence of GRB-SNe in low-metallicity host galaxies (Fynbo et al. 2003; Prochaska et al. 2004; Sollerman et al. 2005; Modjaz et al. 2006; Wiersema et al. 2007; Christensen et al. 2008; Modjaz et al. 2008; Levesque et al. 2010a; Chornock et al. 2010; Starling et al. 2011). Challenging this view is the recent discovery of SN 2009bb, a broad-lined, engine-driven Type-Ic supernova found in a high-metallicity host environment (Soderberg et al. 2010; Levesque et al. 2010d; Pignata et al. 2011). In SN 2010ay, we have found the opposite case – a broad-lined Type Ic supernova found in a low-metallicity host

Table 2.5. Comparison between SN 2010ay and GRB 100316D/SN 2010bh

Property	SN 2010bh	SN 2010ay
Host galaxy properties		
$\log(\text{O}/\text{H})+12$ ^a	8.2	8.19
Redshift (z)	0.059	0.06717
M_R	-18.5	-18.94
Explosion properties		
SN type	Ic-BL	Ic-BL
v_{Si}^{30} (10^3 km s^{-1}) ^b	24 ± 3	21 ± 2
M_R	-18.60 ± 0.08	-20.2 ± 0.2
M_{Ni} (M_{\odot})	0.10 ± 0.01	$0.9_{-0.1}^{+0.1}$
M_{ej} (M_{\odot})	1.93-2.24	$\gtrsim 4.7$
$E_{K,51}$	12.0-13.9	$\gtrsim 10.8$
GRB energy (E_{iso} , erg)	$\gtrsim 5.9 \times 10^{49}$ ^c	$\lesssim 6 \times 10^{48}$

Note. — The observed properties of SN 2010bh and its host galaxy are given by Chornock et al. (2010) and light curve modelling was performed by Cano et al. (2011a). The properties of SN 2010ay are derived in this paper.

^aThe oxygen abundance derived from the PP04 O3N2 metallicity diagnostic, as discussed in §2.6.

^bThe absorption velocity at 30 days after explosion, as measured from the Si II $\lambda 6355\text{\AA}$ feature in §2.3.

^cThe lower limit of the total isotropic energy release estimated by Starling et al. (2011).

environment, but without any indication (via either radio or gamma-ray emission) of a central engine. The existence of SNe 2009bb and 2010ay emphasizes that progenitor metallicity is not the key factor that distinguishes GRB-SNe from broad-lined SNe Ic without associated relativistic ejecta.

We compare the absorption velocity of SNe Ic-BL and engine-driven SNe (GRB-SNe and SN 2009bb) to the metallicity of their host environments in Figure 2.10. This comparison emphasizes the diversity of explosion and host galaxy properties observed in both engine-driven SNe and SNe Ic-BL. The engine-driven SNe with the largest velocity gradients (2003dh, $\alpha = -0.9 \pm 0.1$; 2009bb, $\alpha = -0.86 \pm 0.08$) occur at metallicities different by a factor of 5 (2003dh, $\log(\text{O}/\text{H})+12 = 8.0$; 2009bb, $\log(\text{O}/\text{H})+12 = 8.7$ on the PP04 scale). Furthermore, the velocity gradient of engine-driven SNe seems to be uncorrelated with the velocity at late times; 2010bh ($\alpha = -0.22 \pm 0.07$) and 2006aj ($\alpha = -0.3 \pm 0.2$) have similar velocity gradients, but 2010bh had velocities $\sim 10,000 \text{ km s}^{-1}$ larger at 30 days after explosion. Among SNe Ic-BL from low metallicity environments ($\log(\text{O}/\text{H})+12 < 8.5$), there is a large range in both the characteristic velocity and velocity gradient ($v_{\text{Si}}^{30} = [10 \pm 1, 9 \pm 2, \text{vthirtyay}]$ and $\alpha = [-0.5 \pm 0.2, -0.3 \pm 0.2, -0.4 \pm 0.3]$ for SNe [2003jd,2007bg,2010ay]). For the three SNe Ic-BL at higher metallicities, the characteristic velocities tend to be lower and the velocity gradients tend to be stronger ($v_{\text{Si}}^{30} = [6 \pm 2, 5 \pm 2, 10.3 \pm 0.7]$ and $\alpha = [-0.8 \pm 0.4, -1.5 \pm 0.7, -0.5 \pm 0.1]$ for SNe [1997ef,2002ap,2007ru]). However, a larger sample is needed to exclude the possibility of SNe Ic-BL from super-solar metallicity environments that have high characteristic velocities or shallow velocity gradients.

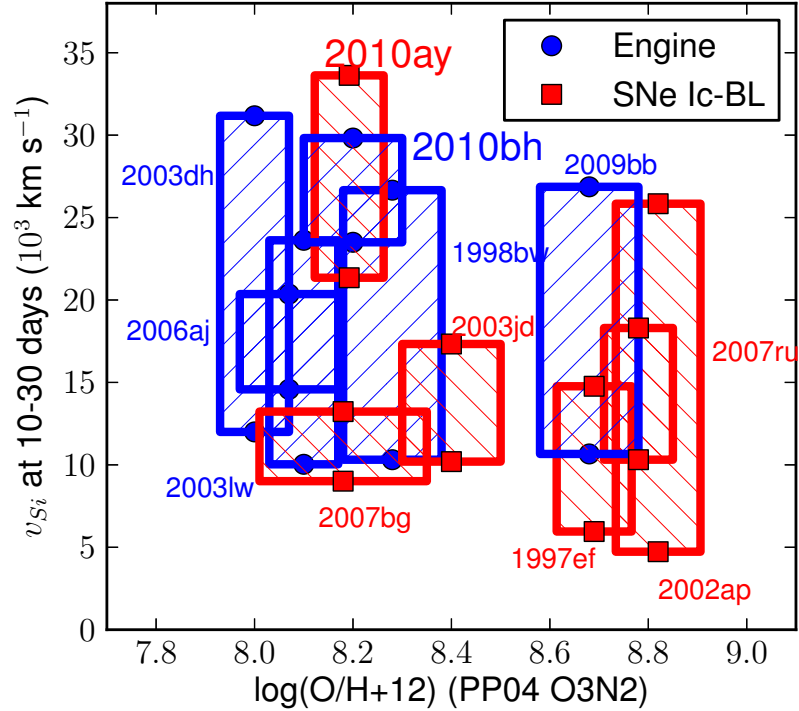


Figure 2.10.— SN absorption velocity, as traced by the Si II $\lambda 6355\text{\AA}$ feature, versus host galaxy oxygen abundance for SN 2010ay and other Ic-BL (red) and engine-driven explosions (blue) from the literature (as in Figure 2.5). The range of velocities hatched for each object comes from the velocity at 10 days and at 30 days after explosion, according to the power law fits presented in Figure 2.5. The oxygen abundance measurements using the PP04 O3N2 diagnostic are from Levesque et al. (2010a) (GRB-SNe), Sahu et al. (2009) (SN2007ru), Young et al. (2010) (SN 2007bg), and Modjaz et al. (2011a) (other SNe Ic-BL). The range of oxygen abundance hatched reflects the error bars quoted in the literature (when stated) plus the ~ 0.07 dex systematic error of the PP04 O3N2 diagnostic (Kewley & Ellison 2008).

The fact that a GRB was not detected in association with SN 2010ay, despite its similarities to the GRB-SNe, could indicate that the relativistic jet produced by this explosion was “suffocated” before it emerged from the progenitor star (MacFadyen et al. 2001). In this scenario, the duration of the accretion event onto the newly-formed central engine is short-lived and the jet post-breakout outflow is not ultra-relativistic. In the process of being suffocated, the jet transfers momentum to the ejecta such that the spectrum is broad lined and the ejecta velocity is very high, even at late times, as we observe (§2.3). However, the low host environment metallicity we measure for SN 2010ay, which is similar to GRB-SNe, does not suggest high angular momentum loss that would help to weaken the jet. Another alternative is that binary interaction plays a key role in the commonality of relativistic outflows among SNe Ic-BL.

Looking forward, additional SNe Ic-BL in sub-solar metallicity host environments will be found through current and future generations of untargeted transient searches. Untargeted searches are required to find supernovae from low-metallicity host environments, because targeted searches only probe the highest metallicity galaxies due to the luminosity-metallicity relationship (Modjaz et al. 2011a; Leloudas et al. 2011).

2.8 CONCLUSIONS

The optical photometric and spectroscopic, radio, and gamma-ray observations of SN 2010ay presented here provide an example of a Type Ic-BL SN with explosion and host properties similar to the known GRB-SN SN 2010bh. This

object demonstrates that SNe in low-metallicity environments with high-velocity ejecta are not necessarily accompanied by the traditional signature of radio emission associated with long-lived relativistic jets. The existence of SN 2010ay and SN 2009bb (a central-engine driven event from a high-metallicity host environment) indicates that progenitor metallicity may not be the key factor that distinguishes GRB-SNe from normal broad-lined Type Ic supernovae.

We conclude that:

1. Pre-discovery imaging of the SN 2010ay from the Pan-STARRS1 3π survey allows us to tightly constrain the early-time light-curve of SN 2010ay (see Figure 2.2) and explosion date (2010 February 21.3 ± 1.3), allowing us to search for gamma-ray emission that may have been associated with the explosion. By fitting the template SN Ib/c light-curve of Drout et al. (2011), we derive an R-band peak absolute magnitude of -20.2 ± 0.2 mag – making SN 2010ay among the most luminous SNe Ib/c ever observed. This peak magnitude suggests that a large mass of nickel, $M_{\text{Ni}} \sim 0.9^{+0.1}_{-0.1} M_{\odot}$, has been synthesized. We estimate a ratio of M_{Ni} to M_{ej} that is $\sim 2 \times$ larger than in known GRB-SNe.
2. Spectroscopy (see Figure 2.3) at the explosion site in the host galaxy of SN 2010ay indicates that the host environment of the progenitor star had a significantly sub-solar metallicity ($Z \sim 0.3 Z_{\odot}$), similar to the host environments of known GRB-SNe progenitors.
3. The Type Ic-BL SN 2010ay strongly resembles the GRB-SN 2010bh, particularly in light of its unusually high absorption velocities at late times

($v_{\text{Si}} \approx 19.2 \times 10^3 \text{ km s}^{-1}$ at 14 days after peak) and low metallicity host environment. The comparison between these two SNe is summarized in Table 2.5.

4. Non-detections in late-time EVLA radio observations of the SN rule out the association of a GRB of the nature of the spectroscopically-confirmed GRB-SNe, except for the radio afterglow associated with XRF 060218. Our radio observations imply limits on the velocity, energy, and density of any associated relativistic jet and the mass loss rate of the progenitor (see Figures 2.4, 2.6, 2.7, and 2.8). Additionally, no coincident gamma-ray emission was detected by satellites: the non-detection by the interplanetary network indicates $E_\gamma \lesssim 6 \times 10^{48} \text{ erg}$, while the non-detection by the Swift BAT indicates that the peak energy of the burst was $\lesssim 1 \times 10^{47} \text{ erg s}^{-1}$ if the burst occurred during the $\sim 20\%$ of the explosion window when it was in the field of view of the instrument. This rules out associated prompt emission similar to that of GRBs 031203, 030329, or 100316D, but not GRBs 980425 or 060218.

The pre-discovery imaging of SN 2010ay demonstrates the capability of the untargeted PS1 survey for identifying and monitoring exotic transients, not only in its high-cadence Medium-Deep Fields, but also in the all-sky 3π survey. Additional detections and multi-wavelength follow-up observations of SNe Ic-BL will help to illuminate the role that ejecta velocity and progenitor metallicity play in the GRB-SNe connection.

Chapter 3

The Metallicity Profile of M31 from Spectroscopy of Hundreds of HII Regions and PNe

N. E. Sanders, N. Caldwell, J. McDowell, & P. Harding 2012, *The Astrophysical Journal*, Vol. 758, 133

Abstract

The oxygen abundance gradients among nebular emission line regions in spiral galaxies have been used as important constraints for models of chemical evolution. We present the largest-ever full-wavelength optical spectroscopic sample of emission line nebulae in a spiral galaxy (M31). We have collected spectra of 253 HII regions and 407 planetary nebulae with the Hectospec multi-fiber

spectrograph of the MMT. We measure the line-of-sight extinction for 199 HII regions and 333 PNe; we derive oxygen abundance directly, based on the electron temperature, for 51 PNe; and we use strong line methods to estimate oxygen abundance for 192 HII regions and nitrogen abundance for 52 HII regions. The relatively shallow oxygen abundance gradient of the more extended HII regions in our sample is generally in agreement with the result of Zaritsky et al. (1994), based on only 19 M31 HII regions, but varies with the strong-line diagnostic employed. Our large sample size demonstrates that there is significant intrinsic scatter around this abundance gradient, as much as ~ 3 times the systematic uncertainty in the strong line diagnostics. The intrinsic scatter is similar in the nitrogen abundances, although the gradient is significantly steeper. On small scales (deprojected distance < 0.5 kpc), HII regions exhibit local variations in oxygen abundance that are larger than 0.3 dex in 33% of neighboring pairs. We do not identify a significant oxygen abundance gradient among PNe, but we do find a significant gradient in the [N II] ratio that varies systematically with surface brightness. Our results underscore the complex and inhomogeneous nature of the ISM of M31, and our dataset illustrates systematic effects relevant to future studies of the metallicity gradients in nearby spiral galaxies.

3.1 INTRODUCTION

The galactocentric radial gradient of chemical abundance within spiral galaxies has become an important parameter in modeling the chemical evolution of galaxies (Henry & Worthey 1999). The gradient is the manifestation of a

variety of physical processes acting from galaxy formation to the present, including gas infall, star formation history, stellar initial mass function, and radial migration. Historically, the observation of abundance gradients has motivated the development of analytic models of chemical evolution (Lynden-Bell 1975, and references therein) and served as a valuable constraint for detailed modeling (Maciel et al. 2005; Mollá & Díaz 2005; Scannapieco et al. 2008; Magrini et al. 2009; Carigi & Peimbert 2010). Moreover, the characterization of the abundance profiles of spiral galaxies has significant applications to other problems, including the interpretation of stellar populations (Massey & Johnson 1998) and the study of supernova explosion sites (Levesque et al. 2011).

The oxygen abundance of gas throughout the disk of star-forming galaxies can be measured via optical spectroscopy. O is the most easily accessible metallicity proxy due to its high relative abundance and its strong optical emission lines from both its major ionization states (O^+ and O^{++}). A variety of diagnostics have been developed to estimate O abundance from the flux ratios of prominent optical emission lines (see e.g. Stasińska 2002; Kewley & Ellison 2008; López-Sánchez & Esteban 2010b). These include "direct" methods, whereby the electron temperature of the nebula is derived from measurement of the weak auroral line $[O III] \lambda 4363$ (Osterbrock & Ferland 2006; Garnett 1992), and "statistical" or "strong line" measures, where the abundance is inferred from ratios of only the brightest elemental lines. Different abundance diagnostics carry systematic discrepancies as large as 0.7 dex (a factor of 5), which must be carefully considered when interpreting results (Kewley & Ellison 2008).

Strong line methods have enabled extensive observational studies of the

abundance distribution of distant spiral galaxies. While high quality spectra can be obtained for the nearby HII regions of the Milky Way, galactocentric distance can be determined more easily for external galaxies (Stanghellini et al. 2008; Henry et al. 2010). Shields & Searle (1978) derived a negative (outward-decreasing) abundance gradient from just three HII regions in M101, and by this time it was already expected from theory that negative radial abundance gradients would be characteristic of all spiral galaxies. Zaritsky et al. (1994) compiled radial O abundance profiles for 39 spiral galaxies, finding gradients ranging from 0 to $-0.23 \text{ dex kpc}^{-1}$ —only the abundance profile of NGC 2541 was inconsistent with a negative or flat gradient.

Because PNe abundances should reflect the older ISM of their progenitors, differences between the HII region and PNe abundance gradients can be used to infer time-variation in the radial abundance trend of a galaxy (e.g. Magrini et al. 2009, for M33). A sample of high-luminosity PNe should reflect current oxygen abundances in a galaxy, by selecting massive progenitors which would have formed recently. The oxygen abundances in a sample containing only the brightest PNe in a galaxy would represent populations with ages from $\sim 3 \times 10^7 - 10^{10}$ years earlier than the HII regions in the same galaxy (Magrini et al. 2009). For surveys penetrating more deeply, the proportion of PNe from less massive progenitors will grow quickly both because less massive stars are more common and because their resulting PNe are longer lasting. However, stars of mass $\lesssim 1.5 M_{\odot}$ may not form PNe because their envelope is ejected so slowly as to disperse before being ionized (Stasińska 2002).

While $\sim 10^3$ bright HII regions ($L_{\text{H}\alpha} \gtrsim 5 \times 10^{34} \text{ ergs s}^{-1}$) are known in M31

(Baade & Arp 1964; Pellet et al. 1978; Walterbos & Braun 1992; Azimlu et al. 2011), previous spectroscopic surveys to determine abundance have provided abundance estimates for $\lesssim 7\%$ of them. Blair et al. (1982) found a significant radial abundance gradient in a sample of 11 HII regions: O/H decreases by a factor of 4 from about 4 – 23 kpc in galactocentric distance. This gradient is in agreement with an earlier study of 8 HII regions in M31 by Dennefeld & Kunth (1981). In an analysis of the data from both Blair et al. (1982) and Dennefeld & Kunth (1981), Zaritsky et al. (1994) quantified the oxygen abundance gradient as relatively shallow among their sample of galaxies: -0.020 ± 0.007 dex/kpc¹. In comparison, the largest gradient in the Zaritsky et al. (1994) sample was -0.231 ± 0.022 dex/kpc (NGC 3344). Most recently, Galarza et al. (1999) surveyed 46 HII regions out to about 20 kpc in the Northeastern portion of M31, finding a radial gradient in R_{23} that is consistent with Blair et al. (1982), but only among objects whose morphology was classified as "center-brightened" by Walterbos & Braun (1992). Among HII regions of other morphologies, they report a flat abundance profile. Each of these previous surveys has relied on various strong line abundance diagnostics. Additionally, abundance gradients have been derived from surveys of M31's stellar population. Trundle et al. (2002) found a flat radial metallicity profile among seven young B stars. Worthey et al. (2005) estimated abundances for an older population, red giant stars, from color-magnitude diagrams of 11 fields in M31. For radii < 25 kpc, they find a

¹Hereafter, we quote physical values for M31 based on a distance of 770 kpc (Freedman & Madore 1990). Zaritsky et al. (1994) used an earlier distance measurement of 700 kpc, so we apply a 10% correction to their measured abundance gradient.

negative gradient similar to the nebular result of Dennefeld & Kunth (1981) and Blair et al. (1982), but they report a flattening at larger radii.

M31 hosts as many as 10^4 PNe, about twice as many as the Milky Way (Nolthenius & Ford 1987). In a kinematic survey, Merrett et al. (2006) cataloged 2615 of M31's PNe. Abundances have been previously derived for less than 1% of these. Jacoby & Ford (1986) determined abundances for three PNe: two in the halo and one in the outer disk. The results of the largest previous spectroscopic survey of M31 PNe, including 70 objects, have not yet been published (Kniazev et al. 2005). A survey of 30 nebulae in the bulge of the galaxy was performed by Richer et al. (1999), but only a lower limit of abundance could be derived for 14 of the nebulae. Because the survey only extended out to $\lesssim 4$ kpc and because only the bulge population is sampled, Richer et al. (1999) did not investigate the radial abundance gradient. Recently, Kwitter et al. (2012) have derived abundances for 16 PNe in the outer disk of M31.

By providing a more thorough characterization of the abundance profile of in M31, this paper seeks to enable an improved understanding of the chemical evolution of M31 and similar spiral galaxies. In Tables A.1-A.4 we present the largest available spectroscopic catalogs of HII regions and PNe in M31. Our observations come from the Hectospec multifiber spectrograph on the MMT, whose multiplexing ability provides a large advantage over previous surveys of these objects. In Section 3.2 we describe the observational parameters and analytical techniques used to produce the catalog. In Section 3.3 we compare our results to previous publications and discuss trends and implications identified in the catalog. Our principal findings are that a significant negative abundance

gradient is only demonstrated among the brightest and most diffuse HII regions. The radial profile is more flat among dimmer or more compact HII regions, and in general there is a large amount of scatter in the physical properties of the ISM of M31. We characterize this scatter in terms of the radial distribution of extinction and abundance in HII regions and PNe, and also in terms of the discrepancies among neighboring objects. We provide a summary of major results in Section 3.4.

3.2 OBSERVATIONS

3.2.1 Data collection

Small, resolved objects and unresolved $H\alpha$ features were selected as HII region candidates by inspecting the images of the Local Group Galaxies Survey (LGGS, Massey et al. 2007). Additionally, some objects observed as part of the M31 cluster survey of Caldwell et al. (2009) had strong emission, and are included in the present study. Some objects from the planetary nebula catalog of Merrett et al. (2006) as well as strong and unresolved [O III] features from the LGGS images were observed as PN candidates. We have excluded from our sample any objects identified as emission line stars by Massey et al. (2007), one object which was found to have broad emission lines characteristic of supernova remnants, and ~ 20 objects which showed broad emission features characteristic of WR stars.

We note that many M31 HII regions have diameters greater than $50''$ (Arp & Brueckel 1973), far too large to be encompassed by a single Hectospec fiber, which

subtends 1.5" on the sky (~ 5 pc at the distance of M31). Moreover, to facilitate a future study of the kinematic properties of nebulae in M31, we attempted to avoid HII regions which would have a large internal velocity dispersion. For both these reasons, the largest HII regions were therefore intentionally omitted from the sample, although some objects remain (mostly the star clusters) that were estimated by Blair et al. (1982) as at least 48 pc in diameter. We assume that any inhomogeneities in spectral properties within each HII region are small and random and therefore that the region sampled by the Hectospec fiber is representative of the whole (see e.g. McCall et al. 1985; Pellegrini et al. 2010).

Optical spectra were obtained with the Hectospec multi-fiber positioner and spectrograph on the 6.5m MMT telescope (Fabricant et al. 2005). The Hectospec 270 gpm grating was used and provided spectral coverage from 3650 – 9200Å at a resolution of ~ 5 Å. Some spectra did not cover [O II] λ 3727, because of the design of the spectrograph (alternate fibers are shifted by 30Å), and the small blueshift of M31. The observations were made in the period from 2004 – 2011 as a component of a survey previously described in Caldwell et al. (2009) and were reduced in the uniform manner outlined there. The frames were first debiased and flat fielded. Individual spectra were then extracted and wavelength calibrated. Standard star spectra obtained intermittently were used for flux calibration and instrumental response. Sky subtraction is achieved with Hectospec by averaging spectra from “blank sky” fibers from the same exposures or by offsetting the telescope by a few arcseconds (see Caldwell et al. 2009). Because local background subtraction could potentially subtract object flux from extended HII regions, we compare the spectra reduced from repeated observations of the same objects using different

sky spectra, local and distant. For both stellar and diffuse objects, we find only small differences in the ratios of $H\alpha/H\beta$ and also $[N II]/H\alpha$. The rms of the discrepancy in the log of the flux ratio is ~ 0.05 dex and the mean difference is ~ 0.01 dex. We therefore conclude that the sky subtraction is adequate.

Each of 25 1 degree fields in M31 was exposed for between 1800 and 4800 s. The spectra of objects that were observed multiple times (in overlapping fields) have been combined, effectively summing those integration times. Sample spectra are shown in Figure 3.1. The locations of emission nebulae included in this study are shown in Figure 3.2. Many of our HII regions fall in the “Ring of Fire,” a circular feature visible in HI density maps extending from about 8 to 15 kpc in the disk of M31 (Sofue & Kato 1981).

Velocities were measured using the SAO xcsao software and emission line templates (one typical of HII regions and another of PNe). Repeat measurements of 114 objects gave an rms of a single measurement of 2.1 km s^{-1} . We also compared our velocities with the work of Halliday et al. (2006), who also used a multifiber spectrograph, and Merrett et al. (2006) who used the Planetary Nebula Spectrograph (which imaged in $[O III]$). The Halliday et al. (2006) comparison revealed a mean offset of $+7.1 \text{ km s}^{-1}$ with an rms of 5.4 km s^{-1} , while the Merrett et al. (2006) comparison resulted in a mean offset of $+2.9 \text{ km s}^{-1}$ with an rms of 15.6 km s^{-1} . The Merrett et al. (2006) rms was expected to be larger because of their use of the single emission line. These comparisons led us to estimate our mean error to be 3 km s^{-1} . The final step in the reduction was the transformation of the spectra to zero velocity using the observed velocities.

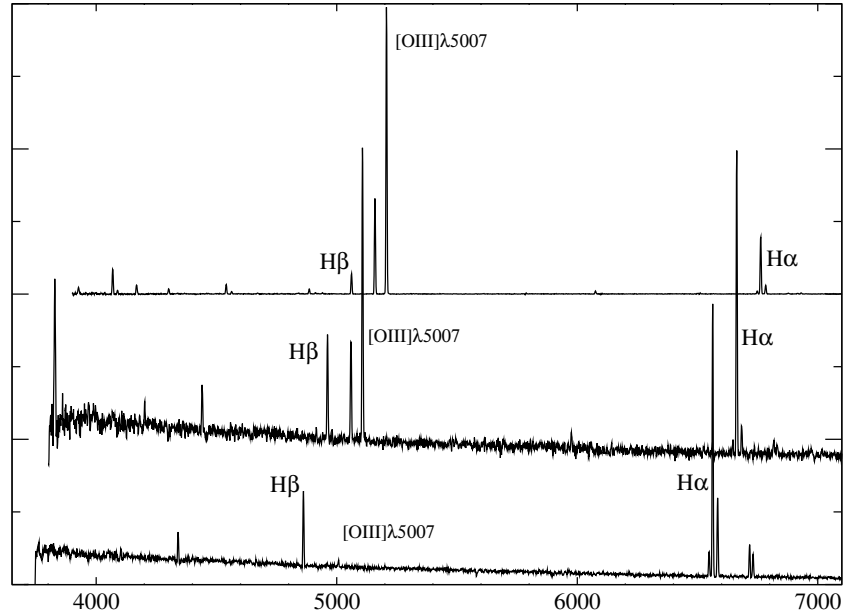


Figure 3.1.— Three spectra from Hectospec. From the bottom, a high-metallicity HII region (object HII166), a low-metallicity HII region (object HII153), and a PNe (object PN130). The two HII regions are separated by only $1.93'$ on the sky, corresponding to a separation of ~ 0.4 kpc at the distance of M31. For clarity, the relative flux scales were set such that the strongest emission line in each spectrum ($H\alpha$ for HII regions and $[O\ III]\lambda 5007$ for the PN) are the same height and the wavelength zero point was offset by 100 and 200\AA for the two upper spectra. $[O\ II]\lambda 3727$ falls off of the original spectrum for the upper and lower spectra.

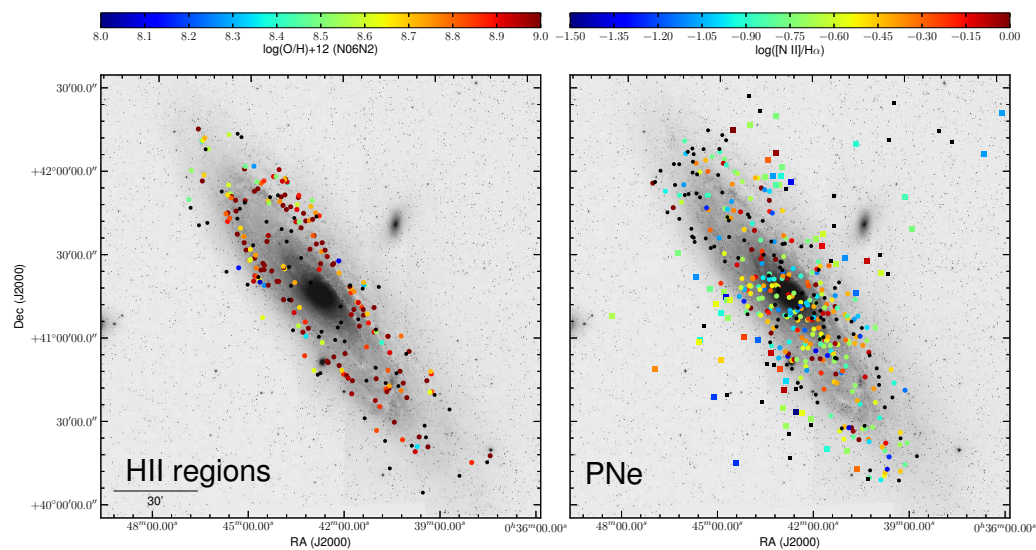


Figure 3.2.— Locations of M31 HII regions and PNe observed with Hectospec, overlaid on the M31 mosaic from the Digitized Sky Survey (DSS). The HII region symbols are colored to oxygen abundance, using the N06 N2 diagnostic, and the PNe are colored according to their N2 flux ratio (see Section 3.2.7). Halo PNe are denoted with squares and objects whose abundance/flux ratio could not be measured are marked in black.

3.2.2 Classification

These candidates were formally classified according to two-dimensional emission line ratio tests of excitation mechanism (BPT diagrams, Baldwin et al. 1981). Specifically, we apply equation 1 of (Kniazev et al. 2008), which distinguishes HII regions from PNe based on their locations in a diagram of $[\text{O III}]/\text{H}\beta$ (O3) versus $[\text{N II}]/\text{H}\alpha$ (N2) (Figure 3.3). These tests have the advantage of relying on ratios of strong emission lines that are near to each other in wavelength and therefore not sensitive to reddening corrections or instrumental response. The measurement of line fluxes is described in Section 3.2.4. We adopt a slight amendment to the dividing line proposed by (Kniazev et al. 2008), illustrated by the dashed line in Figure 3.3. This amendment is favored because it classifies as PNe a number of objects that we have reason to believe are not HII regions. These objects have stellar morphologies (see below) and many of them are in the halo, based on their position along the minor axis ($|Y| > 4$ kpc), as is illustrated in Figure 3.3. It is not surprising that there may be small offsets in the appropriate line ratio diagnostics for different samples given slight differences in flux-measurement methodology. The amended classification we adopt to distinguish HII regions from PNe is:

$$\text{O3} > (0.61/(\text{N2} - 0.47)) + 1.0 \quad (3.1)$$

In total, we identify 407 PNe and 253 HII regions among our spectroscopic sample. Of these objects, 392 PNe and 200 HII region spectra were observed with the atmospheric dispersion compensator (ADC, Fabricant et al. 2008). For

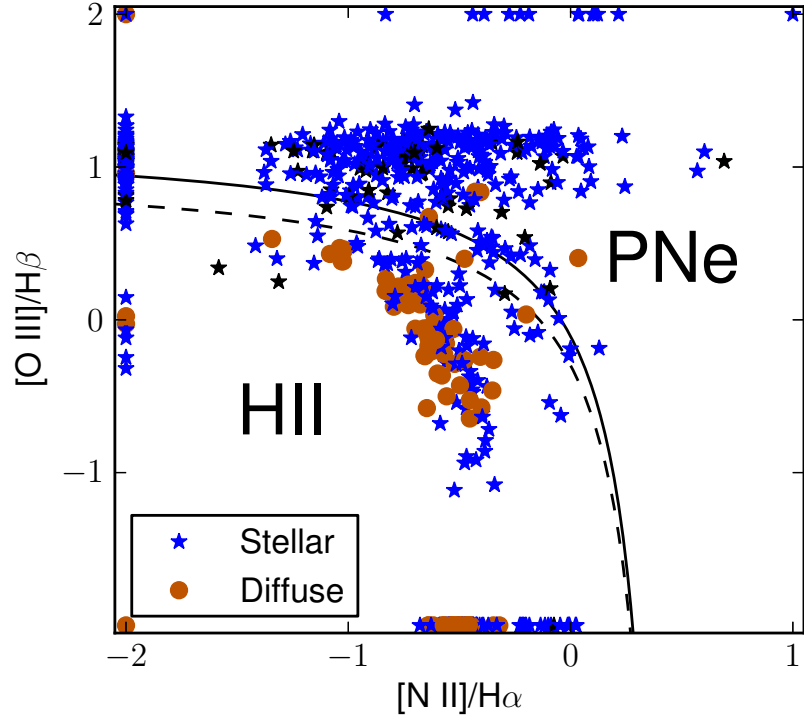


Figure 3.3.— Excitation mechanism diagnostic diagram (Baldwin et al. 1981) distinguishing PNe from HII regions for M31 emission line nebulae observed in this study. Emission line flux ratio error bars are typically smaller than the points. The solid black classification divider is from Kniazev et al. (2008); the dashed line is our amended divider, on which our spectroscopic classification is based. The data points are color coded according to $H\alpha$ morphology (stellar or diffuse); objects identified as being in the halo based on their position along the minor axis ($|Y| > 4$ kpc) are colored black. Objects shown on the edge of the figure denote flux ratio limits for lines which were not detected.

some spectra, the ADC malfunctioned, and for those we do not present quantities derived from emission line flux ratios with large wavelength separations. 81 of the PNe do not appear to be projected onto the disk of M31 (according to the distance along the minor axis, $|Y| > 4$ kpc, see Section 3.2.3), and we therefore assume they are associated with the halo population. 23 of the PNe are hosted by the dwarf satellite galaxy NGC 205 rather than in M31, according to their position and velocity in the kinematic survey of Merrett et al. (2006). Because the S/N of these spectra are such that it is not possible to derive their abundances, we remove them from the sample and do not discuss them further. An additional 25 objects could not be classified because the S/N in their [O III] and $H\beta$ emission lines were too weak. We do not discuss these unclassified objects further.

In addition to this spectroscopic classification, we have made a morphological classification for each object based on its appearance in the LGGs $H\alpha$ images. Objects whose $H\alpha$ emission appears unresolved at the resolution of these images ($\sim 1''$) are classified as “stellar” and those that appear extended and nebulous are classified as “diffuse.” We note that this is similar to the classification scheme of Walterbos & Braun (1992) referred to by Galarza et al. (1999), where their type “C” or “center-brightened” corresponds to our “stellar” and their type “D” or “diffuse” corresponds to the same. We find that 7 spectroscopically-classified PNe are diffuse. Because most of these objects are near the dividing line in the BPT diagram, it is difficult to determine whether these are PNe embedded in HII regions or simply poor spectroscopic classifications. However, these only amount to $\sim 1\%$ of our full sample of PNe.

About half of our spectroscopically-classified HII regions are stellar. From

Figure 3.3, it is clear that the stellar HII regions are more likely to have high O3 or N2 ratios relative to diffuse HII regions and are therefore nearer to the dividing line in the BPT diagram. It is possible that some of these objects are PNe with an unusually low value of $[\text{O III}]/\text{H}\beta$. Among the sample of Galactic PNe in Henry et al. (2010), there are some objects (M1-11 and M1-12) that fall on a similar region of the BPT diagram. According to the Catalogue of Galactic Planetary Nebulae (Kohoutek 2001), these objects were originally classified as PNe by Minkowski (1946), whose classifications were essentially morphological. It is also possible that these are extended HII regions whose $\text{H}\alpha$ emission is simply dominated by the emission in the immediate vicinity of one bright star, and therefore appear compact on the LGSS images. Therefore the diffuse subset of HII regions in our sample may represent a cleaner sample, less likely to have PN contamination.

3.2.3 Galactocentric distance

The deprojected galactocentric distance was calculated following Haud (1981). We assume a distance to M31 of 770 kpc (Freedman & Madore 1990) and an inclination of $i = 12.5^\circ$ (Simien et al. 1978). The adopted coordinates of the galactic center and position angle of the major axis, precessed from Haud (1981), are:

$$\alpha_0 = 00^\circ 42' 44''.52 \quad (\text{J2000})$$

$$\delta_0 = +41^\circ 16' 08''.69 \quad (\text{J2000})$$

$$\phi_0 = 37^\circ 42' 54''$$

Hereafter, we use “galactocentric distance” to refer to this deprojected distance. Any PNe with a distance projected along the semiminor axis (Y) greater than 4 kpc, we associate with the halo population and do not consider in our sample when fitting for radial trends in the disk. Additionally, there are 3 objects that we consider halo PNe given their projected distance $|Y| > 5$ kpc, despite the fact that they fall in the HII region regime of the BPT diagram.

3.2.4 Emission line fluxes

The line fluxes were measured using the line profile-fitting capabilities provided by the IRAF package `fitprofs`. We fit Gaussian profiles to a wavelength range 20 Å in width centered on the rest frame wavelength of each line. We fit a linear continuum to 20 Å regions of the spectra off the wings of each line. For groups of nearby lines likely to be blended, we fit simultaneous Gaussians. The line flux is estimated as the integral of the fitted profile with the continuum subtracted. We estimate the uncertainty in the line fluxes using the Monte Carlo methodology implemented by `fitprofs`. In these Monte Carlo simulations, random noise is repeatedly added to the spectrum according to a simple linear noise model dependent on two parameters: the gain of the CCD and a noise floor. We estimate the gain and noise floor for each individual line profile by comparing the spectrum of the background regions to the corresponding variance spectrum. We have compared this estimate of the line flux uncertainty to the discrepancy between line flux ratios measured in repeated observations of the same objects and find them

to be comparable; for the $H\alpha/H\beta$ ratio, the Monte Carlo uncertainty estimate and the discrepancy among the repeated observations are each $\sim 3\%$ in the mean. Based on the Monte Carlo estimate of the uncertainty in the line flux, we require that $S/N > 3$ and otherwise report a non-detection. Additionally, we record the equivalent width as measured by `fitprofs`, if the sky-subtracted continuum level is more than 2σ greater than zero (where the continuum level and its standard deviation, σ , are measured from the background regions of each line).

The [O II] $\lambda\lambda 3726 - 3729$ doublet is not resolved in these spectra, and the sum effectively measured will henceforth be referred to as [O II] $\lambda 3727$. Moreover, because $\lambda 3727$ is on the very edge of our spectral range, it has a large flux-calibration uncertainty associated with it, which is propagated through to our estimate of the flux uncertainty. As mentioned above, for some spectra, $\lambda 3727$ is outside of the observed spectral range.

We note that we have made no correction for underlying stellar absorption, but we estimate that this will not significantly affect the measurement of the Balmer line fluxes. Using models from Starburst99 (Leitherer et al. 1999), we subtracted off underlying continua for populations with ages ranging from 4 to 20 Myr for a representative low- and high-metallicity HII region (objects HII166 and HII153), see Figure 3.1). We then measured $H\gamma$ and $H\beta$. The ratios of those two lines changes at worst by 1% from the uncorrected values (the worst case results from assuming the youngest age for the underlying population). As a further test of the small effect that the underlying continuum has on our measurements, we also measured $H\alpha$ equivalent widths and compared those with A_v (derived from the $H\alpha/H\beta$ emission line ratio), and found no significant

correlation. This indicates in general that Balmer absorption doesn't significantly affect the measured Balmer ratios for the objects in our sample.

We present the measured line fluxes and their uncertainties for each object in Table A.2. For all parameters derived from these line fluxes, we propagate the uncertainty in the line flux via Monte Carlo simulations. In these simulations, we sample from a Gaussian line flux probability distribution with a mean and standard deviation as reported in Table A.2. We then report the median and standard deviation of the resulting distribution as our best estimate of the derived parameters and its uncertainty.

We characterize the surface brightness of each emission line region based on its observed $H\alpha$ emission line flux, even if the objects are unresolved. $H\alpha$ is used for this purpose because it is strong and easily detected in nearly every spectrum. However, the 1.5" Hectospec fibers generally do not cover the entire area of the diffuse emission nebulae. Moreover, as the observation nights were not all photometric, there could be photometric uncertainties of a factor of a few. We attempted to place all the spectra on the same photometric scale by using the multiple observations, and find that this was successful to within a factor of 1.3.

We therefore divide our sample into three surface brightness classes (1: "dim," 2: "normal", 3: "bright"; see Figure 3.4) based on the extinction-corrected $H\alpha$ line flux, rather than assert a precise flux measurement. We establish separate brightness classes for the HII regions (based on the diffuse subset only) and PNe. For spectra where the $H\beta$ line is not detected, we assume the median A_V for that class (HII region or PNe) for the purpose of calculating the extinction corrected

H α line flux. The diffuse HII regions in our sample are at ~ 2.4 times higher surface brightness than the PNe, in the median (or ~ 4.4 times brighter after extinction correction). Moreover, the HII regions encompass a larger range in surface brightness, extending to nearly two orders of magnitude brighter in H α .

We have estimated the apparent brightness limits corresponding to these surface brightness classes by matching the HII regions in our sample to the catalog of Azimlu et al. (2011), using the nearest objects within 5". They use an automated code to segment diffuse emission in continuum-subtracted H α images of M31 for the identification of HII regions and PNe and to measure the H α flux and diameter. Figure 3.4 shows the relation between our spectroscopic H α flux measurements and the photometry from Azimlu et al. (2011). The scatter in the relation is correlated with the HII region diameter, because HII regions which Azimlu et al. (2011) segment as larger objects are have a correspondingly smaller fraction of their flux fall on our Hectospec fibers. Among small objects ($D < 16$ pc), the scatter is ~ 0.3 dex. This relation implies that our HII region flux bins have edges at $\sim [7.0, 31.1] \times 10^{-15}$ ergs cm $^{-2}$ s $^{-1}$ and, for PNe, $\sim [2.6, 5.4] \times 10^{-15}$ ergs cm $^{-2}$ s $^{-1}$.

3.2.5 Extinction

A reddening correction was applied to restore the Balmer recombination decrement of each spectrum to its theoretical value. We assume H α /H β =2.85, which corresponds to T=10,000K and $n_e = 10^4$ cm $^{-3}$ for Case B recombination. However, the Balmer ratios are not very sensitive to any of these parameters: the

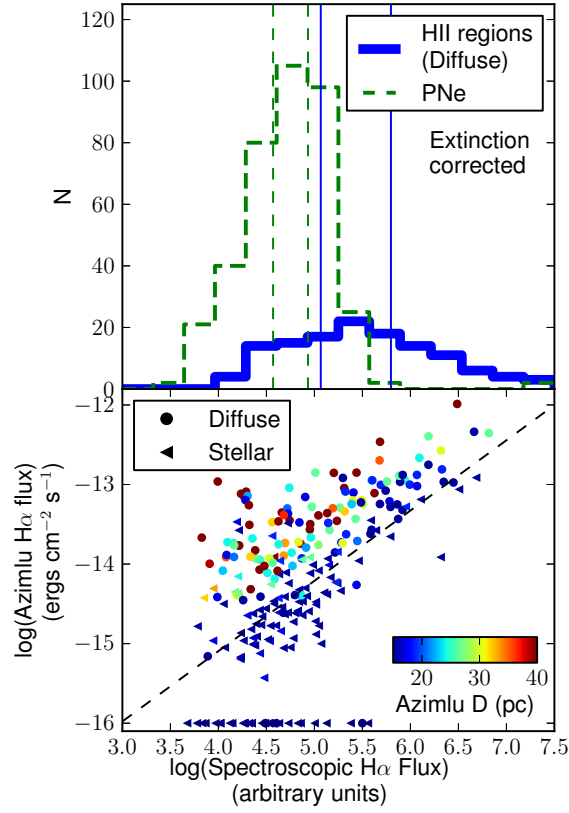


Figure 3.4.— Top: The surface brightness distribution of diffuse HII regions (blue) and disk PNe (green), as measured spectroscopically from the extinction-corrected $\text{H}\alpha$ emission line flux (arbitrary units). The solid and dashed vertical lines denote the surface brightness limits which split the sample into three equally sized bins of HII regions and PNe, respectively. Bottom: Comparison of spectroscopically-measured $\text{H}\alpha$ fluxes (not extinction corrected) and the photometric catalog of Azimlu et al. (2011) for HII regions only, with color coding by the catalog diameter. Symbol shape denotes our morphological types. Points on the edge of the figure do not have matches within $5''$. The dashed line is the best fit among small ($D < 20$ pc) objects.

assumption of Case A only alters the ratio by $\lesssim 0.05$ and extreme temperatures and densities also have little effect: $H\alpha/H\beta = 3.04$ for $T = 5,000$ K and $n_e = 10^2$ cm $^{-3}$, $H\alpha/H\beta = 2.73$ for $T = 20,000$ K and $n_e = 10^6$ cm $^{-3}$ (Osterbrock & Ferland 2006). The extinction curve given in Cardelli et al. (1989) was applied, with a value of 3.1 adopted for R_V . In cases where we derive a negative value of the extinction in the visual band ($A_V < 0$), we instead assume $A_V = 0$.

The value of the extinction derived for each object is presented in Tables A.3 and A.4.

3.2.6 Direct abundance estimation

We derive “direct” oxygen abundance estimates for PNe by estimating the electron temperature of the gas’ dominant excitation zone, which can be done only if a temperature-sensitive line is detected. We use [O III] $\lambda 4363$ exclusively for this purpose; although auroral lines from other ions (e.g., [N II] $\lambda 5755$) are detected in a few spectra, their numbers are not sufficient for a statistical sample and their S/N is typically much lower than [O III] $\lambda 4363$. This prescription is also applied to our HII regions, however direct abundances can be derived for only 4 HII regions due to the weakness of the [O III] $\lambda 4363$ line.

The electron temperatures are estimated using IRAF’s five-level nebular modeling package `nebular` (Shaw & Dufour 1994). The `nebular` task `temden` is first applied to iteratively estimate the O $^{++}$ temperature ($T_e(\text{O}^{++})$) and density (n_e) of the nebula from the [O III] and [S II] line ratios, respectively. When the [S II] lines are not available, we assume a reasonable range of densities,

$n_e = 15 \pm 2 \times 10^3 \text{ cm}^{-3}$ (see e.g. Kwitter et al. 2012). If the measured line ratios correspond to unphysical conditions (outside the range for which `temden` is calibrated, $500 < T_e(\text{O}^{++}) < 10^5 \text{ K}$ and $1 < n_e < 10^8 \text{ cm}^{-3}$), we do not calculate the direct abundance. The O^+ temperature is then estimated using the linear empirical relation of Garnett (1992). The O^+ and O^{++} abundances are then estimated using the density, ionic temperatures, and $[\text{O II}]$ and $[\text{O III}]$ line ratios following the ionization correction factor (ICF) prescription of Shi et al. (2006). The total oxygen abundance is taken to be the sum of these two ionic abundances. This methodology is similar to that applied in, for example, Bresolin et al. (2010).

A variety of studies have shown that stellar evolution of PNe progenitors should not modify oxygen abundance at a level significant for the identification of abundance gradients from the nebulae (Richer & McCall 2007, and references therein). Furthermore, it has been shown that bright PNe (within ~ 2 mag of the brightest in the galaxy), presumably from more massive stars with shorter lifetimes, have approximately the same oxygen abundances as the surrounding ISM and HII regions, to within the observational uncertainty (Richer & McCall 2007). It has been demonstrated that O, as well as Ar and Ne, abundance gradients in the Milky Way as measured with HII regions are reflected in observations of PNe (Pottasch & Bernard-Salas 2006). However, oxygen may be dredged up in some low-metallicity cases ($\log(\text{O}/\text{H})+12 \lesssim 8$) and thereby enrich the PNe relative to its progenitor by $\Delta\log(\text{O}/\text{H}) \lesssim 0.3$ dex (Richer & McCall 2007; Hernandez-Martinez et al. 2009; Magrini & Gonçalves 2009). In high-mass PNe, oxygen may be depleted by $\Delta\log(\text{O}/\text{H}) \lesssim 0.1$ dex during the lifetime of the progenitor via the ON-cycle (Hernandez-Martinez et al. 2009). Moreover,

it has been observed that the N abundance of PNe will often exceed that of the local ISM (Richer & McCall 2007; Hernandez-Martinez et al. 2009)—justified theoretically by nitrogen production via the CN or ON cycle during the first and second dredge ups. Henry et al. (2010) have established empirically that the oxygen abundance gradient of Milky Way PNe does not depend on the Peimbert type of the PNe or the vertical distance from the plane of the Galaxy; we therefore do not consider these parameters here.

3.2.7 Strong line diagnostics

HII region abundances were calculated from the extinction-corrected line flux ratios according to a number of independently calibrated abundance diagnostics from the literature. These diagnostics each depend on a different combination of emission line ratios. Each calibration has its own characteristic scatter and systematic offset as compared to the other methods (Kewley & Ellison 2008). It is unclear that any particular method is superior, and some methods may be more applicable than others for certain comparisons. In particular, diagnostics tied to the direct abundance scale may agree better with stellar oxygen abundances within the same galaxy (see e.g. Bresolin et al. 2009). We therefore employ multiple methods and keep their differences in mind when discussing results. We report the abundance derived from each method in Tables A.3 (HII regions) and A.4 (PNe).

First, we apply the R_{23} oxygen abundance calibration of Zaritsky et al. (1994), an average of three earlier methods, hereafter referred to as “Z94.” Z94

is only calibrated for the higher-metallicity upper branch of the well-known R_{23} -abundance degeneracy. The majority of M31 HII regions may be expected to fall on this upper branch, given that all the M31 HII regions in the compilation of Zaritsky et al. (1994) did. If the measured line ratios correspond to an abundance outside of the range for which Z94 is calibrated (generously, $8.4 < \log(\text{O}/\text{H})+12 < 9.6$), we do not record the measurement.

Second, we apply the $[\text{N II}]/[\text{O II}]$ oxygen abundance calibration of Kewley & Dopita (2002), hereafter referred to as “KD02.” Kewley & Dopita (2002) synthesize a variety of modern photoionization models and observational calibrations to produce recommendations for producing an abundance estimate given different permutations of available emission lines. We implement the prescription outlined in the appendix of Kewley & Ellison (2008), as follows. We use the $[\text{N II}]/[\text{O II}]$ ratio to break the degeneracy between the upper and lower branches of R_{23} . For the upper branch, we employ the $[\text{N II}]/[\text{O II}]$ calibration of Kewley & Dopita (2002). For the rare lower branch cases, we average the R_{23} diagnostics of McGaugh (1991) and Kobulnicky & Kewley (2004). If the measured line ratios correspond to an abundance outside of the range for which KD02 is calibrated ($8.2 < \log(\text{O}/\text{H})+12 < 9.6$), we do not record the measurement.

Third, we apply the empirical $[\text{N II}]/\text{H}\alpha$ (“N2”) and $[\text{O III}]/[\text{N II}]$ (“O3N2”) oxygen abundance calibrations of Nagao et al. (2006), hereafter referred to as “N06.” We prefer the N06 diagnostic to the similar “PP04” N2 and O3N2 diagnostics of Pettini & Pagel (2004) because N06 is well-calibrated in the high-metallicity regime of M31 using data from the SDSS galaxies (Tremonti et al. 2004). If the measured line ratios correspond to an abundance outside of the

range for which N06 is calibrated ($7.0 < \log(\text{O}/\text{H})+12 < 9.5$), we do not record the measurement. Because this diagnostic relies on the N II lines to measure the O abundance, scatter is introduced by variations in the N/O ratio (Pérez-Montero & Contini 2009). We note also that the O3N2 diagnostic is not reliable when $\text{O3N2} \gtrsim 100$, due to line saturation, but this only occurs in a metallicity regime lower than that sampled here ($\log(\text{O}/\text{H})+12 \lesssim 7.5$; Pettini & Pagel 2004; Nagao et al. 2006).

Fourth, we apply the excitation parameter (“*P* method”) oxygen abundance calibration of Pilyugin & Thuan (2005), hereafter referred to as “PT05.” This is an updated version of the calibration first defined in Pilyugin (2001b) (P01). *P* is calculated from the ratio of [O III] to ([O II]+[O III]). PT05 additionally relies on the R_{23} line ratio, so the [N II]/[O II] ratio is used to break the R_{23} degeneracy. If the measured line ratios correspond to an abundance outside of the range for which PT05 is calibrated ($6.8 < \log(\text{O}/\text{H})+12 < 9.1$), we do not record the measurement.

Fifth, we apply the nitrogen abundance calibration of Pilyugin et al. (2010) hereafter referred to as ‘PVT,’ relying on the combination of *P* and [O III], [N II], and [S II] (“ONS”) line ratios. The PVT diagnostic is calibrated separately for each of three different [N II] regimes. If the measured line ratios correspond to an abundance outside of the range for which PVT is calibrated ($7.3 < \log(\text{N}/\text{H})+12 < 8.9$), we do not record the measurement.

We have not attempted to factor in the systematic error in the abundance diagnostics, although they are typically much larger (~ 0.1 dex) than our reported

errors, which are derived by propagation of the line flux uncertainties. For example, Kewley & Ellison (2008) estimates the rms scatter between relative metallicities measured with the Z94 diagnostic, as compared to other popular diagnostics, is 0.07 dex based on a sample of 30,000 SDSS galaxies. They find that the scatter in the other diagnostics are similar, the largest mean rms belonging to P01 (related to PT05) at 0.11 dex. Because the only references for the accuracy of each abundance estimation technique are estimates from other diagnostics, which are not necessarily independent, any quantification of uncertainty must be interpreted with caution.

We have compared the oxygen abundance measurements made for the same HII region in different diagnostics. Among the strong line methods, there is very good agreement between the Z94 and KD02 methods (standard deviation of 0.07 dex). There is fairly good agreement between Z94 and N06 N2 (median offset of -0.10 dex and standard deviation of 0.21 dex) and between the N06 N2 and O3N2 diagnostics (negligible median offset, standard deviation of 0.12 dex). The PT05 diagnostic does not agree well with the other strong line methods, having a median offset as large as -0.50 dex (Z94) and a standard deviation as large as 0.30 dex (N06 N2).

In Figure 3.5 we show the cumulative distribution functions (CDFs) of oxygen abundance for the HII regions and PNe in our sample as derived by the different diagnostics. The total range in PNe abundances is about $7.6 \lesssim \log(\text{O}/\text{H})+12 \lesssim 8.8$ (a factor of 16). The range of HII region abundances varies widely by diagnostic. For example, PT05 abundances range from $8.0 \lesssim \log(\text{O}/\text{H}) + 12 \lesssim 8.5$ while N06 N2 abundances range from $7.9 \lesssim \log(\text{O}/\text{H}) + 12 \lesssim 9.5$.

The difference in both the shape and median value of the CDFs of different diagnostics are due to two factors: the systematic discrepancy between the calibrations, and the selection effects imposed by the requirement for certain emission lines to be detected in order to apply each diagnostic. One additional selection effect is the range over which the diagnostics are calibrated; for example, the Z94 abundance scale is only calibrated down to $\log(\text{O}/\text{H})+12 = 8.4$, as described above. If the diagnostic transformations of Kewley & Ellison (2008) are applied (along with the trivial transformation between PP04 N2 and N06 N2), the CDFs for the N06 N2, KD02, and Z94 diagnostics agree reasonably well (Kolmogorov-Smirnov p -value $\gtrsim 0.01$), despite the selection effects. The discrepancy is largest between the PT05 diagnostic and the other strong line methods. The median abundance for the N06 N2 diagnostic is $\log(\text{O}/\text{H})+12 = 8.89$, while for PT05 it is 8.34 dex. While this offset is approximately equal to the offset determined for the SDSS galaxies with these diagnostics (Kewley & Ellison 2008, and also considering the conversion from N06 N2 to PP04 N2 and PT05 to P01). However, Kewley & Ellison (2008) determined that no reliable transformation can be established between PT05 and the other diagnostics because the relation is highly non-linear and has high scatter ($\gtrsim 0.1$ dex). From Figure 3.5 it is clear that the direct abundances may only be derived for the lowest-metallicity objects where the auroral line is accessible.

The combination of selection effects and calibration discrepancies should be kept in mind as we investigate the oxygen abundance profile of M31. Results should only be compared if they are quoted in the same diagnostic, due to the systematic deviations and scatter that exist between different diagnostics.

Moreover, if a diagnostic does not probe the full range of abundances in the population, then the measured abundance profile in the diagnostic should not be used to infer physical properties of the galaxy. In particular, we suggest that care be used in interpreting the abundance profile derived from the direct diagnostic, because it imposes severe selection effects (the availability of the auroral line) that selectively exclude high-metallicity objects from samples, and the PT05 diagnostic, because it produces abundances discrepant with other strong line diagnostics. However, measurements from these diagnostics are still useful. The direct abundance is the only diagnostic based on a measurement of the true electron temperature of the nebulae, and it provides a useful comparison to Galactic work (e.g. Shaver et al. 1983). Moreover, the direct method must be applied to PNe, for which strong line methods are not available. The PT05 diagnostic is the most modern calibration of the P method, which typically reflects the oxygen abundance as measured by the direct method more closely than other strong line methods (Pilyugin 2001a, as well as our results above).

3.3 DISCUSSION

Our analyses are primarily concerned with looking for radial trends in the interstellar medium properties of M31, with the goal of identifying any information that describes the chemical evolution history of the galaxy. For this purpose, we focus on objects in the disk of the galaxy. While all HII regions studied in this survey are attributed to the disk, a large population ($N = 81$) of PNe appear in projection to be outside of the disk ($|Y| > 4$ kpc); this is the

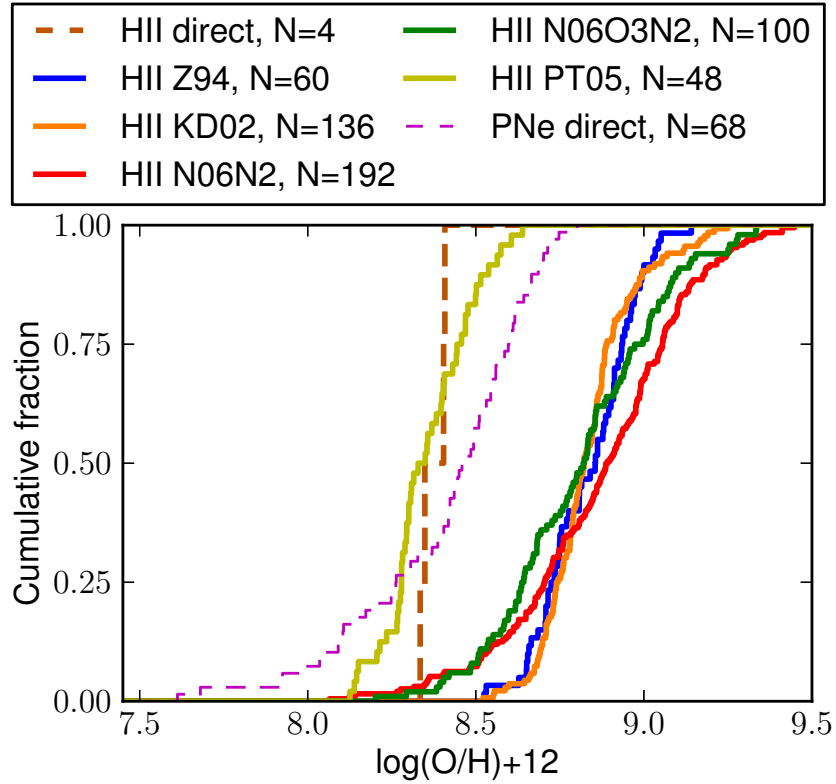


Figure 3.5.— The cumulative distribution functions (CDFs) of oxygen abundance for M31 HII regions and PNe (both disk and halo) as derived by different diagnostics. The strong line methods are shown as solid lines, while the direct abundances are dashed. The number (N) of objects for each diagnostic is noted in the legend and is limited by the available line flux ratios from each spectrum and the abundance range over which the diagnostic is calibrated. PNe include halo objects. A color version of this figure is available in the electronic journal.

halo population discussed in Section 3.2.3. We exclude these disk PNe from our analysis, except where explicitly described.

We look for radial trends in the optical extinction, oxygen abundance, and nitrogen abundance of HII regions and PNe in M31. Our initial analyses, fitting linear trends and looking for correlations, are summarized in Table A.5. This table summarizes the significance of radial trends in two different ways:

Bootstrap We fit a line by ordinary least squares to the radial distribution of the parameter, and then repeat many times with resampling. We simultaneously resample from the set of all objects with measurements of that parameter (with replacement) and also from the probability distribution function of the derived parameter. In this way, we can estimate the slope and intercept (extrapolated value at the center of M31) of the radial trend in a way that is not sensitive to outliers or objects with poor-quality spectra.

Spearman We report the Spearman rank correlation statistic ρ and its p value. A ρ value much less than zero indicates a strongly negative gradient. A p value much greater than zero would indicate that any apparent correlation with radius could be due merely to chance.

We discuss these gradient analyses in the following section.

3.3.1 Extinction

The estimated values of extinction in the visual band (A_V) as derived from the Balmer decrement are reported in Tables A.3 and A.4 and vary from 0 to nearly

5 mag. Blair et al. (1982) sampled HII regions with extinction up to ~ 2.3 mag and Galarza et al. (1999) up to ~ 4 mag.

Figure 3.6 illustrates the A_V distribution versus galactocentric distance for 199 HII regions and 333 PNe. The extinction is patchy. Because reddening imposes a selection effect on our sample, the maximum extinction we observe at a given radius is just a lower limit. Nonetheless, the maximum extinction varies radially: as high as ~ 5 mag from $\sim 10 - 15$ kpc, in the Ring of M31, to $\lesssim 1.5$ mag beyond 20 kpc, in the outskirts of the disk. However, objects fill the figure down to ~ 0 mag at all radii. The maximum extinction of PNe follow a similar radial trend, but typically have smaller extinction than HII regions ($A_{V,\text{PNe}} \lesssim 3$ mag). It is expected that HII regions will have higher extinction than PNe, because they are near the large dust clouds associated with star formation and because they are primarily found in spiral arms rather than evenly throughout the disk. PNe from the halo population are also likely to be found above the disk of M31 where extinction should be negligible. Moreover, HII regions are typically an order of magnitude brighter than PNe and therefore may be observed through greater extinction (Panagia 1978). Kumar (1979) asserted that a plateau at $\lesssim 1$ mag in the extinction of HII regions begins at 12 kpc, while our data demonstrate that large (> 2 mag) values of extinction are common out to nearly twice this distance.

PNe in the halo population have consistently small extinction values.

The median (and 16th, 84 percentile) value for extinction among halo PNe is

$$A_{V\text{halo}} = 0.08_{-0.08}^{+0.19} \text{ mag for } N_{\text{halo}} = 75, \text{ while for disk PNe it is much larger:}$$

$$A_{V\text{disk}} = 0.47_{-0.46}^{+0.76} \text{ mag for } N_{\text{disk}} = 333.$$

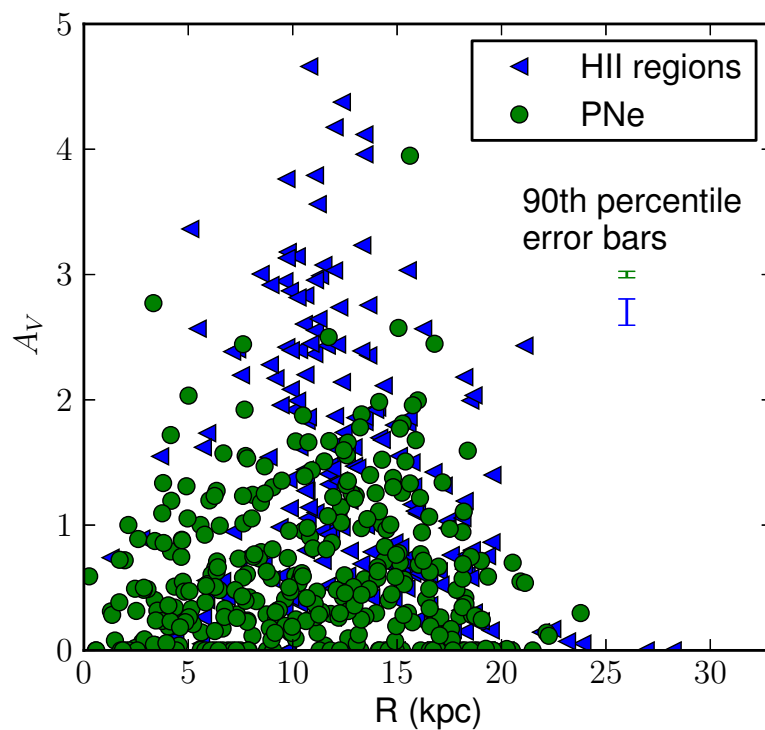


Figure 3.6.— Radial extinction profile for HII regions and disk PNe in M31. The procedure for estimating A_V is described in the text. Typical error bars are smaller than the size of the points, but 90th percentile error bars are shown to illustrate the uncertainty for the least-constrained PNe (green) and HII regions (blue).

It is reasonable to expect the extinction to trace abundance, because dust grains that cause reddening are composed of heavy elements (Shields 1990). Some studies have reported such parallel gradients in spiral galaxies (Sarazin 1976; Viallefond & Goss 1986; van der Hulst et al. 1988, for M33, M101, and M51, respectively), while others have measured flat extinction profiles (Viallefond & Goss 1986; Kaufman et al. 1987, for M33 and M81). In Figure 3.7 we show the oxygen abundance of HII regions and PNe in M31 against the extinction (A_V). This figure illustrates that there is not a clear correlation between extinction and oxygen abundance among the objects in our survey.

Regardless of any trends in the extinction with radius or abundance, it is clear that the extinction in M31 is patchy. For example, neighboring HII regions (< 0.5 kpc in deprojected distance, or $\approx 2.2'$ separation on the sky) differ in extinction by as much as 2.9 mag. Among the 98 such neighboring pairs in our sample with extinction measurements, 33% have a discrepancy in A_V of more than 1.1 mag (Figure 3.11). Some of this deviation is attributable to the large inclination of M31 introducing somewhat disparate column densities into the line of sight for apparently adjacent objects that are in front of and behind the disk.

3.3.2 Radial oxygen abundance gradient

The measurement of any abundance gradient among the M31 HII regions depends strongly on the choice of abundance diagnostic. For example, if we employ the N06 N2 diagnostic, we measure a gradient (-0.0195 ± 0.0055 dex kpc $^{-1}$) that is negative at the $\sim 4\sigma$ -level and consistent with the canonical value

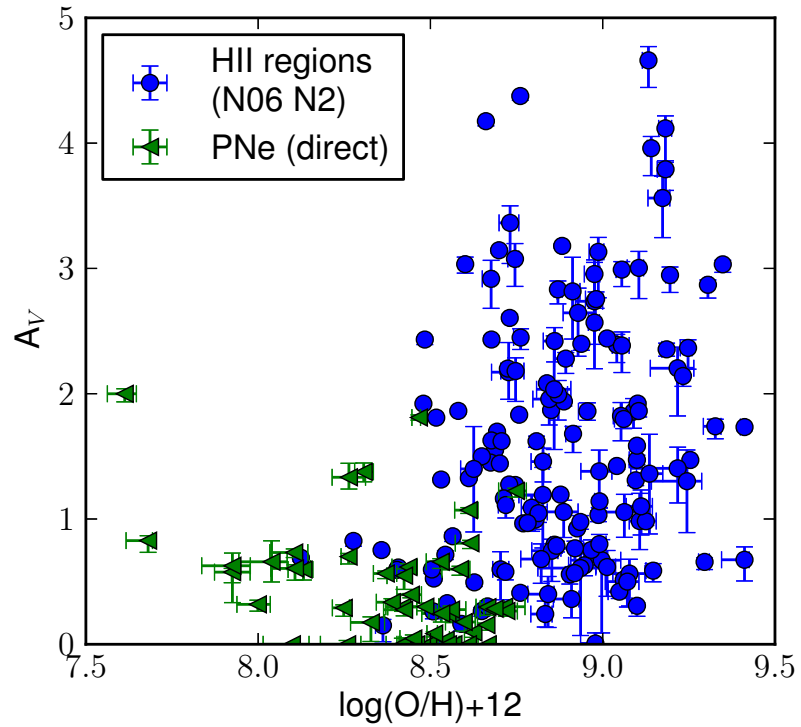


Figure 3.7.— The oxygen abundance of HII regions (N06 N2) and disk PNe (direct) in M31 vs the extinction (A_V) as measured from the Balmer decrement. Statistical error bars (derived as described in the text) are shown for each dimension, but are typically too small to be visible.

$(-0.020 \pm 0.007 \text{ dex kpc}^{-1})$ of Zaritsky et al. (1994). If we instead use the Z94 diagnostic, we find a gradient that is much less steep and only different from zero at the $\sim 1\sigma$ level $(-0.0208 \pm 0.0048 \text{ dex kpc}^{-1})$. The N06 O3N2 $(-0.0130 \pm 0.0068 \text{ dex kpc}^{-1})$ and KD02 $(-0.0096 \pm 0.0049 \text{ dex kpc}^{-1})$ diagnostics yield similar results. The p -value of the Spearman test suggests that a real correlation exists in all four cases, to varying degrees ($p_{\text{N2}} = 3 \times 10^{-04}$, $p_{\text{Z94}} = 2 \times 10^{-06}$, $p_{\text{O3N2}} = 0.06$, $p_{\text{KD02}} = 1 \times 10^{-04}$). If the PT05 diagnostic is used, however, we do not find a significant gradient $(-0.0054 \pm 0.0064 \text{ dex kpc}^{-1})$. The Spearman test reflects the lesser significance of the radial trend in this diagnostics ($p_{\text{PT05}} = 0.60$). Moreover, different results can be achieved if the sample is divided by morphological type or surface brightness (Section 3.3.4). We do not detect the temperature-sensitive auroral lines for enough HII regions to investigate the abundance gradient in the direct diagnostic.

An illustrative radial oxygen abundance profile of M31 HII regions is shown in Figure 3.8, using the N06 N2 diagnostic. This diagnostic is highlighted because it relies on only the brightest emission lines and is insensitive to flux calibration and reddening correction. It therefore produces reliable abundance estimates for a very large number of HII regions ($N = 192$). Also shown is the abundance gradient as fit by the bootstrap method: $(8.98 \pm 0.08) \text{ dex} + (-0.0195 \pm 0.0055) \text{ dex kpc}^{-1}$. This represents a relatively shallow gradient among the nearby spiral galaxies studied by Zaritsky et al. (1994), falling in the 11 – 26 percentile range based on the 1σ errorbars quoted above. Employing the isophotal radius $\rho_0 = 16 \text{ kpc}$ they define for M31, the size normalized gradient falls in the 16 – 32 percentile range.

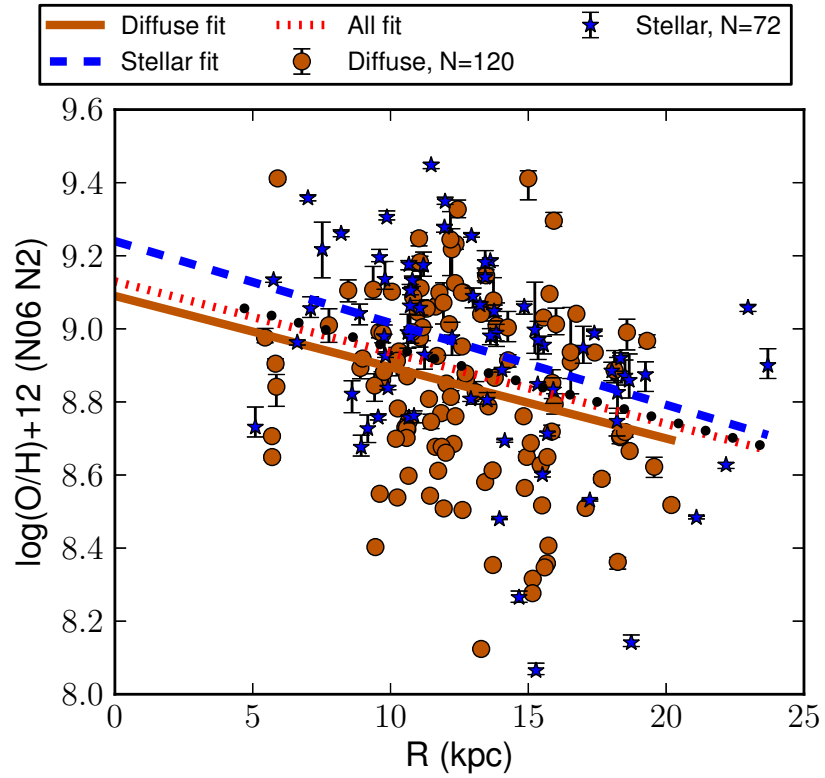


Figure 3.8.— The radial oxygen abundance profile of HII regions in M31 using the N06 N2 diagnostic. Each point is color-coded by the surface brightness of the H α emission line, as discussed in Section 3.2.4. The thick line is the best-fit linear abundance gradient, as derived using the bootstrap method described in the text. The lower and upper dashed lines are constructed from the 33rd and 66th percentile slope and offset parameters calculated in the bootstrap simulation, respectively, shown to illustrate the possible variation in the fitted gradient. The dotted line is the canonical gradient from Zaritsky et al. (1994). Statistical error bars (derived as described in the text) are shown for the oxygen abundance, but are frequently too small to be visible.

The radial oxygen abundance profile of M31 PNe is shown in Figure 3.9, using the direct abundance diagnostic. Also shown in the figure is the abundance gradient as fit by the bootstrap method, (-0.0056 ± 0.0076) dex kpc^{-1} , which is consistent with zero. The Spearman p -value is fairly large (0.45), emphasizing that there is no significant correlation between the PNe abundances and galactocentric radius. However, various systematic effects influence the interpretation of this correlation, as we will discuss in Section 3.3.5.

3.3.3 Intrinsic scatter

It is clear from Figures 3.8 and 3.9 that, regardless of what the true slope of the abundance gradients may be, there is significant intrinsic scatter about the trend.

In Figure 3.10 we characterize this scatter by calculating the standard deviation of the abundance of all HII regions in different radial bins for each abundance diagnostic. By dividing the sample into radial bins, as opposed to calculating the standard deviation of the entire sample, we partially remove the variance that would be introduced by an abundance gradient. While the KD02, PT05, and Z94 diagnostics seem to produce the least scatter (~ 0.1 dex), this could be in part due to selection effects; the emission lines necessary for calculating the R_{23} ratio are not accessible in fainter HII regions. If we consider the diagnostics with the largest sample size, N06 N2, the scatter in abundance rises from $\sim 0.2 - 0.3$ dex from the inner to outer regions of the disk. This is significantly larger than the scatter inherent to the abundance diagnostics themselves (e.g. ~ 0.07 dex for Z94 and PP04 N2, Kewley & Ellison 2008).

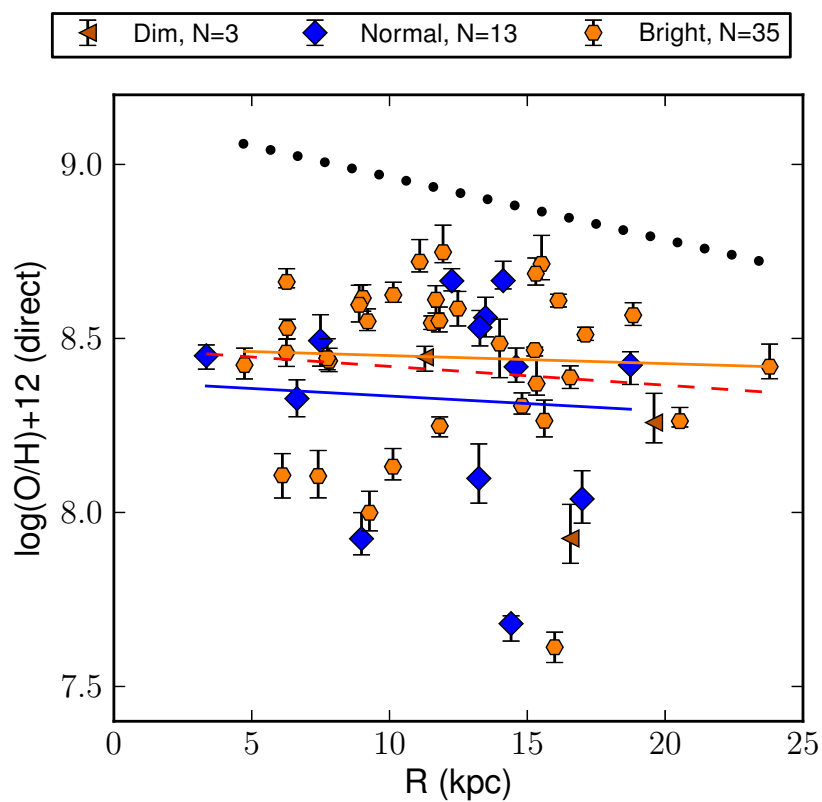


Figure 3.9.— The radial oxygen abundance profile of PNe in M31 using the direct diagnostic. The sample of PNe is divided into 3 luminosity classes as described in Section 3.2.4. A radial gradient is fit to the sample of each flux class, and the dashed red line illustrates the gradient fit to the full sample.

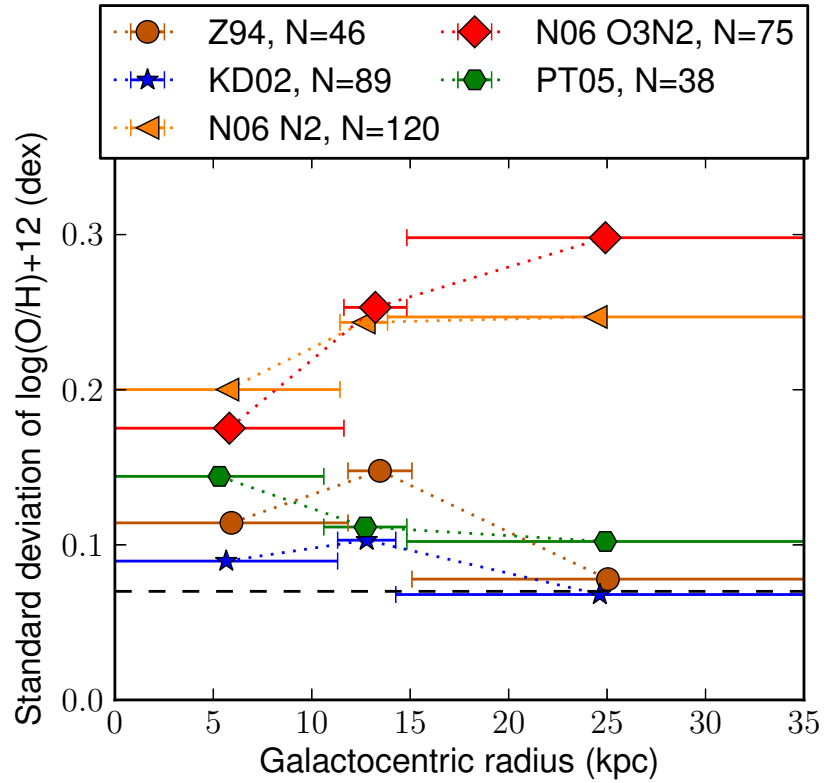


Figure 3.10.— The scatter in the radial oxygen abundance profile of the diffuse HII regions in M31. The horizontal dashed line at 0.07 dex represents the typical systematic error in the diagnostic (the mean rms error in the Z94 diagnostic from Kewley & Ellison 2008). The scatter is the standard deviation of the abundance of all HII regions in each of three different radial bins. The bins are chosen such that each bin has an equal number of objects. The bin edges are therefore different for each diagnostic, because the sample changes when different line ratios are required. Various abundance diagnostics are employed, with sample sizes as noted in the legend.

The conclusion that the intrinsic scatter in the abundance gradient is larger than the observational uncertainty reflects some studies in the literature. If the best-fit gradient is subtracted from the M31 HII region abundances measured in Zaritsky et al. (1994), then the standard deviation among the abundances is ~ 0.16 dex — similar to what we measure with the Z94 diagnostic. Rosolowsky & Simon (2008) found an intrinsic scatter of 0.11 dex among their 61 HII regions in M33, and asserted that this is larger than the precision of the measurements. However, Bresolin (2011) have argued that certain systematic effects have artificially increased the scatter measured by Rosolowsky & Simon (2008), particularly the inclusion of high-excitation HII regions and low S/N spectra. Because only 4 of our spectra meet the strict S/N threshold suggested by Bresolin (2011) (e.g. $S/N ([O\ III] \lambda 4363) > 5$), our dataset is not sufficient to address the intrinsic scatter in a subset of the data as they recommend. However, any high-excitation objects in our sample of the type discussed by Bresolin (2011) would instead be classified as PNe (Section 3.2.2), and therefore would not contaminate the HII region statistics. Moreover, the uncertainties in the strong line abundance measurements are negligible compared to the measures intrinsic scatter. For example, for the N06 N2 diagnostic our measurement uncertainties as propagated from the emission line flux uncertainties have a median of 0.03 dex and 90th percentile value 0.10 dex, much smaller than the $\gtrsim 0.2$ dex intrinsic scatter we measure in the radial abundance profile. Future spectroscopic studies of HII regions in M31 should acquire spectra of sufficient S/N in $[O\ III] \lambda 4363$ to measure the intrinsic scatter in the direct diagnostics.

In Figure 3.11, we investigate local fluctuations in the ISM of M31. We do

so by considering the discrepancy in extinction and abundance measurements among HII regions and disk PNe separated by less than $\approx 2.2'$ on the sky, corresponding to < 0.5 kpc in deprojected distance in M31. As we have previously discussed in Section 3.3.1, local fluctuations in extinction are often quite large — $\Delta(\text{O}/\text{H}) > 0.3$ dex and $\Delta A_V > 1.1$ mag for one third of HII regions and $\Delta(\text{O}/\text{H}) > 0.2$ dex for one third of disk PNe.

As illustrated in Figure 3.2, the oxygen abundance of the ISM of M31 is inhomogeneous. Neighboring HII regions (< 0.5 kpc in deprojected distance) differ in oxygen abundance (N06 N2) by as much as 0.6 dex, an order of magnitude. Among the 132 such neighboring pairs in our sample with N06 N2 abundance measurements, 33% have a discrepancy in $\log(\text{O}/\text{H})$ of more than 0.3 dex (Figure 3.11). These discrepancies could be partially explained by measurement uncertainty, however 0.4 dex is $\sim 5\times$ the scatter expected from the systematic uncertainties in the diagnostic (~ 0.07 dex for the similar PP04 N2 diagnostic, Kewley & Ellison 2008). This scatter is similar to the maximum discrepancy among the 8 PNe and 5 HII regions (~ 0.3 and ~ 0.2 dex, respectively) in the immediate solar neighborhood ($\lesssim 2$ kpc) observed by Rodríguez & Delgado-Inglada (2011). Only 20 neighboring PNe pairs have direct abundance estimates, so we do not consider their distribution of discrepancies.

We present spectra for an example of two neighboring HII regions with discrepant abundances in Figure 3.1. These are two diffuse HII regions (objects HII153 and HII166) that are separated by only $1.93'$ on the sky, corresponding to a separation of ~ 0.4 kpc at the distance of M31. When we calculate their galactocentric radii, the difference is 0.84 kpc, and their velocities only

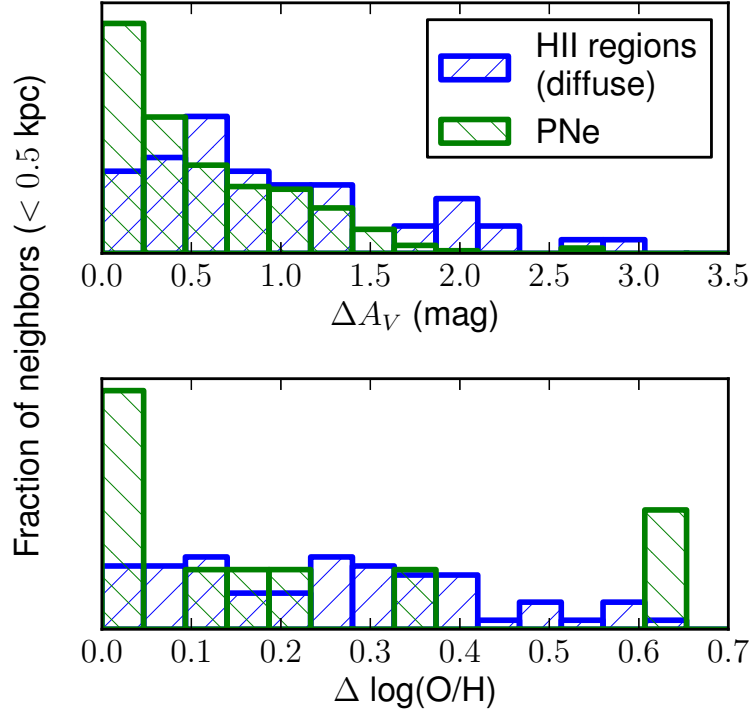


Figure 3.11.— The distribution of discrepancies between the extinction value and oxygen abundance (N06 N2 for HII regions, direct for PNe) of neighboring HII regions and PNe. Neighbors are defined as any pair of objects that are separated by $< 2.2'$ on the sky, corresponding to < 0.5 kpc in deprojected distance in M31. Halo PNe are excluded. There are 98 such neighboring HII region pairs with extinction measurements and 132 such pairs with oxygen abundance measurements in our sample; 502 and 20 PNe pairs, respectively.

differ by 24 km s^{-1} . Despite being so nearby, object HII153 is low metallicity ($\log(\text{O}/\text{H})_{\text{N06 N2}} + 12 = 8.36 \pm 0.04$) and object HII166 is high metallicity ($\log(\text{O}/\text{H})_{\text{N06 N2}} + 12 = 8.94 \pm 0.02$).

While it would be interesting to search for non-linearity in the abundance profile (such as breaks near the well-known star-forming ring of M31), the high-level of intrinsic abundance scatter present throughout the disc would make it difficult to evaluate different models.

For PNe, we estimate the intrinsic scatter in the O abundance of M31 disk PNe as $\gtrsim 0.26$ dex. Because we find no evidence of a significant radial trend in oxygen abundance for PNe, we simply calculate this number as the standard deviation of the 51 disk PNe with directly measured abundances. We consider this to be a lower limit because high-metallicity PNe are systematically excluded from our direct abundance sample due to the weakness of the auroral line. The median oxygen abundance is $\log(\text{O}/\text{H})+12 = 8.46$ dex. For the 17 PNe in the halo of M31 for which we can measure direct abundances, we find a median value and standard deviation of $\log(\text{O}/\text{H})+12 = 8.50 \pm 0.22$ dex. The median abundance in the halo is therefore lower than that in the disk, but this distinction is small given the intrinsic scatter in the abundances of each population.

Henry et al. (2010) derive the oxygen abundance gradient in the Galaxy from observations of 124 PNe with high-quality spectra and well-determined distances. They report a best-fit gradient of $-0.058 \pm 0.006 \text{ dex kpc}^{-1}$. They assert that the scatter around this best-fit gradient is $\sim 40\%$ larger than the uncertainties they ascribe to the abundance estimates. Similarly, we find an intrinsic scatter

in PNe abundances that is larger than the measurement error. the scatter in the M31 disk PNe abundances we report above is $\gtrsim 2\times$ larger than the median uncertainty in our disk PNe direct abundance estimates ($\sigma \sim 0.10$ dex, as derived by propagation of the line flux uncertainties). An accounting of systematic errors could inflate the asserted measurement error, but they could not account for the intrinsic scatter unless they alter the measured abundances by a factor of $\gtrsim 2$.

Rosolowsky & Simon (2008) and Magrini et al. (2010) invoke inefficient azimuthal mixing to explain local fluctuations in the ISM metallicity of M33 (but see also Bresolin 2011). In this scenario, mixing performed by velocity shear due to differential rotation occurs on a longer timescale ($\sim 10^8$ yrs) than enrichment by star formation in the spiral arms of the galaxy. Such a scenario could also apply to the inhomogeneities we observe in the ISM of M31.

3.3.4 Dependence on HII region properties

Due to its size and proximity, M31 provides a unique laboratory for studying the ISM of a spiral galaxy; for many extragalactic studies, only the brightest HII regions in the galaxy are accessible to spectroscopy. While the large number of relatively-dim HII regions included in our survey (Section 3.2.4) allows us to probe the ISM properties of M31 more thoroughly than ever before, it also has the potential to introduce discrepancies with past work. Here we investigate whether the measured abundance profile varies systematically with the brightness or compactness of the HII regions in the sample.

In Figure 3.12 we investigate the fitted abundance gradient parameters (slope

and characteristic abundance at 12 kpc) for the diffuse HII regions as a function of H α emission line flux density by dividing our sample into surface brightness bins (see Section 3.2.4). Although the bins are comprised of equal numbers of HII regions, because the S/N of spectral lines depends strongly on surface brightness, there are typically fewer abundance measurements available in the lower surface brightness bins. We adopt a minimum of 5 abundance measurements for performing abundance gradient analysis, which is the minimum number of HII regions sampled for any galaxy by Zaritsky et al. (1994). There are not sufficient PT05 abundance measurements to perform this analysis with that diagnostic. We find that the fitted slope and characteristic abundance parameters are essentially independent of surface brightness, varying by amounts consistent with the error bars on the fitted parameters.

This result contrasts with that reported by Magrini et al. (2010), who found that the abundance gradient in M33 was more than twice as steep for bright “giant” HII regions than for the less-luminous objects in their sample. Given the distance of M33 (840 kpc), their threshold for bright HII regions ($F_{\text{H}\alpha} \approx 1.2 \times 10^{34}$ ergs s $^{-1}$) is similar to our threshold for normal/bright HII regions. They attribute the surface-brightness dependence of the gradient to self-enrichment in giant HII regions. However, Magrini et al. (2010) derive metallicity gradients based on direct abundance measurements. Because Magrini et al. (2010) exclude $\sim 1/3$ of their spectroscopic sample due to insufficient S/N in the emission lines necessary to derive direct abundances, one possible systematic explanation for the stronger gradient they measure among brighter HII regions is that the [O III] $\lambda 4363$ line is weaker in high-metallicity HII regions.

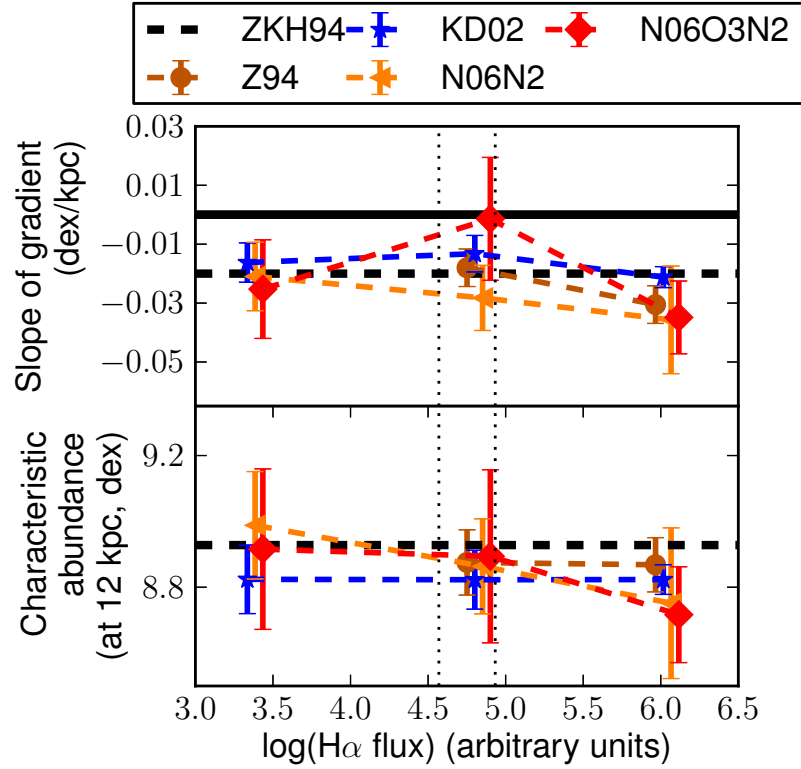


Figure 3.12.— The fitted parameters of the oxygen abundance ($\log(\text{O}/\text{H})+12$) gradient for diffuse HII regions in M31 in bins of $\text{H}\alpha$ emission line flux density. The bins were chosen such that they each have an equal sample size, as described in Section 3.2.4. The dotted vertical lines denote the width of the bin. The points are given small x-offsets for clarity. The y-errorbars are the bootstrap parameter uncertainties as described in the text. Different abundance diagnostics are used as noted in the legend.

Therefore high-metallicity HII regions may be systematically excluded from their lower-luminosity (not giant) HII region sample. Similarly, the strong-line methods we apply in this study carry certain selection effects (see Section 3.2.7), but we do not find that the gradient parameters vary significantly with brightness.

We can also investigate the abundance gradient as a function of HII region morphology (as described in Section 3.2.2). As described in Section 3.2.4, the morphological and surface brightness classifications are quite different, and the stellar HII regions may have PN contamination. Galarza et al. (1999) only found a significant radial abundance trend in the R_{23} line ratio for "center-brightened" (stellar) HII regions, and no gradient for HII regions of more extended morphology (diffuse). Generally, the abundance gradient slopes for diffuse HII regions reported in Table A.5 are in good agreement with the canonical value from Zaritsky et al. (1994), while the slopes for stellar HII regions are more shallow or consistent with zero. For example, in the Z94 diagnostic, the Spearman test indicates a significant gradient among diffuse HII regions ($p = 6 \times 10^{-05}$), but not stellar ($p = 0.06$). In detail, Table A.5 demonstrate that for most abundance diagnostics (e.g. N06 N2), the radial gradient slopes derived from objects of either morphology agree to within their errorbars ($\Delta \log(\text{O}/\text{H})_{+12\text{N06 N2}}^{\text{[diffuse,stellar]}} = [-0.0195 \pm 0.0070, -0.0224 \pm 0.0082]$ dex kpc $^{-1}$). Galarza et al. (1999) do not report a trend in $[\text{N II}]/\text{H}\alpha$ for objects of any classification, whereas we report significant and similar abundance gradients for this line ratio in both diffuse ($\Delta \log([\text{N II}]/\text{H}\alpha)_{\text{diffuse}} = -0.0177 \pm 0.0049$ dex kpc $^{-1}$) and stellar ($\Delta \log([\text{N II}]/\text{H}\alpha)_{\text{stellar}} = -0.0080 \pm 0.0056$ dex kpc $^{-1}$) HII regions, equivalent to the gradient measured in N06 N2 oxygen abundance. We do find a systematic offset in the N06N2 diagnostic, such that the best fit gradient

intercept (metallicity at the galactic center) for the [diffuse,stellar] HII regions is $\log(\text{O}/\text{H}) + 12 = [\text{HII} \text{diffuse} \text{Gradient} \text{Nohsix} \text{Ntwo} \text{Aboot}, 9.24 \pm 0.11]$ in the N06N2 diagnostic. This can be explained by a systematic difference in the hardness of the ionizing radiation in HII regions of these two morphological classes, which causes strong line methods which do not account for the ionization parameter to overestimate the metallicity of compact HII regions.

However, there are particularly strong disagreements between stellar and diffuse HII regions among the KD02 and PT05 diagnostics (Table A.5). In detail, these discrepancies are driven by the presence of anomalously high-metallicity ($\log(\text{O}/\text{H}) + 12 > 9.0$ on the KD02 scale) stellar HII regions. Because these HII regions are also dim, with surface brightness consistent with PNe in our sample, they are likely to be PN contaminants.

3.3.5 Time-variation in the abundance gradient

The HII regions in our sample are in general more enriched than the PNe, as is demonstrated by Figure 3.5. Similarly, the difference in the abundances of HII regions and PNe in M33 reported by Magrini et al. (2010) was ~ 0.1 dex and interpreted in the context of the time-varying composition of the ISM.

The median oxygen abundance and standard deviation for M31 disk PNe is $\log(\text{O}/\text{H}) + 12 = 8.46 \pm 0.26$ dex. Among HII regions studied with the N06 N2 diagnostic, the typical abundances are much larger ($\log(\text{O}/\text{H}) + 12 = 8.89 \pm 0.24$). This would suggest a similar discrepancy between HII regions and PNe as in M33; however, the median abundance we measure for PNe may be depressed

because of the selection effect on the [O III] $\lambda 4363$ line required to estimate direct abundances. Moreover, using a diagnostic that typically correlates between with direct abundance measurements, PT05, we find a smaller median metallicity for HII regions ($\log(\text{O}/\text{H})+12 = 8.34 \pm 0.12$); again, selection effects should act to exclude higher-metallicity objects. This illustrates the complicating role of systematic effects in comparing abundance measurements for a statistical sample of extragalactic HII regions and PNe.

In Figure 3.13, we bin the PNe by surface brightness to investigate the potential time-dependence of the abundance gradient. As discussed in Section 3.1, the luminosity of PNe are related to the masses of their progenitor stars and therefore to their ages. As in Section 3.3.4, we adopt a minimum of 5 measurements for performing gradient analysis in each bin, and we are therefore not able to fit an abundance gradient for the least bright PNe.

If the radial abundance gradient has strengthened over time, we would expect to find a gradient that is more negative with increasing PN surface brightness. In fact, the trend in the direct abundance is never strongly inconsistent with zero for either surface brightness bin. Among the brightest PNe, the slope is $-0.0023 \pm 0.0097 \text{ dex kpc}^{-1}$. We do find that the median metallicity increases with brightness class, with [8.26,8.42,8.49] dex for [Dim, Normal, Bright] PNe. However, because the auroral lines are only detectable in lower-metallicity PNe, selection effects could be eliminating high-metallicity PNe from our sample which could reveal a significant abundance gradient. Moreover, this selection effect would act more strongly to remove high-metallicity objects among the dimmer PNe, which would mimic the signature of increasing metallicity with PN surface

brightness.

Because direct abundance estimates can only be made for 51 of our 326 disk PNe spectra, it is worthwhile to look for gradients in strong line ratios such as R_{23} and $[\text{N II}]/\text{H}\alpha$. While these PN line ratios are not directly abundance-sensitive as they are in HII regions, significant gradients (if present) could indicate interesting trends in other physical properties. For $[\text{N II}]/\text{H}\alpha$, the gradient is positive at the $\sim 2\sigma$ level for the lowest-surface brightness bin ($0.0178 \pm 0.0108 \text{ dex kpc}^{-1}$), and increases significantly with surface brightness such that it is positive among the brightest PNe ($-0.0122 \pm 0.0059 \text{ dex kpc}^{-1}$). The existence of this N2 gradient, and its correlation with surface brightness, could indicate a time-varying gradient in excitation, chemical composition, or both. For R_{23} , the slope is never significantly different from zero in any brightness bin.

It would be difficult to distinguish time evolution in the abundance profile of M31 by comparing its PNe to HII regions, due to the intrinsic scatter in the populations and the uncertainties in the determination of the abundance gradients. Results would be particularly influenced by the choice of strong line diagnostic for HII region abundances, and by the cuts made on morphology/surface brightness (Section 3.3.2).

3.3.6 HII region nitrogen abundance gradient

While the oxygen abundance gradient is the most observationally accessible (Section 3.1), the radial nitrogen gradient is of particular interest because it may be the steepest of any observable element (e.g. in M33, Magrini et al.

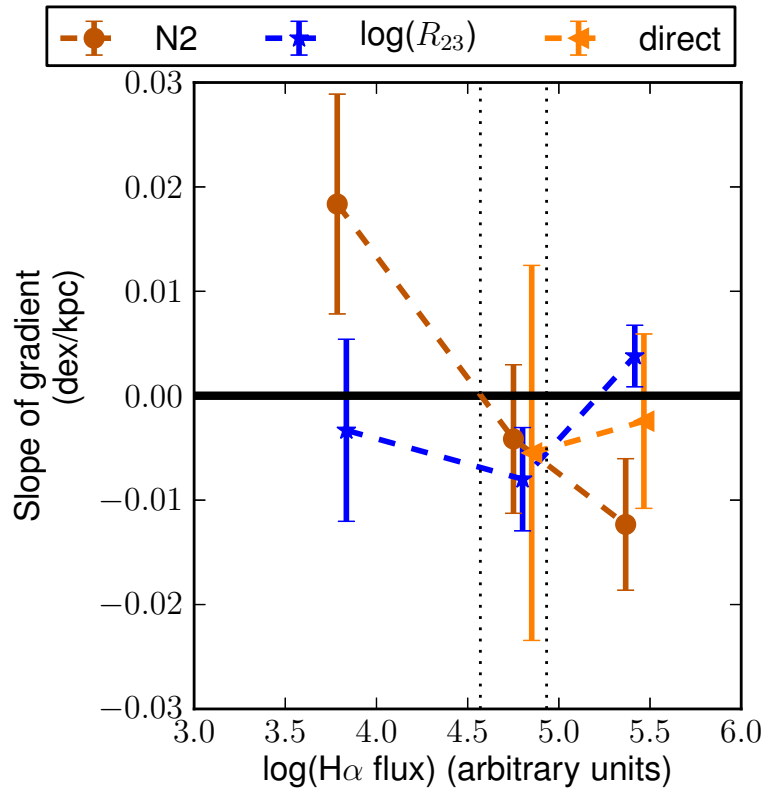


Figure 3.13.— The fitted parameters of the oxygen abundance ($\log(\text{O}/\text{H})+12$) gradient and line ratios for PNe in M31 in bins of $H\alpha$ emission line flux density. The figure is constructed similarly to Figure 3.12.

2010). The models of Magrini et al. (2010) show that the N gradient should be steeper than the O gradient due to the different timescales for production; N is produced primarily in low and intermediate-mass stars, while high-mass stars more efficiently produce O.

The radial nitrogen abundance profile of M31 HII regions is shown in Figure 3.14, using the diagnostics of Pilyugin et al. (2010). Also shown is the highly-significant ($\sim 4\sigma$) radial gradient for the diffuse objects as fit by the bootstrap method, $(7.83 \pm 0.08) \text{ dex} + (-0.0300 \pm 0.0058) \text{ dex kpc}^{-1}$. This slope is approximately as steep or steeper than all the oxygen abundance gradients reported for any diagnostic and morphological selection in Table A.5. However, it is only one third as steep as the nitrogen gradient in M33 ($-0.08 \pm 0.03 \text{ dex kpc}^{-1}$, Magrini et al. 2010). If we include the stellar HII regions ($N = 10$), we find a gradient that is similar ($-0.0303 \pm 0.0049 \text{ dex kpc}^{-1}$).

As for the oxygen abundances, we find a large intrinsic scatter about this gradient. Subtracting the fitted trend among all the HII regions, we find an rms scatter of 0.11 dex. This is significantly larger (~ 2 times) the systematic uncertainty attributable to the strong line diagnostic of (Pilyugin et al. 2010), who report an rms scatter of 0.05 dex (smaller than for the equivalent oxygen abundance diagnostic).

3.3.7 Comparison to previous observations of M31

A variety of authors have previously derived abundance gradients for M31 from other surveys of HII regions, as well as O and B stars.

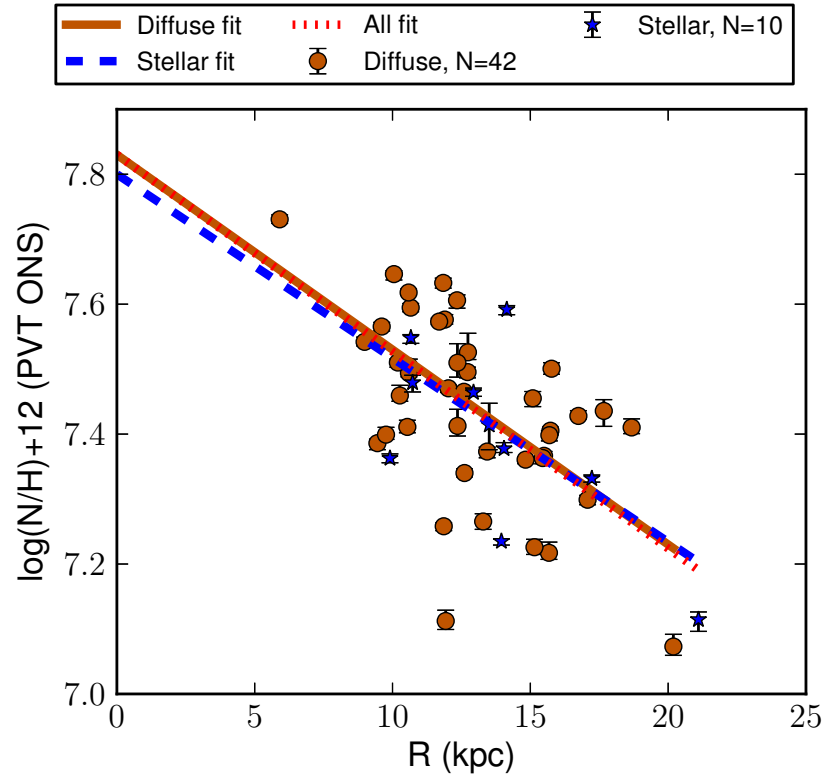


Figure 3.14.— The radial nitrogen abundance profile of HII regions in M31 using the diagnostic of Pilyugin et al. (2010). The figure is constructed similarly to Figure 3.8

As we have discussed, Dennefeld & Kunth (1981), Blair et al. (1982), Zaritsky et al. (1994), and Galarza et al. (1999) have previously derived the abundance gradient of M31 from surveys of HII regions. From those works, we have the canonical result of -0.020 ± 0.007 dex kpc^{-1} , produced by Zaritsky et al. (1994) from the combined sample of 19 HII regions from Dennefeld & Kunth (1981) and Blair et al. (1982). In their survey of 46 HII regions in M31, Galarza et al. (1999) found agreement with this gradient, but only among center-brightened HII regions. Among HII regions of other morphologies, they found no significant trends.

Trundle et al. (2002) derived oxygen abundances for 7 stars of type O and B from about 5 to 30 kpc in the disk of M31. Additionally, they provided a re-analysis of the HII regions of Blair et al. (1982) using modern diagnostics, producing gradients that range from -0.013 (P-method) to -0.027 (M91) dex kpc^{-1} . Their least squares fit to the stars yielded an abundance gradient of -0.017 ± 0.02 dex kpc^{-1} , in good agreement with the canonical result. However, they noted that if they omitted the possible multiple system OB 8-76, then they instead measured a slope consistent with zero (-0.006 ± 0.02 dex kpc^{-1}). Worthey et al. (2005) produced color-magnitude diagrams from HST images to derive the stellar abundance gradient in M31, finding (with some uncertainty in their zero point) good agreement between the upper bound of the metallicity of the stellar population and the HII regions surveyed by Blair et al. (1982) and Dennefeld & Kunth (1981) at a given radius.

The results of previous surveys of HII regions and high-mass stars suggest that any discrepancy between the M31 abundance gradients derived from

different sources are dependent on systematic effects related to sample selection and diagnostic. Similarly, Urbaneja et al. (2005) have found that the nebular abundance gradient can be smaller than, similar to, or larger than the stellar abundance gradient in the late-type spiral NGC 300 depending on the choice of diagnostic.

3.4 CONCLUSIONS

We have presented optical spectroscopy of an unprecedented sample of HII regions and PNe in a massive spiral galaxy, M31. In total, we reported line flux measurements for 253 HII regions and 407 PNe. We have derived the extinction, nitrogen abundance, and oxygen abundance for subsets of these objects using a variety of methods, as described in Section 3.2. From the analysis of these observations, we emphasize the following conclusions:

1. For HII regions, we find an oxygen abundance gradient generally consistent with that found by Zaritsky et al. (1994). Using the N06 N2 diagnostic, we find a gradient of (-0.0195 ± 0.0055) dex kpc^{-1} among 100HII regions. We find a significantly steeper gradient in nitrogen abundance, (-0.0303 ± 0.0049) dex kpc^{-1} among 52 HII regions. These represent relatively shallow gradients as compared to other nearby spiral galaxies.
2. For PNe, we detect no significant oxygen abundance gradient among 51 objects for which the [O III] $\lambda 4363$ line is detected and the direct method can be applied. However, using the line ratio $[\text{N II}]/\text{H}\alpha$, which is

measurable for most PNe ($N = 277$), we find significant gradients which vary systematically with PN brightness, as illustrated in Figure 3.13.

3. The ISM of M31 is highly inhomogeneous. Both the visual extinction (A_V) and oxygen abundance vary significantly among even very nearby HII regions (2.9 mag and 0.6 dex for some HII regions separated by < 2 kpc, see Figures 3.2 and 3.11). Moreover, the intrinsic scatter observed about the HII region oxygen abundance gradient ($\sim 0.1 - 0.3$ dex, see Figure 3.10) is larger than the uncertainty inherent to the strong line diagnostics (~ 0.1 dex). Similarly, the scatter among PNe in our sample is $\gtrsim 0.26$ dex.

4. The abundance gradient derived for HII regions in M31 is dependent upon the strong line metallicity diagnostic employed, and can be affected systematically by sample characteristics such as HII region morphology and surface brightness. In particular, for observations to a given depth, some diagnostics can only be applied to low or high-metallicity HII regions, unless they have sufficient surface brightness. Among more compact (not extended, i.e. “stellar”) nebulae that are spectroscopically classified as HII regions, we find evidence of PN contamination that can lead to erroneous strong line abundance measurements. Sample characteristics of this type should be taken into careful consideration to mitigate systematic effects in future surveys of the ISM of nearby spiral galaxies.

Chapter 4

A Spectroscopic Study of Type Ibc Supernova Host Galaxies from Untargeted Surveys

N. E. Sanders, A. M. Soderberg, E. M. Levesque, R. J. Foley, R. Chornock, D. Milisavljevic, R. Margutti, E. Berger, M. R. Drout, I. Czekala, J. A. Dittmann
2012, *The Astrophysical Journal*, Vol. 758, 132

Abstract

We present the first spectroscopic study of the host environments of Type Ibc supernovae (SN Ibc) discovered exclusively by untargeted SN searches. Past studies of SN Ibc host environments have been biased towards high-mass, high-metallicity galaxies by focusing on SNe discovered in galaxy-targeted SN searches.

Our new observations more than double the total number of spectroscopic stellar population age and metallicity measurements published for untargeted SN Ibc host environments. For the 12 SNe Ib and 21 SNe Ic in our metallicity sample, we find median metallicities of $0.62 Z_{\odot}$ and $0.83 Z_{\odot}$, respectively, but determine that the discrepancy in the full distribution of metallicities is not statistically significant. This median difference would correspond to only a small difference in the mass loss via metal-line driven winds ($\lesssim 30\%$), suggesting this does not play the dominant role in distinguishing SN Ib and Ic progenitors. However, the median metallicity of the 7 broad-lined SN Ic (SN Ic-BL) in our sample is significantly lower, $0.45 Z_{\odot}$. The age of the young stellar population of SN Ic-BL host environments also seems to be lower than for SN Ib and Ic, but our age sample is small. Combining all SN Ibc host environment spectroscopy from the literature to date does not reveal a significant difference in SN Ib and Ic metallicities, but reinforces the significance of the lower metallicities for SN Ic-BL. This combined sample demonstrates that galaxy-targeted SN searches introduce a significant bias for studies seeking to infer the metallicity distribution of SN progenitors, and we identify and discuss other systematic effects that play smaller roles. We discuss the path forward for making progress on SN Ibc progenitor studies in the LSST era.

4.1 INTRODUCTION

Core-collapse supernovae show a diversity of absorption features in their spectra near maximum light, reflecting a diversity in the composition of the outer envelope

of their massive star progenitors at the ends of their lives (Filippenko 1997; Woosley et al. 2002). In particular, some SNe show no evidence of hydrogen (Type Ib) or no evidence for either hydrogen or helium (Type Ic), suggesting extensive mass loss in the progenitor star sufficient to complete stripping of the H and He layers of its outer envelope (Elias et al. 1985; Filippenko & Sargent 1985; Wheeler & Levreault 1985; Uomoto & Kirshner 1985; Clocchiatti et al. 1996; Hachinger et al. 2012, but see also Dessart et al. 2012). Stellar evolutionary considerations point to two likely channels for these stripped-envelope core-collapse supernovae (Type Ibc supernovae).¹ These channels are: (i) high-mass Wolf-Rayet (WR) stars with strong metal line-driven winds with rotation likely playing an important role (Woosley et al. 1995; Georgy et al. 2012), and (ii) lower-mass helium-stars in close-binary systems who lose their envelopes via Roche lobe overflow or common envelope evolution (Podsiadlowski et al. 1992; Yoon et al. 2010; Dessart et al. 2011). Searches for the progenitor stars of SN Ibc in pre-explosion imaging have yet to yield a progenitor detection, but have provided upper limits that challenge the hypothesis that their progenitors are massive WR stars like those seen in the Local Group (Smartt 2009).

By measuring the metallicity of the host environments of Type Ibc SNe as a proxy for the metallicity of the progenitor stars, we may be able to distinguish between these two progenitor models. Mass loss in WR stars is enhanced at

¹Hereafter we use “SN Ibc” to refer to the class of stripped-envelope core-collapse supernovae generally. We define SN Ibc to include SNe of subtypes Ib, Iib, Ic, and Ic-BL. We use “SN Ib/c” to refer to supernovae whose spectroscopic type is uncertain, but likely to be one of the SN Ibc subtypes.

high metallicity (Vink & de Koter 2005). If the primary SN Ibc progenitor channel is single WR stars, then the rate of SN Ibc relative to SNe that show H features (SN II) would be enhanced at high metallicity (see e.g. Prantzos & Boissier 2003) and the ratio of SN Ic to Ib should similarly be higher. In binary progenitor systems, massive primary stars may still strip their envelopes primarily via WR winds, but there exists an additional channel for SN Ic to be produced by relatively low mass ($\sim 12 M_{\odot}$) stars which may dominate at low metallicity. This channel calls for the mass transfer to occur while the star is in the core helium burning or later phases (Yoon et al. 2010). Because either channel calls for massive, short-lived stars to produce the explosions, the metallicity of the SN host environment should be an appropriate proxy for the metallicity of the progenitor star.

Additionally, a connection has emerged between long-duration Gamma Ray Bursts (long GRBs) and one particular subtype of SN Ibc: broad-lined Type Ic SNe (Ic-BL; Kulkarni et al. 1998; see Woosley & Bloom 2006 for a review). The broad and highly blueshifted absorption features of SNe Ic-BL indicate high photospheric expansion velocities, $v_{\text{ph}} > 2 \times 10^4 \text{ km s}^{-1}$ (Iwamoto et al. 1998). This GRB-SN connection can be explained by the gravitational collapse of a massive ($M \gtrsim 20 M_{\odot}$) progenitor star that produces a rapidly rotating and accreting compact object (central engine) that powers a relativistic outflow (the collapsar model, MacFadyen et al. 2001). However, radio observations demonstrate that only a small fraction ($\lesssim 1/3$) of SNe Ic-BL harbor relativistic outflows (Soderberg et al. 2006a, 2010). Because angular momentum loss due to metal line-driven winds could prevent the compact remnant from rotating fast

enough to produce a relativistic outflow, a metallicity threshold ($Z \lesssim 0.3 Z_{\odot}$) has been proposed for collapsars (Woosley & Heger 2006).

Recent observations fundamentally challenge the role of metallicity in GRB production (Fryer et al. 2007). SN 2009bb provides an example of a SN Ic-BL produced in a super-solar metallicity environment and harboring a central engine (Levesque et al. 2010d; Soderberg et al. 2010), and LGRBs with relatively high-metallicity host environments have now been identified (Levesque et al. 2010c; Graham et al. 2009). In contrast, SN 2010ay was a SN Ic-BL with extreme explosion properties that occurred in a sub-solar metallicity environment and without evidence for a central engine (Sanders et al. 2012d; see also SN 2007bg, Young et al. 2010).

In the past few years, several observational studies have sought to measure the characteristics of the host environments of SN Ibc. Prieto et al. (2008) used SDSS spectroscopy to study the metallicity distribution of 115 SNe (19 SN Ibc) and found that SN Ibc host environments are metal-enriched compared to those of SN II. Extending the work of Prantzos & Boissier (2003), Boissier & Prantzos (2009) reach a similar result using SDSS photometry to estimate metallicities for 701 SN (98 SN Ibc) host galaxies. Arcavi et al. (2010) examine the host galaxies of core-collapse SNe discovered by the Palomar Transient Factory (PTF) and find that SN Ic are more common in high-metallicity environments (“giant” host galaxies, $M_r < -18$ mag), while SN Ib, Iib and Ic-BL dominate in low-metallicity environments (“dwarf” host galaxies). Anderson et al. (2010) and Leloudas et al. (2011) perform spectroscopy to measure the metallicity of the host environments of 28 and 20 SN Ibc, respectively, finding no statistically significant difference

between the metallicity distribution of SN Ib and Ic. Extending the work of Modjaz et al. (2008), Modjaz et al. (2011b) performed a similar spectroscopy study of 35 SN Ibc host environments, finding that SN Ic come from significantly higher-metallicity host environments than SN Ib, with SN Ic-BL falling in between. Following Kelly et al. (2008), Kelly & Kirshner (2012) have examined SDSS spectroscopy of 519 SNe (67 SN Ibc), finding that SN Ic-BL preferentially occur in low-mass, low-metallicity host galaxies relative to other core-collapse SNe.

However, there is a prominent observational bias that affects the progenitor metallicity distribution inferred from observations of most known SN host galaxies. The well-known relation between the luminosity and global-metallicity of star-forming galaxies (the $L - Z$ relation, see e.g. Tremonti et al. 2004) indicates that a metallicity distribution measured only from objects found in targeted SN searches, which look for transients in fields centered on nearby and luminous galaxies, will be biased towards high metallicities.

Here we describe a new spectroscopic study of SN Ibc host galaxy metallicities unbiased with respect to the $L - Z$ relation. We have obtained spectra of 60 host environments of SN Ibc discovered only by untargeted transient searches (13 SNe Ib, 10 SNe I Ib, 24 SNe Ic, 8 SNe Ic-BL, 3 of indeterminate type SN Ib/c, and 2 with AGN-dominated host environments, Section 4.2.3). Previous spectroscopic studies of SN Ibc host environments have included relatively few SNe discovered by untargeted searches, totaling $\lesssim 40$ objects. Our study doubles the existing sample of host environment spectroscopy for untargeted SN Ibc, offering considerable constraining power for inferring the metallicity distribution

of the parent population.

In Section 4.2 we describe the characteristics of this sample, our optical observations, and our spectroscopic methodology. We present and analyze the host galaxy metallicities and other physical properties derived from these observations in Section 4.3 and combine with previous spectroscopic surveys of SN Ibc host environments in Section 4.4. In Section 4.5 we discuss possible systematics affecting our results. In Section 4.6 we discuss our results in relation to SN Ibc progenitor models and the SN-GRB connection and we suggest implications for future studies of SN Ibc. We conclude in Section 4.7.

4.2 SAMPLE CONSTRUCTION

4.2.1 SN sample

We have observed the host galaxies of 60 SNe Ibc reported in the International Astronomical Union Circulars (IAUCs)² and/or Astronomer’s Telegrams³ between 1990-2011. When transient searches operate by returning repeatedly to a pre-selected, typically bright, set of galaxies, we refer to the SNe found in those galaxies by those searches to be “targeted.” We refer to any SN discovered by other means as “untargeted,” including discoveries by wide-field optical surveys, SNe identified by targeted searches in anonymous background galaxies, and

²f1.html

³<http://www.astronomerstelegram.org/>

SNe discovered serendipitously during observations of unrelated objects. We observed only untargeted discoveries and prioritized those SNe with reliable classifications, host galaxies which did not already have previously published metallicity measurements, and which were visible at low airmass during the time of our observations.

In total, we present optical spectroscopy with S/N sufficient for metallicity measurements for 50 host galaxies, with median redshift $z = 0.036$. The discoverer of each SN in our sample is listed in Table 4.1. Acronyms for untargeted SN searches are as follows: Catalina Real-time Transient Survey (CRTS; Drake et al. 2009a), the Equation of State: SupErNovae trace Cosmic Expansion program (ESSENCE; Miknaitis et al. 2007), the La Silla-QUEST Variability Survey (LSQ; Hadjiyska et al. 2011), the Palomar Transient Factory (PTF; Law et al. 2009), the Sloan Digital Sky Survey-II Supernova Survey (SDSS; Frieman et al. 2008), and the Nearby Supernova Factory (SNF, including supernovae discovered by NEAT; Aldering et al. 2002). Some objects were discovered serendipitously in background galaxies during targeted SN searches or other wide-field surveys, including the CHilean Automatic Supernova sEarch (CHASE; Pignata et al. 2009) and the Lick Observatory Supernova Search (LOSS; Li et al. 2011). Spectroscopic metallicity estimates have been previously published for only 15 of these galaxies. A comparison to previous spectroscopic studies of SN Ibc host environments is presented in Section 4.4.1; additionally, the host environment of SN 2009jf was previously studied by Valenti et al. (2011) (see also Sahu et al. 2011).

Table 4.1. Properties of SNe in Untargeted Sample

SN	Type ^a	Sample ^b	z	Slit ^c	Discoverer ^d	Classification ^e
1991R	Ibc	S	0.035	0.7	McNaught & McKenzie (1991)	Leibundgut et al. (1991)
2002ex	Ib	G	0.037	1.1	SNF	S.
2002gz	I l b-pec	S	0.085	1.1	SNF	Hamuy et al. (2003)
2003ev	Ic	G	0.024	0.5	LOSS	Filippenko & Chornock (2003)
2004cf	Ib	S	0.248	5.8	Riello et al. (2004b)	M. T. Botticella
2004ib	Ic	G	0.056	1.1	SDSS	G. Leloudas
2005hm	Ib	G	0.034	1.0	SDSS	Leloudas et al. (2011)
2005nb	Ic-BL	G	0.024	0.5	Quimby et al. (2006)	Modjaz et al. (2011b)
2006ip	Ic	G	0.031	0.6	SNF	Modjaz et al. (2011b)
2006ir	Ic	G	0.021	0.4	SNF	Leloudas et al. (2011)
2006jo	Ib	G	0.077	1.4	SDSS	Leloudas et al. (2011)
2006lc	Ib	G	0.016	0.3	SDSS	Blondin et al. (2006b)
2006nx	Ic-BL	G	0.137	2.4	SDSS	Modjaz et al. (2011b)
2006tq	Ic	S	0.261	3.0	ESSENCE	Challis et al. (2007) ^f
2007I	Ic-BL	G	0.022	0.4	LOSS	Modjaz et al. (2011b)
2007az	Ib	G	0.035	1.0	LOSS	Silverman et al. (2007)
2007br	I l b	G	0.053	1.0	SNF	R. Thomas
2007ce	Ic-BL	S	0.046	0.9	Quimby et al. (2007)	Odehahn & Terrazas (2007)
2007db	Ic	G	0.048	0.7	SNF	R. Thomas
2007ea	I l b	G	0.040	0.8	SNF	R. Thomas
2007ff	Ic	S	0.049	0.7	SNF	R. Thomas
2007gg	Ib	G	0.038	0.8	SNF	R. Thomas
2007gl	Ic	G	0.028	0.4	SNF	R. Thomas
2007hb	Ic	G	0.021	0.4	SNF	R. Thomas
2007hl	Ic	S	0.056	1.1	SNF	R. Thomas
2007hn	Ic	G	0.028	0.6	SNF	Leloudas et al. (2011)
2008ao	Ic	G	0.015	0.3	Dimai (2008)	Steele et al. (2008)
2008fi	I l b	G	0.026	0.5	Skvarc & Mikuz (2008)	Silverman et al. (2008)
2008gc	Ib	G	0.049	0.7	CHASE	Stritzinger et al. (2008a)
2008ik	Ic	G	0.064	0.9	CHASE	Stritzinger et al. (2008b)
2008im	Ib	G	0.008	0.2	Oksanen (2008)	S.
2008iu	Ic-BL	S	0.130	1.6	CRTS	Drake et al. (2009b)
2009hu	Ib	G	0.117	2.1	Sand et al. (2009)	Sand et al. (2009)
2009jf	Ib	G	0.008	0.1	LOSS/PTF	Valenti et al. (2011)
2009nl	Ic	G	0.113	1.8	CRTS	A. Drake
2010Q	Ic	G	0.054	1.0	CRTS	A. Drake
2010ah	Ic-BL	G	0.050	1.0	PTF	Corsi et al. (2011)
2010am	I l b	G	0.020	0.4	CRTS	Cenko et al. (2010)

Table 4.1—Continued

SN	Type ^a	Sample ^b	z	Slit ^c	Discoverer ^d	Classification ^e
2010ay	Ic-BL	G	0.067	1.3	CRTS	Sanders et al. (2012d)
2010cn	Ib/I Ib-pec	G	0.026	0.5	CHASE	^g
2010lz	Ic	G	0.090	1.2	CRTS	A. Drake
2011D	I Ib	G	0.023	0.3	CRTS	Marion et al. (2011)
2011V	I Ib	G	0.014	0.3	CRTS	Milisavljevic et al. (2011)
2011bv	I Ib	G	0.072	1.0	CRTS	Prieto (2011)
2011cs	Ic	G	0.101	1.8	CRTS	Drake et al. (2011b)
2011gh	Ib/c	S	0.018	0.4	CRTS	Magill et al. (2011)
2011hw	I bn	G	0.021	0.4	Dintinjana et al. (2011)	Smith et al. (2012)
2011ip	Ic	S	0.051	1.0	Denisenko et al. (2011)	S., S. Valenti
2011it	Ic	G	0.016	0.3	Ciabattari et al. (2011)	S.
LSQ11JW	Ib	G	0.020	0.4	LSQ	S.
PTF09dfk	Ib	G	0.016	0.2	PTF	A. Gal-Yam
PTF09dxv	I Ib	G	0.032	0.4	PTF	A. Gal-Yam
PTF09iqd	Ic	G	0.034	0.7	PTF	A. Gal-Yam
PTF09q	Ic	G	0.090	1.7	PTF	A. Gal-Yam
PTF10aavz	Ic-BL	G	0.063	0.9	PTF	S.
PTF10bip	Ic	G	0.051	1.0	PTF	A. Gal-Yam
PTF10vgv	Ic	G	0.015	0.3	PTF	Corsi et al. (2012)
PTF11hyg	Ic	G	0.028	0.6	PTF	A. Gal-Yam

^aA detailed discussion of SN classification is given in Section 4.2.1.

^bG indicates the Gold sample and S indicates the Silver sample, as defined according to security of spectroscopic classification in Section 4.2.1.

^cThe width of the spectroscopic slit in (see Table 4.2) in physical units (kpc) at the distance of the SN.

^dReference for the discovery of the supernova.

^eReference for spectroscopic classification of SN type. Author names refer to private communications with observers who performed spectroscopy of the SN. “S.” indicates our own spectroscopy.

^fAdditionally, private communication with S. Blondin (2012) indicates that the classification spectrum for SN 2006tq is not of S/N sufficient for the Gold sample.

^gVarying spectroscopic classifications of SN 2010cn are reported by Marion et al. (2010); Silverman et al. (2010); Folatelli & Stritzinger (2010); we consider it a SN I Ib for the purposes of our analysis.

Table 4.2. SN Host Galaxy Sample and Observing Configurations

SN	SN α_{2000}	SN δ_{2000}	Date (UT)	Instrument	Disperser ^a	Exp. time) ^b (s) ^b	Slit width	E/N ^c
1991D ^d	13:41:13.58	-14:38:47.6	2008 May 30	LDSS3	VPH_All	600	1.0''	E
1991R	15:54:53.52	+19:00:43.9	2008 May 30	LDSS3	VPH_All	600	1.0''	E
2002ex	22:09:00.79	-10:36:25.8	2008 June 29	LDSS3	VPH_Blue/Red	1200/1020	1.5''	E
2002gz	02:34:10.36	-00:53:18.2	2008 June 29	IMACS	300-17.5	1200	0.7''	E
2003ev	13:10:31.80	-21:39:49.6	2008 June 1	LDSS3	VPH_All	900	1.0''	E
2003jpd	23:26:03.28	-08:59:22.7	2007 Dec. 17	LDSS3	VPH_All	600	0.75''	N
2004cf	14:11:05.77	-11:44:09.4	2006 June 30	LDSS3	VPH_Red	1800	1.5''	N
2004ib	02:40:56.40	-00:10:48.3	2007 Dec. 16	LDSS3	VPH_All	1200	1.0''	E
2005hm	21:39:00.65	-01:01:38.7	2006 June 30	LDSS3	VPH_Blue/Red	2100/1500	1.5''	E
2005nb	12:13:37.61	+16:07:16.2	2008 May 31	LDSS3	VPH_All	415	1.0''	E
2006ip	23:48:31.68	-02:08:57.3	2007 Dec. 16	LDSS3	VPH_All	1200	1.0''	N
2006ir	23:04:35.68	+07:36:21.5	2007 Dec. 14	LDSS3	VPH_All	1200	1.0''	E
2006jo	01:23:14.72	-00:19:46.7	2006 Dec. 24	LDSS3	VPH_Blue/Red	1000/600	1.0''	N
2006lc	22:44:24.48	-00:09:53.5	2007 Dec. 14	LDSS3	VPH_All	900	1.0''	N
2006nx	03:33:30.63	-00:40:38.2	2006 Dec. 24	LDSS3	VPH_Blue/Red	1500/750	1.0''	N
2006tq	02:10:00.70	+04:06:00.9	2012 Jan. 18	LDSS3	VPH_ALL	1200	0.75''	N
2007I	11:59:13.15	-01:36:18.9	2008 Jan. 17	LDSS3	VPH_All	1800	1.0''	N
2007az	08:25:23.80	+69:54:29.4	2011 Dec. 24	BC	300GPM	1200	1.5''	E
2007br	11:15:39.93	-04:22:47.8	2007 Dec. 14	LDSS3	VPH_All	1200	1.0''	N
2007ce	12:10:17.96	+48:43:31.5	2012 Jan. 01	BC	300GPM	1800	1.0''	E
2007db	11:17:10.30	-06:11:48.6	2007 Dec. 15	LDSS3	VPH_All	900	0.75''	N
2007ea	15:53:46.27	-27:02:15.5	2008 May 30	LDSS3	VPH_All	1200	1.0''	E
2007ff	01:24:10.24	+09:00:40.5	2007 Dec. 17	LDSS3	VPH_All	1200	0.75''	N
2007gg	00:28:12.51	+00:07:04.8	2011 Sep. 06	BC	300GPM	1200	1.0''	E
2007gl	01:05:50.11	+00:08:41.3	2011 Sep, 21	IMACS	300-17.5	1200	0.7''	E
2007hb	05:02:01.28	-21:07:55.1	2011 Nov. 19	IMACS	300-17.5	600	0.9''	E
2007hl	20:50:07.76	-01:58:36.4	2008 May 30	LDSS3	VPH_All	900	1.0''	E
2007hn	21:02:46.85	-04:05:25.2	2008 May 30	LDSS3	VPH_All	600	1.0''	N
2008ao	03:07:46.66	+38:22:06.2	2012 Jan. 01	BC	300GPM	1800	1.0''	E
2008fi	01:53:23.17	+29:21:28.4	2012 Jan. 19	BC	300GPM	1200	1.0''	E
2008gc	02:10:36.63	-53:45:59.5	2012 Jan. 18	LDSS3	VPH_All	600	0.75''	E
2008ik	03:36:09.54	-35:13:00.7	2012 Jan. 20	LDSS3	VPH_All	600	0.75''	E
2008im	04:01:02.15	+74:05:48.5	2011 Dec. 24	BC	300GPM	500	1.5''	E
2008iu	04:36:55.20	-00:21:35.6	2011 Sep. 21	IMACS	300-17.5	1200	0.7''	E
2009hu	14:53:29.82	+18:35:31.1	2012 Jan. 01	BC	300GPM	1800	1.0''	E
2009jf	23:04:52.98	+12:19:59.5	2011 Nov. 18	IMACS	300-17.5	600	0.7''	E
2009nl	03:39:47.78	-11:13:25.0	2011 Sep. 20	IMACS	300-17.5	1200	0.9''	E

Table 4.2—Continued

SN	SN α_{2000}	SN δ_{2000}	Date (UT)	Instrument	Disperser ^a	Exp. time) ^b (s) ^b	Slit width	E/N ^c
2010Q	10:26:27.11	+39:01:50.9	2012 Jan. 18	BC	300GPM	1800	1.0''	E
2010ah	11:44:02.99	+55:41:27.6	^e	BC	300GPM	1500+1200	1.0''	E
2010am	09:33:01.75	+15:49:08.8	2012 Jan. 01	BC	300GPM	1800	1.0''	E
2010ay	12:35:27.19	+27:04:02.8	2010 Apr. 11	GMOS	R400	1800	1.0''	E
2010cn	11:04:06.57	+04:49:58.7	2012 Jan. 18	BC	300GPM	1200	1.0''	E
2010lz	01:50:20.32	-21:44:31.9	2012 Jan. 19	LDSS3	VPH_All	1500	0.75''	E
2011D	03:02:14.58	+17:20:58.9	2011 Nov. 29	IMACS	300-17.5	500	0.7''	E
2011V	09:27:38.76	+28:47:27.2	2012 Jan. 01	BC	300GPM	1800	1.0''	E
2011bv	13:02:53.57	-04:02:36.0	2012 Jan. 19	LDSS3	VPH_All	1200	0.75''	E
2011cs	12:08:01.08	+49:13:33.0	2012 Jan. 19	BC	300GPM	1500	1.0''	E
2011gh	03:16:54.20	+25:54:14.6	2012 Jan. 18	BC	300GPM	600	1.0''	E
2011hw	22:26:14.54	+34:12:59.1	2011 Nov. 29	BC	300GPM	600	1.0''	E
2011ip	1:13:47.59	-12:41:06.0	2011 Dec. 31	BC	300GPM	1800	1.0''	E
2011it	22:02:44.45	+31:41:49.1	2011 Dec. 31	BC	300GPM	600	1.0''	E
LSQ11JW	02:04:47.40	+00:50:06.0	2011 Dec. 31	BC	300GPM	1200	1.0''	E
PTF09q	12:24:50.11	+08:25:58.8	2012 Jan. 18	BC	300GPM	600	1.0''	E
PTF09dfk	23:09:13.42	+07:48:15.4	2011 Sep. 21	IMACS	300-17.5	900	0.7''	E
PTF09dxv	23:08:34.73	+18:56:13.7	2011 Nov. 18	IMACS	300-17.5	500	0.7''	N
PTF09iqd	02:35:23.23	+40:17:08.7	2012 Jan. 18	BC	300GPM	500	1.0''	N
PTF10aavz1	12:20:13.36	+03:44:45.2	2011 Jan. 13	LDSS3	VPH_All	1200	0.75''	E
PTF10bip	12:34:10.52	+08:21:48.5	2012 Jan. 01	BC	300GPM	1800	1.0''	E
PTF10vgv	22:16:01.17	+40:52:03.3	2011 Sep. 06	BC	300GPM	1200	1.0''	E
PTF11hyg	23:27:57.34	+08:46:38.0	2011 Sep. 06	BC	300GPM	1200	1.0''	E

^aThe grism or grating used in the spectroscopic observation. When multiple configurations were used, we list both, separated with a slash.

^bThe exposure time of the spectroscopic observations. When two times are given separated by a slash, they correspond to two different dispersers.

^cE indicates a slit position on the SN explosion site, N indicates slit placement at the galaxy center (see Section 4.2.2)

^dObjects excluded from the sample due to AGN contamination; see Section 4.2.3.

^eSpectra acquired on 2011 May 06 and 2012 Jan. 18 were coadded.

For those SNe in our sample whose classification spectroscopy is not well discussed in the circulars or the literature, we confirm the spectroscopic classification by contacting the authors of the classification circular to re-evaluate their original spectra using e.g., the Supernova Identification tool (Blondin & Tonry 2007) (see private communications in Table 4.1). We construct a “Gold” sample of 48 SNe for which the classification spectrum suggests a clear subtype (but see Section 4.5.3); a “Silver” sample of 10 SN where the classification is based on a spectrum with poor S/N. SNe where we are not able to distinguish between two sub-types are listed as “Undetermined Ibc.” For the purposes of this study, we consider the peculiar object SN 2011hw (classified as Type Ibn; Smith et al. 2012) to be of indeterminate type, we consider SN 2006lc (whose He lines were weak) a Type Ib (Leloudas et al. 2011), and we group the peculiar Type IIb SNe 2002gz and 2010cn together with the other Type IIb SNe.

4.2.2 Spectroscopic Observations

We obtained acquisition images in r -band and long-slit spectra ($\sim 3600 - 8500 \text{ \AA}$) of 25 SN Ibc host galaxies using the Low Dispersion Survey Spectrograph 3 (LDSS3) instrument on the Magellan-Clay Telescope, 23 using the BlueChannel Spectrograph (BC) on the MMT (for which there is no associated imager), 9 using the Inamori-Magellan Areal Camera & Spectrograph (IMACS) instrument on the Magellan-Baade Telescope, and 1 using the Gemini Multi-Object Spectrograph (GMOS) instrument on the Gemini-North Telescope. The host galaxies were observed at the parallactic angle, except for some IMACS spectra which were

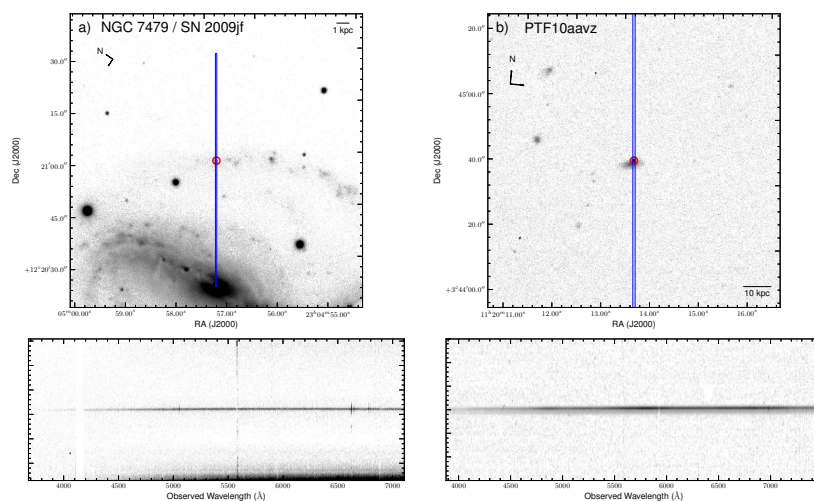


Figure 4.1.— Example of optical spectroscopy procedure for two SN Ibc host galaxies in our sample. Shown are the r -band acquisition images (top) and 2D-spectrum (bottom) obtained using Magellan/IMACS and LDSS3 (see Table 4.2) for a) the Type Ib SN 2009jf host environment in the galaxy NGC 7479 ($z = 0.008$) and b) the Type Ic-BL PTF10aavz ($z = 0.063$). The slit (blue rectangle) was aligned with the SN explosion site (red circle). The IMACS chip gap is visible in the spectrum at $\sim 4100 \text{ \AA}$.

obtained with the atmospheric dispersion compensator.

When possible, the spectrum was extracted at the location of the SN explosion site within the host galaxy. We consider the spectrum to sample the explosion site (“E”; 43 SNe) when we extract at the position of the explosion site and the slit width corresponds to a physical size $\lesssim 2$ kpc ($z \leq 0.11$ for a 1” slit), and otherwise consider the spectrum nuclear (“N”; 15 SNe, see Table 4.2). Explosion site spectroscopy represents a luminosity-weighted average of the physical properties of the star-forming gas within the extracted region. However, because our SN sample consists of events discovered by galaxy-impartial surveys, the host galaxies are typically smaller and more distant than those observed in previous studies. In some cases, the explosion sites of SNe in the outskirts of their host galaxies did not have sufficient flux for spectroscopy and instead we extract at the galaxy nucleus. Some intrinsically-dim host galaxies have apparent sizes so small that a significant fraction of all the galaxy light will fall in the slit, even at relatively-low redshift (see Figure 4.1). For comparison, the explosion site spectroscopy of Modjaz et al. (2011b) includes host galaxies at a maximum redshift of $z = 0.183$ using a 1” slit (~ 3 kpc) and the studies of Prieto et al. (2008) and Kelly & Kirshner (2012) employ 3” SDSS fiber spectroscopy for SN Ibc at $z \lesssim 0.04$ (~ 2 kpc) and 0.07 (~ 4 kpc), respectively.

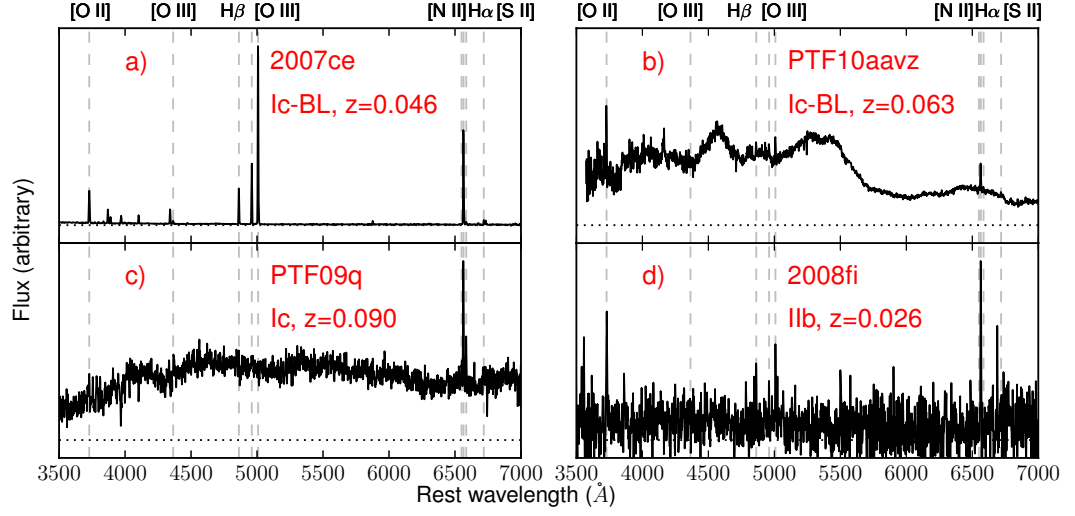


Figure 4.2.— Examples of spectra from our SN Ibc host environment observations. The panels are labeled with the names, classifications, and redshifts of the SNe and represent a) a high-S/N spectrum dominated by nebular emission from the host environment, b) a spectrum dominated by SN flux, c) a spectrum dominated by stellar continuum, and d) a low S/N spectrum dominated by nebular emission from the host environment. The gray vertical lines illustrate the position of the major nebular emission features used in the metallicity analysis. The continuum level can be judged against the dashed horizontal line, illustrating zero flux.

4.2.3 Spectroscopic analysis

We employed standard two-dimensional long-slit image reduction and spectral extraction routines in IRAF⁴. Examples of reduced spectra are displayed in Figure 4.2.

The line fluxes of prominent nebular emission lines ($H\alpha$ and $H\beta$; [O II] $\lambda 3727$ ⁵, [O III] $\lambda 4363$, [O III] $\lambda 4959$, [O III] $\lambda 5007$, [N II] $\lambda\lambda 6548, 6584$; and [S II] $\lambda\lambda 6717, 6731$) were measured by fitting Gaussian functions to their profiles using a Markov Chain Monte Carlo (MCMC) technique (Patil et al. 2010). We fit the profiles to a wavelength range 20 \AA in width centered on the rest frame wavelength of each line. We fit a linear continuum to 20 \AA regions of the spectra off the wings of each line and use this continuum measurement to calculate equivalent widths for spectral lines. We constrain the amplitude of the Gaussian to be positive and fit a single redshift and line width for the set of Balmer lines and an independent redshift and width for the forbidden lines. We adopt the fitted redshift of the Balmer lines as the redshift of the host galaxy. We obtain estimates of the uncertainty in the line flux from the MCMC trace and require a detection confidence of 99%⁶.

⁴IRAF is distributed by the National Optical Astronomy Observatory, which is operated by the Association of Universities for Research in Astronomy (AURA) under cooperative agreement with the National Science Foundation.

⁵The [O II] $\lambda\lambda 3726, 3729$ doublet is not resolved in these spectra, and we refer to the sum we effectively measure as [O II] $\lambda 3727$.

⁶Assuming a normal distribution, the 99% confidence interval corresponds to the requirement that the median value be 2.576σ greater than zero. Here we calculate σ as the difference between the 50th and 16th percentile values of the amplitude distribution in the MCMC trace.

The line fluxes measured for each host environment are presented in Table 4.3. We use observations of standard stars from the same night as the host environment observations to achieve relative flux calibration. No correction for underlying stellar absorption has been made, which could potentially affect the measurement of the Balmer line fluxes (particularly $H\beta$) for galaxies with significant stellar continuum flux. Only 5 of 58 spectra (those of SN 2002ex, 2006ip, 2007I, 2007ff, and PTF10vgv) have stellar continuum levels that may indicate significant underlying absorption, and we therefore do not measure quantities that depend on $H\beta$ for these objects, including extinction (A_V).

We tested for AGN contamination using a Baldwin et al. (1981) excitation-mechanism diagnostic diagram and the classification scheme of (Kauffmann et al. 2003a). We found emission lines from the host galaxies to be consistent with typical star-forming galaxies with few exceptions. The host environments of SN 1991D and 2003jp were excluded from our sample (and all analysis below) due to significant AGN contamination that would bias certain metallicity diagnostics (Kewley & Ellison 2008). We neglect the potential effects of AGN contamination for SN 2006jo (Type Ib) and PTF10xla (Ib/c), whose host environments show evidence for a composite classification. Some objects have supernova flux contamination (2010ay, 2011bv, 2011gh, 2011ip, LSQ11JW, PTF10aav), although the broad SN absorption features do not affect the measurement of the flux in the narrow galaxy emission lines.

4.3 HOST ENVIRONMENT PROPERTIES

From our optical spectra we measure the magnitude of dust extinction, metallicity, young stellar population ages, and Wolf-Rayet star populations of the host environments of the SN Ibc in our sample. We discuss each of these in the following sections.

4.3.1 Dust extinction

We estimate the line-of-sight extinction for each SN host galaxy spectrum (including both Galactic and intrinsic reddening) from the Balmer flux decrement. We assume $H\alpha/H\beta = 2.85$, which corresponds to $T = 10,000$ K and $n_e = 10^4$ cm⁻³ for Case B recombination (Osterbrock & Ferland 2006). The extinction curve of Cardelli et al. (1989) was applied to correct individual line fluxes for reddening, assuming $R_V = 3.1$. The value of the extinction derived for each host galaxy is presented in Table 4.3.

Table 4.3. Nebular Emission Line Fluxes From SN Host Galaxies

SN	A_V	[O II]	[O III]	H β	[O III]	[O III]	[N II]	H α	[N II]	[S II]	[S II]
		λ 3727	λ 4363	λ 4861	λ 4959	λ 5007	λ 6548	λ 6562	λ 6584	λ 6717	λ 6731
<i>SN Type: Ib</i>											
2007br	...	170 \pm 30	30 \pm 10	...	100 \pm 30	38 \pm 8	45 \pm 8	34 \pm 7
2007ea	0.8 $^{+0.2}_{-0.3}$	350 \pm 6	...	100 \pm 2	84 \pm 5	250 \pm 10	17 \pm 1	360 \pm 20	51 \pm 3	54 \pm 3	36 \pm 2
2010am	0.0 $^{+0.0}_{-0.0}$	373 \pm 3	...	100 \pm 2	104 \pm 7	290 \pm 20	11 \pm 2	220 \pm 20	35 \pm 3	49 \pm 4	32 \pm 3
2010cn	0.0 $^{+0.2}_{-0.0}$	300 \pm 10	...	100 \pm 7	104 \pm 10	290 \pm 30	...	270 \pm 30	27 \pm 5	45 \pm 6	23 \pm 5
2011D	5.6 $^{+1.1}_{-1.0}$	100 \pm 30	60 \pm 20	200 \pm 50	120 \pm 30	1500 \pm 400	130 \pm 40	220 \pm 70	140 \pm 40
2011V	0.0 $^{+0.6}_{-0.0}$	140 \pm 20	...	100 \pm 40	80 \pm 20	300 \pm 100	100 \pm 20	80 \pm 20	80 \pm 20
PTF09dx	5.0 $^{+0.8}_{-0.7}$	100 \pm 40	140 \pm 30	1200 \pm 400	430 \pm 60	320 \pm 50	170 \pm 30
<i>SN Type: Ib</i>											
2002ex	5.8 \pm 0.2	20.4 \pm 0.3	7.2 \pm 0.6	100 \pm 10	22 \pm 2	25 \pm 2	18 \pm 1
2004cf	1.3 $^{+0.5}_{-0.6}$	100 \pm 10	110 \pm 10	300 \pm 20	...	410 \pm 70	59 \pm 8	...	150 \pm 20
2005hm	0.0 $^{+0.5}_{-0.0}$...	20 \pm 6	100 \pm 4	180 \pm 20	590 \pm 50	...	290 \pm 50	27 \pm 8	74 \pm 8	47 \pm 7
2006jo	0.2 $^{+0.4}_{-0.2}$	450 \pm 10	...	100 \pm 5	110 \pm 10	200 \pm 20	55 \pm 6	310 \pm 40	190 \pm 20	56 \pm 6	46 \pm 5
2006lc	3.1 $^{+0.3}_{-0.3}$	100 \pm 20	60 \pm 10	700 \pm 100	200 \pm 20	76 \pm 6	58 \pm 5
2007az	0.0 $^{+0.0}_{-0.0}$	215 \pm 3	...	100 \pm 2	126 \pm 7	400 \pm 20	6 \pm 1	260 \pm 20	12 \pm 2	35 \pm 3	17 \pm 2
2007gg	0.7 $^{+0.6}_{-0.6}$	310 \pm 10	...	100 \pm 20	100 \pm 20	240 \pm 30	...	350 \pm 50	80 \pm 10	120 \pm 20	70 \pm 10
2008gc	0.4 $^{+0.3}_{-0.3}$	290 \pm 20	...	100 \pm 5	80 \pm 7	220 \pm 20	26 \pm 3	320 \pm 30	30 \pm 3	52 \pm 4	37 \pm 4
2009hu	...	12 \pm 5	22 \pm 7	100 \pm 20	34 \pm 9
2009jf	5.1 $^{+0.7}_{-0.6}$	100 \pm 10	150 \pm 20	190 \pm 20	160 \pm 30	1300 \pm 200	310 \pm 40	110 \pm 20	140 \pm 30
LSQ11JW	0.0 $^{+0.1}_{-0.0}$	300 \pm 8	...	100 \pm 8	50 \pm 6	150 \pm 10	...	260 \pm 30	44 \pm 6	40 \pm 6	...
PTF09df	3.5 $^{+0.5}_{-0.5}$	79 \pm 6	...	100 \pm 4	110 \pm 10	350 \pm 30	30 \pm 4	800 \pm 100	110 \pm 10	170 \pm 20	130 \pm 10
<i>SN Type: Ic</i>											
2003ev	30 \pm 7	15 \pm 5	100 \pm 30	62 \pm 7	36 \pm 5	22 \pm 5
2004ib	2.4 $^{+0.3}_{-0.3}$	630 \pm 20	...	100 \pm 6	73 \pm 7	230 \pm 10	25 \pm 5	570 \pm 40	108 \pm 8	128 \pm 9	93 \pm 6
2006ip	...	42 \pm 2	2.4 \pm 0.8	3.9 \pm 0.9	9.8 \pm 0.9	100 \pm 10	32 \pm 2	17 \pm 1	14 \pm 1
2006ir	0.8 $^{+0.2}_{-0.3}$	190 \pm 10	...	100 \pm 3	79 \pm 6	260 \pm 20	12 \pm 3	360 \pm 20	39 \pm 3	54 \pm 4	34 \pm 3
2006tq	...	160 \pm 10	50 \pm 10	100 \pm 20	...	100 \pm 20	80 \pm 30	...	90 \pm 30
2007db	0.9 $^{+0.4}_{-0.4}$	600 \pm 20	...	100 \pm 5	76 \pm 7	220 \pm 10	34 \pm 6	370 \pm 40	63 \pm 6	92 \pm 7	66 \pm 6
2007ff	...	30 \pm 10	100 \pm 20	63 \pm 8	13 \pm 3	13 \pm 3
2007gl	20 \pm 10	100 \pm 100	90 \pm 20	30 \pm 10	40 \pm 10
2007hb	2.1 $^{+0.4}_{-0.4}$	100 \pm 20	17 \pm 4	17 \pm 4	44 \pm 9	500 \pm 100	160 \pm 20
2007hl	2.5 $^{+0.2}_{-0.2}$	460 \pm 10	...	100 \pm 5	41 \pm 4	91 \pm 5	59 \pm 4	600 \pm 40	159 \pm 9	137 \pm 7	93 \pm 5
2007hn	...	140 \pm 40	33 \pm 8	100 \pm 40	91 \pm 9	57 \pm 6	36 \pm 5
2008sao	1.5 $^{+0.3}_{-0.3}$	97 \pm 1	...	100 \pm 3	12 \pm 1	37 \pm 2	50 \pm 4	450 \pm 40	150 \pm 10	74 \pm 6	58 \pm 5
2008sik	1.9 $^{+0.6}_{-0.5}$	370 \pm 10	...	100 \pm 20	90 \pm 10	500 \pm 100	370 \pm 30	170 \pm 20	130 \pm 10

Table 4.3—Continued

SN	A_V	[O II]	[O III]	H β	[O III]	[O III]	[N II]	H α	[N II]	[S II]	[S II]
		λ 3727	λ 4363	λ 4861	λ 4959	λ 5007	λ 6548	λ 6562	λ 6584	λ 6717	λ 6731
2009nl	$3.8^{+0.8}_{-0.7}$	100 ± 20	900 ± 200	120 ± 40	150 ± 30	...
2010Q	$0.0^{+0.1}_{-0.0}$	212 ± 5	10 ± 3	100 ± 4	160 ± 10	480 ± 40	10 ± 2	260 ± 30	12 ± 3	55 ± 5	18 ± 2
2011it	$0.7^{+0.5}_{-0.5}$	260 ± 10	...	100 ± 9	33 ± 6	110 ± 10	45 ± 6	350 ± 50	100 ± 10	96 ± 10	69 ± 8
PTF09iqd	...	140 ± 20	40 ± 10	100 ± 30	50 ± 20	70 ± 20	40 ± 10
PTF09q	...	10 ± 3	10 ± 2	100 ± 10	21 ± 3
PTF10bij	$0.6^{+0.3}_{-0.4}$	393 ± 5	...	100 ± 4	85 ± 7	250 ± 20	18 ± 3	340 ± 30	34 ± 4	72 ± 6	46 ± 5
PTF10vgv	...	35.5 ± 0.8	8 ± 1	22 ± 2	9 ± 1	100 ± 10	30 ± 3	24 ± 2	19 ± 2
PTF11hyg	$0.2^{+0.6}_{-0.6}$	144 ± 10	...	100 ± 30	...	50 ± 10	80 ± 10	400 ± 100	200 ± 20	70 ± 10	51 ± 9
<i>SN Type: Ic-BL</i>											
2005nb	$1.0^{+0.5}_{-0.4}$	100 ± 10	50 ± 10	140 ± 20	...	380 ± 40	70 ± 10	70 ± 10	50 ± 10
2006nx	$0.1^{+0.6}_{-0.1}$	600 ± 20	...	100 ± 4	120 ± 10	350 ± 40	17 ± 5	290 ± 60	38 ± 7	80 ± 10	33 ± 6
2007I	...	130 ± 10	7 ± 3	29 ± 4	...	100 ± 10	23 ± 3	41 ± 4	20 ± 3
2007ce	$0.0^{+0.2}_{-0.0}$	119 ± 1	9.8 ± 0.8	100.0 ± 1.0	200 ± 10	550 ± 20	2.5 ± 0.4	270 ± 30	7.4 ± 0.7	14 ± 1	12 ± 1
2008iu	$0.0^{+0.0}_{-0.0}$	110 ± 7	23 ± 4	100 ± 2	210 ± 20	640 ± 70	13 ± 2	230 ± 40	11 ± 1	12 ± 2	...
2010ah	$0.7^{+0.5}_{-0.5}$	380 ± 20	...	100 ± 10	60 ± 10	180 ± 20	...	350 ± 40	33 ± 9	70 ± 10	43 ± 10
2010ay	$0.0^{+0.0}_{-0.0}$	233 ± 7	4.6 ± 0.6	100.0 ± 0.6	170 ± 20	582 ± 4	7.7 ± 0.6	250 ± 30	25 ± 2	29 ± 3	22 ± 2
<i>SN Type: Undetermined Ibc</i>											
1991R	$1.6^{+0.3}_{-0.3}$	560 ± 30	...	100 ± 6	49 ± 6	180 ± 10	41 ± 5	460 ± 30	106 ± 8	77 ± 6	54 ± 6
2011gh	$2.0^{+0.4}_{-0.4}$	193 ± 7	...	100 ± 10	12 ± 4	48 ± 6	56 ± 7	520 ± 80	190 ± 20	93 ± 9	72 ± 7
2011hw	...	40 ± 10	23 ± 7	100 ± 20	61 ± 9	40 ± 10	50 ± 10

Note. — A_V has been derived from the Balmer decrement as described in the text, but fluxes reported here have not been dereddened. Fluxes are reported relative to H β = 100 when possible; H α or oxygen lines are used for normalization when necessary.

In Figure 4.3, we show the distribution of visual-band extinction (A_V) derived for the SN host environments from the Balmer decrement, for all spectra (solid lines) and for only explosion-site spectroscopy (dashed lines). Galactic extinction has been subtracted using the infrared dust map of Schlafly & Finkbeiner (2011). The difference introduced by restricting the sample to explosion sites is small.

Using the Kolmogorov-Smirnov (KS) test, we do not identify a statistical difference between the extinction distributions of SN Ib and Ic (with KS p -value, $p_{\text{KS}} = 0.85$). Combining the 12 SN Ib and 23 SN Ic with A_V measurements and subtracting Galactic extinction, the median and 14th and 86th percentile values (1σ) are $A_V = 0.2_{-0.2}^{+3.2}$ mag. The median extinction values for the SN IIb and Ic-BL are consistent with 0, but given the small sample sizes ($N = 9$ and 6, respectively), the difference from the SN Ib+Ic distribution is not significant ($p_{\text{KS}} \gg 0.1$).

In Figure 4.3 we also show the A_V distribution measured by Kelly & Kirshner (2012) for SN II and for the combination of SN Ib and Ic. A consistent extinction distribution was estimated for 19 SN Ibc by Drout et al. (2011) based on light curve colors. For SN Ibc, Kelly & Kirshner (2012) find median and 1σ values of $A_V = 1.1_{-0.6}^{+1.1}$ mag, with smaller values for SN II. We find A_V values with a more extreme range, with some SNe having no measurable reddening and some as large as $A_V \approx 5$ mag. This discrepancy is likely due to methodological differences. Because they employ 3" SDSS fibers, Kelly & Kirshner (2012) probe gas in the nuclear region of the host galaxy, whereas most of our spectra are from the SN explosion site where the line of sight could be significantly different. However, in some cases the discovery magnitudes reported for the SNe do not allow for

extinctions as large as we measure for the host environment⁷. This implies that the line of sight to the SN may be substantially different than that represented by the integrated light from the star forming gas we observe.

4.3.2 Metallicity Estimation

Host galaxy oxygen abundances were calculated from the extinction-corrected line flux ratios according to a number of independently calibrated abundance diagnostics, described below. We report the abundance derived from each method in Table 4.4.

⁷e.g. SN 2011D, discovered at $m = 18.2$ mag by Narla et al. 2011, implying $M < -20$ adopting the Balmer decrement extinction

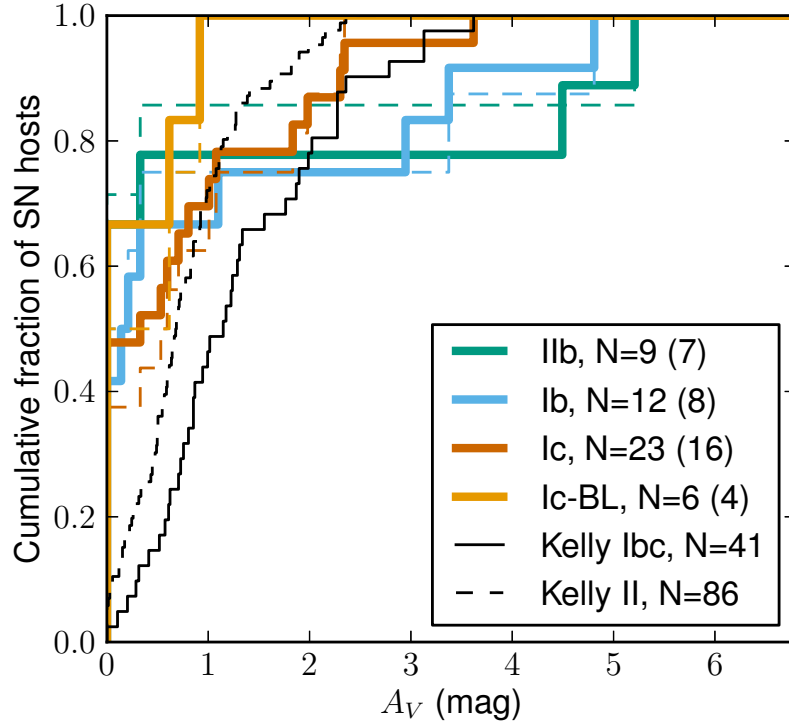


Figure 4.3.— Cumulative distribution of visual-band extinction (A_V) measured for host environments of SN of different types from the spectra collected in our sample. The dashed lines illustrate the same distributions, for only explosion-site spectroscopy. The number of objects included in each sample is given in the legend, with explosion-site only numbers in parentheses. The distributions measured by Kelly & Kirshner (2012) for SDSS fiber spectra are shown in black.

Table 4.4. Metallicities and Ages of SN Host Environments

SN Host Galaxy	log(O/H)+12						Age ^a (Myr)
	Direct	Z94	KD02	PP04N2	PP04O3N2	PT05	
<i>SN Type: IIb</i>							
2007br	8.66 ± 0.09
2007ea	...	8.46 ± 0.04	8.55 ± 0.07	8.42 ± 0.02	8.33 ± 0.01	...	5.2 ± 0.4
2010am	...	8.47 ± 0.03	8.58 ± 0.03	8.45 ± 0.03	8.33 ± 0.02	8.16 ± 0.02	6.0 ± 0.5
2010cn	...	8.54 ± 0.07	8.54 ± 0.08	8.33 ± 0.05	8.26 ± 0.03	8.26 ± 0.06	6.3 ± 0.4
2011D	8.30 ± 0.10	8.33 ± 0.06	...	5.4 ± 0.3
2011V	9.04 ± 0.07	8.6 ± 0.1	8.4 ± 0.9
PTF09dxv	8.64 ± 0.09	8.3 ± 0.9
<i>SN Type: Ib</i>							
2002ex	8.52 ± 0.04
2004cf	8.42 ± 0.05	8.31 ± 0.03	...	8.1 ± 0.6
2005hm	8.32 ± 0.09	8.16 ± 0.05	...	7.3 ± 0.4
2006jo	8.93 ± 0.05	8.79 ± 0.04	8.57 ± 0.02	...	8.4 ± 0.9
2006lc	8.59 ± 0.05	8.2 ± 0.8
2007az	...	8.50 ± 0.03	...	8.15 ± 0.04	8.12 ± 0.02	8.3 ± 0.2	5.4 ± 0.2
2007gg	8.7 ± 0.1	8.52 ± 0.05	8.40 ± 0.03	...	9.0 ± 0.8
2008gc	...	8.62 ± 0.07	8.51 ± 0.08	8.31 ± 0.03	8.29 ± 0.02	8.25 ± 0.08	6.0 ± 0.3
2009hu	8.64 ± 0.09
2009jf	8.55 ± 0.06	8.47 ± 0.03	...	9.0 ± 0.8
LSQ11JW	...	8.78 ± 0.06	8.71 ± 0.04	8.46 ± 0.04	8.43 ± 0.03	8.30 ± 0.05	...
PTF09dfk	...	8.58 ± 0.08	8.7 ± 0.1	8.42 ± 0.04	8.30 ± 0.02	8.32 ± 0.08	9.0 ± 0.6
<i>SN Type: Ic</i>							
2003ev	8.78 ± 0.08
2004ib	8.49 ± 0.03	8.40 ± 0.02	...	8.7 ± 0.7
2006ip	8.62 ± 0.04
2006ir	...	8.69 ± 0.05	8.66 ± 0.06	8.35 ± 0.03	8.29 ± 0.02	8.37 ± 0.05	5.7 ± 0.3
2006tq	8.9 ± 0.1
2007db	8.46 ± 0.04	8.38 ± 0.02	...	7.9 ± 0.6
2007ff	8.78 ± 0.07
2007gl	8.9 ± 0.2
2007hb	8.61 ± 0.06	8.82 ± 0.04	...	6.3 ± 0.7
2007hl	8.43 ± 0.09	8.57 ± 0.02	8.57 ± 0.01	...	8.2 ± 0.8
2007hn	8.88 ± 0.10
2008ao	...	9.13 ± 0.02	9.02 ± 0.04	8.63 ± 0.03	8.73 ± 0.01	8.44 ± 0.04	6.6 ± 0.7
2008ik	8.87 ± 0.09	8.83 ± 0.06	8.4 ± 0.9

Table 4.4—Continued

SN Host Galaxy	log(O/H)+12						Age ^a (Myr)
	Direct	Z94	KD02	PP04N2	PP04O3N2	PT05	
2009nl	8.4 ± 0.1	8.1 ± 0.5
2010Q	8.14 ± 0.07	8.09 ± 0.04	8.2 ± 0.1	5.3 ± 0.2
2011it	...	8.82 ± 0.09	8.85 ± 0.08	8.60 ± 0.04	8.55 ± 0.02	8.26 ± 0.10	8.1 ± 0.8
PTF09iqd	8.7 ± 0.1
PTF09q	8.52 ± 0.05
PTF10bip	8.33 ± 0.04	8.29 ± 0.02	...	6.9 ± 0.4
PTF10vgv	8.61 ± 0.04
PTF11hyg	9.03 ± 0.08	8.72 ± 0.07	8.72 ± 0.04	...	7.9 ± 0.9
<i>SN Type: Ic-BL</i>							
2005nb	8.46 ± 0.05	8.44 ± 0.03	...	6.4 ± 0.5
2006nx	8.39 ± 0.07	8.28 ± 0.04	...	6.7 ± 0.5
2007I	8.53 ± 0.05
2007ce	7.92 ± 0.05	8.01 ± 0.03	7.99 ± 0.02	8.3 ± 0.2	3.8 ± 0.1
2008iu	8.58 ± 0.05	8.14 ± 0.05	8.05 ± 0.03	8.27 ± 0.04	4.7 ± 0.2
2010ah	...	8.6 ± 0.1	...	8.31 ± 0.08	8.32 ± 0.05	...	8.0 ± 0.4
2010ay	8.35 ± 0.07	...	8.62 ± 0.03	8.33 ± 0.04	8.16 ± 0.02	8.18 ± 0.01	...
<i>SN Type: Undetermined Ibc</i>							
1991R	8.4 ± 0.1	8.54 ± 0.02	8.46 ± 0.02	...	8.1 ± 0.8
2011gh	...	8.85 ± 0.10	8.85 ± 0.06	8.65 ± 0.04	8.70 ± 0.02
2011hw	8.78 ± 0.07

Note. — The oxygen abundance, log(O/H)+12, is estimated using the following diagnostics, as described in the text: Direct (based on [O III] λ 4363), Z94 (Smartt 2009), KD02 (Kewley & Dopita 2002), PP04N2 and PP04O3N2 (Pettini & Pagel 2004), and PT05 (Pilyugin & Thuan 2005).

^aThe age of the young stellar population has been estimated based on the rest-frame equivalent width of the H β line, following Levesque et al. (2010a) (see Section 4.3.5).

We derive “direct” oxygen abundance estimates by estimating the electron temperature of the gas’ dominant excitation zone, which is only possible if the [O III] $\lambda 4363$ line is detected. Following Levesque et al. (2010a), the electron temperatures are estimated using IRAF’s five-level nebular modeling package `nebular` (Shaw & Dufour 1994). The `nebular` task `temden` is first applied to iteratively estimate the O^{++} temperature ($T_e(O^{++})$) and density (n_e) of the nebula from the [O III] and [S II] line ratios, respectively. If the measured line ratios correspond to unphysical conditions (outside the range for which `temden` is calibrated, $500 < T_e(O^{++}) < 10^5$ K and $1 < n_e < 10^8$ cm^{-3}), we do not calculate the direct abundance. The O^+ temperature is then estimated using the linear empirical relation of Garnett (1992). The O II and O III abundances are then estimated using the density, ionic temperatures, and [O II] and [O III] line ratios following the ionization correction factor (ICF) prescription of Shi et al. (2006). The total oxygen abundance is taken to be the sum of these two ionic abundances.

We employ several strong line diagnostics chosen to represent each of the major classes calibrated in the literature: R_{23} , N2O2, N2, O3N2, and P (see López-Sánchez & Esteban 2010b, for a recent review). First, we apply the R_{23} oxygen abundance calibration of Smartt (2009), an average of three earlier methods, hereafter referred to as “Z94.” Z94 is only calibrated for the higher-metallicity upper branch of the R_{23} -abundance degeneracy ($8.4 < \log(O/H)+12 < 9.6$); in every case where we apply Z94, the [N II]/[O II] ratio suggests an upper branch solution. Second, we apply the [N II]/[O II] oxygen abundance calibration of Kewley & Dopita (2002) (as updated by Kewley & Ellison 2008), hereafter referred to as “KD02.” Kewley & Dopita (2002) synthesize

a variety of modern photoionization models and observational calibrations to produce recommendations for producing an abundance estimate given different permutations of available emission lines and uses the $[\text{N II}]/[\text{O II}]$ ratio to break the degeneracy between the upper and lower branches of R_{23} . Third, we apply the empirical $[\text{N II}]/\text{H}\alpha$ (“N2”) and $[\text{O III}]/[\text{N II}]$ (“O3N2”) oxygen abundance calibrations of Pettini & Pagel (2004), hereafter referred to as “PP04.” Fourth, we apply the excitation parameter (“ P method”) oxygen abundance calibration of Pilyugin & Thuan (2005), hereafter referred to as “PT05.” P is calculated from the ratio of $[\text{O III}]$ to $([\text{O II}]+[\text{O III}])$ (Pilyugin 2001b), and the $[\text{N II}]/[\text{O II}]$ ratio is used to break the R_{23} degeneracy.

There are well-known offsets between the diagnostics which are particularly large between empirically and theoretically-calibrated diagnostics (see e.g. Stasińska 2002). However, the relative metallicity difference measured between a given pair of galaxies in different diagnostics is consistent with an rms scatter typically ~ 0.07 dex, and 0.15 dex between the most discrepant diagnostics (Kewley & Ellison 2008). Comparing the metallicities we measure for the same host galaxies in different diagnostics, we find discrepancies consistent with the rms scatter reported by Kewley & Ellison (2008). Hereafter we refer to this uncertainty intrinsic to the diagnostics as the “systematic uncertainty;” we do not factor the systematic uncertainty into the metallicities reported in Table 4.4, but we do consider this systematic uncertainty in our statistical analysis (Section 4.3.4). The systematic uncertainty is typically as large as the “statistical uncertainty” associated with the line flux and A_V measurement errors; for example, the median statistical uncertainty associated with our PP04N2 measurements is 0.09 dex.

The galaxy sample varies with the diagnostic chosen. The PP04N2 diagnostic can be applied to nearly all galaxies in our sample ($N = 50$), while the similar PP04O3N2 diagnostic can only be applied to the 31 galaxies which have measurements of the potentially fainter [O III] and $H\beta$ lines. The [PT05,Z94] diagnostics can only be applied to [13,12] galaxies, due to their strict dependence on the full complement of [O II] and [O III] lines. We can apply the direct diagnostic to only 2 galaxies due to its reliance on the auroral line which is weak at the metallicity regime probed here. However, the N2 diagnostic produces relative metallicity estimates consistent with the other strong line methods Kewley & Ellison (2008). N2 is also less sensitive to systematic effects: it employs lines with a very small wavelength separation (so extinction correction may be neglected) and the effect of underlying absorption is less important (because the absorption equivalent width of $H\alpha$ is typically equal to or less than $H\beta$, despite the ~ 3 times stronger flux, e.g. Brinchmann et al. 2004). However, in N2 diagnostics no correction is made for ionization parameter and the N2 ratio can saturate at high metallicities when nitrogen becomes the dominant coolant (Kewley & Dopita 2002).

4.3.3 Metallicity Distribution of SN Ibc Progenitor Environments

Using the PP04N2 abundance diagnostic, we measure metallicities for 12 SN Ib host galaxies and find values ranging from $\log(O/H)+12 = 8.15 - 8.79$, with a median abundance and standard deviation of $\log(O/H)+12 = 8.48$ and 0.16 dex,

respectively (Figure 4.4). The characteristics of the 21 SN Ic host galaxies in this diagnostic are similar, with metallicities ranging from $\log(\text{O}/\text{H})+12 = 8.14 - 8.88$ and median and standard deviation of $\log(\text{O}/\text{H})+12 = 8.61$ and 0.22 dex. Among the 7 SNe I Ib for which we measure PP04N2 metallicities, we find a range of $\log(\text{O}/\text{H})+12 = 8.30 - 8.66$ with median $\log(\text{O}/\text{H})+12 = 8.46$ and the standard deviation is 0.18 dex, similar to the SN Ib. In contrast, the 7 SN Ic-BL host environments typically have lower metallicities, with median $\log(\text{O}/\text{H})+12 = 8.34$ and standard deviation of 0.21 dex. The minimum metallicity for SNe Ic-BL host galaxies ($\log(\text{O}/\text{H})+12 = 8.01$) is only ~ 0.1 dex lower than that of SN Ib and Ic host galaxies, but the highest metallicity measured for an SN Ic-BL host galaxy ($\log(\text{O}/\text{H})+12 = 8.53$) is similar to the median for SN Ib and Ic.

We report the results from the other diagnostics in Table 4.5. We also note that Stoll et al. (2012) have developed an empirical, linear conversion between oxygen and iron abundance. Applying this to our host environment metallicities yields $[\text{Fe}/\text{H}] = [-0.6 \pm 0.2, -0.4 \pm 0.3, -0.6 \pm 0.2, -0.8 \pm 0.3]$ using our full sample of SNe [Ib,Ic,I Ib,Ic-BL].

Table 4.5 illustrates that the effect of restricting our sample to only those objects with Gold classifications and explosion site spectroscopy is modest. Among the 21 SNe Ic host galaxies in our sample for which the PP04N2 diagnostic was applied, 13 have Gold classifications and explosion site spectroscopy. The difference between the median metallicity measured between this subsample and the full sample is -0.01 dex. For SNe [Ib,I Ib,Ic-BL], the subsample fraction is $[8/12, 5/7, 3/7]$ and the difference in the median is similarly small at $[-0.05, -0.04, 0.02]$ dex. These differences, smaller than the systematic

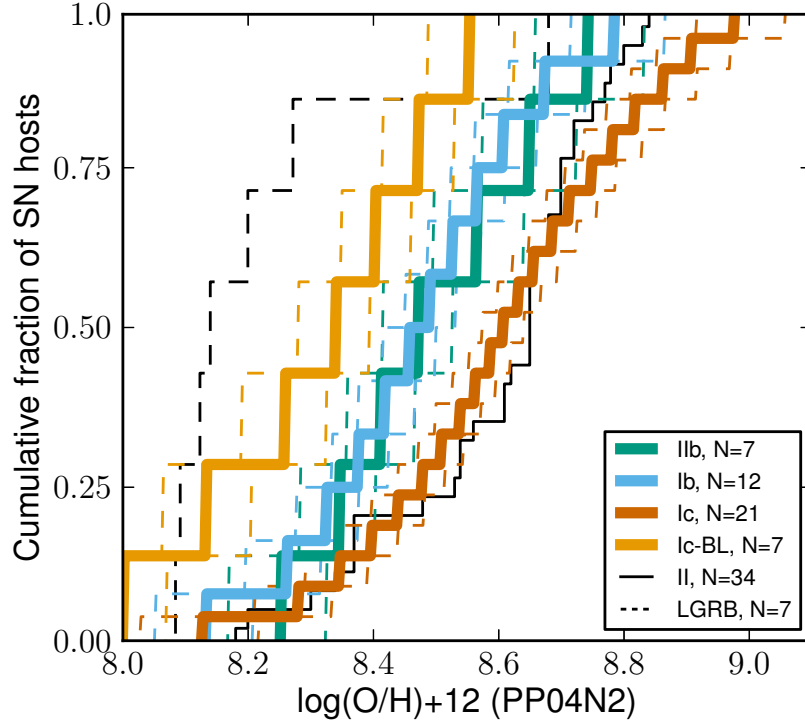


Figure 4.4.— Cumulative metallicity functions for SN host galaxies from this study, using the PP04N2 diagnostic. The 16th and 84th percentiles (1σ limits) of the probability distribution for the CDFs are illustrated by the dashed lines, as computed by propagation of the uncertainties in the line flux measurements and the 0.07 dex diagnostic systematic error. For comparison, we show the distribution of PP04N2 explosion site metallicities of SN II discovered by the untargeted PTF survey as measured by Stoll et al. (2012), and that of low-redshift ($z < 0.3$) LGRBs from Levesque et al. (2010a), Levesque et al. (2010d), and Chornock et al. (2010).

uncertainty associated with the abundance diagnostics (Section 4.3.2), generally reflect the lower metallicities of the SN explosion sites as compared to the galaxy nuclei.

Table 4.5. Statistics of Measured Host Galaxy Metallicity ($\log(\text{O}/\text{H})+12$)

Distribution

Diagnostic	N	Minimum	Maximum	Median	σ
<i>SN Type: Ib</i>					
direct	0 (0)	... (...)	... (...)	... (...)	... (...)
Z94	3 (3)	8.46 (8.46)	8.54 (8.54)	8.48 (8.48)	0.06 (0.06)
KD02	4 (4)	8.54 (8.54)	9.04 (9.04)	8.58 (8.58)	0.25 (0.25)
PP04N2	7 (5)	8.30 (8.30)	8.66 (8.65)	8.46 (8.42)	0.18 (0.13)
PP04O3N2	4 (4)	8.26 (8.26)	8.33 (8.33)	8.32 (8.32)	0.04 (0.04)
PT05	2 (2)	8.16 (8.16)	8.26 (8.26)	8.17 (8.17)	0.07 (0.07)
<i>SN Type: Ib</i>					
direct	0 (0)	... (...)	... (...)	... (...)	... (...)
Z94	4 (4)	8.50 (8.50)	8.78 (8.78)	8.57 (8.60)	0.13 (0.13)
KD02	5 (4)	8.51 (8.51)	8.93 (8.73)	8.69 (8.65)	0.21 (0.16)
PP04N2	12 (8)	8.15 (8.15)	8.79 (8.55)	8.48 (8.43)	0.16 (0.14)
PP04O3N2	9 (7)	8.12 (8.12)	8.57 (8.47)	8.32 (8.31)	0.16 (0.16)
PT05	4 (4)	8.25 (8.25)	8.32 (8.32)	8.29 (8.30)	0.10 (0.09)
<i>SN Type: Ib/c</i>					
direct	0 (0)	... (...)	... (...)	... (...)	... (...)
Z94	1 (0)	... (...)	... (...)	... (...)	... (...)
KD02	2 (0)	8.44 (...)	8.85 (...)	8.78 (...)	0.24 (...)
PP04N2	3 (1)	8.54 (...)	8.78 (...)	8.65 (...)	0.12 (...)
PP04O3N2	2 (0)	8.46 (...)	8.70 (...)	8.57 (...)	0.13 (...)
PT05	0 (0)	... (...)	... (...)	... (...)	... (...)
<i>SN Type: Ic</i>					
direct	0 (0)	... (...)	... (...)	... (...)	... (...)
Z94	3 (3)	8.69 (8.69)	9.13 (9.13)	8.72 (8.72)	0.33 (0.33)
KD02	6 (5)	8.43 (8.66)	9.03 (9.03)	8.74 (8.83)	0.29 (0.28)
PP04N2	21 (13)	8.14 (8.14)	8.88 (8.86)	8.61 (8.60)	0.22 (0.22)
PP04O3N2	10 (8)	8.09 (8.09)	8.82 (8.82)	8.45 (8.45)	0.23 (0.24)
PT05	4 (4)	8.23 (8.23)	8.44 (8.44)	8.31 (8.31)	0.15 (0.15)
<i>SN Type: Ic-BL</i>					
direct	2 (1)	7.92 (...)	8.35 (...)	7.98 (...)	0.25 (...)

Table 4.5—Continued

Diagnostic	N	Minimum	Maximum	Median	σ
Z94	1 (1)	... (...)	... (...)	... (...)	... (...)
KD02	2 (1)	8.58 (...)	8.62 (...)	8.55 (...)	0.12 (...)
PP04N2	7 (3)	8.01 (8.31)	8.53 (8.46)	8.34 (8.36)	0.21 (0.09)
PP04O3N2	6 (3)	7.99 (8.16)	8.44 (8.44)	8.20 (8.32)	0.19 (0.14)
PT05	3 (1)	8.18 (...)	8.31 (...)	8.20 (...)	0.12 (...)

Note. — The statistical properties of the distribution of metallicities measured for the host galaxies, divided by SN type. The first values listed represent all the SNe in the sample; the values in parenthesis reflect only those SNe with secure typing (Gold sample; Section 4.2.1) and explosion site spectroscopy (Section 4.2.2). The oxygen abundance diagnostics applied are described in Section 4.3.2. SNe of type “Ib/c” have uncertain typing. The medians and standard deviations (σ) have been calculated from the MCMC samplings.

Finally, there are several SN host environments at which we performed spectroscopy, but could not measure metallicities. For 7 objects, we detect narrow emission lines in the host galaxy, but they are not sufficient to estimate the metallicity in any of the strong line diagnostics: 2002gz (IIb), 2008fi (IIb), 2008im (Ib), 2011bv (IIb), 2011cs (Ic), 2011ip (Ic), and PTF10aavz (Ic-BL). For 2 objects, we did not detect any narrow emission lines in our host galaxy spectrum: 2004ai (Ib) and 2010lz (Ic). With the exception of SN 2004ai, these host galaxies are not at exceptionally high redshifts with respect to the remainder of the sample, and poor S/N in the spectroscopy is due to the intrinsic low luminosity of the host galaxies.

We place upper limits on the host environment metallicity of these SNe using archival photometry combined with the $L - Z$ relation of Tremonti et al. (2004)⁸ and, when $H\alpha$ is detected, the the 3σ upper limit measured for the [N II] flux combined with the PP04N2 diagnostic. We summarize this investigation in Table 4.6 and note a few special cases here, but we do not use these metallicity limits in our figures or statistics except where explicitly noted. The security of the spectral classification (Silver, S, or Gold, G; see Section 4.2.1) is indicated in parenthesis in hte table. Unless otherwise noted, we retrieve photometry for these host galaxies from NED, the NASA/IPAC Extragalactic Database operated by the Jet Propulsion Laboratory, California Institute of Technology, under contract with the National Aeronautics and Space Administration. When photometry is

⁸Converting the Tremonti et al. (2004) $L - Z$ relation from the Tremonti04 to the PP04N2 scale and adopting $\log(O/H)_{\odot} + 12 = 8.9$ on the Tremonti04 scale (Delahaye & Pinsonneault 2006), a galaxy with $M_B \sim -19.8$ mag should have solar metallicity.

not available in NED (not detected in DSS), we assume $m_B > 20$ mag. Redshifts are taken from NED or our own spectroscopy, except where noted.

SN 2008im occurred ~ 8 kpc from the nucleus of the Sb galaxy UGC 02906 (Oksanen 2008, with $z = 0.008$). In our spectrum, light from an older stellar population dominates over any signature of star formation. Given that the host galaxy has an absolute magnitude $M_B \approx -19$ mag, the explosion site is likely to be of sub-solar metallicity. The only one of these nine host environments for which we cannot place useful constraints on metallicity is that of SN 2004ai, reported as a SN Ic by Riello et al. (2004a), but revised to SN Ib (M. T. Botticella, private communication). The supernova spectrum indicates $z \sim 0.59$, making it by far the most distant SN in our sample. $H\alpha$ is redshifted out of our spectral range and nothing is visible in DSS images at this position, from which we infer that $M_B > -23$ mag, which does not allow us to distinguish between sub- or super-solar metallicities. The remaining seven host environments are constrained to be at sub-solar metallicities, although for SN 2008im and 2010lz we do not have sufficient S/N in $H\alpha$ to place spectroscopic limits on the metallicity.

Table 4.6. Host environments without metallicity measurements

SN	SN Type	z	M_B (mag)	Z (phot.) ^a	Z (spec.) ^b
2002gz	I Ib-pec (G)	0.085	> -18	$\lesssim 8.4$	$\lesssim 8.5$
2004ai	Ib (S)	0.590	> -23	$\lesssim 8.9$...
2008fi	I Ib (G)	0.026	> -15	$\lesssim 8.2$	$\lesssim 8.2$
2008sim	Ib (G)	0.008	-19	~ 8.5	...
2010lz	Ic (G)	0.090 ^c	> -12	< 8.0 ^d	...
2011bv	I Ib (G)	0.072	> -17	$\lesssim 8.3$	$\lesssim 8.3$
2011cs	Ic (G)	0.101	> -18	$\lesssim 8.4$	$\lesssim 8.1$
2011ip	Ic (G)	0.051	> -17	$\lesssim 8.3$	$\lesssim 8.5$
PTF10aavz	Ic-BL (G)	0.063	-16.5	~ 8.2	$\lesssim 8.1$

^aMetallicity ($\log(\text{O}/\text{H}) + 12$) limit implied by the $L - Z$ relation using the photometry listed, on the PP04 scale.

^bMetallicity ($\log(\text{O}/\text{H}) + 12$) limit implied by the PP04N2 diagnostic using the 3σ upper limit measured for the [N II] flux, stated when $\text{H}\alpha$ is detected.

^cDrake et al. (2011a)

^dThe absolute magnitude limit places this host galaxy below the range over which the $L - Z$ relation of Tremonti et al. (2004) is calibrated ($\sim 8.0 - 9.2$ on the Tremonti04 scale).

4.3.4 Statistical tests on metallicity distributions

We apply the KS test to our metallicity measurements (Table 4.7) and interpret $p_{\text{KS}} < 0.05$ to indicate statistically significant evidence for a difference in the parent populations of the two sets being compared. When Monte Carlo simulations⁹ indicate that p_{KS} rises above this threshold (> 0.05) in at least 14% of trials, we refer to this as “marginal” evidence of statistical significance.

We find no significant difference between the metallicity distribution of SN Ib and Ic, with $p_{\text{KS}} = 0.10^{+0.20}_{-0.08}$ using the PP04N2 diagnostic ($p_{\text{KS}} = 0.07^{+0.21}_{-0.05}$ if restricted to Gold classifications and explosion site metallicity measurements). This contrasts with the finding of Modjaz et al. (2011b), that the distributions disagree at the $p_{\text{KS}} = 0.01$ level using the equivalent PP04O3N2 diagnostic, but is consistent with the null result of Anderson et al. (2010); Kelly & Kirshner (2012); Leloudas et al. (2011). We note that when we apply the KS test to the sample of SN Ib and Ic from Modjaz et al. (2011b) using our methodology, we find $p_{\text{KS}} = 0.08^{+0.26}_{-0.06}$. The difference is that we separate SN I Ib and Ibn from Ib, which changes the metallicity distribution and reduces the SN Ib sample size by 5 objects.

We find different metallicity distributions for SN Ic and Ic-BL, with $p_{\text{KS}} = 0.01^{+0.03}_{-0.01}$ using the PP04N2 diagnostic. Given the smaller sample size

⁹Following Leloudas et al. (2011), we incorporate the uncertainty in the individual metallicity estimates (but not the diagnostic systematic uncertainty) by repeating the KS test through Monte Carlo simulations where we sample from the full probability distribution for the metallicity of each host galaxy.

Table 4.7. KS test p -values for SNe Ibc

	I Ib	Ib	Ic	Ic-BL
I Ib	...	$0.75^{+0.22}_{-0.23}$	$0.34^{+0.17}_{-0.27}$	$0.42^{+0.00}_{-0.29}$
Ib	$0.67^{+0.27}_{-0.30}$...	$0.10^{+0.20}_{-0.08}$	$0.21^{+0.31}_{-0.16}$
Ic	$0.16^{+0.28}_{-0.09}$	$0.07^{+0.21}_{-0.05}$...	$0.01^{+0.03}_{-0.01}$
Ic-BL				...

Note. — The values in the table are KS test p -values (p_{KS}) for the probability that the measured host galaxy metallicities of the SNe of the two indicated types were drawn from the same parent populations. Above the diagonal, all objects in our sample are considered; below the diagonal, only objects with Gold spectroscopic classification and explosion site spectroscopy are considered. The PP04N2 diagnostic is used for metallicity estimation. The KS test is performed only if metallicity measurements are available for ≥ 4 SN of each type. The upper and lower limits listed are the 16th and 84th percentile values of the results of the KS test Monte Carlo simulations.

and lower median metallicity of the SN Ib, the evidence for a difference in the Ic-BL and Ib metallicity distributions is not significant ($p_{\text{KS}} = 0.21_{-0.16}^{+0.31}$). We find no evidence for a significant difference between the SN Ib and IIb populations ($p_{\text{KS}} = 0.75_{-0.23}^{+0.22}$).

4.3.5 Young stellar population ages

We estimate the age of the young stellar population using the method of Levesque et al. (2010a), assuming an instantaneous-burst star formation history (for a review see Stasińska & Leitherer 1996). The age estimate is based on the rest frame equivalent width of the $\text{H}\beta$ line ($W_{\text{H}\beta}$) and evolutionary synthesis models for starburst galaxies based on the Geneva HIGH evolutionary tracks (Meynet et al. 1994; Schaerer & Vacca 1998). We use the PP04N2 diagnostic to break the metallicity degeneracy, restrict the sample to spectra obtained at the explosion site, and exclude objects with supernova flux contamination (SNe 2010ay, 2011bv, 2011gh, 2011ip, LSQ11JW, PTF10aav).

As illustrated in Figure 4.5, we find that the ages of young stellar populations in Type Ib and Ic SN host environments are not discrepant, with median ages of [8.1, 7.4] Myr and standard deviations of [1.5, 1.1] Myr for $N = [6, 10]$ SN [Ib,Ic] with explosion site spectra, and $p_{\text{KS}} = 0.21$. However, the ages of SN Ic-BL environments ($N = 4$) are somewhat lower, with a median of 5.6 Myr and standard deviation of 1.6 Myr. Given the small sample size, the KS test cannot confirm statistical significance, $p_{\text{KS}} = 0.34$. Similarly, the age of SN IIb environments seems to be lower than that of SN Ib and Ic, with median age

6.0 Myr and standard deviation of 1.2 Myr, but the sample size is small ($N = 5$).

We note that the distribution of ages for SN Ic-BL host environments in our sample are similar to that of the low-redshift ($z < 0.3$) LGRB hosts studied in Levesque et al. (2010a), which have a median age of ~ 5 Myr. The KS test does not suggest that the LGRB and SN Ic-BL age distributions are significantly different ($p_{\text{KS}} = 0.48$), but with only 5 low- z LGRBs the sample sizes are small. Moreover, the observation that SN Ic-BL and IIb occur in younger stellar populations is consistent with the finding of Kelly & Kirshner (2012) that these types of SNe have bluer explosion site $u' - z'$ colors.

With some caveats, we can interpret the young stellar population ages in terms of the lifetime of massive stars. For consistency with the $W_{\text{H}\beta}$ models of Levesque et al. (2010a), we use the stellar lifetimes from the ‘‘Geneva HIGH’’ (high mass loss) solar-metallicity ($Z = 0.02$) evolutionary tracks computed by Meynet et al. (1994) (shown in Figure 4.5). The measured ages therefore imply progenitor stars with initial masses $M_i \sim 20 - 40 M_{\odot}$ for SN Ib and Ic. This is similar to the mass range for SN Ib/c progenitors expected from stellar evolutionary theory and indicated by the relative rate of SN Ibc and SN II (Boissier & Prantzos 2009), but may be discrepant with progenitor non-detection upper limits from pre-explosion imaging (for a review, see Smartt 2009). For SN IIb and Ic-BL, the young stellar population ages imply progenitor stars that are somewhat more massive, $M_i \lesssim 60 M_{\odot}$. While stars of a given mass are longer-lived at lower metallicity in the Geneva models, and the SN Ic-BL progenitor stars are found in lower metallicity environment, the effect is small because the lifetimes vary by $\sim 10\%$ over a factor of ~ 3 in metallicity. However, because the ages are estimated

assuming an instantaneous burst of star formation and neglecting any ongoing star formation, the possibility of younger progenitor stars within the population is not precluded. Further assumptions inherent to this $W_{H\beta}$ diagnostic include complete absorption of ionizing photons, spatially uniform dust extinction in both nebular and stellar emission regions, and it is based on evolutionary tracks that do not include the effects of stellar rotation.

4.3.6 Wolf-Rayet star populations

Broad Wolf-Rayet (WR) features (“bumps”) in galaxy spectra, reflecting the existence of evolved, massive stars ($M \gtrsim 25 M_{\odot}$), can be used to characterize the nature of ongoing star formation in the galaxy (Allen et al. 1976; Kunth & Sargent 1981; Schaerer & Vacca 1998; Schaerer et al. 1999). In particular, the “blue bump” which is primarily due to the He II $\lambda 4686$ line is an indicator of late-type WN Wolf-Rayet (WNL) stars. A visual inspection of the spectra of our SN Ibc host environments does not reveal any recognizable blue bumps. We estimate the 3σ upper limit of the flux in the blue bump feature as 3 times the rms of the continuum flux in a 40 Å window at its location.

We follow the method of López-Sánchez & Esteban (2010a) to place limits on the fraction of WNL stars in the young stellar population, $WNL/(WNL + O)$, based on the ratio of the upper limit flux of the blue bump to $H\beta$. For WR galaxies in their dataset, this fraction ranges from $WNL/(WNL + O) \sim 0.03 - 0.3$, smaller than we can constrain with most of our spectra due to the continuum S/N. However, there are 3 host environments for which we can rule out WNL

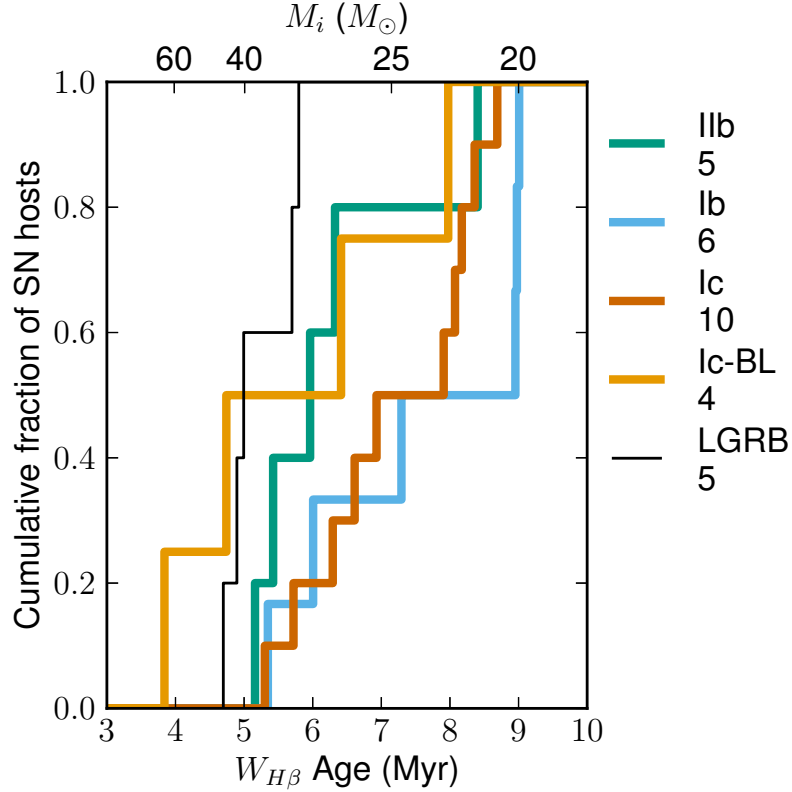


Figure 4.5.— Cumulative young stellar population age distribution for the SN Ibc host galaxies, based on the rest frame equivalent width of the $H\beta$ line ($W_{H\beta}$) measured from explosion-site spectroscopy only. The color coding and number of objects of each type are listed on the right. The low-redshift ($z < 0.3$) LGRB host environment ages come from Levesque et al. (2010a). The top axis illustrates the initial masses of rotating Wolf-Rayet stars with lifetimes equivalent to the stellar population ages, as predicted by Meynet et al. (1994).

populations at that level (2007az, 2008iu, 2010Q; all explosion site spectra) and one for which we can rule out $\text{WNL}/(\text{WNL} + \text{O}) > 0.1$ (2007ce). Significantly higher S/N spectroscopy or narrow-band imaging could provide stricter constraints for typical SN host galaxies. This analysis demonstrates that investigations of the WR populations of SN host environments requires a significantly different observing strategy than a study designed for strong line metallicity measurements, and will likely be limited to nearby SN host galaxies.

4.4 Combined SN Ibc Dataset

Next we combine our dataset with those of previous/concurrent spectroscopic studies of SNe Ibc (Anderson et al. 2010, Kelly & Kirshner 2012, Leloudas et al. 2011, Modjaz et al. 2011b, and this work). We summarize the characteristics of these surveys in Table 4.8.

4.4.1 Criteria of the Combined SN Ibc dataset

For the purposes of assembling a statistical sample, we consider only measurements made on the PP04 scale (see Section 4.3.2)¹⁰. Among these five samples, there are metallicity measurements for 171 unique SN Ibc host galaxies, of which 133 had

¹⁰For our observations and those of Anderson et al. (2010) and Leloudas et al. (2011), we employed measurements made using the PP04N2 diagnostic; for Kelly & Kirshner (2012) and Modjaz et al. (2011b), who do not report PP04N2 measurements, we instead employ the PP04O3N2 measurements and apply the small transformation from Kewley & Ellison (2008).

Table 4.8. Host Galaxy Samples by type

SN Type	A+10	K+11	L+11	M+11	S+12	TW
Targeted SNe						
I Ib	1	13	2	3	0	0
I b	10	10	3	7	0	0
I b/c	3	2	2	1	0	0
I c	14	23	1	10	0	0
I c-BL	0	5	0	6	0	0
<i>z</i>	0.005	0.011	0.016	0.012
Untargeted SNe						
I Ib	0	1	0	1	2	10
I b	0	3	6	6	3	13
I b/c	0	1	1	0	0	3
I c	0	5	4	4	3	24
I c-BL	0	4	0	9	1	8
<i>z</i>	...	0.034	0.037	0.037	0.036	0.036
All SNe						
I Ib	1	14	2	4	2	10
I b	10	13	9	13	3	13
I b/c	3	3	3	1	0	3
I c	14	28	5	14	3	24
I c-BL	0	9	0	15	1	8
<i>z</i>	0.005	0.015	0.022	0.017	0.036	0.036

Note. — The number of host galaxies in each of the literature samples divided by SN type, and median redshifts, *z*. The numbers are given for SNe discovered by untargeted (targeted) surveys. SNe of type “Ib/c” have uncertain typing. The samples come from the following references: A+10, Anderson et al. (2010); K+11, Kelly & Kirshner (2012) (only objects with metallicities measured); L+11, Leloudas et al. (2011); M+11, Modjaz et al. (2011b); S+12, Stoll et al. (2012); TW, this work.

metallicity measurements predating our study. To ensure consistency between authors when propagating uncertainties, we add in quadrature a representative systematic uncertainty of 0.07 dex (see Section 4.3.2) to the metallicity estimates from our study, Leloudas et al. (2011), and Modjaz et al. (2011b); for Kelly & Kirshner (2012) and Stoll et al. (2012), who do not report metallicity uncertainties, we assume this is the sole uncertainty.

Following the authors' own evaluations, we consider all observations from Modjaz et al. (2011b) and all but three from Leloudas et al. (2011) to be at the explosion site. If we were to apply our own criteria (Section 4.2.2), 4 of the observations from Modjaz et al. (2011b) would not qualify as explosion site due to their high redshift (SNe 2007jy, 2007qw, 2005kr, and 2006nx). For Anderson et al. (2010), following Section 4.2.2, we consider the 25/28 observations where the spectrum was extracted < 2 kpc from the SN position to be at the explosion site. For Kelly & Kirshner (2012), who employ 3" fiber spectroscopy from the SDSS, we consider all of the observations to be nuclear rather than explosion site measurements, as they sample the global properties of the host galaxy. We have investigated the discrepancies between those host galaxies whose metallicity measurements were performed by multiple authors and they are typically $\lesssim 0.15$ dex. When SNe have metallicities reported by multiple authors (see Table 4.9), we adopt the average and use only explosion site metallicities where possible. We neglect any systematic uncertainty introduced by differences in instrumental characteristics and spectroscopic analysis between the samples.

Of this combined sample, 75 of the SNe were discovered by untargeted searches and 114 of the metallicity measurements come from explosion site

spectroscopy. Before our observations, these sample sizes were only 37 and 84, respectively. Our results therefore approximately double the number of untargeted SN Ibc for which host galaxy metallicity measurements have been published, and significantly increase the number of explosion-site metallicity measurements.

Figure 4.6 compares the metallicity measurements made in this work to 18 previous measurements of the same host galaxies from the combined sample. Generally, discrepancies are small, with a mean residual of 0.06 dex and rms of 0.15 dex. In the median, the discrepancy is $1.6\times$ the statistical error in our measurement. The largest outliers can be explained by clear differences in spectroscopic methodology between our sample and the previous works. For example, for PTF09q we measured $\log(\text{O}/\text{H}) + 12 = 8.52$ in our explosion site spectrum, whereas Stoll et al. (2012) measure a higher $\log(\text{O}/\text{H}) + 12 = 8.81$ from their SDSS spectrum due to the nuclear placement of the Sloan fiber (~ 5 kpc from the SN site). There are 5 cases where we can compare an explosion site measurement from our sample to an equivalent measurement from the literature, and in those cases the rms discrepancy is only half as large (0.08 dex).

4.4.2 SN Ib vs. Ic metallicities

Figure 4.7 illustrates the metallicity distribution for all the SN Ibc host galaxies from the combined sample. First we consider the distributions with no selection criteria for SN discovery or spectroscopy methodology. With sample sizes of [47,68], we find the median metallicity of SN [Ib,Ic] to be $\log(\text{O}/\text{H})+12 = [8.56, 8.65]$. The difference between the distributions is not

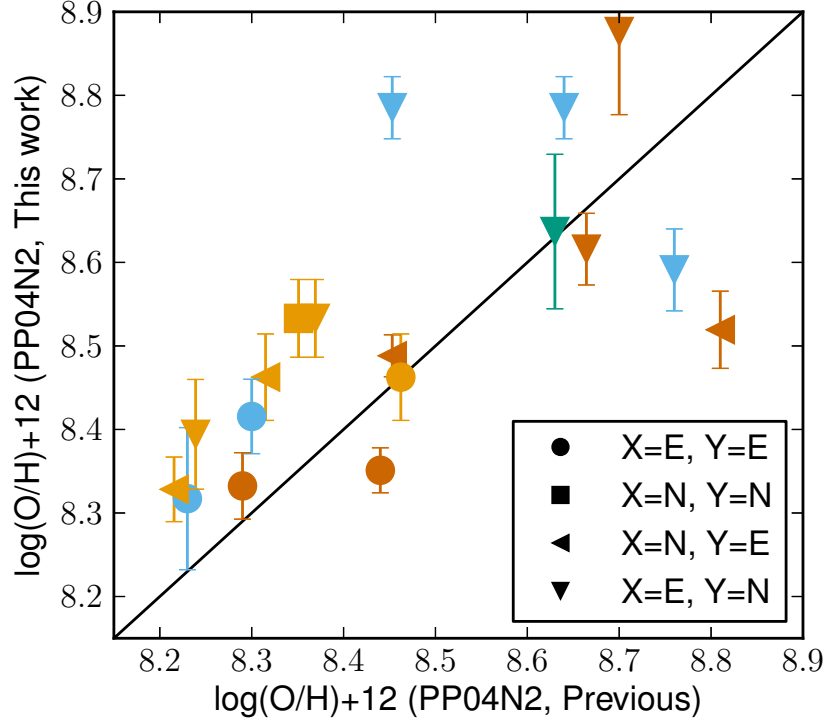


Figure 4.6.— Comparison of SN host galaxy metallicity measurements this work and previous studies in the combined sample. The overlap between these samples is described in Table 4.9. The error bars correspond to the statistical error estimated in this work, from propagation of the line flux errors. The marker shapes defined in the legend as “X, Y” correspond to the spectroscopy type (explosion site, “E” and nuclear, “N”) of the previous work (X) and this work (Y). The colors correspond to SN types as in Figure 4.4.

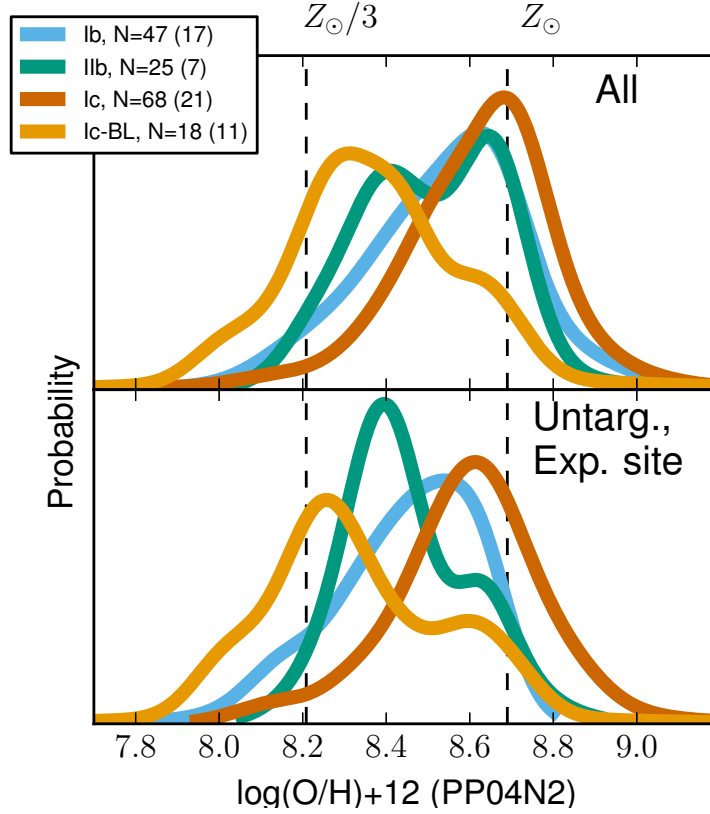


Figure 4.7.— Continuous probability distribution of SN Ibc host environment metallicities from the combined sample. The curves are sums of Gaussians defined by the metallicity measurement and their associated uncertainties. Top: All SN Ibc (sample size N noted in legend); Bottom: Only SN Ibc from untargeted surveys with explosion site metallicity measurements (sample size in parenthesis in legend).

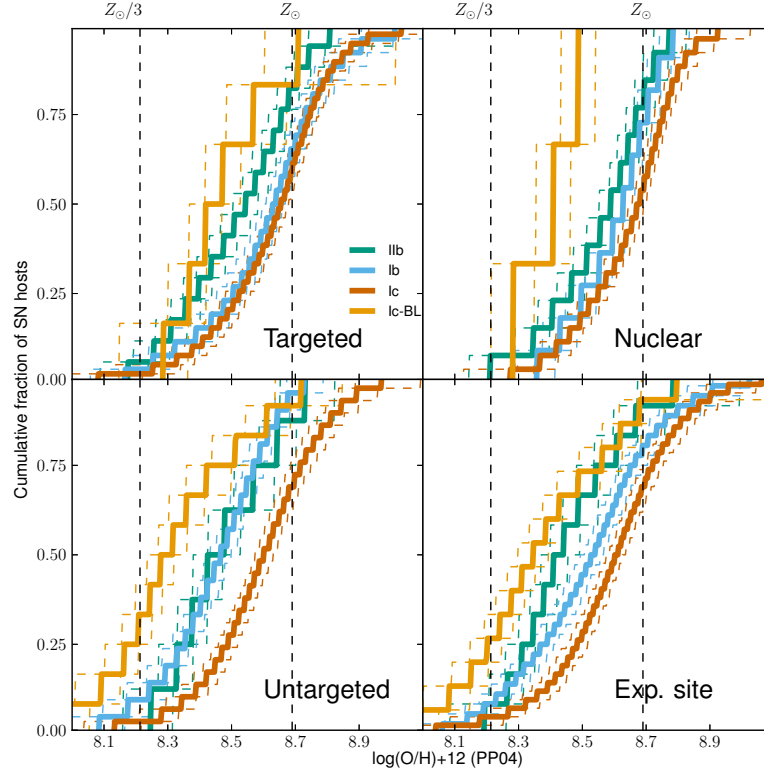


Figure 4.8.— Cumulative metallicity functions for SN host environments from the combined sample, using the PP04 diagnostic. The colors corresponding to SN types are given in the first panel; the sample sizes are given in Table 4.10. As labeled, the panels correspond to different cuts on the discovery mode of the supernova (galaxy-targeted or untargeted) and the method of spectroscopy (nuclear or explosion site). The dashed colored lines are 1σ limits for the CDFs as in Figure 4.4, but incorporating the systematic uncertainty of 0.07 dex (Section 4.3.2). The dashed vertical lines illustrate Z_{\odot} and $Z_{\odot}/3$.

statistically significant ($p_{\text{KS}} = 0.08^{+0.21}_{-0.06}$) and the difference in the medians is small relative to the width of the distributions ([0.16, 0.13] dex standard deviation).

If instead we only consider SNe discovered by targeted SN searches, we find SN host environments with systematically higher metallicities (as quantified in Section 4.5.1) and we find that the differences between the metallicity distributions for SNe of different types are reduced (Figure 4.8). The median metallicity of the $N = [26, 39]$ SN [Ib,Ic] from the targeted searches is $\log(\text{O}/\text{H})+12 = [8.66, 8.65]$ ($p_{\text{KS}} = 0.65^{+0.24}_{-0.43}$). Among the subsample with spectroscopy at the SN explosion site ($N = [19, 21]$ SN [Ib,Ic]) we find median metallicities of $\log(\text{O}/\text{H})+12 = [8.62, 8.62]$ ($p_{\text{KS}} = 0.63^{+0.28}_{-0.38}$).

Looking exclusively to untargeted SNe, for $N = [21, 29]$ SN [Ib,Ic] we find median metallicities of $\log(\text{O}/\text{H})+12 = [8.46, 8.61]$ (Figure 4.8). While this difference is marginally statistically significant ($p_{\text{KS}} = 2.0^{+6.8}_{-1.7} \times 10^{-2}$), it is biased by an unequal numbers of galaxy-nucleus versus explosion site spectroscopy in the SN Ib and Ic samples (19 and 28% nuclear spectroscopy, respectively). This sample construction bias raises the metallicities of SN Ic relative to SN Ib (see Section 4.5.2). If the sample is restricted to only explosion site measurements, the median difference is similar (~ 0.15 dex), but the difference in the full distribution is not significant ($p_{\text{KS}} = 0.06^{+0.12}_{-0.05}$). The difference in the distributions is most apparent at the high-metallicity end, where very few SN Ib discovered by untargeted surveys are found at super-solar metallicities. However, the explosion site spectroscopy in Figure 4.8 illustrates that SN Ib discovered by targeted searches do occur in super-solar metallicity environments, and therefore their absence among the untargeted objects must be attributed to small sample size.

How many observations would be required to distinguish between a true difference in the underlying distribution of progenitor metallicities for SN Ib and Ic? If we assume that the metallicity distribution of SN Ic progenitors is enriched by 0.1 dex with respect to SN Ib progenitors (as we find in Section 4.3.3) and that both distributions are Gaussians with standard deviation $\sigma = 0.2$ dex, then we can randomly sample from these distributions to investigate the value of p_{KS} we would infer from studies of different sizes (see Figure 4.9). We take statistical significance to be indicated by the KS test when $p_{\text{KS}} < 0.05$ and we assume a sample ratio $N_{\text{Ic}}/N_{\text{Ib}} = 1.6$.

We find that, in the absence of systematics, only $N \sim 50$ (20) SN Ibc would be required to distinguish the discrepancy in 85% (50%) of trials given a difference in the median metallicity of 0.2 dex (as suggested by Modjaz et al. 2011b). The combined sample includes $N = [47, 68]$ SN [Ib,Ic] metallicity measurements; $N = [21, 29]$ of these come from untargeted SN searches and therefore have substantially reduced systematics (see Section 4.5.1). Therefore, the observations to date should be sufficient to distinguish a median metallicity difference of 0.2 dex between SN Ib and Ic (even among exclusively-untargeted surveys), which is not supported by the data in the combined sample. However, a much larger sample of $N \sim 200$ (100) observations of SN Ib and Ic would be necessary to distinguish a median difference of 0.1 dex in the progenitor distribution in 84% (50%) of trials. Therefore a sample $\gtrsim 2\times$ as large as the combined sample would be required to unambiguously distinguish a relatively subtle discrepancy of 0.1 dex.

The host environment metallicity measurements made for 34 untargeted Type II SNe by Stoll et al. (2012) (shown in Figure 4.4) constitute an interesting

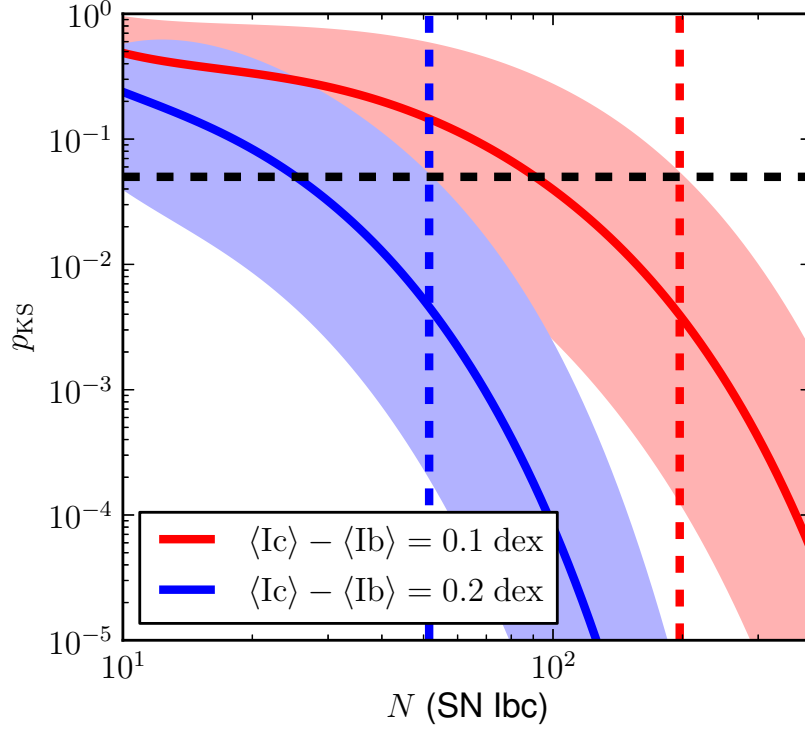


Figure 4.9.— Simulations demonstrating the sample size N of SN Ibc necessary to distinguish a difference in the median metallicity of SN Ib and Ic of [0.1, 0.2] dex ([red, blue]) assuming an underlying Gaussian distribution with $\sigma = 0.2$ dex. The shaded regions illustrate the 1σ range in p_{KS} over random draws from the distribution. The horizontal dashed line illustrates the threshold for statistical significant, $p_{KS} = 0.05$ at the 1σ level. The vertical lines mark the sample size necessary to distinguish the difference in the metallicity distribution to this threshold.

proxy for the metallicity distribution of the massive star progenitors of core-collapse SNe. Applying the KS test using all the untargeted objects in the combined sample, we do not find a significant difference between the metallicities of SN Ic and SN II ($p_{\text{KS}} = 0.52$), although there is a significant difference between SN II and [Ib,Ic-BL] ($p_{\text{KS}} = [1 \times 10^{-3}, 8 \times 10^{-4}]$). Combining all the SN Ibc in our sample, we find that they have a median metallicity 0.13 dex lower than the SN II and the difference in the full distribution is significant at $p_{\text{KS}} = 0.01$. A higher median metallicity for SN II than Ibc would conflict with several previous findings (e.g. Prieto et al. 2008; Boissier & Prantzos 2009; Anderson et al. 2010; Kelly & Kirshner 2012) and would not be consistent with metal-line driven winds stripping the progenitors of SN Ibc, unless combined with a significantly more bottom-heavy IMF at low metallicities. This discrepancy may instead indicate differences in sample construction. The relatively bright SN Ic-BL may be over-represented in the combined sample relative to a volume limited survey (see Section 4.5.4), biasing the SN Ibc metallicity downward, and some low-luminosity SN II and Ibc host galaxies do not have metallicity measurements (see Section 4.5.5 in this work and Section 3 of Stoll et al. 2012).

4.4.3 SN Ic vs. Ic-BL metallicities

When no cut is placed on SN discovery or spectroscopy characteristics, the SN Ic-BL in the combined sample ($N = 18$) have an appreciably smaller ($\gtrsim 0.2$ dex) median metallicity ($\log(\text{O}/\text{H})+12 = 8.36$) than other SN Ibc, and the difference relative to the SN Ic distribution is significant with $p_{\text{KS}} = 1.3_{-1.2}^{+9.8} \times 10^{-4}$

(see Figure 4.8). Restricting our scope to SNe discovered by targeted searches, the sample of targeted SN Ic-BL is limited ($N = 6$). The SN Ic-BL again show a median metallicity ($\log(\text{O}/\text{H})+12 = [8.45]$) ~ 0.2 dex smaller than other SN Ibc, but the difference compared to the SN Ic has only marginal statistical significance ($p_{\text{KS}} = 4.4_{-3.8}^{+16.1} \times 10^{-2}$). However, for $N = 12$ SN Ic-BL from untargeted surveys (primarily from this work and Modjaz et al. (2011b)), we find a median metallicity ($\log(\text{O}/\text{H})+12 = 8.30$) that is ~ 0.15 dex lower than from the targeted SN searches. This median metallicity is significantly different¹¹ from the distribution of either SN Ic (~ 0.3 dex lower median, $p_{\text{KS}} = 1.7_{-1.5}^{+6.0} \times 10^{-3}$) or the combination of the $N = 54$ SN Ib, Ic, and Ib/c ($p_{\text{KS}} = 3.1_{-2.7}^{+12.9} \times 10^{-3}$). As the SN Ic-BL metallicities derive almost exclusively from explosion site spectroscopy, this difference is not dependent on spectroscopic methodology ($p_{\text{KS}} = 7.2_{-6.0}^{+12.9} \times 10^{-3}$ for SN Ic vs SN Ic-BL with explosion-site spectroscopy only).

It has been suggested that the metallicity distribution of SNe Ic-BL may be bimodal (see e.g. Modjaz et al. 2008). This question is entangled with SN search methodology, because some SN Ic-BL are discovered via associated GRBs (by untargeted gamma-ray searches), while many SN Ic-BL without GRBs have been found by targeted SN searches. While we have shown SN Ic-BL are preferentially found at lower metallicity than other SN Ibc, Figure 4.7 illustrates that the metallicity distribution of SN Ic-BL is broad, extending to super-solar

¹¹Statistical significance is verified despite a smaller sample size than in the SN Ib versus Ic comparison because the difference in the distributions is much larger. Simulations of the type illustrated by Figure 4.9 indicate that a sample of ~ 30 SN Ic+Ic-BL is sufficient to expose a 0.3 dex median difference at the $p_{\text{KS}} < 0.05$ level in $\geq 84\%$ of trials.

metallicities. The Figure is visually suggestive of a bimodality, even among objects only from untargeted SN searches and with explosion-site metallicity measurements, but given the sample size the distribution is not significantly different than a Gaussian. Further studies comparing SN Ic-BL explosion properties (optical luminosity, photospheric velocity, etc.) with explosion site metallicity may inform the discussion of progenitor (sub)classes for these objects.

4.4.4 SN IIb vs. Ibc metallicities

Arcavi et al. (2010) reported that SN IIb preferentially occur in low-luminosity, likely low-metallicity, host environments. However, when no cut is placed on SN discovery or spectroscopy characteristics, the difference between the combined sample distributions for SN Ib ($N = 47$) and IIb ($N = 25$) is not significant, with $p_{\text{KS}} = 0.56^{+0.31}_{-0.35}$ (see Figure 4.8). Among only objects with explosion site spectroscopy ($N_{\text{IIb}} = 5$ SN IIb), the SN IIb median $\log(\text{O}/\text{H})+12 = 8.55$, ~ 0.1 dex lower than SN Ib, but this difference is not significant ($p_{\text{KS}} = 0.32^{+0.42}_{-0.24}$). Among SNe discovered by untargeted searches ($N_{\text{IIb}} = 8$, mostly from this work), there is no suggestion of a difference between the host environment metallicity of SN IIb and SN Ib, with $p_{\text{KS}} = 0.75^{+0.19}_{-0.32}$. As with SN Ic-BL, Figure 4.7 points to a bimodality in the SN IIb metallicity distribution that cannot be statistically verified with the present sample size.

4.4.5 Type Ic supernovae from dwarf host galaxies

Investigating SNe discovered in the first year of operation of PTF, Arcavi et al. (2010) found that SN I Ib and Ic-BL occur preferentially in dwarf host galaxies (defined by $M_r > -18$ mag), while they found SN Ic only in giant host galaxies ($M_r < -18$ mag). They interpret this as evidence for a dependence of the SN explosion properties on the metallicity of the explosion site. Transforming the $L - Z$ relation of Tremonti et al. (2004) to the r band, they find that this threshold corresponds to a characteristic metallicity of $0.35 Z_\odot$, or $\log(\text{O}/\text{H})+12 = 8.23$ on the PP04 scale. However, this photometric approach has several limitations (see Section 3.1 of Arcavi et al. 2010). In particular, the statistics are limiting, with only 6 SN Ibc in dwarf galaxies, and the absolute magnitude of the host galaxy does not necessarily reflect the metallicity of the explosion site accurately (Section 4.5.2). Moreover, while the mass-metallicity relation for star-forming galaxies is relatively tight (Tremonti et al. 2004 find $\sigma = 0.10$ dex), the scatter is larger when luminosity is used as a proxy for mass (Tremonti et al. 2004 find $\sigma = 0.16$ dex for M_B) and the scatter increases by a factor of $\gtrsim 2$ at low-luminosities/masses in the dwarf regime (see e.g. Kewley & Ellison 2008; Mannucci et al. 2011). Additional scatter is introduced in the survey of Arcavi et al. (2010) because they use a statistical transformation to convert their r -band magnitudes to the B -band and because they do not correct for extinction of the host galaxies, which Tremonti et al. (2004) find is typically $A_B \approx 0.3$ mag (~ 0.05 dex in Z). Finally, the statistical analysis of Arcavi et al. (2010) depends on the arbitrary choice of the luminosity threshold ($M_r = -18$ mag).

Using the spectroscopic metallicity threshold $\log(\text{O}/\text{H})+12 \leq 8.23$, 4% of the combined sample of SN Ibc host galaxy observations we consider here are in dwarf hosts (6/171 with PP04 metallicity measurements). Of these six, two are SN Ic-BL discovered by untargeted surveys (2007ce and 2008iu, both with explosion-site metallicity measurements presented by this work), one is an untargeted SN Ib (2007az; this work), one is a targeted SN Iib (2008ax; nuclear metallicity from Kelly & Kirshner 2012), and two are SN Ic. The SN Ic are SN 2002jz, discovered by a targeted survey with an explosion site metallicity measured by Anderson et al. (2010), and SN 2010Q, discovered by the untargeted CRTS survey and with explosion site metallicity measured as a member of our Gold spectroscopic sample. However, the spectral classification of SN 2002jz is somewhat uncertain, as Hamuy et al. (2002) suggest that it possibly displays $\text{H}\alpha$ absorption reflective of Type Iib SNe. Additionally, there are 3 SN Ic (all Gold classifications) in our sample for which we can not measure metallicities using strong line diagnostics, but are likely to be in sub-solar metallicity hosts and at least one of these (SN 2010lz) is in an exceptionally low-luminosity host galaxy (see Section 4.5). Finally, we note SN 2005kf, which Modjaz et al. (2011b) report as a Type Ic SN from a $M_B = -17$ mag dwarf host galaxy with super-solar metallicity ($\log(\text{O}/\text{H})+12 \approx 8.8$).

In summary, spectroscopic metallicity measurements of the host environments of SN Ibc do not support the conclusion of Arcavi et al. (2010) that SN Ic do not occur in low-metallicity host galaxies. This discrepancy may be due to the small number of objects included in the sample of Arcavi et al. (2010). Moreover, because secondary metallicity estimates made using host galaxy photometry

introduce additional scatter, their role in detecting the subtle difference that could exist between the metallicity distributions of SN Ib and Ic may be limited. In Section 4.4.2 we show that existing observations demonstrate that the difference in the median metallicity of SN Ib and Ic host galaxies is almost certainly < 0.2 dex, while the systematic uncertainty in photometric metallicity measurements is ~ 0.2 dex.

4.5 Systematic Effects

4.5.1 Targeted vs. Untargeted SN Searches

Galaxy-targeted supernova searches can bias SN host environment studies towards higher metallicities due to the galaxy $L - Z$ relation, as illustrated in Figure 4.10. The median metallicity measured for SNe discovered by targeted searches is $\log(\text{O}/\text{H}) + 12 = 8.64$, while for untargeted searches it is $\log(\text{O}/\text{H}) + 12 = 8.52$ ($\sim 24\%$ lower). The difference between the distributions is statistically significant ($p_{\text{KS}} = 3 \times 10^{-4}$). The fraction of galaxies with metallicity $< 1/3 Z_{\odot}$ is larger by a factor of $N_U/N_T \approx 5.1$ in untargeted surveys, meaning that low-metallicity galaxies are strongly underrepresented in targeted surveys. This ratio is still appreciable for $1/2 Z_{\odot}$ ($N_U/N_T \approx 2.4$), and even galaxies of solar metallicity are somewhat under-represented in targeted searches ($N_U/N_T \approx 1.2$).

Consequently, galaxy-targeted SN searches offer a smaller baseline over which to probe for differences in metallicity distributions. The 1σ spread in the metallicity distribution of SN Ibc discovered by targeted SN searches in the

combined sample is only 70% as large as that of untargeted surveys. As a result, the metallicity distributions of SNe are compressed and differences are reduced, as illustrated by Figure 4.8.

This $L - Z$ bias has important consequences for studies which combine observations of SNe discovered by both targeted and untargeted surveys. To illustrate this, we take the assumption that SN Ib and Ic share the same metallicity distribution and randomly draw samples from the targeted and untargeted SN Ibc metallicity distributions shown in Figure 4.10. We produce simulated samples constructed identically to that of Modjaz et al. (2011b) with respect to SN discovery characteristics: [6,11] targeted and [6,4] untargeted SN [Ib,Ic]. We find the SN Ic in the simulated samples to have higher average metallicities than the SN Ib in 64.2% of simulated trials, due solely to the $L - Z$ bias. The average difference in the SN Ic and SN Ib metallicities reported by Modjaz et al. (2011b) (≥ 0.14 dex, depending on the diagnostic scale) is reproduced or exceeded in 3.3% of the trials. Similarly, we find that in 5.0% of trials, a KS test on the simulated observations would indicate that SN Ic host environments are significantly different ($p_{\text{KS}} \leq 0.05$) from Ib environments. This represents a systematic effect biasing the results of the study, above and beyond the statistical ambiguity indicated by the KS test p -value. We conclude that differences in sample construction alone (the ratio of supernovae from targeted versus untargeted searches) can lead to erroneous differences in the metallicity distribution measured for the host environments of different SN types.

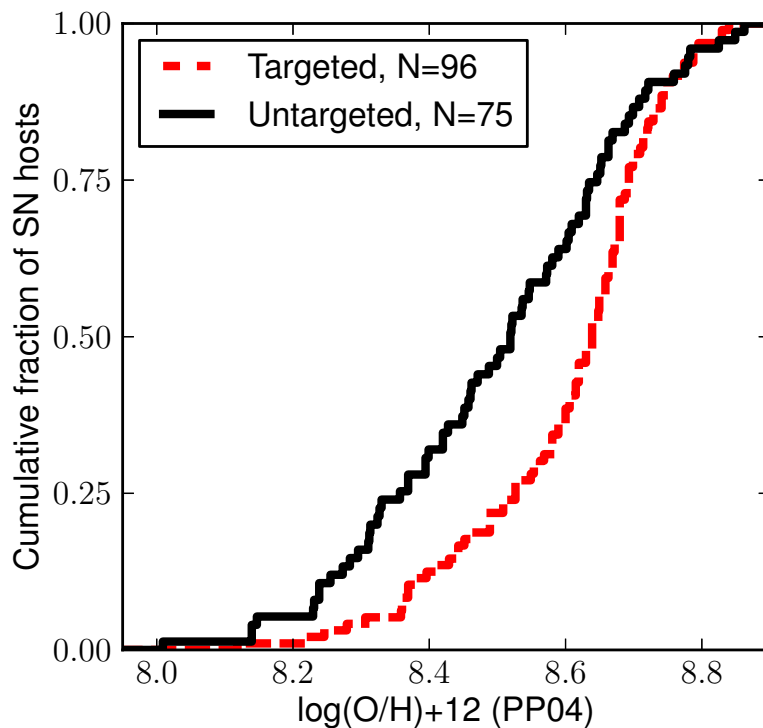


Figure 4.10.— Cumulative metallicity distribution for the host galaxies SN Ibc (of all subtypes) discovered by targeted and untargeted searches, from the combined dataset (Section 4.4). SNe with and without explosion site spectroscopy are shown (adopting only the explosion site measurement when both are available); if we restrict the sample to objects with explosion site spectroscopy, the effect is to shift to lower metallicities by $\ll 0.05$ dex.

4.5.2 Isolating the SN Explosion Site

Relative to nearby galaxies observed in targeted surveys, host galaxies in our exclusively-untargeted sample will typically have smaller intrinsic radii and luminosities and are typically found at greater distances. As a result, we are not able to resolve and measure the local metallicity at the explosion site of every host galaxy in our sample. As we discuss in Section 4.2.2, many of our measurements reflect integrated galaxy flux or only light from the brightest region of the galaxy (the nucleus). The situation is similar for SNe hosted by edge-on galaxies, where the host environment spectrum is necessarily integrated over the full line-of-sight.

It has been shown that SN Ic preferentially occur in the innermost regions of galaxies, more so than SN Ib or IIb (Prieto et al. 2008; Kelly et al. 2008; Anderson & James 2009; Habergham et al. 2012). In cases where we resort to measuring the galaxy nuclear metallicity, this implies that we would overestimate the metallicities of SN Ib relative to Ic in the presence of a strong gradient (e.g. Smartt 2009). We would therefore be less sensitive to the scenario where SN Ib come from lower metallicity environments than SN Ic within galaxies of similar nuclear characteristics.

However, the role of gradients is not clear cut and the ability to resolve explosion environments is limited, even for surveys of local galaxies. Individual SN Ibc host environments (HII regions) can only be resolved from nearby emission nebulae for the most local events (e.g. $z \lesssim 0.005$ for a 100 pc HII region and a 1" slit). Moreover, long-slit spectroscopy of nearby spiral galaxies illustrates that the oxygen abundance difference between the galaxy nucleus and disk outskirts is

modest (very rarely as large as 0.3 dex; Moran et al. 2012). Metallicity gradients in galaxies should play an even smaller role for explosion sites close to the galaxy nucleus, where SNe Ibc usually occur (Kelly et al. 2008). Moreover, nearby spiral galaxies show significant intrinsic scatter in metallicity gradients (e.g. Fabbiano et al. 2004, Rosolowsky & Simon 2008, Sanders et al. 2012a; but see also Bresolin 2011).

We investigate the effect of physical resolution on the median metallicity difference measured between SN Ib and Ic host environments in Figure 4.11. Monte Carlo simulations incorporating the uncertainties in the individual metallicity measurements demonstrate that the difference in the median metallicity of SN Ib and Ic is never significantly larger than the uncertainty in the median for any sample. For comparison, we show a model where the true median difference of 0.2 dex that can be measured accurately at $z = 0$, but is diminished linearly with increasing physical resolution until it is apparently 0 dex at a modest redshift ($z \approx 0.1$, resolution of ~ 2 kpc). The model is shown cumulatively for a sample with the redshift distribution of the combined sample.

Comparing the model to the existing datasets in Figure 4.11 suggests that physical resolution is not the limiting factor obscuring a difference in the median metallicity of SN Ib and Ic. The median difference in the combined sample is not greater than 0.1 dex at any redshift (and always consistent with 0 dex at 1σ), even though the corresponding model suggests that a 0.15 – 0.2 dex metallicity difference would be preserved in the sample out to $z \gtrsim 0.2$. We conclude that limitations due to physical resolution are not sufficient to mask a significant difference between the metallicity distributions of the SN Ib and Ic in

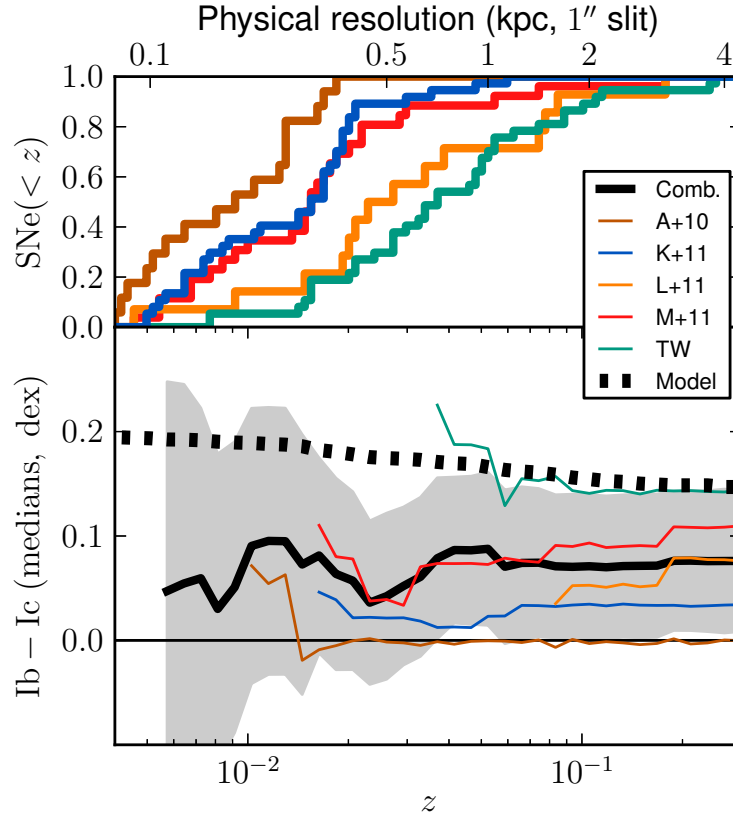


Figure 4.11.— Bottom: the cumulative difference measured between the median metallicity of SN Ib and Ic host environments at redshift $< z$ where > 4 SN Ib and Ic are available, using $\log(\text{O}/\text{H})$ as estimated from the PP04 diagnostic. The black dashed line illustrates the model for the effect of physical resolution on the measurement of a 0.2 dex difference in the median, described in the text. Except for the K+11 sample, only objects with explosion site spectroscopy claimed are considered (see Section 4.4.1). The shaded region illustrates the 1σ bootstrap errors on the median difference in the combined sample. Top: redshift distribution of SN Ib and Ic in the individual studies of the combined sample (see Table 4.8).

the combined sample.

A related issue is the methodological difference between explosion site and galaxy-nucleus spectroscopy. In the combined sample (Section 4.4), there are 30 SNe which have metallicity estimates at both the galaxy nucleus and explosion site. Figure 4.12 indicates that nuclear metallicity measurements introduce both a small additional scatter (rms discrepancy of 0.13 dex) and bias (median difference of -0.08 dex) relative to explosion site spectroscopy. The sign of the effect is consistent with offset explosion sites being systematically lower-metallicity environments than galaxy nuclei due to galactic metallicity gradients, with the effect strongest among the highest-metallicity host galaxies (nuclear $Z > Z_{\odot}$). In the median the discrepancy between the nuclear and explosion site metallicity measurements is only 0.68 times the uncertainties in the individual metallicity measurements. We do not find evidence for a significant difference between the explosion site versus nuclear metallicity discrepancies of SN Ib and Ic in the combined sample; their medians are different by only 0.03 dex, which is much smaller than the rms.

Simulations of the type illustrated in Figure 4.9 indicate that the bias and scatter introduced by nuclear spectroscopy should be small for studies of SN Ibc host environments. Introducing an additional 0.1 dex scatter for all measurements, the sample size necessary to recover a 0.1 dex metallicity difference between SN Ib and Ic increases by only a small amount ($\sim 20\%$). Introducing a 0.1 dex bias only for objects with super-solar metallicity (and assuming intrinsic median metallicities of $\log(\text{O}/\text{H})+12= 8.5$ and 8.6 for SN Ib and Ic, respectively), we find a negligible effect on the significance indicated by the KS test. In summary,

the combined sample demonstrates that nuclear metallicity measurements can be used as effectively unbiased tracers of SN Ibc progenitor metallicity.

A third issue relating to the isolation of the SN explosion site is the use of photometry to estimate the nuclear galaxy metallicity (e.g. Arcavi et al. 2010), or additionally using a simple metallicity gradient model to estimate the explosion site metallicity (e.g. Boissier & Prantzos 2009). In either case, photometric metallicity estimates will carry the same scatter as spectroscopic nuclear metallicity measurements (~ 0.1 dex, see above) and an additional uncertainty $\gtrsim 0.16$ dex due to the scatter in the $L - Z$ relation (see Section 4.4.5). Assuming a representative 0.2 dex uncertainty for photometric metallicity estimates and performing the same simulations as in Figure 4.9, we find that a small (0.1 dex median) metallicity difference between SN Ib and Ic host environments can only be detected with a sample ~ 2 times as large as an equivalent sample of spectroscopic metallicity measurements. Our conclusion that the combined sample of > 100 SN Ibc has not revealed a difference between the metallicity distributions of SN Ib and Ic may therefore conflict with the suggestion by Arcavi et al. (2010) that a sample of 18 photometric metallicity measurements for SN Ibc host galaxies could reveal a significant difference.

In summary, the role of explosion site spectroscopy in SN host environment studies is complex. The ability to isolate SN explosion sites is limited for smaller galaxies and at larger redshifts (e.g. those found by untargeted surveys). However, given the significantly larger baseline for making measurements of metallicity distributions offered by untargeted SN searches (Section 4.5.1), the effect of physical resolution is likely to play a secondary role. Substituting

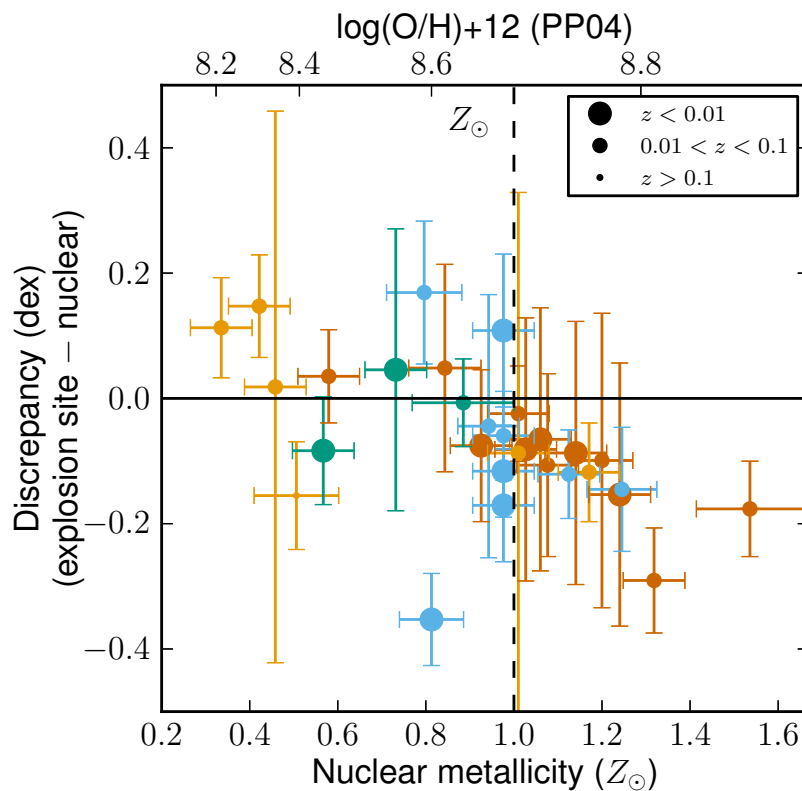


Figure 4.12.— Comparison of PP04 metallicity measurements for 30 SN Ibc host environments from galaxy nucleus and explosion site spectroscopy, from the combined dataset. The horizontal line marks equality and the dashed vertical line marks the solar metallicity. The colors reflect SN type as in Figure 4.8 and the sizes encode the redshift of the object.

nuclear for explosion site spectroscopy can lead to discrepancies in metallicity of ~ 0.1 dex, but we find that small differences in metallicity distributions could still be recovered by studies employing nuclear spectroscopy. However, the additional uncertainty introduced by photometric metallicity measurements is larger and may limit the role of these investigations in discovering differences in metallicity distributions, unless sufficient statistical power can be gained by larger sample size.

4.5.3 Uncertainties in SN classification

The spectral classification of SNe could also potentially effect the metallicity distribution inferred for the host environments of each SN type (see also Section 4.2.1).

It is unlikely that a SN Ic would be mistaken for a SN Ib, if the type is designated based on a clear detection of He I lines, but it is possible for a SN Ib to be classified as an SN Ic if the He lines are weak and S/N is poor, or if the He lines have not yet developed at the epoch of spectroscopy (Hamuy 2003b). Misidentifying SN Ib as SN Ic could act to blur any distinctions in the metallicity distribution of their host environments. We evaluate the possibility that this blurring could hide a large (0.2 dex) difference in the metallicity distributions of SN Ib and Ic host environments for a dataset as large as the combined sample using simulations. We randomly draw SN Ib and Ic metallicities from Gaussian distributions with widths of 0.2 dex and then mis-attribute a certain fraction of the draws to SN Ic. We find that the KS test indicates a statistically significant

difference ($p_{\text{KS}} < 0.05$ at 1σ) unless a large percentage ($\gtrsim 2/3$) of SN Ib are mis-classified as SN Ic.

It can be difficult to distinguish normal SN Ib from SN Iib, especially if spectra are not available near peak. There is a diversity in the hydrogen mass surrounding SNe Iib (Chevalier & Soderberg 2010) and, spectroscopically, SN Iib seem to represent a transitional type between SN Ib and SN II (Milisavljevic et al. 2012). However, Arcavi et al. (2010) have suggested that SN Iib prefer low-mass, low-metallicity host galaxies. It is difficult to reconcile these observations into a consistent progenitor model, but the conclusions of Arcavi et al. (2010) imply that grouping SN Ib and Iib together (as Leloudas et al. 2011 and Modjaz et al. 2011b have done explicitly) could bias downward the metallicity distribution inferred for SN Ib environments.

Similarly, if SN Ic-BL are grouped together with SN Ic, the SN Ic metallicity distribution could also be biased downward (Section 4.4.3). There is no clear definition of the ejecta velocity or line width that distinguishes SN Ic-BL from SN Ic, and any distinction will strongly depend on the spectroscopy epoch due to the velocity evolution of the photosphere (see e.g. Pian et al. 2006; Sanders et al. 2012d).

We have attempted to reduce the effects of SN classification errors by revisiting the SN spectroscopy on a case-by-case basis, rather than relying on the classification reported in the IAUCs, and by separating our dataset based on our degree of confidence in the classifications (Gold and Silver samples; Section 4.2.1). Of the previous studies in our combined sample (Section 4.4),

Leloudas et al. (2011) and Modjaz et al. (2011b) made similar revisions to SN classifications, while Anderson et al. (2010) and Kelly & Kirshner (2012) have relied on classifications reported in the circulars.

4.5.4 Selection effects in spectroscopic follow-up

The number of optical transients detected by SN searches often exceeds the resources available for spectroscopic follow-up. For example, because SNe without host galaxies clearly detected in discovery images may be mistaken for non-SN optical transients, the spectroscopic follow-up for some SN searches will be biased against SNe with low-luminosity host galaxies (Drake et al. 2009a). Similarly, some untargeted SN searches such as ESSENCE and SDSS-II have focused on discovering SNe Ia at the exclusion of core-collapse SNe (Sako et al. 2008; Foley et al. 2009b). Because the host galaxy properties of SN Ia differ systematically from those of SN Ibc (see e.g. Kelly et al. 2008; Mannucci et al. 2008), this selection effect could influence resulting studies of SN Ibc host environments. Moreover, some optical surveys are less sensitive to SN detection in the central regions of galaxies. However, because the photometric and host galaxy properties of SN Ib and Ic are significantly more similar to other subclasses of SNe, the systematic effects of biases in SN search spectroscopic follow-up is likely to effect SN Ib and Ic in similar ways. Therefore we expect it to be a second order effect influencing the results of this study, likely much smaller than the previous effects discussed.

In a magnitude limited survey, the ratio of SN Ic to Ib has been estimated

to be ~ 1.6 (Li et al. 2011). In our study, this ratio is similar, 1.8, suggesting no significant bias for or against SN Ib or Ic. For comparison, this ratio is 1.4 for Anderson et al. (2010), 2.1 for Kelly & Kirshner (2012), 0.5 for Leloudas et al. (2011), and 1.25 for Modjaz et al. (2011b).

SN Ic-BL, comprising 13% of our sample, are over-represented in our sample with respect to galaxy-targeted, volume-limited surveys (e.g. $< 5\%$ of SN Ibc in LOSS, not including SN I Ib, Li et al. 2011). This is a natural consequence of two factors. First, SN Ic-BL typically have brighter peak luminosities than other SNe Ibc (~ 1 mag in R -band, Drout et al. 2011) and can therefore be discovered over a larger volume in a magnitude-limited survey. Indeed, the median redshift of SNe Ic-BL in our sample ($z = 0.056$) is nearly twice that of the other SNe Ibc in our sample ($z = 0.034$). Second, we have found that Ic-BL preferentially occur in low-metallicity galaxies that will have preferentially lower luminosities (see also Arcavi et al. 2010; Kelly & Kirshner 2012). These galaxies are therefore under-represented in galaxy-targeted SN searches, but are not excluded from the untargeted SN searches we draw our sample from. We further note that the percentage of SN I Ib in our sample (17%) is similar to the value found by Smartt et al. (2009) among those SN classified and reported in the IAU circulars: $\sim 16\%$ of SN Ibc. However, Li et al. (2011) report an SN I Ib rate > 2 times this value based on SNe found by LOSS. Li et al. (2011) that the LOSS classifications are based primarily on photometry (in particular, identification of the double-peaked SN I Ib lightcurve shape), while classifications reported in the circulars are primarily based on single-epoch spectroscopic observations. Finally, we note that any effect due to the cosmic star formation history should be negligible over the

modest redshift range ($z \lesssim 0.3$) of our sample (Grieco et al. 2012).

An additional systematic effect could act if the host galaxy properties of SN Ibc are found to correlate with the explosion peak magnitude, as has been found for SN Ia (Hamuy et al. 1996). For example, if it were the case that SN Ic-BL in low-mass/metallicity galaxies are brighter than their counterparts in brighter galaxies, they would be over-represented in samples of host galaxy spectroscopy. This potential effect could be evaluated more thoroughly with more extensive studies of SN Ibc lightcurve properties, as the sample size of existing studies are small (Richardson et al. 2006; Drout et al. 2011; Li et al. 2011), or by performing a volume-limited survey. Moreover, dust obscuration could prevent the discovery of a significant fraction of SNe (Mattila et al. 2012), and could potentially be correlated with both host galaxy and explosion properties.

4.5.5 Depth limits for host galaxy spectroscopy

Due to the galaxy $L - Z$ relation, the lowest metallicity galaxies will also have the lowest luminosities, and may therefore be under-represented in spectroscopic studies that require sufficient S/N in the nebular emission lines to derive metallicity. Table 4.6 indicates that we are potentially excluding 3 SN Ic in low-metallicity hosts from our sample due to insufficient S/N, while we are likely only excluding one such SN Ib. The effect of these exclusions is significant: if we suppose that each of the excluded galaxies falls at the low-metallicity end of the observed distribution, than the median metallicities we measure for the SN [Ib,Ic] in our sample become $\log(\text{O}/\text{H})+12 = [8.46, 8.42]$. Considering these excluded

galaxies indicates that the median metallicity for SN Ic host environments could be *lower* than for SN Ib in our sample. Such a revision would not conflict with the results of our statistical tests, which indicate that the difference we measure in the metallicity distributions of SN Ib and Ic host environments is not significant (Section 4.3.4). This illustrates the role of small number statistics in spectroscopic studies of SN Ibc host environments. Moreover, it advocates for continued follow up of supernova host environments with facilities capable of measuring metallicity for the low-luminosity, relatively high-redshift host galaxies discovered by untargeted SN searches.

4.6 DISCUSSION

4.6.1 SN Ib and Ic progenitor models

The new observations presented in this work, and previous observations synthesized in our combined dataset, suggest and constrain differences in the progenitor star population of SNe Ibc. The modest difference observed in the median metallicity of SN Ib and Ic host environments corresponds to a very small difference in mass-loss rates for single star progenitors. In general, the mass loss rates of massive stars is taken to scale as $\dot{M} \sim (Z/Z_{\odot})^m$ where $m = 0.5$ (Kudritzki et al. 1987) or perhaps $m = 0.86$ for WR winds (Vink & de Koter 2005). The difference in median metallicity we measure for SN Ib and Ic from explosion site spectroscopy of Gold-classification SNe in our untargeted study (Section 4.3.3) then corresponds to a difference in mass loss rates of a factor

of $\dot{M}_{Ic}/\dot{M}_{Ib} \sim 1.17$ (1.32) for the power law slope $m = 0.5$ (0.86). If we use instead the median difference inferred from the combined sample using only explosion-site spectroscopy (Section 4.4.2), the mass loss rate differs by a factor of $\dot{M}_{Ic}/\dot{M}_{Ib} \sim 1.11$ (1.20). In this simplistic analysis, it seems improbable that this small difference in mass loss rate is sufficient to strip the entire He layer from the progenitor star in order to produce the envelope composition indicated by the spectrum of the explosion.

In more detail, the difference in the SN Ib and Ic metallicity distributions can be interpreted in terms of a metallicity-dependence for the critical initial-mass required for a progenitor star to explode as SN Ib or Ic. Boissier & Prantzos (2009) estimated how this critical mass depends on metallicity by comparing the observed difference in the rates of SN Ib and Ic in different metallicity bins to a model that has an explicit dependence of the threshold mass for SN Ib and Ic explosions. Using photometric metallicity estimates, they find that the critical mass varies by a factor of ~ 2 over a factor of ~ 3 in metallicity. However, our combined dataset indicates that a difference in the metallicity distribution of SN Ib and Ic has yet to be measured robustly (Section 4.4.2), suggesting that the metallicity-dependence of this critical mass may be much more subtle.

Moreover, the observed relation between galaxy mass, metallicity, and star formation rate implies that metal-poor galaxies typically have higher specific star formation rates (Lara-López et al. 2010; Mannucci et al. 2010). In a single star progenitor model where SN Ic are produced by more massive stars, this could indicate an elevated rate of SN Ic relative to SN Ib in metal-poor galaxies if the star formation events are short-lived. This could potentially mask the

effect of metal-line dependent winds. Our measurements of the ages of young stellar populations of SN Ibc host galaxies do not indicate that SN Ic come from younger stellar populations (Section 4.3.5), but a larger sample is needed to address this question in detail. A metallicity-dependent slope for the initial mass function could also effect SN Ibc rates (Prantzos & Boissier 2003). Assuming SN Ic progenitors are more massive than those of SN Ib, a top-heavy IMF in low-metallicity environments would elevate the SN Ic/Ib rate and could push the metallicity distribution of SN Ic downward.

Smartt et al. (2009) suggest that luminosity limits from pre-explosion imaging and ejecta masses from light-curve modeling rule out massive WR progenitors for a sample of nearby SN Ibc. However, the SN Ibc studied by Smartt et al. (2009) are primarily in nearby, high-mass host galaxies that are likely to reflect high-metallicity progenitor stars. In essentially all progenitor models, SN Ibc progenitors are expected to be less massive (and less luminous) at higher metallicities. Indeed, the rate of SN Ibc in nearby ($z \lesssim 0.04$), low-metallicity environments is expected to be quite low (at best a few per year), making direct progenitor detection observationally challenging (Young et al. 2008). Moreover, local extinction may play a larger role in obscuring SN progenitor stars than previously recognized (Walmswell & Eldridge 2012).

Podsiadlowski et al. (1992) suggested that Roche lobe overflow via binary interaction could be responsible for stripping significant amounts of material from the progenitor stars of SN Ibc. Observations of OB stars indicate that a significant percentage of potential Type Ibc SN progenitors are likely to be in interacting binary systems (Kobulnicky & Fryer 2007; Kouwenhoven et al.

2007; Sana et al. 2012). Eldridge et al. (2008) have shown that the observed metallicity-dependence of the relative rates of SN II and Ibc can be reproduced using binary population synthesis models informed by the observed populations of red supergiants, Wolf-Rayet, and other massive stars. Smith et al. (2011a) have argued based on SN rates that the majority of SN Ibc progenitors may come from binary star systems. However, additional modeling is needed to predict the relative metallicity-distribution of SN Ib and Ic that would result from binary progenitor stars. Moreover, the effect of mixing may further complicate the comparison of observations to SN Ibc progenitor models for both single and binary stars (Dessart et al. 2012).

4.6.2 Comparison to nearby GRB-SNe

In the “collapsar” model, the progenitors of LGRBs found in association with SNIc-BL (GRB-SNe) are massive stars with high rates of core rotation, implying sub-solar metallicities ($Z \lesssim 0.3 Z_{\odot}$) in order to minimize angular momentum losses due to line-driven winds (Woosley & Bloom 2006). The observational result that most LGRBs and GRB-SNe are discovered in dwarf, sub-solar metallicity galaxies has been interpreted as evidence supporting this model (Fruchter et al. 2006; Stanek et al. 2006; Levesque et al. 2010a). Because SNIc-BL have traditionally been found in higher-metallicity environments, a “cut-off” metallicity has been proposed to distinguish stars which will produce GRB-SNe from those that will produce non-relativistic SNIc-BL (Modjaz et al. 2008; Kocevski et al. 2009).

However, several discoveries have challenged the role of metallicity in the production of LGRBs. LGRBs and relativistic, engine-driven SNe have been found in super-solar metallicity environments (Berger et al. 2007; Levesque et al. 2010d; Soderberg et al. 2010; Levesque et al. 2010c; Graham et al. 2009). Moreover, SNIc-BL with strong limits on the association of relativistic ejecta have been found in sub-solar metallicity environments (see e.g. Sanders et al. 2012d). This shift in the discovery environments of GRBs and SNIc-BL can be explained in terms of the transient search strategy — GRBs are discovered via their gamma-ray emission through untargeted searches, while past studies of SNIbc host environments drew primarily from galaxy-targeted searches, which are heavily biased towards higher-metallicity host environments (see Section 4.5.1). The advent of wide-field, untargeted SN searches has enabled the discovery of SNIc-BL in sub-solar metallicity environments. Indeed, the results from this work and Kelly & Kirshner (2012) demonstrate that SNIc-BL preferentially occur in lower-metallicity environments than SNIb or Ic (see Section 4.3.3 and Section 4.4.3).

Alternatively, the observed metallicity distribution of LGRB host environments has been interpreted as a secondary manifestation of a preference for high-star formation rate environments (Kocevski & West 2011; Mannucci et al. 2011). Our results are consistent with this view. In Section 4.3.5 we found that SNIc-BL host environments potentially have younger stellar populations than those of other SNIbc and more similar to nearby LGRBs. In Section 4.3.3 we find that the untargeted SNIc-BL in our sample have a median metallicity ~ 0.2 dex higher than that of the nearby LGRBs ($z < 0.3$), but given the small size of

both samples ($N = 7$ and 7 , respectively), the KS test indicates no significant difference between the distributions ($p_{\text{KS}} = 0.13$).

In summary, observations of SNe discovered by untargeted searches have substantially reduced the discrepancy reported between the metallicity distribution of SNIc-BL with and without associated LGRBs, while verifying a shared preference for environments with high-star formation rates and/or very young stellar populations. These findings are consistent with the view that massive stars ($M \gtrsim 40 M_{\odot}$) are the common progenitor for both these types of explosions, but suggest that metallicity does not play the primary role in the formation of a central engine. Similarly, Levesque et al. (2010e) have found that host environment metallicity does not correlate to the gamma-ray energy release of LGRBs. Georgy et al. (2012) have suggested, using the models of Ekström et al. (2012), that differential rotation in LGRB progenitors could moderate the coupling between WR winds and the stellar core and may be responsible for reducing the role of metallicity in the explosion.

4.6.3 Studies of SN Ibc in the LSST era

In the coming years, the discovery rate for SNe promises to grow dramatically as existing high-cadence, wide field surveys continue to operate and new surveys such as the Dark Energy Survey and the Large Synoptic Survey Telescope (LSST) come online. As LSST could discover $\sim 10^6$ SNe per year, it is anticipated that the SN discovery rate in this era will far outstrip the capacity to perform spectroscopic follow-up on individual objects (LSST Science Collaboration et al.

2009). This significant increase in the SN discovery rate could permit studies of untargeted SN Ibc host environments with sample sizes sufficient to detect even small ($\lesssim 0.1$ dex) differences in the SN Ib and Ic metallicity distributions without statistical ambiguity. We suggest that a sample of $\gtrsim 100$ such objects would be required for that purpose (see Section 4.4.2), but caution that attention must continue to be paid to the systematic effects discussed in Section 4.5.

Moreover, such an SN discovery rate suggests that SN classification will become the limiting factor for certain science goals. Investigating the GRB-SN connection will be more difficult if a sample of well-classified SN Ic-BL cannot be identified. In SN Ia samples for precision cosmology that are assembled using light curve-based classification alone, SN Ibc may be major contaminants ($\sim 20\%$) because their light curve shape resembles that of SN Ia (Gong et al. 2010; Kessler et al. 2010; Gjergo et al. 2012). The potential for ambiguity between SN Ia and SN Ibc light curves is especially great in the case of SN Ic-BL, because the average absolute peak magnitude is more similar to SN Ia than for normal SN Ib or Ic (Drout et al. 2011).

We therefore suggest that information about the distribution of host galaxy properties for SN Ia and Ibc could be used to inform photometric SN classification in the LSST era. Because SN Ic-BL preferentially occur in lower luminosity, lower metallicity host galaxies than other SN Ibc or SN Ia (Li et al. 2011; Kelly & Kirshner 2012), the difference in flux between the SN and the host galaxy could be used to distinguish SN Ic-BL from other SN types for the dual purposes of 1) identifying SN Ic-BL for follow-up SN studies and 2) filtering SN Ibc from samples of SN Ia for precision cosmology. However, a study using information about the

host galaxy distribution to inform SN classification would sacrifice the ability to make unbiased inferences about the properties of the host galaxy populations (similar to the case of galaxy-targeted SN surveys) and could introduce systematic effects if used to construct samples for SN Ia cosmology. Moreover, it would also exclude events with unexpected properties, such as the engine-driven Type Ic-BL SN 2009bb that exploded in a luminous, high-metallicity host galaxy (Levesque et al. 2010d).

4.7 CONCLUSIONS

We have presented the largest study to date of SN Ibc host environments unbiased with respect to the galaxy $L - Z$ relation as imposed by galaxy-targeted SN searches. By reporting metallicity measurements for 50 objects, we more than double the number of host environment metallicity measurements for SN Ibc discovered by untargeted surveys.

We conclude that:

1. SN Ibc host environments discovered through targeted surveys are significantly biased towards higher metallicities, representing host environments that are typically more enriched by $\sim 24\%$. The ratio of low-metallicity ($Z_{\odot}/3$) host environments probed by untargeted versus targeted SN searches is $N_U/N_T \approx 5.1$, and galaxy-targeted SN searches offer a smaller baseline for probing metallicity distribution differences.
2. In our own sample and combining observations from all spectroscopic

studies of SN Ibc host environments to date, we find no statistical difference between the metallicity distributions of SN Ib and Ic or between SN Ib and IIb. We place a limit on the median metallicity difference between SN Ib and Ic ($\lesssim 0.1$ dex) and find that a sample $\gtrsim 2\times$ as large would be required to unambiguously confirm a difference at that level. This limit corresponds to a very small difference in the mass loss rate of metal line-driven winds, suggesting that it may not be the dominant factor distinguishing SN Ib and Ic progenitors.

3. SN Ic-BL are found in host environments with substantially lower metallicity than SN Ic, confirming the result of Kelly & Kirshner (2012). We show that the median metallicity of SN Ic-BL found by untargeted SN searches is ~ 0.15 dex lower than those found by targeted SN searches, yielding closer agreement to LGRB host environments. Moreover, the young stellar population ages of SN Ic-BL appear to be lower than SN Ib and Ic, but the sample is not large enough to be significant.
4. Evaluating the systematic effects afflicting studies of SN Ibc host environment metallicities, we find that the bias introduced by galaxy-targeted SN searches is most significant. Galaxy-nucleus spectroscopy can serve as a good proxy for explosion site metallicity measurements, but studies using photometric metallicity estimates would require sample sizes ~ 2 times larger. Biases in spectroscopic follow-up of SNe discovered by optical transient searches and uncertainties in SN classification play smaller roles.

In the era of wide-field, untargeted SN searches, we anticipate that significant progress will be made towards unveiling the progenitors of SN Ibc through the study of their host environments. We advocate for continued spectroscopic studies of the host environments of SN Ibc discovered by untargeted surveys to uncover or place stricter limits on the difference in the metallicity distribution of SN Ib and Ic. Optical facilities with large light-gathering power are required to measure metallicities in the low-luminosity, relatively high-redshift galaxies hosting SNe discovered by untargeted surveys. To identify SN Ic-BL in this era and make progress on the GRB-SN connection in the face of limited resources for spectroscopic follow up, we suggest that host galaxy properties will become a significant aid to future photometric SN classification schemes.

Table 4.9. Overlap between SN Ibc host galaxy samples

	A+10	K+11	L+11	M+11	S+12	TW
A+10	28	7	0	0	0	0
K+11		67	3	12	3	4
L+11			20	5	0	5
M+11				47	0	5
S+12					9	4
TW						58

Note. — The numbers on the diagonal represent the total number of SNe Ibc in each sample; the numbers above the diagonal represent the intersection of the samples. The samples are the same as in Table 4.8.

Table 4.10. Statistics of the combined SN Ibc sample

	All	Nuclear	Exp. Site
SN Ib vs Ic			
All	47; 68; $0.08^{+0.21}_{-0.06}$	11; 26; $0.48^{+0.37}_{-0.34}$	36; 42; $0.16^{+0.33}_{-0.13}$
Targeted	26; 39; $0.65^{+0.24}_{-0.43}$	7; 18; $0.57^{+0.30}_{-0.35}$	19; 21; $0.63^{+0.28}_{-0.38}$
Untargeted	21; 29; $2.0^{+6.8}_{-1.7} \times 10^{-2}$	4; 8; $0.38^{+0.36}_{-0.33}$	17; 21; $0.06^{+0.12}_{-0.05}$
SN IIb vs Ib			
All	25; 47; $0.56^{+0.31}_{-0.35}$	13; 11; $0.60^{+0.31}_{-0.33}$	12; 36; $0.31^{+0.40}_{-0.25}$
Targeted	17; 26; $0.21^{+0.39}_{-0.15}$	12; 7; $0.15^{+0.18}_{-0.12}$	5; 19; $0.32^{+0.42}_{-0.24}$
Untargeted	8; 21; $0.75^{+0.19}_{-0.32}$	1; 4;	7; 17; $0.70^{+0.20}_{-0.35}$
SN Ic-BL vs Ic			
All	18; 68; $1.3^{+9.8}_{-1.2} \times 10^{-4}$	3; 26;	15; 42; $1.8^{+12.3}_{-1.5} \times 10^{-3}$
Targeted	6; 39; $4.4^{+16.1}_{-3.8} \times 10^{-2}$	2; 18;	4; 21; $0.38^{+0.42}_{-0.29}$
Untargeted	12; 29; $1.7^{+6.0}_{-1.5} \times 10^{-3}$	1; 8;	11; 21; $7.2^{+12.9}_{-6.0} \times 10^{-3}$
SN Ic-BL vs Ibc			
All	18; 127; $2.3^{+21.0}_{-2.1} \times 10^{-4}$	3; 41;	15; 86; $4.5^{+19.5}_{-3.8} \times 10^{-3}$
Targeted	6; 73; $4.7^{+13.1}_{-4.0} \times 10^{-2}$	2; 29;	4; 44; $0.39^{+0.38}_{-0.31}$
Untargeted	12; 54; $3.1^{+12.9}_{-2.7} \times 10^{-3}$	1; 12;	11; 42; $1.1^{+3.1}_{-0.9} \times 10^{-2}$

Note. — This table lists the KS test p -value (p_{KS}) and sample size (N) for SN Ibc metallicity distributions (PP04 scale) in the combined sample. Each table entry reflects a different cut on the SN discovery (galaxy-targeted or untargeted) and spectroscopic methods (nuclear or explosion site; see also Figure 4.8). Each entry is given as $N_1; N_2; p_{\text{KS}}$. “SN Ibc” is a combination of SN Ib, Ic, and Ib/c.

Chapter 5

Using Colors to Improve Photometric Metallicity Estimates for Galaxies

N. E. Sanders, E. M. Levesque, A. M. Soderberg 2013, *The Astrophysical Journal*,
Vol. 775, 125

abstract

There is a well known correlation between the mass and metallicity of star-forming galaxies. Because mass is correlated with luminosity, this relation is often exploited, when spectroscopy is not available, to estimate galaxy metallicities based on single band photometry. However, we show that galaxy color is typically more effective than luminosity as a predictor of metallicity. This is a consequence

of the correlation between color and the galaxy mass-to-light ratio and the recently discovered correlation between star formation rate (SFR) and residuals from the mass-metallicity relation. Using Sloan Digital Sky Survey spectroscopy of $\sim 180,000$ nearby galaxies, we derive “*LZC* relations,” empirical relations between metallicity (in seven common strong line diagnostics), luminosity, and color (in ten filter pairs and four methods of photometry). We show that these relations allow photometric metallicity estimates, based on luminosity and a single optical color, that are $\sim 50\%$ more precise than those made based on luminosity alone; galaxy metallicity can be estimated to within $\sim 0.05 - 0.1$ dex of the spectroscopically-derived value depending on the diagnostic used. Including color information in photometric metallicity estimates also reduces systematic biases for populations skewed toward high or low SFR environments, as we illustrate using the host galaxy of the supernova SN 2010ay. This new tool will lend more statistical power to studies of galaxy populations, such as supernova and gamma-ray burst host environments, in ongoing and future wide field imaging surveys.

5.1 INTRODUCTION

The gas-phase metallicity of galaxies, as measured from their nebular emission spectrum, is correlated with galaxy luminosity (Lequeux et al. 1979; Garnett & Shields 1987). This relation has been used as a key observational tool in the study of populations such as supernova host galaxies (e.g. Prantzos & Boissier 2003; Arcavi et al. 2010), where gas-phase metallicity is an important proxy for

the properties of their short lived progenitor stars. However, using Sloan Digital Sky Survey (SDSS) imaging and spectroscopy for $\sim 53,000$ galaxies, Tremonti et al. (2004) showed that the luminosity-metallicity relation has a large intrinsic scatter of $\sigma = 0.16$ dex (50%), in terms of metallicity residuals, which limits the utility of this relation as an effective indicator of metallicity.

There are two primary causes for the scatter in the luminosity-metallicity relation. First, while the scatter in the *mass*-metallicity relation is fairly small ($\sigma = 0.10$ dex, Tremonti et al. 2004), luminosity is not a perfect proxy for mass. The mass-to-light ratio of galaxies is highly correlated with galaxy color, such that redder galaxies at a fixed luminosity are more massive (Bell & de Jong 2001; Kauffmann et al. 2003b). Second, a more fundamental relation has been uncovered between mass (M), metallicity (Z), and star formation rate (SFR) (Lara-López et al. 2010; Mannucci et al. 2010). This “fundamental plane” or “Fundamental Metallicity Relation” has remarkably small residual scatter ($\sigma = 0.05$ dex), indicating that variations in SFR are responsible for much of the scatter in the mass-metallicity relation. The existence of this fundamental plane is a valuable constraint for models of galaxy evolution, and likely an expression of galaxy outflows, infall, downsizing, and/or gas-rich mergers (Mannucci et al. 2010; Peeples & Shankar 2011; Yates et al. 2012). To improve the precision of photometric metallicity estimates, a readily accessible observable must be used to break the degeneracy between luminosity, mass, and SFR.

In this paper, we show that the addition of color information significantly decreases the scatter in photometric metallicity estimates. We derive the optimal projection of the fundamental plane for star-forming galaxies, in terms of the

observable properties luminosity and color, that we call the *LZC* relation. We describe the sample of SDSS galaxies we use to study these correlations and methods for spectroscopic metallicity estimation in Section 5.2. In Section 5.3, we derive analytic expressions for the *LZC* as expressed in a variety of different filter sets, methods of photometry, and metallicity diagnostics and we discuss the limitations of these calibrations in Section 5.4. Finally, in Section 5.5, we describe how specific observational studies may benefit from the *LZC* relation in making precise metallicity determinations from imaging available from wide field sky surveys.

5.2 GALAXY SAMPLE

We used spectroscopic data and derived quantities from the MPA/JHU catalog¹ of 927,552 star-forming galaxies from the SDSS-DR7 (Abazajian et al. 2009).² The catalog includes emission line fluxes, stellar masses (based on SED fitting to *ugriz* photometry), and star formation rates for each galaxy, as described in Kauffmann et al. (2003b); Brinchmann et al. (2004); Salim et al. (2007). While the MPA/JHU line fluxes are corrected for Galactic extinction, we additionally correct them for intrinsic reddening using the Balmer flux decrement. The fluxes are measured on continuum-subtracted spectra and therefore the $H\alpha$ and $H\beta$ line fluxes are corrected for Balmer absorption from the underlying stellar

¹The MPA/JHU catalog is available at <http://www.mpa-garching.mpg.de/SDSS>

²We assume a standard Λ CDM cosmology throughout this work, adopting the Hubble constant $H_0 = 73 \text{ km s}^{-1} \text{ Mpc}^{-1}$, $\Omega_m = 0.3$, and $\Lambda = 0.7$.

population (Tremonti et al. 2004). We assume $F_{\text{H}\alpha}/F_{\text{H}\beta} = 2.85$ (corresponding to $T = 10,000$ K and $n_e = 10^4 \text{ cm}^{-3}$ for Case B recombination; Osterbrock & Ferland 2006) and the extinction curve of Cardelli et al. (1989), assuming $R_V = 3.1$.

We joined the MPA/JHU catalog data with the photometric data from the SDSS-DR9 (SDSS-III Collaboration et al. 2012). To compare the effects of different methods of photometry, we include the SDSS model, cModel, Petrosian, and 3" fiber magnitudes (for details see Stoughton et al. 2002). We adopt the model/cModel and Petrosian magnitude K -corrections provided in the NYU Value Added Galaxy Catalog (Blanton et al. 2005; Blanton & Roweis 2007; Padmanabhan et al. 2008), and for the fiber magnitudes we adopt the K -corrections from the MPA/JHU catalog (only available for the g, r, i filters).³ We correct the photometry for foreground Galactic dust extinction (Schlegel et al. 1998).

We perform preliminary sample cuts on the catalog following a modified version of the prescription of Mannucci et al. (2010), as follows. First, we require that the galaxy be included in the SDSS MAIN spectroscopic sample, i.e. $r < 17.77$ mag after Galactic reddening correction. Second, we limit the sample to galaxies with $0.03 < z < 0.3$. This guarantees the availability of [O II] $\lambda 3727$ and is more inclusive than the $0.07 < z < 0.3$ cut of Mannucci et al. 2010. Third, we adopt the data quality cut from Mannucci et al. (2010), $(\text{S/N})_{\text{H}\alpha} > 25$, $F_{\text{H}\alpha}/F_{\text{H}\beta} > 2.5$, which they chose to provide high data quality (high signal to

³All K -corrections are made to the $z = 0$ frame.

noise and not saturated) in all relevant emission lines without biasing the sample explicitly towards higher metallicities. Fourth, we require the fraction of the r -band flux within the SDSS fiber to the full Petrosian flux to be > 0.05 , to exclude $\sim 0.1\%$ galaxies where the SDSS spectroscopy includes very little of the total flux and may not reflect the galaxy global properties.

Fifth, we reject AGN following Kauffmann et al. (2003a). Finally, we require that K corrections be available (see methodology below) and that the derived metallicity (see methodology below) be within a reasonable physical range ($7 < \log(\text{O}/\text{H}) + 12 < 9.5$). We make no selection based on the internal extinction within the galaxies (A_V ; Mannucci et al. 2010 excluded high-reddening galaxies).

For each galaxy, we compute oxygen abundance as a proxy for metallicity using a variety of strong line diagnostics that are widely used in the literature (Table 5.1; see Lopez-Sanchez et al. 2012 for a recent review). First, we employ several diagnostics relying on the R23 ratio, which depends on the fluxes of O II $\lambda\lambda 3726, 3729$, O III $\lambda 4959$ and $\lambda 5007$, and $\text{H}\beta$. The R23 diagnostic suffers from a degeneracy (see e.g. Kewley & Dopita 2002) that we break using either the N2O2 (N II $\lambda 6584$ to O II $\lambda 3727$) or N2 (N II $\lambda 6584$ to $\text{H}\alpha$) ratios, following the authors' prescriptions. Next we employ diagnostics depending on N2, N2O2, and O3N2, the flux ratio of O III $\lambda 5007$ and N II $\lambda 6584$. Finally, we employ diagnostics based on the ionization parameter, P , the ratio of O III $\lambda 4959$ and $\lambda 5007$ to R23. It is necessary to calibrate for multiple diagnostics because they exhibit well known systematic discrepancies, which are particularly strong between those diagnostics calibrated empirically and those calibrated against photoionization models (Kewley & Ellison 2008). Yates et al. (2012) have already shown that the

fundamental metallicity relation varies with the diagnostic used.

The number of galaxies in our final sample, following the cuts described, varies somewhat with the choice of filter set, photometric system, and metallicity diagnostic. We consider $\sim (110 - 120) \times 10^3$ galaxies with Tremonti04 metallicities and $\sim (160 - 180) \times 10^3$ galaxies for other metallicity diagnostics.

Figure 5.1 demonstrates two correlations in the galaxy sample. First, it shows the well known luminosity-metallicity correlation (shown using M_g), where more luminous galaxies typically have higher metallicities. However, there is significant scatter in this relation, with a standard deviation of $\sigma_0 = 0.13$ dex in the metallicity residuals from the g band luminosity-metallicity relation. Second, the figure demonstrates that there is a correlation between the residual in metallicity (the offset from the luminosity-metallicity relation) and galaxy color.

5.3 LUMINOSITY-METALLICITY-COLOR RELATION

Following Mannucci et al. (2010), we project the LZC relation onto an axis μ with components of color and luminosity:

$$\mu = M_i - \alpha \times (m_i - m_j) \quad (5.1)$$

$$12 + \log(\text{O}/\text{H}) = p_0 + p_1 \mu + p_2 \mu^2 + p_3 \mu^3 \quad (5.2)$$

where i, j are choices of filters and p_l are parameters of a third order polynomial.

Table 5.1. Metallicity Diagnostics Used

Name	Method	Source
M91	R23	McGaugh 1991 ^a
KD02	N2O2	Kewley & Dopita 2002 ^b
KK04	R23	Kobulnicky & Kewley 2004
PP04	N2,O3N2	Pettini & Pagel 2004
Tremonti04	model ^c	Tremonti et al. 2004
PVT	P	Pilyugin et al. 2010 ^d

^aWe have adopted the revised prescription suggested by Kobulnicky et al. (1999).

^bFollowing Kewley & Ellison (2008), we adopt the average of the M91 and KK04 for the lower branch solution.

^cThe Tremonti04 metallicities are estimated based on simultaneous fits of all major emission lines to photoionization models and are provided in the MPA/JHU catalog

^dWe use the “ONS” solution, which includes a dependence on the S II flux, for the conditions $\log(\text{N2}) > -0.1$ and $\log(\text{N2/S2}) > -0.25$ (which is true for $\sim 98\%$ of the SDSS galaxies).

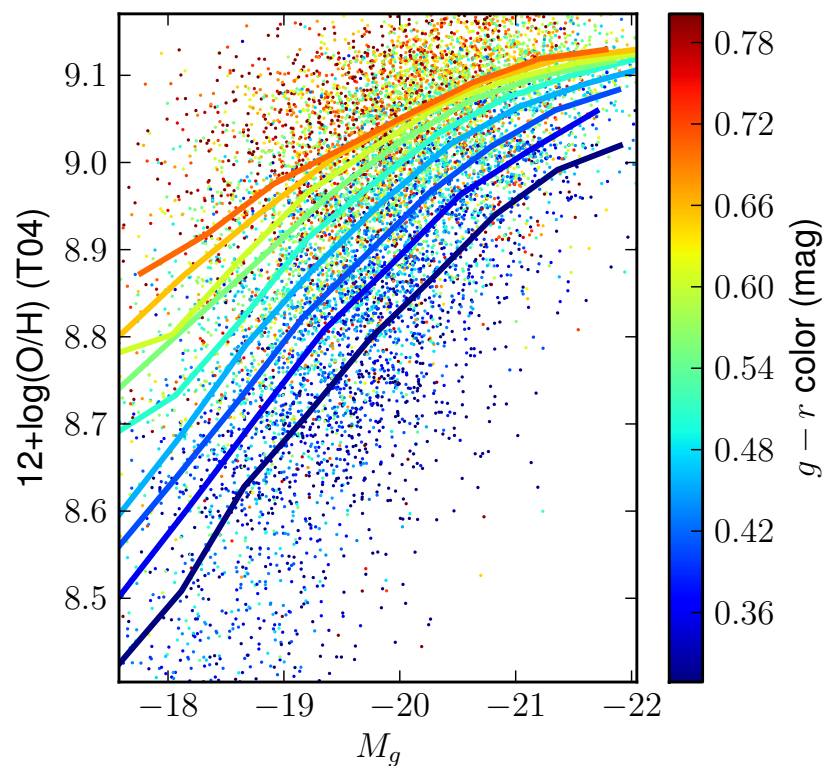


Figure 5.1.— A luminosity-metallicity (g -band, Tremonti04 metallicity, Model magnitudes) plot showing a random subset of 10,000 SDSS galaxies, color coded by $g - r$ color. The solid lines show the median luminosity-metallicity relation for the galaxies divided into 10 equal-sample-size bins in $g - r$ color.

For each combination of metallicity diagnostic, luminosity band, and color, we determine the optimal projection of the galaxy LZC relation by sampling from a grid of α parameters and selecting the value that minimizes the variance in the residuals of metallicity. We calculate the best-fit polynomial using the median value for metallicity in 15 equally-spaced bins along the projected axis, as shown in Figure 5.2. We report the optimal value of α and corresponding best fit LZC parameters p in Table 5.2 (for α values in terms of the physical parameters mass and SFR, see Andrews & Martini 2013).

We find a correlation between the luminosity-metallicity relation and color which varies in strength depending on the choice of metallicity diagnostic and filter set. Figure 5.2 demonstrates this optimization for one filter set (g, r) and three choices of metallicity diagnostic: Tremonti04, KD02, and PP04 O3N2. For PP04 O3N2, the scatter in the metallicity residuals of the LZC relation is $\sigma_Z = 0.07$ dex, as compared to the LZ relation ($\alpha = 0$), $\sigma_{Z,0} = 0.10$ dex (an improvement of 37% on a linear scale).

The decrease in residual scatter is similar in other metallicity diagnostics, ranging from 17 – 51%. For further statistics, see Table 5.2.

A nominal correction for the mass-to-light ratio only will account for much, but not all, of the reduction in scatter. For example, for M_g and $(g - r)$, $\alpha = 5.4$ would correspond to the mass-to-light ratio necessary to convert luminosity (M_g) to stellar mass (Kauffmann et al. 2003b), but this value of α is smaller than the optimal value in any metallicity diagnostic ($\alpha \sim 6 - 19$, see Table 5.2).

Note that, regardless of the choice of diagnostic or filters, the residual scatter

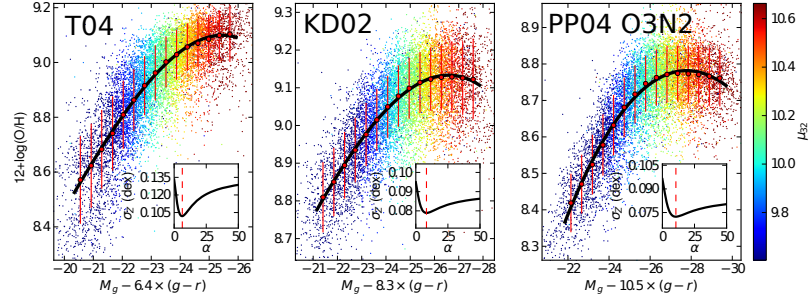


Figure 5.2.— The optimal projection of the LZO relation for M_g , $g-r$ color, and three different metallicity diagnostics (Tremonti04, KD02, and PP04 O3N2; all in the Model photometric system). The red points and lines show the median and standard deviation of the metallicity for galaxies in 15 bins. The projected LZO relation is shown for the optimal value of α , with the best fit third order polynomial LZO relation in black, extending over the calibrated range (2 – 98th percentile). The color coding shows the optical physical parameter (μ_{32}) from Mannucci et al. (2010). The insets display the standard deviation in the residuals in metallicity from the LZO as a function of the color-weighting parameter α , with the optimal value marked by the dashed line.

is lower for asymptotically high values of α than it is for $\alpha = 0$. This implies that, in general, color is more effective than luminosity as a predictor of metallicity.

In contrast, the residual scatter achieved by Mannucci et al. (2010) in terms of the optimal projection of the physical parameters stellar mass (M_*) and SFR, $\mu_{0.32} = \log(M_*) - 0.32 \log(\text{SFR})$, was only 0.05 dex. However, estimation of $\mu_{0.32}$ is based on full *ugriz* imaging and $R \sim 2000$ optical spectroscopy, while the *LZC* relation relies on imaging in just two bands and a redshift estimate. The coloring in Figure 5.2 illustrates that the optimal projection of the photometric properties is highly correlated with $\mu_{0.32}$, with Pearson correlation coefficient $\rho \sim 0.6 - 0.9$ for all metallicity diagnostics and filters. We calculated $\mu_{0.32}$ for the galaxies in our sample using the photometric mass measurement and aperture-corrected SFR estimates from the MPA-JHU catalog.

In general, filter sets that include bluer filters and/or incorporate a greater separation in central wavelengths produce a greater improvement in σ_Z (see Figure 5.3). The three most effective filter combinations are $[g - r, g - i, u - z]$, producing $\sigma_Z/\sigma_{Z,0} = [0.78, 0.80, 0.80]$ (taking the median across all metallicity diagnostics and methods of photometry). The three least effective are $[i - z, u - g, r - i]$, with $\sigma_Z/\sigma_{Z,0} = [0.94, 0.91, 0.91]$.

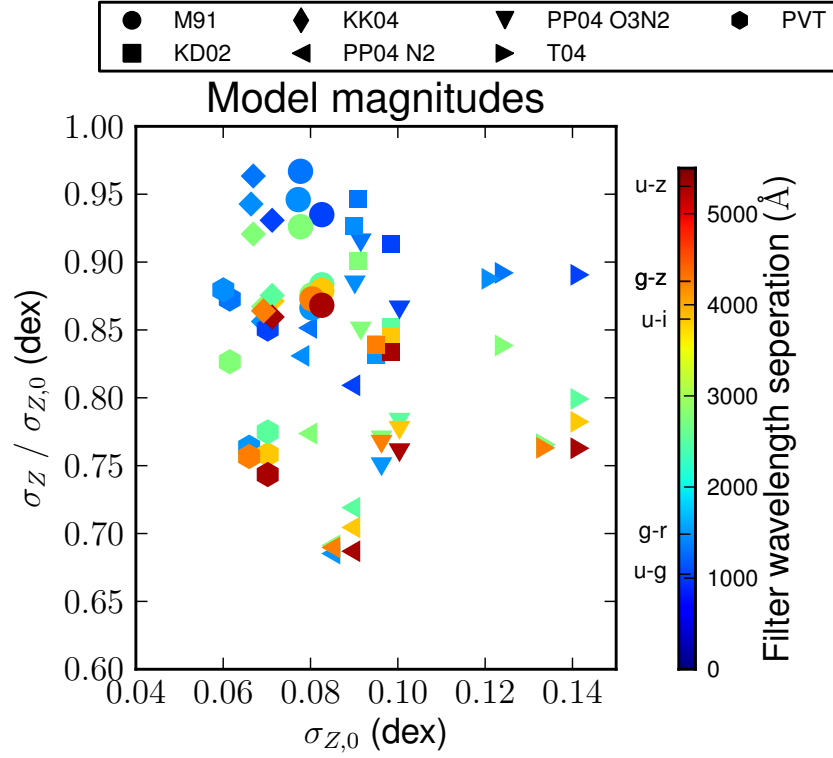


Figure 5.3.— Summary statistics of the LZC calibrations. The axes show $\sigma_{Z,0}$, the scatter in metallicity around the luminosity-metallicity relation, and the ratio of σ_Z , the scatter in metallicity around the optimal LZC relation, to $\sigma_{Z,0}$. Smaller values on the y -axis represent improvement in scatter due to the addition of color information. Each point shown represents an independent calibration for a particular choice of luminosity filter, color filter pair (see color coding), and metallicity diagnostic (different symbols). The color coding is based on the separation in Angstroms of the effective wavelength of the two color filters, and a few filter combinations are indicated in the colorbar at right. Only results from the model photometric method is shown – results for other methods are similar.

Table 5.2. Parameters of the LZC relations

L	Color	α	$p_3 \times 10^5$	$p_2 \times 10^3$	$p_1 \times 10^3$	p_0	$\sigma_{Z,0}$	σ_Z	μ range
PP04 O3N2 – model									
u	$u - g$	5.8	-98.57	-94.43	-2951.55	-21.48	0.100	0.087	[-29.0,-22.8]
u	$u - r$	4.1	-55.79	-59.71	-2023.09	-13.30	0.100	0.079	[-29.4,-22.7]
u	$u - i$	3.9	-83.33	-82.75	-2687.82	-19.90	0.100	0.078	[-30.5,-23.5]
u	$u - z$	3.5	-47.07	-51.13	-1769.68	-11.02	0.100	0.076	[-30.6,-23.0]
g	$g - r$	10.5	-9.02	-18.82	-836.54	-1.87	0.096	0.072	[-29.7,-21.9]
g	$g - i$	7.5	-68.65	-68.11	-2210.54	-14.79	0.096	0.074	[-30.5,-23.0]
g	$g - z$	6.2	-19.35	-25.61	-993.07	-3.20	0.096	0.074	[-30.9,-22.3]
r	$r - i$	11.0	-241.03	-198.54	-5431.00	-40.58	0.092	0.084	[-26.9,-21.7]
r	$r - z$	9.6	-16.28	-24.51	-977.73	-2.96	0.092	0.078	[-29.2,-21.6]
i	$i - z$	11.3	84.65	45.53	699.29	11.03	0.090	0.080	[-26.1,-19.1]

Note. — Parameters of the LZC relation defined in Equation 5.1; L is the photometric band of the luminosity, α is the optimal value of the color weighting factor to minimize the scatter in metallicity, and p_l are the parameters of the best-fit LZC polynomial for the corresponding value of α . The range of μ , the optimal projection of luminosity and color, over which the diagnostic is calibrated. The μ range is defined by the 2nd and 98th percentiles in μ (see Equation 5.1) of the SDSS galaxies in the calibration sample. Table 5.2 is published in its entirety the electronic edition of the Astrophysical Journal. A portion is shown here for guidance regarding its form and content.

5.4 CAVEATS

Here we note certain caveats and limitations of the *LZC* calibrations presented in this work and caution users not to apply them outside of the regime of the calibration data.

First, we recommend that the SDSS model magnitudes be used when applying the *LZC* relations to estimate galaxy metallicity. Model magnitudes should provide the most accurate measurements of galaxy colors⁴, although Petrosian and cModel magnitudes are typically in agreement with model magnitudes to within < 0.1 mag. We provide calibrations using the other SDSS photometric methods here for completeness and to support applications to datasets where photometry is only available in a particular method (i.e. Petrosian photometry). Fiber magnitudes, which are integrated over a fixed 3" aperture, may not encompass the full galaxy for large or nearby objects. The fiber magnitude calibrations may be useful for explorations of aperture effects (see e.g. Kewley et al. 2005).

Second, the redshift range of the calibration data is $0.03 < z < 0.3$ (Section 5.2). The *LZC* relations need to be tested for evolution at higher redshifts due to evolution in the fundamental plane for star-forming galaxies and passive evolution of galaxy colors. It is unclear to what extent the fundamental plane evolution would effect the calibrations. Cresci et al. (2012) found no evolution to $z \sim 0.8$ and Lara-López et al. (2010) concluded that there is no detectable evolution out to $z \sim 3.5$. However, Perez-Montero et al. (2012)

⁴<http://www.sdss3.org/dr9/algorithms/magnitudes.php>

investigate a larger sample of ~ 5000 zCOSMOS galaxies to $z \sim 1.3$ and report evolution of the SFR-corrected mass-metallicity relation starting at $z \gtrsim 0.4$. As data is assembled to corroborate evolution in these fundamental plane relations, it may also be used to calibrate the redshift dependence of the *LZC* relations.

Third, redshift estimates are needed to evaluate luminosity and apply *K*-corrections to estimate metallicity using the rest-frame *LZC* calibrations we present here. Using *ugriz* photometry of SDSS main sample galaxies ($r < 17.77$ mag, $z < 0.4$), photometric redshift estimates for galaxies can be achieved with scatter $\delta z \sim 0.02$ (Ball et al. 2008), while *K*-corrections can be determined to $\lesssim 20\%$ (Blanton & Roweis 2007). In some applications of the *LZC*, galaxy redshift may already be known through e.g. observations of a hosted supernova. When using only 2 bands of photometry (the minimal use case for the *LZC*), *K*-corrections have a larger uncertainty (an additional scatter of $\sim 5 - 20\%$ versus full-photometric corrections; Chilingarian et al. 2010).

To test the uncertainty in metallicity introduced by use of photometric redshifts (photo-*z*) and 2-band *K*-corrections, we recompute metallicities for the subset of $\sim 70,000$ galaxies in the MPA-JHU catalog with photo-*z* estimates in the SDSS-DR9. We use the *kd*-tree nearest neighbor fit photo-*z* estimates, as described in Csabai et al. (2007). We compute *K*-corrections using the analytic prescriptions of Chilingarian et al. (2010), using both the spectroscopic and photometric redshifts for each galaxy. We apply the *LZC* relation as calibrated for the PP04 O3N2 metallicity diagnostic using the M_g luminosities and $g - r$ colors (model magnitudes). The resulting distribution of metallicity residuals (δZ) for the spectroscopic versus photometric redshifts suggests that there is no

systematic bias introduced by photo- z (median $\delta Z = 0.000$ dex). The typical uncertainty added to the metallicity estimates is negligible (standard deviation $\delta Z = 0.008$ dex) and therefore the photometric metallicity estimate is dominated by the scatter in the LZC relation.

Some additional properties of galaxies may effect their metallicity as estimated from the LZC relation. Edge-on galaxies may be redder than face-on equivalents, leading towards an upward bias in their LZC metallicity. Galaxy inclination could be included as an additional parameter in a future calibration of the LZC . Early-type galaxies may contaminate photometric samples of star-forming galaxies. Early-types should be excluded by careful application of color-magnitude diagrams; they may not lie along the extrapolation of the LZC relation to redder colors, and the gas-phase metallicity of early-types may not be of interest in any case.

Fourth, we caution that the statistics presented here describe the bulk of the galaxy distribution (e.g. median and 1σ contours), while individuals may be outliers from this population. Like any photometric method for galaxy metallicity estimation, the LZC relations are most robust when applied to a statistical sample of galaxies.

5.5 APPLICATIONS

The calibrated LZC relation we present could benefit several disciplines, allowing for precise and accurate metallicity estimates for galaxies based on photometry

alone. Spectroscopic metallicity measurement demands considerably more observational resources, while full SED modeling provides only weak constraints on metallicity (1σ scatter of ~ 0.2 dex, e.g. Pacifici et al. 2012) and accesses the chemical composition in the older, stellar population rather than the gas phase. In contrast, the *LZC* relation can be employed to make precise measurements of gas phase metallicity using existing multi-band photometry from wide-field surveys such as SDSS or newly acquired, targeted observations, so long as an estimate for the redshift of each galaxy is available.

Studies of supernova (SN) host galaxies can support inferences into progenitor star populations (e.g. Modjaz et al. 2008; Prieto et al. 2008; Sanders et al. 2012c), with some studies relying on photometry rather than spectroscopy to measure the host galaxy metallicity (e.g. Prantzos & Boissier 2003; Boissier & Prantzos 2009; Arcavi et al. 2010). However, Sanders et al. (2012c) have shown that the statistical uncertainty associated with metallicity estimates based on the galaxy luminosity-metallicity relation is a significant barrier to detecting subtle differences in metallicity among SN populations. Moreover, because some SNe strongly prefer blue galaxies (high SFR environments; Levesque et al. 2010b; Kelly & Kirshner 2012), photometric metallicity estimates will be biased if color information is not incorporated. Using the *LZC* relation will effectively remove this bias, and significantly reduce the uncertainty in metallicity measurements. The additional uncertainty introduced by photo- z should be minor, as SN host galaxies studies are almost exclusively done in the $z < 0.15$ regime (see compilation in Sanders et al. 2012c), and spectroscopic redshift estimates are often available from the SN spectroscopy. We note that the *LZC* relation predicts

the galaxy metallicity in the inner few kpc of the galaxy, as probed by the 3" SDSS spectroscopic fibers, and significant offsets may exist from the SN host environment metallicity due to metallicity gradients in galaxies. However, these metallicity offsets are typically small ($\lesssim 0.1$ dex; Sanders et al. 2012c), and the intrinsic scatter in the radial metallicity profiles of galaxies limits observers' ability to spatially isolate the explosion site with spectroscopy (Rosolowsky & Simon 2008; Sanders et al. 2012a).

Similarly, galaxy metallicity measurements are key to the discussion of the progenitor properties of long-duration gamma-ray bursts (LGRBs, see e.g. Fynbo et al. 2003; Sanders et al. 2012d). While the host environments of LGRBs typically fall below the mass-metallicity relation (Levesque et al. 2010b), it has been shown that these host galaxies do follow the fundamental plane relation (Mannucci et al. 2011, but see also Kocevski & West 2011). Because LGRBs are frequently discovered at high redshift ($z > 1$), the *LZC* relation could potentially be used to derive metallicity estimates at considerably lower expense than deep NIR spectroscopy (e.g. Maiolino et al. 2008). However, in order to study the high redshift extremely lowest metallicity environments preferred by LGRBs ($Z \lesssim 0.3 Z_{\odot}$, see e.g. Mannucci et al. 2011), additional calibration is needed to extend the *LZC* relation beyond the range probed by the SDSS galaxy sample, which is $0.4 Z_{\odot} \lesssim Z \lesssim 1.3 Z_{\odot}$ and $z < 0.3$ (with only 10% of the galaxies in our sample being at $0.2 < z < 0.3$).

As a usage example, we apply the *LZC* relation to the unusual host galaxy of the SN 2010ay. In Sanders et al. (2012d), we report that this host galaxy is a 2σ outlier from the luminosity-metallicity relation. The median and 1σ

metallicity interval for SDSS galaxies with luminosity similar to this host galaxy ($M_B = -18.3$ mag) is $12 + \log(\text{O}/\text{H}) = 8.93 \pm 0.17$ (Tremonti04). This is a factor of $\gtrsim 2$ greater than the spectroscopically-measured Tremonti04 metallicity of $12 + \log(\text{O}/\text{H}) = 8.58$. The discrepancy is due to the extremely low mass-to-light ratio and high SFR of the host galaxy. The *LZC* relation cannot be applied in all filter combinations because the host lies outside the calibrated range for μ . Using the *LZC* relation for M_r and $r - i$ color, we find a Tremonti04 metallicity of $12 + \log(\text{O}/\text{H}) = 8.58 \pm 0.03$ (with an additional systematic uncertainty of 0.1 dex from the spread in the *LZC* relation). This agrees well with the spectroscopically measured value and has a significantly lower associated uncertainty than the estimate from the luminosity-metallicity relation. Because the *LZC* relation cannot be applied in all filter combinations, this cases illustrates the importance of extending the calibration presented here to lower-metallicity host galaxies not well-represented in the SDSS spectroscopic sample.

Finally, we suggest that the next generation of wide field, multi-band, photometric surveys could use the *LZC* relation to characterize the metallicity distribution of galaxies in the local universe, and perhaps its evolution with redshift. The Pan-STARRS1 (PS1) survey is already operating, and will provide $g_{\text{P1}} r_{\text{P1}} i_{\text{P1}} z_{\text{P1}} y_{\text{P1}}$ photometry for $\sim 2 \times 10^8$ galaxies over 3/4 of the sky (Saglia et al. 2012). In the future, the Large Synoptic Survey Telescope (LSST) will provide *ugrizy* photometry of $\sim 10^{10}$ galaxies to $z \sim 6$ (LSST Science Collaboration et al. 2009). With the advent of such datasets, the *LZC* relation may play an important role in defining the metallicity distribution of galaxies that has emerged from the cosmic evolution of star formation and galaxy mass.

To fulfill that role, the calibrations presented here must first be extended to higher redshift using data from ongoing spectroscopic surveys of the high redshift universe.

Chapter 6

PS1-12sk is a Peculiar Supernova

From a He-rich Progenitor

System in a Brightest Cluster

Galaxy Environment

N. E. Sanders, A. M. Soderberg, R. J. Foley, R. Chornock, D. Milisavljevic, R. Margutti, M. R. Drout, M. Moe, E. Berger, W. R. Brown, R. Lunnan, S. J. Smartt, M. Fraser, R. Kotak, L. Magill, K. W. Smith, D. Wright, K. Huang, Y. Urata, J. S. Mulchaey, A. Rest, D. J. Sand, L. Chomiuk, A. S. Friedman, R. P. Kirshner, G. H. Marion, J. L. Tonry, W. S. Burgett, K. C. Chambers, K. W. Hodapp, R. P. Kudritzki, P. A. Price 2013, *The Astrophysical Journal*, Vol. 769,

abstract

We report on our discovery and observations of the Pan-STARRS1 supernova (SN) PS1-12sk, a transient with properties that indicate atypical star formation in its host galaxy cluster or pose a challenge to popular progenitor system models for this class of explosion. The optical spectra of PS1-12sk classify it as a Type Ibn SN (c.f. SN 2006jc), dominated by intermediate-width ($3 \times 10^3 \text{ km s}^{-1}$) and time variable He I emission. Our multi-wavelength monitoring establishes the rise time $dt \sim 9 - 23$ days and shows an NUV-NIR SED with temperature $\gtrsim 17 \times 10^3 \text{ K}$ and a peak magnitude of $M_z = -18.88 \pm 0.02 \text{ mag}$. SN Ibn spectroscopic properties are commonly interpreted as the signature of a massive star ($17 - 100 M_\odot$) explosion within a He-enriched circumstellar medium. However, unlike previous Type Ibn supernovae, PS1-12sk is associated with an elliptical brightest cluster galaxy, CGCG 208-042 ($z = 0.054$) in cluster RXC J0844.9+4258. The expected probability of an event like PS1-12sk in such environments is low given the measured infrequency of core-collapse SNe in red sequence galaxies compounded by the low volumetric rate of SN Ibn. Furthermore, we find no evidence of star formation at the explosion site to sensitive limits ($\Sigma_{\text{H}\alpha} \lesssim 2 \times 10^{-3} M_\odot \text{ yr}^{-1} \text{ kpc}^{-2}$). We therefore discuss white dwarf binary systems as a possible progenitor channel for SNe Ibn. We conclude that PS1-12sk represents either a fortuitous and statistically unlikely discovery, evidence for a top-heavy IMF in galaxy cluster cooling flow filaments, or the first clue suggesting an alternate progenitor channel for Type Ibn SNe.

6.1 INTRODUCTION

Traditionally, hydrogen-poor supernovae (Type I SNe) have been classified into three sub-classes based on the presence of Si (Type Ia), He (Type Ib), or the absence of both features (Type Ic) in their optical spectra (see Filippenko 1997 for a review). Since the discovery of SN 1999cq (Matheson et al. 2000), a new sub-class of “Type Ibn” SNe have emerged, characterized by intermediate-width (FWHM $\sim 3 \times 10^3$ km s $^{-1}$) He I emission. The most well studied of these SNe Ibn is SN 2006jc (Pastorello et al. 2007), while other examples identified in the literature are limited to 2000er (Pastorello et al. 2008a), 2002ao (Foley et al. 2007), 2011hw (Smith et al. 2012), and perhaps SN 2005la (Pastorello et al. 2008b).

Several lines of evidence point to a massive star ($\sim 17 - 100 M_{\odot}$) origin for SNe Ibn. First, the He I emission is representative of a dense circumstellar medium (CSM), suggesting a progenitor with an He-rich envelope and high mass loss rate, such as a Wolf Rayet star (Foley et al. 2007; Pastorello et al. 2008a; Smith et al. 2008; Tominaga et al. 2008). Second, a Luminous Blue Variable (LBV)-like eruption was observed at the location of SN 2006jc ~ 2 yr before the SN explosion (Pastorello et al. 2007). Third, late-time (~ 2 months) IR and spectroscopic observations of SN 2006jc suggest hot carbon dust formation in the SN ejecta, with total $M_{ej} \sim 5 M_{\odot}$ (Di Carlo et al. 2008; Mattila et al. 2008; Nozawa et al. 2008; Smith et al. 2008; Tominaga et al. 2008; Sakon et al. 2009). Fourth, all past SNe Ibn have been found in star-forming galaxies, consistent with a massive star progenitor. Intermediate-width H emission has been detected in

the spectra of some SNe Ibn, with strengths significantly weaker than the He I lines (Pastorello et al. 2008a; Smith et al. 2008, 2012). Intermediate-width H α emission suggests a connection between SNe Ibn and IIn – a class whose spectra are dominated by intermediate-width H spectral features and are in some cases associated with LBV-like progenitors (Pastorello et al. 2008b; Gal-Yam et al. 2007; Gal-Yam & Leonard 2009; Smith et al. 2011b; Kochanek et al. 2011; Mauerhan et al. 2012). The close temporal connection between these LBV-like events and the SN explosions suggests a massive star progenitor, but also challenges models for massive star evolution that predict stars should spend the final ~ 1 Myr of their lives in a core-He burning Wolf-Rayet phase (Heger et al. 2003; Smith et al. 2012).

Here we present observations of a newly discovered SN Ibn found in a host environment with no direct evidence of a young stellar population. The optical transient PS1-12sk was discovered on 2012 March 11 by the Panoramic Survey Telescope & Rapid Response System 1 survey (Pan-STARRS1, abbreviated PS1, Kaiser et al. 2002) at $z_{P1} = 18.66 \pm 0.01$ mag at position $08^{\text{h}}44^{\text{m}}54.86^{\text{s}} + 42^{\circ}58'16.89''$ (J2000), within the galaxy cluster RXC J0844.9+4258. The object was spectroscopically classified as the first Type Ibn SN discovered by Pan-STARRS1 after just ~ 2 years of survey operation. At $z = 0.054$, PS1-12sk is more distant than any previously discovered SN Ibn.¹

We describe our multi-wavelength (radio through X-ray) observations of

¹We assume a standard Λ CDM cosmology throughout this work, adopting the Hubble constant $H_0 = 71 \text{ km s}^{-1} \text{ Mpc}^{-1}$, a distance modulus for PS1-12sk and its host environment (CGCG 208-042) of $\mu = 36.88$, and a luminosity distance of 238 Mpc.

PS1-12sk in Section 6.2. In Section 6.3, we discuss the observed properties of PS1-12sk and compare to past SNe Ibn. Our multi-wavelength monitoring of PS1-12sk provides the most detailed information to date on the rise phase and NUV-NIR SED of a Type Ibn SN. Deep stacks of pre-explosion PS1 imaging and optical spectroscopy allow us to characterize the host environment of PS1-12sk in depth (Section 6.4), pointing to the massive elliptical brightest cluster galaxy CGCG 208-042 as the most likely host galaxy and placing strong limits on star formation levels at the explosion site. We infer characteristics of the progenitor system from our observations of PS1-12sk in Section 6.5. In light of the observed explosion and host environment properties, we discuss several possible massive star and white dwarf progenitor channels for this SN in Section 6.6, and speculate on their implications for the initial mass function (IMF) and star formation in the cluster environment. We conclude in Section 6.7.

6.2 OBSERVATIONS

6.2.1 Optical Photometry

After discovery with PS1 on MJD 55997, we monitored the optical evolution of PS1-12sk through MJD 56049 (see Figure 6.3), after which it went into conjunction with the sun. These observations are summarized in Table 6.1 and described below.

PS1 is a high-extended wide-field imaging system, designed for dedicated survey observations. The system is installed on the peak of Haleakala on the

island of Maui in the Hawaiian island chain. Routine observations are conducted remotely, from the University of Hawaii–Institute for Astronomy Advanced Technology Research Center (ATRC) in Pukalani. A complete description of the PS1 system, both hardware and software, is provided by Kaiser et al. (2002). The PS1 optical design is described in Hodapp et al. (2004), the imager is described in Tonry & Onaka (2009), and the survey design and execution strategy are described in Chambers (in preparation). The standard reduction, astrometric solution, and stacking of the nightly images is done by the Pan-STARRS1 IPP system (Magnier 2006; Magnier et al. 2008). The nightly Medium Deep stacks are transferred to the Harvard FAS Research Computing cluster, where they are processed through a frame subtraction analysis using the *photpipe* image differencing pipeline developed for the SuperMACHO and ESSENCE surveys (Rest et al. 2005; Garg et al. 2007; Miknaitis et al. 2007). A summary of details of PS1 operations relevant to SN studies is given in Chomiuk et al. (2011), and additional PS1 SN studies were presented by Gezari et al. (2010); Botticella et al. (2010); Chomiuk et al. (2011); Narayan et al. (2011); Berger et al. (2012); Sanders et al. (2012d); Valenti et al. (2012); Chornock et al. (2013); Lunnan et al. (2013b).

The PS1 observations are obtained through a set of five broadband filters, which we have designated as g_{P1} , r_{P1} , i_{P1} , z_{P1} , and y_{P1} (Stubbs et al. 2010). Although the filter system for PS1 has much in common with that used in previous surveys, such as the Sloan Digital Sky Survey (SDSS: York et al. 2000; Aihara et al. 2011), there are important differences. The g_{P1} filter extends 200 Å redward of g_{SDSS} , and the z_{P1} filter is cut off at 9200 Å. SDSS has no corresponding y_{P1} filter. Further information on the passband shapes is described in Stubbs et al.

(2010). Photometry is in the “natural” PS1 system, $m = 2.5 \log(\text{flux}) + m'$, with a single zero-point adjustment m' made in each band to conform to the AB magnitude scale (Tonry et al. 2012). We assume a systematic uncertainty of 1% for our PS1 observations due to the asymmetric PS1 point spread function and uncertainty in the photometric zero-point calibration (Tonry et al. 2012).

PS1 observed the field of PS1-12sk in two prior seasons dating to December 2009 (MJD 55174), but we detect no transient flux before the March 2012 explosion. Considering observations in all filters, the [2009 – 2010, 2010 – 2011, 2011 – 2012] pre-explosion observing seasons had durations of [10, 27, 15] weeks and typical cadences of [4, 4, 1] days, respectively. The pre-explosion imaging consists of [16, 18, 22, 32, 21] frames in $[g_{\text{P1}}, r_{\text{P1}}, i_{\text{P1}}, z_{\text{P1}}, y_{\text{P1}}]$ band with median 3σ limiting absolute magnitude of $M_{g,r,i,z,y} \gtrsim [-14.1, -13.8, -15.4, -14.6, -15.0]$ mag, respectively. These pre-explosion limits are not strongly constraining in the context of a SN 2006jc-like pre-explosion outburst, an LBV-like flare with peak magnitude $M_r \sim -14.1$ mag that was detected for just nine days (Pastorello et al. 2007).

Additional *ugriz* imaging was acquired with the 2.0 m Liverpool Telescope with the optical CCD camera RATCam from MJD 56015 – 56039. RATCam data were reduced following Valenti et al. (2011). Fixed aperture (3”) photometry of PS1-12sk was performed using SExtractor (Bertin & Arnouts 1996) and zero points were measured from comparison with field stars in the SDSS catalog. Flux from CGCG 208-042 at the position of PS1-12sk was below the noise level of the RATcam observations, so template subtraction was not performed.

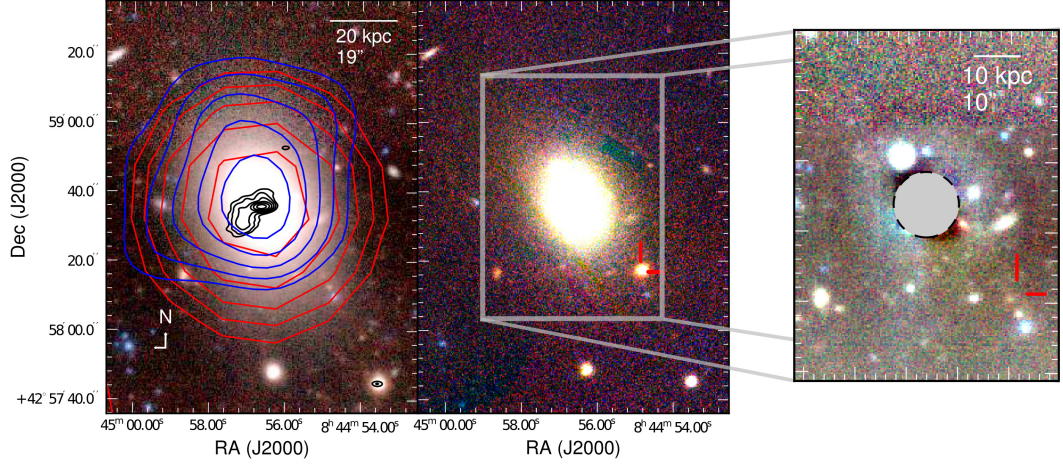


Figure 6.1.— Multiwavelength observations of the field of PS1-12sk. Left: optical composite of $g_{P1}r_{P1}z_{P1}$ pre-explosion PS1 images from December 2009 to May 2012, shown with log stretch. Contours from our 5.9 GHz JVLA observations are overlaid in black (beam FWHM $\sim 3.5''$), NVSS 1.4 GHz radio observations are overlaid in red (beam FWHM $\sim 45''$), and XMM-Newton X-ray observations are overlaid in blue (FWHM $\sim 6''$). The radio and X-ray emission is centered on CGCG 208-042, the brightest cluster galaxy. Middle: PS1 $g_{P1}r_{P1}z_{P1}$ imaging of the environment near the peak of PS1-12sk (2012 March 13; MJD 55999), shown with linear stretch. The SN position is marked. Right: The deep composite with the model for the BCG subtracted (linear stretch; a $1 \times 1.33'$ field). The circular mask excludes the inner $7''$ of the residual image for source detection.

UV/optical observations of PS1-12sk with the Swift-UVOT instrument (Roming et al. 2005) were acquired from MJD 56013 – 56032. Observations were performed using all of its six broad band filters, spanning the wave-length range $\lambda_c = 1928$ Angstroms (*W2* filter) - $\lambda_c = 5468$ Angstroms (*V* filter, central wavelength). Starting from MJD 56041 the SN was too faint in the UV wavelength range and we therefore limited our follow up to the *U*, *B* and *V* filters. Data have been analyzed following the prescriptions by Brown et al. (2009). In particular: a 3" aperture has been used to maximize the signal-to-noise ratio. The AB photometry presented in Table 6.1 is based on the UVOT photometric system of Poole et al. (2008). Host galaxy imaging was not available for template subtraction, but the host galaxy flux at the explosion site is not significant compared to the uncertainty in the SN flux.

6.2.2 Optical spectroscopy

Our spectroscopic observations are summarized in Table 6.2 and displayed in Figure 6.2. Spectroscopy of PS1-12sk was first obtained with the BlueChannel (BC) spectrograph of the MMT (Schmidt et al. 1989a) on MJD 56012.5. A moderate resolution (0.7\AA px^{-1}) BC spectrum was taken on MJD 56014.2. Subsequent spectroscopy was performed with the Andalucia Faint Object Spectrograph and Camera of the Nordic Optical Telescope on MJD 56016.5, the Intermediate Dispersion Spectrograph of the Isaac Newton Telescope on MJD 56023.5, and BC on MJD 56041.5. All spectra were reduced using standard two-dimensional long-slit image reduction and spectral extraction routines in

Table 6.1. PS1-12sk Optical/NIR Photometry

MJD	Filter	m (AB mag)	Instrument
56021.3	H	21.24 ± 0.06	CFHT
56021.3	J	20.29 ± 0.08	CFHT
56021.3	K	21.80 ± 0.06	CFHT
56028.2	H	21.87 ± 0.08	CFHT
56028.2	J	21.02 ± 0.07	CFHT
56028.2	K	22.21 ± 0.06	CFHT
56013.1	H	> 19.27	PAIRITEL
56013.1	J	18.86 ± 0.10	PAIRITEL
56013.1	K	> 18.35	PAIRITEL
56014.2	H	> 19.08	PAIRITEL

Note. — Uncertainties reflect 1σ ranges while upper limits are 3σ . Table 6.1 is published in its entirety in the electronic edition. A portion is shown here for guidance regarding its form and content.

IRAF² and flux calibrated using observations of spectrophotometric standard stars obtained on the same night.

6.2.3 NIR imaging

We obtained NIR photometry of PS1-12sk using simultaneous *JHK* imaging from the robotic 1.3 m Peters Automated Infrared Imaging Telescope (PAIRITEL; Bloom et al. 2006) at Mount Hopkins, Arizona in 18 epochs from MJD 56013 – 56034. PAIRITEL images were reduced using the CfA pipeline described in Wood-Vasey et al. (2008) and Mandel et al. (2009), with more detailed discussion of the updated mosaic and photometry pipelines to be discussed in Friedman et al. (2013, in prep.). We did not perform template subtraction to remove the host flux, as the NIR flux from CGCG 208-042 at the position of PS1-12sk was below the noise level of the PAIRITEL observations. We use the 2MASS point source catalog to establish the photometric zero points (Cutri et al. 2003).

We obtained further imaging of PS1-12sk with WIRCAM (Puget et al. 2004) on the 3.6 m Canada-France-Hawaii Telescope (CFHT). NIR *J*, *H* and *Ks*-band observations were carried out on MJD 56021 and 56028. The data were processed with the standard WIRCAM pipeline. The photometric calibrations were performed against with the 2MASS point source catalog.

²IRAF is distributed by the National Optical Astronomy Observatory, which is operated by the Association of Universities for Research in Astronomy (AURA) under cooperative agreement with the National Science Foundation.

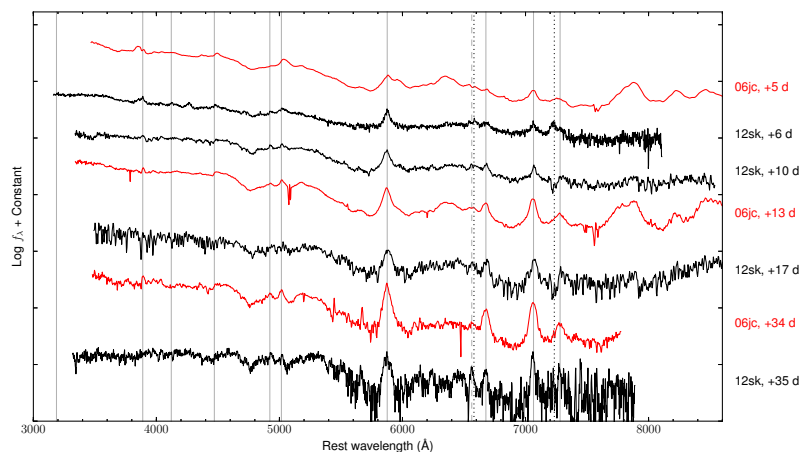


Figure 6.2.— Low-resolution spectroscopic sequence of PS1-12sk, with time since z -band peak noted at right. See Table 6.2 for observing details. The moderate resolution MMT/BC spectrum is shown separately in Figure 6.5. The locations of the He I features $\lambda\lambda 3188, 3889, 4121, 4471, 4922, 5016, 5876, 6678, 7065, 7281 \text{ \AA}$ are marked with solid lines; $H\alpha$ with a dashed line; and C II $\lambda\lambda 6580, 7234$ with dotted lines. Spectra of SN 2006jc at representative epochs (Pastorello et al. 2008a) are shown in red.

The NIR photometry from both instruments is listed in Table 6.1.

6.2.4 Radio Observations

We observed PS1-12sk with the Karl G. Jansky Very large Array (JVLA; Perley et al. 2009) on two epochs, MJD 56013.0 and 56059.0 ([+7,+53] d after z -band peak). All JVLA observations were obtained with two 1 GHz sidebands centered at 5.0 and 6.75 GHz, averaging to 5.9 GHz. We used calibrator J0818+4222 to monitor the phase and 3C147 for flux calibration. Data were reduced using the standard packages of the Astronomical Image Processing System (AIPS).

We do not detect a radio counterpart to PS1-12sk in these observations (Figure 6.1) and place upper limits of $F_\nu \lesssim [16, 22] \mu\text{Jy}$ (3σ) for each epoch respectively, corresponding to upper limits on the spectral luminosity of $L_\nu \lesssim [1.1, 1.5] \times 10^{27} \text{ erg s}^{-1}$. The SN 2006jc radio peak was 415 μJy at 8.46 GHz (VLA program AS887, PI Soderberg; see also Soderberg 2006). Given the distance to SN 2006jc of 28 Mpc the luminosity is $3.9 \times 10^{26} \text{ erg s}^{-1} \text{ Hz}^{-1}$ at ~ 80 days after explosion, a factor of ~ 3 below our upper limits for PS1-12sk. Figure 6.1 illustrates that the 5.9 GHz morphology of the host galaxy cluster emission is asymmetric and peaked at the center of brightest cluster galaxy CGCG 208-042, suggesting evidence of an active nucleus. Optical line emissions ratios verify the presence of AGN activity (Section 6.4).

The host environment of PS1-12sk is included in the NRAO VLA Sky Survey (NVSS) 1.4 GHz continuum survey (Condon et al. 1998). These observations are displayed in Figure 6.1, which shows that the 1.4 GHz flux of $16.4 \pm 0.6 \text{ mJy}$

($1.1 \times 10^{23} \text{ W Hz}^{-1}$ at $z = 0.054$) listed in the NVSS catalog is centered at the core of CGCG 208-042.

6.2.5 X-ray Observations

We observed PS1-12sk with the X-Ray Telescope (XRT, Burrows et al. 2005) onboard the *Swift* spacecraft (Gehrels et al. 2004), in the time period MJD 56013 – 56056, for a total of 26.4 ks. *Swift*-XRT data have been analyzed using the latest version of the HEASOFT package available at the time of writing (v. 6.12) and corresponding calibration files. Standard filtering and screening criteria have been applied. No point-like X-ray source is detected at the SN position. However, we find evidence for spatially extended X-ray emission from RXCJ0844.9+4258, the host galaxy cluster, at the SN location at the level of $(3 \pm 1) \times 10^{-14} \text{ erg s}^{-1} \text{ cm}^{-2}$, corresponding to a luminosity of $(2.0 \pm 0.7) \times 10^{41} \text{ erg s}^{-1}$ (0.3-10 keV). We assumed a simple power-law spectral model corrected for Galactic absorption in the direction of the SN with neutral H column density $N_H = 2.93 \times 10^{20} \text{ cm}^{-2}$ (Kalberla et al. 2005). Assuming the same spectral model, at the cluster core we measure a similar flux, $(4 \pm 1) \times 10^{-14} \text{ erg s}^{-1} \text{ cm}^{-2}$ (0.3-10 keV). For comparison, Immler et al. (2008) detected SN 2006jc with the Swift XRT at several epochs, finding a luminosity of $\sim 1 \times 10^{39} \text{ erg s}^{-1} \sim 1$ month after explosion, rising to ~ 4 times that level at ~ 4 months. The luminosity of SN 2006jc at any epoch was therefore well below the cluster background level we observe at the position of PS1-12sk.

We analyzed archival XMM-Newton data of the host galaxy cluster from

2007 November 6 (Program 50360; PI Mulchaey). The 26.8 ks observation was significantly impacted by high background levels due to solar flares. Following the procedure outlined in Jeltema et al. (2006), but using version 12.0.0 of the SAS reduction software, we identified periods of high flaring and removed these times from the dataset. The final effective exposure times are approximately 23 ksec for the MOS detectors and 13 ksec for the PN detector. Within the usable portion of the dataset, we find ~ 200 photons associated with the cluster. The cluster X-ray emission is extended and detected out to a radius $\sim 40''$ that includes the explosion site of PS1-12sk. The morphology of the X-ray emission shows that the emission is peaked at the center of the core of CGCG 208-042 as shown in Figure 6.1.

6.3 Comparison to Past Type Ib_n Supernovae

6.3.1 Light curve evolution

We present the full, multi-band light curve constructed from our observations of PS1-12sk in Figure 6.3. During the course of PS1 z -band observations, PS1-12sk rose by ~ 1 mag over ~ 9 days and then faded by ~ 3 mag over ~ 50 days.

Using a fifth-order polynomial fit, we estimate the peak magnitude in z -band to be -18.88 ± 0.02 mag at MJD = 56006.1 ± 0.3 . Similarly, in $[g, r, i]$ -band we find $M_{\text{peak}} = [-19.24 \pm 0.02, -19.08 \pm 0.02, -18.44 \pm 0.03]$ mag.

We estimate the foreground extinction affecting PS1-12sk to be insignificant. The Galactic extinction at its position is $E(B - V) = 0.03$ mag (Schlafly &

Finkbeiner 2011) and the host galaxy is unlikely to have significant local dust obscuration (see Section 6.4). Furthermore, the SED of the SN is not consistent with significant reddening given reasonable assumptions about the photospheric temperature (see Figure 6.4). We therefore do not correct for extinction in the following analysis.

Our z -band PS1 observations of PS1-12sk, tracking the rise of the SN in 4 epochs over ~ 9 d, are significant because, as noted by Pastorello et al. (2008a), no past SN Ibn was observed during the rise to maximum. A possible exception is SN 2011hw, which was observed to rise to over ~ 7 d after discovery, but only by ~ 0.1 mag (Smith et al. 2012). This is within the photometric uncertainty in the observations. Our pre-explosion non-detections constrain the rise time of PS1-12sk to be $9 \lesssim \tau \lesssim 23$ d. In contrast, pre-detection limits for the Type Ibn SN 1999cq suggest a very steep rise ($\lesssim 4$ d in unfiltered light) (Matheson et al. 2000). For SN 2006jc, pre-explosion limits suggest a rise time $\lesssim 17$ d (Itagaki et al. 2006), and similarly for SN 2002ao (~ 20 d, Pastorello et al. 2008a), while constraining pre-explosion limits are not available for SNe 2000er and 2011hw.

$BVRI$ photometry for SN 2006jc is also shown in Figure 6.3. Because the rise phase of SN 2006jc was not observed, the epoch of peak luminosity is not well constrained. At discovery, SN 2006jc had observed AB magnitudes of $M_{B,V,R,I} = [-17.9, -17.7, -17.6, -17.6]$ mag (based on photometry in Foley et al. 2007), ~ 1.5 mag less luminous than PS1-12sk at peak. Pastorello et al. (2008a) compile the optical light curves of SNe Ibn and report that SN 1999cq was discovered at $M \sim -20$ mag (unfiltered) and SN 2000er was discovered at $M_R \sim -19.5$ mag, $\sim 0.5 - 1$ mag more luminous than PS1-12sk. Based on the

spectroscopic phase of the SNe, Pastorello et al. (2008a) argue that SN 2002ao and 2006jc may have been similarly luminous at peak (before discovery). The r and i -band luminosity of PS1-12sk is similar to the observed peak of SN 2011hw (Smith et al. 2012), although SN 2011hw declined more slowly and was brighter in B by ~ 1 mag.

The $(g - r)$ color curve of PS1-12sk does not show significant evolution at the precision of our photometry, maintaining $(g - r) \approx 0 \pm 0.1$ mag from $\sim -5 - +35$ d (Figure 6.3). For the purpose of comparison to the PS1-12sk data, we have approximately transformed the $(B - R)$ colors of SN 2006jc and 2011hw to $(g - r)$ via Lupton (2005)^{3,4}. During the observed rise, the $(g - r)$ color of PS1-12sk reddens only slightly (~ 0.07 mag over 7 d; measured only at the $\sim 1\sigma$ level in our PS1 photometry). SN 2006jc evolved from $(g - r) \sim -0.5$ mag at discovery to $(g - r) \sim -0.8$ mag about two weeks later and then returned to $(g - r) \sim -0.5$ mag. This indicates bluer colors than PS1-12sk, although this level of color evolution cannot be ruled out for PS1-12sk given the uncertainty in our photometry after peak. The color of SN 2011hw was $(g - r) \sim -0.8$ mag, significantly bluer than that of PS1-12sk, and remained essentially constant from $\sim 15 - 60$ days (Smith et al. 2012).

The NIR-optical SED of PS1-12sk, shown in Figure 6.4, resembles a single-component power law. We use a Markov Chain Monte Carlo method

³<http://www.sdss3.org/dr9/algorithms/sdssUBVRITransform.php>

⁴Using the observed spectrum of PS1-12sk near peak, we estimate that K -correction from $z = 0.054$ would have a $\lesssim 0.1$ mag effect on the $(g - r)$ color, which we neglect here.

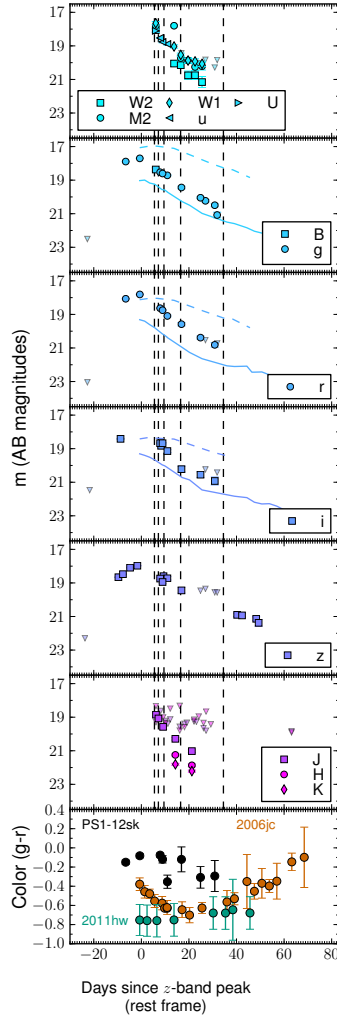


Figure 6.3.— The multi-band light curve of PS1-12sk and 3σ upper limits (triangles). The thin lines are the *BVRI* light curves (AB magnitudes) of SN 2006jc (solid, Foley et al. 2007) and SN 2011hw (dashed, Smith et al. 2012), shifted temporally so the brightest/first observation corresponds to the epoch of *z*-band peak for PS1-12sk (MJD = 56006.1 ± 0.3) and rescaled to $z = 0.054$. The bottom panel shows the optical color (AB magnitudes), corrected for Galactic extinction, of PS1-12sk, SN 2006jc, and SN 2011hw (Smith et al. 2012). No extinction or K-corrections have been applied. The dashed vertical lines indicate the epochs of our optical spectroscopy.

(Foreman-Mackey et al. 2012) to fit a blackbody model to the NUV-NIR portion of the SED. The spectral peak of the SED is not well constrained by our NUV observations, and the NUV spectrum of SNe Ibn is known to be contaminated by iron emission due to X-ray fluorescence (Foley et al. 2007). We therefore adopt a nominal temperature for our blackbody fit by introducing a Gaussian prior of $T = (17 \pm 2) \times 10^3$ K. This is similar to the temperatures near peak of other SNe showing strong circumstellar interaction (see e.g. Smith et al. 2010, and references therein). Given this prior, we obtain a radius of $(1.4 \pm 0.3) \times 10^{15}$ cm for the photosphere near the epoch of peak brightness. We place a limit of $\sim 10^{-17}$ ergs s^{-1} \AA^{-2} on any NIR excess above a blackbody SED within the first 1–3 weeks after maximum brightness. In SN 2006jc, an NIR excess corresponding to an additional warm (dust) blackbody component was detected at the onset of NIR monitoring at $\gtrsim 50$ d (Di Carlo et al. 2008; Smith et al. 2008). In the case of the more luminous SNe Ibn PS1-12sk and 2011hw, dust condensation may be delayed due to the higher equilibrium temperatures (Smith et al. 2012). Similarly, dust signatures in the ejecta of SNe IIn are usually not observed until $\gtrsim 200$ d (see e.g. Fassia et al. 2000; Fox et al. 2011).

6.3.2 Spectroscopic evolution

The spectra of PS1-12sk strongly resemble that of the Type Ibn SN 2006jc at similar epochs (Figure 6.2). The most prominent features in the spectra are the intermediate-width He I emission lines at $\lambda 5876$ \AA (Gaussian FWHM ~ 3000 km s^{-1}) and $\lambda 7065$ \AA (FWHM ~ 2000 km s^{-1}). The equivalent

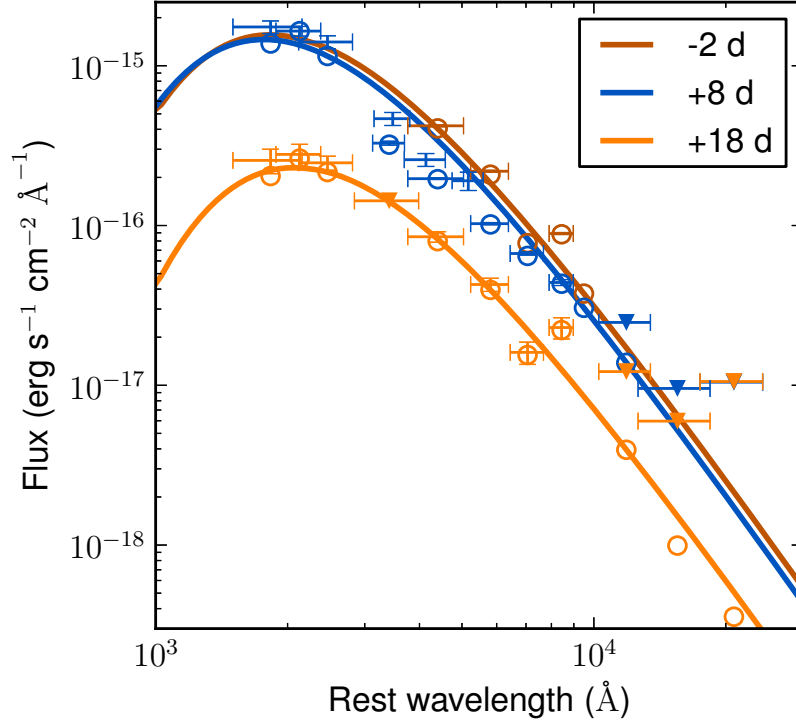


Figure 6.4.— The SED of PS1-12sk from photometry at three epochs (MJD = [56005, 56015, 56025] \pm 1.5). The circles show the linearly-interpolated light curve value in each filter at each precise epoch, error bars show the flux and filter width for the measured NUV-NIR photometric points nearest to each epoch (only when within 1.5 days), and triangles show the nearest 3σ upper limit. The solid-lines show the blackbody fit to the interpolated photometry. The NIR observations do not suggest a significant infrared excess for PS1-12sk within a few weeks of peak brightness.

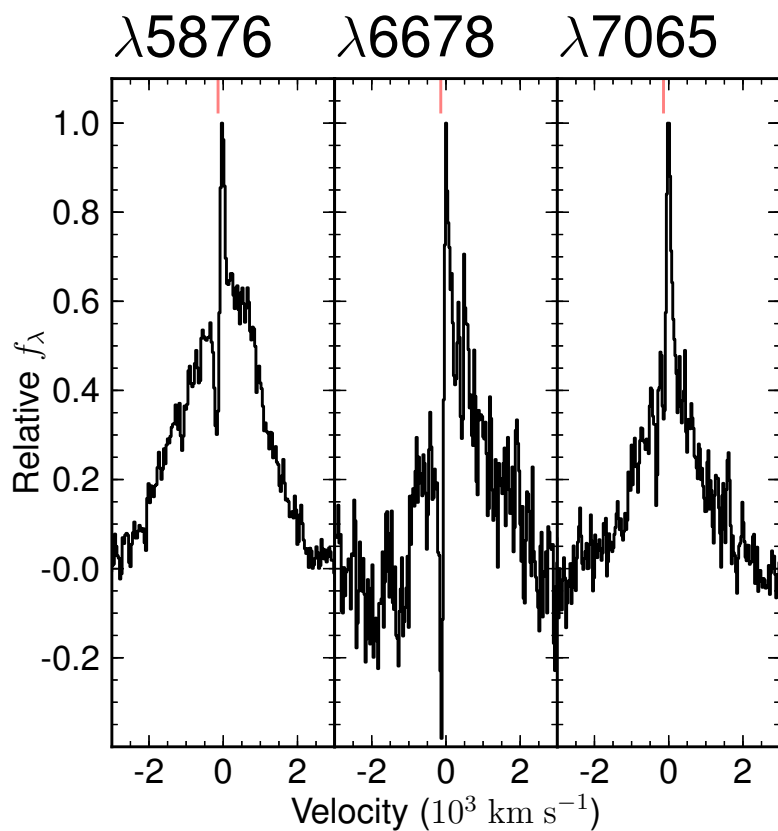


Figure 6.5.— Moderate resolution MMT/BC spectroscopy of He I features in PS1-12sk from MJD 56014.2, +8 d after z -band peak. The velocity scale is centered on the narrow emission component of the P-Cygni profiles, blueshifted by 190 km s^{-1} from the recession velocity of CGCG 208-042. The solid red line marks the center of the narrow absorption component, blueshifted by 140 km s^{-1} relative to the emission.

width of both lines increases substantially ($EW_{5876} \sim 50 - 100 \text{ \AA}$) from +6 to +35 days as the continuum fades. Weaker intermediate-width He I features at $\lambda\lambda 3188, 3889, 4121, 4471, 4922, 5016, 6678, 7281 \text{ \AA}$ are also visible in the spectra.

In Figure 6.5 we display our moderate resolution MMT/BC spectrum of PS1-12sk at +8 d. This spectrum reveals narrow ($\sim 100 \text{ km s}^{-1}$) P-Cygni profiles superimposed on the intermediate-width ($\sim 3000 \text{ km s}^{-1}$) He I emission lines. The narrow emission component is blueshifted from the recession velocity of CGCG 208-042 by 190 km s^{-1} , indicating a velocity offset for the progenitor star that is consistent with the velocity dispersion of CGCG 208-042 ($\sigma = 269 \pm 5 \text{ km s}^{-1}$, from SDSS DR9 spectroscopy; SDSS-III Collaboration et al. 2012). Relative to the narrow emission, the P-Cygni absorption features have a blueshift of $\sim 140 \text{ km s}^{-1}$ that is consistent between the three strong He I lines ($\lambda 5876, 6678, 7065$) visible in this spectrum.

We detect no systematic evolution in the He I line profiles. Smith et al. (2008) quantify the shape of the line profiles of SN 2006jc as the ratio of the flux summed on the red and blue sides of the He I $\lambda\lambda 5876, 7065$ lines. Calculating this ratio for the spectra of PS1-12sk, we find Pearson correlation coefficients of $r = -0.22$ and -0.66 , respectively, indicating no statistically significant trends with time. Significant reddening of the He I lines in SN 2006jc did not begin until $\sim +50$ days, beyond where our spectral series terminates. The available spectroscopy does not rule out later dust formation in PS1-12sk, or dust formation enshrouded by optically thick material at higher velocities.

While $H\alpha$ features are not apparent in our PS1-12sk spectra near peak,

intermediate-width $H\alpha$ (FWHM $\sim 1600 \text{ km s}^{-1}$) emission is present in the +35 day spectrum (see Figure 6.6). Similarly, late-developing $H\alpha$ features in the spectra of SNe 2002ao and 2006jc, narrower than those of He I, was interpreted by Pastorello et al. (2007) as evidence for an H-rich circumstellar shell beyond the He shell, which is ionized when the SN flux propagates through the He-rich shell or by the circumstellar interaction. Significantly stronger $H\alpha$ features were observed in the spectra of SN 2011hw, and discussed by Smith et al. (2012) in the context of a CSM with higher H/He abundance than SN 2006jc. We revisit the evolution of the He I and $H\alpha$ features in Section 6.5.2.

Intermediate-width C II $\lambda\lambda 6580, 7234$ emission is evident in the earliest two MMT/BC spectra (+6 and +8 days after peak). C II $\lambda 6580$ is a blend of lines at 6578 and 6583 Å, and in our moderate resolution spectrum we identify narrow absorption components corresponding to both lines at a blueshift consistent with that of the He I P-Cygni absorption components (320 km s^{-1} relative to the velocity of CGCG 208-042; see Figure 6.6). We note that this intermediate-width C II emission feature is also visible in the early time (+7 and +13 d) spectra of SN 2011hw (see Figure 3 of Smith et al. 2012), although there is significant blending with the stronger $H\alpha$ feature in this object. Broad photospheric C II absorption has previously been detected in SN Ia spectra (Tanaka et al. 2008; Parrent et al. 2011), and a few SNe Ibc (e.g., SN 2004aw; Taubenberger et al. 2006). The energy levels for these features are high (16 – 18 eV), and Parrent et al. (2011) show that the C II emission is found more often among SNe Ia with higher effective temperatures. This temperature dependence is consistent with our detection of C II lines only in the earlier spectra of PS1-12sk. Finally, we do

not detect the intermediate-width O I, Mg II, and Ca II emission features that are prominent in the red spectrum of SN 2006jc within ~ 2 weeks of discovery (Anupama et al. 2009; Chugai 2009).

6.4 Host environment properties

PS1-12sk is located $26.5''$ E and $18.8''$ N of the giant elliptical galaxy CGCG 208-042, with separation of $27.1''$ (projected distance 28.1 kpc, ~ 1.3 times the SDSS DR9 r -band Petrosian radius). CGCG 208-042 has redshift $z = 0.05402$ (from SDSS DR9 spectroscopy) and its morphological type is identified as elliptical with 96% confidence in the Galaxy Zoo I catalog (Lintott et al. 2011). Tempel et al. (2012) list CGCG 208-042 as the Brightest Cluster Galaxy (BCG) in their friends-of-friends group sample for SDSS DR8. The galaxy’s host cluster is RXC J0844.9+4258, listed as a point source in the Northern ROSAT All-Sky X-ray galaxy cluster catalog (Böhringer et al. 2000), with $L_X = 0.16 \times 10^{44} h_{50}^{-2}$ ergs s $^{-1}$ (0.1 – 2.4 keV).

For our adopted value $H_0 = 71$ km s $^{-1}$ Mpc $^{-1}$, the factor $h_{50}^{-2} \sim 0.50$. Using the best-fit X-ray scaling relation of Reiprich & Böhringer (2002), this corresponds to a total cluster halo mass of $\log(M_{200}) = 14.1_{-1.1}^{+1.1} h_{50}^{-1} M_{\odot}$ ($h_{50}^{-1} \sim 0.70$). This is consistent with the cluster mass derived by Yang et al. (2007) from the combined SDSS DR4 optical luminosity of 15 cluster members: $\log(M) = 14.0 h^{-1} M_{\odot}$.

We produce deep $g_{P1}r_{P1}i_{P1}z_{P1}y_{P1}$ stacks of PS1 pre-explosion imaging (exposure times of [45375, 47309, 118320, 151200, 75180] s, respectively) at the

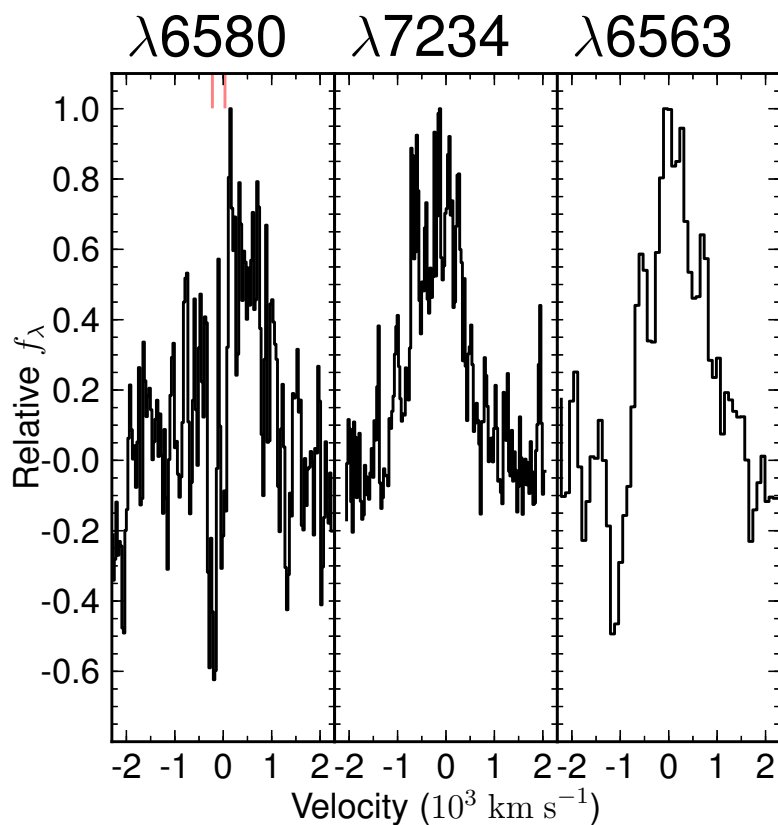


Figure 6.6.— Left: moderate resolution MMT/BC spectroscopy of C II $\lambda\lambda 6580, 7234$ features in PS1-12sk from +8 d after z -band peak. The narrow absorption components corresponding to $\lambda\lambda 6578, 6583$ are marked with the red solid lines. Right: The H α feature from the lower-resolution +35 days MMT spectrum. The velocity scale is relative to the He I narrow emission component, as in Figure 6.5.

host environment (Figure 6.1a). We use the two-dimensional fitting algorithm *GALFIT* (Peng et al. 2002, 2010) to model the galaxies within a $1 \times 1.33'$ rectangular region centered on CGCG 208-042 based on the PS1 pre-explosion stacks. We fit CGCG 208-042 with a Sersic model with Fourier components (to allow for asymmetry) and fit the remaining objects in the field simultaneously as point (PSF models) or extended sources (Sersic profiles; see Figure 6.1b).

We subtract the best fit model for CGCG 208-042 and perform object detection and photometry on the BCG-subtracted image (Figure 6.1c) using SExtractor. We exclude objects in a $7''$ radius from the BCG center, where residuals from the BCG model are strong, and require that sources be detected in the r and i band images. Assuming all sources in the image are galaxies associated with the cluster, we show a color-magnitude diagram for these 47 galaxies in Figure 6.7. One galaxy in the field has $M_r = -18.6$ mag, while the rest are dwarf galaxies, with luminosity in the range $M_r \sim [-11, -16]$ mag. The radial distribution of the dwarf galaxies is similar to the light distribution of the BCG, approximately following a r^{-2} profile.

The BCG-subtracted PS1 deep stack reveals no source at the position of the supernova PS1-12sk. By comparison to the faintest objects we detect, this implies a limit of $M_r \gtrsim -10.5$ mag for any unseen, positionally coincident host galaxy. In our moderate resolution MMT spectrum of PS1-12sk, we do not detect superimposed narrow $H\alpha$ emission with a 3σ upper limit of $L_{H\alpha} \lesssim 2 \times 10^{38}$ ergs s^{-1} kpc^{-2} given our ~ 1 kpc^2 aperture. This limit rules out the association of PS1-12sk with an individual giant HII region located within a few hundred parsecs, as seen for nearby SN Ib/c (Crowther 2012).

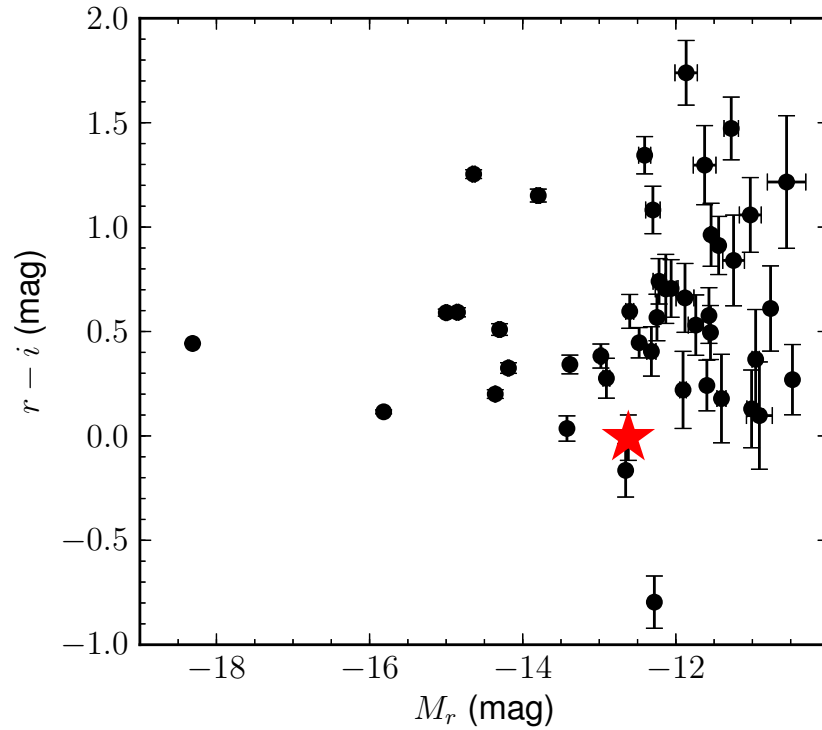


Figure 6.7.— Color-magnitude diagram for sources in the field of CGC 208-042, assumed to be galaxies in the cluster RXC J0844.9+4258. The sources were detected on the BCG-subtracted PS1 images displayed in Figure 6.1. The source closest to PS1-12sk is marked with the red star. CGC 208-042, with $M_r \sim -22.9$ mag and $(r - i) \sim 0.5$ mag, is not shown.

We place a limit on the star formation rate of the local host environment of $\lesssim 2 \times 10^{-3} M_{\odot} \text{ yr}^{-1} \text{ kpc}^{-2}$ (Kennicutt 1998, Salpeter IMF), an intensity similar to that of M101 and ~ 3 orders of magnitude below that of a starburst irregular like NGC 1569 (Crowther 2012). While internal extinction could relax this SFR limit, the color of PS1-12sk is not consistent with significant dust reddening (Section 6.3.1).

The source nearest to the SN site (separation ~ 2.4 kpc, assuming it is associated with the cluster) is unresolved in our PS1 images and has flux $[g_{P1}, r_{P1}, i_{P1}, z_{P1}] = [24.9 \pm 0.2, 24.3 \pm 0.1, 24.3 \pm 0.1, 24.7 \pm 0.2]$ mag. Adopting the redshift of the cluster, these magnitudes indicate a source with brightness and color $M_{[g_{P1}, r_{P1}, i_{P1}, z_{P1}]} = [-12.0 \pm 0.2, -12.6 \pm 0.1, -12.6 \pm 0.1, -12.2 \pm 0.2]$ mag) similar to blue ultra-compact galaxies found near NGC 4874 in the Coma cluster (Chiboucas et al. 2011). For comparison, UGC 4904, the host galaxy of SN 2006jc, has $M_g \approx -17$, similar to the Small Magellanic Cloud and ~ 60 times brighter than that of the faint source near the PS1-12sk explosion site. SN 2006jc was located near a spiral arm of UGC 4904, visible in SDSS imaging (SDSS-III Collaboration et al. 2012), at an offset of ~ 1.2 kpc from the galaxy center.

The dominant source of background flux at the SN explosion site is CGCG 208-042, while no flux is detected from the fainter source at this position. Based on our *GALFIT* modeling, we estimate that CGCG 208-042 is 3 times brighter at this position than the 3σ upper limit of flux contributed by other sources. We test the hypothesis that the spatial association of PS1-12sk and the putative dwarf galaxy is due to random chance using simulations. We randomly draw simulated SN positions from a radial distribution consistent with the BCG

light over the range $7'' < r < 25''$. For each simulated SN, we searched for dwarf galaxies within $2''$. We find that the likelihood of chance association with a dwarf galaxy is $\sim 14\%$. Because the dwarf galaxy near PS1-12sk is among the bluest in the field, with $r - i \sim 0$ mag, the likelihood decreases if the association is limited to bluer galaxies. For $(r - i) < [0.5, 1.0]$ mag, the likelihood is $\sim [7, 12]\%$. Additionally, we use the method of the SN Legacy Survey (Sullivan et al. 2006) to order the likelihood of association with potential host galaxy candidates, including the BCG and the nearby faint source described above.

We calculate the dimensionless R parameter, the elliptical SN-galaxy separation normalized by galaxy size, using the revised formula presented by Sand et al. (2011) and the elliptical aperture measured by SExtractor from the r_{P1} -band stacked image. For CGCG 208-042, $R \sim 3.1$, while for the fainter host galaxy candidate, $R \sim 5.6$. Using PS1 images in other bands ($g_{P1}i_{P1}z_{P1}$), the R value for CGCG 208-042 is similar and for the fainter candidate is larger ($R \approx 7 - 16$). We therefore conclude that available observations favor CGCG 208-042 as the most likely host galaxy of PS1-12sk.

While we do not detect evidence for star formation at the PS1-12sk explosion site, there is evidence for centrally-concentrated star formation in CGCG 208-042. Nebular emission line fluxes are detected in the SDSS $3''$ fiber spectrum of CGCG 208-042. The aperture-corrected star formation rate (SFR) listed in the MPIA/JHU catalog (Brinchmann et al. 2004) is $0.1^{+0.5}_{-0.1} M_{\odot} \text{ yr}^{-1}$. Using the SDSS DR9 spectroscopy and the emission line ratio diagnostics of Kewley et al. (2006), CGCG 208-042 is classified as a LINER/Composite galaxy, which suggests Active Galactic Nucleus (AGN) contamination of the emission lines

which could significantly inflate the SFR estimate (Salim et al. 2007). The FUV flux measured by GALEX ($F_{\text{FUV}} = 29 \pm 4 \mu\text{Jy}$ in General Release 6; Martin et al. 2005) provides an independent constraint on the SFR. Using the Kennicutt (1998) scaling relations, the extinction-corrected SFR is $0.33 \pm 0.03 M_{\odot} \text{ yr}^{-1}$ (assuming $A_{\text{FUV}} = 0.21 \text{ mag}$), which is reconcilable with the MPIA/JHU estimate given the observational uncertainties, AGN contamination, and the ~ 0.3 dex scatter observed between FUV and $\text{H}\alpha$ -based SFR estimates by Lee et al. (2009). The mass listed for the elliptical galaxy in the MPIA/JHU catalog is $2.62_{-0.52}^{+0.56} \times 10^{11} M_{\odot}$ indicating a specific star formation rate of $4.9_{-2.9}^{+16.6} \times 10^{-4} \text{ Gyr}^{-1}$.

We discuss the possibility of undetected star formation associated with a cluster cool core or dwarf galaxy tidal tail in Section 6.6.1.

6.5 Discussion

The observations we present in Section 6.2 suggest several key properties for the progenitor star of PS1-12sk. First, the most prominent features in the optical spectrum are intermediate-width He I features, reflecting a shock accelerated shell of dense circumstellar medium (CSM) material similar to that accompanying SN 2006jc (Pastorello et al. 2007; Foley et al. 2007; Smith et al. 2008). Second, the spectrum shows intermediate-width $\text{H}\alpha$ and C II features indicating additional material within the CSM, as well as unshocked material evidenced by blueshifted narrow absorption features corresponding to He I and C II. Third, the light curve shows a peak magnitude ($\sim -19 \text{ mag}$) consistent with a luminous SNe Ib, but declines at a rate similar to SN 1994I and significantly faster than typical SNe

Ibc (Drout et al. 2011). This suggests that the SN has unusual ejecta mass and kinetic energy properties, or that the light curve is powered by a source other than the radioactive decay of ^{56}Ni . Fourth, PS1-12sk was found within a galaxy cluster, with no evidence for ongoing star formation at the explosion site.

6.5.1 Basic Physical Constraints

Our z -band monitoring of PS1-12sk constrains the rise time to be $\sim 9 - 23$ days. Adopting the rise time as the delay for the forward shock to reach the edge of the He-rich circumstellar material, we use characteristic ejecta velocity to infer the radius of the dense CSM. While the FWHM of the observed He I $\lambda 5876$ Å line is ~ 3000 km s $^{-1}$, this may be representative of only the shocked circumstellar material and represents a lower limit for the SN ejecta velocity, v . A velocity, $v \sim 10,000$ km s $^{-1}$, is typical of core-collapse SN photosphere velocities (Filippenko 1997). Adopting this value, we find $R \sim (8 - 20) \times 10^{14} \left(\frac{v}{10000 \text{ km s}^{-1}} \right)$ cm. This is consistent with the photosphere radius we infer from the blackbody SED (Section 6.3.1). If we further interpret the absorption minimum of the He I P-Cygni profiles as indicative of the velocity of the mass ejection which populated the He-rich shell, then we infer that the mass ejection event would have taken place within the past 1.8 – 4.5 yrs. We note that our pre-SN PS1 photometry constrains a putative pre-SN transient to $\gtrsim -14$ mag, but the temporal coverage is not well matched to the expected duration of such an event (see Section 6.2.1).

As a basic estimate of the explosion energy, we estimate the integrated

bolometric flux of PS1-12sk using our observed photometry. We interpolate the light curve of PS1-12sk in our most well-sampled band (z -band) from -10 to 49 days. We derive a quasi-bolometric correction for the SN based on photometry from the epoch that is most well-sampled from NUV-NIR ($+6$ days; Figure 6.4). We assume this correction is constant during the duration of our observations, given that we do not find evidence for $g - r$ color evolution (Section 6.3.1). Performing Monte Carlo simulations drawing from the uncertainty distribution of our photometry, we find an integrated bolometric energy of $E \gtrsim 6.4 \pm 0.4 \times 10^{49}$ ergs. If we entirely neglect the NUV ($\lambda < 3000 \text{ \AA}$) flux, the total energy is decreased by only a factor of ~ 2 ; this could be more realistic if the high NUV flux we observe near peak is not maintained at later times.

If we attribute the full bolometric energy output of the SN near peak to interaction with a He-dominated CSM, we can roughly estimate the He ejected in the pre-explosion mass loss. Using the bolometric energy output estimated for the observed portion of the SN light curve in Section 6.6.1 ($E \sim 6.4 \pm 0.4 \times 10^{49}$ ergs) we find that a mass of $M_{He} \sim 0.06 M_{\odot} (10,000 \text{ km s}^{-1}/v_s)^2$ is required assuming full efficiency and pure He composition. This corresponding mass loss rate is $\dot{M} \sim 0.01 M_{\odot} \text{ yr}^{-1}$ given a wind velocity $v_w = 100 \text{ km s}^{-1}$ and CSM radius $R = 2 \times 10^{15} \text{ cm}$. Reducing the efficiency increases this M_{He} estimate while decreasing the He fraction decreases it.

6.5.2 Radioactive Decay

If we treat the light curve of PS1-12sk like that of Type I SNe powered by the radioactive decay of ^{56}Ni , without contributions from circumstellar interaction, we can estimate the physical parameters of the SN explosion using the SN Ibc light curve scaling relations of Drout et al. (2011). These relations are based on the original formalism derived by Arnett (1982) and modified by Valenti et al. (2008). In this framework, our estimates are upper limits and would be reduced by the additional contribution from circumstellar interaction. Converting the measured peak r_{P1} -band magnitude to R -band (Windhorst et al. 1991), we find $M_R \sim -19.6$ mag (Vega), which corresponds to a nickel mass of $M_{\text{Ni}} \lesssim 0.5 M_{\odot}$. This upper limit is $\sim 2\sigma$ above the population median for SNe Ib from the Drout et al. (2011) sample, $\langle M_{\text{Ni}} \rangle = 0.2 \pm 0.16 M_{\odot}$. Pastorello et al. (2008a) invoked a range of models with $M_{\text{Ni}} = 0.25 - 0.40 M_{\odot}$ to fit the bolometric light curve of SN 2006jc, while Tominaga et al. (2008) report an estimate, $M_{\text{Ni}} = 0.22 M_{\odot}$. While these masses are larger than those of typical core-collapse SNe, they fall far below the tens of solar masses of ^{56}Ni produced by models of the most massive exploding stars, e.g. pair instability supernovae (Heger & Woosley 2002).

The measured luminosity and light-curve width for PS1-12sk imply an ejecta mass $M_{\text{ej}} \sim 0.3 M_{\odot}$ and kinetic energy $E_{K,51} \sim 0.2$ in units of 10^{51} ergs. From our polynomial fit to the r -band light curve, we find $\Delta m_{15} = 1.44 \pm 0.07$ mag, which reflects a faster decline than any object in the sample of Drout et al. (2011) (except perhaps the fast-fading SN 1994I, $\Delta m_{15} \sim 1.4$ mag) and corresponds to a light curve width parameter, $\tau \sim 5$ d. These values are significantly lower than

typical SN Ib, which have $\langle M_{\text{ej}} \rangle = 2.0 \pm 1.0 M_{\odot}$ and $\langle E_{K,51} \rangle = 1.2 \pm 0.6 \times 10^{51}$ ergs. The result that $M_{\text{Ni}} > M_{\text{ej}}$ suggests that a process other than radioactive decay, presumably circumstellar interaction, is the dominant power source for the light curve.

Using our z -band detection of the SN at +59 days, we report an independent limit on the ^{56}Ni mass. To estimate the limit, we fit the analytic Type I SN nebular phase ($t \gtrsim 60$ d) light curve model from Valenti et al. (2008) assuming $M_{\text{ej}} = M_{\text{Ni}}$, $E_{K,51} = 1$, applying a bolometric correction based on the SED observed near peak ($BC = -4.33 \pm 0.06$ mag, see Section 6.6.1 and Figure 6.4), and interpreting the flux observed at this epoch to be wholly powered by the decay of $^{56}\text{Co} \rightarrow ^{56}\text{Fe}$. We find $M_{\text{Ni}} < 2.0 M_{\odot}$ if we model incomplete gamma-ray trapping using the exponential gamma-ray absorption probability and homologous density profile adopted by Valenti et al. (2008). If we assume full trapping, which may be more realistic when the inner regions of the SN ejecta is dense (Maeda et al. 2003), we find $M_{\text{Ni}} < 1.5 M_{\odot}$. These models are displayed in Figure 6.8. Adopting a more conservative estimate for the rise time, using the date of the latest z -band non-detection as the explosion date, has only a small effect on these limits ($M_{\text{Ni}} < [2.4, 1.7] M_{\odot}$ for [incomplete,full] trapping). These limits are likely inflated by contributions to the lightcurve from circumstellar interaction, the assumption of Ni-dominated ejecta, and/or if the ejecta is not yet fully nebular at this epoch.

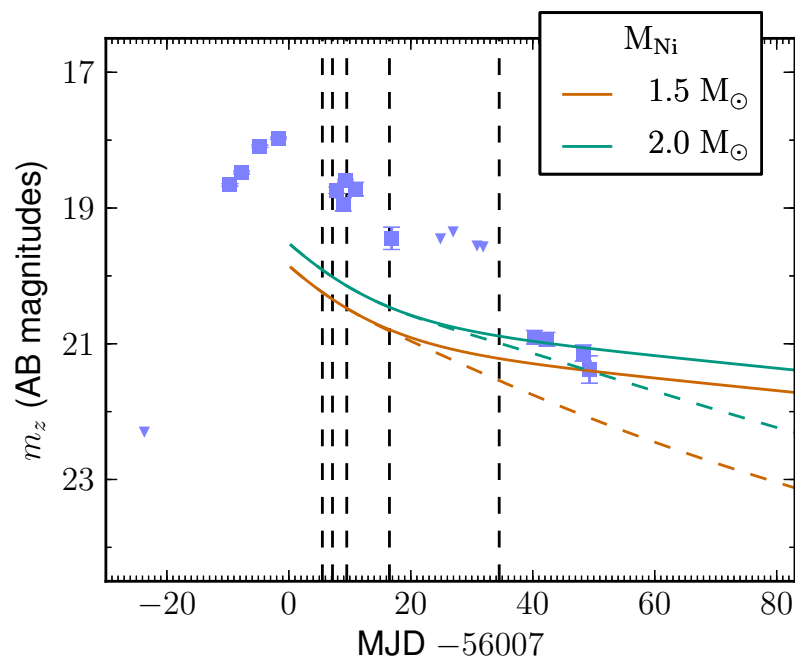


Figure 6.8.— The z -band light curve of PS1-12sk alongside the nebular phase Type I SN light curve models described in Section 6.6.1. The models are shown with full (solid) and incomplete (dashed) gamma-ray trapping and assuming the explosion date is the same as the discovery date.

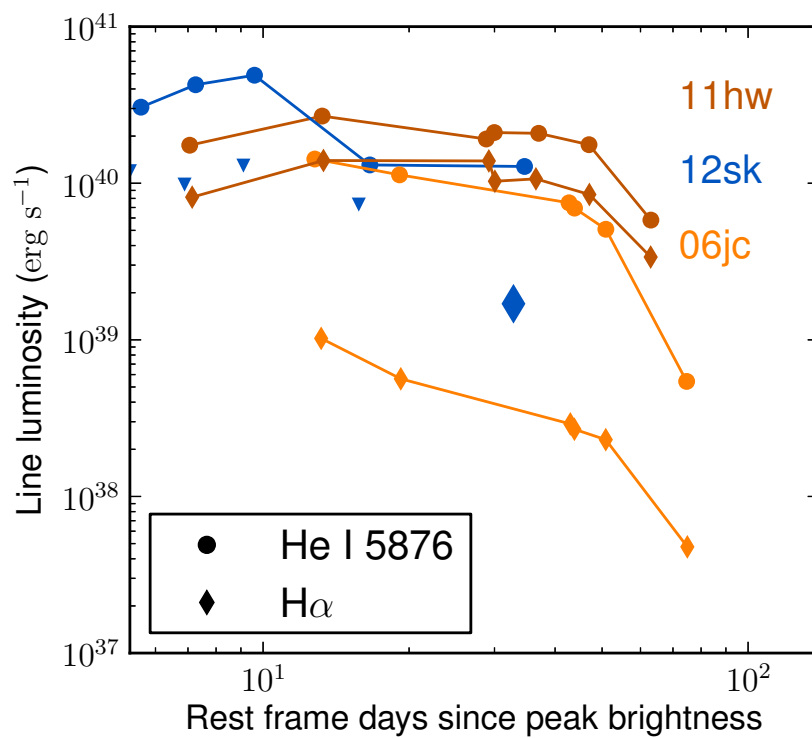


Figure 6.9.— Comparison of intermediate-width line luminosity between PS1-12sk and the SNe Ibn 2006jc and 2011hw (Smith et al. 2012), $H\alpha$ is only detected in the final spectrum (blue diamond) and limits (triangles) are plotted at earlier epochs.

H Emission

The detection of intermediate-width $H\alpha$ emission suggests a significant amount of H remains in the progenitor star near the time of explosion. To first order, we can estimate M_H by starting from our estimate of total CSM mass based on the bolometric energy output, assuming the standard abundance (90% He), and attributing the remaining mass to H rather than α elements (Section 6.6.2). H would then comprise 3% of the total mass, or $M_H \lesssim 0.002 M_\odot$, however the same order of magnitude uncertainties in velocity, efficiency, and composition apply as in the M_{He} calculation.

The $H\alpha$ emission line flux varies by about an order of magnitude in observed SNe Ibn, both in absolute terms and relative to the strength of the dominant He I $\lambda 5876$ line. Figure 6.9 shows the evolution of these emission lines for well-studied SNe Ibn. SN 2006jc had $H\alpha$ emission line fluxes an order of magnitude lower than He I $\lambda 5876$, but growing relative to He at late times. SN 2011hw was characterized by much stronger $H\alpha$ emission, only a few times lower than He I $\lambda 5876$. In the only epoch where we detect $H\alpha$ in PS1-12sk, it is about an order of magnitude weaker than He I $\lambda 5876$. $H\alpha$ emission was not detected in spectra of SN 1999cq (Matheson et al. 2000).

6.5.3 Host Environment

The host environments of past SNe Ibn 1999cq, 2000er, 2002ao, 2006jc, and 2011hw have exclusively been blue, spiral galaxies (Pastorello et al. 2008a; Smith et al. 2012). However, the fact that the first 5 known examples of SN Ibn occurred

in spiral galaxies is not, by itself, strong evidence of a massive star progenitor. The host environment statistics of SNe Ia, thermonuclear explosions of white dwarfs, are illustrative. Only $\sim 15\%$ of SN Ia occur in elliptical galaxies (Li et al. 2011), which would suggest a $\sim 44\%$ chance that any 5 arbitrary SNe Ia would be found in spiral hosts. The host galaxy type statistics of past SNe Ibn are therefore not sufficient to rule out a low-mass progenitor population like that observed for SNe Ia.

A massive star progenitor of PS1-12sk carries with it the expectation of significant star formation in its host environment, which is uncharacteristic of the outskirts of massive elliptical galaxies like CGCG 208-042. Core-collapse SNe are extremely rare in early-type host galaxies, and we know of no core-collapse SNe discovered in association with a BCG. In an examination of 2104 morphologically-classified SN host galaxies in the SDSS field, Hakobyan et al. (2012) report only four core-collapse supernovae in S0 or elliptical galaxies. Core-collapse SN hosting ellipticals often show atypical evidence for star formation via LINER activity and/or galaxy interaction. In an earlier study, Hakobyan et al. (2008) had shown that all other reports of core-collapse supernovae with early type hosts were in fact hosted by mis-classified star forming galaxies.⁵ Similarly, of the SNe discovered by the Lick Observatory Supernova Search (LOSS; Leaman et al. 2011), 13/536 SNe II and Ibc were found in early-type galaxies, all having S0 or S0/a morphology or strong galaxy interaction, or belong to the class of Ca-rich SNe Ib which may not result from core-collapse

⁵The SN 2005md discussed in Hakobyan et al. (2008), reportedly hosted by an elliptical galaxy, was later revealed to be a Galactic cataclysmic variable star (Leonard 2010).

in massive stars (see Perets et al. 2010; Kasliwal et al. 2012). Suh et al. (2011) consider a sample of 7 SN II with early-type host galaxies and find that they systematically show more evidence for star formation than SN Ia hosts, typically being NUV-bright ($\text{NUV} - r < 5.6$ mag) indicating the existence of recent star formation. The most likely host galaxy of PS1-12sk, CGCG 208-042, has GALEX NUV = 19.8 ± 0.1 mag and $(\text{NUV} - r) = 5.9 \pm 0.1$ mag, larger than any of the core-collapse SN host galaxies in Suh et al. (2011). The Multi-Epoch Nearby Cluster Survey (MENeACS) reported one core-collapse SN discovered in a red-sequence cluster galaxy, indicating a rate per unit mass of core-collapse (SN II) to thermonuclear (SN Ia) supernovae of $\sim 1/5$ in this environment (Graham et al. 2012; Sand et al. 2012). In an earlier survey of 723 cluster early type galaxies and 1326 field early-types, Mannucci et al. (2008) reported a core-collapse SN rate of zero. These rates can be reconciled due to small number statistics; e.g. the MENeACS rate is based on the detection of only one SN II, so the 1σ statistical uncertainty permits relative rates about an order of magnitude below this.

Ongoing star formation in the PS1-12sk host environment could be associated with cooling flow filaments like those seen near Abell 1795, Abell 2597, and other nearby clusters (see e.g. O’Dea et al. 2008; McDonald & Veilleux 2009; McDonald et al. 2011; Tremblay et al. 2012). The archival XMM-Newton observation of the cluster RXC J0844.9+4258 (Section 6.2.4) has insufficient photons to construct a robust temperature profile to determine whether or not the cluster has a cool core. However, the global properties of the cluster point towards a cool core. The BCG 1.4 GHz radio luminosity (Section 6.2.4) nearly meets the threshold established

by Sun (2009), $2 \times 10^{23} \text{ W Hz}^{-1}$ at 1.4 GHz, above which all 69 clusters in their sample have cool cores. Furthermore, the cluster X-ray emission is centered on the BCG to within the spatial resolution of the XMM-Newton observation ($\sim 10''$ or $\sim 10 \text{ kpc}$; Figure 6.1). Clusters without cool cores typically have separations $\gtrsim 50 \text{ kpc}$ between the BCG and X-ray emission peak (see e.g. Hudson et al. 2010). High resolution and sensitive imaging (e.g. Hubble Space Telescope) is required to search for evidence of optical cooling flow filaments near the explosion site of PS1-12sk.

6.6 Progenitor Scenarios

6.6.1 Core Collapse Progenitor Models

Several lines of evidence, summarized in Section 6.1, have suggested massive star progenitors for past SN Ibn events. Given the strong spectroscopic similarity between PS1-12sk and past SN Ibn such as SN 2006jc (Section 6.2.2), it is reasonable to assume that their progenitor channel is physically related. In particular, the spectroscopic detection of intermediate-width He and H features is consistent with the explosion of a massive Wolf-Rayet (WR) or Luminous Blue Variable (LBV)-like star which recently ejected He-rich material into its CSM. Previously proposed progenitor models for SNe Ibn call for very massive stars, like the WR and LBV stars we observe undergoing severe mass loss events in the Local Group. Pastorello et al. (2007) discuss outbursts of LBV stars with initial mass $60 - 100 M_{\odot}$ as analogs to the 2004 pre-explosion brightening of SN 2006jc,

but known outbursting LBV stars have H-rich atmospheres inconsistent with the He-dominated CSM inferred for SNe Ibn. Pastorello et al. (2007, 2008a) further a binary progenitor system for SN 2006jc, composed of a $\sim 30 M_{\odot}$ WR star and $50 M_{\odot}$ LBV. Binary common envelope interaction provides a possible mechanism for the ejection of a dense, He-rich shell from the progenitor star while providing another source for the LBV-like eruption observed in conjunction with SN 2006jc. Foley et al. (2007) suggested a progenitor star for SN 2006jc which has recently transitioned from a LBV to a WR star. Smith et al. (2012) interpret the Type Ibn SN 2011hw, with relatively strong $H\alpha$ emission, as an intermediate example between SN 2006jc and H-rich Type IIn SNe. Smith et al. (2012) invoke a progenitor belonging to the Ofpe/WN9 class with initial masses $17 - 100 M_{\odot}$.

Under the assumption that PS1-12sk had a massive star progenitor, this event represents the first core-collapse supernova residing within a BCG environment. Given the low rate of SNe Ibn relative to all core-collapse SNe ($\lesssim 1\%$, Pastorello et al. 2008a), PS1-12sk is a statistically unlikely harbinger of massive star explosions in this unique environment. If we suppose that ongoing star formation in the environment of CGCG 208-042 functions similarly to classical star formation, then we would expect to see of order 10^2 SNe II for each SN Ibn found in galaxy clusters.

Over-representation of SNe Ibn among core-collapse SNe in red-sequence cluster galaxies could point toward a top-heavy IMF, preference for particular binary evolution scenarios, or overproduction of main sequence stars in a narrow mass range. Few observational constraints have been placed on the IMF of star formation in galaxy clusters. Maoz & Gal-Yam (2004) and Maoz et al. (2010)

have found that the iron enrichment level in galaxy clusters paired with the observed cluster SN Ia rate may point to a top-heavy IMF. However, Mannucci et al. (2008) find that the rate of SN II in late type galaxies is independent of environment (cluster or field), which they interpret as evidence for a consistent IMF. In the cluster core environment, McDonald et al. (2011) posed that the FUV/H α excess seen in cooling flow filaments could be interpreted as either evidence for a modest level of dust extinction or a top-heavy IMF.

The association of PS1-12sk with the cluster BCG, rather than another red sequence cluster galaxy, is consistent with a massive progenitor star originating from a cooling flow. The global properties of the cluster are consistent with a cool core (Section 6.5.3). Narrow-band H α imaging or spatial high-resolution X-ray observations could reveal the presence of a gas filament at the position of the PS1-12sk explosion site, which would be indicative of star formation below the level of our spectroscopic limits. Additionally, HI radio observations could reveal or constrain the presence of star forming gas near the SN explosion site.

The SN could also be associated with the fainter candidate host galaxy discussed in Section 6.4 if it has an unobserved, low surface brightness tidal tail. In that case, the likelihood of association we calculate based on the PS1 pre-explosion stacks could be underestimated. However, such a large offset from a star-forming host galaxy would be unusual for a core-collapse SN. Among the 36 SNe Ibs and 35 SNe IIins in the sample of Kelly & Kirshner (2012), the median offset is < 1 host galaxy half-light radii and the largest offset among these types is only 2.5 radii. The offset of PS1-12sk from the faint host galaxy candidate is 3.3 half-light radii, and this number may be underestimated as the faint source

is unresolved. It is also unlikely that the SN progenitor is a runaway star. To achieve the ~ 2.4 kpc separation observed from the faint host galaxy candidate would require a progenitor lifetime after ejection of ~ 10 Myr given a velocity ~ 200 km s $^{-1}$ (e.g. Hoogerwerf et al. 2001). A core-collapse SN is unlikely to result from a star that has achieved a separation $\gtrsim 100$ pc (Eldridge et al. 2011).

Finally, we consider the possibility that the event PS1-12sk is not a SN explosion, but rather a non-destructive eruptive mass loss event from a massive star. This issue is raised not only by the 2004 flare that preceded SN 2006jc, which was relatively dim at ~ -14 mag. but also by the recent “restlessness” of SN 2009ip (Mauerhan et al. 2012, Pastorello et al. 2012, Margutti et al. in prep.). The progenitor of SN 2009ip is an LBV which has undergone three luminous (~ -14 to -18 mag) outbursts in the past 4 yrs (Foley et al. 2011a; Mauerhan et al. 2012), and is located ~ 4 kpc (~ 2 half light radii, Lauberts & Valentijn 1989) from the center of its spiral host galaxy, NGC 7259 ($M_B \sim -18$ mag), similar to the remote placement of PS1-12sk (Section 6.4). Given that $< 10^{50}$ ergs was needed to power the light curve of PS1-12sk, and assuming a radiative efficiency $\lesssim 0.3$ (Falk & Arnett 1977), this leaves open the possibility that there was not sufficient energy to unbind the progenitor star, and we may see additional flares from PS1-12sk in the future.

6.6.2 A Degenerate Progenitor?

While the unusual spectroscopic features of PS1-12sk point to the explosion of a massive star, its host environment is dominated by an old stellar population

and shows no direct evidence for ongoing star formation. The environment is reminiscent of those associated with Type Ia SNe, the thermonuclear explosions of white dwarfs (WDs) which dominate the supernova population within cluster elliptical galaxies including BCGs (see e.g. Gal-Yam et al. 2002a, 2003; Maoz & Gal-Yam 2004; Sharon et al. 2007; Mannucci et al. 2008; Li et al. 2011; Sand et al. 2011). Examples of SNe Ia exploding within H-rich CSM have been found in SN 2002ic (Hamuy 2003a; Kotak et al. 2004), SN 2005gj (Aldering et al. 2006), and PTF11kx (Dilday et al. 2012). Along this line, we consider the possibility that PS1-12sk marks the disruption of a degenerate progenitor system. Below we discuss constraints on the range of possible white dwarf progenitor models provided by the observational features of PS1-12sk.

Spectroscopic properties

A degenerate progenitor system model for PS1-12sk must be able to eject H, He, and C a few years prior to the SN explosion. To explain the significant He, a putative WD progenitor system must contain a He star: either a degenerate WD or non-degenerate He-burning star (see e.g. Benetti et al. 2002). It is unclear how a He-burning star could produce a significant outburst a few years before explosion since the accretion rate of such a system is typically $10^{-8} M_{\odot} \text{ yr}^{-1}$. Moreover, the lifetime of a He-burning star is relatively short (500 Myr), and therefore these systems are expected to be rare in elliptical galaxies.

Merger models for WD-WD systems with high mass ratios (i.e. a CO WD and He WD pair) predict a significant amount of He ejected from the

lower-mass companion into the circumbinary environment. Such a merger model would require fine tuning to match the observed properties of PS1-12sk. Using smoothed-particle hydrodynamics simulations, Dan et al. (2011) find that $\sim 3\%$ of the secondary star mass is ejected from the merger of a 0.5 and $1.2 M_{\odot}$ WD system (this fraction is 10% in similar simulations by Guerrero et al. 2004). This enriches the CSM with a He mass lower than the estimate we infer for PS1-12sk, but within an order of magnitude. In order for the ejected material to reach the 10^{15} cm radius inferred for the SN shock, the merger scenario enforces a strict timescale of a few years for the explosion mechanism.

In double-detonation models for the thermonuclear explosion of merging WD binaries, material from the disrupted secondary WD typically accretes unstably onto the primary star on the dynamical timescale of the system ($10^2 - 10^3$ s; Shen et al. 2012). A delayed detonation on the viscous timescale of the system ($10^4 - 10^8$ s; e.g. Schwab et al. 2012) would be required to allow the ejected material to reach the radius observed in SNe Ibn. If physically possible, the secondary star of such a system would necessarily fall in the transitional regime where the donor star is intermediate between low mass ($\lesssim 0.3 M_{\odot}$) He WDs expected to produce long-lived AM CVn or R Coronae Borealis stars and higher mass ($\gtrsim 0.5 M_{\odot}$) CO WDs expected to produce thermonuclear, sub-Chandrasekhar explosions by direct impact mass transfer (see e.g. Dan et al. 2011). Additional simulations are needed to determine if a delayed detonation on the viscous timescale is possible, while also ejecting sufficient material into the CSM to produce the He (and also H and C) features observed in SNe Ibn.

Typical $0.6 - 1.0 M_{\odot}$ CO WD stars have low masses for H ignition

($\sim 10^{-5} - 10^{-4} M_{\odot}$; Townsley & Bildsten 2004). Nova events could therefore prevent the accretion of significant H on the surface of the white dwarf, as is suggested by the appearance of intermediate-width H features in the ejecta of PS1-12sk. However, lower mass WDs have higher H ignition masses (see e.g. Shen & Bildsten 2009a). Low mass, $0.3 M_{\odot}$ He WDs are expected to have $\sim 3 \times 10^{-3} M_{\odot}$ of H remaining on their surface as they emerge from binary evolution (Driebe et al. 1998). This may be consistent with our observational upper limit (Section 6.5.2). The gradual burning and depletion of this H does not significantly constrain the timescale over which a putative SN Ibn binary progenitor system must merge. For $0.3 M_{\odot}$ He WDs, Panei et al. (2007) predict that the H surface mass is depleted by a factor of ~ 2 after 27 Myr, and is only depleted by a factor of ~ 5 from the initial value after 6 Gyr. Moreover, in a degenerate progenitor model, nova ejecta may contribute to the CSM formation around the SN progenitor. The detection of H emission features only at late times could be a clue to the geometry of the system. The emission may only develop once the ejecta reaches an outlying region of H-rich CSM.

R Coronae Borealis (RCB) stars are surrounded by He-rich circumstellar media and their progenitors therefore may share some similarities to the progenitors of SNe Ibn. Leading progenitor channels for RCBs are the merger of He and C-O white dwarfs or the final-helium-shell flash of a post-Asymptotic Giant Branch (AGB) central star of a planetary nebula (Clayton et al. 2011). While we know of no explosion mechanisms for RCB stars, we consider the comparison between their outflows and the inferred circumstellar properties of PS1-12sk. The 10^{15} cm radius we associate with the PS1-12sk shock is

$\sim 10^2$ times larger than the envelopes of RCB stars ($\sim 70 R_{\odot}$; Schoenberner 1975), but $\sim 10^4$ times smaller than the maximum extent of the diffuse shell of material surrounding RCB (~ 4 pc; Clayton et al. 2011). RCB stars have a mass loss rate of $\dot{M} \sim 10^{-5} M_{\odot} \text{ yr}^{-1}$ (Clayton et al. 2011), several orders of magnitude lower than that necessary to populate the CSM of PS1-12sk within the radius of the shocked region. With a lower mass transfer rate are AM CVn stars, consisting of a white dwarf accreting from a degenerate helium donor star, showing evidence for mass loss rates of $\dot{M} \sim 10^{-13} - 10^{-5} M_{\odot} \text{ yr}^{-1}$ (Iben & Tutukov 1989; Solheim 2010) and could possibly produce a short lived (5 – 10 d), low luminosity ($M_V = -15$ to -18 mag) thermonuclear SN (Bildsten et al. 2007; Shen & Bildsten 2009b).

Light Curve Properties

When contributions due to circumstellar interaction are removed, the luminosity of PS1-12sk ($M_{r_{P1}} = -19.08 \pm 0.02$ mag) and other SNe Ibn due to radioactive decay of ^{56}Ni is significantly less than that of typical SNe Ia (M_R typically -18.5 to -19 mag Li et al. 2011, with dust extinction). A white dwarf progenitor for PS1-12sk may therefore require a sub-Chandrasekhar mass, for which there are several possible explosion mechanisms including runaway He ignition, He shell deflagration, and CO core detonation (see e.g. Bildsten et al. 2007; Kromer et al. 2010; Woosley & Kasen 2011).

Thermonuclear explosion models for sub-Chandrasekhar WD-WD merger are typically invoked to explain low-luminosity, sub-energetic SNe Ia. However,

higher-mass primary stars will produce more ^{56}Ni and correspondingly brighter explosions, as luminous as $M_V \sim -20$ mag with $\Delta m_{15} \sim 1.3$ mag for a $1.4 M_\odot$ primary WD (Kromer et al. 2010). A primary star mass sufficient to produce the $M_R \sim -19$ mag peak luminosity and $\Delta m_{15} > 1$ mag light curve width of PS1-12sk calls for a large mass ratio, sufficient to eject significant material from the secondary star during the merger. However, the contributions of circumstellar interaction to the light curve need to be modeled in more detail.

Alternatively, the “enshrouded” accretion induced collapse (AIC) scenario described by Metzger et al. (2009) has been proposed to explain SN 2008ha-like events, sub-luminous Type Ia SNe with fast rise times (~ 10 d) and low peak magnitudes (~ -14 mag; Foley et al. 2009a; Valenti et al. 2009). In this model, a super-Chandrasekhar binary white dwarf pair merges, stripping $\sim 0.1 M_\odot$ of potentially He-rich material into a disk surrounding the explosion. If the circumstellar density is sufficiently high, and a Ni-rich outflow is produced from the accretion disk, a much brighter SN with spectroscopic signatures of circumstellar interaction (like SN Ibn) could be produced. However, AIC progenitors would not be expected to have a significant H envelope remaining at the time of explosion and may not be capable of producing the $\text{H}\alpha$ emission observed in the spectra of SN Ibn. We note that Piro & Kulkarni (2012) predict that AIC explosions will produce a radio transient due to synchrotron emission from the resulting pulsar wind nebula. The predicted timescale for the radio transient to reach peak luminosity is a few months with luminosity $\sim 10^{28} - \sim 10^{29}$ ergs s^{-1} in the 1 – 10 GHz range. This is 1 – 2 orders of magnitude below our JVLA luminosity limit for PS1-12sk at a similar epoch (Section 6.2.4).

6.7 CONCLUSIONS

We have assembled multi-wavelength observations of the first ~ 2 months of the supernova PS1-12sk (Figure 6.3) and its host galaxy cluster, RXC J0844.9+4258. While the explosion properties of PS1-12sk are similar to past examples of SNe Ibn and may be explained by massive-star progenitor models, its unique host environment is suggestive of an origin from an older stellar population.

Spectroscopy of PS1-12sk clearly classifies it as the sixth discovered Type Ibn SN, with intermediate-width He I and $H\alpha$ features similar to SN 2006jc. Our high-resolution spectrum obtained ~ 1 week after peak brightness shows P-cygni profiles associated with the He I features (Figure 6.5), with absorption minima suggesting a wind velocity of 140 km s^{-1} for the circumstellar material, and also reveals the presence of narrow C II absorption.

The PS1 MDS first detected the SN ~ 9 d before peak, providing the most detailed constraints to date on the rise of a Type Ibn SN. The luminosity of PS1-12sk (with peak $M_{r_{p1}} = -19.08 \pm 0.02$ mag) is intermediate between the archetypal Type Ibn SNe 2006jc and brighter examples like SN 2000er. The NUV-NIR SED (Figure 6.4) of the SN within a few weeks of peak brightness is consistent with a single-component blackbody. Assuming a temperature of $T \sim 17 \times 10^3$ K, we measure a radius of $\sim 1.4 \times 10^{15}$ cm for the blackbody photosphere, and a similar value based on the rise time and wind velocity. We do not detect an NIR excess or reddening of He I line profiles in our optical spectra, suggesting no significant dust formation in the ejecta of PS1-12sk in the first month after peak brightness.

The host environment of PS1-12sk is unique among Type Ibn SNe, and is unprecedented among core-collapse SNe. We use deep imaging from pre-explosion stacks of PS1 MDS observations to characterize the host cluster RXC J0844.9+4258 (Figure 6.1). We find that the most likely host galaxy for the SN is the BCG of the cluster, CGCG 208-042, at a separation of 28 kpc. There is no evidence of star formation at the PS1-12sk explosion site, and our spectroscopy yields a limit of $L_{\text{H}\alpha} \lesssim 2 \times 10^{38} \text{ ergs s}^{-1} \text{ kpc}^{-2}$. We identify a nearby faint source which may be a dwarf galaxy and could be responsible for star formation near the host environment, although the separation is several times the source’s half-light radius at ~ 2.4 kpc. The radio and X-ray characteristics of the host galaxy cluster also suggest a cooling flow may exist that could support star formation in low-luminosity filaments.

The discovery of PS1-12sk in association with a brightest cluster galaxy either represents surprisingly vigorous star formation, possibly with a top-heavy IMF, in this unique environment or suggests the possibility of a progenitor channel other than the WR or LBV-like, massive star models favored for SN 2006jc. However, the observational constraints we present for PS1-12sk make it challenging to formulate a degenerate progenitor model capable of producing the He-rich circumstellar medium attributed to SNe Ibn. Additional theoretical work is needed to interpret the power source for the light curve of PS1-12sk, the pre-explosion mass loss rate of H and He into the circumstellar medium, and the star formation properties of the explosion environment in terms of a consistent physical progenitor model. Additional deep optical imaging observations of the cluster RXC J0844.9+4258 are needed to search for filamentary emission at the

explosion site of PS1-12sk. Future SN discoveries will provide the sample size necessary to unambiguously associate SNe Ibn with a stellar population older or younger than typical core-collapse SNe (see e.g. Kelly et al. 2008; Kelly & Kirshner 2012; Leloudas et al. 2011; Sanders et al. 2012c), shedding light on the nature of their progenitor stars.

Table 6.2. PS1-12sk Optical Spectroscopy

MJD	Telescope /Instrument	Epoch ^a (Days)	Range (Å)	Dispersion (Å px ⁻¹)
56012.5	MMT/BC	+6	3330 – 8530	1.9
56014.2	MMT/BC	+8	5870 – 7770	0.7
56016.5	NOT/AFOSC	+10	3520 – 8980	3.0
56023.5	INT/IDS	+17	3695 – 9485	4.1
56041.5	MMT/BC	+35	3535 – 8410	1.9

^aEpoch relative to z -band peak.

Chapter 7

Towards Characterization of the Type IIP Supernova Progenitor Population: a Statistical Sample of Light Curves from Pan-STARRS1

N. E. Sanders, A. M. Soderberg, S. Gezari, M. Betancourt, R. Chornock, E. Berger, R. J. Foley, P. Challis, M. Drout, R. P. Kirshner, R. Lunnan, G. H. Marion, R. Margutti, R. McKinnon, D. Milisavljevic, G. Narayan, A. Rest, E. Kankare, S. Mattila, S. J. Smartt, M. E. Huber, W. S. Burgett, P.W. Draper, K. W. Hodapp, N. Kaiser, R. P. Kudritzki, E. A. Magnier, N. Metcalfe, J. S. Morgan, P. A. Price, J. L. Tonry, R. J. Wainscoat, C. Waters 2014, *arXiv:1404.2004*

abstract

We find no evidence for the existence of a discontinuous sub-population of fast-declining explosions (historically referred to as “Type IIL” SNe). However, we identify a highly significant continuous relation between the plateau phase decay rate and peak luminosity among our SNe IIP. These results argue in favor of a single predominant explosion parameter, likely determined by initial stellar mass, controlling the most significant observational outcomes of red supergiant explosions. We compare each light curve to physical models from hydrodynamic simulations to estimate progenitor initial masses and other properties of the Pan-STARRS1 Type IIP SN sample. We show that correction of certain systematic discrepancies between modeled and observed SN IIP light curve properties, and an expanded grid of progenitor mass and explosion energy ranges, are needed to enable robust progenitor inferences from multi-band light curve samples of this kind. This work will serve as a pathfinder for photometric studies of core-collapse SNe to be conducted through future wide field transient searches.

7.1 INTRODUCTION

Core-collapse supernovae (SNe) mark the explosive deaths of massive stars. Several independent lines of evidence including explosion modeling (Nadyozhin 2003; Maguire et al. 2012; Jerkstrand et al. 2013; Takáts et al. 2013), progenitor star photometry (Li et al. 2007; Smartt et al. 2009; Walmswell & Eldridge 2012),

rate statistics (Smith et al. 2011a), and theory (Heger et al. 2003; Ekström et al. 2012) combine to suggest a lower main sequence initial mass (M_{in}) limit for achieving core collapse of $M_{in} \gtrsim 8 - 12 M_{\odot}$. Red supergiant progenitor stars in this mass range are known to produce Type IIP (hydrogen rich) SN explosions, the most common form of core-collapse SN. The upper mass limit for SNe IIP progenitors is more uncertain, with stars of $M_{in} \gtrsim 16 - 30 M_{\odot}$ realizing significant mass loss depending on their mass, metallicity, rotation rate, binarity, and other properties; and even more massive stars ending their lives through more exotic explosion mechanisms. These mass limits for CC-SN progenitor stars have profound implications throughout stellar and galactic astrophysics and cosmology, including as an input to and constraint on models of stellar evolution for massive stars (Groh et al. 2013a; Meynet et al. 2013), chemical evolution (Timmes et al. 1995; Nomoto et al. 2006, 2013), supernova feedback in the interstellar medium and galaxy formation (Leitherer et al. 1992; Stilp et al. 2013), and astrobiological planetary sterilization rates (Clark et al. 1977; Lineweaver et al. 2004).

The electromagnetic signatures of these core-collapse explosions are diverse, depending sensitively on the properties of both the core and the outer envelope of the progenitor star at the time of explosion. Supernovae with hydrogen features detected in their optical spectra are referred to as Type II SNe, with a variety of subtypes defined by more specific spectroscopic and/or photometric criteria (see e.g. Filippenko 1997; Li et al. 2011). The most common subclass, Type IIP, are typified by broad ($\sim 10,000 \text{ km s}^{-1}$) hydrogen Balmer P-Cygni spectroscopic features, fast rise times of a few days and optical light curves dominated by a long lived, ~ 100 day “plateau” phase of roughly constant luminosity. The

plateau phase is understood to arise from hydrogen recombination in the ejecta, with cooling temperature balancing the expansion of the blastwave to essentially equilibrate the R -band luminosity (see e.g. Kasen & Woosley 2009). The Type IIL sub-class is historically designated based on spectroscopic properties similar to SNe IIP, but faster, “linearly” declining optical light curves rather than a long lived plateau. Type I Ib supernovae are classified spectroscopically based on the disappearance of H features and the prominence of He absorptions. Type I Ib light curves feature slow rise times and rapid decline rates (in each case, a few weeks) typical of Type I (H deficient) SNe. The most extreme subclass, Type I In, are identified by intermediate width ($\sim 10^3$ km s $^{-1}$) H emission features reflecting interaction with circumstellar material, and contributions from this interaction can power these explosions to reach extreme luminosities at peak.

The optical evolution of Type IIP SNe has been explored in light curve studies by a number of authors, including Patat et al. (1994); Chieffi et al. (2003); Hamuy (2003a); Nadyozhin (2003); Bersten & Hamuy (2009); Li et al. (2011); Arcavi et al. (2012); Anderson et al. (2014); Faran et al. (2014). The relationship between these observables and the properties of SN progenitor stars has been explored in theoretical parameter studies by Arnett (1980); Litvinova & Nadezhin (1985); Young (2004); Kasen & Woosley (2009); Dessart et al. (2013), and others. Combining a uniform analysis of a statistical population of Type IIP supernova light curves with consistent physical models for inferring the properties of their stellar progenitors represents a path forward for characterizing the progenitor population.

Here we describe an analysis of a statistical sample of SN IIP light curve

properties, performed using observations from the Panoramic Survey Telescope & Rapid Response System 1 survey (Pan-STARRS1, abbreviated PS1). This represents the first such population analysis of SN IIP light curves based on a homogeneously-collected and multi-band photometric sample from a wide field optical survey. In Section 7.2 we describe the PS1 optical observations and follow-up optical spectroscopy program used to construct the light curve sample. We have developed a novel Bayesian methodology for self-consistently modeling the full population of light curves in the sample and obtaining robust measurements of physically-meaningful light curve parameters (Section 8.2). We discuss the population wide distributions of these parameters and compare to previous observational studies (Section 7.4). By comparison to theoretical light curve models, we recover estimates of the progenitor properties of the objects in our sample, and discuss the limitations of the available models in Section 7.5. We summarize and conclude in Section 8.6.

7.2 OBSERVATIONS

7.2.1 Pan-STARRS1 imaging

We select a Type II SN light curve sample from the transients discovered and monitored by PS1 since the initiation of the survey in 2010, consisting of 18,837 relevant photometric data points, 5,056 of which are robust transient detections. PS1 is a high-etendue wide-field imaging system, designed for dedicated survey observations and located on the peak of Haleakala on the island of Maui in the

Hawaiian island chain. Routine observations are conducted remotely, from the University of Hawaii–Institute for Astronomy Advanced Technology Research Center (ATRC) in Pukalani. A summary of details of PS1 operations relevant to SN studies is given in Rest et al. (2013), and we discuss its key features here.

A complete description of the PS1 system, both hardware and software, is provided by Kaiser et al. (2002). The 1.8 m diameter primary mirror, 3.3° field of view, and other PS1 optical design elements are described in Hodapp et al. (2004); the array of sixty 4800×4800 , 0.258" pixel detectors, and other attributes of the PS1 imager is described in Tonry & Onaka (2009); and the survey design and execution strategy are described in Chambers (in preparation). The PS1 Medium Deep Survey (MDS) consists of 10 pencil beam fields observed with a typical cadence of 3 days in each filter, to a 5σ depth of ~ 23.3 mag in *griz* filters, and ~ 21.7 mag in the *y*-filter (with observations taken near full moon).

The PS1 observations are obtained through a set of five broadband filters, which we refer to interchangeably as g_{P1} , r_{P1} , i_{P1} , z_{P1} , and y_{P1} or simply *grizy* (Stubbs et al. 2010). Although the filter system for PS1 has much in common with that used in previous surveys, such as the Sloan Digital Sky Survey (SDSS: York et al. 2000; Aihara et al. 2011), there are important differences. The g_{P1} filter extends 200 Å redward of g_{SDSS} , and the z_{P1} filter is cut off at 9200 Å. SDSS has no corresponding y_{P1} filter. Further information on the passband shapes is described in Stubbs et al. (2010). Photometry is in the “natural” PS1 system, $m = 2.5 \log(\text{flux}) + m'$, with a single zero-point adjustment m' made in each

band to conform to the AB magnitude scale (Tonry et al. 2012).¹ We assume a systematic uncertainty of 1% for our PS1 observations due to the asymmetric PS1 point spread function and uncertainty in the photometric zero-point calibration (Tonry et al. 2012). See Figure 7.1 for an illustration of the PS1 photometric sampling and the range in data quality.

The standard reduction, astrometric solution, and stacking of the nightly images is done by the Pan-STARRS1 IPP system (Magnier 2006; Magnier et al. 2008). The nightly MDS stacks are transferred to the Harvard Faculty of Arts and Sciences “Odyssey” Research Computing cluster, where they are processed through a frame subtraction analysis using the *photpipe* image differencing pipeline developed for the SuperMACHO and ESSENCE surveys (Rest et al. 2005; Garg et al. 2007; Miknaitis et al. 2007).

7.2.2 Optical spectroscopy

We begin with a selection of PS1-discovered SNe which were classified as Type II through our spectroscopic follow-up campaign: 112 objects in total. One object in our sample, PS1-10ae (SN 2010aq), has previously been reported on in Gezari et al. (2010). We note that the PS1 spectroscopic follow-up is not complete; brighter objects, those with longer plateau durations, and those with the highest ratio of SN to underlying galaxy light are most likely to be over-represented in our sample, due to their availability for spectroscopy.

¹The magnitudes quoted throughout this paper are in the AB system, except where explicitly noted.

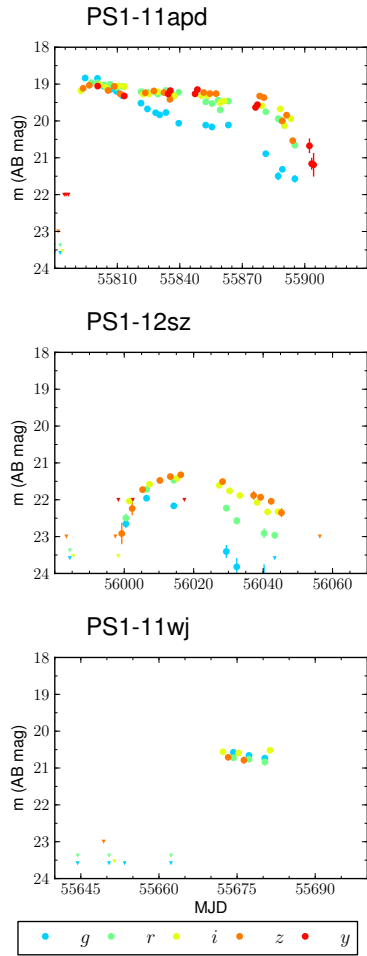


Figure 7.1.— Sample PS1 multi-band light curves from the Type II SN dataset. Top: PS1-11apd, a bright Type IIP SN with a light curve sampled from peak through the plateau and the transition to the radioactive decay phase, covering ~ 100 days. Middle: PS1-12sz, a Type IIb supernova which peaked at ~ 21 st magnitude with a well sampled light curve. Bottom: PS1-11wj, a Type IIP SN with photometry sampled only during the plateau phase. In each plot, the filters are specified by the colors shown in the legend and the triangles represent non-detection upper limits (with values set from the 2σ level of the distribution of detected magnitudes from the full photometric dataset in each filter).

Spectra were obtained using the Blue Channel and Hectospec spectrographs of the 6.5 m MMT telescope (Schmidt et al. 1989b; Fabricant et al. 2005), the Low Dispersion Survey Spectrograph (LDSS3) and Inamori-Magellan Areal Camera and Spectrograph (IMACS; Dressler et al. 2006) of the 6.5 m Magellan telescopes, the Gemini Multi-Object Spectrograph of the 8 m Gemini telescopes (GMOS; Hook et al. 2004), and the Andalucia Faint Object Spectrograph and Camera at the Nordic Optical Telescope (ALFOSC). Objects were classified as Type II by identification of $H\alpha$ emission not associated with the host galaxy. This selection could possibly include Type II SNe of the Type IIP, IIL, I Ib, and Type IIn subclasses; we will discuss sub-classification in Section 7.3.4.

Additionally, we obtain host galaxy redshift measurements for each object from these spectra, which we use for K -correction (see Section 7.2.3) and to estimate distance.² Figure 7.2 shows the host galaxy redshift distribution of the SNe in the sample, which has [16,50,84]th percentile values of [0.07, 0.12, 0.21]. The sub-sample classified as SNe IIP (see Section 7.3.4) have distribution percentile values of [0.07, 0.10, 0.16], reflecting a population of luminous, distant SNe IIn excluded from the sub-sample.

Details of our final SN IIP sample, as described in Section 7.3.4, are listed in Table 7.2.

²We assume a standard Λ CDM cosmology with $H_0 = 70 \text{ km s}^{-1} \text{ Mpc}^{-1}$, $\Omega_\Lambda = 0.73$, and $\Omega_M = 0.27$

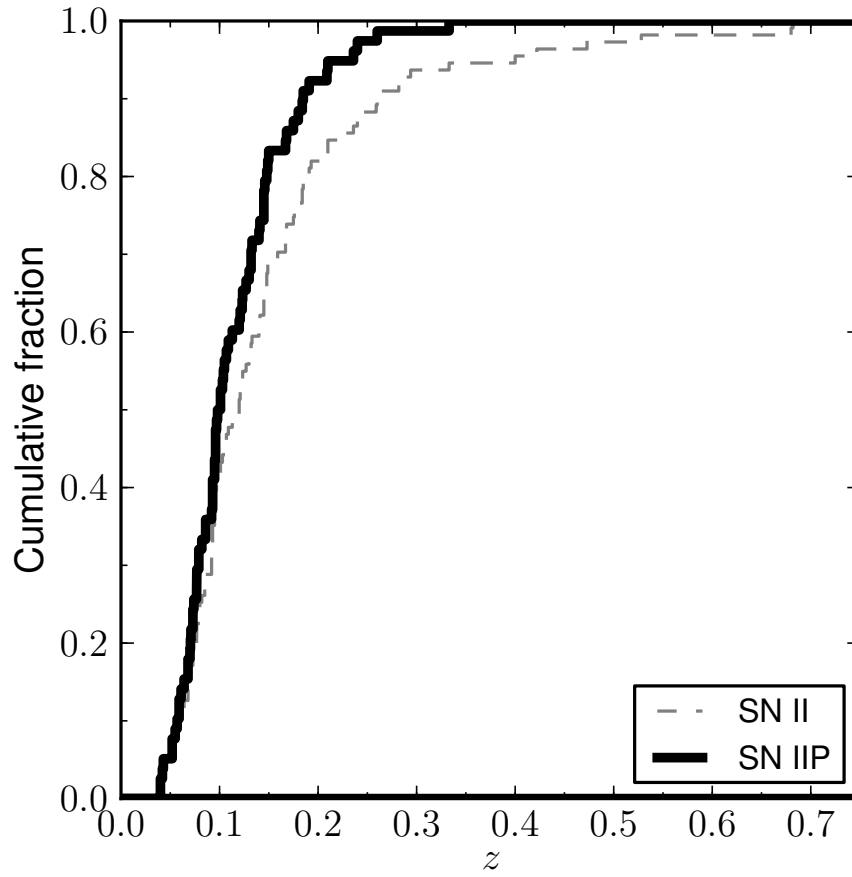


Figure 7.2.— Cumulative redshift distribution for PS1 SNe II. The sub-sample classified as SNe IIP (see Section 7.3.4) are shown with the thick line.

7.2.3 *K*-corrections

We use *K*-corrections to account for the difference between the observed and rest frame wavelengths of the light collected through the PS1 filters, as a function of the redshift of each object in our sample. We define this correction, $K = m_R - M_Q - DM$, where m_R is the observed-frame magnitude, M_Q is the emitted-frame absolute magnitude, and DM is the distance modulus (Hogg et al. 2002). We estimate *K*-corrections using the SN IIP spectral templates provided by P. Nugent (based on observations of SN 1999em; Gilliland et al. 1999; Baron et al. 2004)³. We interpolate linearly between the spectral templates to obtain *K*-corrections for arbitrary epochs. We note that we do not warp the spectral templates to match the observed color of the SN, due to the computational cost involved in doing so dynamically within our probabilistic light curve fitting methodology (see Appendix 8.7). By testing the effects of warping the spectral templates on the *K*-correction calculation, we estimate that neglecting this effect will introduce an uncertainty of ~ 0.02 mag in the *K*-correction per 0.1 mag of $(V - I)$ color offset, which is much smaller than typical uncertainties in our color estimates.

Figure 7.3 illustrates the resulting *K*-corrections for an illustrative set of epochs. The $t = 0$ *K*-correction is linear with z because the post-shock breakout cooling phase spectral model is a blackbody; thereafter the *K*-correction evolution becomes more complex, with spectral features evolving and shifting between

³Spectral templates obtained from P. Nugent at http://supernova.lbl.gov/~nugent/nugent_templates.html

bandpasses. The bluer bands have K -corrections more highly dependent on time, as the onset of line blanketing in the spectral model depresses the flux redward of $\sim 5000 \text{ \AA}$.

7.3 LIGHT CURVE MODELING

In order to consistently compare the photometric properties of the SN IIPs in our sample, we have produced models of the full, multi-band light curve evolution of each SN using a Bayesian methodology. We apply weakly informative priors to regularize the shape of the light curve fits to conform to SN IIP phenomenology. The product of the modeling is a posterior predictive probability distribution for the luminosity of the SN at every phase, and joint posterior probability distributions for associated light curve parameters. This methodology enables us to model the full pseudo-bolometric light curve evolution of all objects in our sample from explosion through the radioactive decay phase, regardless of variation in photometric coverage and data quality, while fully accounting for statistical uncertainty. Throughout, we interpret these marginal parameter probability distributions in the context of the influence of the weakly informative priors to avoid introducing bias on our inference.

7.3.1 Parameterized light curve model

To model the light curve, we use a simple, physically-motivated parameterization that captures the essential components of the rise, plateau, and decline phases

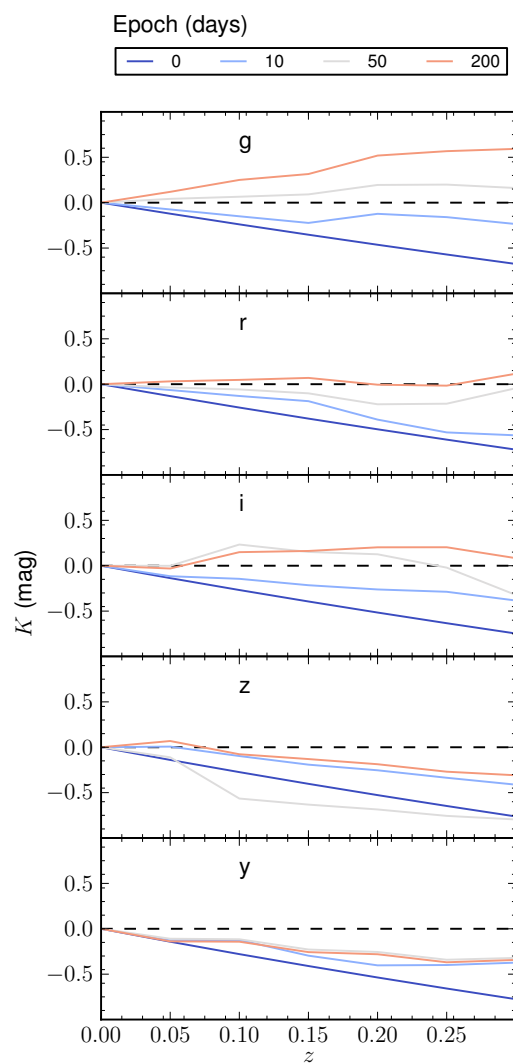


Figure 7.3.— Estimated SN IIP K -corrections in PS1 filters (different panels), derived as described in the text. The line colors correspond to different epochs (rest frame days since explosion; key at top).

of the Type IIP light curve. Our model is constructed so that the most salient features of the SN IIP light curve (the plateau duration, peak magnitude, and the luminosity evolution of the radioactive decay phase) are represented by directly interpretable parameters.

The light curve model for the luminosity measured from our PS1 forced photometry, l , in a given optical filter, F , consists of 5 piecewise components (see Figure 8.1): a power law fast rise phase, a plateau phase divided into exponential rising and declining components, a transitional phase representing the end of the plateau, and a post-plateau exponential decay phase:

$$l[t, \dots] = \begin{cases} 0, & \text{if } t < t_0 \\ M_1 (t/t_1)^\alpha, & \text{if } t_0 < t < t_1 \\ M_1 \exp(\beta_1(t - t_1)), & \text{if } t_1 < t < t_p \\ M_p \exp(-\beta_2(t - (t_p + t_1))), & \text{if } t_p < t < t_2 \\ M_2 \exp(-\beta_{dN}(t - (t_2 + t_p + t_1))), & \text{if } t_2 < t < t_d \\ M_d \exp(-\beta_{dC}(t - (t_d + t_2 + t_p + t_1))), & \text{if } t_d < t \end{cases} \quad (7.1)$$

These parameters have the following definitions and interpretations. The time parameters are defined where t is the MJD epoch of an observation, t_0 is the epoch of explosion, t_1 is the rest frame duration of the power law rise phase, t_p is the duration of the exponential rise phase (ending at peak flux), t_2 is the duration of the falling component of the plateau phase, and t_d is the duration of the transitional phase. The flux parameters are defined such that M_1 is the flux

at the transition from the power law to the exponential rise phases, M_p is the peak flux, M_2 is the flux at the end of the plateau phase, and M_d is the flux at the transition to the Co decay-dominated phase. The rate parameters are defined such that α is the power law rise slope, β_1 is the exponential rate constant during the rising phase of the plateau, β_2 is the rate constant during the declining phase of the plateau, β_{dN} is the exponential decline rate of the transition phase following the plateau, and β_{dC} is the exponential decay constant corresponding to ^{56}Co to ^{56}Fe decay. Each parameter is defined independently for each photometric filter, with the exception of t_0 . For numerical convenience, we define l in arbitrary scaled units relative to the absolute magnitude M , such that $M = -2.5 \log_{10}(10^7 \times l)$.

Note that, in order for the light curve model to be continuous, not all of the parameters may be independent. In particular, for each filter,

$$M_1 = M_p / \exp(\beta_1 t_p) \quad (7.2)$$

$$M_2 = M_p / \exp(-\beta_2 t_2) \quad (7.3)$$

$$M_d = M_2 / \exp(-\beta_{dN} t_d) \quad (7.4)$$

Furthermore, we note that the post-peak decay rate β_2 is directly related to the quantity Δm_{15} , the decline in magnitudes of the light curve in the 15 days following peak:

$$\Delta m_{15} = \frac{15 \times 2.5}{\log_e 10} \beta_2 \sim 16.3 \beta_2 \quad (7.5)$$

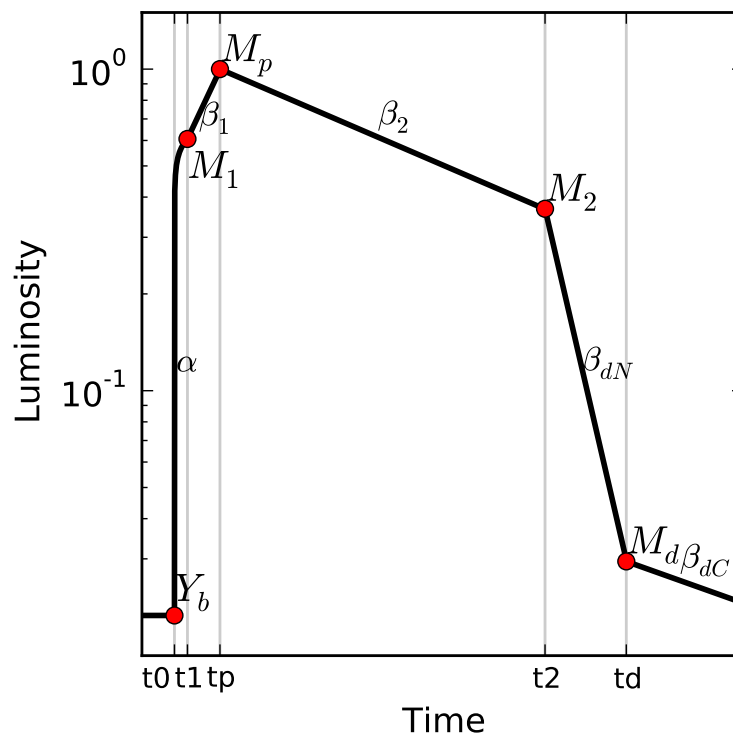


Figure 7.4.— Schematic illustration of the 5-component SN II light curve model defined in Equation 7.1. The gray vertical lines denote the duration (t_x) between epochs of transition between the piecewise components of the model. The background level (Y_b) and turnover fluxes (M_x) are marked and labeled (red points). The power law (α) and exponential (β_x) rate constant for each phase are labeled adjacent to each light curve segment.

Our model is similar to the linear segmented light curve fitting approach of e.g. Patat et al. (1993), but (as we will discuss in Section 7.3.2) our fitting methodology for the knot properties is fully probabilistic rather than manual. We prefer this piecewise analytic formulation to the additive components model used by e.g. Olivares (2008) because it will in principal have weaker parameter interactions, therefore reducing the posterior curvature and increasing the efficiency of Markov Chain Monte Carlo methods for sampling from the posterior. While this parameterization is designed to capture the phenomenology of Type IIP SNe, it is sufficiently flexible that reasonably descriptive fits are obtained to the light curves of other Type II SN light curves (e.g. SNe IIn and IIb).

7.3.2 Fitting methodology

We estimate the posterior distributions of these model parameters using a Markov Chain Monte Carlo (MCMC) method. We employ the C++ library *Stan* (Stan Development Team 2013), which implements the adaptive Hamiltonian Monte Carlo (HMC) *No-U-Turn Sampler* of Hoffman & Gelman (2013). For each multi-band SN light curve, we use *Stan* to return 1000 samples (250 samples each from 4 independent MCMC chains) from the posterior distribution of the model.⁴

In addition to the light curve parameterization outlined in Section 8.2, our *Stan* model includes certain features representing the data acquisition process. To account for uncertainty in the PS1 background template subtractions, we fit for the background level in each filter using an independent set of luminosity

⁴The full *Stan* code for our statistical model is discussed in Appendix 8.7.

parameters, $Y_b[F]$, and an intrinsic model variance, $V[F]$. We pre-compute K -correction curves for the redshift of each object in our sample (see Section 7.2.3), and apply them to the model during the likelihood calculation using the phases corresponding to the sampled explosion date at each step in the MCMC chain.

We employ weakly informative priors (see e.g. Gelman et al. 2008) to regularize the fitted models to the characteristic SN IIP light curve shape. These prior distributions are constructed to more than encompass the observed variance in parameter values from well-identified light curves in the dataset. The *Stan* model in Section 8.7 fully defines the fixed prior distributions we employ, and we discuss their most salient properties here. Figure 7.5 illustrates the prior distribution construction procedure for the priors which we have defined individually per filter in the model. To t_2 , we apply a (lognormal) $\log N(\log(100), 0.3)$ day prior. Together with our prior on t_p (Figure 7.5), this effectively provides a prior on the plateau duration which has [5, 50, 95]th percentile values of [70, 110, 180] days in i -band (and similar in other bands). This prior is constructed to be weakly informative, having significantly more variance than previously reported SN IIP plateau duration distributions (Arcavi et al. 2012) and covering a range of values similar to that predicted from theoretical modeling (Kasen & Woosley 2009). Perhaps the most informative prior we apply is that on the peak-magnitude distribution, which is observationally motivated. A strong prior is desirable for this parameter because it has the effect of regularizing the light curve shape in cases where photometric observations before peak are not available. We set this prior to $(-17.5, 0.8)$ mag to match the Type II SN luminosity function predicted for an R -band magnitude-limited survey by Li

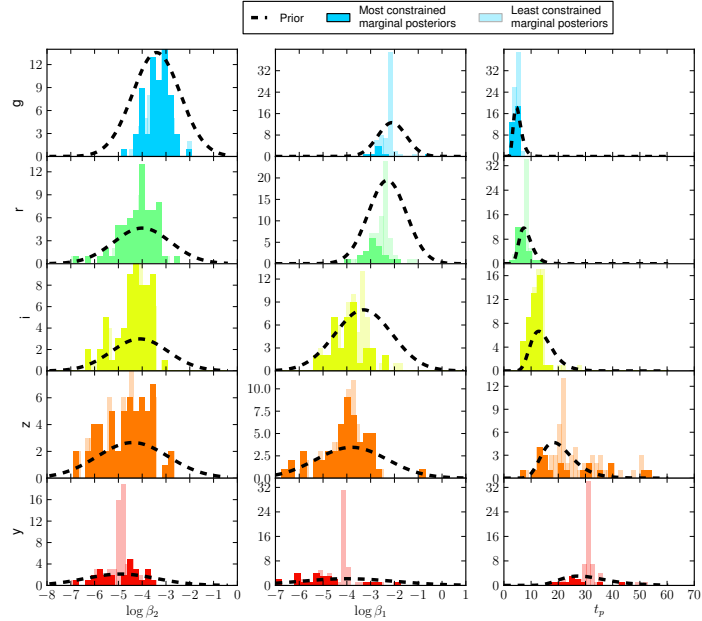


Figure 7.5.— Illustration of prior distribution construction for parameters of the Bayesian SN IIP light curve model. Filters are displayed by row; parameters by column. Only parameters with priors defined per-filter are shown. The bars show the distribution of the marginalized posterior medians for the fitted light curve model parameters. The least constrained posterior medians (with variance 80% or more of the variance in the prior) are shown with the faded bars, and more constrained posterior medians are shown with darker bars. The chosen prior distribution is shown with the dashed lines. Posteriors fitted exclusively with information from the prior (no constraint provided by the data; e.g. the least constrained marginal posteriors) would appear exactly at the position of the prior mean.

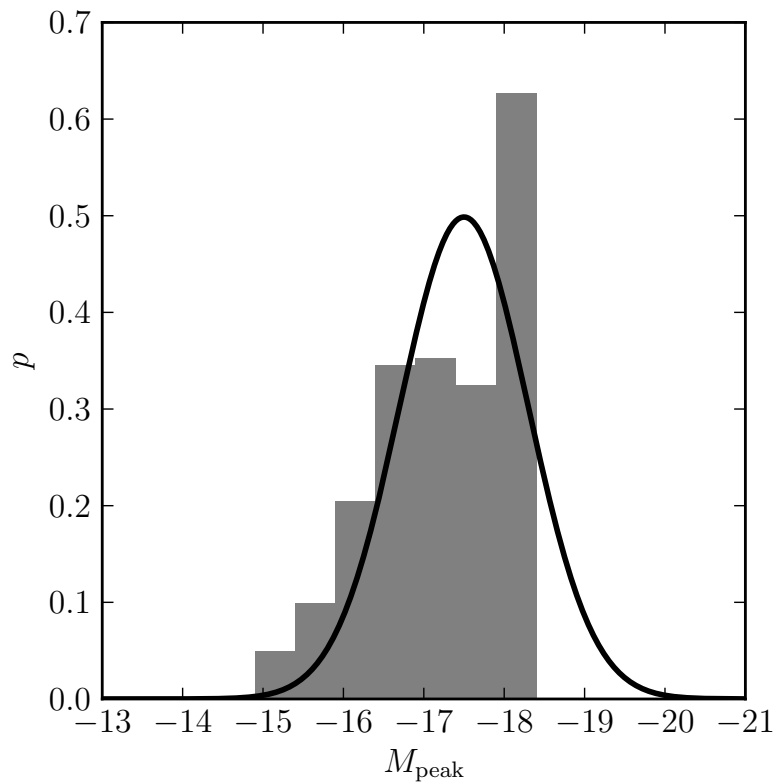


Figure 7.6.— The prior adopted for the SN II peak magnitude distribution (solid line) compared to the observed SN II luminosity function determined by Li et al. (2011) for an ideal, magnitude-limited survey with a 1 day cadence (their Figure 10) is shown with gray bars.

et al. (2011) based on observations from the Lick Observatory Supernova Search (LOSS; Figure 7.6).

In total, including the independent parameters for each light curve segment and filter, the fitted model for each SN has 61 independent parameters (12 per filter and t_0). We reproduce the fitted light curve parameters for each object in our sample in Table 7.3.

7.3.3 Fitting validation

Following execution of *Stan* and posterior sampling, we reconstruct a posterior predictive distribution for each light curve from the model parameter samples (Gelman et al. 2013). This distribution represents the probability for the physical supernova light curve to have the luminosity l_m on a grid of times t_m .

Figure 7.7 illustrates a posterior predictive check for the model fit to the object PS1-11apd, whose well-sampled observations illustrate both the strengths and weaknesses of the 5-component model. The rising phase in each band is well-constrained by the tightest pre-explosion limit, in the y -band. The two-component (rising then falling) plateau phase provides an accurate description of the data in the i -band, but not in the g -band, where the evolution of iron line blanketing (see e.g. Kasen & Woosley 2009) causes a behavior not captured by the model (falling then rising/plateauing). As is characteristic of the PS1 data, the y -band light curve is more poorly sampled and higher in variance than the other bands. In general, the model parameter inferences are therefore most reliable and directly interpretable in the r , i , and z bands.

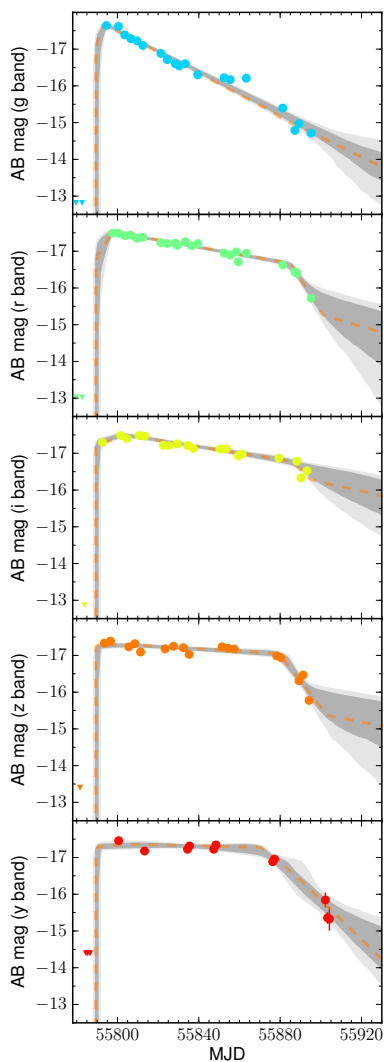


Figure 7.7.— An example of the 5-component SN II light curve model fit to the SN PS1-11apd in each of the *grizy* bands (top to bottom). The PS1 photometry and uncertainties in each of five optical bands are displayed by the circles and errorbars. The model posterior distribution is displayed by the shaded intervals; the shading boundaries correspond to the [5, 16, 84, 95]th percentile values of the posterior. The maximum likelihood model in each band is displayed by the red dashed line. *K*-corrections have been applied to both the data and model, but not reddening correction. The triangles denote photometric upper limits.

Figure 7.8 illustrates fitting behavior for a well-sampled and a poorly-sampled PS1 light curve. The top panel shows PS1-12bku, a SN with observations from the rise phase through the end of the plateau. Note that the nonlinear behavior of the light curve during the rise, due to shock breakout and post-shock breakout cooling envelope effects (see e.g. Nakar & Sari 2010; Rabinak & Waxman 2011) are not captured by the power law rise model, but the explosion epoch itself is fit accurately in the fitted model. PS1-10zu is shown in the bottom panel, an object which apparently exploded during the gap between observing seasons. With observations only available starting a few weeks before the end of the plateau phase, and no direct constraints on the explosion epoch, the model fit includes a range of possible explosion dates reflecting the prior distributions for the plateau duration and peak magnitude.

7.3.4 Type II SN sub-classification

We apply a supervised machine learning methodology (see e.g. Faraway et al. 2014) to classify the Type II SNe in this sample into their appropriate subclasses and, in particular, to identify SNe IIP for further analysis. Our approach is to first apply “expert knowledge” to manually label a subset of clearly-classifiable objects from our sample of 112 SNe II, then we uniformly measure light curve features using the methodology described in Section 7.3.1, then train a Support Vector Machine (SVM) classifier to a deliberately-selected subset of these features, and finally apply that classifier to assign labels to the remaining objects in the sample. In general, spectral classification of distant ($z \gtrsim 0.1$) transients is complicated by

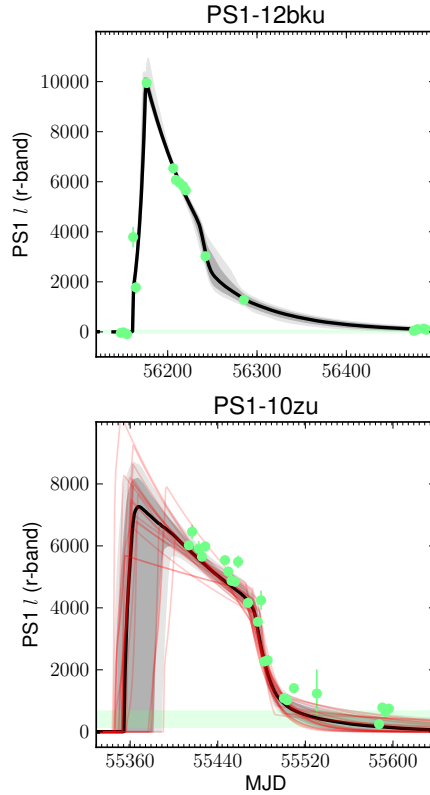


Figure 7.8.— Examples of fitting the 5-component SN II light curve model defined in Equation 7.1 over a range in light curve quality. Top: r -band photometry for the SN IIP PS1-12bku (green points and errorbars), showing clear detections during each of the five phases on the light curve model. The dashed red line shows the maximum likelihood 5-component model fit, the shaded areas show the 1 and 2 σ confidence intervals for the posterior distribution of the model (see Section 7.3.2), and the solid black line shows the median of that confidence interval. The horizontal green bar shows the range fitted for the zero-point flux offset. Bottom: The same, for PS1-10zu. In this case, no observations constrain the rise phase, and models with a diversity of plateau durations and rise behaviors are explored by the MCMC chain (a sampling of these models is shown in red).

spectral evolution (see e.g. Milisavljevic et al. 2013 for a discussion of SNe IIB), exacerbated by the observational cost of obtaining a well sampled spectral series, and the difficulty in robustly identifying spectral features, exacerbated by the low signal-to-noise of the spectroscopy relative to nearby objects. The methodology discussed below is intended to capitalize on photometric information to help overcome these limitations.

Our procedure is as follows. We begin by manually assigning SN IIP, IIB, IIn, and “II?” (undetermined) classifications to each object in the sample by inspection of their light curves and optical spectra. See e.g. Li et al. (2011) for a discussion of the photometric and spectroscopic properties of SN II sub-classes. We do not establish a label for SNe IIL separate from SNe IIP, but discuss that sub-class later in Section 7.4.2. We assign SN IIn classifications to 23 objects based on the detection of intermediate-width H emission features and/or exceptional luminosity ($\gtrsim -20$ mag); SN IIB classifications to 5 objects based on the detection of He features (in addition to broad H features) in the optical spectrum and/or a SN I-like light curve, with slow rise and fast decline rate; and SN IIP to 67 objects based on the presence of a broad $H\alpha$ spectral feature and/or a clearly-exhibited plateau-like light curve. Finally, we liberally apply the SN II? classification to 17 objects for which we do not have sufficient data to assign a classification and/or do not neatly fit the preceding criteria.

We apply our Bayesian light curve model (Section 7.3.1) to uniformly measure features of the light curves of every SN II in our PS1 sample. To mirror our expert knowledge, we focus on the peak absolute magnitude (M), the rise time to peak magnitude (t_p), and the post-peak decay rate (β_2) as features capable of

distinguishing objects in these subclasses. We identify the i band as the filter in which these features are most discriminating. For self-consistency, we apply the SN IIP theoretical K -corrections (Section 7.2.3) to every object in the sample.

We then fit a linear SVM classifier (Pedregosa et al. 2011) to the features of the training set. The SVM consists of a series of hyperplanes that optimally divide the feature space to discriminate the training set based on their class labels. The results of this fit are displayed in Figure 7.9. In summary, the classifier identifies SNe IIn as luminous (primarily $M_i < -18$ mag) and slowly-evolving ($\log \beta_2 \lesssim -3$), SNe IIb as intermediate-luminosity and quickly evolving, and SNe IIP as slowly-evolving and spanning a range from sub-luminous ($M_i > -17$ mag) to luminous ($M_i \sim -20$ mag), accurately reflecting our expert knowledge applied in construction of the training set. Disagreement between object location and shaded labeling in Figure 7.9 is partially due to variance in the observational data, which limits the efficiency of the classifier, and partially due to the coarse binning of the display slices. We have configured the classifier with the penalty parameter $C = 1$ and class weights calculated from their representation in the training set.

Finally, we apply the classifier to the unclassified (SNII?) objects to infer their subclasses. While “SN IIb” and “IIn” classifications can only be assigned by spectroscopy, by definition, here we are using photometric information to supplement available spectroscopy for the purpose of predicting the most likely spectroscopic sub-classification. The classifier identifies 9 of these objects as SNe IIP, which we hereafter incorporate in our SN IIP sample; 6 as SNe IIb; and 2 as SNe IIn.

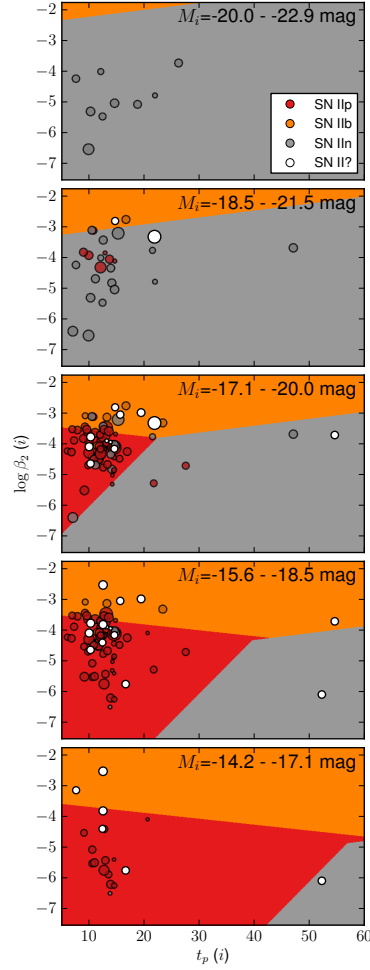


Figure 7.9.— Support Vector Machine classifier trained to the SN II light curve feature data. The subplots display 5 slices of the 3-dimensional feature space (β_2, t_p, M_i) , representing different bins of absolute i -band magnitude. The shaded regions indicate the labeling regimes identified by the classifier, and the points represent observed objects from the sample of different manually-assigned subclasses. The colored points represent the training set, and the white (“SNII?”) points represent the objects to be classified. The point size reflects the uncertainty in the feature posterior distribution for each object, with larger points indicating smaller uncertainty.

When applied to the training set, the classifier achieves 82% accuracy across all sub-types, and 88% accuracy for SNe IIP. It mistakenly classifies SNe I Ib and I In as SNe IIP only 22% of the time (the false positive rate), and mistakenly classifies SNe IIP as other classes only 12% of the time (the false negative rate). These statistics imply that, of our sample of 17 SNe II?, ~ 3 may be incorrectly classified as SNe IIP and ~ 3 legitimate SNe IIP may be inadvertently excluded. In combination with our sample of 67 securely-identified SNe IIP, this level of false positives would imply a $\sim 4\%$ contamination rate within the sample. Given the relatively low S/N of the SN II? objects, the classifier may perform more poorly than on the training dataset; but for the same reason, the influence of these objects on our light curve parameter inferences will be correspondingly suppressed.

7.4 RESULTS

In this section, we present the results of our analysis of the observational properties of the PS1 SN IIP light curves. The parameters calculated for individual objects are summarized in Table 7.5.

7.4.1 SN IIP Light Curve Template

We construct *grizy* SN IIP template light curves based on scaled stacks of our PS1 photometric sample. Figure 7.10 (left) shows these stacked SN light curves. In each band, we only include objects with a 1σ uncertainty in the peak magnitude

of < 0.5 mag and with an uncertainty in the plateau epoch of < 10 days, as estimated from the marginal posterior of the fitted light curve model. In total, we include [66, 68, 65, 64, 32] objects in the $[g, r, i, z, y]$ -band templates.

Figure 7.10 (right) shows the template light curves constructed from this data. The template magnitudes are calculated based on the range of observed photometry within a moving window of 6 rest frame days in width, between ~ -10 –110 days from peak magnitude. Template values are only reported if at least 4 photometric observations fall in the window. In total, we include [449, 610, 762, 798, 267] observations in constructing the $[g, r, i, z, y]$ -band templates. The templates are reproduced in Table 7.4.

7.4.2 Search for an SN IIL sub-population

Past studies have varied widely in their interpretation of a putative, fast-declining sub-class of SNe II commonly labeled “SNe IIL.” The SN IIL classification was coined by Barbon et al. (1979), in recognition of a set of 6 Type II SNe with an unusually fast decline rate of ~ 0.05 mag day $^{-1}$ in the B -band, constituting $\sim 26\%$ of their SN II sample. From a theoretical perspective, a fast declining SN II suggests a less massive H envelope and consequently less sustained power contribution from H recombination. Likely explanations for diversity in H envelope mass among SN II progenitors include variation in progenitor initial mass, with SNe IIL likely to arise from either progenitors with intrinsically less massive envelopes (e.g. initial masses of $\sim 7 - 10 M_{\odot}$; Swartz et al. 1991) or from more massive stars which have been stripped by strong radiation driven winds

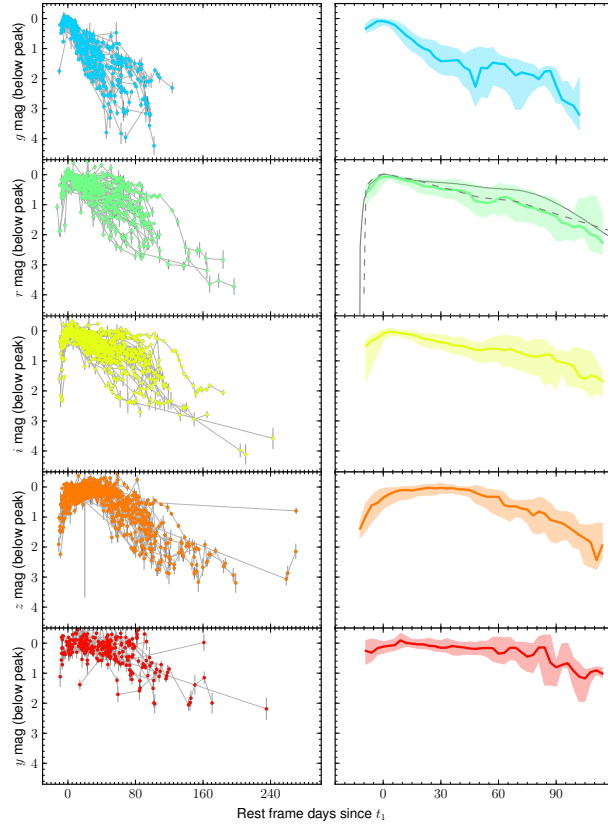


Figure 7.10.— Left: Stacked SN IIP light curve constructed from objects in the PS1 sample. The magnitudes are shown relative to the fitted value of M_{peak} (see Section 7.3.1). Right: Template light curves derived from the stacks, zoomed in relative to the stacked light curves. The solid line shows the median value of stacked photometry at each reference epoch, and the shaded region shows the 1σ (16-84th percentile) range. The grey lines displayed against the r -band curve show the unfiltered SN IIP (solid line) and IIL (dashed line) templates from Li et al. (2011). K -corrections have been applied using the method described in Section 7.2.3, including uncertainties accounting for the range of epochs allowed for each photometric point by the model fit.

($\gtrsim 18 M_{\odot}$; Smith et al. 2011a), and/or stars which have been partially stripped by interaction with binary companions (Nomoto et al. 1995).

Observationally, no widely adopted criteria for SN IIL classification have emerged. Patat et al. (1994) divided their SN II light curve set into “linear” and “plateau” classes based on the Barbon et al. (1979) criterion, but they describe the decline rate distribution of these objects as continuous and find no statistical evidence for two modes in the distribution. In their population study of the LOSS SNe, Li et al. (2011) define SN IIL as having SN IIP-like spectroscopic features, but exhibiting an R -band decline of > 0.5 mag after explosion. By their selected criterion, they identify 7 unambiguous SNe IIL among 81 SNe II, and they determine SNe IIL to represent 10% of the volume-limited SN II population. They find that the SN IIL are on average over-luminous compared to SNe IIP, and therefore would represent $\sim 25\%$ of a magnitude-limited SN II survey sample. By inspection of a set of 22 SN II light curves from the CCCP and the literature, Arcavi et al. (2012) identify a set of 5 objects which they describe as SNe IIL. Their selection corresponds to a decline rate criteria of $\gtrsim 0.3$ mag within 50 days of explosion. They suggest that these objects form a class “distinct” from SNe IIP, and that the two classes together do not form a continuum of decline rates. Most recently, Anderson et al. (2014) have characterized the decline rate distribution of hydrogen-rich SNe as continuous.

We take an empirical approach to searching for evidence of a fast-declining mode in the sample of PS1 objects classified nominally as SNe IIP (see Section 7.3.4). Figure 7.11 shows the distribution of mean posterior values for the β_2 plateau decline rate parameter in our fitted light curve models, among objects

with significant constraints on the plateau phase decay behavior. We employ Gaussian kernel density estimation (KDE) to estimate the underlying form of the decline rate distribution from the observed data. We select a KDE bandwidth factor of 0.42 in r -band (and similar in other bands) based on the number of objects in the well constrained sample, following Scott (1992). Inspection of the KDE models in Figure 7.11 does not indicate the presence of any fast-declining modes, e.g. within the shaded regions corresponding to the Barbon et al. (1979) and Li et al. (2011) criteria. Given the limited sample size, this test would not be sensitive to the existence of a small SN IIL sub-population if subsumed within the fast-declining tail of a more numerous SN IIP population. However, a significant sub-population ($\sim 20\%$) as proposed by previous authors should emerge if present.

We therefore conclude that empirical evidence for a distinct SN IIL sub-population is not present within the PS1 SN II dataset, and hereafter we do not distinguish between SNe IIL and IIP. Discounting the existence of an SN IIL subclass differs from the interpretation applied in many past studies, but does not disagree quantitatively with past results. Li et al. (2011) adopted an SN IIL classification scheme defined arbitrarily by previous authors (Barbon et al. 1979) for the purpose of estimating volumetric rates. Patat et al. (1994) applied a similar criterion, then tested for a discontinuity between the properties of this sub-population and the “normal” SN IIP population. They reported a negative result. Arcavi et al. (2012) identified a slow declining subset of objects in their sample, but did not quantitatively test for a discontinuity. Moreover, we note that our sample, consisting of 112 SNe II in total, is $\sim 40\%$ larger than the Li et al.

(2011) SN II sample and ~ 5 times larger than the Arcavi et al. (2012) sample. Using a similarly sized sample, Anderson et al. (2014) have reported independent results in agreement with the continuum of decline rates we report here.

Figure 7.10 further illustrates this result, showing our SN IIP r -band photometry in comparison to the averaged unfiltered SN IIP and SN IIL light curves of Li et al. (2011). Both their templates fall within the photometric range of our observed sample, with their SN IIP template falling near the $+1\sigma$ range of our light curves and their SN IIL template falling near the median of our light curves. Note that their photometry was collected with an unfiltered photometric system, which Li et al. (2011) compare to R band. This would suggest that their response function includes redder wavelengths than our r -band photometry. This may partially explain the slower decline rates in their sample, as redder filters (e.g. izy -bands) exhibit more gradual SN IIP decline rates in the plateau phase. Regardless, this comparison illustrates that the long-recognized range of decline rates among SNe with broad $H\alpha$ features falls within the observed, continuous range of decline behavior exhibited by objects classified as SNe IIP in our sample, with no evidence for a second, fast-declining mode in the population.

7.4.3 Plateau duration distribution

Recent observational studies have suggested that the plateau durations of SNe IIP are tightly distributed around ~ 100 days (Poznanski et al. 2009; Arcavi et al. 2012), in stark contrast to theoretical predictions that they should vary from $\sim 80 - 200$ days given the expected range of progenitor properties including

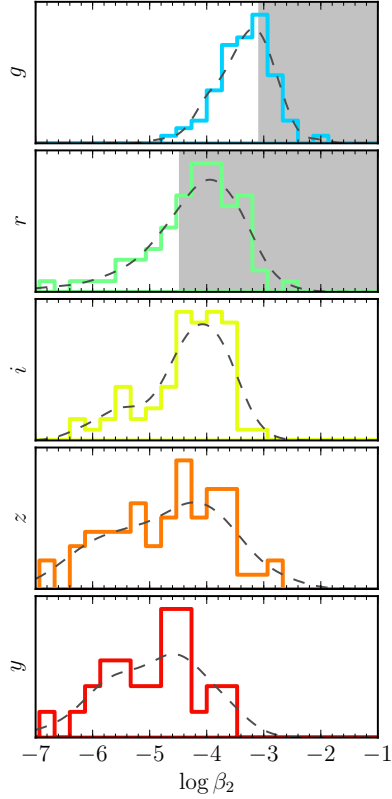


Figure 7.11.— Investigation of a potential SN IIL sub-population. The histograms display the distribution of mean posterior values for the β_2 plateau decline rate parameter in our fitted light curve models in each photometric band. Only objects classified nominally as SNe IIP (i.e. not classified as SNe IIc or IIb, see Section 7.3.4), and only objects with well constrained β_2 posteriors (with variance $\leq 80\%$ of the prior variance), are included. The dashed lines display the Gaussian kernel density estimate models for the distributions. The *g*-band shaded region shows the approximate range for objects that would be classified as SNe IIL under the Barbon et al. (1979) *B*-band criterion (with more positive β_2 values reflecting faster decline rates), and the *r*-band shaded region shows the Li et al. (2011) *R*-band criterion.

mass, energy, and radius (see e.g. Kasen & Woosley 2009). Poznanski (2013) have interpreted this as evidence that the joint parameter space of progenitor properties must be tightly constrained, with the explosion energy scaling precisely with the cube of the mass to produce a roughly constant plateau duration.

We quantitatively assess the plateau duration distribution of our SNe IIP sample. In agreement with Arcavi et al. (2012), Poznanski (2013), and Faran et al. (2014), the r -band plateau duration distribution of our sample (Figure 7.12) is peaked around $\sim 90 - 100$ days, with median value of 91 days and 1σ variation of 13 days. However, the full observed range of plateau durations is significantly larger, $64 - 127$ days. Note that we do not include in this distribution poorly-constrained light curves, where the marginalized posterior uncertainty is $> 80\%$ of the prior variance (24 days at 1σ). For those poorly constrained objects, as Figure 7.12 illustrates, the posterior is typically peaked around the mean of the prior distribution.

Our PS1 sample therefore suggests that the observed variation in SN IIP plateau durations is not as highly constrained as suggested by Poznanski et al. (2009) and Arcavi et al. (2012). However, we do not detect objects with plateaus as long lived as the least energetic objects produced in the model grid of Kasen & Woosley (2009) (e.g. ~ 200 days for kinetic explosion energy of $0.3 B$ at infinity). However, all wide field surveys will be insensitive to identifying the longest duration objects for two primary reasons. First, such low energy explosions will have correspondingly low luminosities ($L_{50} \sim 41.8$, similar to the least luminous objects in our sample; see Table 7.5) and therefore be subject to Malmquist bias. Second, because the length of the observing seasons of each PS1 MD field

(typically $\lesssim 160$ days) are similar to the SN IIP plateau duration, there will be an observational bias towards measuring well-constrained plateau durations only for short-duration objects. We therefore interpret the results presented here as a lower limit on the true variation in the SN IIP plateau duration distribution. In a companion paper, we use a hierarchical Bayesian methodology to assess the influence of these biases on our inferred plateau duration distribution, and to estimate the underlying plateau duration distribution.

7.4.4 Line of sight extinction

We correct for total extinction (Galactic and host environment) using the $(V - I)$ color excess method of Nugent et al. (2006) as revised by Kasen & Woosley (2009)—see Figure 7.13. We calculate $E(V - I)$ by comparing to the theoretical baseline $(V - I)$ color⁵ for the given V -band luminosity (Equation 15 of Kasen & Woosley 2009), and convert to extinction in each *griz* band using the extinction curve of Cardelli et al. (1989) and assuming $R_V = 3.1$. We apply a physically-motivated uniform prior enforcing $E(V - I) \geq 0$ mag. The median

⁵We convert our *griz* photometry to the Landolt and Vega systems using a color-based S correction obtained by integrating over the temporally nearest available UVOIR spectrum of SN 1999em, the $\sim +37$ day spectrum from Leonard et al. (2002). We find that s -corrections based on the spectrophotometric templates applied in Section 7.2.3 would introduce a systematic discrepancy in the $(I - i)$ color relative to SN IIP corrections in past works (e.g. D’Andrea et al. 2010) of ~ 0.4 mag, due to differences in the equivalent width of the NIR Ca II emission feature. We estimate a ~ 0.1 mag systematic uncertainty may remain in our I -band magnitude estimates due to variation in this feature. We apply the AB offset of Blanton & Roweis (2007).

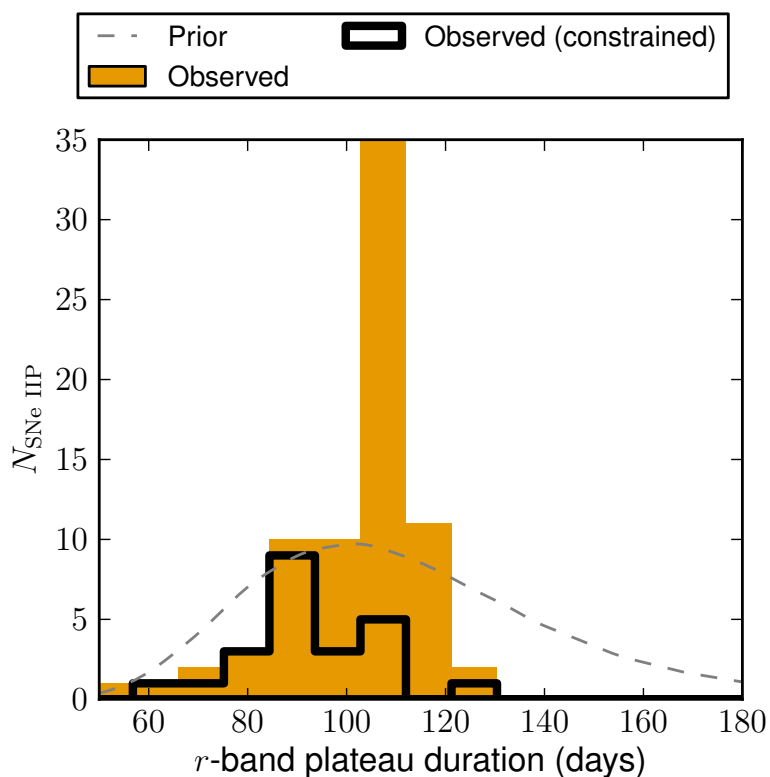


Figure 7.12.— The distribution of r -band plateau durations ($t_p + t_2$) among the SNe IIP in our sample, as derived from the posterior medians of our Bayesian light curve fits. The solid line shows the subset of objects with well-constrained marginalized posterior uncertainties (< 15 days at 1σ ; $N = 29$). The dashed line shows the lognormal mixture prior on the plateau duration.

uncertainty for the extinction estimate of an individual SN is 0.4 mag.

We find extinctions varying from 0.0 – 4.6 mag, with median value of $\langle A_V \rangle = 1.3$ mag. In this distribution we have excluded objects with extinction uncertainties ≥ 2 mag, affecting 9 objects. This median is somewhat higher than the mean extinction reported by Smartt et al. (2009) for their sample of SNe IIP with progenitor imaging, $\langle A_V \rangle = 0.7 \pm 1.1$ mag. The discrepancy may result from a combination of differences in methodology (the estimates from Smartt et al. 2009 are derived from a heterogeneous set of sources and techniques) and sample selection (given that our PS1 transient search operates in red bands, particularly i and z , it may be relatively insensitive to selection against high extinction objects). Both observations and theory show that there is significant scatter around the fiducial $(V - I)$ color, indicating intrinsic color variation not accounted for in our color excess-based extinction estimate. Moreover, the color excess method may be particularly vulnerable to under estimates for low-metallicity progenitors where decreased iron line blanketing would reduce suppression of blue flux. We note that Faran et al. (2014) have recently shown that both photometric and spectroscopic SN IIP extinction correction prescriptions have limited effectiveness (as measured by their ability to reduce the scatter in observed colors), and exhibit systematic offsets relative to each other.

7.4.5 Peak magnitude distribution

We show the peak absolute magnitude distribution for our PS1 SN IIP sample in each photometric filter in Figure 7.14. We correct for extinction using the

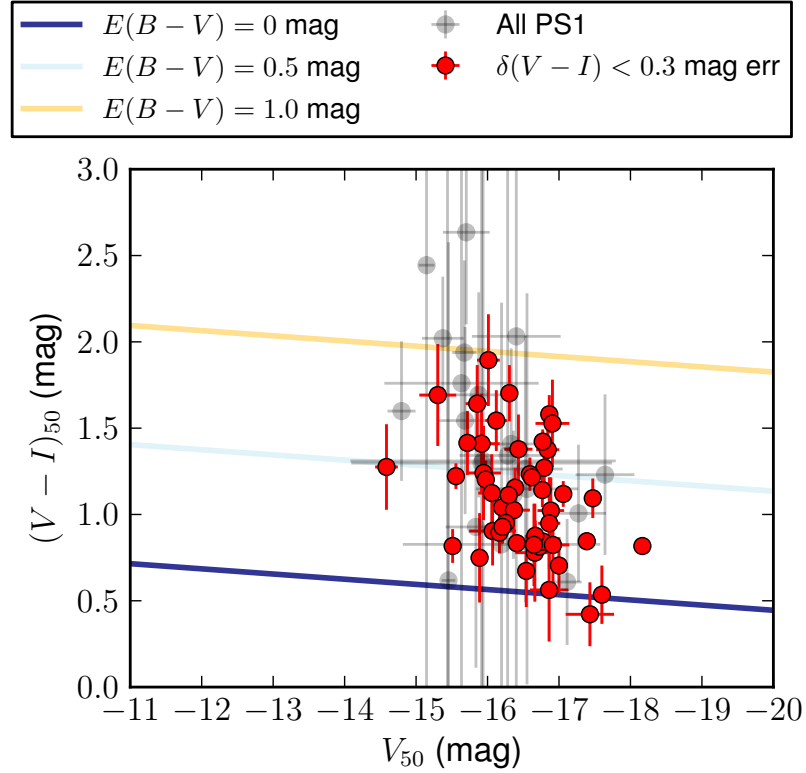


Figure 7.13.— Illustration of $(V - I)$ color excess method for extinction estimation. The points show the V magnitude and $(V - I)$ color (in the Vega magnitude system) at 50 days for objects from our SN IIP sample, with error bars representing 1σ variation in the posterior predictive luminosity distribution for each object. Objects with strong posterior color constraints are highlighted in red. The solid lines show theoretical color-magnitude relations for SNe IIP with different levels of reddening, based on the fiducial relation of Kasen & Woosley (2009).

($V - I$) color excess method, as described in Section 7.4.4. Statistics of these distributions are given in Table 7.1. In this table and hereafter, we include only objects with well constrained posterior distributions: $\delta M_{peak} < 0.1$ mag at 1σ without extinction correction, and $\delta M_{peak} < 0.2$ mag with correction. The median uncertainty for the absolute magnitude measurement (1σ posterior width) is δM_{peak} of 0.08 mag in r band without extinction correction, and 0.32 mag after correction.

The observed peak magnitude distribution agrees well with the R band luminosity function of Li et al. (2011), reflected in the prior distribution shown in Figure 7.14 (see also Section 7.3.2 and Figure 7.6). The comparison is somewhat limited, as Li et al. (2011) examined a different filter (R) and did not correct for extinction (although the objects in their sample should have low extinction). Note that this similarity represents a true agreement between the observed distribution of peak magnitudes between our surveys; if the prior were simply dominating our inferred peak magnitudes, the posterior medians would all be centered at the prior mean ($M_{peak} = -17.5$). This effect can be seen in the y -band peak magnitude distribution shown in Figure 7.14, where prior information does dominate for a substantial fraction of objects. Extinction correction shifts the median of the distribution by ~ 0.6 mag in g -band, and only ~ 0.1 mag in z -band. We regard the y -band distribution as least reliable due to the small number of objects ($N = 17$) that pass our posterior width cut, and therefore do not include them in Table 7.1.

The extinction corrected peak magnitude distribution spans a 1σ range of -17.50 to -19.40 mag in r -band, indicating a factor of ~ 3 spread in the

luminosity distribution of these SNe. This wide range in SN properties has important implications for the mass distribution of their progenitor stars, which we will model and discuss in Section 7.5.4. Richardson et al. (2014) found a B -band volume limited peak magnitude distribution with mean and standard deviation of $M_B \sim -17 \pm 1$ among 74 SNe IIP from the literature, ~ 1.5 mag dimmer than the g -band mean peak magnitude we report. The discrepancy in the mean of the absolute magnitude distributions between our studies is likely due to a combination of sample selection effects and extinction correction methodology. Richardson et al. (2014) have considered SNe IIL separately from SNe IIP, which systematically lowers their SN IIP peak magnitude distribution relative to ours (see Section 7.4.2). Moreover, Richardson et al. (2014) have applied a statistical correction for extinction, assuming a mean value of ~ 0.3 mag for each core-collapse SN, which is typically ~ 1 mag lower than the extinction correction we measure among our SNe IIP with the $(V - I)$ color excess method (Section 7.4.4).

7.4.6 Decline rate–peak magnitude relation

Upon investigation of the joint posterior parameter distributions among our fitted SN IIP light curves, we identified a highly significant relation between the plateau phase decline rate (β_2) and the extinction corrected peak magnitude (M_{peak}) of the SNe. Figure 7.15 illustrates that these parameters are highly correlated in r -band, with Pearson correlation coefficient of -0.62 (p -value of 2×10^{-09}). We have evaluated the strength of the correlation between these parameters in all

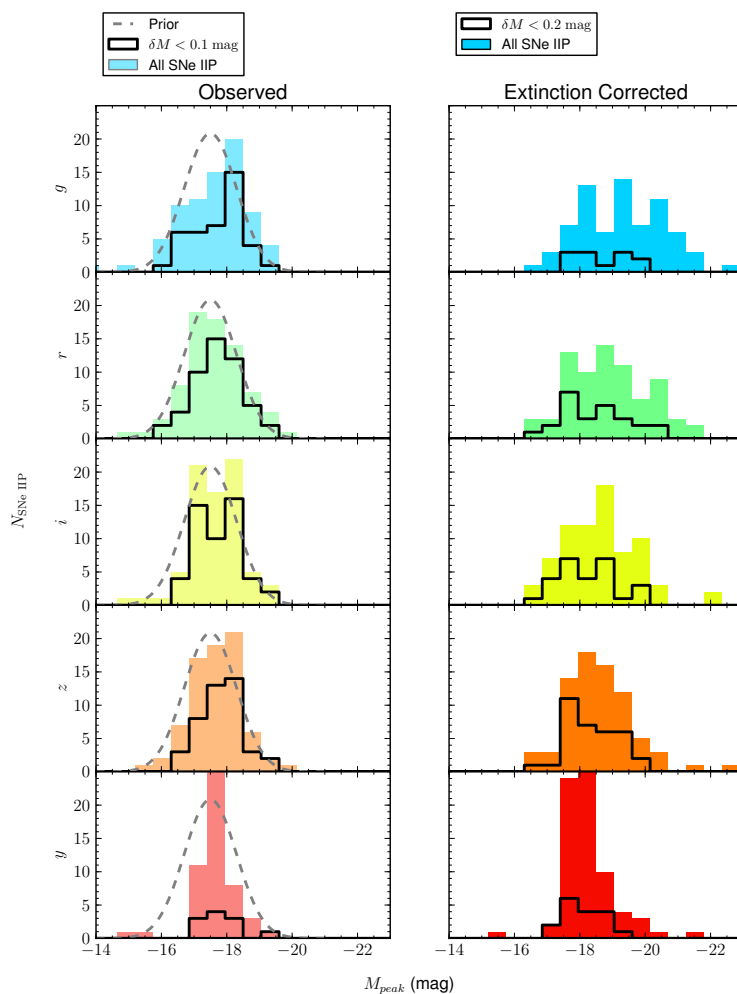


Figure 7.14.— The peak absolute magnitude distribution among the SNe IIP in our PS1 sample, as derived from the posterior medians of our Bayesian light curve fits, without (left) and with (right) correction for extinction (see Section 7.4.4). The solid line shows the subset of objects with well-constrained marginalized posteriors (< 0.1 mag at 1σ without extinction correction, < 0.2 mag with correction). The dashed line shows the prior distribution discussed in Section 7.3.2. All data are K -corrected.

combinations of photometric filters available from the PS1 dataset (Figure 7.16) and identified this relation to be significant in every band (except y , where the PS1 photometry is limited), though it is strongest in the r and i -bands.

In the r -band, the relation between these parameters is best fit with the relation:

$$\log \beta_2[r] = (-12.5 \pm 1.1) + M_{peak}[r] (-0.44 \pm 0.06) \quad (7.6)$$

This linear fit was obtained using a Bayesian methodology accounting for the two dimensional covariance of the M_{peak} and β_2 posterior distributions for each SN, and modeling the relationship between these values with an intrinsic scatter V orthogonal to the axis of the fit line (Hogg et al. 2010).

The [16, 50, 84]th percentile values of the intrinsic scatter parameter, projected to the peak magnitude axis, are [0.13, 0.16, 0.18] mag. No samples among the 20,000 returned from our MCMC fit of this model have positive slopes for the linear fit, supporting the low p -value reported from the Pearson correlation coefficient test above. When we perform the same analysis on the observed absolute peak magnitudes, not corrected for extinction, we find a similar trend, but with somewhat decreased significance (p -value of 2×10^{-08} and projected intrinsic scatter median $V = 0.26$ mag). This result suggests that application of the color-excess based extinction estimates provides measurable success in recovering the intrinsic distribution of light curve properties, despite the shortcomings described in Section 7.4.4.

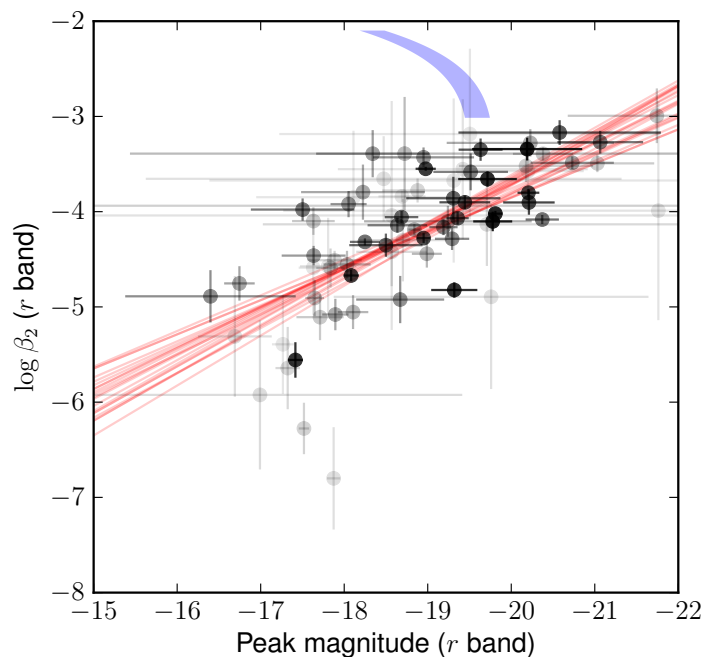


Figure 7.15.— Relation between the plateau phase decay rate (β_2 , r -band) and the extinction corrected r -band peak magnitude (M_{peak}) among SNe IIP in the PS1 sample. The red lines show posterior samples of linear fits to the parameter values. The opacity of the points is drawn in proportion to the inverse of their posterior variance. The blue band shows the SN Ia width–luminosity relation of Phillips et al. (1999), assuming $M_r^{max,Ia} = -19.45$ mag and a dispersion of 0.15 mag.

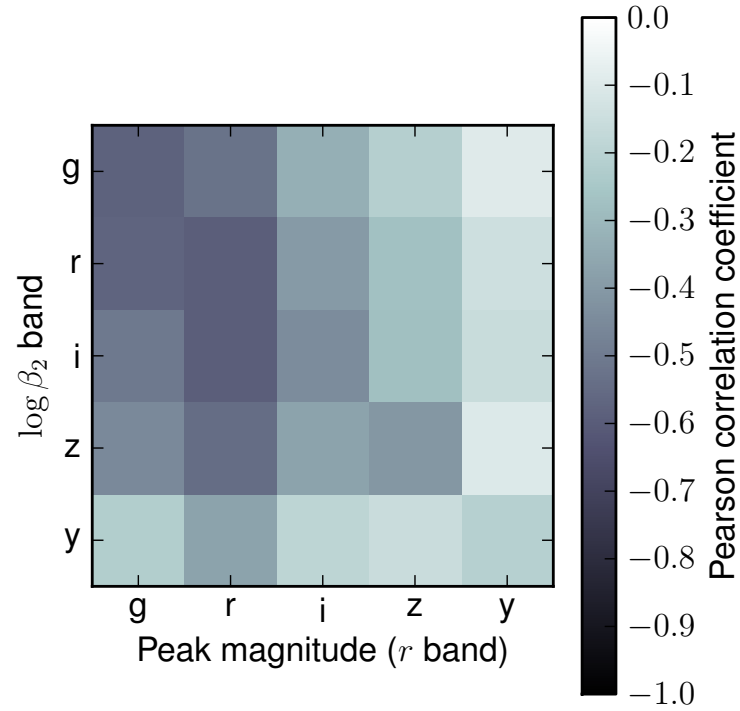


Figure 7.16.— Comparison of $\beta_2 - M_{peak}$ (extinction corrected) relation for different photometric filter sets. The shading represents the strength of the correlation between the two variables in each pair of photometric filters, as measured by the Pearson correlation coefficient (key at right).

In past studies, divisions of SN IIP samples into “normal” SN IIP and SN IIL (see Section 7.4.2) sub-classes may have obscured this relation by reducing the dynamic range available for correlations against the decline rate. Anderson et al. (2014) have recently reported an independent discovery of this relation using a similarly-sized sample of V -band light curves from a variety of past SN searches. This independent discovery, and the multi-band manifestation of the relation that we explore here, underscores its physical significance. This result echoes past conclusions that “SNe IIL” are on average more luminous than more slowly declining SNe IIP (e.g. Patat et al. 1994; Li et al. 2011).

The existence of a decline rate–peak magnitude relation for SNe IIP is reminiscent of the well known width–luminosity relation for SNe Ia (e.g. Phillips et al. 1999). However, while brighter SNe Ia have more slowly declining light curves, brighter SNe IIP instead have faster declining light curves (Figure 7.15). Moreover, the SN IIP relation has significant intrinsic scatter: $V \sim 0.2$ mag. That the SN IIP decline rate–peak magnitude relation is recoverable at all is testament to the wide range of variation in their plateau phase decline rates, which ranges a factor of ~ 20 .

The SN Ia decline rate–peak magnitude relation is interpreted as evidence for a fundamental plane or single-parameter family among SNe Ia light curves, and a similarly sparse dimensionality may apply to SNe IIP. Several authors have argued for a single parameter source of variation among SNe IIP light curves (Hamuy 2003a; Poznanski 2013), particularly with respect to the luminosity–velocity relation applied in the standardizable candle method (Hamuy & Pinto 2002; Olivares 2008; D’Andrea et al. 2010). Interpreted together with

the results of Section 7.4.2, this would seem to point to the explosion energy, likely determined by the progenitor initial mass through its influence on the mass of the hydrogen envelope at the time of explosion, as the predominant single parameter continuously determining the fundamental observational properties of the explosions of hydrogen-rich red supergiants, as Anderson et al. (2014) also concluded. However, the presence of significant scatter around the SN IIP decline rate–peak magnitude relation presented here suggests additional correlations with secondary factors, as have emerged among SNe Ia (Foley et al. 2011b). Relevant secondary characteristics of the progenitor stars are likely to include metallicity and rotation velocity.

In general, more massive H-rich envelopes should have longer radiative diffusion times ($t_{\text{diff}} \propto M/R$), suggesting slower light curve evolution and lower peak magnitudes. However, Poznanski (2013) have found an empirical linear relation between the progenitor initial mass of SNe IIP and their expansion velocities in the plateau phase. With these two factors in opposition, this would suggest that the diffusion time, and perhaps the β_2 parameter, should be nearly constant among SNe IIP. This discrepancy could result from nonlinearity in the relationship between progenitor initial mass and the mass of the hydrogen envelope at the time of explosion or variation in the velocity evolution between SNe IIP. Alternatively, it may challenge the robustness of the linear mass–velocity relation constructed by Poznanski (2013).

7.5 Progenitor Modeling

We compare the light curve models for each SN IIP in our sample to relevant theoretical models to estimate the physical properties of their progenitor stars.

7.5.1 Bolometric luminosity

For the purpose of comparing to the full-wavelength spectrophotometric models of Kasen & Woosley (2009), we estimate the pseudo-bolometric (OIR) luminosity of each SN by integrating over the multi-band (*grizy*) light curve model described in Section 7.3.2. We apply a correction (pBC) to the pseudo-bolometric light curves to, primarily, account for unobserved IR flux and some UV emission. We calculate this correction by integrating a SN IIP spectral template from a similar epoch ($t = +61$ days; Gilliland et al. 1999; Baron et al. 2004) over the '*griz*' bands, obtaining $\text{pBC} = 0.38$ mag. By using a fixed spectral template, we neglect any intrinsic variation in the SN IIP spectral properties. The modeling in Kasen & Woosley (2009) suggests that any intrinsic color variation among SNe IIP is small, with the bolometric correction estimated to vary by ~ 0.1 mag based on differences in progenitor metallicity and initial mass (their Figure 14).

7.5.2 Ejected Ni mass

We estimate the ejected mass of radioactive ^{56}Ni (M_{Ni}) by comparison to the late-time light curve of SN 1987A (see Figure 7.17), following the method of Pastorello et al. (2004). We compare our pseudo-bolometric light curves

(Section 7.5.1) to the SN 1987A light curve using the late-time (> 125 days) rest frame epoch where the model is most tightly constrained and assuming complete gamma-ray trapping, as in Pastorello et al. (2004); but see also the discussion of gamma-ray trapping in Anderson et al. (2014).

The distribution of M_{Ni} among our PS1 SNe IIP has [16, 50, 84]th percentile values of [0.04, 0.12, 0.20] M_{\odot} . We include in this distribution only objects with photometry to directly constrain their light curve evolution in the radioactive decay dominated phase. We identify such objects by looking at the posterior variance in the β_{dN} parameter, which is $\delta\beta_{dN} = 1$ dex at 1σ in cases where the prior alone sets the parameter value. We therefore adopt a cut at $\delta\beta_{dN} < 0.9$ dex to exclude poorly constrained Ni masses. We note that, among the entire sample, the typical uncertainty in M_{Ni} is fairly large (median of 0.4 dex) due to the relatively poor photometric coverage of the late phases of SNe in the sample. Among the excluded objects, some have unphysically large median estimates for the ejected ^{56}Ni mass ($M_{\text{Ni}} > 1 M_{\odot}$); the high uncertainty in these estimates is appropriately reflected in the confidence intervals quoted in Table 7.5.

Our results suggest a factor of ~ 2 smaller M_{Ni} for most SNe IIP in comparison to typical SNe Ib and Ic, which have $\langle M_{\text{Ni}} \rangle \approx 0.20 \pm 0.16 M_{\odot}$ (Drout et al. 2011). This is consistent with the expectation that SNe Ib and Ic are produced by more massive stellar progenitors than SNe IIP. Our measured M_{Ni} distribution is similar to that reported by Nadyozhin (2003), who derive M_{Ni} ranging from 0.03 – 0.4 M_{\odot} for a set of 11 SNe IIP from the literature, with a mean value of 0.10 M_{\odot} .

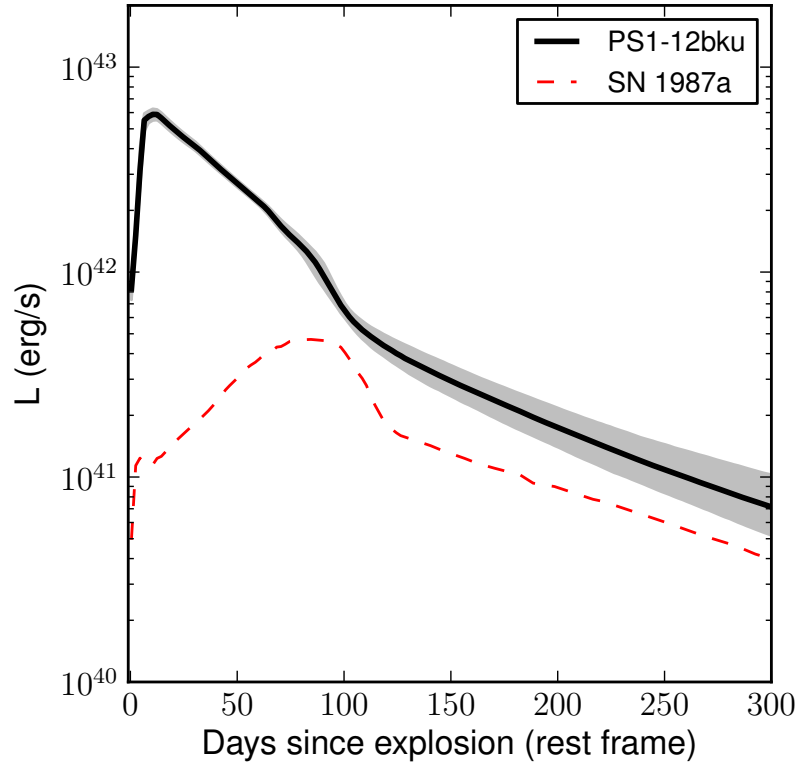


Figure 7.17.— Illustration of ejected nickel mass (M_{Ni}) measurement methodology. The pseudo-bolometric (optical-infrared) light curve for PS1-12bku (black solid line) is shown in comparison to the late time bolometric light curve of SN 1987A (red dashed line; from Pastorello et al. 2004 and references therein). The 1σ uncertainty in the bolometric luminosity as derived from the multi-band light curve model is illustrated with the shaded region, including the uncertainty in the explosion epoch.

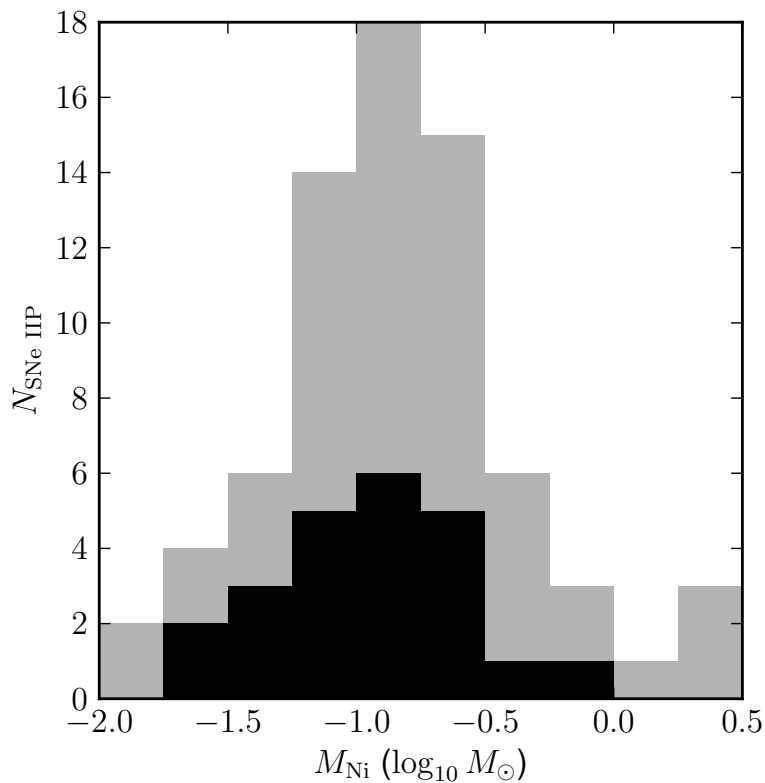


Figure 7.18.— The distribution of ejected nickel mass (M_{Ni}) among the SNe IIP in our sample, as derived from the late time bolometric luminosity. The gray shaded area shows the distribution estimated among all objects in our sample, and the black shaded region shows only objects with photometry constraining the light curve evolution in the radioactive decay phase (based on the variance in the β_{aC} posterior; see text).

7.5.3 Comparison to hydrodynamic models

We derive physical parameters (including progenitor initial mass, radius, and explosion energy) for the progenitor stars of our SN IIP sample by comparison to the modeling of Kasen & Woosley (2009). In general, more massive progenitor stars produce plateaus that are brighter and of longer duration. There is a secondary contribution from M_{Ni} which has the effect of increasing the plateau duration. Kasen & Woosley (2009) provide scaling relations for the observable parameters L_{50} (bolometric luminosity at 50 days after explosion) and $t_{p,0}$ (plateau phase duration, corrected for extension by ejected ^{56}Ni) as a function of E_{51} (total explosion energy in units of 10^{51} ergs) and M_{in} (initial mass of progenitor star). We note that there is a well known discrepancy between masses derived from hydrodynamic light curve modeling and direct progenitor searches, with progenitor searches yielding lower mass estimates (Utrobin & Chugai 2008; Maguire et al. 2010).

We derive $t_{p,0}$ using their Equation 13, which requires an estimate for M_{Ni} (see Section 7.5.2), R_0 (the progenitor radius at the time of explosion) and M_{ej} (the total ejected mass). Following the recommendations of Kasen & Woosley (2009), we calculate values for R_0 and M_{ej} strictly as a function of M_{in} by interpolating over the progenitor star model grid used in their study. Solving this system of equations for every sample in the posterior distribution of the light curve model, we obtain estimates for M_{in} , M_{ej} , and E_{51} for each SN IIP in our sample.

7.5.4 Progenitor initial mass inference

In Figure 7.19, we compare the observed plateau duration and L_{50} to model curves from Kasen & Woosley (2009). This comparison illustrates that the observed variation in SN IIP light curve phenomenology is significantly larger than the range explored by the Kasen & Woosley (2009) model grid, preventing us from performing progenitor parameter estimation for a substantial number of the objects in our sample. Given the observed M_{Ni} values measured for each individual light curve, 64 of our SNe IIP have light curve properties outside the region covered by the Kasen & Woosley (2009) models, and we can produce mathematically valid comparisons to model light curves from the Kasen & Woosley (2009) grid for only 12 SNe IIP (see Table 7.5). Even these comparisons typically yield explosion energies at or above the most energetic models in their grid ($E_{51} > 5$). A large number of objects in our sample have luminosities lower than the range of theoretical values for a given plateau duration (falling in the blue shaded region of Figure 7.19); accounting for 58 of the 64 objects for which we do not report progenitor inferences.

We therefore advocate for further theoretical exploration of the SN IIP light curve parameter phase space through additional hydrodynamic modeling, in order to provide more robust model grids and scaling relations for comparison to observational surveys. In particular, certain modeling systematics should be addressed to enable inference on objects occupying the low-luminosity and short plateau duration parameter space. Dessart & Hillier (2011) have previously recognized a systematic discrepancy between SN IIP model and observed light

curves, and identified over-sized radii in model progenitor stars as the likely cause. Hydrodynamic explosion simulations based on more advanced progenitor star models, taking into account important effects such as rotation on the stellar radius (e.g. Georgy et al. 2013), are needed to overcome this bias. Moreover, synthetic light curves for SNe with progenitor initial masses $< 12 M_{\odot}$, down to the limit for core-collapse (e.g. $8 M_{\odot}$, see Smartt et al. 2009 and references therein), and higher explosion energies should be produced. Such low mass progenitors have already been explored in the context of extremely low luminosity SN IIP like SN 1997D (Chugai & Utrobin 2000), and model light curves of this kind calculated with full self-consistency across the mass and energy spectrum are needed.

Additionally, other progenitor physical parameters will play important secondary roles in determining SN light curve properties and should be included in future simulations. In particular, lower metallicity can serve to lower the plateau luminosity by decreasing the opacity of the H envelope, therefore lowering plateau luminosities, and by decreasing mass loss, causing longer lived H recombination and plateau durations (Kasen & Woosley 2009; Dessart et al. 2013). Dessart et al. (2013) have recently performed a theoretical survey of SN IIP radiative properties using a grid of synthetic progenitor stars expanded in parameter scope with respect to the grid of Kasen & Woosley (2009), including core overshoot, rotation, mixing, and metallicity. However, the Dessart et al. (2013) grid was limited to a single progenitor initial mass of $15 M_{\odot}$. An expanded survey of the kind performed by Dessart et al. (2013), to provide updated observationally-applicable scaling relations of the kind provided by Kasen & Woosley (2009), would be an invaluable

tool for inference on the progenitor population of massive star explosions in the nascent untargeted survey era. Photometric galaxy metallicity diagnostics like that presented in Sanders et al. (2013) can be used to observationally estimate metallicities for the progenitor stars of observed SNe to facilitate model comparison.

7.5.5 Implications for the Red Supergiant Problem

While theoretical stellar evolution modeling has historically predicted that stars undergoing core-collapse up to $\sim 25 M_{\odot}$ should produce Type IIP SNe (see e.g. Eldridge et al. 2008; Smartt 2009 and references therein), a variety of observational techniques have failed to identify SN IIP progenitors with masses greater than $\sim 16 M_{\odot}$. The shape of the stellar initial mass function can at least help to explain this absence, with $\sim 8 M_{\odot}$ progenitors being a factor of 10–15 times more common than $\sim 25 M_{\odot}$ progenitors. However, even accounting for IMF prescriptions of varying steepness, Smartt (2009) reported an upper limit for the SN IIP progenitor mass of $16.5 M_{\odot}$ based on their direct progenitor detection search. Similarly, in an X-ray analysis of SN IIP progenitor mass loss rates, Dwarkadas (2014) estimated a maximum mass loss rate of $\sim 19 M_{\odot}$. Black hole fallback formation (Fryer 1999; Heger et al. 2003) and / or progenitor rotation (Georgy et al. 2013; Groh et al. 2013b) may provide a theoretical solution to this “Red Supergiant Problem.”

Our results have only indirect implications for the Red Supergiant Problem. While our progenitor mass estimates (e.g. Figure 7.19) show no evidence for an

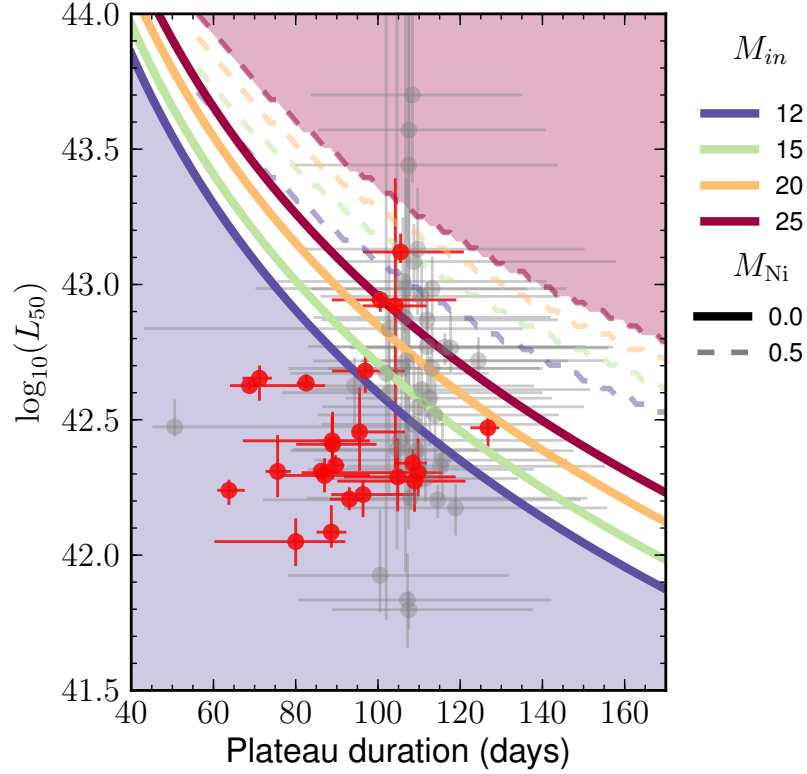


Figure 7.19.— Comparison of observed SNe IIP light curve properties to hydrodynamic light curve models. The points show the plateau duration (t_p+t_2 , rest frame; not corrected for M_{Ni}) of SNe IIP from the PS1 sample versus their bolometric luminosity at 50 days after explosion (L_{50}). Red points have well-constrained values for the plateau duration ($\delta t_p < 20\%$), while gray points have poorer constraints. The solid lines show interpolated values for progenitors of different initial masses (M_{in} ; key at right) from the model grid of Kasen & Woosley (2009). Different curves are plotted to illustrate the range of variation with the mass of ejected radioactive nickel ($M_{\text{Ni}} = [0, 0.50] M_{\odot}$ for [solid, dashed] line styles, respectively). The shaded curves illustrate physical parameter space not explored by the Kasen & Woosley (2009) model grid, ostensibly corresponding to masses < 12 or $> 25 M_{\odot}$.

absence of SN IIP progenitor stars at the high mass end of the Kasen & Woosley (2009) progenitor grid, our mass estimates are only as reliable as the calibration of the hydrodynamic modeling underpinning them. As we have discussed, there are known systematic offsets between the masses inferred from hydrodynamic modeling and progenitor star photometry, and additional theoretical investigation of this discrepancy is needed to conclusively resolve the Red Supergiant Problem.

However, our observations and modeling suggest that there is no discontinuous distinction between Type IIP and IIL SNe (Section 7.4.2). Given the correlation between plateau phase decline rate and luminosity (Section 7.4.6), and the theoretical connection between luminosity and progenitor mass, the exclusion of luminous “SNe IIL” could obscure the high-mass end of the SNe IIP progenitor population. Emphasizing the role of small number statistics in this regime, we note that Smartt (2009) report a progenitor mass upper limit that is already consistent with $20 M_{\odot}$ at 2σ , and consistent with $> 25 M_{\odot}$ at 2σ if only events with robust progenitor detections are included in the analysis. Walmswell & Eldridge (2012) have recently considered the extinction due to the dust produced by red supergiant winds and revised the SN IIP upper mass limit to $20_{-3}^{+6} M_{\odot}$ (with 2σ uncertainty). As the direct progenitor search technique has so far only been applied to a handful of objects, we look to future detections of the progenitors of luminous SNe IIP to address the Red Supergiant Problem (see e.g. Fraser et al. 2010; Elias-Rosa et al. 2011).

7.6 CONCLUSIONS

We have assembled and studied the full sample of Type IIP SN light curves from the Pan-STARRS1 Medium Deep Survey, totaling 18,837 photometric data points (5,056 robust transient detections) in *grizy* filters for 112 individual SNe (76 SNe IIP). We have developed a Bayesian light curve fitting methodology for SNe II based on a physically-motivated 5-component segmentation of the SN IIP light curve (Section 7.3.1). We present an implementation of our SN IIP model for use with the Hamiltonian Monte Carlo library *Stan* in Appendix 8.7. We have interpreted our light curve modeling in terms of the hydrodynamic Type IIP SN progenitor model grid of Kasen & Woosley (2009).

The primary conclusions of this work are as follows:

- We present photometric K-corrections and SN IIP light curve templates in the *grizy* bands (Sections 7.2.3 and 7.4.1). Our templates are based on 2,886 individual photometric detections for 68 individual SNe IIP from -15 to $+114$ days from peak magnitude.
- Consistent with theoretical expectations, our SN IIP sample spans a diverse range of light curve parameters: a factor of ~ 20 in plateau phase decay rate (Figure 7.11), ~ 2 orders of magnitude in ejected ^{56}Ni (Figure 7.18), a factor of ~ 2 in plateau duration (Figure 7.12), and $\gtrsim 4$ mag in absolute magnitude (Figure 7.14). This evidence stands in contrast to recent suggestions by Arcavi et al. (2012) and Poznanski (2013) that the SN IIP plateau duration distribution, a critical observational parameter tied to

progenitor initial mass, is tightly distributed (Section 7.4.3).

- Addressing a longstanding debate in the literature, we have searched for the existence of a fast declining “SN IIL” sub-population in the decline rate distribution of our SN IIP sample (Section 7.4.2). We find no evidence for a discontinuity in this distribution for any photometric band, questioning the existence of a discrete SN IIL sub-population.
- We identify a highly significant statistical correlation between the peak magnitude and plateau phase decline rate of SNe IIP (Section 7.4.6). Together with the previous results, this supports the interpretation of core-collapse among hydrogen-rich red supergiants as a predominantly single parameter family of explosions, whose observational behavior is determined primarily by the explosion energy and likely set by the initial mass of the progenitor star. This represents an independent discovery and confirmation of results recently reported in Anderson et al. (2014).
- Through the largest systematic comparison to date of SN IIP lightcurves to hydrodynamic progenitor models, we have derived mass, radius, and explosion energy estimates for the objects in our sample (Section 7.5.4). However, we find that the available theoretical model grids are insufficient to cover the full range of observed variation in SN IIP light curve properties. We point to the need for additional hydrodynamic modeling to produce updated and expanded self-consistent model grids, particularly in the low luminosity regime.
- Though our progenitor inferences are based on hydrodynamic light curve

models, which are known to produce systematically higher masses than direct progenitor detection searches, we do not find evidence for an absence of high-mass SN IIP progenitors (Section 7.5.5). We point to future direct progenitor detections of luminous SNe IIP as having the potential to ease the discrepancy between the maximum SN IIP progenitor mass identified by various theoretical and observational methods, known as the Red Supergiant Problem.

In a companion paper, we discuss and demonstrate a hierarchical expansion of the model presented here to provide a general framework for the analysis of supernova light curve populations in the coming era of next generation wide field transient searches. We advocate continued investment in statistical and computational tools in the future as a means to compensate for the relative decline anticipated in the availability of detailed spectroscopic and other follow-up information on individual transients.

7.7 Appendix A: Individual Light Curve Stan Model

Below we reproduce the full Bayesian model for our 5-component segmented SN II light curve model described in Section 7.3.2, in the *Stan* modeling language. The Stan model specification format is documented in the Stan Modeling Language Users Guide and Reference Manual (Stan Development Team 2014).

The model takes the following data as input: `N_obs`, the total number of

photometric data points; `N_filt`, the number of photometric filters; `t`, a vector of MJD dates of the photometric observations; `fL`, a vector of luminosities corresponding to the photometric observations (with units as described in Section 7.3.1); `dfL` a corresponding vector of luminosity uncertainties; `z` the redshift; `t0_mean` an initial estimate of the explosion date (for initialization and for centering the explosion date prior distribution); `J` a vector of integers specifying the filter ID of each photometric observation; `Kcor_N`, a matrix of pre-computed K -corrections for each filter, in magnitudes with spacing of 1 day; `fluxscale` the zero-point of the luminosity unit system (`fluxscale = 107` in the system we have employed); and `duringseason`, a boolean value specifying whether the object exploded within or between observing seasons, for selection of the explosion date prior distribution parameters. The calculation of the model light curve flux and application of the K -correction values is performed in the `transformed parameters` section, and the prior and likelihood calculations are performed in the `model` section. Certain vector-valued prior distribution parameters are specified in the `transformed data` section for convenience.

The *Stan* model is then compiled and run (Stan Development Team 2014) to yield MCMC samples from the posterior distribution of light curve parameters. We have used PyStan version 2.2.0⁶.

We configured the *No-U-Turn Sampler* to use fixed 0 initialization of the parameter values, an adaptation phase of 250 steps, a maximum treedepth of 22, and otherwise employed the default sampler parameters. Using this configuration,

⁶<https://github.com/stan-dev/stan/releases/tag/v2.2.0>

we achieve a Gelman-Rubin between-to-within chain variance ratio of $\hat{R} < 1.02$ for 95% of parameters, indicating excellent convergence. The typical run time is 1 minute per chain.

```
data {
  int<lower=0> N_obs;
  int<lower=0> N_filt;
  vector[N_obs] t;
  vector[N_obs] fL;
  vector[N_obs] dfL;
  real z;
  real t0_mean;
  int<lower=1,upper=N_filt> J[N_obs];
  int<lower=0> Kcor_N;
  real Kcor[N_filt,Kcor_N];
  real<lower=0> fluxscale;
  real<lower=0,upper=1> duringseason;
}

transformed data {
  vector[N_filt] prior_tp;
  vector[N_filt] prior_sig_tp;
  vector[N_filt] prior_lbeta1;
  vector[N_filt] prior_sig_lbeta1;
  vector[N_filt] prior_lbeta2;
  vector[N_filt] prior_sig_lbeta2;
  prior_tp[1] <- log(5);
  prior_tp[2] <- log(8);
  prior_tp[3] <- log(14);
  prior_tp[4] <- log(20);
  prior_tp[5] <- log(30);
  prior_sig_tp[1] <- 0.3;
  prior_sig_tp[2] <- 0.3;
  prior_sig_tp[3] <- 0.3;
  prior_sig_tp[4] <- 0.3;
  prior_sig_tp[5] <- 0.3;
  prior_lbeta1[1] <- -2.1;
  prior_lbeta1[2] <- -2.3;
  prior_lbeta1[3] <- -3.3;
  prior_lbeta1[4] <- -3.8;
  prior_lbeta1[5] <- -4.0;
  prior_sig_lbeta1[1] <- 0.6;
  prior_sig_lbeta1[2] <- 0.8;
  prior_sig_lbeta1[3] <- 1.2;
  prior_sig_lbeta1[4] <- 1.5;
  prior_sig_lbeta1[5] <- 2;
  prior_lbeta2[1] <- -3.4;
  prior_lbeta2[2] <- -4;
```

```
prior_lbeta2[3] <- -4.1;
prior_lbeta2[4] <- -4.4;
prior_lbeta2[5] <- -4.9;
prior_sig_lbeta2[1] <- 1;
prior_sig_lbeta2[2] <- 1.2;
prior_sig_lbeta2[3] <- 1.2;
prior_sig_lbeta2[4] <- 1.5;
prior_sig_lbeta2[5] <- 1.5;
}
parameters {
  real pt0;
  vector<lower=0>[N_filt] t1;
  vector<lower=0>[N_filt] t2;
  vector<lower=0>[N_filt] td;
  vector<lower=0>[N_filt] tp;
  vector<upper=0>[N_filt] lalpha;
  vector<upper=0>[N_filt] lbeta1;
  vector<upper=0>[N_filt] lbeta2;
  vector<upper=0>[N_filt] lbetadN;
  vector<upper=0>[N_filt] lbetadC;
  vector<lower=0>[N_filt] Mp;
  vector[N_filt] Yb;
  vector<lower=0>[N_filt] V;
}
transformed parameters {
  vector[N_obs] mm;
  vector[N_obs] dm;
  vector<lower=0>[N_filt] M1;
  vector<lower=0>[N_filt] M2;
  vector<lower=0>[N_filt] Md;
  M1 <- Mp ./ exp( exp(lbeta1) .* tp );
  M2 <- Mp .* exp( -exp(lbeta2) .* t2 );
  Md <- M2 .* exp( -exp(lbetadN) .* td );
  for (n in 1:N_obs) {
    real N_SNc;
    int Kc_up;
    int Kc_down;
    real t_exp;
    int j;
    int k;
    real mm_1;
    real mm_2;
    real mm_3;
    real mm_4;
    real mm_5;
    real mm_6;
    j <- J[n];
    t_exp <- ( t[n] - (t0_mean + pt0) ) / (1 + z);
    if (t_exp < 0) {
```



```

        mm_1 <- Yb[j];
    } else {
        mm_1 <- 0;
    }
    if ((t_exp>=0) && (t_exp < t1[j])) {
        mm_2 <- Yb[j] + M1[j] * pow(t_exp / t1[j] , exp(lalpha[j]));
    } else {
        mm_2 <- 0;
    }
    if ((t_exp >= t1[j]) && (t_exp < t1[j] + tp[j])) {
        mm_3 <- Yb[j] + M1[j] * exp(exp(lbeta1[j]) * (t_exp - t1[j]));
    } else {
        mm_3 <- 0;
    }
    if ((t_exp >= t1[j] + tp[j]) && (t_exp < t1[j] + tp[j] + t2[j])) {
        mm_4 <- Yb[j] + Mp[j] * exp(-exp(lbeta2[j]) * (t_exp - t1[j] - tp[j]));
    } else {
        mm_4 <- 0;
    }
    if ((t_exp >= t1[j] + tp[j] + t2[j]) && (t_exp < t1[j] + tp[j] + t2[j] + td[j])) {
        mm_5 <- Yb[j] + M2[j] * exp(-exp(lbetadN[j]) * (t_exp - t1[j] - tp[j] - t2[j]));
    } else {
        mm_5 <- 0;
    }
    if (t_exp >= t1[j] + tp[j] + t2[j] + td[j]) {
        mm_6 <- Yb[j] + Md[j] * exp(-exp(lbetadC[j]) * (t_exp - t1[j] - tp[j] - t2[j] - td[j]));
    } else {
        mm_6 <- 0;
    }
    dm[n] <- sqrt(pow(dfL[n],2) + pow(V[j],2));
    if (t_exp<0) {
        N_SNC <- 0;
    } else if (t_exp<Kcor_N-2){
        Kc_down <- 0;
        while ((Kc_down+1) < t_exp) {
            Kc_down <- Kc_down + 1;
        }
        Kc_up <- Kc_down+1;
        N_SNC <- Kcor[j,Kc_down+1] + (t_exp - floor(t_exp)) * (Kcor[j,Kc_up+1]-Kcor[j,Kc_down+1]);
    } else {
        N_SNC <- Kcor[j,Kcor_N];
    }
    mm[n] <- (mm_1+mm_2+mm_3+mm_4+mm_5+mm_6)
        / (pow(10, N_SNC/(-2.5)));
}
}
model {
    if (duringseason == 1) {
        pt0 ~ skew_normal(-1, 1, -0.5);
    }
}

```

```
} else {
  pt0 ~ skew_normal(-30, 20, -1);
}
t1 ~ lognormal(log(1), 0.3);
tp ~ lognormal(prior_tp, prior_sig_tp);
t2 ~ lognormal(log(100), 0.3);
td ~ lognormal(log(10), 0.5);
lalpha ~ normal(-1, 0.3);
lbeta1 ~ normal(prior_lbeta1, prior_sig_lbeta1);
lbeta2 ~ normal(prior_lbeta2, prior_sig_lbeta2);
lbetadN ~ normal(-3, 0.5);
lbetadC ~ normal(-5, 1);
Mp ~ lognormal(log(1), 0.7);
Yb ~ normal(0, 0.3);
V ~ cauchy(0, 0.01);
fL ~ normal(mm, dm);
}
```

Table 7.1. SN IIP Absolute Magnitude Distribution Statistics

F	N	Observed			Extinction Corrected			
		16th	50th	84th	N	16th	50th	84th
<i>g</i>	40	-16.85	-17.96	-18.44	12	-17.82	-18.61	-19.61
<i>r</i>	50	-16.94	-17.79	-18.47	25	-17.50	-18.25	-19.40
<i>i</i>	51	-17.08	-17.79	-18.33	27	-17.33	-18.02	-18.98
<i>z</i>	43	-17.18	-17.86	-18.42	34	-17.61	-18.09	-19.23

Note. — The [16, 50, 84]th columns correspond to percentile values within the SN IIP absolute, K -corrected peak magnitude distribution, without (“observed”) and with extinction correction (Section 7.4.4). Only PS1 SNe IIP with low posterior uncertainty in their peak magnitudes are included ($\delta M < 0.1$ mag at 1σ without extinction correction, $\delta M < 0.2$ mag with); the total number of objects in each distribution (N) is given. Each row corresponds to a PS1 photometric filter (F).

Table 7.2. Pan-STARRS1 Type IIP SN Sample

PS1 SN	Field	RA	DEC	Disc. MJD	z	N_g	N_r	N_i	N_z	N_y
PS1-10a	02	03:29:48.735	-29:04:29.91	55207	0.071	2	2	5	4	0
PS1-10b	03	08:37:02.587	+43:44:16.85	55207	0.260	4	4	5	0	0
PS1-10q	06	12:19:37.533	+46:01:56.03	55212	0.057	15	17	16	13	0
PS1-10t	04	09:55:30.959	+01:29:01.18	55214	0.093	11	11	11	11	0
PS1-10ae	04	10:02:09.742	+01:14:00.93	55242	0.086	4	5	8	6	0
PS1-10jr	07	14:07:33.470	+52:38:17.87	55362	0.333	2	4	3	0	0
PS1-10lv	09	22:13:00.969	+00:46:24.49	55389	0.127	10	21	22	23	0
PS1-10mb	08	16:11:44.435	+56:05:08.39	55389	0.064	2	12	13	10	0
PS1-10zu	01	02:18:54.489	-04:14:42.96	55407	0.059	11	18	21	24	0
PS1-10abd	01	02:20:04.175	-03:30:46.10	55414	0.132	5	15	18	16	0
PS1-10agh	01	02:21:04.532	-03:06:14.81	55428	0.141	8	12	14	18	0
PS1-10awc	02	03:30:12.902	-28:38:22.19	55467	0.123	8	11	12	15	0
PS1-10biu	09	22:14:20.250	-00:19:00.10	55499	0.184	2	3	5	2	0
PS1-10blk	01	02:22:51.457	-03:24:18.58	55510	0.074	7	6	9	5	0
PS1-11u	05	10:41:11.486	+58:14:11.61	55566	0.040	7	8	7	5	0
PS1-11z	04	10:03:16.250	+03:23:54.14	55566	0.105	8	9	11	7	0
PS1-11ai	04	09:56:42.562	+00:55:47.69	55567	0.092	3	6	7	5	0
PS1-11ak	02	03:33:29.222	-28:45:26.54	55568	0.120	0	1	2	1	0
PS1-11bl	05	10:49:31.565	+56:43:05.92	55572	0.150	4	10	15	8	0
PS1-11bo	04	09:56:45.045	+00:58:08.29	55576	0.093	8	12	10	10	0
PS1-11fl	07	14:05:19.148	+53:07:24.25	55597	0.096	5	9	14	8	0
PS1-11jg	06	12:21:42.116	+47:23:00.01	55597	0.082	0	1	12	1	0
PS1-11kf	08	16:09:05.620	+54:07:19.71	55602	0.210	1	3	4	2	0
PS1-11li	06	12:16:14.114	+46:20:45.99	55605	0.068	4	11	0	9	0
PS1-11lj	06	12:16:56.601	+46:18:56.29	55605	0.070	12	14	16	14	0
PS1-11lr	03	08:37:58.889	+43:48:22.28	55615	0.055	4	4	7	5	0
PS1-11lq	04	09:57:11.372	+02:32:40.35	55615	0.101	8	9	7	5	0
PS1-11md	03	08:41:11.752	+43:22:51.45	55633	0.145	4	4	6	4	0
PS1-11pf	07	14:18:29.828	+53:43:31.79	55636	0.148	4	9	19	7	0
PS1-11qe	07	14:19:13.704	+54:09:15.03	55648	0.191	7	9	18	8	0

Table 7.2—Continued

PS1 SN	Field	RA	DEC	Disc. MJD	z	N_g	N_r	N_i	N_z	N_y
PS1–11si	05	10:43:40.661	+58:02:38.18	55666	0.133	0	2	5	2	0
PS1–11sm	07	14:20:18.612	+53:59:28.70	55666	0.209	4	4	9	2	0
PS1–11ua	08	16:12:00.684	+54:41:31.66	55675	0.236	2	3	7	1	0
PS1–11uv	05	10:48:48.970	+57:47:35.99	55675	0.073	6	5	7	7	0
PS1–11vn	07	14:19:17.217	+53:45:07.20	55675	0.168	3	5	12	2	0
PS1–11wj	04	10:00:49.340	+02:52:46.68	55675	0.077	3	3	3	2	0
PS1–11yh	07	14:11:11.466	+51:59:12.63	55705	0.146	4	8	13	8	0
PS1–11amh	09	22:11:47.815	+01:09:00.95	55795	0.077	11	9	4	6	5
PS1–11amv	08	16:12:40.632	+56:11:18.38	55803	0.052	1	1	3	2	3
PS1–11anm	10	23:29:26.246	−01:51:18.09	55775	0.061	3	20	29	20	5
PS1–11aof	10	23:25:59.575	−00:30:55.16	55792	0.095	30	36	37	29	14
PS1–11apd	10	23:28:56.422	−01:05:18.45	55800	0.043	25	26	23	30	13
PS1–11asz	02	03:34:46.879	−29:12:32.51	55831	0.103	11	13	22	21	6
PS1–11awd	02	03:34:37.528	−27:04:31.47	55852	0.068	9	3	14	11	13
PS1–11azd	10	23:31:47.673	−01:25:51.41	55883	0.059	5	9	0	11	3
PS1–11azi	02	03:37:45.601	−28:14:25.71	55883	0.180	4	4	9	11	7
PS1–11azt	01	02:27:34.018	−03:50:34.07	55883	0.175	4	4	9	8	0
PS1–11azv	03	08:39:58.993	+45:11:36.90	55883	0.145	7	12	18	24	6
PS1–11bbg	03	08:49:51.815	+44:41:17.26	55893	0.132	4	15	17	24	8
PS1–12c	05	10:36:06.755	+57:47:01.85	55911	0.040	6	13	23	30	4
PS1–12d	05	10:39:55.485	+58:49:27.53	55911	0.123	11	16	18	30	9
PS1–12y	04	09:58:01.639	+00:43:14.16	55941	0.093	8	8	14	10	6
PS1–12bt	04	10:05:16.844	+01:40:39.57	55948	0.042	8	11	15	13	5
PS1–12rk	06	12:25:55.129	+47:36:06.38	56000	0.079	11	10	23	25	6
PS1–12wn	04	09:59:11.437	+01:08:38.27	56013	0.107	4	6	12	15	2
PS1–12zd	04	09:56:48.772	+01:01:45.56	56029	0.104	5	5	13	7	2
PS1–12zp	06	12:14:45.637	+48:19:13.49	56029	0.101	8	6	9	9	2
PS1–12auw	08	16:15:35.435	+56:11:26.92	56091	0.096	3	3	6	4	7
PS1–12bku	09	22:16:40.194	−01:08:24.35	56166	0.096	7	11	15	11	8
PS1–12bmp	02	03:29:28.318	−28:42:15.61	56207	0.070	10	12	18	23	21

Table 7.2—Continued

PS1 SN	Field	RA	DEC	Disc. MJD	z	N_g	N_r	N_i	N_z	N_y
PS1–12blz	01	02:21:10.849	−05:27:22.91	56210	0.086	9	12	16	24	13
PS1–12boi	09	22:22:40.280	−00:07:21.02	56210	0.145	4	6	8	6	1
PS1–12bza	03	08:36:23.991	+43:38:26.14	56235	0.109	9	13	26	26	19
PS1–12cey	01	02:21:27.462	−03:18:56.45	56240	0.140	3	5	9	13	4
PS1–13hp	04	10:04:16.974	+02:35:50.61	56326	0.149	11	12	19	20	5
PS1–13vs	04	09:57:24.212	+03:34:46.75	56353	0.079	6	7	17	17	6
PS1–13wr	07	14:15:57.954	+52:03:10.57	56385	0.077	10	16	27	29	27
PS1–13alz	04	09:57:52.631	+01:52:21.07	56399	0.098	1	1	7	5	5
PS1–13arp	06	12:18:25.108	+46:37:01.30	56408	0.167	6	9	14	12	0
PS1–13ave	07	14:08:52.904	+53:15:25.98	56417	0.185	13	12	21	24	16
PS1–13atm	04	09:59:16.605	+03:18:28.43	56417	0.240	1	1	5	5	1
PS1–13bvb	09	22:18:54.478	+01:41:32.70	56478	0.113	8	11	14	20	9
PS1–13cqb	10	23:23:35.356	−00:20:33.23	56513	0.097	4	9	16	26	6
PS1–13cua	01	02:24:04.137	−04:21:25.21	56564	0.095	13	16	17	20	7
PS1–13eck	04	09:54:25.733	+02:19:30.73	56624	0.121	3	4	8	11	9
PS1–13esn	04	09:57:23.048	+02:31:09.22	56659	0.130	3	2	7	3	0

Note. — This table includes only SNe classified as SNe IIP by the criteria of Section 7.3.4. PS1 SN is the PS1 designation of the transient; field is the PS1 Medium Deep Field where the transient was discovered, RA and DEC are in J2000 coordinates, Disc. MJD is the date of discovery, z is the redshift obtained from our follow-up spectroscopy (Section 7.2.2), and N_x is the number of detections of the object included in our dataset in each PS1 filter (additional photometric non-detections are also used to constrain the explosion date and decay behavior).

Table 7.3. Pan-STARRS1 Type IIP SN Light Curve Parameters

SN	t_0	$\log \alpha$	$\log \beta_1$	$\log \beta_2$	$\log \beta_{dN}$	$\log \beta_{dC}$	t_1	t_p	t_2	t_d	M_p	V
<i>g</i> -band												
PS1-10a	55200.9 ^{+0.7} _{-0.8}	-1.0 ^{+0.3} _{-0.3}	-2.4 ^{+0.5} _{-0.5}	-3.1 ^{+0.4} _{-0.3}	-3.0 ^{+0.5} _{-0.5}	-4.9 ^{+1.2} _{-1.2}	1.0 ^{+0.4} _{-0.3}	5 ⁺¹ ₋₁	108 ⁺³⁴ ₋₂₈	11 ⁺⁷ ₋₄	2.12 ^{+0.49} _{-0.26}	0.005 ^{+0.005} _{-0.004}
PS1-10b	55203.9 ^{+0.4} _{-0.5}	-1.0 ^{+0.3} _{-0.3}	-2.8 ^{+0.3} _{-0.4}	-2.7 ^{+0.2} _{-0.2}	-3.0 ^{+0.4} _{-0.5}	-5.0 ^{+0.9} _{-1.0}	1.1 ^{+0.4} _{-0.3}	7 ⁺¹ ₋₁	99 ⁺³⁶ ₋₂₆	10 ⁺⁶ ₋₄	1.94 ^{+0.10} _{-0.11}	0.008 ^{+0.018} _{-0.006}
PS1-10q	55200.5 ^{+0.7} _{-0.8}	-1.0 ^{+0.3} _{-0.3}	-2.4 ^{+0.5} _{-0.6}	-3.1 ^{+0.0} _{-0.0}	-2.9 ^{+0.6} _{-0.5}	-4.9 ^{+1.1} _{-1.1}	1.0 ^{+0.3} _{-0.3}	4 ⁺¹ ₋₁	109 ⁺³⁰ ₋₂₅	11 ⁺⁷ ₋₅	0.77 ^{+0.03} _{-0.04}	0.016 ^{+0.004} _{-0.003}
PS1-10t	55205.2 ^{+0.9} _{-0.9}	-1.0 ^{+0.3} _{-0.3}	-2.2 ^{+0.6} _{-0.6}	-3.5 ^{+0.1} _{-0.1}	-3.0 ^{+0.4} _{-0.5}	-5.1 ^{+1.0} _{-0.9}	1.0 ^{+0.3} _{-0.2}	4 ⁺¹ ₋₁	98 ⁺³³ ₋₂₂	10 ⁺⁶ ₋₄	0.38 ^{+0.02} _{-0.02}	0.012 ^{+0.006} _{-0.006}
PS1-10ae	55239.3 ^{+0.1} _{-0.1}	-1.1 ^{+0.2} _{-0.3}	-2.6 ^{+0.5} _{-0.5}	-3.3 ^{+0.1} _{-0.1}	-3.0 ^{+0.6} _{-0.5}	-5.6 ^{+0.7} _{-0.8}	0.9 ^{+0.2} _{-0.2}	3 ⁺¹ ₋₀	75 ⁺²⁷ ₋₂₀	9 ⁺⁶ ₋₃	0.84 ^{+0.02} _{-0.02}	0.005 ^{+0.006} _{-0.004}
PS1-10jr	55359.1 ^{+0.4} _{-0.5}	-1.0 ^{+0.3} _{-0.3}	-2.9 ^{+0.5} _{-0.4}	-2.1 ^{+0.3} _{-0.3}	-3.0 ^{+0.5} _{-0.5}	-5.0 ^{+1.0} _{-1.0}	1.0 ^{+0.3} _{-0.3}	4 ⁺² ₋₁	99 ⁺³³ ₋₂₅	10 ⁺⁶ ₋₄	4.16 ^{+0.39} _{-0.27}	0.010 ^{+0.030} _{-0.008}
PS1-10lv	55380.5 ^{+2.0} _{-4.3}	-1.0 ^{+0.3} _{-0.3}	-2.1 ^{+0.6} _{-0.6}	-3.1 ^{+0.1} _{-0.0}	-3.1 ^{+0.5} _{-0.5}	-4.8 ^{+0.8} _{-1.0}	1.0 ^{+0.4} _{-0.3}	5 ⁺² ₋₁	102 ⁺³⁶ ₋₂₇	10 ⁺⁷ ₋₄	1.91 ^{+0.23} _{-0.12}	0.008 ^{+0.012} _{-0.006}
PS1-10mb	55374.3 ^{+0.9} _{-0.9}	-1.0 ^{+0.3} _{-0.3}	-2.4 ^{+0.5} _{-0.6}	-3.7 ^{+0.2} _{-0.2}	-3.0 ^{+0.5} _{-0.5}	-5.0 ^{+1.1} _{-1.1}	1.0 ^{+0.3} _{-0.2}	4 ⁺¹ ₋₁	101 ⁺³³ ₋₂₄	10 ⁺⁶ ₋₄	0.11 ^{+0.02} _{-0.01}	0.008 ^{+0.005} _{-0.005}
PS1-10zu	55354.3 ^{+25.5} _{-5.5}	-1.0 ^{+0.3} _{-0.3}	-2.1 ^{+0.6} _{-0.6}	-3.7 ^{+0.1} _{-0.1}	-2.8 ^{+0.5} _{-0.6}	-4.5 ^{+1.1} _{-1.0}	1.0 ^{+0.3} _{-0.3}	5 ⁺² ₋₁	120 ⁺³⁰ ₋₂₄	11 ⁺⁷ ₋₅	0.75 ^{+0.23} _{-0.27}	0.017 ^{+0.005} _{-0.004}
PS1-10abd	55387.6 ^{+3.8} _{-4.0}	-1.0 ^{+0.3} _{-0.3}	-2.1 ^{+0.6} _{-0.6}	-2.8 ^{+0.1} _{-0.1}	-3.0 ^{+0.5} _{-0.5}	-5.1 ^{+1.0} _{-0.9}	1.0 ^{+0.3} _{-0.3}	5 ⁺² ₋₁	93 ⁺³⁵ ₋₂₈	10 ⁺⁷ ₋₄	4.33 ^{+1.28} _{-0.88}	0.033 ^{+0.024} _{-0.026}
PS1-10agh	55434.0 ^{+0.4} _{-0.5}	-1.0 ^{+0.3} _{-0.3}	-2.1 ^{+0.6} _{-0.6}	-2.9 ^{+0.0} _{-0.0}	-3.0 ^{+0.5} _{-0.5}	-5.0 ^{+0.9} _{-0.9}	1.0 ^{+0.3} _{-0.3}	5 ⁺² ₋₁	100 ⁺²⁷ ₋₂₆	10 ⁺⁶ ₋₄	3.01 ^{+0.30} _{-0.32}	0.015 ^{+0.017} _{-0.011}
PS1-10awc	55454.2 ^{+0.2} _{-0.3}	-1.0 ^{+0.3} _{-0.3}	-2.5 ^{+0.2} _{-0.3}	-3.1 ^{+0.1} _{-0.1}	-3.1 ^{+0.4} _{-0.5}	-5.0 ^{+1.0} _{-0.9}	1.0 ^{+0.3} _{-0.2}	6 ⁺¹ ₋₁	93 ⁺⁴⁰ ₋₃₀	10 ⁺⁶ ₋₄	1.62 ^{+0.09} _{-0.08}	0.007 ^{+0.009} _{-0.005}
PS1-10biu	55495.0 ^{+0.6} _{-0.7}	-1.0 ^{+0.3} _{-0.3}	-2.3 ^{+0.6} _{-0.6}	-2.8 ^{+0.2} _{-0.2}	-3.0 ^{+0.5} _{-0.5}	-4.9 ^{+0.9} _{-1.0}	0.9 ^{+0.3} _{-0.2}	3 ⁺¹ ₋₁	102 ⁺³² ₋₂₈	10 ⁺⁷ ₋₃	2.38 ^{+0.15} _{-0.14}	0.008 ^{+0.016} _{-0.006}
PS1-10blk	55508.3 ^{+0.1} _{-0.2}	-1.0 ^{+0.3} _{-0.3}	-2.5 ^{+0.4} _{-0.3}	-3.4 ^{+0.1} _{-0.1}	-3.0 ^{+0.5} _{-0.5}	-5.1 ^{+1.0} _{-0.9}	1.0 ^{+0.3} _{-0.2}	4 ⁺¹ ₋₁	97 ⁺³⁹ ₋₃₃	10 ⁺⁶ ₋₄	2.00 ^{+0.13} _{-0.11}	0.010 ^{+0.011} _{-0.007}
PS1-11u	55497.2 ^{+21.0} _{-13.0}	-1.0 ^{+0.3} _{-0.3}	-2.1 ^{+0.6} _{-0.6}	-3.6 ^{+0.2} _{-0.3}	-2.7 ^{+0.5} _{-0.5}	-2.8 ^{+0.4} _{-1.7}	1.0 ^{+0.4} _{-0.2}	5 ⁺² ₋₁	82 ⁺¹⁴ ₋₁₈	14 ⁺¹¹ ₋₆	0.56 ^{+0.33} _{-0.20}	0.001 ^{+0.001} _{-0.000}
PS1-11z	55539.2 ^{+7.6} _{-15.0}	-1.0 ^{+0.3} _{-0.3}	-2.1 ^{+0.6} _{-0.6}	-3.1 ^{+0.1} _{-0.1}	-3.0 ^{+0.5} _{-0.5}	-4.8 ^{+1.0} _{-1.0}	1.0 ^{+0.4} _{-0.3}	5 ⁺² ₋₁	108 ⁺³¹ ₋₂₃	10 ⁺⁶ ₋₄	2.86 ^{+1.87} _{-0.75}	0.046 ^{+0.017} _{-0.016}
PS1-11ai	55496.2 ^{+13.3} _{-10.9}	-1.0 ^{+0.3} _{-0.3}	-2.1 ^{+0.6} _{-0.6}	-3.6 ^{+0.3} _{-0.3}	-3.0 ^{+0.5} _{-0.5}	-4.7 ^{+0.9} _{-1.0}	1.0 ^{+0.3} _{-0.3}	5 ⁺² ₋₁	111 ⁺²⁹ ₋₂₉	10 ⁺⁶ ₋₄	1.11 ^{+0.69} _{-0.45}	0.008 ^{+0.009} _{-0.006}
PS1-11ak	55592.8 ^{+0.9} _{-0.9}	-1.0 ^{+0.3} _{-0.3}	-2.1 ^{+0.6} _{-0.6}	-3.4 ^{+1.0} _{-0.9}	-3.0 ^{+0.5} _{-0.5}	-5.0 ^{+1.0} _{-1.1}	1.0 ^{+0.4} _{-0.3}	5 ⁺² ₋₁	98 ⁺³⁷ ₋₂₅	10 ⁺⁷ ₋₄	0.96 ^{+1.04} _{-0.48}	0.010 ^{+0.025} _{-0.007}
PS1-11bl	55568.0 ^{+0.7} _{-0.7}	-1.0 ^{+0.3} _{-0.3}	-2.3 ^{+0.5} _{-0.5}	-3.2 ^{+0.1} _{-0.1}	-3.0 ^{+0.5} _{-0.5}	-5.0 ^{+1.1} _{-1.0}	0.9 ^{+0.3} _{-0.2}	4 ⁺¹ ₋₁	102 ⁺³³ ₋₂₉	10 ⁺⁶ ₋₄	1.77 ^{+0.14} _{-0.14}	0.006 ^{+0.009} _{-0.004}
PS1-11bo	55574.2 ^{+0.8} _{-1.1}	-1.0 ^{+0.3} _{-0.3}	-2.1 ^{+0.6} _{-0.6}	-3.9 ^{+0.1} _{-0.1}	-3.0 ^{+0.5} _{-0.5}	-5.0 ^{+1.0} _{-0.9}	1.0 ^{+0.3} _{-0.2}	5 ⁺² ₋₁	107 ⁺³⁴ ₋₂₁	10 ⁺⁶ ₋₄	0.54 ^{+0.04} _{-0.04}	0.005 ^{+0.004} _{-0.003}
PS1-11fl	55568.9 ^{+4.7} _{-21.4}	-1.0 ^{+0.3} _{-0.3}	-2.1 ^{+0.6} _{-0.6}	-3.4 ^{+0.1} _{-0.1}	-2.9 ^{+0.5} _{-0.5}	-4.7 ^{+1.1} _{-1.1}	1.0 ^{+0.4} _{-0.3}	5 ⁺² ₋₁	113 ⁺³² ₋₂₈	11 ⁺⁸ ₋₄	1.33 ^{+0.88} _{-0.86}	0.045 ^{+0.017} _{-0.013}
PS1-11jg	55497.8 ^{+10.6} _{-10.0}	-1.0 ^{+0.3} _{-0.3}	-2.1 ^{+0.6} _{-0.6}	-3.4 ^{+1.0} _{-0.9}	-3.0 ^{+0.5} _{-0.5}	-5.0 ^{+1.0} _{-1.0}	1.0 ^{+0.3} _{-0.3}	5 ⁺² ₋₁	99 ⁺³² ₋₂₄	10 ⁺⁶ ₋₄	1.02 ^{+0.96} _{-0.52}	0.010 ^{+0.028} _{-0.007}
PS1-11kf	55580.9 ^{+6.3} _{-8.3}	-1.0 ^{+0.3} _{-0.3}	-2.1 ^{+0.6} _{-0.6}	-3.0 ^{+0.2} _{-0.2}	-2.9 ^{+0.5} _{-0.5}	-4.8 ^{+1.2} _{-1.1}	1.0 ^{+0.4} _{-0.3}	5 ⁺² ₋₁	113 ⁺³² ₋₂₆	11 ⁺⁶ ₋₄	4.88 ^{+1.49} _{-0.97}	0.009 ^{+0.020} _{-0.007}
PS1-11li	55600.6 ^{+0.7} _{-0.8}	-1.0 ^{+0.3} _{-0.3}	-2.2 ^{+0.5} _{-0.5}	-3.5 ^{+0.1} _{-0.1}	-3.0 ^{+0.5} _{-0.5}	-5.0 ^{+1.0} _{-1.0}	1.0 ^{+0.4} _{-0.2}	4 ⁺¹ ₋₁	100 ⁺³⁷ ₋₁₇	10 ⁺⁶ ₋₄	0.27 ^{+0.04} _{-0.03}	0.006 ^{+0.003} _{-0.003}
PS1-11lj	55603.4 ^{+0.7} _{-0.6}	-1.0 ^{+0.3} _{-0.3}	-2.7 ^{+0.5} _{-0.4}	-3.9 ^{+0.1} _{-0.1}	-2.5 ^{+0.3} _{-0.4}	-4.5 ^{+1.8} _{-1.2}	0.9 ^{+0.3} _{-0.2}	4 ⁺¹ ₋₁	81 ⁺³ ₋₅	17 ⁺⁹ ₋₇	0.52 ^{+0.03} _{-0.03}	0.004 ^{+0.004} _{-0.003}
PS1-11lr	55611.5 ^{+0.5} _{-0.5}	-1.0 ^{+0.3} _{-0.3}	-2.1 ^{+0.6} _{-0.6}	-4.0 ^{+0.1} _{-0.1}	-3.0 ^{+0.5} _{-0.5}	-5.0 ^{+0.9} _{-0.8}	1.0 ^{+0.4} _{-0.3}	5 ⁺² ₋₁	99 ⁺³⁵ ₋₂₆	10 ⁺⁷ ₋₄	0.46 ^{+0.03} _{-0.03}	0.003 ^{+0.003} _{-0.002}
PS1-11lq	55612.4 ^{+0.7} _{-0.7}	-1.0 ^{+0.3} _{-0.3}	-2.6 ^{+0.4} _{-0.5}	-2.9 ^{+0.1} _{-0.1}	-3.0 ^{+0.5} _{-0.5}	-4.9 ^{+0.9} _{-1.1}	0.9 ^{+0.3} _{-0.2}	4 ⁺¹ ₋₁	98 ⁺³² ₋₂₄	10 ⁺⁶ ₋₄	1.32 ^{+0.08} _{-0.09}	0.010 ^{+0.007} _{-0.007}
PS1-11md	55616.3 ^{+4.7} _{-5.6}	-1.0 ^{+0.3} _{-0.3}	-2.1 ^{+0.6} _{-0.7}	-3.1 ^{+0.1} _{-0.1}	-3.0 ^{+0.5} _{-0.5}	-5.1 ^{+1.0} _{-1.0}	1.0 ^{+0.4} _{-0.2}	5 ⁺² ₋₁	100 ⁺³⁶ ₋₂₆	10 ⁺⁷ ₋₄	2.84 ^{+0.62} _{-0.37}	0.006 ^{+0.010} _{-0.004}
PS1-11pf	55633.2 ^{+0.2} _{-0.3}	-1.0 ^{+0.3} _{-0.3}	-2.1 ^{+0.5} _{-0.6}	-2.8 ^{+0.1} _{-0.1}	-3.0 ^{+0.5} _{-0.5}	-4.9 ^{+1.0} _{-1.0}	1.0 ^{+0.3} _{-0.3}	5 ⁺² ₋₁	102 ⁺³¹ ₋₂₆	10 ⁺⁶ ₋₄	2.28 ^{+0.35} _{-0.34}	0.007 ^{+0.011} _{-0.005}
PS1-11qe	55644.3 ^{+0.5} _{-1.2}	-1.0 ^{+0.3} _{-0.3}	-2.2 ^{+0.6} _{-0.6}	-3.2 ^{+0.1} _{-0.1}	-2.3 ^{+0.3} _{-0.4}	-4.5 ^{+1.1} _{-1.1}	0.9 ^{+0.3} _{-0.3}	4 ⁺¹ ₋₁	46 ⁺²⁸ ₋₄	16 ⁺⁷ ₋₆	5.39 ^{+0.26} _{-0.22}	0.009 ^{+0.022} _{-0.007}
PS1-11si	55671.0 ^{+0.6} _{-0.7}	-1.0 ^{+0.3} _{-0.3}	-2.1 ^{+0.6} _{-0.6}	-3.4 ^{+0.9} _{-1.0}	-3.0 ^{+0.5} _{-0.5}	-5.0 ^{+0.9} _{-1.0}	1.0 ^{+0.4} _{-0.3}	5 ⁺² ₋₁	101 ⁺³⁷ ₋₂₆	10 ⁺⁶ ₋₄	1.03 ^{+0.96} _{-0.49}	0.009 ^{+0.025} _{-0.007}
PS1-11sm	55659.4 ^{+0.6} _{-0.9}	-1.0 ^{+0.3} _{-0.3}	-2.7 ^{+0.5} _{-0.5}	-2.6 ^{+0.2} _{-0.1}	-3.0 ^{+0.5} _{-0.5}	-5.0 ^{+1.1} _{-0.9}	1.0 ^{+0.3} _{-0.2}	4 ⁺¹ ₋₁	100 ⁺³³ ₋₂₃	10 ⁺⁷ ₋₄	2.24 ^{+0.15} _{-0.15}	0.018 ^{+0.043} _{-0.014}
PS1-11ua	55644.6 ^{+8.1} _{-9.9}	-1.0 ^{+0.3} _{-0.3}	-2.1 ^{+0.6} _{-0.5}	-2.9 ^{+0.1} _{-0.1}	-3.0 ^{+0.5} _{-0.4}	-5.0 ^{+0.9} _{-1.0}	1.0 ^{+0.4} _{-0.3}	6 ⁺² ₋₁	104 ⁺³³ ₋₂₅	10 ⁺⁷ ₋₄	5.35 ^{+2.51} _{-1.43}	0.008 ^{+0.020} _{-0.006}
PS1-11uv	55670.8 ^{+0.6} _{-1.4}	-1.0 ^{+0.3} _{-0.3}	-2.5 ^{+0.6} _{-0.5}	-3.5 ^{+0.1} _{-0.1}	-3.0 ^{+0.5} _{-0.5}	-5.0 ^{+1.0} _{-0.9}	0.9 ^{+0.3} _{-0.2}	3 ⁺¹ ₋₁	101 ⁺²⁶ ₋₂₃	10 ⁺⁶ ₋₄	0.42 ^{+0.01} _{-0.01}	0.002 ^{+0.003} _{-0.002}
PS1-11vn	55673.1 ^{+0.4} _{-0.5}	-1.0 ^{+0.3} _{-0.3}	-3.1 ^{+0.4} _{-0.4}	-2.8 ^{+0.2} _{-0.1}	-3.0 ^{+0.5} _{-0.5}	-5.0 ^{+1.0} _{-1.1}	0.9 ^{+0.2} _{-0.2}	4 ⁺¹ ₋₂	100 ⁺³⁵ ₋₂₇	10 ⁺⁷ ₋₅	1.58 ^{+0.16} _{-0.10}	0.041 ^{+0.024} _{-0.027}
PS1-11wj	55669.5 ^{+0.6} _{-0.9}	-1.0 ^{+0.3} _{-0.3}	-2.2 ^{+0.6} _{-0.6}	-3.3 ^{+0.7} _{-0.9}	-3.0 ^{+0.6} _{-0.5}	-5.0 ^{+1.0} _{-1.0}	1.0 ^{+0.3} _{-0.2}	4 ⁺¹ ₋₁	101 ⁺³⁵ ₋₂₅	10 ⁺⁶ ₋₄	0.78 ^{+0.11} _{-0.10}	0.110 ^{+0.037} _{-0.033}
PS1-11yh	55688.7 ^{+4.8} _{-3.5}	-1.0 ^{+0.3} _{-0.3}	-2.1 ^{+0.6} _{-0.5}	-3.1 ^{+0.1} _{-0.1}	-3.0 ^{+0.5} _{-0.5}	-5.0 ^{+0.8} _{-1.1}	1.0 ^{+0.3} _{-0.2}	5 ⁺² ₋₁	100 ⁺³⁵ ₋₂₄	10 ⁺⁶ ₋₄	2.20 ^{+0.41} _{-0.33}	0.009 ^{+0.018} _{-0.006}
PS1-11amh	55790.1 ^{+0.7} _{-1.2}	-1.0 ^{+0.3} _{-0.3}	-2.2 ^{+0.7} _{-0.7}	-3.5 ^{+0.0} _{-0.0}	-3.5 ^{+0.4} _{-0.5}	-5.4 ^{+0.7} _{-0.7}	0.8 ^{+0.3} _{-0.2}	3 ⁺¹ ₋₁	35 ⁺⁴ ₋₂	6 ⁺³ ₋₂	2.15 ^{+0.06} _{-0.06}	0.050 ^{+0.009} _{-0.007}
PS1-11amv	55802.1 ^{+0.1} _{-0.9}	-1.0 ^{+0.3} _{-0.3}	-1.7 ^{+0.5} _{-0.6}	-3.4 ^{+1.0} _{-1.0}	-3.0 ^{+0.5} _{-0.5}	-5.0 ^{+1.0} _{-1.0}	1.0 ^{+0.4} _{-0.3}	6 ⁺² ₋₂	101 ⁺³⁴ ₋₂₆	10 ⁺⁷ ₋₄	0.46 ^{+0.36} _{-0.17}	0.003 ^{+0.001} _{-0.001}
PS1-11anm	55763.5 ^{+0.8} _{-0.9}	-1.0 ^{+0.3} _{-0.3}	-2.0 ^{+0.9} _{-0.6}	-1.8 ^{+0.9} _{-1.6}	-3.0 ^{+0.4} _{-0.5}	-5.0 ^{+0.9} _{-0.9}	1.0 ^{+0.3} _{-0.2}	4 ⁺¹ ₋₁	99			

Table 7.3—Continued

SN	t_0	$\log \alpha$	$\log \beta_1$	$\log \beta_2$	$\log \beta_{dN}$	$\log \beta_{dC}$	t_1	t_p	t_2	t_d	M_p	V
PS1-11aof	55777.1 ^{+0.4} _{-0.3}	-1.0 ^{+0.3} _{-0.3}	-2.7 ^{+0.5} _{-0.4}	-2.6 ^{+0.1} _{-0.1}	-3.0 ^{+0.5} _{-0.5}	-4.9 ^{+1.0} _{-1.1}	0.9 ^{+0.3} _{-0.2}	3 ⁺¹ ₋₁	99 ⁺³⁵ ₋₂₇	10 ⁺⁶ ₋₄	3.46 ^{+0.19} _{-0.16}	0.146 ^{+0.014} _{-0.012}
PS1-11apd	55789.4 ^{+0.9} _{-0.8}	-1.0 ^{+0.3} _{-0.3}	-2.2 ^{+0.7} _{-0.6}	-3.6 ^{+0.0} _{-0.0}	-3.0 ^{+0.5} _{-0.5}	-4.6 ^{+0.9} _{-0.8}	0.9 ^{+0.3} _{-0.2}	4 ⁺¹ ₋₁	111 ⁺³⁷ ₋₂₄	10 ⁺⁷ ₋₄	1.16 ^{+0.03} _{-0.03}	0.033 ^{+0.004} _{-0.003}
PS1-11asz	55823.1 ^{+1.4} _{-0.3}	-1.0 ^{+0.3} _{-0.3}	-1.1 ^{+0.5} _{-0.9}	-3.1 ^{+0.2} _{-0.2}	-3.0 ^{+0.5} _{-0.6}	-5.0 ^{+1.0} _{-1.0}	1.0 ^{+0.4} _{-0.3}	4 ⁺¹ ₋₁	102 ⁺³⁴ ₋₂₇	10 ⁺⁷ ₋₄	0.89 ^{+0.10} _{-0.09}	0.072 ^{+0.019} _{-0.014}
PS1-11awd	55849.3 ^{+0.4} _{-1.1}	-1.0 ^{+0.3} _{-0.3}	-2.7 ^{+0.6} _{-0.6}	-4.0 ^{+0.1} _{-0.1}	-2.9 ^{+0.5} _{-0.5}	-4.7 ^{+0.7} _{-0.6}	0.9 ^{+0.3} _{-0.2}	3 ⁺¹ ₋₁	106 ⁺³⁴ ₋₁₈	11 ⁺⁸ ₋₄	0.64 ^{+0.02} _{-0.02}	0.013 ^{+0.004} _{-0.004}
PS1-11azd	55880.3 ^{+0.0} _{-0.1}	-1.0 ^{+0.3} _{-0.3}	-2.6 ^{+0.3} _{-0.4}	-4.3 ^{+0.3} _{-0.4}	-2.9 ^{+0.5} _{-0.5}	-3.9 ^{+0.5} _{-0.5}	0.9 ^{+0.3} _{-0.2}	4 ⁺¹ ₋₁	100 ⁺³⁸ ₋₂₅	10 ⁺⁸ ₋₄	0.72 ^{+0.02} _{-0.02}	0.014 ^{+0.003} _{-0.002}
PS1-11azi	55877.4 ^{+0.5} _{-0.5}	-1.0 ^{+0.3} _{-0.3}	-2.1 ^{+0.6} _{-0.6}	-2.8 ^{+0.2} _{-0.2}	-3.0 ^{+0.5} _{-0.5}	-5.2 ^{+1.0} _{-1.0}	1.0 ^{+0.3} _{-0.3}	6 ⁺² ₋₂	94 ⁺³⁵ ₋₂₆	9 ⁺⁶ ₋₃	4.15 ^{+0.55} _{-0.50}	0.192 ^{+0.036} _{-0.028}
PS1-11azt	55878.8 ^{+0.3} _{-0.4}	-1.0 ^{+0.3} _{-0.3}	-2.1 ^{+0.5} _{-0.6}	-3.4 ^{+0.2} _{-0.2}	-3.0 ^{+0.5} _{-0.5}	-5.2 ^{+1.0} _{-0.9}	1.0 ^{+0.3} _{-0.2}	5 ⁺¹ ₋₁	96 ⁺³⁰ ₋₂₃	10 ⁺⁶ ₋₄	1.48 ^{+0.10} _{-0.08}	0.012 ^{+0.025} _{-0.009}
PS1-11azv	55876.7 ^{+0.8} _{-1.2}	-1.0 ^{+0.3} _{-0.3}	-2.0 ^{+0.7} _{-0.7}	-3.9 ^{+0.1} _{-0.1}	-3.0 ^{+0.5} _{-0.5}	-5.1 ^{+1.0} _{-0.8}	1.0 ^{+0.3} _{-0.3}	5 ⁺² ₋₁	105 ⁺³⁴ ₋₃₂	10 ⁺⁶ ₋₄	0.49 ^{+0.04} _{-0.05}	0.007 ^{+0.008} _{-0.005}
PS1-11bbg	55888.2 ^{+8.4} _{-0.8}	-1.0 ^{+0.3} _{-0.3}	-2.1 ^{+0.5} _{-0.7}	-3.1 ^{+0.2} _{-0.1}	-3.0 ^{+0.5} _{-0.5}	-4.8 ^{+0.8} _{-1.0}	1.0 ^{+0.4} _{-0.2}	4 ⁺¹ ₋₁	102 ⁺³⁵ ₋₂₉	10 ⁺⁷ ₋₄	1.71 ^{+0.14} _{-0.13}	0.082 ^{+0.012} _{-0.011}
PS1-12c	55848.4 ^{+8.4} _{-9.3}	-1.0 ^{+0.3} _{-0.3}	-2.1 ^{+0.5} _{-0.7}	-4.0 ^{+0.2} _{-0.3}	-2.3 ^{+0.2} _{-0.2}	-4.7 ^{+0.7} _{-0.6}	1.0 ^{+0.3} _{-0.3}	5 ⁺² ₋₁	89 ⁺⁹ ₋₉	17 ⁺⁶ ₋₅	0.29 ^{+0.12} _{-0.09}	0.006 ^{+0.002} _{-0.001}
PS1-12d	55899.5 ^{+13.6} _{-2.0}	-1.0 ^{+0.3} _{-0.3}	-2.1 ^{+0.5} _{-0.6}	-3.3 ^{+0.0} _{-0.0}	-3.1 ^{+0.5} _{-0.4}	-4.8 ^{+0.9} _{-1.0}	1.0 ^{+0.4} _{-0.3}	5 ⁺² ₋₁	110 ⁺³² ₋₂₂	10 ⁺⁶ ₋₄	1.49 ^{+0.15} _{-0.12}	0.023 ^{+0.007} _{-0.007}
PS1-12y	55911.8 ^{+19.7} _{-19.7}	-1.0 ^{+0.3} _{-0.3}	-2.1 ^{+0.7} _{-0.6}	-3.6 ^{+0.1} _{-0.1}	-1.8 ^{+0.3} _{-0.3}	-5.1 ^{+1.3} _{-1.1}	1.0 ^{+0.4} _{-0.2}	5 ⁺² ₋₁	67 ⁺²⁵ ₋₅	16 ⁺⁸ ₋₅	2.01 ^{+1.31} _{-0.34}	0.019 ^{+0.010} _{-0.010}
PS1-12bt	55827.7 ^{+14.1} _{-13.1}	-1.0 ^{+0.3} _{-0.3}	-2.1 ^{+0.6} _{-0.6}	-3.2 ^{+0.3} _{-0.3}	-2.9 ^{+0.5} _{-0.6}	-5.0 ^{+0.3} _{-0.2}	1.0 ^{+0.3} _{-0.2}	5 ⁺² ₋₁	77 ⁺¹⁶ ₋₁₅	10 ⁺⁶ ₋₄	0.81 ^{+0.82} _{-0.41}	0.001 ^{+0.001} _{-0.001}
PS1-12rk	55996.2 ^{+0.5} _{-0.6}	-1.0 ^{+0.3} _{-0.3}	-2.4 ^{+0.7} _{-0.6}	-4.0 ^{+0.1} _{-0.1}	-3.0 ^{+0.5} _{-0.5}	-5.0 ^{+1.0} _{-0.7}	0.9 ^{+0.3} _{-0.2}	3 ⁺¹ ₋₁	102 ⁺³⁴ ₋₂₆	10 ⁺⁶ ₋₄	0.26 ^{+0.02} _{-0.02}	0.015 ^{+0.003} _{-0.004}
PS1-12wn	55999.3 ^{+0.6} _{-0.4}	-1.0 ^{+0.3} _{-0.3}	-1.9 ^{+0.5} _{-0.5}	-3.3 ^{+0.2} _{-0.2}	-3.0 ^{+0.5} _{-0.5}	-4.8 ^{+0.9} _{-1.0}	1.0 ^{+0.4} _{-0.3}	6 ⁺¹ ₋₁	102 ⁺³⁵ ₋₂₆	10 ⁺⁶ ₋₄	0.23 ^{+0.03} _{-0.03}	0.010 ^{+0.008} _{-0.007}
PS1-12zd	56016.1 ^{+0.1} _{-0.5}	-1.0 ^{+0.3} _{-0.3}	-2.1 ^{+0.6} _{-0.6}	-3.2 ^{+0.1} _{-0.1}	-3.0 ^{+0.5} _{-0.5}	-4.7 ^{+0.9} _{-0.9}	1.0 ^{+0.4} _{-0.3}	5 ⁺² ₋₁	109 ⁺³⁸ ₋₂₈	10 ⁺⁶ ₋₄	1.69 ^{+0.12} _{-0.13}	0.014 ^{+0.006} _{-0.006}
PS1-12zp	56019.4 ^{+0.0} _{-0.1}	-1.0 ^{+0.3} _{-0.3}	-2.1 ^{+0.6} _{-0.6}	-3.2 ^{+0.1} _{-0.1}	-3.0 ^{+0.5} _{-0.4}	-5.0 ^{+1.0} _{-0.9}	1.0 ^{+0.4} _{-0.3}	6 ⁺³ ₋₂	102 ⁺²⁹ ₋₂₉	10 ⁺⁶ ₋₄	1.10 ^{+0.11} _{-0.11}	0.008 ^{+0.009} _{-0.006}
PS1-12auw	56080.7 ^{+0.4} _{-0.5}	-1.0 ^{+0.3} _{-0.3}	-2.1 ^{+0.6} _{-0.6}	-3.0 ^{+0.2} _{-0.2}	-3.0 ^{+0.5} _{-0.5}	-4.9 ^{+0.9} _{-0.9}	1.0 ^{+0.3} _{-0.2}	5 ⁺¹ ₋₁	105 ⁺³⁴ ₋₂₄	10 ⁺⁷ ₋₄	1.64 ^{+0.11} _{-0.07}	0.004 ^{+0.004} _{-0.003}
PS1-12bku	56160.7 ^{+0.2} _{-0.1}	-0.9 ^{+0.3} _{-0.3}	-0.6 ^{+0.3} _{-0.4}	-3.5 ^{+0.0} _{-0.0}	-3.0 ^{+0.5} _{-0.4}	-5.3 ^{+0.5} _{-0.7}	1.0 ^{+0.3} _{-0.2}	5 ⁺¹ ₋₁	104 ⁺²¹ ₋₂₁	10 ⁺⁶ ₋₄	2.46 ^{+0.11} _{-0.11}	0.005 ^{+0.006} _{-0.004}
PS1-12bmp	56201.1 ^{+0.3} _{-0.4}	-1.0 ^{+0.3} _{-0.3}	-2.1 ^{+0.6} _{-0.6}	-4.3 ^{+0.1} _{-0.1}	-2.8 ^{+0.4} _{-0.4}	-4.3 ^{+0.8} _{-0.5}	0.9 ^{+0.3} _{-0.2}	4 ⁺¹ ₋₁	79 ⁺⁹ ₋₁₁	12 ⁺⁷ ₋₄	0.64 ^{+0.01} _{-0.01}	0.012 ^{+0.004} _{-0.005}
PS1-12blz	56201.6 ^{+0.8} _{-1.1}	-1.0 ^{+0.3} _{-0.3}	-2.4 ^{+0.6} _{-0.6}	-3.0 ^{+0.0} _{-0.0}	-2.9 ^{+0.5} _{-0.6}	-4.9 ^{+0.9} _{-0.9}	1.0 ^{+0.3} _{-0.3}	4 ⁺¹ ₋₁	108 ⁺³² ₋₂₆	10 ⁺⁷ ₋₄	2.97 ^{+0.05} _{-0.05}	0.012 ^{+0.005} _{-0.005}
PS1-12boi	56201.7 ^{+0.7} _{-0.9}	-1.0 ^{+0.3} _{-0.3}	-2.3 ^{+0.6} _{-0.7}	-4.0 ^{+0.3} _{-0.3}	-2.9 ^{+0.4} _{-0.5}	-4.2 ^{+0.7} _{-1.0}	0.9 ^{+0.3} _{-0.2}	3 ⁺¹ ₋₁	106 ⁺³⁹ ₋₂₇	11 ⁺⁸ ₋₅	2.01 ^{+0.08} _{-0.08}	0.007 ^{+0.011} _{-0.005}
PS1-12bza	56228.6 ^{+0.6} _{-0.7}	-1.0 ^{+0.3} _{-0.3}	-2.1 ^{+0.6} _{-0.6}	-3.3 ^{+0.0} _{-0.0}	-2.9 ^{+0.4} _{-0.5}	-4.8 ^{+0.7} _{-0.8}	1.0 ^{+0.3} _{-0.2}	5 ⁺¹ ₋₁	91 ⁺³⁰ ₋₁₄	10 ⁺⁶ ₋₄	1.28 ^{+0.08} _{-0.07}	0.014 ^{+0.006} _{-0.009}
PS1-12cey	56237.2 ^{+0.2} _{-0.7}	-1.0 ^{+0.2} _{-0.3}	-2.6 ^{+0.6} _{-0.6}	-2.6 ^{+0.1} _{-0.1}	-3.1 ^{+0.5} _{-0.7}	-5.1 ^{+1.0} _{-0.7}	0.9 ^{+0.3} _{-0.2}	5 ⁺¹ ₋₁	97 ⁺³⁴ ₋₁₉	10 ⁺⁶ ₋₃	3.48 ^{+0.75} _{-0.66}	0.005 ^{+0.008} _{-0.004}
PS1-13hp	56323.4 ^{+0.4} _{-0.5}	-1.0 ^{+0.3} _{-0.3}	-3.0 ^{+0.3} _{-0.4}	-3.2 ^{+0.0} _{-0.0}	-3.0 ^{+0.4} _{-0.5}	-5.1 ^{+1.0} _{-0.8}	1.0 ^{+0.3} _{-0.3}	5 ⁺¹ ₋₁	101 ⁺³⁰ ₋₂₃	10 ⁺⁷ ₋₄	2.34 ^{+0.06} _{-0.07}	0.015 ^{+0.018} _{-0.011}
PS1-13vs	56342.7 ^{+0.7} _{-0.8}	-1.0 ^{+0.3} _{-0.3}	-2.1 ^{+0.6} _{-0.6}	-3.6 ^{+0.1} _{-0.1}	-2.9 ^{+0.5} _{-0.5}	-4.7 ^{+0.8} _{-0.9}	1.0 ^{+0.3} _{-0.2}	5 ⁺³ ₋₂	105 ⁺²⁵ ₋₂₃	10 ⁺⁸ ₋₄	1.00 ^{+0.06} _{-0.07}	0.007 ^{+0.008} _{-0.005}
PS1-13wr	56300.4 ^{+2.3} _{-2.4}	-1.0 ^{+0.3} _{-0.3}	-2.1 ^{+0.6} _{-0.6}	-4.2 ^{+0.2} _{-0.2}	-2.8 ^{+0.4} _{-0.4}	-4.8 ^{+0.9} _{-1.2}	1.0 ^{+0.4} _{-0.3}	5 ⁺² ₋₁	126 ⁺⁹ ₋₈	14 ⁺⁸ ₋₆	0.48 ^{+0.14} _{-0.12}	0.007 ^{+0.004} _{-0.004}
PS1-13alz	56397.2 ^{+0.1} _{-0.8}	-1.0 ^{+0.3} _{-0.3}	-2.1 ^{+0.6} _{-0.6}	-3.2 ^{+0.5} _{-0.6}	-3.0 ^{+0.5} _{-0.5}	-4.6 ^{+1.0} _{-1.2}	1.0 ^{+0.4} _{-0.3}	5 ⁺² ₋₁	104 ⁺³⁴ ₋₂₇	10 ⁺⁶ ₋₄	2.01 ^{+0.59} _{-0.38}	0.005 ^{+0.006} _{-0.004}
PS1-13arp	56396.6 ^{+0.5} _{-0.5}	-1.0 ^{+0.3} _{-0.3}	-2.8 ^{+0.5} _{-0.5}	-3.0 ^{+0.1} _{-0.1}	-3.0 ^{+0.5} _{-0.5}	-5.0 ^{+0.9} _{-1.0}	0.9 ^{+0.3} _{-0.2}	4 ⁺¹ ₋₁	98 ⁺³⁷ ₋₂₄	10 ⁺⁶ ₋₄	1.20 ^{+0.12} _{-0.11}	0.010 ^{+0.015} _{-0.007}
PS1-13ave	56404.4 ^{+0.1} _{-0.2}	-1.0 ^{+0.3} _{-0.3}	-2.2 ^{+0.6} _{-0.6}	-3.6 ^{+0.1} _{-0.0}	-3.2 ^{+0.6} _{-0.6}	-5.0 ^{+1.0} _{-1.0}	1.0 ^{+0.4} _{-0.2}	5 ⁺² ₋₁	94 ⁺³⁵ ₋₃₇	9 ⁺³ ₋₃	4.03 ^{+0.21} _{-0.20}	0.072 ^{+0.020} _{-0.033}
PS1-13atm	56352.8 ^{+0.9} _{-0.9}	-1.0 ^{+0.3} _{-0.3}	-1.7 ^{+0.6} _{-0.6}	-4.8 ^{+0.7} _{-0.8}	-3.0 ^{+0.5} _{-0.5}	-5.0 ^{+1.1} _{-1.0}	1.0 ^{+0.4} _{-0.3}	6 ⁺² ₋₂	100 ⁺³³ ₋₂₄	10 ⁺⁶ ₋₄	0.43 ^{+0.13} _{-0.12}	0.155 ^{+0.059} _{-0.073}
PS1-13bvb	56451.6 ^{+0.5} _{-0.7}	-1.0 ^{+0.3} _{-0.3}	-2.1 ^{+0.6} _{-0.6}	-3.3 ^{+0.1} _{-0.1}	-3.0 ^{+0.5} _{-0.5}	-4.9 ^{+1.1} _{-1.1}	1.0 ^{+0.3} _{-0.3}	5 ⁺² ₋₁	104 ⁺³⁹ ₋₂₇	10 ⁺⁶ ₋₄	1.49 ^{+0.19} _{-0.16}	0.022 ^{+0.023} _{-0.017}
PS1-13cqb	56503.7 ^{+1.0} _{-1.0}	-1.0 ^{+0.3} _{-0.3}	-2.3 ^{+0.5} _{-0.5}	-3.5 ^{+0.3} _{-0.3}	-3.0 ^{+0.5} _{-0.5}	-5.0 ^{+0.9} _{-0.9}	1.0 ^{+0.3} _{-0.2}	5 ⁺¹ ₋₁	102 ⁺³⁴ ₋₂₆	10 ⁺⁷ ₋₄	0.22 ^{+0.03} _{-0.03}	0.005 ^{+0.006} _{-0.004}
PS1-13cua	56544.8 ^{+0.2} _{-0.2}	-1.1 ^{+0.3} _{-0.3}	-2.6 ^{+0.4} _{-0.4}	-4.0 ^{+0.1} _{-0.1}	-3.1 ^{+0.5} _{-0.5}	-5.0 ^{+0.9} _{-1.0}	0.9 ^{+0.3} _{-0.2}	4 ⁺¹ ₋₁	110 ⁺³² ₋₂₄	10 ⁺⁶ ₋₄	0.58 ^{+0.04} _{-0.03}	0.004 ^{+0.004} _{-0.003}
PS1-13eck	56613.7 ^{+0.3} _{-0.4}	-1.0 ^{+0.3} _{-0.3}	-2.1 ^{+0.5} _{-0.6}	-3.2 ^{+0.2} _{-0.3}	-3.0 ^{+0.5} _{-0.5}	-5.0 ^{+1.0} _{-1.0}	1.0 ^{+0.3} _{-0.3}	5 ⁺² ₋₁	99 ⁺³³ ₋₂₇	10 ⁺⁶ ₋₄	0.39 ^{+0.07} _{-0.06}	0.010 ^{+0.016} _{-0.007}
PS1-13esn	56637.0 ^{+0.9} _{-1.0}	-1.0 ^{+0.3} _{-0.3}	-2.1 ^{+0.5} _{-0.6}	-2.9 ^{+0.2} _{-0.2}	-3.0 ^{+0.5} _{-0.5}	-5.1 ^{+1.0} _{-0.9}	1.0 ^{+0.3} _{-0.3}	5 ⁺² ₋₁	101 ⁺³⁵ ₋₂₈	10 ⁺⁶ ₋₄	1.38 ^{+0.27} _{-0.23}	0.013 ^{+0.016} _{-0.010}
r-band												
PS1-10a	55200.9 ^{+0.7} _{-0.8}	-1.0 ^{+0.3} _{-0.3}	-2.8 ^{+0.5} _{-0.6}	-3.6 ^{+0.7} _{-0.7}	-2.9 ^{+0.5} _{-0.5}	-4.4 ^{+0.9} _{-1.3}	1.0 ^{+0.4} _{-0.3}	8 ⁺² ₋₂	104 ⁺³⁷ ₋₂₈	11 ⁺⁷ ₋₄	1.72 ^{+0.35} _{-0.24}	0.005 ^{+0.005} _{-0.003}
PS1-10b	55203.9 ^{+0.4} _{-0.5}	-1.0 ^{+0.3} _{-0.3}	-2.8 ^{+0.4} _{-0.4}	-3.2 ^{+0.1} _{-0.1}	-3.0 ^{+0.5} _{-0.4}	-5.1 ^{+1.0} _{-0.9}	1.0 ^{+0.3} _{-0.2}	7 ⁺¹ ₋₁	101 ⁺³⁶ ₋₂₅	10 ⁺⁶ ₋₄	2.46 ^{+0.16} _{-0.14}	0.008 ^{+0.016} _{-0.006}
PS1-10q	55200.5 ^{+0.7} _{-0.8}	-1.0 ^{+0.3} _{-0.3}	-3.4 ^{+0.6} _{-0.6}	-4.1 ^{+0.1} _{-0.1}	-2.3 ^{+0.4} _{-0.4}	-5.3 ^{+1.2} _{-1.1}	1.0 ^{+0.3} _{-0.2}	6 ⁺² ₋₁	89 ⁺⁶ ₋₃	15 ⁺⁷ ₋₅	0.67 ^{+0.03} _{-0.02}	0.022 ^{+0.006} _{-0.005}
PS1-10t	55205.2 ^{+0.9} _{-0.9}	-1.0 ^{+0.3} _{-0.3}	-2.5 ^{+0.8} _{-0.8}	-4.9 ^{+0.3} _{-0.3}	-2.7 ^{+0.4} _{-0.5}	-4.4 ^{+1.0} _{-0.8}	1.0 ^{+0.3} ₋					

Table 7.3—Continued

SN	t_0	$\log \alpha$	$\log \beta_1$	$\log \beta_2$	$\log \beta_{dN}$	$\log \beta_{dC}$	t_1	t_p	t_2	t_d	M_p	V
PS1-10ae	55239.3 ^{+0.1} _{-0.1}	-1.0 ^{+0.2} _{-0.2}	-3.8 ^{+0.7} _{-0.6}	-4.0 ^{+0.1} _{-0.1}	-3.0 ^{+0.5} _{-0.5}	-4.7 ^{+1.0} _{-1.3}	0.9 ^{+0.3} _{-0.2}	5 ⁺³ ₋₁	104 ⁺²⁷ ₋₂₆	10 ⁺⁶ ₋₄	0.73 ^{+0.03} _{-0.03}	0.006 ^{+0.005} _{-0.004}
PS1-10jr	55359.1 ^{+0.4} _{-0.5}	-0.9 ^{+0.3} _{-0.3}	-2.8 ^{+0.5} _{-0.6}	-2.6 ^{+0.2} _{-0.2}	-3.0 ^{+0.5} _{-0.5}	-5.0 ^{+1.0} _{-0.9}	1.0 ^{+0.3} _{-0.2}	6 ⁺² ₋₁	100 ⁺³⁶ ₋₂₇	10 ⁺⁶ ₋₄	5.63 ^{+0.67} _{-0.55}	0.009 ^{+0.024} _{-0.007}
PS1-10lv	55380.5 ^{+2.0} _{-4.3}	-1.0 ^{+0.3} _{-0.3}	-2.5 ^{+0.7} _{-0.7}	-4.1 ^{+0.0} _{-0.0}	-2.9 ^{+0.5} _{-0.5}	-4.0 ^{+0.8} _{-0.8}	1.0 ^{+0.3} _{-0.3}	10 ⁺³ ₋₂	97 ⁺¹⁷ ₋₈	12 ⁺⁹ ₋₅	2.36 ^{+0.08} _{-0.08}	0.037 ^{+0.015} _{-0.014}
PS1-10mb	55374.3 ^{+0.9} _{-0.9}	-1.0 ^{+0.3} _{-0.3}	-2.7 ^{+0.6} _{-0.6}	-5.3 ^{+0.5} _{-0.6}	-2.9 ^{+0.5} _{-0.5}	-4.4 ^{+0.9} _{-1.0}	1.0 ^{+0.3} _{-0.3}	7 ⁺³ ₋₂	101 ⁺³⁰ ₋₂₅	11 ⁺⁷ ₋₄	0.15 ^{+0.03} _{-0.02}	0.025 ^{+0.010} _{-0.007}
PS1-10zu	55354.3 ^{+25.5} _{-5.5}	-1.0 ^{+0.3} _{-0.3}	-2.3 ^{+0.8} _{-0.7}	-5.1 ^{+0.2} _{-0.2}	-2.7 ^{+0.3} _{-0.6}	-3.9 ^{+1.0} _{-0.9}	1.0 ^{+0.4} _{-0.3}	8 ⁺³ ₋₂	101 ⁺⁸ ₋₂₅	17 ⁺⁸ ₋₇	0.53 ^{+0.06} _{-0.07}	0.019 ^{+0.005} _{-0.004}
PS1-10abd	55387.6 ^{+3.8} _{-4.0}	-1.0 ^{+0.3} _{-0.3}	-2.3 ^{+0.8} _{-0.8}	-3.9 ^{+0.1} _{-0.1}	-2.9 ^{+0.4} _{-0.4}	-4.3 ^{+0.6} _{-1.0}	1.0 ^{+0.3} _{-0.2}	8 ⁺³ ₋₂	87 ⁺⁴¹ ₋₁₂	11 ⁺⁶ ₋₄	2.61 ^{+0.28} _{-0.24}	0.049 ^{+0.020} _{-0.018}
PS1-10agh	55434.0 ^{+0.4} _{-0.5}	-1.0 ^{+0.3} _{-0.4}	-2.3 ^{+0.8} _{-0.8}	-3.8 ^{+0.0} _{-0.0}	-2.4 ^{+0.4} _{-0.5}	-4.4 ^{+1.3} _{-1.3}	1.0 ^{+0.3} _{-0.3}	8 ⁺² ₋₂	95 ⁺¹⁶ ₋₁₆	14 ⁺⁸ ₋₅	2.68 ^{+0.11} _{-0.12}	0.018 ^{+0.020} _{-0.013}
PS1-10awc	55454.2 ^{+0.2} _{-0.3}	-1.0 ^{+0.3} _{-0.3}	-2.5 ^{+0.3} _{-0.3}	-4.2 ^{+0.1} _{-0.1}	-2.3 ^{+0.6} _{-0.6}	-4.4 ^{+1.8} _{-1.4}	1.0 ^{+0.3} _{-0.3}	8 ⁺² ₋₁	89 ⁺¹⁰ ₋₈	16 ⁺⁹ ₋₇	1.48 ^{+0.06} _{-0.06}	0.012 ^{+0.016} _{-0.009}
PS1-10biu	55495.0 ^{+0.6} _{-0.7}	-1.0 ^{+0.3} _{-0.3}	-3.2 ^{+0.7} _{-0.6}	-3.5 ^{+0.2} _{-0.2}	-3.0 ^{+0.5} _{-0.5}	-4.8 ^{+0.8} _{-1.0}	1.0 ^{+0.3} _{-0.2}	6 ⁺³ ₋₂	102 ⁺³⁸ ₋₂₆	10 ⁺⁶ ₋₄	2.75 ^{+0.23} _{-0.18}	0.008 ^{+0.012} _{-0.006}
PS1-10blk	55508.3 ^{+0.1} _{-0.2}	-1.0 ^{+0.3} _{-0.3}	-3.9 ^{+0.5} _{-0.5}	-4.6 ^{+0.1} _{-0.1}	-2.9 ^{+0.3} _{-0.3}	-5.0 ^{+1.1} _{-1.0}	0.9 ^{+0.2} _{-0.2}	6 ⁺² ₋₁	70 ⁺³ ₋₃	11 ⁺⁶ ₋₄	1.22 ^{+0.08} _{-0.06}	0.027 ^{+0.012} _{-0.008}
PS1-11u	55497.2 ^{+21.0} _{-13.0}	-1.0 ^{+0.3} _{-0.3}	-2.3 ^{+0.8} _{-0.8}	-4.1 ^{+0.1} _{-0.1}	-3.2 ^{+0.1} _{-0.1}	-1.8 ^{+0.4} _{-0.3}	1.0 ^{+0.3} _{-0.3}	8 ⁺³ ₋₂	73 ⁺¹⁴ ₋₁₉	20 ⁺³ ₋₂	0.67 ^{+0.21} _{-0.17}	0.001 ^{+0.001} _{-0.000}
PS1-11z	55539.2 ^{+7.6} _{-15.0}	-1.0 ^{+0.3} _{-0.3}	-0.9 ^{+0.6} _{-1.4}	-4.5 ^{+0.1} _{-0.1}	-2.6 ^{+0.3} _{-0.3}	-4.2 ^{+1.5} _{-1.4}	1.0 ^{+0.4} _{-0.3}	13 ⁺¹² ₋₅	83 ⁺⁴ ₋₄	19 ⁺⁹ ₋₈	1.03 ^{+0.07} _{-0.06}	0.005 ^{+0.008} _{-0.004}
PS1-11ai	55496.2 ^{+13.3} _{-10.9}	-1.0 ^{+0.3} _{-0.3}	-2.3 ^{+0.8} _{-0.8}	-4.6 ^{+0.4} _{-0.5}	-2.5 ^{+0.5} _{-0.6}	-3.9 ^{+1.0} _{-1.4}	1.0 ^{+0.3} _{-0.2}	8 ⁺³ ₋₂	95 ⁺¹⁴ ₋₁₄	14 ⁺⁹ ₋₆	0.80 ^{+0.30} _{-0.20}	0.050 ^{+0.015} _{-0.011}
PS1-11ak	55592.8 ^{+0.9} _{-0.9}	-1.0 ^{+0.3} _{-0.3}	-2.2 ^{+0.6} _{-0.7}	-4.0 ^{+1.2} _{-1.2}	-3.0 ^{+0.5} _{-0.5}	-5.0 ^{+0.9} _{-0.9}	1.0 ^{+0.4} _{-0.3}	8 ⁺³ ₋₂	99 ⁺³¹ ₋₂₅	10 ⁺⁶ ₋₄	0.72 ^{+0.50} _{-0.24}	0.030 ^{+0.044} _{-0.025}
PS1-11bl	55568.0 ^{+0.7} _{-0.7}	-1.0 ^{+0.3} _{-0.3}	-3.0 ^{+0.6} _{-0.6}	-4.3 ^{+0.1} _{-0.1}	-2.8 ^{+0.5} _{-0.5}	-4.1 ^{+1.0} _{-1.3}	1.0 ^{+0.3} _{-0.3}	7 ⁺² ₋₁	87 ⁺¹⁷ ₋₇	12 ⁺⁹ ₋₅	1.51 ^{+0.10} _{-0.11}	0.010 ^{+0.018} _{-0.007}
PS1-11bo	55574.2 ^{+0.8} _{-1.1}	-1.0 ^{+0.3} _{-0.3}	-2.3 ^{+0.8} _{-0.7}	-5.4 ^{+0.2} _{-0.5}	-3.1 ^{+0.5} _{-0.5}	-5.2 ^{+1.0} _{-0.9}	1.0 ^{+0.4} _{-0.2}	8 ⁺³ ₋₂	101 ⁺³⁸ ₋₃₉	9 ⁺⁷ ₋₃	0.43 ^{+0.03} _{-0.04}	0.020 ^{+0.014} _{-0.013}
PS1-11fl	55568.9 ^{+4.7} _{-21.4}	-1.0 ^{+0.3} _{-0.3}	-2.3 ^{+0.8} _{-0.8}	-4.5 ^{+0.1} _{-0.1}	-2.6 ^{+0.5} _{-0.8}	-3.0 ^{+0.5} _{-2.1}	1.0 ^{+0.3} _{-0.3}	8 ⁺³ ₋₂	97 ⁺¹⁷ ₋₁₅	15 ⁺¹¹ ₋₇	1.00 ^{+0.16} _{-0.09}	0.005 ^{+0.006} _{-0.003}
PS1-11jg	55497.8 ^{+10.6} _{-10.0}	-1.0 ^{+0.3} _{-0.3}	-2.3 ^{+0.9} _{-0.8}	-3.7 ^{+0.3} _{-0.4}	-3.1 ^{+0.5} _{-0.5}	-5.4 ^{+0.5} _{-0.7}	1.0 ^{+0.4} _{-0.3}	8 ⁺³ ₋₂	86 ⁺¹⁸ ₋₁₇	9 ⁺⁶ ₋₄	0.70 ^{+0.70} _{-0.37}	0.005 ^{+0.004} _{-0.003}
PS1-11kf	55580.9 ^{+6.3} _{-8.3}	-1.0 ^{+0.3} _{-0.3}	-2.3 ^{+0.8} _{-0.8}	-3.5 ^{+0.1} _{-0.1}	-2.8 ^{+0.5} _{-0.5}	-4.4 ^{+1.1} _{-1.2}	1.0 ^{+0.4} _{-0.2}	9 ⁺³ ₋₂	96 ⁺³⁹ ₋₂₂	11 ⁺⁷ ₋₅	7.58 ^{+1.48} _{-0.95}	0.009 ^{+0.017} _{-0.006}
PS1-11li	55600.6 ^{+0.7} _{-0.8}	-1.0 ^{+0.3} _{-0.3}	-2.6 ^{+0.6} _{-0.6}	-4.1 ^{+0.4} _{-0.4}	-3.0 ^{+0.4} _{-0.5}	-5.0 ^{+1.0} _{-1.0}	1.0 ^{+0.4} _{-0.3}	8 ⁺² ₋₂	95 ⁺³⁵ ₋₂₁	11 ⁺⁷ ₋₄	0.32 ^{+0.09} _{-0.07}	0.060 ^{+0.012} _{-0.012}
PS1-11lj	55603.4 ^{+0.7} _{-0.7}	-1.0 ^{+0.3} _{-0.3}	-2.3 ^{+0.4} _{-0.4}	-4.9 ^{+0.2} _{-0.2}	-3.8 ^{+0.1} _{-0.1}	-2.9 ^{+0.1} _{-0.1}	1.0 ^{+0.3} _{-0.2}	8 ⁺² ₋₂	56 ⁺⁴ ₋₄	26 ⁺³ ₋₅	0.58 ^{+0.03} _{-0.02}	0.002 ^{+0.003} _{-0.002}
PS1-11lr	55611.5 ^{+0.5} _{-0.5}	-1.0 ^{+0.3} _{-0.3}	-2.3 ^{+0.8} _{-0.7}	-6.8 ^{+0.4} _{-0.5}	-3.0 ^{+0.5} _{-0.5}	-5.0 ^{+1.0} _{-0.9}	1.0 ^{+0.4} _{-0.3}	8 ⁺³ ₋₂	100 ⁺³⁴ ₋₂₆	10 ⁺⁷ ₋₄	0.54 ^{+0.01} _{-0.01}	0.002 ^{+0.002} _{-0.001}
PS1-11lq	55612.4 ^{+0.7} _{-0.7}	-1.0 ^{+0.3} _{-0.3}	-2.3 ^{+0.8} _{-0.8}	-4.1 ^{+0.1} _{-0.1}	-2.9 ^{+0.5} _{-0.5}	-5.0 ^{+1.0} _{-1.0}	1.0 ^{+0.4} _{-0.3}	8 ⁺² ₋₂	99 ⁺³³ ₋₂₅	10 ⁺⁷ ₋₄	1.00 ^{+0.05} _{-0.05}	0.006 ^{+0.008} _{-0.004}
PS1-11md	55616.3 ^{+4.7} _{-5.6}	-1.0 ^{+0.3} _{-0.3}	-2.4 ^{+0.7} _{-0.8}	-3.8 ^{+0.2} _{-0.1}	-3.0 ^{+0.5} _{-0.5}	-5.1 ^{+1.0} _{-1.0}	1.0 ^{+0.3} _{-0.3}	8 ⁺³ ₋₂	98 ⁺³³ ₋₂₅	10 ⁺⁶ ₋₄	2.14 ^{+0.22} _{-0.16}	0.008 ^{+0.011} _{-0.005}
PS1-11pf	55633.2 ^{+0.2} _{-0.3}	-1.0 ^{+0.3} _{-0.3}	-2.3 ^{+0.7} _{-0.8}	-3.9 ^{+0.1} _{-0.1}	-3.2 ^{+0.6} _{-0.5}	-5.0 ^{+0.8} _{-0.9}	1.0 ^{+0.4} _{-0.2}	8 ⁺² ₋₂	99 ⁺³⁷ ₋₄₀	9 ⁺⁵ ₋₄	1.71 ^{+0.13} _{-0.12}	0.029 ^{+0.027} _{-0.021}
PS1-11qe	55644.3 ^{+0.5} _{-1.2}	-1.0 ^{+0.3} _{-0.3}	-2.9 ^{+1.0} _{-0.9}	-3.3 ^{+0.1} _{-0.1}	-2.6 ^{+0.4} _{-0.6}	-4.8 ^{+0.9} _{-1.0}	0.9 ^{+0.3} _{-0.2}	5 ⁺² ₋₁	48 ⁺⁶⁸ ₋₇	11 ⁺⁷ ₋₄	6.78 ^{+0.22} _{-0.24}	0.049 ^{+0.081} _{-0.044}
PS1-11si	55671.0 ^{+0.6} _{-0.7}	-1.0 ^{+0.3} _{-0.3}	-2.2 ^{+0.4} _{-0.4}	-5.9 ^{+0.7} _{-0.8}	-3.0 ^{+0.5} _{-0.5}	-5.0 ^{+1.0} _{-1.1}	1.0 ^{+0.4} _{-0.3}	10 ⁺² ₋₂	99 ⁺³⁴ ₋₂₇	10 ⁺⁷ ₋₄	0.41 ^{+0.04} _{-0.04}	0.014 ^{+0.024} _{-0.011}
PS1-11sm	55659.4 ^{+0.6} _{-0.9}	-1.0 ^{+0.3} _{-0.3}	-2.8 ^{+0.7} _{-0.8}	-3.3 ^{+0.1} _{-0.1}	-3.0 ^{+0.5} _{-0.5}	-5.0 ^{+1.0} _{-1.0}	0.9 ^{+0.3} _{-0.2}	5 ⁺¹ ₋₁	99 ⁺³⁸ ₋₂₇	10 ⁺⁶ ₋₄	2.36 ^{+0.17} _{-0.17}	0.052 ^{+0.088} _{-0.045}
PS1-11ua	55644.6 ^{+8.1} _{-9.9}	-1.0 ^{+0.3} _{-0.3}	-2.3 ^{+0.8} _{-0.8}	-3.3 ^{+0.1} _{-0.1}	-2.9 ^{+0.5} _{-0.5}	-4.8 ^{+1.0} _{-1.1}	1.0 ^{+0.4} _{-0.3}	9 ⁺³ ₋₂	100 ⁺³⁵ ₋₃₂	10 ⁺⁸ ₋₄	5.42 ^{+1.49} _{-1.17}	0.010 ^{+0.021} _{-0.007}
PS1-11uv	55670.8 ^{+0.6} _{-1.4}	-1.0 ^{+0.3} _{-0.3}	-2.7 ^{+0.9} _{-0.9}	-4.8 ^{+0.2} _{-0.2}	-3.0 ^{+0.5} _{-0.5}	-5.0 ^{+1.0} _{-1.1}	0.9 ^{+0.3} _{-0.2}	6 ⁺¹ ₋₁	102 ⁺³³ ₋₂₃	10 ⁺⁷ ₋₄	0.33 ^{+0.01} _{-0.01}	0.002 ^{+0.002} _{-0.001}
PS1-11vn	55673.1 ^{+0.4} _{-0.5}	-1.0 ^{+0.3} _{-0.3}	-3.3 ^{+0.6} _{-0.6}	-3.9 ^{+0.2} _{-0.2}	-3.0 ^{+0.5} _{-0.5}	-5.1 ^{+1.0} _{-0.9}	0.9 ^{+0.3} _{-0.2}	6 ⁺² ₋₁	100 ⁺³⁵ ₋₂₄	10 ⁺⁶ ₋₄	1.24 ^{+0.19} _{-0.17}	0.117 ^{+0.033} _{-0.029}
PS1-11wj	55669.5 ^{+0.6} _{-0.9}	-1.0 ^{+0.3} _{-0.3}	-3.0 ^{+0.8} _{-0.8}	-3.7 ^{+0.7} _{-0.9}	-3.0 ^{+0.5} _{-0.5}	-5.0 ^{+0.9} _{-1.0}	0.9 ^{+0.3} _{-0.2}	4 ⁺¹ ₋₁	102 ⁺³⁴ ₋₂₈	10 ⁺⁷ ₋₄	0.70 ^{+0.03} _{-0.02}	0.002 ^{+0.003} _{-0.002}
PS1-11yh	55688.7 ^{+4.8} _{-3.5}	-1.0 ^{+0.3} _{-0.3}	-2.4 ^{+0.8} _{-0.8}	-4.1 ^{+0.1} _{-0.1}	-3.0 ^{+0.6} _{-0.5}	-5.0 ^{+1.0} _{-1.0}	1.0 ^{+0.3} _{-0.3}	8 ⁺² ₋₂	100 ⁺³² ₋₂₅	10 ⁺⁶ ₋₄	1.96 ^{+0.16} _{-0.15}	0.010 ^{+0.020} _{-0.008}
PS1-11amh	55790.1 ^{+0.7} _{-1.2}	-1.0 ^{+0.3} _{-0.3}	-2.8 ^{+1.0} _{-1.0}	-4.8 ^{+0.1} _{-0.1}	-3.0 ^{+0.5} _{-0.5}	-5.0 ^{+1.1} _{-1.0}	0.8 ^{+0.3} _{-0.2}	3 ⁺¹ ₋₁	105 ⁺³² ₋₂₅	10 ⁺⁷ ₋₄	2.00 ^{+0.05} _{-0.04}	0.066 ^{+0.010} _{-0.008}
PS1-11amv	55802.1 ^{+0.1} _{-0.9}	-1.0 ^{+0.3} _{-0.3}	-1.9 ^{+0.5} _{-0.5}	-4.0 ^{+1.1} _{-1.2}	-3.0 ^{+0.5} _{-0.5}	-5.0 ^{+1.0} _{-1.0}	1.0 ^{+0.4} _{-0.3}	8 ⁺³ ₋₂	100 ⁺³⁶ ₋₂₅	10 ⁺⁶ ₋₄	0.59 ^{+0.59} _{-0.25}	0.002 ^{+0.001} _{-0.001}
PS1-11anm	55763.5 ^{+0.8} _{-0.9}	-1.0 ^{+0.3} _{-0.3}	-2.7 ^{+0.6} _{-0.6}	-3.9 ^{+0.4} _{-0.3}	-2.9 ^{+0.5} _{-0.5}	-4.9 ^{+1.1} _{-1.0}	1.0 ^{+0.4} _{-0.3}	10 ⁺⁷ ₋₄	95 ⁺³² ₋₁₉	11 ⁺⁷ ₋₄	0.08 ^{+0.01} _{-0.01}	0.014 ^{+0.003} _{-0.002}
PS1-11aof	55777.1 ^{+0.4} _{-0.3}	-1.0 ^{+0.3} _{-0.3}	-3.0 ^{+0.6} _{-0.6}	-3.3 ^{+0.1} _{-0.1}	-3.0 ^{+0.5} _{-0.5}	-4.9 ^{+0.9} _{-0.9}	0.9 ^{+0.3} _{-0.2}	5 ⁺¹ ₋₁	99 ⁺³⁸ ₋₃₀	10 ⁺⁶ ₋₄	2.73 ^{+0.22} _{-0.21}	0.241 ^{+0.022} _{-0.021}
PS1-11apd	55789.4 ^{+0.9} _{-0.8}	-1.0 ^{+0.3} _{-0.3}	-2.5 ^{+0.9} _{-0.8}	-4.7 ^{+0.1} _{-0.1}	-2.7 ^{+0.3} _{-0.4}	-4.0 ^{+0.9} _{-0.5}	1.0 ^{+0.3} _{-0.2}	6 ⁺¹ ₋₁	83 ⁺² ₋₃	12 ⁺⁸ ₋₄	1.02 ^{+0.02} _{-0.02}	0.03

Table 7.3—Continued

SN	t_0	$\log \alpha$	$\log \beta_1$	$\log \beta_2$	$\log \beta_{dN}$	$\log \beta_{dC}$	t_1	t_p	t_2	t_d	M_p	V
PS1-11azi	55877.4 ^{+0.5} _{-0.5}	-1.0 ^{+0.3} _{-0.3}	-2.3 ^{+0.8} _{-0.7}	-3.5 ^{+0.1} _{-0.1}	-3.0 ^{+0.6} _{-0.5}	-4.6 ^{+0.9} _{-0.9}	1.0 ^{+0.3} _{-0.3}	8 ⁺² ₋₂	107 ⁺³⁴ ₋₂₅	10 ⁺⁷ ₋₄	3.65 ^{+0.27} _{-0.32}	0.007 ^{+0.011} _{-0.005}
PS1-11azt	55878.8 ^{+0.3} _{-0.4}	-1.0 ^{+0.3} _{-0.3}	-2.4 ^{+0.8} _{-0.8}	-4.3 ^{+0.3} _{-0.4}	-2.9 ^{+0.5} _{-0.5}	-4.5 ^{+0.8} _{-0.8}	1.0 ^{+0.3} _{-0.2}	6 ⁺¹ ₋₁	102 ⁺³⁶ ₋₂₇	11 ⁺⁷ ₋₅	1.51 ^{+0.09} _{-0.09}	0.007 ^{+0.010} _{-0.005}
PS1-11azv	55876.7 ^{+0.8} _{-1.2}	-1.0 ^{+0.3} _{-0.3}	-2.4 ^{+0.8} _{-0.8}	-4.6 ^{+0.1} _{-0.2}	-2.6 ^{+0.4} _{-0.4}	-5.1 ^{+1.7} _{-0.7}	1.0 ^{+0.4} _{-0.3}	8 ⁺² ₋₂	80 ⁺¹⁰ ₋₁₃	15 ⁺⁹ ₋₆	0.60 ^{+0.04} _{-0.04}	0.010 ^{+0.012} _{-0.007}
PS1-11bbg	55888.2 ^{+2.2} _{-0.8}	-0.9 ^{+0.3} _{-0.3}	-2.0 ^{+0.3} _{-0.4}	-3.7 ^{+0.1} _{-0.1}	-3.0 ^{+0.5} _{-0.5}	-4.6 ^{+0.7} _{-0.8}	1.1 ^{+0.4} _{-0.3}	8 ⁺¹ ₋₁	113 ⁺³⁶ ₋₂₉	10 ⁺⁷ ₋₄	1.88 ^{+0.14} _{-0.13}	0.049 ^{+0.012} _{-0.010}
PS1-12c	55848.4 ^{+8.4} _{-9.3}	-1.0 ^{+0.3} _{-0.3}	-2.3 ^{+0.8} _{-0.9}	-4.1 ^{+0.1} _{-0.2}	-2.6 ^{+0.3} _{-0.3}	-4.8 ^{+0.6} _{-0.5}	1.0 ^{+0.3} _{-0.2}	8 ⁺³ ₋₂	96 ⁺¹⁰ ₋₉	15 ⁺⁷ ₋₅	0.49 ^{+0.12} _{-0.09}	0.015 ^{+0.002} _{-0.002}
PS1-12d	55899.5 ^{+5.4} _{-2.0}	-1.0 ^{+0.3} _{-0.3}	-2.6 ^{+0.8} _{-0.8}	-4.3 ^{+0.0} _{-0.0}	-2.5 ^{+0.4} _{-0.7}	-3.2 ^{+0.8} _{-1.3}	1.0 ^{+0.3} _{-0.3}	7 ⁺³ ₋₂	99 ⁺⁴ ₋₅	15 ⁺¹⁰ ₋₇	1.18 ^{+0.04} _{-0.03}	0.014 ^{+0.009} _{-0.008}
PS1-12y	55911.8 ^{+13.6} _{-19.7}	-1.0 ^{+0.3} _{-0.3}	-2.4 ^{+0.7} _{-0.7}	-3.8 ^{+0.0} _{-0.1}	-1.8 ^{+0.2} _{-0.2}	-5.4 ^{+1.4} _{-1.0}	1.0 ^{+0.3} _{-0.3}	8 ⁺³ ₋₂	70 ⁺¹⁹ ₋₁₁	21 ⁺⁶ ₋₆	2.63 ^{+1.25} _{-0.58}	0.016 ^{+0.008} _{-0.007}
PS1-12bt	55827.7 ^{+14.1} _{-13.1}	-1.0 ^{+0.3} _{-0.3}	-2.3 ^{+0.8} _{-0.7}	-3.8 ^{+0.4} _{-0.7}	-3.0 ^{+0.5} _{-0.5}	-4.6 ^{+0.1} _{-0.1}	1.0 ^{+0.4} _{-0.2}	8 ⁺³ ₋₂	76 ⁺¹⁵ ₋₁₅	10 ⁺⁶ ₋₄	0.77 ^{+0.78} _{-0.36}	0.003 ^{+0.001} _{-0.001}
PS1-12rk	55996.2 ^{+0.5} _{-0.6}	-1.0 ^{+0.3} _{-0.3}	-3.0 ^{+0.6} _{-0.5}	-5.6 ^{+0.4} _{-0.4}	-2.9 ^{+0.5} _{-0.5}	-4.2 ^{+0.6} _{-0.4}	1.0 ^{+0.3} _{-0.3}	7 ⁺² ₋₁	99 ⁺³⁵ ₋₂₆	11 ⁺⁶ ₋₄	0.28 ^{+0.01} _{-0.01}	0.013 ^{+0.003} _{-0.003}
PS1-12wn	55999.3 ^{+0.6} _{-0.4}	-1.0 ^{+0.3} _{-0.3}	-2.1 ^{+0.5} _{-0.6}	-3.8 ^{+0.3} _{-0.3}	-2.9 ^{+0.5} _{-0.5}	-4.3 ^{+0.8} _{-1.0}	1.0 ^{+0.3} _{-0.2}	6 ⁺¹ ₋₁	107 ⁺⁴⁰ ₋₃₀	11 ⁺⁷ ₋₄	0.36 ^{+0.05} _{-0.04}	0.029 ^{+0.006} _{-0.006}
PS1-12zd	56016.1 ^{+0.1} _{-0.5}	-1.0 ^{+0.3} _{-0.3}	-2.4 ^{+0.8} _{-0.8}	-3.4 ^{+0.1} _{-0.1}	-3.0 ^{+0.6} _{-0.5}	-4.8 ^{+0.8} _{-0.9}	1.0 ^{+0.3} _{-0.3}	8 ⁺² ₋₂	105 ⁺³² ₋₂₆	10 ⁺⁷ ₋₄	1.48 ^{+0.11} _{-0.10}	0.021 ^{+0.005} _{-0.005}
PS1-12zp	56019.4 ^{+0.0} _{-0.1}	-1.0 ^{+0.3} _{-0.4}	-2.5 ^{+0.7} _{-0.8}	-3.9 ^{+0.1} _{-0.1}	-3.0 ^{+0.5} _{-0.5}	-4.4 ^{+0.7} _{-0.6}	1.0 ^{+0.4} _{-0.2}	9 ⁺¹ ₋₁	106 ⁺³² ₋₂₈	10 ⁺⁷ ₋₄	0.93 ^{+0.03} _{-0.02}	0.013 ^{+0.011} _{-0.008}
PS1-12auw	56080.7 ^{+0.4} _{-0.5}	-1.0 ^{+0.3} _{-0.3}	-2.6 ^{+0.8} _{-0.8}	-3.0 ^{+0.3} _{-0.3}	-3.0 ^{+0.5} _{-0.5}	-5.1 ^{+1.0} _{-1.0}	1.0 ^{+0.3} _{-0.2}	6 ⁺¹ ₋₁	101 ⁺³⁴ ₋₂₆	10 ⁺⁷ ₋₄	1.46 ^{+0.05} _{-0.04}	0.002 ^{+0.003} _{-0.002}
PS1-12bku	56160.7 ^{+0.2} _{-0.1}	-1.2 ^{+0.3} _{-0.4}	-2.0 ^{+0.2} _{-0.2}	-4.2 ^{+0.1} _{-0.1}	-2.8 ^{+0.3} _{-0.3}	-4.3 ^{+0.2} _{-0.2}	0.8 ^{+0.4} _{-0.2}	13 ⁺¹ ₋₂	56 ⁺¹⁸ ₋₅	11 ⁺⁶ ₋₄	1.98 ^{+0.07} _{-0.07}	0.014 ^{+0.006} _{-0.005}
PS1-12bmp	56201.1 ^{+0.3} _{-0.3}	-1.0 ^{+0.3} _{-0.3}	-2.7 ^{+0.9} _{-0.9}	-6.3 ^{+0.2} _{-0.3}	-2.6 ^{+0.2} _{-0.3}	-3.9 ^{+0.6} _{-0.4}	0.9 ^{+0.3} _{-0.2}	4 ⁺¹ ₋₁	82 ⁺³ ₋₂	14 ⁺⁶ ₋₅	0.61 ^{+0.01} _{-0.01}	0.004 ^{+0.004} _{-0.003}
PS1-12blz	56201.6 ^{+0.8} _{-0.9}	-1.0 ^{+0.3} _{-0.3}	-3.1 ^{+0.8} _{-0.7}	-3.5 ^{+0.0} _{-0.0}	-3.0 ^{+0.5} _{-0.5}	-4.5 ^{+0.8} _{-0.7}	0.9 ^{+0.3} _{-0.3}	5 ⁺¹ ₋₁	114 ⁺³⁶ ₋₂₆	10 ⁺⁷ ₋₄	2.45 ^{+0.04} _{-0.04}	0.018 ^{+0.005} _{-0.005}
PS1-12boi	56201.7 ^{+0.7} _{-0.9}	-1.0 ^{+0.3} _{-0.3}	-3.2 ^{+0.7} _{-0.6}	-3.4 ^{+0.2} _{-0.2}	-3.0 ^{+0.5} _{-0.5}	-4.8 ^{+0.9} _{-1.0}	0.9 ^{+0.3} _{-0.2}	6 ⁺¹ ₋₁	105 ⁺³² ₋₂₅	10 ⁺⁷ ₋₄	1.90 ^{+0.08} _{-0.08}	0.006 ^{+0.009} _{-0.004}
PS1-12bza	56228.6 ^{+0.6} _{-0.7}	-1.0 ^{+0.3} _{-0.3}	-2.5 ^{+0.8} _{-0.8}	-4.3 ^{+0.0} _{-0.1}	-2.2 ^{+0.2} _{-0.2}	-5.5 ^{+0.6} _{-0.6}	1.0 ^{+0.3} _{-0.3}	7 ⁺¹ ₋₂	75 ⁺² ₋₂	17 ⁺³ ₋₃	1.21 ^{+0.03} _{-0.03}	0.003 ^{+0.005} _{-0.004}
PS1-12cey	56237.2 ^{+0.2} _{-0.7}	-1.0 ^{+0.2} _{-0.3}	-2.8 ^{+0.3} _{-0.6}	-3.4 ^{+0.1} _{-0.1}	-2.9 ^{+0.4} _{-0.5}	-5.2 ^{+0.8} _{-1.1}	0.9 ^{+0.3} _{-0.2}	5 ⁺¹ ₋₁	105 ⁺⁴⁵ ₋₂₅	11 ⁺⁵ ₋₅	2.61 ^{+0.12} _{-0.12}	0.006 ^{+0.012} _{-0.005}
PS1-13hp	56323.4 ^{+0.4} _{-0.5}	-1.0 ^{+0.3} _{-0.3}	-3.5 ^{+0.2} _{-0.3}	-4.1 ^{+0.1} _{-0.1}	-2.9 ^{+0.5} _{-0.5}	-4.0 ^{+0.6} _{-0.8}	1.0 ^{+0.3} _{-0.2}	10 ⁺¹ ₋₁	105 ⁺⁴² ₋₂₈	11 ⁺⁸ ₋₅	2.03 ^{+0.07} _{-0.06}	0.046 ^{+0.016} _{-0.018}
PS1-13vs	56342.7 ^{+0.7} _{-0.8}	-1.0 ^{+0.3} _{-0.3}	-2.3 ^{+0.9} _{-0.8}	-5.1 ^{+0.1} _{-0.2}	-2.9 ^{+0.5} _{-0.5}	-4.5 ^{+0.3} _{-0.5}	1.0 ^{+0.4} _{-0.2}	8 ⁺² ₋₂	105 ⁺³⁴ ₋₂₄	11 ⁺⁷ ₋₄	0.82 ^{+0.03} _{-0.03}	0.021 ^{+0.007} _{-0.006}
PS1-13wr	56300.4 ^{+2.3} _{-2.4}	-1.0 ^{+0.3} _{-0.3}	-2.2 ^{+0.8} _{-0.8}	-5.1 ^{+0.2} _{-0.2}	-2.7 ^{+0.2} _{-0.2}	-4.6 ^{+0.8} _{-1.0}	1.0 ^{+0.3} _{-0.3}	8 ⁺² ₋₂	118 ⁺⁴ ₋₅	21 ⁺⁵ ₋₅	0.62 ^{+0.05} _{-0.05}	0.004 ^{+0.004} _{-0.003}
PS1-13alz	56397.2 ^{+0.1} _{-0.8}	-1.0 ^{+0.3} _{-0.3}	-2.3 ^{+0.7} _{-0.8}	-3.2 ^{+0.6} _{-0.9}	-2.9 ^{+0.5} _{-0.5}	-4.3 ^{+1.1} _{-1.3}	1.0 ^{+0.4} _{-0.3}	9 ⁺³ ₋₂	106 ⁺³⁴ ₋₂₈	11 ⁺⁸ ₋₅	2.29 ^{+0.73} _{-0.37}	0.004 ^{+0.004} _{-0.003}
PS1-13arp	56396.6 ^{+0.5} _{-0.5}	-1.0 ^{+0.3} _{-0.3}	-2.5 ^{+0.5} _{-0.5}	-3.6 ^{+0.2} _{-0.2}	-3.0 ^{+0.5} _{-0.5}	-5.0 ^{+1.1} _{-1.0}	1.0 ^{+0.4} _{-0.3}	8 ⁺² ₋₂	99 ⁺³⁵ ₋₂₄	10 ⁺⁶ ₋₄	1.03 ^{+0.13} _{-0.11}	0.039 ^{+0.024} _{-0.030}
PS1-13ave	56404.4 ^{+0.1} _{-0.2}	-1.0 ^{+0.3} _{-0.3}	-2.6 ^{+0.8} _{-0.8}	-4.0 ^{+0.0} _{-0.0}	-3.0 ^{+0.5} _{-0.4}	-5.0 ^{+1.1} _{-1.0}	1.0 ^{+0.4} _{-0.3}	10 ⁺¹ ₋₂	101 ⁺³⁴ ₋₂₅	10 ⁺⁵ ₋₄	4.88 ^{+0.12} _{-0.10}	0.013 ^{+0.024} _{-0.010}
PS1-13atm	56352.8 ^{+0.9} _{-0.9}	-1.0 ^{+0.3} _{-0.3}	-2.2 ^{+0.8} _{-0.7}	-4.9 ^{+1.0} _{-1.0}	-3.0 ^{+0.5} _{-0.5}	-5.0 ^{+1.1} _{-0.9}	1.0 ^{+0.3} _{-0.2}	8 ⁺² ₋₂	102 ⁺³⁴ ₋₂₇	10 ⁺⁷ ₋₄	0.62 ^{+0.23} _{-0.22}	0.348 ^{+0.061} _{-0.051}
PS1-13bvb	56451.6 ^{+0.5} _{-0.7}	-1.0 ^{+0.3} _{-0.3}	-2.3 ^{+0.8} _{-0.8}	-4.4 ^{+0.1} _{-0.1}	-2.4 ^{+0.4} _{-0.8}	-2.9 ^{+0.7} _{-2.1}	1.0 ^{+0.4} _{-0.2}	8 ⁺² ₋₂	63 ⁺⁴ ₋₅	14 ⁺¹³ ₋₆	1.41 ^{+0.09} _{-0.09}	0.014 ^{+0.019} _{-0.011}
PS1-13ccb	56503.7 ^{+1.0} _{-1.0}	-1.0 ^{+0.3} _{-0.3}	-2.2 ^{+1.2} _{-0.7}	-4.9 ^{+0.2} _{-0.2}	-3.0 ^{+0.5} _{-0.5}	-5.0 ^{+1.0} _{-1.0}	1.0 ^{+0.3} _{-0.2}	6 ⁺³ ₋₁	101 ⁺³⁸ ₋₂₄	10 ⁺⁶ ₋₄	0.44 ^{+0.03} _{-0.03}	0.012 ^{+0.011} _{-0.009}
PS1-13cua	56544.8 ^{+0.2} _{-0.2}	-1.0 ^{+0.3} _{-0.3}	-2.9 ^{+0.4} _{-0.5}	-5.6 ^{+0.2} _{-0.2}	-3.0 ^{+0.4} _{-0.3}	-4.7 ^{+1.1} _{-1.1}	1.0 ^{+0.3} _{-0.3}	7 ⁺² ₋₂	85 ⁺⁴ ₋₅	13 ⁺⁷ ₋₅	0.57 ^{+0.02} _{-0.02}	0.006 ^{+0.005} _{-0.004}
PS1-13eck	56613.7 ^{+0.3} _{-0.4}	-1.0 ^{+0.3} _{-0.3}	-2.3 ^{+0.7} _{-0.9}	-3.6 ^{+0.2} _{-0.4}	-2.8 ^{+0.6} _{-0.6}	-5.0 ^{+1.0} _{-0.9}	1.0 ^{+0.4} _{-0.3}	7 ⁺² ₋₂	88 ⁺³⁷ ₋₅₁	11 ⁺⁶ ₋₅	1.03 ^{+0.09} _{-0.07}	0.043 ^{+0.016} _{-0.031}
PS1-13esn	56637.0 ^{+0.9} _{-1.0}	-1.0 ^{+0.3} _{-0.3}	-2.3 ^{+0.9} _{-0.8}	-4.4 ^{+0.3} _{-0.4}	-3.0 ^{+0.5} _{-0.5}	-5.0 ^{+0.9} _{-1.0}	1.0 ^{+0.3} _{-0.2}	8 ⁺³ ₋₂	99 ⁺³⁷ ₋₂₄	10 ⁺⁷ ₋₄	1.02 ^{+0.08} _{-0.07}	0.008 ^{+0.012} _{-0.005}
<i>i</i> -band												
PS1-10a	55200.9 ^{+0.7} _{-0.8}	-1.0 ^{+0.3} _{-0.3}	-2.4 ^{+0.1} _{-0.1}	-3.9 ^{+0.1} _{-0.2}	-3.1 ^{+0.5} _{-0.5}	-4.7 ^{+0.4} _{-0.7}	0.9 ^{+0.3} _{-0.2}	7 ⁺¹ ₋₁	90 ⁺²¹ ₋₁₆	9 ⁺⁵ ₋₃	1.76 ^{+0.06} _{-0.05}	0.003 ^{+0.003} _{-0.002}
PS1-10b	55203.9 ^{+0.4} _{-0.5}	-1.0 ^{+0.3} _{-0.3}	-2.1 ^{+0.4} _{-0.5}	-3.7 ^{+0.3} _{-0.3}	-3.0 ^{+0.6} _{-0.5}	-5.1 ^{+1.0} _{-1.0}	1.0 ^{+0.3} _{-0.3}	10 ⁺² ₋₂	99 ⁺³⁶ ₋₂₆	10 ⁺⁶ ₋₄	1.66 ^{+0.19} _{-0.18}	0.026 ^{+0.099} _{-0.022}
PS1-10q	55200.5 ^{+0.7} _{-0.8}	-1.0 ^{+0.3} _{-0.3}	-4.6 ^{+0.9} _{-0.9}	-4.4 ^{+0.1} _{-0.1}	-2.6 ^{+0.5} _{-0.4}	-5.1 ^{+1.3} _{-1.1}	1.0 ^{+0.4} _{-0.3}	11 ⁺³ ₋₂	88 ⁺⁹ ₋₇	14 ⁺⁸ ₋₅	0.69 ^{+0.05} _{-0.05}	0.032 ^{+0.007} _{-0.006}
PS1-10t	55205.2 ^{+0.9} _{-0.9}	-1.0 ^{+0.3} _{-0.3}	-4.0 ^{+0.9} _{-1.0}	-4.4 ^{+1.0} _{-1.0}	-3.0 ^{+0.6} _{-0.5}	-5.1 ^{+1.0} _{-1.0}	1.0 ^{+0.3} _{-0.3}	12 ⁺⁴ ₋₃	103 ⁺³⁰ ₋₂₂	10 ⁺⁶ ₋₄	0.33 ^{+0.08} _{-0.08}	0.142 ^{+0.027} _{-0.022}
PS1-10ae	55239.3 ^{+0.1} _{-0.1}	-0.5 ^{+0.2} _{-0.2}	-3.5 ^{+0.3} _{-0.4}	-3.4 ^{+0.1} _{-0.2}	-2.8 ^{+0.5} _{-0.6}	-5.3 ^{+1.2} _{-1.3}	2.1 ^{+0.4} _{-0.3}	13 ⁺² ₋₂	82 ⁺³⁶ ₋₃₂	10 ⁺⁷ ₋₄	0.95 ^{+0.06} _{-0.07}	0.012 ^{+0.014} _{-0.007}
PS1-10jr	55359.1 ^{+0.4} _{-0.5}	-1.0 ^{+0.3} _{-0.3}	-4.6 ^{+0.7} _{-0.8}	-3.9 ^{+0.6} _{-0.8}	-2.9 ^{+0.5} _{-0.5}	-4.6 ^{+1.0} _{-1.0}	1.0 ^{+0.3} _{-0.3}	13 ⁺⁵ ₋₃	100 ⁺³¹ ₋₂₅	11 ⁺⁸ ₋₅	3.87 ^{+0.26} _{-0.22}	0.010 ^{+0.021} _{-0.007}
PS1-10lv	55380.5 ^{+2.0} _{-4.3}	-1.0 ^{+0.3} _{-0.3}	-3.3 ^{+1.2} _{-1.2}	-4.4 ^{+0.1} _{-0.1}	-3.0 ^{+0.4} _{-0.4}	-3.8 ^{+0.4} _{-0.5}	1.0 ^{+0.3} _{-0.3}	14 ⁺⁴ ₋₃	89 ⁺⁶ ₋₇	11 ⁺⁷ ₋₄	2.26 ^{+0.11} _{-0.}	

Table 7.3—Continued

SN	t_0	$\log \alpha$	$\log \beta_1$	$\log \beta_2$	$\log \beta_{dN}$	$\log \beta_{dC}$	t_1	t_p	t_2	t_d	M_p	V
PS1–10abd	55387.6 ^{+3.8} _{-4.0}	-1.0 ^{+0.3} _{-0.3}	-3.3 ^{+1.2} _{-1.2}	-4.0 ^{+0.2} _{-0.2}	-2.7 ^{+0.5} _{-0.6}	-4.4 ^{+1.1} _{-1.2}	1.0 ^{+0.4} _{-0.3}	14 ⁺⁴ ₋₃	85 ⁺³¹ ₋₁₃	12 ⁺⁸ ₋₅	2.03 ^{+0.23} _{-0.20}	0.160 ^{+0.039} _{-0.031}
PS1–10agh	55434.0 ^{+0.4} _{-0.5}	-1.0 ^{+0.3} _{-0.3}	-4.8 ^{+0.6} _{-0.8}	-3.9 ^{+0.0} _{-0.0}	-2.3 ^{+0.3} _{-0.3}	-4.9 ^{+1.0} _{-1.0}	0.9 ^{+0.3} _{-0.2}	10 ⁺¹ ₋₁	78 ⁺⁶ ₋₅	16 ⁺⁷ ₋₅	2.62 ^{+0.05} _{-0.05}	0.006 ^{+0.008} _{-0.004}
PS1–10awc	55454.2 ^{+0.2} _{-0.3}	-1.0 ^{+0.3} _{-0.3}	-2.9 ^{+0.2} _{-0.2}	-4.4 ^{+0.1} _{-0.1}	-2.4 ^{+0.3} _{-0.3}	-4.7 ^{+1.5} _{-1.2}	1.0 ^{+0.3} _{-0.3}	11 ⁺² ₋₁	95 ⁺⁶ ₋₆	15 ⁺⁷ ₋₅	1.37 ^{+0.04} _{-0.04}	0.008 ^{+0.010} _{-0.005}
PS1–10biu	55495.0 ^{+0.6} _{-0.7}	-1.0 ^{+0.3} _{-0.3}	-5.1 ^{+0.7} _{-0.9}	-3.6 ^{+0.1} _{-0.1}	-2.9 ^{+0.5} _{-0.6}	-4.5 ^{+0.7} _{-0.6}	0.9 ^{+0.3} _{-0.2}	7 ⁺¹ ₋₁	113 ⁺³⁵ ₋₃₁	11 ⁺⁷ ₋₄	2.60 ^{+0.09} _{-0.09}	0.008 ^{+0.014} _{-0.006}
PS1–10blk	55508.3 ^{+0.1} _{-0.2}	-1.0 ^{+0.3} _{-0.3}	-3.8 ^{+0.9} _{-1.1}	-4.4 ^{+0.2} _{-0.3}	-2.9 ^{+0.5} _{-0.5}	-4.6 ^{+1.0} _{-1.0}	1.0 ^{+0.3} _{-0.2}	11 ⁺⁴ ₋₃	104 ⁺³¹ ₋₂₆	11 ⁺⁷ ₋₄	1.26 ^{+0.17} _{-0.16}	0.162 ^{+0.037} _{-0.030}
PS1–11u	55497.2 ^{+21.0} _{-13.0}	-1.0 ^{+0.3} _{-0.3}	-3.2 ^{+1.1} _{-1.1}	-4.1 ^{+0.5} _{-0.4}	-2.8 ^{+1.4} _{-0.5}	-2.1 ^{+0.7} _{-3.0}	1.0 ^{+0.4} _{-0.2}	15 ⁺²⁵ ₋₄	70 ⁺¹³ ₋₃₃	17 ⁺⁶ ₋₃	0.60 ^{+0.18} _{-0.22}	0.001 ^{+0.001} _{-0.000}
PS1–11z	55539.2 ^{+7.6} _{-15.0}	-1.0 ^{+0.3} _{-0.3}	-3.2 ^{+1.1} _{-1.3}	-5.3 ^{+0.4} _{-0.5}	-2.3 ^{+0.3} _{-0.3}	-4.5 ^{+1.7} _{-1.3}	1.0 ^{+0.4} _{-0.3}	14 ⁺⁴ ₋₃	84 ⁺¹² ₋₇	19 ⁺⁸ ₋₇	0.78 ^{+0.07} _{-0.06}	0.027 ^{+0.020} _{-0.019}
PS1–11ai	55496.2 ^{+13.3} _{-10.9}	-1.0 ^{+0.3} _{-0.3}	-3.4 ^{+1.2} _{-1.1}	-4.8 ^{+0.4} _{-0.5}	-2.5 ^{+0.6} _{-0.6}	-3.4 ^{+0.7} _{-1.5}	1.0 ^{+0.4} _{-0.3}	14 ⁺⁵ ₋₄	88 ⁺¹⁵ ₋₁₃	14 ⁺¹⁰ ₋₆	0.82 ^{+0.15} _{-0.13}	0.048 ^{+0.012} _{-0.010}
PS1–11ak	55592.8 ^{+0.9} _{-0.9}	-1.0 ^{+0.3} _{-0.3}	-3.3 ^{+0.9} _{-1.1}	-4.2 ^{+1.2} _{-1.2}	-3.0 ^{+0.5} _{-0.5}	-5.0 ^{+1.2} _{-1.0}	1.0 ^{+0.4} _{-0.2}	14 ⁺⁵ ₋₄	101 ⁺³⁴ ₋₂₇	10 ⁺⁶ ₋₃	0.71 ^{+0.45} _{-0.22}	0.165 ^{+0.054} _{-0.037}
PS1–11bl	55568.0 ^{+0.7} _{-0.7}	-1.0 ^{+0.3} _{-0.3}	-4.8 ^{+0.7} _{-0.9}	-4.6 ^{+0.1} _{-0.1}	-2.3 ^{+0.3} _{-0.3}	-4.9 ^{+1.5} _{-1.1}	1.0 ^{+0.3} _{-0.2}	10 ⁺³ ₋₂	101 ⁺⁴ ₋₇	13 ⁺⁶ ₋₄	1.51 ^{+0.06} _{-0.05}	0.008 ^{+0.012} _{-0.006}
PS1–11bo	55574.2 ^{+0.8} _{-1.1}	-1.0 ^{+0.3} _{-0.3}	-3.1 ^{+0.3} _{-0.3}	-5.5 ^{+0.1} _{-0.1}	-3.0 ^{+0.5} _{-0.5}	-5.0 ^{+0.9} _{-1.0}	1.0 ^{+0.3} _{-0.2}	11 ⁺² ₋₂	115 ⁺³² ₋₂₂	10 ⁺⁷ ₋₄	0.52 ^{+0.02} _{-0.02}	0.004 ^{+0.005} _{-0.003}
PS1–11fl	55568.9 ^{+4.7} _{-21.4}	-1.0 ^{+0.3} _{-0.3}	-3.3 ^{+1.3} _{-1.3}	-4.8 ^{+0.2} _{-0.8}	-2.8 ^{+0.6} _{-0.7}	-3.2 ^{+0.4} _{-1.5}	1.0 ^{+0.3} _{-0.3}	14 ⁺⁴ ₋₃	90 ⁺⁹ ₋₉	13 ⁺⁹ ₋₅	0.85 ^{+0.07} _{-0.10}	0.046 ^{+0.010} _{-0.008}
PS1–11jg	55497.8 ^{+10.6} _{-10.0}	-1.0 ^{+0.3} _{-0.3}	-3.3 ^{+1.2} _{-1.3}	-3.7 ^{+0.4} _{-0.7}	-2.9 ^{+0.4} _{-0.4}	-4.9 ^{+0.2} _{-0.2}	1.0 ^{+0.4} _{-0.2}	13 ⁺⁴ ₋₃	63 ⁺¹¹ ₋₁₀	10 ⁺⁵ ₋₃	0.94 ^{+0.70} _{-0.40}	0.004 ^{+0.004} _{-0.003}
PS1–11kf	55580.9 ^{+6.3} _{-8.3}	-1.0 ^{+0.3} _{-0.3}	-3.2 ^{+1.1} _{-1.2}	-4.0 ^{+0.2} _{-0.2}	-2.7 ^{+0.3} _{-0.3}	-4.1 ^{+0.9} _{-0.6}	1.0 ^{+0.3} _{-0.2}	14 ⁺⁵ ₋₄	68 ⁺⁹ ₋₁₀	13 ⁺⁷ ₋₅	4.43 ^{+0.92} _{-0.87}	0.023 ^{+0.054} _{-0.019}
PS1–11li	55600.6 ^{+0.7} _{-0.8}	-1.0 ^{+0.3} _{-0.3}	-3.3 ^{+1.3} _{-1.1}	-4.1 ^{+1.1} _{-1.2}	-3.0 ^{+0.5} _{-0.5}	-5.0 ^{+1.0} _{-1.0}	1.0 ^{+0.3} _{-0.3}	14 ⁺⁵ ₋₄	99 ⁺³³ ₋₂₃	10 ⁺⁷ ₋₄	0.98 ^{+1.01} _{-0.48}	0.010 ^{+0.033} _{-0.007}
PS1–11lj	55603.4 ^{+0.7} _{-0.6}	-1.0 ^{+0.3} _{-0.3}	-3.7 ^{+1.1} _{-1.0}	-5.4 ^{+0.2} _{-0.2}	-2.9 ^{+0.2} _{-0.2}	-4.3 ^{+0.9} _{-1.3}	1.0 ^{+0.3} _{-0.2}	13 ⁺⁴ ₋₃	74 ⁺³ ₋₄	18 ⁺⁶ ₋₇	0.57 ^{+0.03} _{-0.02}	0.018 ^{+0.007} _{-0.005}
PS1–11lr	55611.5 ^{+0.5} _{-0.5}	-1.0 ^{+0.3} _{-0.3}	-3.8 ^{+0.4} _{-0.4}	-6.2 ^{+0.4} _{-0.5}	-3.0 ^{+0.5} _{-0.5}	-5.0 ^{+1.0} _{-1.0}	1.0 ^{+0.3} _{-0.3}	13 ⁺⁴ ₋₃	99 ⁺³⁴ ₋₂₆	10 ⁺⁶ ₋₄	0.64 ^{+0.02} _{-0.02}	0.018 ^{+0.008} _{-0.006}
PS1–11lq	55612.4 ^{+0.7} _{-0.7}	-1.0 ^{+0.3} _{-0.3}	-4.4 ^{+0.7} _{-0.8}	-4.2 ^{+0.1} _{-0.1}	-3.0 ^{+0.5} _{-0.5}	-5.1 ^{+1.1} _{-0.9}	1.0 ^{+0.3} _{-0.3}	12 ⁺⁴ ₋₃	101 ⁺³⁶ ₋₂₅	10 ⁺⁶ ₋₄	0.88 ^{+0.06} _{-0.05}	0.042 ^{+0.010} _{-0.008}
PS1–11md	55616.3 ^{+4.7} _{-5.6}	-1.0 ^{+0.3} _{-0.3}	-3.6 ^{+1.2} _{-1.3}	-3.8 ^{+0.1} _{-0.1}	-3.0 ^{+0.5} _{-0.5}	-5.0 ^{+0.9} _{-1.0}	1.0 ^{+0.3} _{-0.3}	12 ⁺³ ₋₃	101 ⁺³⁸ ₋₂₆	10 ⁺⁶ ₋₄	1.90 ^{+0.12} _{-0.12}	0.008 ^{+0.016} _{-0.006}
PS1–11pf	55633.2 ^{+0.2} _{-0.3}	-1.0 ^{+0.3} _{-0.3}	-3.7 ^{+0.7} _{-0.7}	-4.4 ^{+0.1} _{-0.1}	-3.1 ^{+0.5} _{-0.5}	-5.1 ^{+1.0} _{-0.9}	1.1 ^{+0.4} _{-0.3}	12 ⁺³ ₋₂	113 ⁺³⁰ ₋₂₀	10 ⁺⁷ ₋₄	1.55 ^{+0.08} _{-0.08}	0.060 ^{+0.025} _{-0.024}
PS1–11qe	55644.3 ^{+0.5} _{-1.2}	-1.0 ^{+0.3} _{-0.3}	-3.7 ^{+0.6} _{-1.0}	-3.1 ^{+0.0} _{-0.0}	-3.4 ^{+0.4} _{-0.4}	-5.0 ^{+0.8} _{-0.9}	0.9 ^{+0.3} _{-0.2}	11 ⁺¹ ₋₁	53 ⁺²² ₋₆	9 ⁺⁵ ₋₃	6.81 ^{+0.28} _{-0.30}	0.107 ^{+0.035} _{-0.026}
PS1–11si	55671.0 ^{+0.6} _{-0.7}	-1.0 ^{+0.3} _{-0.3}	-2.8 ^{+0.4} _{-0.4}	-5.7 ^{+0.7} _{-0.8}	-3.0 ^{+0.5} _{-0.5}	-5.0 ^{+0.9} _{-0.9}	1.0 ^{+0.3} _{-0.2}	16 ⁺⁵ ₋₃	99 ⁺³⁵ ₋₂₄	10 ⁺⁷ ₋₄	0.46 ^{+0.04} _{-0.04}	0.013 ^{+0.024} _{-0.011}
PS1–11sm	55659.4 ^{+0.6} _{-0.9}	-1.0 ^{+0.3} _{-0.3}	-4.4 ^{+0.8} _{-1.0}	-3.5 ^{+0.2} _{-0.1}	-3.0 ^{+0.5} _{-0.5}	-5.0 ^{+0.9} _{-1.0}	0.9 ^{+0.3} _{-0.2}	9 ⁺² ₋₂	99 ⁺³⁴ ₋₂₆	10 ⁺⁷ ₋₄	1.77 ^{+0.16} _{-0.17}	0.162 ^{+0.043} _{-0.036}
PS1–11ua	55644.6 ^{+8.1} _{-9.9}	-1.0 ^{+0.3} _{-0.3}	-3.4 ^{+1.2} _{-1.1}	-3.8 ^{+0.1} _{-0.2}	-2.5 ^{+0.4} _{-0.4}	-5.6 ^{+1.0} _{-1.0}	1.0 ^{+0.4} _{-0.3}	13 ⁺³ ₋₃	61 ⁺⁸ ₋₇	12 ⁺⁶ ₋₄	2.97 ^{+0.37} _{-0.29}	0.009 ^{+0.021} _{-0.007}
PS1–11uv	55670.8 ^{+0.6} _{-1.4}	-1.0 ^{+0.3} _{-0.3}	-3.7 ^{+0.9} _{-1.1}	-4.5 ^{+0.2} _{-0.2}	-3.0 ^{+0.5} _{-0.5}	-5.1 ^{+1.0} _{-1.0}	1.1 ^{+0.5} _{-0.3}	9 ⁺² ₋₂	100 ⁺³⁵ ₋₂₆	10 ⁺⁷ ₋₄	0.35 ^{+0.01} _{-0.02}	0.004 ^{+0.006} _{-0.003}
PS1–11vn	55673.1 ^{+0.4} _{-0.5}	-1.0 ^{+0.3} _{-0.3}	-3.9 ^{+0.6} _{-0.8}	-3.9 ^{+0.1} _{-0.1}	-3.0 ^{+0.5} _{-0.5}	-5.1 ^{+1.0} _{-0.9}	1.0 ^{+0.4} _{-0.3}	12 ⁺⁴ ₋₃	98 ⁺³² ₋₂₅	10 ⁺⁶ ₋₄	1.16 ^{+0.09} _{-0.09}	0.007 ^{+0.010} _{-0.005}
PS1–11wj	55669.5 ^{+0.6} _{-0.9}	-1.0 ^{+0.3} _{-0.3}	-5.0 ^{+0.5} _{-0.6}	-4.1 ^{+1.3} _{-1.1}	-3.0 ^{+0.5} _{-0.5}	-5.0 ^{+1.0} _{-1.0}	1.0 ^{+0.3} _{-0.3}	14 ⁺⁵ ₋₄	101 ⁺³² ₋₂₇	10 ⁺⁷ ₋₄	0.85 ^{+0.05} _{-0.03}	0.004 ^{+0.005} _{-0.003}
PS1–11yh	55688.7 ^{+4.8} _{-3.5}	-1.0 ^{+0.3} _{-0.3}	-3.0 ^{+0.8} _{-1.2}	-4.2 ^{+0.1} _{-0.1}	-3.0 ^{+0.5} _{-0.5}	-5.0 ^{+0.9} _{-1.0}	1.0 ^{+0.3} _{-0.3}	13 ⁺³ ₋₃	101 ⁺³⁵ ₋₂₉	10 ⁺⁷ ₋₄	2.10 ^{+0.09} _{-0.10}	0.009 ^{+0.017} _{-0.007}
PS1–11amh	55790.1 ^{+0.7} _{-1.2}	-1.0 ^{+0.3} _{-0.3}	-3.7 ^{+1.4} _{-0.8}	-5.1 ^{+1.2} _{-1.7}	-3.0 ^{+0.5} _{-0.5}	-5.0 ^{+0.9} _{-0.9}	1.0 ^{+0.4} _{-0.3}	15 ⁺³⁰ ₋₄	88 ⁺⁴² ₋₄₄	10 ⁺⁷ ₋₄	1.95 ^{+0.08} _{-0.14}	0.010 ^{+0.008} _{-0.007}
PS1–11amv	55802.1 ^{+0.1} _{-0.9}	-0.9 ^{+0.3} _{-0.3}	-1.4 ^{+0.0} _{-0.0}	-4.1 ^{+1.2} _{-1.2}	-3.0 ^{+0.5} _{-0.5}	-5.0 ^{+1.0} _{-1.0}	1.0 ^{+0.3} _{-0.3}	10 ⁺² ₋₂	101 ⁺³⁶ ₋₂₆	10 ⁺⁶ ₋₄	2.04 ^{+1.25} _{-0.71}	0.008 ^{+0.001} _{-0.007}
PS1–11anm	55763.5 ^{+0.8} _{-0.9}	-1.0 ^{+0.3} _{-0.3}	-4.4 ^{+0.9} _{-1.0}	-4.4 ^{+0.3} _{-0.4}	-3.1 ^{+0.5} _{-0.5}	-5.2 ^{+1.0} _{-0.9}	1.0 ^{+0.3} _{-0.2}	12 ⁺³ ₋₃	102 ⁺³⁷ ₋₂₈	10 ⁺⁶ ₋₄	0.11 ^{+0.02} _{-0.02}	0.032 ^{+0.004} _{-0.003}
PS1–11aof	55777.1 ^{+0.4} _{-0.3}	-1.0 ^{+0.3} _{-0.3}	-4.5 ^{+0.9} _{-1.0}	-3.6 ^{+0.1} _{-0.1}	-3.0 ^{+0.5} _{-0.5}	-4.6 ^{+0.8} _{-0.8}	1.0 ^{+0.3} _{-0.3}	10 ⁺³ ₋₂	106 ⁺³⁴ ₋₂₃	10 ⁺⁸ ₋₄	2.24 ^{+0.22} _{-0.20}	0.252 ^{+0.026} _{-0.022}
PS1–11apd	55789.4 ^{+0.9} _{-0.8}	-1.0 ^{+0.3} _{-0.3}	-4.2 ^{+0.5} _{-0.6}	-4.8 ^{+0.1} _{-0.1}	-3.1 ^{+0.5} _{-0.5}	-4.3 ^{+0.5} _{-0.4}	1.0 ^{+0.4} _{-0.2}	12 ⁺⁴ ₋₂	85 ⁺⁴³ ₋₈	10 ⁺⁸ ₋₄	1.00 ^{+0.03} _{-0.03}	0.044 ^{+0.004} _{-0.004}
PS1–11asz	55823.1 ^{+1.4} _{-0.3}	-1.0 ^{+0.3} _{-0.3}	-4.4 ^{+0.9} _{-0.9}	-4.7 ^{+0.3} _{-0.3}	-2.8 ^{+0.5} _{-0.5}	-4.4 ^{+0.9} _{-0.7}	1.0 ^{+0.3} _{-0.3}	9 ⁺³ ₋₂	85 ⁺¹³ ₋₁₀	12 ⁺⁶ ₋₄	0.70 ^{+0.06} _{-0.05}	0.096 ^{+0.012} _{-0.010}
PS1–11awd	55849.3 ^{+0.4} _{-1.1}	-1.0 ^{+0.3} _{-0.3}	-3.8 ^{+1.0} _{-1.0}	-5.0 ^{+0.1} _{-0.2}	-2.8 ^{+0.3} _{-0.2}	-4.7 ^{+0.1} _{-0.2}	1.2 ^{+0.4} _{-0.4}	10 ⁺⁴ ₋₃	82 ⁺⁴ ₋₅	11 ⁺⁷ ₋₄	0.68 ^{+0.03} _{-0.02}	0.008 ^{+0.003} _{-0.003}
PS1–11azd	55880.3 ^{+0.0} _{-0.1}	-1.0 ^{+0.3} _{-0.3}	-3.3 ^{+1.2} _{-1.2}	-4.1 ^{+1.1} _{-1.2}	-3.0 ^{+0.5} _{-0.5}	-5.0 ^{+1.0} _{-1.0}	1.0 ^{+0.4} _{-0.3}	14 ⁺⁴ ₋₄	100 ⁺³⁴ ₋₂₅	10 ⁺⁶ ₋₄	0.96 ^{+1.01} _{-0.48}	0.010 ^{+0.028} _{-0.008}
PS1–11azi	55877.4 ^{+0.5} _{-0.5}	-1.0 ^{+0.3} _{-0.3}	-3.7 ^{+0.4} _{-0.4}	-3.8 ^{+0.1} _{-0.1}	-2.6 ^{+0.3} _{-0.3}	-4.2 ^{+0.6} _{-0.7}	0.9 ^{+0.4} _{-0.2}	9 ⁺¹ ₋₂	53 ⁺⁵⁰ ₋₃	12 ⁺⁷ ₋₅	3.35 ^{+0.11} _{-0.09}	0.010 ^{+0.018} _{-0.017}
PS1–11azt	55878.8 ^{+0.3} _{-0.4}	-1.0 ^{+0.3} _{-0.3}	-3.8 ^{+0.7} _{-0.9}	-4.2 ^{+0.3} _{-0.3}	-3.0 ^{+0.5} _{-0.5}	-5.1 ^{+0.5} _{-0.7}	1.0 ^{+0.3} _{-0.3}	11 ⁺⁴ ₋₂	100 ⁺³⁶ ₋₂₅	10 ⁺⁶ ₋₄	1.55 ^{+0.07} ₋	

Table 7.3—Continued

SN	t_0	$\log \alpha$	$\log \beta_1$	$\log \beta_2$	$\log \beta_{dN}$	$\log \beta_{dC}$	t_1	t_p	t_2	t_d	M_p	V
PS1–12d	$55899.5^{+5.4}_{-2.0}$	$-1.0^{+0.3}_{-0.4}$	$-3.4^{+1.2}_{-1.2}$	$-4.9^{+0.1}_{-0.1}$	$-3.0^{+0.3}_{-0.3}$	$-2.8^{+0.2}_{-0.3}$	$1.0^{+0.3}_{-0.3}$	14^{+5}_{-4}	92^{+5}_{-6}	12^{+10}_{-5}	$0.91^{+0.04}_{-0.04}$	$0.020^{+0.006}_{-0.006}$
PS1–12y	$55911.8^{+13.6}_{-19.7}$	$-1.0^{+0.3}_{-0.3}$	$-3.3^{+1.3}_{-1.2}$	$-4.1^{+0.3}_{-0.4}$	$-1.9^{+0.3}_{-0.3}$	$-4.5^{+1.2}_{-1.0}$	$1.0^{+0.3}_{-0.3}$	14^{+4}_{-4}	73^{+13}_{-13}	18^{+8}_{-6}	$1.86^{+0.14}_{-0.13}$	$0.042^{+0.008}_{-0.007}$
PS1–12bt	$55827.7^{+14.1}_{-13.1}$	$-1.0^{+0.3}_{-0.3}$	$-3.4^{+1.2}_{-1.1}$	$-3.8^{+0.4}_{-0.7}$	$-2.9^{+0.5}_{-0.6}$	$-4.4^{+0.1}_{-0.1}$	$1.0^{+0.4}_{-0.3}$	13^{+4}_{-3}	74^{+16}_{-15}	9^{+6}_{-4}	$0.76^{+0.76}_{-0.37}$	$0.001^{+0.001}_{-0.001}$
PS1–12rk	$55996.2^{+0.5}_{-0.6}$	$-1.0^{+0.3}_{-0.3}$	$-4.8^{+0.7}_{-0.8}$	$-5.5^{+0.3}_{-0.3}$	$-2.9^{+0.5}_{-0.5}$	$-4.4^{+0.5}_{-0.4}$	$1.0^{+0.3}_{-0.3}$	11^{+3}_{-3}	100^{+31}_{-26}	11^{+8}_{-5}	$0.37^{+0.02}_{-0.01}$	$0.022^{+0.002}_{-0.002}$
PS1–12wn	$55999.3^{+0.6}_{-0.4}$	$-1.0^{+0.3}_{-0.3}$	$-4.6^{+0.8}_{-0.8}$	$-3.8^{+0.3}_{-0.4}$	$-3.0^{+0.5}_{-0.5}$	$-5.0^{+0.8}_{-1.0}$	$1.0^{+0.3}_{-0.3}$	12^{+4}_{-3}	100^{+33}_{-27}	10^{+6}_{-4}	$0.47^{+0.05}_{-0.05}$	$0.062^{+0.011}_{-0.009}$
PS1–12zd	$56016.1^{+0.1}_{-0.5}$	$-1.0^{+0.3}_{-0.3}$	$-3.9^{+1.1}_{-1.1}$	$-3.6^{+0.3}_{-0.2}$	$-3.0^{+0.5}_{-0.5}$	$-4.6^{+0.9}_{-0.7}$	$1.0^{+0.3}_{-0.2}$	11^{+2}_{-2}	106^{+35}_{-28}	10^{+6}_{-4}	$1.53^{+0.07}_{-0.07}$	$0.075^{+0.012}_{-0.009}$
PS1–12zp	$56019.4^{+0.0}_{-0.1}$	$-0.8^{+0.3}_{-0.3}$	$-4.1^{+0.8}_{-0.7}$	$-3.7^{+0.1}_{-0.1}$	$-3.0^{+0.5}_{-0.5}$	$-4.6^{+0.6}_{-0.7}$	$1.1^{+0.4}_{-0.3}$	13^{+1}_{-2}	107^{+35}_{-27}	11^{+7}_{-4}	$1.06^{+0.03}_{-0.03}$	$0.006^{+0.006}_{-0.004}$
PS1–12auw	$56080.7^{+0.4}_{-0.5}$	$-1.0^{+0.3}_{-0.3}$	$-4.3^{+0.6}_{-0.6}$	$-4.1^{+0.2}_{-0.1}$	$-3.1^{+0.4}_{-0.5}$	$-4.6^{+0.1}_{-0.2}$	$1.0^{+0.3}_{-0.2}$	11^{+4}_{-3}	96^{+35}_{-24}	9^{+6}_{-4}	$1.41^{+0.07}_{-0.03}$	$0.004^{+0.003}_{-0.003}$
PS1–12bku	$56160.7^{+0.2}_{-0.1}$	$-1.0^{+0.3}_{-0.3}$	$-2.6^{+0.3}_{-0.2}$	$-4.3^{+0.0}_{-0.0}$	$-2.9^{+0.3}_{-0.3}$	$-4.5^{+0.1}_{-0.1}$	$1.0^{+0.3}_{-0.2}$	10^{+1}_{-1}	83^{+10}_{-12}	10^{+5}_{-3}	$2.16^{+0.05}_{-0.05}$	$0.008^{+0.006}_{-0.005}$
PS1–12bmp	$56201.1^{+0.3}_{-0.4}$	$-1.0^{+0.3}_{-0.3}$	$-5.2^{+0.6}_{-0.7}$	$-5.5^{+0.1}_{-0.0}$	$-2.8^{+0.1}_{-0.1}$	$-4.7^{+0.2}_{-0.2}$	$0.9^{+0.3}_{-0.2}$	9^{+2}_{-2}	80^{+2}_{-2}	17^{+6}_{-3}	$0.76^{+0.01}_{-0.01}$	$0.014^{+0.003}_{-0.003}$
PS1–12blz	$56201.6^{+0.8}_{-1.1}$	$-1.0^{+0.3}_{-0.3}$	$-3.0^{+0.5}_{-0.3}$	$-3.5^{+0.0}_{-0.0}$	$-3.8^{+0.4}_{-0.4}$	$-4.2^{+0.1}_{-0.1}$	$0.9^{+0.3}_{-0.2}$	7^{+1}_{-1}	44^{+6}_{-6}	8^{+3}_{-3}	$2.38^{+0.05}_{-0.04}$	$0.027^{+0.006}_{-0.005}$
PS1–12boi	$56201.7^{+0.7}_{-0.9}$	$-1.0^{+0.3}_{-0.3}$	$-3.9^{+0.6}_{-0.9}$	$-3.7^{+0.1}_{-0.1}$	$-2.9^{+0.5}_{-0.5}$	$-4.5^{+0.8}_{-1.0}$	$1.0^{+0.3}_{-0.2}$	11^{+4}_{-2}	111^{+38}_{-29}	11^{+7}_{-4}	$1.70^{+0.08}_{-0.07}$	$0.007^{+0.009}_{-0.005}$
PS1–12bza	$56228.6^{+0.6}_{-0.7}$	$-1.0^{+0.3}_{-0.3}$	$-5.1^{+0.7}_{-0.7}$	$-4.3^{+0.0}_{-0.0}$	$-2.8^{+0.1}_{-0.1}$	$-5.0^{+0.2}_{-0.2}$	$0.9^{+0.3}_{-0.2}$	7^{+1}_{-1}	76^{+2}_{-2}	15^{+3}_{-3}	$1.52^{+0.03}_{-0.03}$	$0.013^{+0.008}_{-0.007}$
PS1–12cey	$56237.2^{+0.2}_{-0.5}$	$-0.9^{+0.2}_{-0.3}$	$-3.5^{+0.5}_{-0.5}$	$-3.5^{+0.1}_{-0.1}$	$-3.1^{+0.5}_{-0.8}$	$-4.7^{+0.4}_{-0.7}$	$1.0^{+0.3}_{-0.3}$	9^{+2}_{-2}	97^{+34}_{-22}	9^{+7}_{-3}	$2.30^{+0.28}_{-0.21}$	$0.016^{+0.010}_{-0.010}$
PS1–13hp	$56323.4^{+0.4}_{-0.8}$	$-1.0^{+0.3}_{-0.3}$	$-3.6^{+0.5}_{-0.6}$	$-4.5^{+0.1}_{-0.1}$	$-2.9^{+0.5}_{-0.5}$	$-4.1^{+0.7}_{-0.6}$	$1.0^{+0.4}_{-0.3}$	12^{+2}_{-2}	106^{+34}_{-24}	11^{+7}_{-4}	$1.80^{+0.10}_{-0.09}$	$0.114^{+0.018}_{-0.015}$
PS1–13vs	$56342.7^{+0.7}_{-0.8}$	$-1.0^{+0.3}_{-0.3}$	$-3.9^{+0.7}_{-0.7}$	$-4.5^{+0.1}_{-0.1}$	$-2.9^{+0.5}_{-0.5}$	$-4.6^{+0.8}_{-0.8}$	$1.0^{+0.3}_{-0.3}$	11^{+3}_{-2}	105^{+36}_{-25}	11^{+6}_{-4}	$1.05^{+0.06}_{-0.06}$	$0.082^{+0.014}_{-0.011}$
PS1–13wr	$56300.4^{+2.3}_{-0.8}$	$-1.0^{+0.3}_{-0.3}$	$-3.1^{+1.5}_{-1.4}$	$-6.2^{+0.2}_{-0.2}$	$-2.9^{+0.1}_{-0.1}$	$-5.5^{+0.8}_{-0.8}$	$1.0^{+0.4}_{-0.3}$	14^{+5}_{-4}	113^{+4}_{-5}	29^{+4}_{-3}	$0.67^{+0.03}_{-0.03}$	$0.016^{+0.004}_{-0.003}$
PS1–13alz	$56397.2^{+0.1}_{-0.5}$	$-1.0^{+0.3}_{-0.3}$	$-3.7^{+0.5}_{-0.3}$	$-3.5^{+0.1}_{-0.1}$	$-3.0^{+0.5}_{-0.5}$	$-4.9^{+0.6}_{-0.8}$	$1.0^{+0.3}_{-0.2}$	13^{+2}_{-2}	102^{+29}_{-25}	10^{+6}_{-4}	$1.93^{+0.17}_{-0.09}$	$0.028^{+0.008}_{-0.013}$
PS1–13arp	$56396.6^{+0.5}_{-0.5}$	$-1.0^{+0.3}_{-0.3}$	$-3.2^{+0.3}_{-0.4}$	$-4.2^{+0.2}_{-0.2}$	$-3.0^{+0.5}_{-0.5}$	$-5.0^{+1.0}_{-1.0}$	$1.0^{+0.4}_{-0.3}$	18^{+2}_{-4}	100^{+34}_{-26}	10^{+7}_{-4}	$0.86^{+0.06}_{-0.06}$	$0.061^{+0.018}_{-0.018}$
PS1–13ave	$56404.4^{+0.1}_{-0.2}$	$-1.0^{+0.3}_{-0.3}$	$-3.7^{+0.4}_{-0.5}$	$-4.3^{+0.1}_{-0.1}$	$-3.2^{+0.5}_{-0.4}$	$-5.6^{+0.9}_{-0.6}$	$1.0^{+0.3}_{-0.3}$	12^{+1}_{-1}	39^{+75}_{-3}	6^{+2}_{-2}	$4.25^{+0.11}_{-0.12}$	$0.099^{+0.035}_{-0.027}$
PS1–13atm	$56352.8^{+0.9}_{-0.9}$	$-1.0^{+0.3}_{-0.3}$	$-1.6^{+0.8}_{-1.9}$	$-4.8^{+1.0}_{-1.0}$	$-3.0^{+0.5}_{-0.5}$	$-5.0^{+0.9}_{-1.0}$	$1.0^{+0.4}_{-0.3}$	35^{+5}_{-22}	100^{+37}_{-27}	10^{+7}_{-4}	$1.24^{+0.67}_{-0.73}$	$0.596^{+0.179}_{-0.134}$
PS1–13bvz	$56451.6^{+0.5}_{-0.7}$	$-1.0^{+0.3}_{-0.3}$	$-3.2^{+1.1}_{-1.3}$	$-4.6^{+0.3}_{-0.3}$	$-2.4^{+0.4}_{-0.4}$	$-4.2^{+0.6}_{-0.9}$	$1.0^{+0.3}_{-0.3}$	13^{+4}_{-3}	59^{+4}_{-5}	11^{+5}_{-4}	$1.34^{+0.17}_{-0.14}$	$0.090^{+0.022}_{-0.019}$
PS1–13cqb	$56503.7^{+1.0}_{-1.0}$	$-1.0^{+0.3}_{-0.3}$	$-3.1^{+0.5}_{-0.6}$	$-4.2^{+0.2}_{-0.2}$	$-3.0^{+0.5}_{-0.5}$	$-5.0^{+1.0}_{-1.0}$	$1.0^{+0.4}_{-0.3}$	12^{+2}_{-2}	103^{+36}_{-26}	10^{+7}_{-4}	$0.69^{+0.05}_{-0.06}$	$0.080^{+0.013}_{-0.011}$
PS1–13cua	$56544.8^{+0.2}_{-0.2}$	$-1.0^{+0.3}_{-0.3}$	$-4.4^{+0.7}_{-0.8}$	$-5.7^{+0.3}_{-0.4}$	$-3.0^{+0.6}_{-0.5}$	$-3.4^{+0.8}_{-1.9}$	$1.0^{+0.3}_{-0.3}$	12^{+4}_{-3}	85^{+8}_{-8}	14^{+8}_{-5}	$0.59^{+0.02}_{-0.03}$	$0.031^{+0.007}_{-0.007}$
PS1–13eck	$56613.7^{+0.3}_{-0.4}$	$-1.0^{+0.3}_{-0.3}$	$-3.4^{+1.1}_{-1.3}$	$-3.6^{+0.1}_{-0.1}$	$-3.0^{+0.5}_{-0.5}$	$-5.0^{+1.1}_{-1.0}$	$1.0^{+0.4}_{-0.2}$	14^{+3}_{-3}	97^{+33}_{-24}	11^{+6}_{-4}	$1.31^{+0.12}_{-0.11}$	$0.080^{+0.024}_{-0.022}$
PS1–13esn	$56637.0^{+0.9}_{-1.0}$	$-1.0^{+0.3}_{-0.3}$	$-2.8^{+0.4}_{-0.5}$	$-4.0^{+0.1}_{-0.1}$	$-2.9^{+0.5}_{-0.6}$	$-4.9^{+1.0}_{-1.0}$	$1.0^{+0.4}_{-0.3}$	13^{+3}_{-3}	100^{+36}_{-23}	10^{+6}_{-4}	$1.06^{+0.07}_{-0.05}$	$0.014^{+0.013}_{-0.009}$
z-band												
PS1–10a	$55200.9^{+0.7}_{-0.8}$	$-1.0^{+0.3}_{-0.3}$	$-3.0^{+0.1}_{-0.1}$	$-3.5^{+0.4}_{-0.5}$	$-3.0^{+0.5}_{-0.5}$	$-4.8^{+0.7}_{-1.0}$	$0.9^{+0.3}_{-0.2}$	13^{+1}_{-1}	98^{+28}_{-23}	10^{+7}_{-4}	$1.64^{+0.05}_{-0.06}$	$0.004^{+0.005}_{-0.003}$
PS1–10b	$55203.9^{+0.4}_{-0.5}$	$-1.0^{+0.3}_{-0.3}$	$-3.7^{+1.4}_{-1.6}$	$-4.4^{+1.4}_{-1.4}$	$-3.0^{+0.5}_{-0.4}$	$-5.0^{+1.0}_{-0.9}$	$1.0^{+0.3}_{-0.3}$	20^{+6}_{-5}	100^{+36}_{-25}	10^{+7}_{-4}	$1.03^{+1.03}_{-0.55}$	$0.010^{+0.028}_{-0.008}$
PS1–10q	$55200.5^{+0.7}_{-0.8}$	$-1.0^{+0.3}_{-0.3}$	$-6.1^{+0.8}_{-0.9}$	$-4.7^{+0.2}_{-0.2}$	$-2.8^{+0.3}_{-0.4}$	$-2.9^{+0.4}_{-2.7}$	$1.0^{+0.3}_{-0.3}$	25^{+5}_{-7}	62^{+6}_{-5}	16^{+15}_{-8}	$0.54^{+0.02}_{-0.01}$	$0.015^{+0.005}_{-0.004}$
PS1–10t	$55205.2^{+0.9}_{-0.9}$	$-1.0^{+0.3}_{-0.3}$	$-3.4^{+0.5}_{-0.6}$	$-6.0^{+0.7}_{-1.0}$	$-3.0^{+0.5}_{-0.5}$	$-5.1^{+1.0}_{-0.9}$	$1.0^{+0.4}_{-0.3}$	19^{+6}_{-4}	90^{+38}_{-25}	10^{+7}_{-4}	$0.39^{+0.08}_{-0.06}$	$0.035^{+0.018}_{-0.017}$
PS1–10ae	$55239.3^{+0.1}_{-0.1}$	$-1.0^{+0.3}_{-0.3}$	$-2.9^{+0.2}_{-0.3}$	$-4.5^{+0.3}_{-0.2}$	$-2.9^{+0.5}_{-0.6}$	$-3.9^{+0.6}_{-0.6}$	$1.0^{+0.3}_{-0.2}$	13^{+4}_{-2}	98^{+33}_{-24}	11^{+8}_{-4}	$0.72^{+0.06}_{-0.04}$	$0.009^{+0.010}_{-0.006}$
PS1–10jr	$55359.1^{+0.4}_{-0.5}$	$-1.0^{+0.3}_{-0.3}$	$-3.8^{+1.6}_{-1.5}$	$-4.4^{+1.3}_{-1.5}$	$-3.0^{+0.5}_{-0.5}$	$-4.9^{+0.9}_{-1.1}$	$1.0^{+0.4}_{-0.3}$	20^{+7}_{-5}	100^{+35}_{-27}	10^{+6}_{-4}	$1.01^{+0.89}_{-0.54}$	$0.010^{+0.028}_{-0.007}$
PS1–10lv	$55380.5^{+2.0}_{-4.3}$	$-1.0^{+0.3}_{-0.3}$	$-4.1^{+1.1}_{-0.3}$	$-3.8^{+0.1}_{-2.3}$	$-2.6^{+0.5}_{-0.6}$	$-4.9^{+1.3}_{-1.2}$	$1.0^{+0.4}_{-0.3}$	42^{+3}_{-24}	75^{+11}_{-29}	13^{+8}_{-5}	$3.40^{+0.19}_{-0.34}$	$0.116^{+0.040}_{-0.032}$
PS1–10mb	$55374.3^{+0.9}_{-0.9}$	$-1.0^{+0.3}_{-0.3}$	$-3.0^{+0.7}_{-0.7}$	$-6.1^{+0.8}_{-1.0}$	$-2.9^{+0.5}_{-0.5}$	$-4.5^{+1.0}_{-1.0}$	$1.0^{+0.3}_{-0.3}$	22^{+11}_{-6}	96^{+27}_{-23}	11^{+7}_{-4}	$0.20^{+0.03}_{-0.02}$	$0.038^{+0.013}_{-0.010}$
PS1–10zu	$55354.3^{+25.5}_{-5.5}$	$-1.0^{+0.3}_{-0.3}$	$-4.4^{+1.6}_{-0.8}$	$-5.7^{+1.9}_{-0.3}$	$-2.7^{+0.2}_{-0.3}$	$-4.3^{+0.2}_{-0.5}$	$1.0^{+0.4}_{-0.3}$	22^{+39}_{-3}	95^{+9}_{-11}	11^{+3}_{-3}	$0.61^{+0.04}_{-0.04}$	$0.013^{+0.018}_{-0.017}$
PS1–10abd	$55387.6^{+3.8}_{-4.0}$	$-1.0^{+0.3}_{-0.3}$	$-4.4^{+1.5}_{-0.7}$	$-3.8^{+0.2}_{-0.4}$	$-2.9^{+0.5}_{-0.5}$	$-4.6^{+1.0}_{-1.1}$	$1.0^{+0.3}_{-0.3}$	38^{+6}_{-7}	99^{+32}_{-40}	10^{+7}_{-4}	$2.70^{+0.39}_{-0.28}$	$0.126^{+0.043}_{-0.034}$
PS1–10agh	$55434.0^{+0.4}_{-0.5}$	$-1.0^{+0.3}_{-0.3}$	$-5.9^{+1.2}_{-0.5}$	$-3.2^{+0.2}_{-2.3}$	$-3.0^{+0.5}_{-0.5}$	$-4.5^{+1.4}_{-1.2}$	$1.0^{+0.3}_{-0.3}$	50^{+2}_{-30}	91^{+37}_{-52}	10^{+8}_{-4}	$2.47^{+0.09}_{-0.07}$	$0.008^{+0.013}_{-0.006}$
PS1–10awc	$55454.2^{+0.2}_{-0.3}$	$-0.9^{+0.3}_{-0.3}$	$-3.6^{+0.2}_{-0.3}$	$-4.1^{+0.2}_{-0.2}$	$-2.5^{+0.4}_{-0.4}$	$-4.8^{+1.2}_{-1.1}$	$1.1^{+0.4}_{-0.3}$	35^{+6}_{-3}	69^{+7}_{-8}	12^{+7}_{-4}	$1.89^{+0.11}_{-0.13}$	$0.069^{+0.026}_{-0.024}$
PS1–10biu	$55495.0^{+0.6}_{-0.7}$	$-1.0^{+0.3}_{-0.3}$	$-4.2^{+0.6}_{-1.0}$	$-5.1^{+1.3}_{-1.3}$	$-2.8^{+0.5}_{-0.6}$	$-3.9^{+0.7}_{-1.1}$	$1.0^{+0.3}_{-0.2}$	24^{+11}_{-6}	95^{+31}_{-25}	12^{+8}_{-5}	$2.19^{+0.34}_{-0.23}$	$0.007^{+0.014}_{-0.006}$
PS1–10blk	$55508.3^{+0.1}_{-0.2}$	$-0.8^{+0.3}_{-0.3}$	$-3.7^{+0.5}_{-0.3}$	$-4.7^{+0.2}_{-0.2}$	$-3.0^{+0.5}_{-0.5}$	$-5.1^{+1.0}_{-0.9}$	$1.2^{+0.4}_{-0.3}$	21^{+6}_{-5}	100^{+32}_{-26}	10^{+6}_{-4}	$1.39^{+0.12}_{-0.09}$	$0.052^{+0.016}_{-0.013}$

Table 7.3—Continued

SN	t_0	$\log \alpha$	$\log \beta_1$	$\log \beta_2$	$\log \beta_{dN}$	$\log \beta_{dC}$	t_1	t_p	t_2	t_d	M_p	V
PS1-11u	55497.2 $^{+21.0}_{-13.0}$	-1.0 $^{+0.3}_{-0.3}$	-3.7 $^{+1.6}_{-1.6}$	-3.3 $^{+0.1}_{-0.5}$	-1.9 $^{+0.4}_{-1.3}$	-4.5 $^{+2.4}_{-1.3}$	1.0 $^{+0.3}_{-0.3}$	21 $^{+7}_{-6}$	77 $^{+12}_{-12}$	18 $^{+9}_{-7}$	1.61 $^{+0.84}_{-0.73}$	0.001 $^{+0.001}_{-0.001}$
PS1-11z	55539.2 $^{+7.6}_{-15.0}$	-1.0 $^{+0.3}_{-0.3}$	-3.8 $^{+1.2}_{-1.4}$	-4.6 $^{+0.3}_{-0.9}$	-2.5 $^{+0.5}_{-0.7}$	-3.5 $^{+1.2}_{-1.9}$	1.0 $^{+0.4}_{-0.2}$	20 $^{+8}_{-5}$	71 $^{+19}_{-14}$	16 $^{+10}_{-7}$	1.43 $^{+0.41}_{-0.26}$	0.008 $^{+0.012}_{-0.006}$
PS1-11ai	55496.2 $^{+13.3}_{-10.9}$	-1.0 $^{+0.3}_{-0.3}$	-3.9 $^{+1.4}_{-1.2}$	-3.8 $^{+0.4}_{-0.9}$	-2.9 $^{+0.5}_{-0.5}$	-4.4 $^{+0.9}_{-1.2}$	1.0 $^{+0.3}_{-0.3}$	21 $^{+8}_{-6}$	98 $^{+30}_{-22}$	11 $^{+7}_{-4}$	2.20 $^{+1.32}_{-1.02}$	0.051 $^{+0.022}_{-0.015}$
PS1-11ak	55592.8 $^{+0.9}_{-0.9}$	-1.0 $^{+0.3}_{-0.3}$	-3.4 $^{+0.9}_{-1.4}$	-4.4 $^{+1.4}_{-1.5}$	-3.0 $^{+0.5}_{-0.5}$	-5.0 $^{+0.9}_{-0.9}$	1.0 $^{+0.4}_{-0.3}$	20 $^{+7}_{-5}$	101 $^{+34}_{-24}$	10 $^{+6}_{-4}$	0.73 $^{+0.57}_{-0.29}$	0.151 $^{+0.037}_{-0.026}$
PS1-11bl	55568.0 $^{+0.7}_{-0.7}$	-1.0 $^{+0.3}_{-0.3}$	-4.6 $^{+1.2}_{-1.0}$	-5.1 $^{+0.5}_{-1.2}$	-2.9 $^{+0.5}_{-0.4}$	-3.5 $^{+0.4}_{-1.5}$	1.0 $^{+0.3}_{-0.2}$	18 $^{+10}_{-4}$	72 $^{+14}_{-9}$	12 $^{+9}_{-5}$	1.37 $^{+0.12}_{-0.09}$	0.007 $^{+0.015}_{-0.005}$
PS1-11bo	55574.2 $^{+0.8}_{-1.1}$	-1.0 $^{+0.3}_{-0.3}$	-3.4 $^{+0.2}_{-0.3}$	-4.8 $^{+0.4}_{-0.7}$	-3.0 $^{+0.5}_{-0.5}$	-5.0 $^{+0.9}_{-1.0}$	1.0 $^{+0.3}_{-0.3}$	32 $^{+6}_{-5}$	96 $^{+33}_{-28}$	10 $^{+6}_{-4}$	0.79 $^{+0.11}_{-0.10}$	0.010 $^{+0.016}_{-0.008}$
PS1-11fl	55568.9 $^{+4.7}_{-21.4}$	-1.0 $^{+0.3}_{-0.3}$	-4.1 $^{+1.2}_{-0.6}$	-4.1 $^{+0.3}_{-0.4}$	-2.5 $^{+0.4}_{-0.5}$	-4.0 $^{+1.0}_{-1.4}$	1.0 $^{+0.3}_{-0.3}$	41 $^{+9}_{-21}$	79 $^{+28}_{-15}$	15 $^{+9}_{-6}$	1.32 $^{+0.25}_{-0.13}$	0.020 $^{+0.012}_{-0.010}$
PS1-11jg	55497.8 $^{+10.6}_{-10.0}$	-1.0 $^{+0.3}_{-0.3}$	-3.9 $^{+1.4}_{-1.5}$	-4.1 $^{+0.3}_{-0.4}$	-3.1 $^{+0.5}_{-0.5}$	-4.4 $^{+0.5}_{-1.1}$	1.0 $^{+0.3}_{-0.3}$	20 $^{+6}_{-5}$	114 $^{+35}_{-37}$	9 $^{+6}_{-3}$	0.47 $^{+0.27}_{-0.18}$	0.004 $^{+0.004}_{-0.003}$
PS1-11kf	55580.9 $^{+6.3}_{-8.3}$	-1.0 $^{+0.3}_{-0.3}$	-4.7 $^{+1.3}_{-1.2}$	-3.7 $^{+0.2}_{-0.1}$	-3.0 $^{+0.5}_{-0.5}$	-5.0 $^{+1.0}_{-1.0}$	1.0 $^{+0.4}_{-0.3}$	18 $^{+6}_{-4}$	100 $^{+37}_{-26}$	10 $^{+6}_{-4}$	8.02 $^{+1.02}_{-0.62}$	0.008 $^{+0.019}_{-0.006}$
PS1-11li	55600.6 $^{+0.7}_{-0.8}$	-1.0 $^{+0.3}_{-0.3}$	-3.5 $^{+0.9}_{-1.1}$	-4.3 $^{+0.2}_{-0.4}$	-2.9 $^{+0.4}_{-0.4}$	-4.9 $^{+1.0}_{-1.1}$	1.0 $^{+0.4}_{-0.3}$	21 $^{+6}_{-5}$	91 $^{+31}_{-17}$	10 $^{+7}_{-4}$	0.50 $^{+0.09}_{-0.08}$	0.026 $^{+0.010}_{-0.009}$
PS1-11lj	55603.4 $^{+0.5}_{-0.6}$	-1.0 $^{+0.3}_{-0.3}$	-4.4 $^{+0.4}_{-0.4}$	-3.7 $^{+0.3}_{-2.0}$	-2.6 $^{+0.4}_{-0.6}$	-4.6 $^{+1.3}_{-1.0}$	1.0 $^{+0.3}_{-0.3}$	52 $^{+7}_{-18}$	43 $^{+6}_{-6}$	11 $^{+7}_{-4}$	0.77 $^{+0.05}_{-0.08}$	0.012 $^{+0.013}_{-0.009}$
PS1-11lr	55611.5 $^{+0.5}_{-0.5}$	-1.0 $^{+0.3}_{-0.3}$	-4.5 $^{+0.2}_{-0.2}$	-6.7 $^{+1.1}_{-0.9}$	-3.0 $^{+0.5}_{-0.5}$	-5.0 $^{+1.1}_{-1.0}$	1.0 $^{+0.3}_{-0.3}$	35 $^{+6}_{-3}$	101 $^{+39}_{-29}$	10 $^{+6}_{-4}$	0.61 $^{+0.02}_{-0.01}$	0.004 $^{+0.003}_{-0.003}$
PS1-11lq	55612.4 $^{+0.7}_{-0.7}$	-1.0 $^{+0.3}_{-0.3}$	-4.5 $^{+0.7}_{-0.6}$	-5.3 $^{+0.7}_{-0.9}$	-3.0 $^{+0.5}_{-0.5}$	-5.0 $^{+1.0}_{-1.0}$	1.0 $^{+0.3}_{-0.2}$	29 $^{+7}_{-6}$	102 $^{+34}_{-29}$	10 $^{+6}_{-4}$	1.04 $^{+0.06}_{-0.05}$	0.008 $^{+0.012}_{-0.005}$
PS1-11md	55616.3 $^{+4.7}_{-5.6}$	-1.0 $^{+0.3}_{-0.3}$	-3.3 $^{+0.7}_{-0.7}$	-4.4 $^{+0.4}_{-0.6}$	-3.0 $^{+0.5}_{-0.6}$	-5.0 $^{+0.8}_{-1.0}$	1.0 $^{+0.4}_{-0.3}$	22 $^{+5}_{-5}$	100 $^{+31}_{-28}$	10 $^{+7}_{-4}$	2.16 $^{+0.33}_{-0.25}$	0.007 $^{+0.011}_{-0.005}$
PS1-11pf	55633.2 $^{+0.2}_{-0.3}$	-1.0 $^{+0.3}_{-0.3}$	-3.8 $^{+0.3}_{-0.3}$	-4.0 $^{+0.1}_{-0.1}$	-3.0 $^{+0.5}_{-0.5}$	-5.0 $^{+0.9}_{-1.0}$	1.1 $^{+0.4}_{-0.3}$	32 $^{+4}_{-3}$	100 $^{+35}_{-24}$	10 $^{+7}_{-3}$	2.08 $^{+0.13}_{-0.12}$	0.007 $^{+0.015}_{-0.005}$
PS1-11qe	55644.3 $^{+0.5}_{-0.7}$	-1.0 $^{+0.3}_{-0.3}$	-5.9 $^{+0.8}_{-0.2}$	-3.5 $^{+0.1}_{-0.5}$	-3.0 $^{+0.5}_{-0.5}$	-5.0 $^{+1.1}_{-1.0}$	1.0 $^{+0.4}_{-0.3}$	22 $^{+4}_{-3}$	101 $^{+34}_{-26}$	10 $^{+6}_{-4}$	5.61 $^{+0.26}_{-0.23}$	0.031 $^{+0.097}_{-0.027}$
PS1-11si	55671.0 $^{+0.6}_{-0.7}$	-1.0 $^{+0.3}_{-0.3}$	-3.2 $^{+0.2}_{-0.2}$	-5.1 $^{+1.3}_{-1.3}$	-3.0 $^{+0.5}_{-0.5}$	-5.1 $^{+1.0}_{-0.9}$	1.0 $^{+0.3}_{-0.3}$	37 $^{+8}_{-5}$	99 $^{+34}_{-24}$	10 $^{+6}_{-4}$	0.88 $^{+0.18}_{-0.10}$	0.008 $^{+0.012}_{-0.006}$
PS1-11sm	55659.4 $^{+0.6}_{-0.9}$	-1.0 $^{+0.3}_{-0.3}$	-5.2 $^{+0.9}_{-1.0}$	-3.5 $^{+0.3}_{-0.3}$	-2.9 $^{+0.5}_{-0.5}$	-5.0 $^{+0.9}_{-1.0}$	1.0 $^{+0.3}_{-0.3}$	20 $^{+7}_{-6}$	96 $^{+36}_{-36}$	10 $^{+7}_{-4}$	1.71 $^{+0.22}_{-0.19}$	0.013 $^{+0.048}_{-0.010}$
PS1-11ua	55644.6 $^{+8.1}_{-9.9}$	-1.0 $^{+0.3}_{-0.3}$	-3.7 $^{+1.5}_{-1.5}$	-3.7 $^{+0.3}_{-1.0}$	-2.6 $^{+0.5}_{-0.8}$	-4.7 $^{+1.0}_{-1.2}$	1.0 $^{+0.3}_{-0.3}$	20 $^{+8}_{-5}$	72 $^{+47}_{-19}$	12 $^{+6}_{-5}$	3.51 $^{+1.14}_{-0.57}$	0.009 $^{+0.017}_{-0.007}$
PS1-11uv	55670.8 $^{+0.6}_{-1.4}$	-1.0 $^{+0.3}_{-0.3}$	-3.9 $^{+0.5}_{-0.3}$	-6.1 $^{+0.9}_{-1.0}$	-3.0 $^{+0.5}_{-0.5}$	-5.0 $^{+0.9}_{-1.0}$	1.0 $^{+0.3}_{-0.2}$	23 $^{+10}_{-6}$	99 $^{+37}_{-26}$	10 $^{+7}_{-4}$	0.34 $^{+0.02}_{-0.02}$	0.004 $^{+0.005}_{-0.003}$
PS1-11vn	55673.1 $^{+0.4}_{-0.5}$	-0.9 $^{+0.3}_{-0.3}$	-3.5 $^{+0.7}_{-1.2}$	-4.6 $^{+0.5}_{-0.8}$	-3.0 $^{+0.5}_{-0.5}$	-5.0 $^{+0.9}_{-0.9}$	1.1 $^{+0.4}_{-0.3}$	21 $^{+7}_{-6}$	99 $^{+34}_{-26}$	10 $^{+6}_{-4}$	1.24 $^{+0.25}_{-0.23}$	0.009 $^{+0.019}_{-0.007}$
PS1-11wj	55669.5 $^{+0.6}_{-0.9}$	-1.0 $^{+0.3}_{-0.3}$	-4.9 $^{+0.9}_{-1.0}$	-4.4 $^{+1.5}_{-1.5}$	-3.0 $^{+0.5}_{-0.6}$	-5.0 $^{+1.0}_{-1.0}$	1.0 $^{+0.4}_{-0.2}$	20 $^{+7}_{-5}$	100 $^{+35}_{-27}$	10 $^{+6}_{-4}$	0.78 $^{+0.16}_{-0.07}$	0.006 $^{+0.007}_{-0.005}$
PS1-11yh	55688.7 $^{+4.8}_{-3.5}$	-1.0 $^{+0.3}_{-0.3}$	-4.1 $^{+0.9}_{-0.8}$	-5.7 $^{+0.6}_{-0.6}$	-3.0 $^{+0.5}_{-0.5}$	-4.9 $^{+1.0}_{-1.0}$	1.0 $^{+0.4}_{-0.3}$	22 $^{+6}_{-5}$	99 $^{+36}_{-26}$	10 $^{+6}_{-4}$	2.16 $^{+0.18}_{-0.13}$	0.007 $^{+0.013}_{-0.005}$
PS1-11amh	55790.1 $^{+0.7}_{-1.2}$	-1.0 $^{+0.3}_{-0.3}$	-3.9 $^{+1.6}_{-1.5}$	-6.7 $^{+0.6}_{-0.8}$	-3.0 $^{+0.6}_{-0.5}$	-4.9 $^{+0.9}_{-1.0}$	1.0 $^{+0.3}_{-0.3}$	20 $^{+7}_{-5}$	98 $^{+36}_{-26}$	10 $^{+6}_{-4}$	2.35 $^{+0.07}_{-0.05}$	0.034 $^{+0.009}_{-0.010}$
PS1-11amv	55802.1 $^{+0.1}_{-0.9}$	-0.8 $^{+0.3}_{-0.3}$	-2.7 $^{+1.7}_{-1.4}$	-4.5 $^{+1.4}_{-1.4}$	-3.0 $^{+0.5}_{-0.5}$	-5.0 $^{+1.1}_{-1.0}$	1.1 $^{+0.3}_{-0.3}$	17 $^{+8}_{-8}$	100 $^{+38}_{-27}$	10 $^{+7}_{-4}$	0.82 $^{+2.05}_{-0.46}$	0.002 $^{+0.002}_{-0.001}$
PS1-11anm	55763.5 $^{+0.8}_{-0.9}$	-1.0 $^{+0.3}_{-0.3}$	-2.5 $^{+0.9}_{-1.3}$	-2.7 $^{+1.1}_{-1.0}$	-3.1 $^{+0.5}_{-0.4}$	-5.0 $^{+0.9}_{-1.1}$	1.0 $^{+0.4}_{-0.3}$	18 $^{+4}_{-3}$	99 $^{+39}_{-26}$	10 $^{+6}_{-4}$	0.23 $^{+0.17}_{-0.09}$	0.058 $^{+0.008}_{-0.006}$
PS1-11aof	55777.1 $^{+0.4}_{-0.3}$	-1.0 $^{+0.3}_{-0.3}$	-5.7 $^{+0.8}_{-1.0}$	-3.7 $^{+0.3}_{-0.5}$	-2.8 $^{+0.5}_{-0.5}$	-4.4 $^{+0.9}_{-0.9}$	1.0 $^{+0.3}_{-0.3}$	27 $^{+9}_{-11}$	90 $^{+45}_{-35}$	11 $^{+6}_{-5}$	2.06 $^{+0.14}_{-0.12}$	0.193 $^{+0.021}_{-0.019}$
PS1-11apd	55789.4 $^{+0.9}_{-0.8}$	-1.0 $^{+0.3}_{-0.3}$	-6.3 $^{+0.9}_{-0.9}$	-5.8 $^{+0.3}_{-0.4}$	-2.7 $^{+0.3}_{-0.3}$	-4.6 $^{+0.8}_{-1.0}$	1.0 $^{+0.3}_{-0.3}$	14 $^{+6}_{-4}$	72 $^{+5}_{-6}$	16 $^{+7}_{-5}$	0.82 $^{+0.03}_{-0.02}$	0.046 $^{+0.005}_{-0.005}$
PS1-11asz	55823.1 $^{+1.4}_{-0.3}$	-1.0 $^{+0.3}_{-0.3}$	-4.6 $^{+0.8}_{-1.1}$	-5.9 $^{+0.7}_{-0.9}$	-2.3 $^{+0.3}_{-0.3}$	-3.9 $^{+1.0}_{-0.9}$	1.1 $^{+0.3}_{-0.3}$	18 $^{+4}_{-4}$	70 $^{+5}_{-6}$	17 $^{+7}_{-8}$	0.91 $^{+0.07}_{-0.05}$	0.035 $^{+0.011}_{-0.013}$
PS1-11awd	55849.3 $^{+0.4}_{-1.1}$	-1.0 $^{+0.3}_{-0.3}$	-4.6 $^{+0.1}_{-0.1}$	-4.0 $^{+0.4}_{-0.7}$	-2.8 $^{+0.4}_{-0.4}$	-4.9 $^{+0.4}_{-0.8}$	1.0 $^{+0.3}_{-0.2}$	51 $^{+7}_{-9}$	57 $^{+52}_{-11}$	10 $^{+6}_{-4}$	0.75 $^{+0.07}_{-0.06}$	0.013 $^{+0.005}_{-0.005}$
PS1-11azd	55880.3 $^{+0.0}_{-0.1}$	-0.8 $^{+0.3}_{-0.3}$	-3.7 $^{+0.9}_{-1.3}$	-4.6 $^{+0.7}_{-1.2}$	-3.0 $^{+0.5}_{-0.5}$	-4.4 $^{+0.4}_{-0.6}$	1.1 $^{+0.4}_{-0.3}$	20 $^{+6}_{-5}$	97 $^{+36}_{-24}$	10 $^{+7}_{-4}$	0.79 $^{+0.34}_{-0.13}$	0.021 $^{+0.003}_{-0.003}$
PS1-11azi	55877.4 $^{+0.5}_{-0.5}$	-1.0 $^{+0.3}_{-0.3}$	-3.0 $^{+0.2}_{-0.2}$	-4.5 $^{+0.2}_{-0.2}$	-2.3 $^{+0.4}_{-0.4}$	-4.4 $^{+1.4}_{-0.7}$	1.0 $^{+0.4}_{-0.2}$	11 $^{+1}_{-1}$	49 $^{+3}_{-3}$	16 $^{+8}_{-6}$	3.69 $^{+0.13}_{-0.12}$	0.009 $^{+0.017}_{-0.007}$
PS1-11azt	55878.8 $^{+0.8}_{-0.4}$	-0.9 $^{+0.3}_{-0.3}$	-3.7 $^{+0.4}_{-0.4}$	-4.2 $^{+0.7}_{-1.4}$	-2.8 $^{+0.6}_{-0.6}$	-4.7 $^{+0.9}_{-1.2}$	1.1 $^{+0.5}_{-0.3}$	26 $^{+5}_{-6}$	99 $^{+35}_{-26}$	11 $^{+7}_{-4}$	1.89 $^{+0.25}_{-0.21}$	0.015 $^{+0.031}_{-0.011}$
PS1-11azv	55876.7 $^{+0.8}_{-1.2}$	-1.0 $^{+0.3}_{-0.3}$	-3.6 $^{+0.4}_{-0.3}$	-6.2 $^{+0.8}_{-1.0}$	-2.7 $^{+0.3}_{-0.3}$	-4.4 $^{+0.4}_{-0.3}$	1.0 $^{+0.4}_{-0.2}$	22 $^{+4}_{-5}$	50 $^{+6}_{-6}$	15 $^{+9}_{-4}$	0.81 $^{+0.07}_{-0.05}$	0.008 $^{+0.009}_{-0.005}$
PS1-11bbg	55888.2 $^{+2.2}_{-0.8}$	-1.0 $^{+0.3}_{-0.3}$	-3.5 $^{+0.1}_{-0.2}$	-3.8 $^{+0.1}_{-0.1}$	-2.5 $^{+0.4}_{-0.4}$	-5.0 $^{+1.0}_{-0.7}$	1.1 $^{+0.3}_{-0.3}$	29 $^{+2}_{-2}$	95 $^{+10}_{-9}$	14 $^{+7}_{-6}$	2.08 $^{+0.10}_{-0.09}$	0.011 $^{+0.016}_{-0.008}$
PS1-12c	55848.4 $^{+8.4}_{-9.3}$	-1.0 $^{+0.3}_{-0.3}$	-3.7 $^{+1.3}_{-1.7}$	-4.3 $^{+0.2}_{-0.2}$	-2.8 $^{+0.1}_{-0.1}$	-4.9 $^{+0.2}_{-0.2}$	1.0 $^{+0.4}_{-0.3}$	18 $^{+5}_{-4}$	76 $^{+11}_{-10}$	20 $^{+2}_{-4}$	0.45 $^{+0.09}_{-0.07}$	0.013 $^{+0.002}_{-0.001}$
PS1-12d	55899.5 $^{+5.4}_{-2.0}$	-1.0 $^{+0.3}_{-0.3}$	-3.0 $^{+0.6}_{-0.6}$	-6.6 $^{+2.8}_{-1.8}$	-3.7 $^{+1.3}_{-1.0}$	-3.1 $^{+0.4}_{-0.9}$	1.0 $^{+0.3}_{-0.2}$	18 $^{+35}_{-4}$	48 $^{+13}_{-5}$	45 $^{+10}_{-32}$	1.32 $^{+0.06}_{-0.04}$	0.008 $^{+0.010}_{-0.006}$
PS1-12y	55911.8 $^{+13.6}_{-19.7}$	-1.0 $^{+0.4}_{-0.3}$	-5.8 $^{+3.2}_{-1.4}$	-3.0 $^{+0.8}_{-0.8}$	-2.7 $^{+0.8}_{-0.7}$	-4.9 $^{+2.6}_{-1.2}$	1.0 $^{+0.4}_{-0.3}$	55 $^{+6}_{-18}$	62 $^{+50}_{-12}$	11 $^{+7}_{-5}$	2.25 $^{+1.29}_{-0.35}$	0.007 $^{+0.009}_{-0.005}$
PS1-12bt	55827.7 $^{+14.1}_{-13.1}$	-1.0 $^{+0.3}_{-0.3}$	-3.8 $^{+1.5}_{-1.4}$	-4.3 $^{+0.6}_{-0.6}$	-3.2 $^{+0.5}_{-0.5}$	-4.4 $^{+0.1}_{-0.6}$	1.0 $^{+0.4}_{-0.3}$	19 $^{+6}_{-5}$	85 $^{+56}_{-28}$	9 $^{+5}_{-3}$	0.30 $^{+0.59}_{-0.10}$	0.001 $^{+0.001}_{-0.001}$
PS1-12rk	55996.2 $^{+0.5}_{-0.6}$	-1.0 $^{+0.3}_{-0.3}$	-4.1 $$									

Table 7.3—Continued

SN	t_0	$\log \alpha$	$\log \beta_1$	$\log \beta_2$	$\log \beta_{dN}$	$\log \beta_{dC}$	t_1	t_p	t_2	t_d	M_p	V
PS1-12zd	56016.1 ^{+0.1} _{-0.5}	-0.9 ^{+0.3} _{-0.3}	-3.8 ^{+1.5} _{-1.9}	-3.7 ^{+0.4} _{-0.4}	-3.0 ^{+0.5} _{-0.5}	-4.7 ^{+0.9} _{-1.0}	1.0 ^{+0.4} _{-0.2}	13 ⁺³ ₋₂	103 ⁺³³ ₋₂₇	11 ⁺⁶ ₋₄	1.43 ^{+0.12} _{-0.10}	0.050 ^{+0.011} _{-0.009}
PS1-12zp	56019.4 ^{+0.0} _{-0.1}	-1.0 ^{+0.3} _{-0.3}	-5.0 ^{+0.7} _{-0.6}	-5.7 ^{+1.6} _{-1.2}	-2.9 ^{+0.5} _{-0.6}	-3.6 ^{+0.6} _{-0.7}	1.0 ^{+0.4} _{-0.3}	27 ⁺¹⁰ ₋₉	96 ⁺³² ₋₂₃	11 ⁺⁷ ₋₄	0.93 ^{+0.04} _{-0.04}	0.005 ^{+0.007} _{-0.003}
PS1-12auw	56080.7 ^{+0.4} _{-0.5}	-1.0 ^{+0.3} _{-0.3}	-4.0 ^{+0.3} _{-0.4}	-5.2 ^{+0.7} _{-1.0}	-2.9 ^{+0.5} _{-0.5}	-3.7 ^{+0.5} _{-0.3}	1.0 ^{+0.3} _{-0.2}	18 ⁺⁶ ₋₆	96 ⁺³⁴ ₋₂₄	10 ⁺⁷ ₋₄	1.38 ^{+0.20} _{-0.13}	0.007 ^{+0.005} _{-0.005}
PS1-12bku	56160.7 ^{+0.2} _{-0.1}	-1.0 ^{+0.3} _{-0.3}	-3.2 ^{+0.1} _{-0.1}	-5.3 ^{+0.3} _{-0.4}	-2.3 ^{+0.3} _{-0.3}	-4.8 ^{+1.3} _{-1.1}	1.0 ^{+0.3} _{-0.3}	32 ⁺¹ ₋₁	59 ⁺⁶ ₋₈	15 ⁺⁷ ₋₅	2.33 ^{+0.06} _{-0.05}	0.006 ^{+0.007} _{-0.005}
PS1-12bmp	56201.1 ^{+0.3} _{-0.4}	-1.0 ^{+0.3} _{-0.3}	-4.6 ^{+0.1} _{-0.1}	-3.4 ^{+0.1} _{-0.1}	-3.0 ^{+0.6} _{-0.5}	-4.6 ^{+0.7} _{-0.9}	1.0 ^{+0.4} _{-0.3}	64 ⁺² ₋₂	108 ⁺³⁷ ₋₃₄	10 ⁺⁸ ₋₄	1.02 ^{+0.04} _{-0.04}	0.017 ^{+0.006} _{-0.006}
PS1-12blz	56201.6 ^{+0.8} _{-1.1}	-1.0 ^{+0.3} _{-0.3}	-3.0 ^{+0.2} _{-0.2}	-4.6 ^{+0.1} _{-0.1}	-2.4 ^{+0.3} _{-0.3}	-4.0 ^{+0.2} _{-0.2}	0.9 ^{+0.3} _{-0.2}	8 ⁺² ₋₁	51 ⁺² ₋₂	11 ⁺⁵ ₋₃	2.05 ^{+0.03} _{-0.03}	0.017 ^{+0.007} _{-0.008}
PS1-12boi	56201.7 ^{+0.7} _{-0.9}	-1.0 ^{+0.3} _{-0.3}	-3.1 ^{+0.3} _{-0.5}	-3.5 ^{+0.4} _{-0.4}	-3.0 ^{+0.5} _{-0.5}	-5.0 ^{+0.9} _{-1.0}	1.0 ^{+0.4} _{-0.3}	12 ⁺² ₋₂	99 ⁺³⁵ ₋₂₄	10 ⁺⁷ ₋₄	2.17 ^{+0.15} _{-0.14}	0.008 ^{+0.018} _{-0.006}
PS1-12bza	56228.6 ^{+0.6} _{-0.7}	-1.0 ^{+0.3} _{-0.3}	-6.4 ^{+0.6} _{-1.0}	-6.2 ^{+0.4} _{-0.7}	-2.8 ^{+0.1} _{-0.1}	-4.7 ^{+0.3} _{-0.3}	1.0 ^{+0.3} _{-0.2}	16 ⁺⁶ ₋₄	52 ⁺⁶ ₋₄	27 ⁺³ ₋₄	1.28 ^{+0.03} _{-0.03}	0.014 ^{+0.011} _{-0.010}
PS1-12cey	56237.2 ^{+0.2} _{-0.7}	-0.9 ^{+0.3} _{-0.3}	-2.9 ^{+0.3} _{-2.0}	-4.1 ^{+0.3} _{-0.3}	-2.5 ^{+0.3} _{-0.3}	-4.4 ^{+0.4} _{-0.3}	1.1 ^{+0.3} _{-0.2}	12 ⁺³ ₋₂	46 ⁺¹⁰ ₋₃	12 ⁺⁶ ₋₄	2.19 ^{+0.16} _{-0.14}	0.006 ^{+0.007} _{-0.004}
PS1-13hp	56323.4 ^{+0.4} _{-0.5}	-1.0 ^{+0.3} _{-0.3}	-4.3 ^{+0.2} _{-0.2}	-3.5 ^{+0.2} _{-0.2}	-3.0 ^{+0.4} _{-0.5}	-5.2 ^{+1.0} _{-0.9}	1.0 ^{+0.4} _{-0.3}	51 ⁺³ ₋₃	96 ⁺³¹ ₋₂₄	10 ⁺⁶ ₋₄	2.59 ^{+0.18} _{-0.16}	0.119 ^{+0.026} _{-0.022}
PS1-13vs	56342.7 ^{+0.7} _{-0.8}	-1.0 ^{+0.3} _{-0.3}	-4.2 ^{+0.7} _{-1.1}	-5.7 ^{+0.8} _{-0.9}	-2.9 ^{+0.5} _{-0.5}	-4.4 ^{+0.7} _{-0.7}	1.0 ^{+0.3} _{-0.2}	22 ⁺⁸ ₋₅	96 ⁺³⁴ ₋₂₆	12 ⁺⁷ ₋₅	0.79 ^{+0.09} _{-0.08}	0.110 ^{+0.015} _{-0.013}
PS1-13wr	56300.4 ^{+2.3} _{-2.4}	-1.0 ^{+0.3} _{-0.3}	-3.8 ^{+1.6} _{-1.3}	-5.2 ^{+0.2} _{-0.3}	-2.9 ^{+0.2} _{-0.2}	-4.6 ^{+0.4} _{-0.7}	1.0 ^{+0.3} _{-0.3}	20 ⁺⁸ ₋₅	106 ⁺⁶ ₋₈	22 ⁺⁶ ₋₆	0.89 ^{+0.11} _{-0.09}	0.017 ^{+0.005} _{-0.005}
PS1-13alz	56397.2 ^{+0.1} _{-0.8}	-0.7 ^{+0.5} _{-0.3}	-4.0 ^{+0.3} _{-0.3}	-4.5 ^{+1.0} _{-1.1}	-2.8 ^{+0.6} _{-0.5}	-3.9 ^{+0.5} _{-0.5}	1.2 ^{+1.2} _{-0.4}	16 ⁺³ ₋₄	96 ⁺²⁹ ₋₂₄	11 ⁺⁸ ₋₄	2.10 ^{+0.08} _{-0.07}	0.012 ^{+0.009} _{-0.008}
PS1-13arp	56396.6 ^{+0.5} _{-0.5}	-1.0 ^{+0.3} _{-0.3}	-3.2 ^{+0.4} _{-0.5}	-6.1 ^{+0.8} _{-0.9}	-3.0 ^{+0.5} _{-0.5}	-4.9 ^{+1.0} _{-1.0}	1.0 ^{+0.4} _{-0.3}	21 ⁺⁵ ₋₄	103 ⁺³³ ₋₃₀	10 ⁺⁷ ₋₄	1.06 ^{+0.09} _{-0.09}	0.084 ^{+0.021} _{-0.019}
PS1-13ave	56404.4 ^{+0.1} _{-0.2}	-0.9 ^{+0.3} _{-0.3}	-3.7 ^{+0.3} _{-0.3}	-4.4 ^{+0.7} _{-1.8}	-3.2 ^{+0.5} _{-0.2}	-4.8 ^{+1.0} _{-1.1}	1.2 ^{+0.4} _{-0.3}	34 ⁺⁹ ₋₁₀	42 ⁺⁷² ₋₉	15 ⁺⁸ ₋₇	6.54 ^{+0.56} _{-0.59}	0.077 ^{+0.046} _{-0.069}
PS1-13atm	56352.8 ^{+0.9} _{-0.9}	-1.0 ^{+0.3} _{-0.3}	-0.8 ^{+0.5} _{-0.5}	-5.3 ^{+0.9} _{-1.2}	-3.0 ^{+0.5} _{-0.5}	-5.0 ^{+1.0} _{-1.0}	1.0 ^{+0.4} _{-0.3}	38 ⁺² ₋₁	99 ⁺³⁶ ₋₂₆	10 ⁺⁷ ₋₄	3.62 ^{+0.42} _{-0.40}	0.011 ^{+0.029} _{-0.007}
PS1-13bvj	56451.6 ^{+0.5} _{-0.7}	-1.0 ^{+0.3} _{-0.3}	-5.3 ^{+0.8} _{-0.9}	-5.5 ^{+0.4} _{-0.6}	-2.2 ^{+0.3} _{-0.4}	-4.4 ^{+1.3} _{-1.1}	1.0 ^{+0.3} _{-0.2}	16 ⁺⁶ ₋₄	52 ⁺⁵ ₋₇	15 ⁺⁷ ₋₅	1.76 ^{+0.14} _{-0.11}	0.098 ^{+0.029} _{-0.028}
PS1-13cqb	56503.7 ^{+1.0} _{-1.0}	-1.0 ^{+0.3} _{-0.3}	-3.6 ^{+0.7} _{-0.8}	-5.0 ^{+0.4} _{-0.7}	-3.0 ^{+0.5} _{-0.5}	-5.0 ^{+1.0} _{-1.0}	1.0 ^{+0.4} _{-0.3}	20 ⁺⁶ ₋₄	86 ⁺³⁷ ₋₁₆	10 ⁺⁶ ₋₄	0.78 ^{+0.14} _{-0.11}	0.138 ^{+0.021} _{-0.020}
PS1-13cua	56544.8 ^{+0.2} _{-0.2}	-1.0 ^{+0.3} _{-0.3}	-4.0 ^{+0.1} _{-0.1}	-3.8 ^{+0.1} _{-0.1}	-3.0 ^{+0.5} _{-0.5}	-5.0 ^{+0.9} _{-0.9}	1.0 ^{+0.4} _{-0.3}	54 ⁺² ₋₂	99 ⁺³⁹ ₋₂₅	10 ⁺⁶ ₋₄	1.12 ^{+0.04} _{-0.04}	0.012 ^{+0.009} _{-0.008}
PS1-13eck	56613.7 ^{+0.3} _{-0.4}	-1.0 ^{+0.3} _{-0.3}	-4.8 ^{+0.3} _{-0.3}	-2.7 ^{+0.2} _{-0.2}	-3.0 ^{+0.4} _{-0.5}	-5.0 ^{+1.0} _{-1.0}	1.0 ^{+0.3} _{-0.3}	40 ⁺¹ ₋₁	101 ⁺³⁴ ₋₂₇	10 ⁺⁷ ₋₄	1.46 ^{+0.07} _{-0.07}	0.029 ^{+0.020} _{-0.020}
PS1-13esn	56637.0 ^{+0.9} _{-1.0}	-1.0 ^{+0.3} _{-0.3}	-4.4 ^{+1.2} _{-1.3}	-4.8 ^{+1.2} _{-1.4}	-3.0 ^{+0.5} _{-0.5}	-5.0 ^{+1.0} _{-1.0}	1.0 ^{+0.4} _{-0.3}	19 ⁺⁶ ₋₄	99 ⁺³⁴ ₋₂₅	10 ⁺⁶ ₋₄	1.13 ^{+0.07} _{-0.06}	0.006 ^{+0.008} _{-0.004}
<i>y</i> -band												
PS1-10a	55200.9 ^{+0.7} _{-0.8}	-1.0 ^{+0.3} _{-0.3}	-4.1 ^{+2.1} _{-1.9}	-4.9 ^{+1.5} _{-1.6}	-3.0 ^{+0.6} _{-0.5}	-5.0 ^{+1.0} _{-1.0}	1.0 ^{+0.3} _{-0.2}	30 ⁺¹⁰ ₋₇	101 ⁺³³ ₋₂₇	10 ⁺⁶ ₋₄	0.99 ^{+1.00} _{-0.52}	0.010 ^{+0.020} _{-0.007}
PS1-10b	55203.9 ^{+0.4} _{-0.5}	-1.0 ^{+0.3} _{-0.3}	-4.0 ^{+1.9} _{-2.2}	-4.8 ^{+1.6} _{-1.6}	-3.0 ^{+0.5} _{-0.5}	-4.9 ^{+1.1} _{-1.0}	1.0 ^{+0.3} _{-0.3}	30 ⁺⁹ ₋₉	99 ⁺³⁷ ₋₂₆	10 ⁺⁷ ₋₄	0.97 ^{+1.10} _{-0.48}	0.010 ^{+0.028} _{-0.007}
PS1-10q	55200.5 ^{+0.7} _{-0.8}	-1.0 ^{+0.3} _{-0.3}	-3.9 ^{+1.8} _{-2.1}	-4.9 ^{+1.6} _{-1.5}	-3.0 ^{+0.5} _{-0.5}	-5.0 ^{+1.0} _{-0.9}	1.0 ^{+0.3} _{-0.3}	30 ⁺¹⁰ ₋₇	100 ⁺³² ₋₂₅	10 ⁺⁷ ₋₄	0.99 ^{+1.12} _{-0.50}	0.009 ^{+0.031} _{-0.007}
PS1-10t	55205.2 ^{+0.9} _{-0.9}	-1.0 ^{+0.3} _{-0.3}	-4.1 ^{+1.9} _{-1.9}	-4.8 ^{+1.5} _{-1.5}	-3.0 ^{+0.5} _{-0.5}	-5.1 ^{+1.0} _{-1.0}	1.0 ^{+0.3} _{-0.3}	30 ⁺¹⁰ ₋₈	99 ⁺³⁴ ₋₂₄	10 ⁺⁶ ₋₄	1.00 ^{+1.02} _{-0.50}	0.010 ^{+0.025} _{-0.007}
PS1-10ae	55239.3 ^{+0.1} _{-0.1}	-1.0 ^{+0.3} _{-0.3}	-4.0 ^{+1.9} _{-2.1}	-4.9 ^{+1.6} _{-1.5}	-3.0 ^{+0.4} _{-0.4}	-5.1 ^{+1.1} _{-1.0}	1.0 ^{+0.4} _{-0.3}	30 ⁺¹² ₋₈	100 ⁺³⁴ ₋₂₆	10 ⁺⁶ ₋₄	1.02 ^{+0.94} _{-0.51}	0.010 ^{+0.033} _{-0.008}
PS1-10jr	55359.1 ^{+0.4} _{-0.5}	-1.0 ^{+0.3} _{-0.3}	-4.1 ^{+2.0} _{-1.8}	-5.0 ^{+1.4} _{-1.5}	-3.0 ^{+0.5} _{-0.5}	-5.0 ^{+1.0} _{-1.0}	1.0 ^{+0.3} _{-0.3}	31 ⁺¹¹ ₋₈	99 ⁺³⁶ ₋₂₆	10 ⁺⁶ ₋₄	1.02 ^{+1.16} _{-0.51}	0.010 ^{+0.023} _{-0.007}
PS1-10lv	55380.5 ^{+2.0} _{-4.3}	-1.0 ^{+0.3} _{-0.3}	-4.0 ^{+1.8} _{-2.1}	-4.9 ^{+1.5} _{-1.4}	-3.0 ^{+0.5} _{-0.5}	-5.1 ^{+1.1} _{-1.0}	1.0 ^{+0.3} _{-0.3}	31 ⁺⁹ ₋₈	100 ⁺³⁴ ₋₂₅	10 ⁺⁷ ₋₄	1.02 ^{+0.89} _{-0.47}	0.010 ^{+0.029} _{-0.008}
PS1-10mb	55374.3 ^{+0.9} _{-0.9}	-1.0 ^{+0.3} _{-0.3}	-4.1 ^{+1.9} _{-2.0}	-5.0 ^{+1.6} _{-1.5}	-3.0 ^{+0.5} _{-0.5}	-5.0 ^{+1.0} _{-1.0}	1.0 ^{+0.3} _{-0.2}	30 ⁺¹¹ ₋₈	101 ⁺³² ₋₂₇	10 ⁺⁶ ₋₄	1.05 ^{+1.06} _{-0.55}	0.010 ^{+0.025} _{-0.007}
PS1-10zu	55354.3 ^{+25.5} _{-5.5}	-1.0 ^{+0.3} _{-0.3}	-4.0 ^{+2.0} _{-2.1}	-4.9 ^{+1.5} _{-1.4}	-3.0 ^{+0.4} _{-0.4}	-5.0 ^{+1.0} _{-0.9}	1.0 ^{+0.4} _{-0.3}	30 ⁺¹⁰ ₋₈	103 ⁺³⁹ ₋₂₉	10 ⁺⁷ ₋₄	0.99 ^{+0.91} _{-0.42}	0.011 ^{+0.034} _{-0.008}
PS1-10abd	55387.6 ^{+3.8} _{-4.0}	-1.0 ^{+0.3} _{-0.3}	-4.0 ^{+1.9} _{-2.0}	-4.9 ^{+1.4} _{-1.5}	-3.0 ^{+0.6} _{-0.5}	-4.9 ^{+0.8} _{-1.0}	1.0 ^{+0.3} _{-0.3}	30 ⁺¹⁰ ₋₈	98 ⁺³⁷ ₋₂₅	10 ⁺⁶ ₋₄	0.99 ^{+1.02} _{-0.51}	0.010 ^{+0.026} _{-0.007}
PS1-10agh	55434.0 ^{+0.4} _{-0.5}	-1.0 ^{+0.3} _{-0.3}	-4.1 ^{+2.0} _{-2.0}	-4.9 ^{+1.5} _{-1.7}	-3.0 ^{+0.5} _{-0.5}	-5.0 ^{+1.0} _{-0.9}	1.0 ^{+0.4} _{-0.3}	30 ⁺¹¹ ₋₇	101 ⁺⁴¹ ₋₂₉	10 ⁺⁷ ₋₄	1.02 ^{+0.98} _{-0.53}	0.010 ^{+0.029} _{-0.008}
PS1-10awc	55454.2 ^{+0.2} _{-0.3}	-1.0 ^{+0.3} _{-0.3}	-4.0 ^{+1.8} _{-2.1}	-4.9 ^{+1.4} _{-1.5}	-3.0 ^{+0.5} _{-0.5}	-5.0 ^{+1.0} _{-1.0}	1.0 ^{+0.4} _{-0.3}	30 ⁺¹⁰ ₋₈	99 ⁺³⁵ ₋₂₆	10 ⁺⁶ ₋₄	0.98 ^{+0.96} _{-0.49}	0.010 ^{+0.029} _{-0.007}
PS1-10biu	55495.0 ^{+0.6} _{-0.7}	-1.0 ^{+0.3} _{-0.3}	-4.1 ^{+1.9} _{-2.1}	-4.8 ^{+1.5} _{-1.5}	-3.0 ^{+0.5} _{-0.5}	-5.0 ^{+0.9} _{-0.9}	1.0 ^{+0.4} _{-0.3}	30 ⁺¹¹ ₋₈	100 ⁺³² ₋₂₅	10 ⁺⁶ ₋₄	1.04 ^{+0.93} _{-0.53}	0.011 ^{+0.040} _{-0.009}
PS1-10blk	55508.3 ^{+0.1} _{-0.2}	-1.0 ^{+0.3} _{-0.3}	-3.7 ^{+1.8} _{-2.2}	-5.0 ^{+1.6} _{-1.4}	-3.0 ^{+0.5} _{-0.5}	-5.0 ^{+1.0} _{-1.1}	1.0 ^{+0.4} _{-0.2}	30 ⁺⁹ ₋₇	100 ⁺²⁹ ₋₂₄	10 ⁺⁸ ₋₄	1.01 ^{+1.04} _{-0.50}	0.010 ^{+0.027} _{-0.007}
PS1-11u	55497.2 ^{+21.0} _{-13.0}	-1.0 ^{+0.3} _{-0.3}	-4.0 ^{+2.0} _{-2.0}	-4.9 ^{+1.6} _{-1.5}	-3.0 ^{+0.5} _{-0.5}	-5.0 ^{+0.9} _{-0.9}	1.0 ^{+0.3} _{-0.2}	30 ⁺¹¹ ₋₇	98 ⁺³² ₋₂₄	10 ⁺⁶ ₋₄	0.95 ^{+1.05} _{-0.47}	0.010 ^{+0.030} _{-0.007}
PS1-11z	55539.2 ^{+7.6} _{-15.0}	-1.0 ^{+0.3} _{-0.3}	-4.0 ^{+2.0} _{-2.1}	-5.0 ^{+1.4} _{-1.3}	-3.0 ^{+0.5} _{-0.5}	-4.9 ^{+1.0} _{-1.1}	1.0 ^{+0.3} _{-0.3}	29 ⁺¹⁰ ₋₇	98 ⁺³⁶ ₋₂₄	10 ⁺⁷ ₋₄	1.00 ^{+1.00} _{-0.50}	0.010 ^{+0.027} _{-0.007}
PS1-11ai	55496.2 ^{+13.3} _{-10.9}	-1.0 ^{+0.3} _{-0.3}	-4.0 ^{+1.7} _{-2.0}	-4.9 ^{+1.6} _{-1.6}	-3.0 ^{+0.5} _{-0.6}	-4.9 ^{+0.9} _{-1.0}	1.0 ^{+0.4} _{-0.3}	30 ⁺⁹ ₋₈	100 ⁺³⁶ ₋₂₇	10 ⁺⁶ ₋₄	1.00 ^{+0.97} _{-0.47}	0.010 ^{+0.024} _{-0.008}
PS1-11ak	55592.8 ^{+0.9} _{-0.9}	-1.0 ^{+0.3} _{-0.3}	-4.1 ^{+1.9} _{-2.0}	-4.9 ^{+1.5} _{-1.5}	-3.0 ^{+0.5} _{-0.5}	-5.0 ^{+1.1} _{-1.0}	1.0 ^{+0.3} _{-0.3}	30 ⁺¹⁰ ₋₈	98 ⁺³⁶ ₋₂₄	10 ⁺⁶ ₋₄	1.01 ^{+0.97} _{-0.52}	0.010 ^{+0.026} _{-0.007}
PS1-11bl	55568.0 ^{+0.7} _{-0.7}	-1.0 ^{+0.3} _{-0.3}	-4.2 ^{+1.7} _{-1.8}	-4.8 ^{+1.3} _{-1.4}	-3.0 ^{+0.5} _{-0.5}	-5.0 ^{+1.0} _{-1.0}	1.0 ^{+0.3} _{-0.}					

Table 7.3—Continued

SN	t_0	$\log \alpha$	$\log \beta_1$	$\log \beta_2$	$\log \beta_{dN}$	$\log \beta_{dC}$	t_1	t_p	t_2	t_d	M_p	V
PS1-11bo	55574.2 ^{+0.8} _{-1.1}	-1.0 ^{+0.3} _{-0.3}	-4.1 ^{+1.9} _{-2.0}	-4.9 ^{+1.6} _{-1.6}	-3.0 ^{+0.5} _{-0.5}	-4.9 ^{+1.0} _{-1.0}	1.0 ^{+0.3} _{-0.2}	30 ⁺¹⁰ ₋₈	101 ⁺³² ₋₂₇	10 ⁺⁷ ₋₄	1.02 ^{+0.91} _{-0.51}	0.010 ^{+0.028} _{-0.008}
PS1-11fl	55568.9 ^{+4.7} _{-21.4}	-1.0 ^{+0.3} _{-0.3}	-4.1 ^{+2.2} _{-2.0}	-4.9 ^{+1.4} _{-1.5}	-3.0 ^{+0.5} _{-0.5}	-4.9 ^{+1.0} _{-1.0}	1.0 ^{+0.3} _{-0.2}	30 ⁺¹¹ ₋₇	101 ⁺³⁵ ₋₂₆	10 ⁺⁶ ₋₄	1.01 ^{+1.05} _{-0.52}	0.010 ^{+0.038} _{-0.007}
PS1-11jg	55497.8 ^{+10.6} _{-10.0}	-1.0 ^{+0.3} _{-0.3}	-4.1 ^{+1.7} _{-2.0}	-4.8 ^{+1.5} _{-1.6}	-3.0 ^{+0.5} _{-0.5}	-5.0 ^{+1.0} _{-1.0}	1.0 ^{+0.3} _{-0.2}	30 ⁺¹⁰ ₋₈	99 ⁺³⁵ ₋₂₅	10 ⁺⁷ ₋₄	1.00 ^{+1.11} _{-0.51}	0.010 ^{+0.028} _{-0.008}
PS1-11kf	55580.9 ^{+6.3} _{-8.3}	-1.0 ^{+0.3} _{-0.3}	-4.0 ^{+2.0} _{-1.9}	-4.9 ^{+1.5} _{-1.5}	-3.0 ^{+0.5} _{-0.5}	-5.1 ^{+1.1} _{-0.9}	1.0 ^{+0.3} _{-0.3}	30 ⁺¹¹ ₋₇	101 ⁺³⁷ ₋₂₉	10 ⁺⁶ ₋₄	1.00 ^{+1.05} _{-0.53}	0.009 ^{+0.025} _{-0.007}
PS1-11li	55600.6 ^{+0.7} _{-0.8}	-1.0 ^{+0.3} _{-0.3}	-4.1 ^{+1.8} _{-1.9}	-4.9 ^{+1.4} _{-1.5}	-3.0 ^{+0.5} _{-0.6}	-5.0 ^{+0.9} _{-0.9}	1.0 ^{+0.4} _{-0.3}	30 ⁺¹⁰ ₋₈	99 ⁺⁴⁰ ₋₂₇	10 ⁺⁶ ₋₄	1.01 ^{+1.10} _{-0.56}	0.010 ^{+0.029} _{-0.008}
PS1-11lj	55603.4 ^{+0.7} _{-0.6}	-1.0 ^{+0.3} _{-0.3}	-4.2 ^{+2.1} _{-1.7}	-5.0 ^{+1.4} _{-1.4}	-3.0 ^{+0.5} _{-0.5}	-5.0 ^{+0.9} _{-1.0}	1.0 ^{+0.3} _{-0.3}	30 ⁺¹¹ ₋₈	99 ⁺³⁵ ₋₂₄	10 ⁺⁷ ₋₄	0.97 ^{+0.95} _{-0.53}	0.010 ^{+0.027} _{-0.007}
PS1-11lr	55611.5 ^{+0.5} _{-0.5}	-1.0 ^{+0.3} _{-0.3}	-4.3 ^{+1.9} _{-1.8}	-4.8 ^{+1.4} _{-1.6}	-3.0 ^{+0.5} _{-0.5}	-4.9 ^{+1.0} _{-1.0}	1.0 ^{+0.3} _{-0.3}	29 ⁺¹⁰ ₋₇	98 ⁺³⁵ ₋₂₇	10 ⁺⁶ ₋₄	1.01 ^{+0.87} _{-0.50}	0.010 ^{+0.032} _{-0.007}
PS1-11lq	55612.4 ^{+0.7} _{-0.7}	-1.0 ^{+0.3} _{-0.3}	-4.0 ^{+2.1} _{-2.0}	-4.9 ^{+1.7} _{-1.5}	-3.0 ^{+0.5} _{-0.5}	-5.0 ^{+1.0} _{-1.0}	1.0 ^{+0.3} _{-0.3}	30 ⁺¹⁰ ₋₈	99 ⁺³¹ ₋₂₄	10 ⁺⁶ ₋₄	1.05 ^{+1.10} _{-0.53}	0.010 ^{+0.026} _{-0.007}
PS1-11md	55616.3 ^{+4.7} _{-5.6}	-1.0 ^{+0.3} _{-0.3}	-4.0 ^{+1.8} _{-1.9}	-4.8 ^{+1.5} _{-1.5}	-3.0 ^{+0.5} _{-0.5}	-5.1 ^{+1.0} _{-1.0}	1.0 ^{+0.4} _{-0.2}	30 ⁺¹⁰ ₋₈	99 ⁺³⁸ ₋₂₆	10 ⁺⁶ ₋₄	1.04 ^{+1.11} _{-0.52}	0.010 ^{+0.024} _{-0.007}
PS1-11pf	55633.2 ^{+0.2} _{-0.3}	-1.0 ^{+0.3} _{-0.3}	-4.0 ^{+1.8} _{-2.0}	-4.9 ^{+1.6} _{-1.6}	-3.0 ^{+0.5} _{-0.5}	-5.0 ^{+0.9} _{-1.0}	1.0 ^{+0.3} _{-0.3}	30 ⁺¹⁰ ₋₈	100 ⁺³³ ₋₂₄	10 ⁺⁶ ₋₄	0.96 ^{+0.93} _{-0.49}	0.010 ^{+0.023} _{-0.007}
PS1-11qe	55644.3 ^{+0.5} _{-1.2}	-1.0 ^{+0.3} _{-0.3}	-4.1 ^{+1.8} _{-1.8}	-4.8 ^{+1.6} _{-1.6}	-3.0 ^{+0.5} _{-0.5}	-5.1 ^{+1.0} _{-1.0}	1.0 ^{+0.3} _{-0.3}	30 ⁺¹⁰ ₋₉	99 ⁺³⁶ ₋₂₆	10 ⁺⁷ ₋₄	0.99 ^{+1.19} _{-0.48}	0.010 ^{+0.027} _{-0.007}
PS1-11si	55671.0 ^{+0.6} _{-0.7}	-1.0 ^{+0.3} _{-0.3}	-4.0 ^{+2.0} _{-2.1}	-4.9 ^{+1.4} _{-1.6}	-3.0 ^{+0.5} _{-0.5}	-4.9 ^{+0.9} _{-1.1}	1.0 ^{+0.3} _{-0.2}	30 ⁺¹⁰ ₋₇	102 ⁺³⁵ ₋₂₈	10 ⁺⁷ ₋₄	1.03 ^{+1.04} _{-0.51}	0.009 ^{+0.029} _{-0.007}
PS1-11sm	55659.4 ^{+0.6} _{-0.9}	-1.0 ^{+0.3} _{-0.3}	-4.0 ^{+1.8} _{-2.0}	-4.9 ^{+1.5} _{-1.5}	-3.0 ^{+0.5} _{-0.5}	-5.1 ^{+1.0} _{-0.9}	1.0 ^{+0.3} _{-0.3}	30 ⁺¹⁰ ₋₈	100 ⁺³⁴ ₋₂₄	10 ⁺⁶ ₋₄	1.02 ^{+1.05} _{-0.50}	0.010 ^{+0.021} _{-0.007}
PS1-11ua	55644.6 ^{+8.1} _{-9.9}	-1.0 ^{+0.3} _{-0.3}	-3.8 ^{+1.8} _{-2.2}	-4.9 ^{+1.3} _{-1.4}	-3.0 ^{+0.5} _{-0.5}	-5.0 ^{+1.1} _{-0.9}	1.0 ^{+0.3} _{-0.3}	29 ⁺¹¹ ₋₇	100 ⁺³⁴ ₋₂₅	10 ⁺⁶ ₋₄	1.02 ^{+0.95} _{-0.50}	0.009 ^{+0.027} _{-0.007}
PS1-11uv	55670.8 ^{+0.6} _{-1.4}	-1.0 ^{+0.3} _{-0.3}	-4.1 ^{+1.7} _{-1.8}	-4.8 ^{+1.6} _{-1.6}	-3.0 ^{+0.5} _{-0.5}	-5.0 ^{+1.0} _{-1.0}	1.0 ^{+0.4} _{-0.3}	30 ⁺¹¹ ₋₈	100 ⁺³⁴ ₋₂₆	10 ⁺⁶ ₋₄	1.02 ^{+1.02} _{-0.49}	0.010 ^{+0.035} _{-0.008}
PS1-11vn	55673.1 ^{+0.4} _{-0.5}	-1.0 ^{+0.3} _{-0.3}	-4.0 ^{+2.0} _{-2.1}	-4.9 ^{+1.7} _{-1.7}	-3.0 ^{+0.5} _{-0.5}	-5.0 ^{+1.0} _{-1.0}	1.0 ^{+0.3} _{-0.2}	31 ⁺¹⁰ ₋₉	100 ⁺³⁵ ₋₂₅	10 ⁺⁷ ₋₄	1.03 ^{+0.99} _{-0.54}	0.010 ^{+0.034} _{-0.007}
PS1-11wj	55669.5 ^{+0.6} _{-0.9}	-1.0 ^{+0.3} _{-0.3}	-4.1 ^{+2.0} _{-1.9}	-4.9 ^{+1.5} _{-1.6}	-3.0 ^{+0.5} _{-0.5}	-5.0 ^{+1.1} _{-1.0}	1.0 ^{+0.4} _{-0.3}	30 ⁺¹¹ ₋₇	100 ⁺³³ ₋₂₆	11 ⁺⁶ ₋₄	0.99 ^{+1.03} _{-0.49}	0.010 ^{+0.030} _{-0.007}
PS1-11yh	55688.7 ^{+4.8} _{-3.5}	-1.0 ^{+0.3} _{-0.3}	-3.8 ^{+2.0} _{-2.1}	-4.9 ^{+1.5} _{-1.5}	-3.0 ^{+0.5} _{-0.4}	-5.0 ^{+1.0} _{-1.0}	1.0 ^{+0.4} _{-0.3}	30 ⁺¹¹ ₋₈	101 ⁺³² ₋₂₇	10 ⁺⁷ ₋₄	0.95 ^{+1.00} _{-0.49}	0.010 ^{+0.032} _{-0.007}
PS1-11amh	55790.1 ^{+0.7} _{-1.2}	-1.0 ^{+0.3} _{-0.3}	-5.4 ^{+0.8} _{-1.2}	-6.8 ^{+0.9} _{-1.1}	-3.0 ^{+0.5} _{-0.5}	-5.0 ^{+1.0} _{-1.0}	1.0 ^{+0.4} _{-0.2}	34 ⁺¹³ ₋₉	99 ⁺³⁴ ₋₂₅	10 ⁺⁷ ₋₄	2.11 ^{+0.08} _{-0.08}	0.010 ^{+0.019} _{-0.007}
PS1-11amv	55802.1 ^{+0.1} _{-0.9}	-1.0 ^{+0.3} _{-0.3}	-4.3 ^{+1.4} _{-1.8}	-5.0 ^{+1.4} _{-1.4}	-3.0 ^{+0.5} _{-0.5}	-5.0 ^{+1.1} _{-0.9}	1.0 ^{+0.4} _{-0.3}	28 ⁺¹¹ ₋₇	100 ⁺³⁵ ₋₂₇	10 ⁺⁷ ₋₄	0.78 ^{+0.12} _{-0.04}	0.004 ^{+0.005} _{-0.003}
PS1-11anm	55763.5 ^{+0.8} _{-0.9}	-1.0 ^{+0.3} _{-0.3}	-3.4 ^{+1.6} _{-2.0}	-4.3 ^{+0.9} _{-1.1}	-3.1 ^{+0.4} _{-0.4}	-5.2 ^{+1.0} _{-0.9}	1.0 ^{+0.4} _{-0.2}	30 ⁺⁹ ₋₇	99 ⁺³⁵ ₋₂₄	9 ⁺⁶ ₋₃	0.20 ^{+0.13} _{-0.06}	0.080 ^{+0.015} _{-0.014}
PS1-11aof	55777.1 ^{+0.4} _{-0.3}	-1.0 ^{+0.3} _{-0.3}	-6.0 ^{+1.2} _{-1.4}	-3.8 ^{+0.3} _{-0.3}	-3.0 ^{+0.5} _{-0.5}	-4.8 ^{+0.9} _{-1.0}	1.0 ^{+0.3} _{-0.2}	25 ⁺⁹ ₋₆	104 ⁺³² ₋₂₅	10 ⁺⁶ ₋₄	2.56 ^{+0.33} _{-0.27}	0.370 ^{+0.056} _{-0.047}
PS1-11apd	55789.4 ^{+0.9} _{-0.8}	-1.0 ^{+0.3} _{-0.3}	-7.0 ^{+1.1} _{-1.2}	-4.0 ^{+1.0} _{-2.0}	-2.8 ^{+0.5} _{-0.6}	-4.2 ^{+1.1} _{-1.2}	1.0 ^{+0.4} _{-0.3}	56 ⁺¹⁹ ₋₃₆	72 ⁺⁴⁴ ₋₁₇	11 ⁺⁸ ₋₄	0.87 ^{+0.05} _{-0.03}	0.039 ^{+0.009} _{-0.007}
PS1-11asz	55823.1 ^{+1.4} _{-0.3}	-1.0 ^{+0.3} _{-0.3}	-5.2 ^{+1.4} _{-1.3}	-5.0 ^{+0.7} _{-1.0}	-3.0 ^{+0.5} _{-0.5}	-5.3 ^{+1.0} _{-0.5}	1.0 ^{+0.3} _{-0.3}	29 ⁺⁸ ₋₈	99 ⁺³⁴ ₋₂₇	10 ⁺⁷ ₋₄	0.68 ^{+0.17} _{-0.16}	0.208 ^{+0.044} _{-0.039}
PS1-11awd	55849.3 ^{+0.4} _{-1.1}	-1.0 ^{+0.3} _{-0.3}	-4.7 ^{+1.0} _{-1.0}	-4.9 ^{+1.4} _{-2.8}	-2.9 ^{+0.4} _{-0.4}	-4.3 ^{+0.7} _{-0.9}	1.0 ^{+0.4} _{-0.2}	51 ⁺²⁸ ₋₂₆	70 ⁺⁵¹ ₋₁₂	10 ⁺⁷ ₋₄	0.69 ^{+0.08} _{-0.04}	0.005 ^{+0.007} _{-0.004}
PS1-11azd	55880.3 ^{+0.0} _{-0.1}	-1.0 ^{+0.3} _{-0.3}	-4.5 ^{+1.6} _{-1.9}	-5.4 ^{+0.9} _{-1.2}	-3.0 ^{+0.5} _{-0.5}	-4.5 ^{+0.3} _{-0.4}	1.0 ^{+0.4} _{-0.3}	29 ⁺¹⁰ ₋₇	99 ⁺³⁵ ₋₂₅	10 ⁺⁶ ₋₄	0.92 ^{+0.30} _{-0.08}	0.025 ^{+0.011} _{-0.010}
PS1-11azi	55877.4 ^{+0.5} _{-0.5}	-1.0 ^{+0.3} _{-0.3}	-4.6 ^{+1.5} _{-1.6}	-3.8 ^{+0.4} _{-0.4}	-3.0 ^{+0.5} _{-0.4}	-4.6 ^{+1.1} _{-1.0}	1.0 ^{+0.4} _{-0.3}	25 ⁺⁷ ₋₅	107 ⁺³⁶ ₋₂₉	11 ⁺⁷ ₋₄	2.80 ^{+0.42} _{-0.38}	0.010 ^{+0.026} _{-0.007}
PS1-11azt	55878.8 ^{+0.3} _{-0.4}	-1.0 ^{+0.3} _{-0.3}	-3.9 ^{+1.9} _{-2.2}	-4.9 ^{+1.3} _{-1.5}	-3.0 ^{+0.5} _{-0.5}	-5.1 ^{+0.9} _{-0.9}	1.0 ^{+0.3} _{-0.3}	30 ⁺¹¹ ₋₈	98 ⁺³³ ₋₂₃	10 ⁺⁶ ₋₄	0.94 ^{+1.00} _{-0.46}	0.010 ^{+0.024} _{-0.007}
PS1-11azv	55876.7 ^{+0.8} _{-1.2}	-1.0 ^{+0.3} _{-0.3}	-4.8 ^{+1.4} _{-1.7}	-4.5 ^{+0.6} _{-0.8}	-3.0 ^{+0.5} _{-0.5}	-4.9 ^{+0.9} _{-0.8}	1.0 ^{+0.4} _{-0.2}	28 ⁺⁹ ₋₆	102 ⁺³⁷ ₋₂₇	10 ⁺⁶ ₋₄	0.72 ^{+0.11} _{-0.11}	0.008 ^{+0.015} _{-0.006}
PS1-11bbg	55888.2 ^{+2.2} _{-0.8}	-1.0 ^{+0.3} _{-0.3}	-6.1 ^{+1.1} _{-1.5}	-4.5 ^{+0.4} _{-0.5}	-3.0 ^{+0.5} _{-0.5}	-4.5 ^{+0.8} _{-0.8}	1.0 ^{+0.3} _{-0.2}	29 ⁺⁹ ₋₇	107 ⁺³⁵ ₋₂₇	10 ⁺⁷ ₋₄	1.20 ^{+0.11} _{-0.10}	0.008 ^{+0.016} _{-0.006}
PS1-12c	55848.4 ^{+8.4} _{-9.3}	-1.0 ^{+0.3} _{-0.3}	-4.0 ^{+1.9} _{-2.0}	-3.4 ^{+0.3} _{-0.4}	-3.0 ^{+0.5} _{-0.5}	-5.0 ^{+0.9} _{-0.9}	1.0 ^{+0.3} _{-0.2}	32 ⁺¹⁰ ₋₈	98 ⁺²⁹ ₋₂₄	10 ⁺⁶ ₋₄	1.03 ^{+0.81} _{-0.42}	0.026 ^{+0.010} _{-0.010}
PS1-12d	55899.5 ^{+5.4} _{-2.0}	-1.0 ^{+0.3} _{-0.3}	-4.6 ^{+2.4} _{-1.7}	-5.8 ^{+0.8} _{-1.1}	-2.6 ^{+0.4} _{-0.5}	-4.5 ^{+1.0} _{-0.7}	1.0 ^{+0.4} _{-0.2}	24 ⁺⁷ ₋₅	77 ⁺¹⁴ ₋₁₀	13 ⁺⁹ ₋₅	0.95 ^{+0.06} _{-0.06}	0.010 ^{+0.022} _{-0.007}
PS1-12y	55911.8 ^{+13.6} _{-19.7}	-1.0 ^{+0.3} _{-0.3}	-5.9 ^{+1.2} _{-1.4}	-4.7 ^{+0.8} _{-0.6}	-2.9 ^{+0.6} _{-0.6}	-4.3 ^{+0.9} _{-1.1}	1.0 ^{+0.3} _{-0.3}	26 ⁺⁸ ₋₆	100 ⁺³⁹ ₋₂₅	11 ⁺⁷ ₋₄	2.04 ^{+0.21} _{-0.59}	0.193 ^{+0.304} _{-0.186}
PS1-12bt	55827.7 ^{+14.1} _{-13.1}	-1.0 ^{+0.3} _{-0.3}	-4.2 ^{+1.9} _{-1.9}	-4.8 ^{+0.7} _{-1.0}	-3.1 ^{+0.5} _{-0.5}	-4.9 ^{+0.8} _{-0.7}	1.0 ^{+0.3} _{-0.3}	27 ⁺⁹ ₋₆	105 ⁺³² ₋₃₂	10 ⁺⁷ ₋₄	0.12 ^{+0.11} _{-0.04}	0.007 ^{+0.006} _{-0.005}
PS1-12rk	55996.2 ^{+0.5} _{-0.6}	-1.0 ^{+0.3} _{-0.3}	-4.8 ^{+1.6} _{-1.7}	-5.3 ^{+0.6} _{-0.6}	-2.9 ^{+0.5} _{-0.5}	-3.9 ^{+0.7} _{-0.6}	1.0 ^{+0.3} _{-0.3}	26 ⁺⁸ ₋₅	97 ⁺³⁵ ₋₂₄	11 ⁺⁸ ₋₅	0.61 ^{+0.10} _{-0.10}	0.007 ^{+0.008} _{-0.005}
PS1-12wn	55999.3 ^{+0.6} _{-0.4}	-1.0 ^{+0.3} _{-0.3}	-4.5 ^{+1.0} _{-1.7}	-4.7 ^{+0.9} _{-1.2}	-2.9 ^{+0.5} _{-0.5}	-5.2 ^{+0.9} _{-0.9}	1.0 ^{+0.4} _{-0.3}	29 ⁺¹⁰ ₋₈	98 ⁺³⁰ ₋₂₅	10 ⁺⁷ ₋₄	0.97 ^{+0.45} _{-0.30}	0.021 ^{+0.062} _{-0.017}
PS1-12zd	56016.1 ^{+0.1} _{-0.5}	-1.0 ^{+0.3} _{-0.3}	-4.0 ^{+1.4} _{-1.8}	-4.4 ^{+1.4} _{-1.6}	-3.0 ^{+0.5} _{-0.5}	-4.7 ^{+1.0} _{-1.0}	1.0 ^{+0.3} _{-0.3}	30 ⁺⁹ ₋₈	99 ⁺³⁰ ₋₂₅	10 ⁺⁶ ₋₄	0.71 ^{+0.56} _{-0.50}	0.161 ^{+0.036} _{-0.033}
PS1-12zp	56019.4 ^{+0.0} _{-0.1}	-1.0 ^{+0.3} _{-0.3}	-3.9 ^{+1.5} _{-2.0}	-5.7 ^{+1.1} _{-1.2}	-3.0 ^{+0.5} _{-0.5}	-4.6 ^{+0.7} _{-0.7}	1.0 ^{+0.3} _{-0.3}	34 ⁺¹¹ ₋₁₁				

Table 7.3—Continued

SN	t_0	$\log \alpha$	$\log \beta_1$	$\log \beta_2$	$\log \beta_{dN}$	$\log \beta_{dC}$	t_1	t_p	t_2	t_d	M_p	V
PS1-12blz	56201.6 ^{+0.8} _{-1.1}	-1.0 ^{+0.3} _{-0.3}	-5.2 ^{+1.3} _{-1.4}	-4.0 ^{+0.2} _{-0.2}	-3.0 ^{+0.5} _{-0.5}	-4.6 ^{+0.7} _{-0.7}	1.0 ^{+0.4} _{-0.3}	29 ⁺⁶ ₋₆	111 ⁺³⁵ ₋₂₅	10 ⁺⁷ ₋₄	1.72 ^{+0.16} _{-0.08}	0.007 ^{+0.014} _{-0.006}
PS1-12boi	56201.7 ^{+0.7} _{-0.9}	-1.0 ^{+0.3} _{-0.3}	-5.0 ^{+1.3} _{-1.7}	-3.9 ^{+1.0} _{-1.5}	-3.0 ^{+0.6} _{-0.5}	-4.7 ^{+1.0} _{-1.1}	1.0 ^{+0.3} _{-0.2}	27 ⁺⁹ ₋₇	99 ⁺³³ ₋₂₆	10 ⁺⁷ ₋₄	1.72 ^{+0.54} _{-0.47}	0.012 ^{+0.056} _{-0.009}
PS1-12bza	56228.6 ^{+0.6} _{-0.7}	-1.0 ^{+0.3} _{-0.3}	-6.8 ^{+1.0} _{-1.3}	-4.4 ^{+0.2} _{-0.3}	-2.9 ^{+0.5} _{-0.5}	-4.9 ^{+0.6} _{-0.7}	1.0 ^{+0.4} _{-0.3}	18 ⁺⁹ ₋₄	71 ⁺⁶³ ₋₁₃	10 ⁺⁶ ₋₄	1.15 ^{+0.09} _{-0.10}	0.034 ^{+0.047} _{-0.029}
PS1-12cey	56237.2 ^{+0.2} _{-0.7}	-1.1 ^{+0.4} _{-0.5}	-4.8 ^{+1.8} _{-2.9}	-4.2 ^{+0.3} _{-0.6}	-3.1 ^{+0.5} _{-0.4}	-5.7 ^{+0.9} _{-1.1}	1.0 ^{+0.4} _{-0.2}	26 ⁺⁴ ₋₅	91 ⁺³⁵ ₋₂₁	9 ⁺⁶ ₋₃	1.26 ^{+0.17} _{-0.18}	0.007 ^{+0.022} _{-0.005}
PS1-13hp	56323.4 ^{+0.4} _{-0.5}	-1.0 ^{+0.3} _{-0.3}	-5.1 ^{+1.3} _{-1.6}	-5.8 ^{+0.9} _{-1.1}	-2.9 ^{+0.6} _{-0.5}	-3.9 ^{+0.8} _{-0.7}	1.0 ^{+0.3} _{-0.3}	28 ⁺⁹ ₋₇	93 ⁺³² ₋₂₄	12 ⁺⁸ ₋₅	1.49 ^{+0.23} _{-0.19}	0.009 ^{+0.030} _{-0.007}
PS1-13vs	56342.7 ^{+0.7} _{-0.8}	-1.0 ^{+0.3} _{-0.3}	-4.8 ^{+0.9} _{-1.3}	-4.7 ^{+1.0} _{-1.2}	-2.9 ^{+0.5} _{-0.5}	-4.3 ^{+0.8} _{-1.1}	1.0 ^{+0.4} _{-0.3}	34 ⁺¹⁵ ₋₁₀	100 ⁺³³ ₋₂₆	11 ⁺⁷ ₋₄	0.92 ^{+0.18} _{-0.12}	0.013 ^{+0.033} _{-0.010}
PS1-13wr	56300.4 ^{+2.3} _{-2.4}	-1.0 ^{+0.3} _{-0.3}	-1.9 ^{+0.8} _{-1.1}	-4.3 ^{+0.2} _{-0.3}	-3.1 ^{+0.5} _{-0.5}	-5.1 ^{+0.9} _{-1.0}	1.0 ^{+0.4} _{-0.3}	45 ⁺³ ₋₁₀	103 ⁺³³ ₋₁₉	10 ⁺⁶ ₋₄	1.94 ^{+0.27} _{-0.24}	0.239 ^{+0.041} _{-0.035}
PS1-13alz	56397.2 ^{+0.1} _{-0.8}	-1.0 ^{+0.3} _{-0.3}	-5.8 ^{+1.0} _{-1.4}	-3.6 ^{+0.7} _{-0.7}	-2.9 ^{+0.5} _{-0.5}	-4.9 ^{+1.1} _{-1.1}	1.0 ^{+0.4} _{-0.3}	28 ⁺¹⁰ ₋₇	99 ⁺³³ ₋₂₆	11 ⁺⁷ ₋₄	1.99 ^{+0.19} _{-0.11}	0.014 ^{+0.034} _{-0.011}
PS1-13arp	56396.6 ^{+0.5} _{-0.5}	-1.0 ^{+0.3} _{-0.3}	-4.0 ^{+1.8} _{-1.9}	-4.8 ^{+1.6} _{-1.6}	-3.0 ^{+0.5} _{-0.5}	-4.9 ^{+0.9} _{-1.0}	1.0 ^{+0.3} _{-0.3}	30 ⁺¹⁰ ₋₈	100 ⁺³⁷ ₋₂₅	10 ⁺⁷ ₋₄	0.98 ^{+0.98} _{-0.49}	0.011 ^{+0.032} _{-0.008}
PS1-13ave	56404.4 ^{+0.1} _{-0.2}	-1.0 ^{+0.3} _{-0.3}	-3.0 ^{+0.4} _{-0.4}	-5.1 ^{+0.4} _{-0.5}	-3.0 ^{+0.5} _{-0.5}	-5.0 ^{+1.0} _{-1.0}	1.1 ^{+0.4} _{-0.3}	17 ⁺⁴ ₋₄	100 ⁺³⁵ ₋₂₆	10 ⁺⁷ ₋₄	5.16 ^{+0.37} _{-0.33}	0.010 ^{+0.043} _{-0.008}
PS1-13atm	56352.8 ^{+0.9} _{-0.9}	-1.0 ^{+0.3} _{-0.3}	-2.4 ^{+1.2} _{-1.5}	-5.1 ^{+1.2} _{-1.3}	-3.0 ^{+0.5} _{-0.5}	-5.0 ^{+0.9} _{-1.0}	1.0 ^{+0.4} _{-0.3}	35 ⁺⁷ ₋₇	100 ⁺³⁴ ₋₂₅	10 ⁺⁷ ₋₄	3.18 ^{+0.77} _{-0.67}	0.010 ^{+0.029} _{-0.007}
PS1-13bvb	56451.6 ^{+0.5} _{-0.7}	-1.0 ^{+0.3} _{-0.3}	-5.6 ^{+1.2} _{-1.6}	-4.2 ^{+0.3} _{-0.5}	-2.8 ^{+0.5} _{-0.5}	-5.0 ^{+0.9} _{-1.0}	1.0 ^{+0.3} _{-0.3}	20 ⁺⁶ ₋₅	74 ⁺⁴⁷ ₋₁₄	11 ⁺⁶ ₋₄	1.73 ^{+0.23} _{-0.23}	0.013 ^{+0.045} _{-0.010}
PS1-13cqb	56503.7 ^{+1.0} _{-1.0}	-1.0 ^{+0.3} _{-0.3}	-4.4 ^{+1.5} _{-1.7}	-5.6 ^{+0.9} _{-1.3}	-3.0 ^{+0.5} _{-0.5}	-5.0 ^{+1.0} _{-0.9}	1.0 ^{+0.3} _{-0.2}	29 ⁺¹⁰ ₋₇	103 ⁺³⁵ ₋₂₅	10 ⁺⁶ ₋₄	0.67 ^{+0.14} _{-0.12}	0.167 ^{+0.043} _{-0.034}
PS1-13cua	56544.8 ^{+0.2} _{-0.2}	-1.0 ^{+0.4} _{-0.3}	-4.5 ^{+0.8} _{-1.4}	-6.1 ^{+1.0} _{-1.2}	-2.7 ^{+0.4} _{-0.5}	-4.9 ^{+1.0} _{-1.1}	1.0 ^{+0.3} _{-0.2}	30 ⁺¹⁰ ₋₈	75 ⁺¹² ₋₁₂	12 ⁺⁷ ₋₄	0.58 ^{+0.08} _{-0.07}	0.008 ^{+0.011} _{-0.005}
PS1-13eck	56613.7 ^{+0.3} _{-0.4}	-1.1 ^{+0.3} _{-0.3}	-6.7 ^{+0.9} _{-1.2}	-5.2 ^{+1.1} _{-1.3}	-3.0 ^{+0.6} _{-0.5}	-5.0 ^{+1.1} _{-1.0}	0.8 ^{+0.3} _{-0.2}	29 ⁺¹² ₋₈	101 ⁺³³ ₋₂₅	10 ⁺⁷ ₋₄	1.02 ^{+0.08} _{-0.08}	0.011 ^{+0.043} _{-0.008}
PS1-13esn	56637.0 ^{+0.9} _{-1.0}	-1.0 ^{+0.3} _{-0.3}	-4.1 ^{+1.8} _{-1.9}	-4.9 ^{+1.4} _{-1.7}	-3.0 ^{+0.5} _{-0.5}	-5.0 ^{+1.0} _{-1.0}	1.0 ^{+0.3} _{-0.3}	31 ⁺¹⁰ ₋₈	101 ⁺³⁷ ₋₂₅	10 ⁺⁶ ₋₄	1.01 ^{+0.89} _{-0.49}	0.010 ^{+0.036} _{-0.008}

Note. — Light curve parameters are listed separately for each photometric band, in sequence. The parameters are defined in Section 7.3.1. This table includes only SNe classified as SNe IIP by the criteria of Section 7.3.4.

Table 7.4. SN IIP *grizy* Template Light Curves

Epoch	<i>g</i>	<i>r</i>	<i>i</i>	<i>z</i>	<i>y</i>
-15
-12	1.38 ^{+0.31} _{-0.22}	...
-9	0.33 ^{+0.13} _{-0.15}	0.63 ^{+0.36} _{-0.28}	0.50 ^{+1.19} _{-0.19}	0.96 ^{+0.50} _{-0.42}	0.26 ^{+0.44} _{-0.34}
-6	0.20 ^{+0.20} _{-0.18}	0.42 ^{+0.33} _{-0.29}	0.33 ^{+0.86} _{-0.18}	0.61 ^{+0.56} _{-0.31}	0.32 ^{+0.28} _{-0.46}
-3	0.08 ^{+0.20} _{-0.09}	0.15 ^{+0.47} _{-0.11}	0.24 ^{+0.54} _{-0.21}	0.53 ^{+0.42} _{-0.41}	0.17 ^{+0.21} _{-0.27}
0	0.08 ^{+0.12} _{-0.08}	0.07 ^{+0.22} _{-0.08}	0.08 ^{+0.25} _{-0.11}	0.36 ^{+0.36} _{-0.31}	0.12 ^{+0.22} _{-0.17}
3	0.13 ^{+0.12} _{-0.10}	0.06 ^{+0.06} _{-0.07}	0.03 ^{+0.13} _{-0.12}	0.24 ^{+0.36} _{-0.22}	0.09 ^{+0.19} _{-0.17}
6	0.21 ^{+0.22} _{-0.14}	0.09 ^{+0.15} _{-0.08}	0.04 ^{+0.11} _{-0.10}	0.16 ^{+0.35} _{-0.13}	0.07 ^{+0.17} _{-0.20}
9	0.38 ^{+0.29} _{-0.22}	0.15 ^{+0.17} _{-0.08}	0.08 ^{+0.11} _{-0.09}	0.11 ^{+0.31} _{-0.11}	-0.09 ^{+0.26} _{-0.23}
12	0.56 ^{+0.34} _{-0.28}	0.20 ^{+0.16} _{-0.10}	0.10 ^{+0.16} _{-0.10}	0.10 ^{+0.31} _{-0.12}	-0.01 ^{+0.11} _{-0.23}
15	0.69 ^{+0.39} _{-0.22}	0.22 ^{+0.22} _{-0.11}	0.13 ^{+0.18} _{-0.10}	0.12 ^{+0.26} _{-0.13}	0.02 ^{+0.12} _{-0.13}
18	0.87 ^{+0.31} _{-0.27}	0.30 ^{+0.28} _{-0.15}	0.18 ^{+0.25} _{-0.13}	0.08 ^{+0.20} _{-0.12}	0.04 ^{+0.13} _{-0.15}
21	0.99 ^{+0.36} _{-0.30}	0.38 ^{+0.25} _{-0.23}	0.26 ^{+0.26} _{-0.16}	0.05 ^{+0.22} _{-0.12}	0.04 ^{+0.13} _{-0.17}
24	1.06 ^{+0.52} _{-0.35}	0.40 ^{+0.27} _{-0.25}	0.29 ^{+0.28} _{-0.19}	0.03 ^{+0.24} _{-0.11}	0.09 ^{+0.12} _{-0.25}
27	1.29 ^{+0.42} _{-0.54}	0.42 ^{+0.28} _{-0.27}	0.33 ^{+0.25} _{-0.23}	0.05 ^{+0.22} _{-0.13}	0.10 ^{+0.16} _{-0.21}
30	1.42 ^{+0.43} _{-0.51}	0.47 ^{+0.25} _{-0.28}	0.38 ^{+0.21} _{-0.24}	0.03 ^{+0.18} _{-0.15}	0.16 ^{+0.11} _{-0.24}
33	1.41 ^{+0.47} _{-0.50}	0.50 ^{+0.31} _{-0.32}	0.40 ^{+0.28} _{-0.24}	0.05 ^{+0.16} _{-0.12}	0.15 ^{+0.15} _{-0.30}
36	1.40 ^{+0.49} _{-0.41}	0.49 ^{+0.29} _{-0.34}	0.48 ^{+0.26} _{-0.27}	0.04 ^{+0.16} _{-0.11}	0.10 ^{+0.29} _{-0.18}
39	1.38 ^{+0.57} _{-0.37}	0.52 ^{+0.37} _{-0.37}	0.49 ^{+0.30} _{-0.28}	0.07 ^{+0.17} _{-0.09}	0.12 ^{+0.28} _{-0.16}
42	1.61 ^{+0.63} _{-0.42}	0.55 ^{+0.45} _{-0.32}	0.52 ^{+0.30} _{-0.29}	0.08 ^{+0.20} _{-0.08}	0.14 ^{+0.23} _{-0.16}
45	1.73 ^{+0.67} _{-0.65}	0.64 ^{+0.50} _{-0.39}	0.58 ^{+0.30} _{-0.26}	0.11 ^{+0.21} _{-0.11}	0.18 ^{+0.19} _{-0.22}
48	2.27 ^{+0.64} _{-1.29}	0.89 ^{+0.44} _{-0.54}	0.63 ^{+0.37} _{-0.25}	0.19 ^{+0.34} _{-0.24}	0.19 ^{+0.19} _{-0.21}
51	1.64 ^{+0.94} _{-0.68}	0.91 ^{+0.49} _{-0.54}	0.65 ^{+0.40} _{-0.24}	0.27 ^{+0.35} _{-0.28}	0.17 ^{+0.22} _{-0.23}
54	1.66 ^{+0.98} _{-0.66}	0.94 ^{+0.46} _{-0.48}	0.60 ^{+0.44} _{-0.31}	0.32 ^{+0.39} _{-0.25}	0.16 ^{+0.28} _{-0.22}
57	1.47 ^{+0.76} _{-0.50}	0.90 ^{+0.36} _{-0.49}	0.59 ^{+0.43} _{-0.36}	0.32 ^{+0.55} _{-0.23}	0.17 ^{+0.43} _{-0.37}
60	1.50 ^{+0.75} _{-0.29}	0.80 ^{+0.58} _{-0.53}	0.60 ^{+0.44} _{-0.42}	0.32 ^{+0.63} _{-0.21}	0.35 ^{+0.30} _{-0.55}
63	1.51 ^{+0.84} _{-0.24}	0.74 ^{+0.54} _{-0.39}	0.65 ^{+0.56} _{-0.50}	0.61 ^{+0.43} _{-0.42}	0.33 ^{+0.37} _{-0.50}
66	1.69 ^{+0.87} _{-0.36}	0.79 ^{+0.64} _{-0.44}	0.60 ^{+0.56} _{-0.43}	0.65 ^{+0.50} _{-0.25}	0.16 ^{+0.39} _{-0.35}
69	1.89 ^{+1.13} _{-0.54}	0.91 ^{+0.64} _{-0.53}	0.68 ^{+0.60} _{-0.49}	0.64 ^{+0.33} _{-0.19}	0.16 ^{+0.41} _{-0.18}
72	1.79 ^{+1.21} _{-0.37}	0.99 ^{+0.56} _{-0.53}	0.74 ^{+0.56} _{-0.52}	0.72 ^{+0.32} _{-0.26}	0.30 ^{+0.53} _{-0.34}

Table 7.4—Continued

Epoch	g	r	i	z	y
75	$1.84^{+0.81}_{-0.34}$	$1.09^{+0.50}_{-0.58}$	$0.82^{+0.56}_{-0.43}$	$0.75^{+0.45}_{-0.31}$	$0.45^{+0.49}_{-0.47}$
78	$1.88^{+0.51}_{-0.36}$	$1.09^{+0.51}_{-0.55}$	$0.85^{+0.62}_{-0.56}$	$0.95^{+0.57}_{-0.51}$	$0.39^{+0.58}_{-0.36}$
81	$2.02^{+0.25}_{-0.31}$	$1.19^{+0.54}_{-0.44}$	$0.85^{+0.60}_{-0.56}$	$0.82^{+0.74}_{-0.48}$	$0.14^{+0.44}_{-0.36}$
84	$1.76^{+0.45}_{-0.16}$	$1.25^{+0.50}_{-0.57}$	$0.79^{+1.00}_{-0.49}$	$0.88^{+0.60}_{-0.48}$	$0.14^{+1.25}_{-0.41}$
87	$1.74^{+0.69}_{-0.15}$	$1.30^{+0.60}_{-0.56}$	$0.79^{+0.92}_{-0.33}$	$1.09^{+0.70}_{-0.54}$	$0.65^{+0.75}_{-0.91}$
90	$2.23^{+0.56}_{-0.56}$	$1.39^{+0.81}_{-0.58}$	$1.00^{+0.93}_{-0.33}$	$1.15^{+0.72}_{-0.37}$	$0.81^{+0.63}_{-0.19}$
93	$2.69^{+0.16}_{-0.59}$	$1.60^{+0.60}_{-0.58}$	$1.05^{+0.36}_{-0.38}$	$1.20^{+0.56}_{-0.36}$	$0.72^{+0.09}_{-0.70}$
96	$2.81^{+0.36}_{-0.71}$	$1.63^{+0.52}_{-0.31}$	$1.09^{+0.72}_{-0.38}$	$1.32^{+0.44}_{-0.49}$	$0.67^{+0.14}_{-0.66}$
99	$2.90^{+0.51}_{-0.49}$	$1.75^{+0.44}_{-0.47}$	$1.17^{+0.69}_{-0.61}$	$1.45^{+0.56}_{-0.55}$	$0.92^{+0.56}_{-0.42}$
102	$3.19^{+0.50}_{-1.20}$	$1.69^{+0.41}_{-0.90}$	$1.51^{+0.39}_{-0.95}$	$1.60^{+0.46}_{-0.36}$	$1.12^{+0.82}_{-0.45}$
105	...	$1.79^{+0.32}_{-0.99}$	$1.61^{+0.38}_{-0.94}$	$1.71^{+0.89}_{-0.44}$	$1.18^{+0.76}_{-0.29}$
108	...	$1.99^{+0.54}_{-1.31}$	$1.49^{+0.72}_{-0.82}$	$1.84^{+0.82}_{-0.58}$	$0.96^{+0.33}_{-0.12}$
111	...	$2.04^{+0.53}_{-1.31}$	$1.53^{+0.53}_{-0.54}$	$2.43^{+0.31}_{-1.23}$	$0.91^{+0.12}_{-0.11}$
114	...	$2.26^{+0.39}_{-0.95}$	$1.67^{+0.49}_{-0.29}$	$1.95^{+0.42}_{-0.75}$	$1.01^{+0.13}_{-0.19}$

Note. — The reported epoch is in rest frame days since peak. The *grizy* photometry is reported in terms of magnitude below peak; the ranges reflect the 16-84th percentile variation in observed light curve behavior.

Table 7.5. Light curve and modeled progenitor parameters for PS1 SNe IIP

PS1 SN	$M_{p,r}$ (mag)	$t_{plateau,r}$ (days)	$\log_{10}(L_{50})$ (ergs s $^{-1}$)	$\Delta m_{15,r}$ (mag)	M_{Ni} (mag)	M_{in} (M_{\odot})	R_0 (R_{\odot})	E_{51} (10^{51} ergs)
PS1-10a	$-18.09^{+0.17}_{-0.20}$	111^{+41}_{-29}	$42.61^{+0.47}_{-0.37}$	$-0.47^{+0.24}_{-0.38}$	$0.10^{+0.23}_{-0.07}$
PS1-10q	$-17.07^{+0.04}_{-0.05}$	96^{+11}_{-2}	$42.46^{+0.16}_{-0.14}$	$-0.26^{+0.02}_{-0.02}$	$0.10^{+0.14}_{-0.06}$
PS1-10ae	$-17.16^{+0.04}_{-0.04}$	101^{+31}_{-22}	$41.93^{+0.24}_{-0.14}$	$-0.30^{+0.03}_{-0.04}$	$0.07^{+0.06}_{-0.03}$
PS1-10jr	$-19.38^{+0.11}_{-0.12}$	112^{+29}_{-28}	$45.63^{+0.83}_{-0.89}$	$-1.16^{+0.22}_{-0.31}$	$27.79^{+...}_{-24.07}$
PS1-10lv	$-18.43^{+0.04}_{-0.04}$	106^{+15}_{-9}	$43.12^{+0.07}_{-0.04}$	$-0.27^{+0.01}_{-0.01}$	$0.21^{+0.18}_{-0.13}$	$24.9^{+13.6}_{-8.8}$	1340^{+840}_{-490}	$6.91^{+2.51}_{-2.79}$
PS1-10mb	$-15.46^{+0.14}_{-0.18}$	107^{+35}_{-27}	$41.83^{+0.17}_{-0.18}$	$-0.08^{+0.04}_{-0.05}$	$0.07^{+0.09}_{-0.05}$
PS1-10zu	$-16.82^{+0.15}_{-0.12}$	110^{+6}_{-28}	$42.30^{+0.13}_{-0.09}$	$-0.10^{+0.02}_{-0.02}$	$0.07^{+0.03}_{-0.03}$
PS1-10abd	$-18.54^{+0.11}_{-0.11}$	94^{+44}_{-12}	$42.63^{+0.10}_{-0.14}$	$-0.33^{+0.02}_{-0.02}$	$0.09^{+0.12}_{-0.06}$
PS1-10agh	$-18.57^{+0.05}_{-0.05}$	101^{+18}_{-12}	$42.94^{+0.03}_{-0.04}$	$-0.36^{+0.01}_{-0.01}$	$0.11^{+0.17}_{-0.06}$	$13.0^{+12.9}_{-3.9}$	690^{+710}_{-200}	$6.68^{+2.35}_{-2.92}$
PS1-10awc	$-17.92^{+0.05}_{-0.04}$	97^{+10}_{-8}	$42.68^{+0.07}_{-0.08}$	$-0.25^{+0.02}_{-0.02}$	$0.14^{+0.14}_{-0.06}$
PS1-10biu	$-18.60^{+0.07}_{-0.09}$	112^{+38}_{-29}	$42.77^{+0.24}_{-0.26}$	$-0.48^{+0.07}_{-0.12}$	$0.11^{+0.15}_{-0.07}$	$13.0^{+21.4}_{-7.9}$	690^{+1230}_{-390}	$4.41^{+4.36}_{-2.45}$
PS1-10blk	$-17.71^{+0.06}_{-0.07}$	76^{+3}_{-3}	$42.31^{+0.13}_{-0.10}$	$-0.17^{+0.02}_{-0.02}$	$0.19^{+0.08}_{-0.10}$
PS1-11u	$-17.07^{+0.32}_{-0.29}$	80^{+12}_{-20}	$42.05^{+0.09}_{-0.09}$	$-0.27^{+0.04}_{-0.03}$	$0.00^{+0.00}_{-0.00}$
PS1-11z	$-17.54^{+0.07}_{-0.07}$	96^{+13}_{-8}	$42.22^{+0.05}_{-0.08}$	$-0.19^{+0.02}_{-0.02}$	$0.03^{+0.02}_{-0.02}$
PS1-11ai	$-17.26^{+0.31}_{-0.35}$	105^{+14}_{-13}	$42.29^{+0.14}_{-0.13}$	$-0.17^{+0.07}_{-0.07}$	$0.04^{+0.05}_{-0.03}$
PS1-11bo	$-16.57^{+0.10}_{-0.09}$	115^{+35}_{-42}	$42.20^{+0.05}_{-0.07}$	$-0.07^{+0.03}_{-0.02}$	$0.23^{+0.10}_{-0.08}$
PS1-11fi	$-17.51^{+0.11}_{-0.16}$	109^{+12}_{-19}	$42.27^{+0.10}_{-0.11}$	$-0.18^{+0.02}_{-0.01}$	$0.02^{+0.03}_{-0.01}$
PS1-11kf	$-19.70^{+0.15}_{-0.19}$	110^{+41}_{-28}	$43.13^{+0.23}_{-0.24}$	$-0.49^{+0.04}_{-0.04}$	$0.17^{+0.20}_{-0.11}$
PS1-11li	$-16.27^{+0.26}_{-0.26}$	107^{+36}_{-28}	$43.44^{+1.55}_{-1.34}$	$-0.26^{+0.09}_{-0.11}$	$1.82^{+69.64}_{-1.77}$
PS1-11lj	$-16.91^{+0.04}_{-0.05}$	64^{+4}_{-3}	$42.24^{+0.04}_{-0.05}$	$-0.12^{+0.02}_{-0.02}$	$0.04^{+0.05}_{-0.03}$
PS1-11lr	$-16.84^{+0.02}_{-0.02}$	105^{+33}_{-25}	$42.39^{+0.04}_{-0.03}$	$-0.02^{+0.01}_{-0.01}$	$0.42^{+0.24}_{-0.23}$
PS1-11lq	$-17.50^{+0.06}_{-0.11}$	109^{+38}_{-31}	$42.39^{+0.07}_{-0.07}$	$-0.28^{+0.02}_{-0.02}$	$0.21^{+0.15}_{-0.10}$
PS1-11md	$-18.32^{+0.08}_{-0.11}$	105^{+40}_{-21}	$42.42^{+0.14}_{-0.15}$	$-0.37^{+0.04}_{-0.08}$	$0.17^{+0.11}_{-0.10}$
PS1-11pf	$-18.08^{+0.08}_{-0.08}$	113^{+33}_{-43}	$42.98^{+0.12}_{-0.11}$	$-0.33^{+0.04}_{-0.04}$	$0.61^{+0.39}_{-0.35}$	$13.1^{+22.1}_{-8.5}$	690^{+1280}_{-420}	$8.05^{+8.08}_{-4.27}$
PS1-11qe	$-19.58^{+0.04}_{-0.03}$	51^{+57}_{-5}	$42.47^{+0.10}_{-0.04}$	$-0.57^{+0.06}_{-0.07}$	$0.15^{+0.15}_{-0.09}$
PS1-11sm	$-18.43^{+0.08}_{-0.07}$	103^{+37}_{-26}	$42.60^{+0.34}_{-0.38}$	$-0.61^{+0.08}_{-0.11}$	$0.10^{+0.19}_{-0.06}$
PS1-11ua	$-19.33^{+0.26}_{-0.26}$	106^{+34}_{-28}	$42.69^{+0.26}_{-0.19}$	$-0.58^{+0.07}_{-0.07}$	$0.22^{+0.36}_{-0.14}$
PS1-11uv	$-16.30^{+0.04}_{-0.04}$	108^{+30}_{-19}	$41.80^{+0.07}_{-0.07}$	$-0.14^{+0.02}_{-0.02}$	$0.07^{+0.05}_{-0.02}$
PS1-11vn	$-17.74^{+0.15}_{-0.16}$	113^{+30}_{-21}	$42.58^{+0.15}_{-0.18}$	$-0.34^{+0.07}_{-0.08}$	$0.25^{+0.18}_{-0.14}$
PS1-11wj	$-17.11^{+0.03}_{-0.04}$	102^{+25}_{-23}	$42.67^{+1.44}_{-0.91}$	$-0.41^{+0.24}_{-0.38}$	$0.36^{+5.28}_{-0.31}$
PS1-11yh	$-18.23^{+0.09}_{-0.08}$	112^{+32}_{-26}	$42.87^{+0.08}_{-0.04}$	$-0.27^{+0.03}_{-0.03}$	$0.57^{+0.51}_{-0.27}$
PS1-11amh	$-18.25^{+0.02}_{-0.03}$	107^{+36}_{-22}	$42.88^{+0.11}_{-0.06}$	$-0.13^{+0.01}_{-0.01}$	$2.05^{+1.11}_{-0.68}$
PS1-11anm	$-14.79^{+0.14}_{-0.16}$	105^{+26}_{-17}	$44.32^{+4.44}_{-2.29}$	$-0.32^{+0.08}_{-0.13}$	$7.13^{+...}_{-7.06}$
PS1-11aof	$-18.59^{+0.09}_{-0.08}$	106^{+35}_{-31}	$43.01^{+0.24}_{-0.23}$	$-0.62^{+0.07}_{-0.08}$	$0.17^{+0.30}_{-0.12}$	$16.2^{+21.9}_{-10.5}$	850^{+1300}_{-530}	$6.34^{+7.79}_{-3.42}$
PS1-11apd	$-17.52^{+0.02}_{-0.02}$	90^{+2}_{-3}	$42.33^{+0.04}_{-0.03}$	$-0.15^{+0.01}_{-0.01}$	$0.06^{+0.04}_{-0.03}$
PS1-11asz	$-17.24^{+0.04}_{-0.04}$	89^{+11}_{-9}	$42.41^{+0.12}_{-0.13}$	$-0.21^{+0.02}_{-0.03}$	$0.06^{+0.10}_{-0.04}$
PS1-11awd	$-17.33^{+0.27}_{-0.41}$	89^{+4}_{-4}	$42.08^{+0.10}_{-0.06}$	$-0.17^{+0.06}_{-0.08}$	$0.08^{+0.05}_{-0.03}$
PS1-11azd	$-17.27^{+0.07}_{-0.09}$	107^{+29}_{-23}	$42.98^{+1.84}_{-1.05}$	$-0.55^{+0.25}_{-0.46}$	$0.22^{+7.54}_{-0.20}$	$24.9^{+11.4}_{-20.5}$	1340^{+700}_{-1070}	$6.96^{+539.91}_{-5.97}$
PS1-11azi	$-18.91^{+0.10}_{-0.08}$	109^{+49}_{-19}	$43.08^{+0.14}_{-0.15}$	$-0.50^{+0.03}_{-0.04}$	$0.20^{+0.24}_{-0.12}$	$22.8^{+15.4}_{-11.5}$	1220^{+940}_{-620}	$6.10^{+5.11}_{-2.36}$
PS1-11azt	$-17.95^{+0.07}_{-0.07}$	114^{+30}_{-29}	$42.52^{+0.15}_{-0.16}$	$-0.22^{+0.08}_{-0.08}$	$0.17^{+0.12}_{-0.07}$

Table 7.5—Continued

PS1 SN	$M_{p,r}$ (mag)	$t_{plateau,r}$ (days)	$\log_{10}(L_{50})$ (ergs s $^{-1}$)	$\Delta m_{15,r}$ (mag)	M_{Ni} (mag)	M_{in} (M_{\odot})	R_0 (R_{\odot})	E_{51} (10^{51} ergs)
PS1-11azv	$-16.94^{+0.07}_{-0.06}$	87^{+11}_{-11}	$42.29^{+0.06}_{-0.06}$	$-0.17^{+0.03}_{-0.03}$	$0.13^{+0.07}_{-0.06}$
PS1-11bbg	$-18.19^{+0.08}_{-0.08}$	124^{+30}_{-29}	$42.72^{+0.09}_{-0.07}$	$-0.42^{+0.03}_{-0.03}$	$0.12^{+0.09}_{-0.05}$	$17.1^{+19.4}_{-9.8}$	900^{+1150}_{-500}	$3.39^{+3.07}_{-1.81}$
PS1-12c	$-16.72^{+0.22}_{-0.23}$	104^{+8}_{-8}	$42.92^{+0.47}_{-0.60}$	$-0.27^{+0.04}_{-0.04}$	$0.20^{+0.53}_{-0.14}$
PS1-12d	$-17.68^{+0.03}_{-0.42}$	108^{+3}_{-4}	$42.34^{+0.05}_{-0.03}$	$-0.22^{+0.01}_{-0.01}$	$0.01^{+0.02}_{-0.01}$
PS1-12y	$-18.55^{+0.27}_{-0.06}$	89^{+9}_{-22}	$42.42^{+0.09}_{-0.12}$	$-0.35^{+0.02}_{-0.02}$	$0.02^{+0.01}_{-0.01}$
PS1-12rk	$-16.12^{+0.05}_{-0.07}$	108^{+43}_{-25}	$42.21^{+0.04}_{-0.04}$	$-0.06^{+0.02}_{-0.03}$	$0.09^{+0.05}_{-0.04}$
PS1-12zd	$-17.92^{+0.08}_{-0.07}$	109^{+32}_{-23}	$42.48^{+0.27}_{-0.25}$	$-0.53^{+0.05}_{-0.05}$	$0.05^{+0.07}_{-0.03}$
PS1-12zp	$-17.43^{+0.03}_{-0.03}$	119^{+37}_{-27}	$42.17^{+0.09}_{-0.10}$	$-0.32^{+0.04}_{-0.04}$	$0.03^{+0.02}_{-0.02}$
PS1-12auw	$-17.91^{+0.03}_{-0.04}$	108^{+27}_{-25}	$43.70^{+0.59}_{-0.33}$	$-0.82^{+0.20}_{-0.24}$	$0.62^{+1.26}_{-0.30}$
PS1-12bku	$-18.24^{+0.03}_{-0.04}$	69^{+18}_{-5}	$42.63^{+0.02}_{-0.02}$	$-0.25^{+0.01}_{-0.02}$	$0.16^{+0.06}_{-0.03}$
PS1-12bmp	$-16.96^{+0.02}_{-0.01}$	86^{+2}_{-2}	$42.31^{+0.02}_{-0.02}$	$-0.03^{+0.01}_{-0.01}$	$0.06^{+0.03}_{-0.02}$
PS1-12blz	$-18.47^{+0.02}_{-0.02}$	115^{+40}_{-23}	$42.33^{+0.05}_{-0.05}$	$-0.47^{+0.01}_{-0.01}$	$0.03^{+0.02}_{-0.01}$
PS1-12boi	$-18.20^{+0.04}_{-0.05}$	112^{+23}_{-24}	$42.28^{+0.26}_{-0.09}$	$-0.55^{+0.12}_{-0.14}$	$0.04^{+0.06}_{-0.03}$
PS1-12bza	$-17.71^{+0.03}_{-0.03}$	83^{+1}_{-2}	$42.64^{+0.03}_{-0.02}$	$-0.23^{+0.01}_{-0.01}$	$0.22^{+0.08}_{-0.06}$
PS1-12cey	$-18.54^{+0.04}_{-0.05}$	118^{+38}_{-24}	$42.77^{+0.13}_{-0.09}$	$-0.55^{+0.04}_{-0.05}$	$0.14^{+0.08}_{-0.06}$	$14.4^{+22.3}_{-7.0}$	760^{+1310}_{-350}	$3.91^{+3.12}_{-2.31}$
PS1-13hp	$-18.27^{+0.03}_{-0.04}$	116^{+41}_{-29}	$42.77^{+0.05}_{-0.07}$	$-0.28^{+0.02}_{-0.02}$	$0.13^{+0.10}_{-0.07}$	$13.7^{+22.6}_{-7.6}$	730^{+1310}_{-380}	$4.03^{+4.70}_{-2.40}$
PS1-13vs	$-17.28^{+0.04}_{-0.03}$	110^{+28}_{-27}	$42.32^{+0.08}_{-0.08}$	$-0.10^{+0.02}_{-0.02}$	$0.11^{+0.05}_{-0.04}$
PS1-13wr	$-16.99^{+0.10}_{-0.11}$	127^{+3}_{-4}	$42.47^{+0.06}_{-0.08}$	$-0.10^{+0.02}_{-0.02}$	$0.19^{+0.04}_{-0.05}$
PS1-13alz	$-18.40^{+0.19}_{-0.30}$	107^{+39}_{-23}	$42.72^{+0.68}_{-0.45}$	$-0.67^{+0.40}_{-0.53}$	$0.05^{+0.26}_{-0.04}$	$13.4^{+23.8}_{-8.8}$	710^{+1390}_{-430}	$2.86^{+8.23}_{-1.11}$
PS1-13arp	$-17.54^{+0.12}_{-0.12}$	113^{+26}_{-25}	$42.69^{+0.16}_{-0.13}$	$-0.45^{+0.08}_{-0.09}$	$0.34^{+0.20}_{-0.22}$
PS1-13ave	$-19.22^{+0.02}_{-0.03}$	111^{+34}_{-24}	$42.96^{+0.04}_{-0.04}$	$-0.29^{+0.01}_{-0.01}$	$1.03^{+0.70}_{-0.44}$
PS1-13atm	$-16.99^{+0.47}_{-0.34}$	108^{+33}_{-22}	$43.57^{+0.67}_{-1.39}$	$-0.12^{+0.08}_{-0.21}$	$2.09^{+15.75}_{-1.88}$	$12.5^{+21.4}_{-8.1}$	660^{+1220}_{-390}	$19.39^{+93.09}_{-17.27}$
PS1-13bvb	$-17.87^{+0.07}_{-0.08}$	71^{+3}_{-4}	$42.65^{+0.05}_{-0.08}$	$-0.19^{+0.03}_{-0.02}$	$0.08^{+0.09}_{-0.06}$
PS1-13cqb	$-16.62^{+0.07}_{-0.04}$	110^{+40}_{-23}	$42.55^{+0.18}_{-0.20}$	$-0.12^{+0.03}_{-0.03}$	$0.35^{+0.38}_{-0.16}$
PS1-13cua	$-16.89^{+0.04}_{-0.09}$	93^{+3}_{-5}	$42.21^{+0.04}_{-0.04}$	$-0.06^{+0.01}_{-0.01}$	$0.12^{+0.10}_{-0.08}$
PS1-13eck	$-17.53^{+0.08}_{-0.09}$	103^{+33}_{-60}	$42.84^{+0.29}_{-0.18}$	$-0.46^{+0.14}_{-0.09}$	$0.28^{+0.37}_{-0.20}$
PS1-13esn	$-17.52^{+0.08}_{-0.08}$	116^{+30}_{-31}	$42.35^{+0.14}_{-0.15}$	$-0.20^{+0.06}_{-0.06}$	$0.21^{+0.18}_{-0.14}$

Note. — The r -band peak magnitude ($M_{p,r}$) is derived directly from the model fits (Section 7.3.2), including K -corrections, but not corrected for extinction. The r -band plateau duration ($t_{plateau,r}$) is in rest frame days, not corrected for contamination by ^{56}Ni . The pseudo-bolometric (OIR) luminosity at 50 days (L_{50}) is measured from the fits to the PS1 photometry; the value quoted does not include the bolometric correction described in Section 7.3.2. The decline rate in r -band ($\Delta m_{15,r}$; rest frame days) is measured from the same model fits. The ejected nickel mass is estimated from comparison of the late-time bolometric light curve to that of SN 1987a (but see Section 7.5.2 for a discussion of reliability). The progenitor initial mass (M_{in}), radius (R_0), and explosion energy (E_{51}) estimates come from the comparisons (see Section 7.5.3) to the models of Kasen & Woosley (2009); but see Section 7.5.4 for a discussion of reliability. These theoretical estimates are reported only if the central mass estimate falls within the model grid ($12 - 25 M_{\odot}$); but the full posterior distribution for the reported values includes extrapolations to values beyond the model grid, as reflected in the reported uncertainties. All reported values represent [16,50,84]th percentiles of the posterior distribution.

Chapter 8

Unsupervised Transient Light Curve Analysis Via Hierarchical Bayesian Inference

N. E. Sanders, M. Betancourt, A. M. Soderberg 2014, *arXiv:1404.3619*

abstract

Historically, light curve studies of supernovae (SNe) and other transient classes have focused on individual objects with copious and high signal-to-noise observations. In the nascent era of wide field transient searches, objects with detailed observations are decreasing as a fraction of the overall known SN population, and this strategy sacrifices the majority of the information contained in the data about the underlying population of transients. A population level

modeling approach, simultaneously fitting all available observations of objects in a transient sub-class of interest, fully mines the data to infer the properties of the population and avoids certain systematic biases. We present a novel hierarchical Bayesian statistical model for population level modeling of transient light curves, and discuss its implementation using an efficient Hamiltonian Monte Carlo technique. As a test case, we apply this model to the Type IIP SN sample from the Pan-STARRS1 Medium Deep Survey, consisting of 18,837 photometric observations of 76 SNe, corresponding to a joint posterior distribution with 9,176 parameters under our model. Our hierarchical model fits provide improved constraints on light curve parameters relevant to the physical properties of their progenitor stars relative to modeling individual light curves alone. Moreover, we directly evaluate the probability for occurrence rates of unseen light curve characteristics from the model hyperparameters, addressing observational biases in survey methodology. We view this modeling framework as an unsupervised machine learning technique with the ability to maximize scientific returns from data to be collected by future wide field transient searches like LSST.

8.1 INTRODUCTION

The majority of luminous transients in the universe are core-collapse supernovae (CC-SNe), marking the explosive deaths of massive stars (Heger et al. 2003; Smartt 2009). Stellar evolution theory, as well as both detailed observations of the explosive transient and fortuitous pre-explosion observations of the progenitor star, point to progenitor initial mass as the primary factor determining stars'

eventual death state. Metallicity, rotation rate, binarity, and other properties play important secondary roles, and permutations of these parameters are likely responsible for the extreme diversity of core-collapse supernovae phenomenology observed in the universe (Heger et al. 2003; Smartt 2009; Smith et al. 2011a; Ekström et al. 2012; Jerkstrand et al. 2013). The progenitor star mass distribution for each SN type, as well as the distribution of these secondary factors, have far reaching implications throughout astrophysics, influencing the theory of stellar evolution (Groh et al. 2013a), galactic chemical evolution (Nomoto et al. 2013), hydrodynamic feedback in galaxy formation (Stilp et al. 2013), and astrobiology (Lineweaver et al. 2004).

Studies of individual transients typically focus on well observed cases within each object class, capitalizing on the availability of detailed and high signal-to-noise observations to facilitate comparison to finely tuned hydrodynamic explosion simulations and analytic light curve models (e.g. Mazzali et al. 2003; Utrobin & Chugai 2008). Syntheses of these observations, studies of large samples of SNe of a given class, are then typically composed of samples culled from these well observed cases (see e.g. Nomoto et al. 2006; Bersten & Hamuy 2009; Jerkstrand et al. 2013). However, the properties of luminous and/or high signal-to-noise objects within a survey sample may be systematically different from their lower luminosity / signal-to-noise counterparts, and traditional targeted transient searches themselves are inherently biased towards particular SN progenitor properties like high metallicity (Sanders et al. 2012c,d). To derive truly robust and unbiased inferences about SN progenitor populations, it is therefore necessary to study transient samples in a fashion as complete and observationally

agnostic as possible.

Here we discuss a methodological framework for the simultaneous modeling of multi-band, multi-object photometric observations from wide field transient surveys, which addresses certain biasing factors inherent to transient searches. This method is rooted in “hierarchical” and “multi-level” Bayesian analysis, where information about similar events within a sample is partially pooled through a hierarchical structure applied to the joint prior distribution (see Gelman et al. 2013 and references therein; see Mandel et al. 2009 for applications to SN Ia light curves). We adopt Hamiltonian Monte Carlo as a computational technique to efficiently explore the high-dimensional and strongly correlated posterior distribution of this hierarchical model (Betancourt & Girolami 2013). The result of this modeling is simultaneous inference on physically-relevant light curve parameters describing individual objects in the sample, as well as the parameter distribution among the population, regularized by the application of minimal (“weakly informative”) prior information.

In Section 8.2 we discuss the design and implementation of a hierarchical Bayesian model capable of simultaneously fitting large quantities of raw photometric data from wide field transient surveys to infer the population properties of the underlying SN sample. We test this model with a sample dataset of Type IIP SNe from the Pan-STARRS1 (PS1) survey (Section 8.3), previously published in Sanders et al. (2014). We explore the results of this test in Section 8.4, including comparison with inferences drawn from traditional modeling based on fits to individual light curves. We discuss the implications of this methodology for future wide field transient surveys in Section 8.5 and

conclude in Section 8.6.

8.2 MODEL DESIGN

We have designed a hierarchical Bayesian generalized linear model (GLM) to simultaneously describe the individual multi-band light curves of a set of optical transients, and the population distribution of their light curve parameters. Due to the nature of the sample dataset we discuss in Section 8.3, the non-linear link function of our GLM is tailored for Type IIP SNe (see Section 8.2.1), but the hierarchical structure of the model is generalizable to any transient class.

Type IIP SNe are particularly apt for a hierarchical modeling approach because their long lived light curves reduce the likelihood of any individual object to have fully identifiable light curve parameters. In particular, because the plateau phase of the SN IIP light curve has a duration (~ 3 months) similar to the length of observing seasons for typical pointings of ground based telescopes, individual light curves are typically incomplete. The detected SNe IIP have often exploded between observing seasons, when their field is behind the sun, or their field sets before the plateau phase has ended. As a result, individual objects in the data set do not have the temporal coverage needed to fully identify their light curve parameters. Partial pooling among objects in the sample can compensate, helping to identify unconstrained parameter values for individual objects, while applying information from well-constrained parameters of the individual light curves to all other objects in the sample.

8.2.1 Light curve model

We have designed a physically motivated parameterized model for the SN IIP light curve, composed of 5 piecewise power law and exponential segments. The model is fully specified by a set of 12 independent parameters per optical filter and an explosion date (t_0). These parameters are 4 time durations (t_1, t_p, t_2, t_d) defining the knot locations of the segments, 5 rate parameters describing the slope of each light curve segment ($\alpha, \beta_1, \beta_2, \beta_{dN}, \beta_{dC}$), a luminosity scale (M_p), a background level (Y_b) for the photometric data, and an intrinsic scatter (V) to encompass deviation from the model. The light curve model and its primary parameters are illustrated in Figure 8.1; a full mathematical description of the light curve model is given in Sanders et al. (2014).

8.2.2 Hierarchical structure

We allow for partial pooling between the light curve parameters of this 5-component model using a linear hierarchical structure. This structure is illustrated in Figure 8.2. For the time, rate, luminosity scale, and intrinsic scatter parameters of the model, this structure includes levels for individual photometric filters, individual SNe-filter combinations, and a top-level parameter; a 3-level structure. For the explosion date (t_0) parameter, which is not defined per-filter, we use a modified two-level structure. The structure includes separate hyperprior distributions for objects discovered within and between observing seasons, which will have significantly different delay times between explosion and the epoch of detection. We do not adopt a hierarchical structure for the background level Y_b

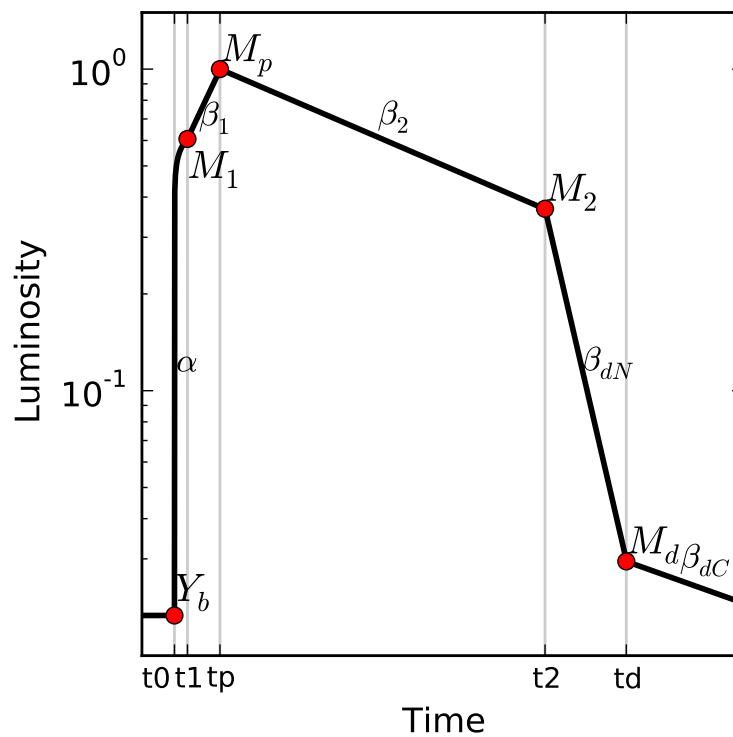


Figure 8.1.— Schematic illustration of the 5-component SN II light curve model defined in Sanders et al. (2014). The gray vertical lines denote the epochs of transition (t_x) between the piecewise components of the model. The background level (Y_b) and turnover fluxes (M_x) are marked and labeled (red points). The power law (α) and exponential (β_x) rate constant for each phase is labeled adjacent to the light curve component.

parameter, which should nominally be 0 except in the presence of artifacts among the PS1 template images used in difference imaging.

In effect, this structure means that a single top level value is drawn for each rate parameter; separate filter-level rate parameters are drawn for each of the *grizy* filters from the hyperprior distribution specified by the top level value; and bottom level rate parameters for each SN-filter combination are drawn from the hyperprior specified by the filter-level draw. In practice, this “centered” multi-level parameterization is non-optimal, because it introduces significant correlations between the hyperparameters in the model that decrease the efficiency of the MCMC sampler. Instead we use a modified, “non-centered parameterization,” where correlations between hyperparameters are exchanged for correlations between hyperparameters and data. This is a general technique applicable for any distribution in the location-scale family, and optimal when the data poorly identify the parameter values (Papaspiliopoulos et al. 2007; Betancourt & Girolami 2013). We therefore adopt normal hyperprior distributions for all the location hyperparameters in our model, and half-cauchy distributions for all scale parameters (including hyperprior width parameters; Gelman et al. 2008).

The hierarchical modeling framework largely eschews the specification of prior information, instead allowing the model to set its own hyperprior distributions learned from the data during fitting. We view this process, as applied to transient optical light curve studies, as a form of unsupervised machine learning. In effect, the model is learning the shape and range of variation among light curves within the transient class, and applying that information to optimally interpret

individual light curves.

However, it is necessary to set prior distributions for the top level hyperparameters, and we adopt weakly informative priors except where needed to enforce regularization of the light curve model. In particular, we assign mean values for the normal prior distribution on the filter-level parameter (t_{hF,t_p}) controlling the plateau phase rise time (t_p) to specify the within filter variation observed in Sanders et al. (2014). We do the same for the filter-level priors controlling the plateau phase rise and decay rates (β_1 and β_2). We specify the prior on the explosion date hyperparameters with means of 1 and 100 days for the within- and between-season objects, respectively. We use a restrictive $\text{cauchy}(0.001)$ hyperprior for the top-level intrinsic scatter parameter (V_h) to regularize its ability to dominate the likelihood evaluation. We note that narrow hyperprior distributions are needed here because the hierarchical model exponentially amplifies variances. Prior information is therefore needed to ensure a reasonable range of variation of the top level parameters and to avoid numerical overflow during sampling. The model then fits optimal values for each of these hyperparameters given the likelihood for the data, and these priors serve largely to regularize the results.

8.2.3 Stan implementation

To sample from this model posterior, we employ the C++ library *Stan* (Stan Development Team 2013), which implements the adaptive Hamiltonian Monte Carlo (HMC) *No-U-Turn Sampler* (NUTS) of Hoffman & Gelman (2013). HMC

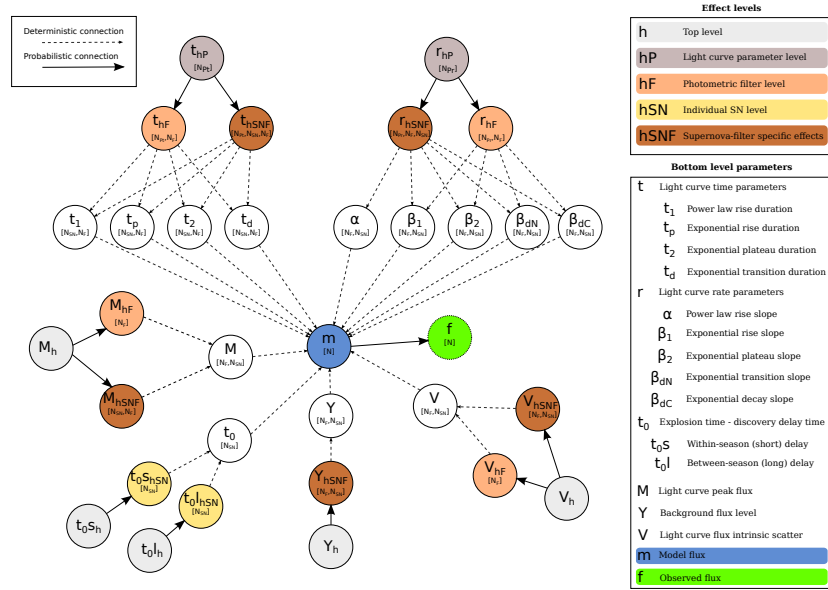


Figure 8.2.— Directed Acyclic Graphical representation of the hierarchical structure of the multi-level light curve model parameters. The color coding of the effects levels and the meanings of the bottom level parameters are given in the key at right. The bracketed numbers indicate the dimensionality (in terms of the number of objects, N_{SN} , the number of filters, N_F , and the number of parameters in the time and rate groups, N_{Pt} and N_{Pr}) of each parameter matrix.

is advantageous for inference on high dimensional multi-level models, because it capitalizes on the gradient of the posterior to efficiently traverse the joint posterior despite the presence of the highly correlated parameters inherent to hierarchical models (Betancourt & Girolami 2013). In practice, HMC will achieve a significantly higher effective sample size ratio (i.e. lower autocorrelation in the trace) than traditional Gibbs samplers for models with highly correlated parameters (Betancourt & Girolami 2013; Stan Development Team 2014).

NUTS operates in two phases; “adaptation” and “sampling.” During adaptation, the algorithm automatically tunes the temporal step size which controls the discretization of the Hamiltonian (Hoffman & Gelman 2013). Additionally, the algorithm estimates a diagonal HMC mass matrix during adaptation, which effectively scales the global step size to the optimal value for each parameter (we do not configure *Stan* to estimate the full, “dense” mass matrix given the significant additional computational overhead). During the sampling phase, the step size and mass matrix are fixed.

We use *Stan* to construct 32 independent MCMC chains from the posterior distribution of the model.¹ We have used the Harvard Faculty of Arts and Sciences “Odyssey” Research Computing cluster to run these chains in parallel, running for the cluster’s maximum job execution time of 3 days per chain, for a total utilization of 2,304 cpu hrs. Given our total yield of 12651 samples, this represents an average chain length of 395 samples and an effective sampling rate of 5.49 samples per hour per chain. For the purposes of convergence testing

¹The full *Stan* code for our statistical model is discussed in Appendix 8.7.

(Section 8.4.1), we consider the full chains including adaptation phase. For the purposes of light curve modeling, we exclude the adaptation phase as well as the first 20 iterations of the sampling phase, yielding 11265 total samples from the approximate posterior stationary distribution.

The high computational cost of sampling from the model posterior distribution is due to the small HMC step size emerging from the NUTS adaptation. Figure 8.3 illustrates this effect, comparing the Hamiltonian discretization step size to the number of leapfrog steps per iteration as the step size varies during NUTS adaptation. As the step size decreases, the number of leapfrog steps needed (the number of posterior calculations, and therefore the execution time) grows exponentially. The horizontal feature at the top of the this figure illustrates saturation of the leapfrog algorithm tree depth, suggesting that yet smaller step sizes may be needed to optimally sample from the posterior. However, given the onerous computation time required to iterate the NUTS algorithm (which is not immediately parallelizable) at the selected maximum tree depth (\gtrsim 1 hour of CPU time at the maximum tree depth of 16), we have elected not to increase the maximum tree depth. As a result, the HMC sampler could potentially become stuck in local minima of the multi-dimensional posterior, biasing the resulting samples away from the tails of the true joint posterior distribution.

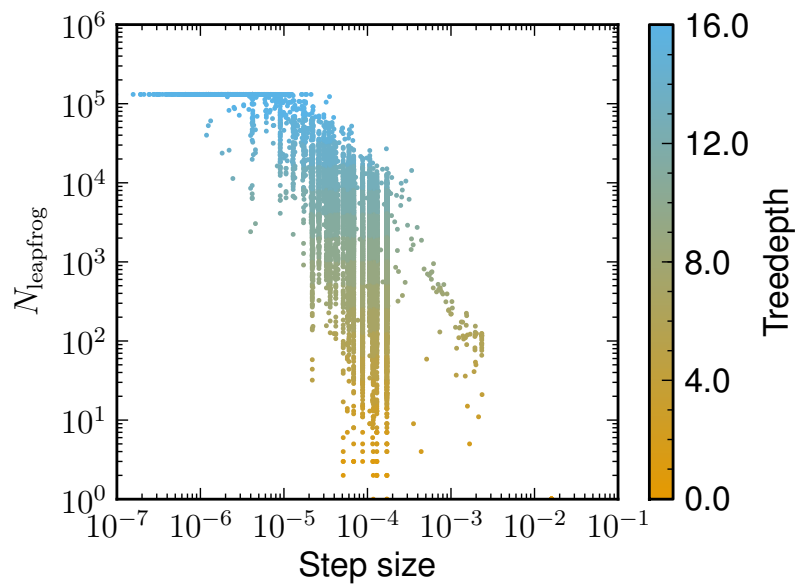


Figure 8.3.— Illustration of the complexity of the HMC sampling procedure. The figure compares the HMC Hamiltonian discretization step size to the number of leapfrog steps (N_{leapfrog}) needed per iteration. All samples from the combined MCMC chain, including adaptation steps, are shown. The color coding shows the NUTS treedepth (key at right). Vertically-correlated features indicate adapted chains (proceeding with fixed step size).

8.3 SAMPLE DATA

8.3.1 Pan-STARRS1 Optical Observations

Our Type IIP supernova light curve sample is selected from four years of systematic Medium Deep Field observations by the Pan-STARRS1 (PS1) telescope, as described in Sanders et al. (2014). PS1 is a high-extended wide-field imaging system, designed for dedicated survey observations and located on a mountaintop site in the Hawaiian island chain. Observations are conducted remotely, from the University of Hawaii–Institute for Astronomy Advanced Technology Research Center (ATRC) in Pukalani. A complete description of the PS1 system, both hardware and software, is provided by Kaiser et al. (2002). The 1.8 m diameter primary mirror, 3.3° field of view, and other PS1 optical design elements are described in Hodapp et al. (2004); the array of $0.258''$ pixel detectors, and other attributes of the PS1 imager is described in Tonry & Onaka (2009); and the survey design and execution strategy are described in Chambers (in preparation). The PS1 Medium Deep Survey (MDS) consists of 10 pencil beam fields observed with a typical cadence of 3 d in each filter.

The PS1 observations are obtained through a set of five broadband filters, which we refer to interchangeably as g_{P1} , r_{P1} , i_{P1} , z_{P1} , and y_{P1} or simply *grizy* (Stubbs et al. 2010). MDS achieves a 5σ depth of ~ 23.3 mag in *griz* filters, and ~ 21.7 mag in the *y*-filter (with observations taken near full moon). Photometry presented here is in the “natural” PS1 system, $m = 2.5 \log(\text{flux}) + m'$, with a single zero-point adjustment m' made in each band to conform to the AB magnitude

scale (Schlafly et al. 2012; Tonry et al. 2012; Magnier et al. 2013).² We assume a systematic uncertainty of 1% for our PS1 observations due to the asymmetric PS1 point spread function and uncertainty in the photometric zero-point calibration (Tonry et al. 2012). The standard reduction, astrometric solution, and stacking of the nightly images is done by the Pan-STARRS1 IPP system (Magnier 2006; Magnier et al. 2008), and the nightly MDS stacks are processed through a frame subtraction analysis using the *photpipe* image differencing pipeline (Rest et al. 2005; Scolnic et al. 2013).

We adopt the final spectroscopic SN IIP sample from Sanders et al. (2014), including all objects sub-classified using the Support Vector Machine machine learning classification method therein. This sample consists of 18,837 total photometric data points, including 5,056 robust detections, for 76 SNe IIP in the *grizy* filters. We note that the photometric observations which are not robust detections still play a significant role in the likelihood of our model, serving to constrain the rise time and decay rate parameters of the model, as well as directly identifying the background parameter Y_b . The particular transients included in this sample and their properties are described in Sanders et al. (2014).

8.3.2 Posterior Probability Convergence

The HMC algorithm quickly and efficiently converges on a maximal value of the global posterior probability for the model by identifying optimal values for each

²The magnitudes quoted throughout this paper are in the AB system, except where explicitly noted.

bottom level light curve parameter for all the SNe and for the hyperparameters. Given that the global model for the PS1 SNe IIP sample has a total of 9,176 individual parameters, this fast convergence is a significant testament to the efficiency of HMC as an optimization engine for high-dimensional functions.

Figure 8.4 shows the posterior probability evolution of the Markov chains as the NUTS sampler adapts and then reaches the sampling phase. Chains typically converge near the maximum achievable posterior probability during our warmup period of only 30 iterations.

8.4 RESULTS

8.4.1 Sampling Characteristics and Fit Convergence

Figure 8.5 shows the MCMC trace for a well identified bottom level parameter; the values drawn from the HMC algorithm for the plateau phase decline rate (β_2) of an object (PS1-12cey) with sufficient r -band photometry to constrain this phase of the light curve. The sampler moves quickly in this dimension, with low autocorrelation between samples, and the parameter is acceptably convergent (with potential scale reduction factor $\hat{R} = 1.14$).

In contrast, Figure 8.6 shows the trace for a moderately well identified top level parameter (r_{hP}), controlling the global plateau phase decay rate across all filters. The trace indicates that the sampler is moving more slowly in this dimension, with significant autocorrelation between samples. This top level

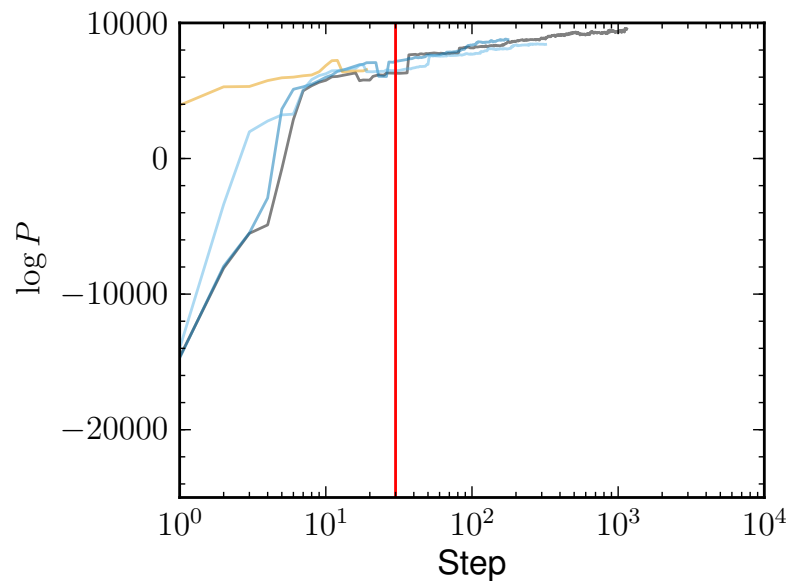


Figure 8.4.— Markov Chain Monte Carlo trace of the global posterior probability from the hierarchical model fit, showing the fast convergence of the HMC algorithm to near the optimal parameter values. A random subset of chains from the hierarchical model fit are shown (different lines). The red vertical line marks the end of the NUTS adaptation phase, at which point the HMC step size is fixed. The probability shown on the y -axis is not normalized and therefore has arbitrary units.

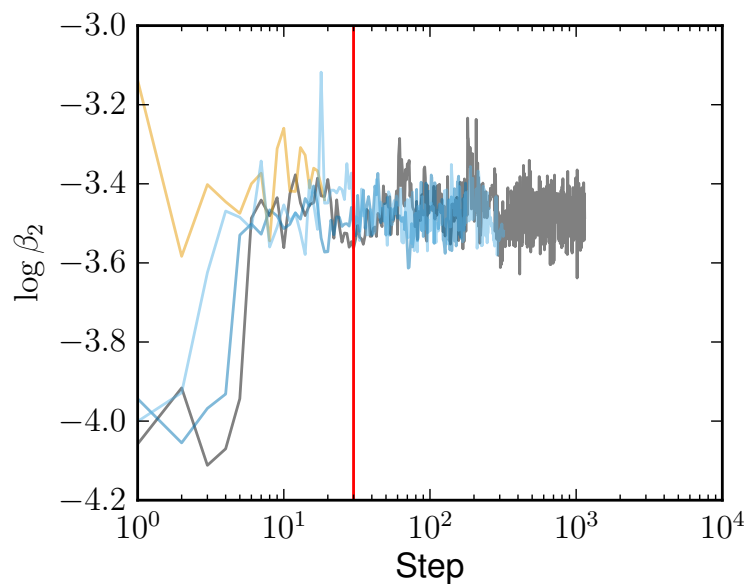


Figure 8.5.— Illustration of convergent HMC sampling for the well identified bottom-level model parameters. Like Figure 8.4, but for the bottom level parameter β_2 for a randomly selected SN (r band).

parameter has apparently not yet converged ($\hat{R} = 1.77$). This suggests that additional sampling is needed to achieve a desirable level of convergence among some hyperparameters, but the computational cost is prohibitive at this time; we discuss alternative methods for achieving convergence with HMC in Section 8.5.

The origin of the convergence challenges facing the HMC algorithm are illustrated in Figure 8.7. The Figure, showing a slice from the joint posterior distribution, illustrates the high correlation between the hierarchically linked parameters in the model. In contrast, Figure 8.8 shows a slice of the joint posterior along the dimensions of the top level and filter-level hyperparameters for the plateau phase time duration. Dependence between these hyperparameters was obviated via selection of the non-centered parameterization (Section 8.2.2) and, indeed, their marginal posteriors have very low correlation.

8.4.2 Posterior Predictive Check Comparison

We validate the success of our model in describing the light curve behavior of objects in our SN IIP sample using posterior predictive checks (Gelman et al. 2013), comparing the distribution of luminosities predicted under our fitted light curve model to the observed photometric data. Figure 8.9 shows a posterior predictive check for PS1-10zu, whose poor temporal coverage illustrates the strengths of the hierarchical model. The figure compares the r -band light curve fit for this object to the fit under the individual-level model presented in Sanders et al. (2014), which uses an identical 5-component light curve model, but does not make use of no partial pooling between SNe. The hierarchical

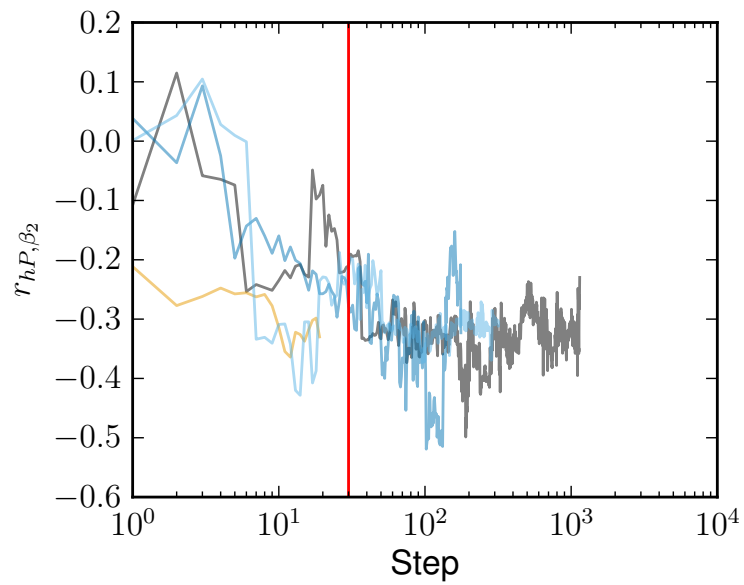


Figure 8.6.— Illustration of slow moving HMC sampling for the higher level model parameters. Like Figure 8.4, but for the hyperparameter r_{hP, β_2} , the top level parameter controlling the β_2 decay rates.

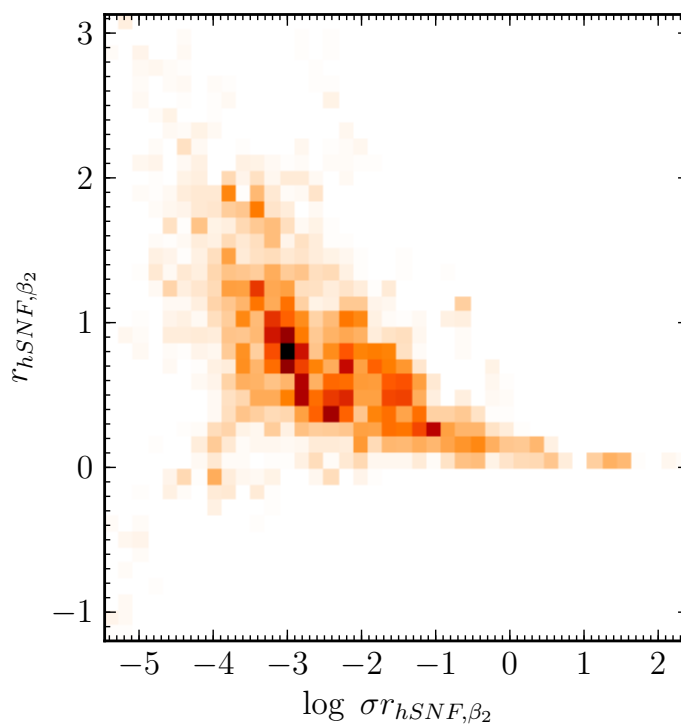


Figure 8.7.— Illustration of the high curvature in the hierarchical model posterior. A histogram of samples from a slice of the joint posterior distribution is shown, along the dimensions of the SN-filter level mean and width (on a log scale) hyperparameters for the plateau phase decay rate (r_{hSNF, β_2}).

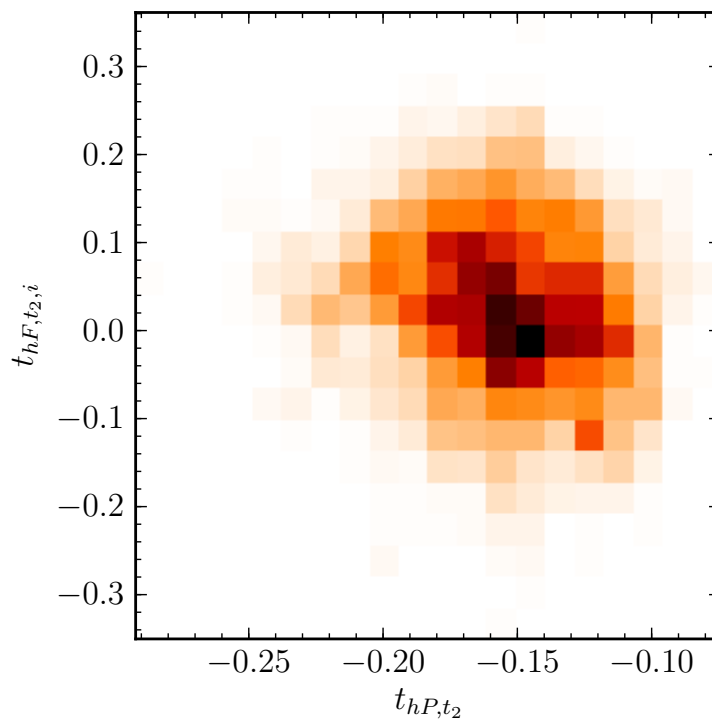


Figure 8.8.— Illustration of the effectiveness of the non-centered parameterization in removing dependency between hyperparameters. Like Figure 8.7, but showing a slice along the dimensions of the top level and filter-level hyperparameters for the plateau phase time duration (t_{hP,t_2} and $t_{hP,t_2,i}$).

fit achieves significantly greater constraints on the parameters describing the rising phases of the SN, resulting in a much tighter distribution of explosion dates and plateau durations (a parameter critical for physical inference on the progenitor star). The improvement is due to the strongly identified plateau duration hyperparameters (Section 8.4.3). In the individual-level model, a weakly informative prior distribution was established for this parameter based on the theoretically predicted range of plateau duration variation; in the multi-level model, the hyperparameters are inferred from the data themselves, resulting in much stronger prior information at the individual SN level. That the fit to the later phases of the light curve, where the data are strongly identifying, is indistinguishable from the fit obtained in the individual model is validation of the unbiased performance of the hierarchical model.

Figure 8.10 shows a comparison of fits for several additional objects, illustrating features of the hierarchical modeling framework under different data scenarios, which we describe here. PS1-11azd was observed only during the rise and initial stages of the plateau phase. The posterior predictive luminosity distribution of the individual and hierarchical models are similar, but the plateau decline phase duration (t_2) parameter is much more constrained in the hierarchical model (Figure 8.10 a).

PS1-12bku (Figure 8.10 b) was observed from explosion through the final, radioactive decay-dominated phase. Generally, this case confirms that, where the data is strongly identifying, the hierarchical model produces fits in agreement with the individual-level model. Interestingly, for this object there is a r -band photometric observation with relatively high uncertainty at $\sim +80$ days, which

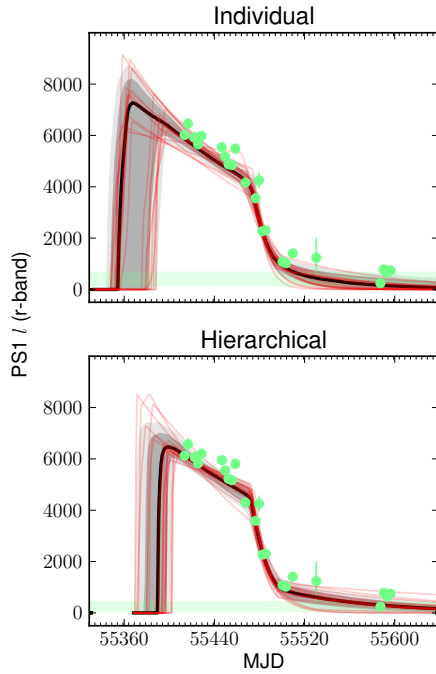


Figure 8.9.— Comparison of posterior predictive checks between the individual light curve fit of Sanders et al. (2014), above, and the hierarchical model fit, below, for the SN PS1-10zu. Each plot shows the r -band photometry for the SN (green points and errorbars), which has detection only of the final phases of the light curve because the object exploded between observing seasons. The units of luminosity, l , are described in (Sanders et al. 2014). The shaded areas show the 1 and 2 σ confidence intervals for the posterior predictive distribution of the 5-component light curve model (see Section 8.4.2), and the solid black line shows the median of that confidence interval. The red lines show a random subset of sampled light curve models corresponding to parameter values from the MCMC chain. The horizontal green bar shows the range fitted for the zero-point luminosity offset.

introduces a degeneracy in the posterior—whether this point should be assigned to the plateau or transition phase of the light curve. The fit for this SN under the hierarchical model looks similar to the individual-level model fit, exploring both forks of the degeneracy. However, the two fits favor opposite sides of the fork. The individual fit maximizes the likelihood of the r -band photometry for the object alone, placing the point on the transition phase, while the hierarchical fit prefers the solution where the point falls on the plateau. Because the fork favored by the hierarchical model is more consistent with the modeled distribution of plateau durations among SNe IIP (based on partial pooling from the other objects in the sample), it is the more well justified solution.

In Figure 8.10 c, the hierarchical z -band fit for the SN PS1-11ai is much more highly regularized to match the shape of other z -band light curves than the individual fit. This leads to significantly improved constraints on the peak magnitude and plateau duration for this object. For PS1-12wn (y -band; Figure 8.10 d), only 1 robust photometric detection is available, and all the photometry is highly uncertain ($\delta m \sim 0.5$ mag at 1σ). The individual light curve fit in this case is very poorly regularized, obeying the peak magnitude suggested by the detection and the limits suggested by the non-detections, but otherwise has very poorly constrained light curve properties like plateau duration and decline rate. The hierarchical fit in this case is far superior in regularization, showing a characteristic y -band SN IIP light curve shape matched to the available photometry.

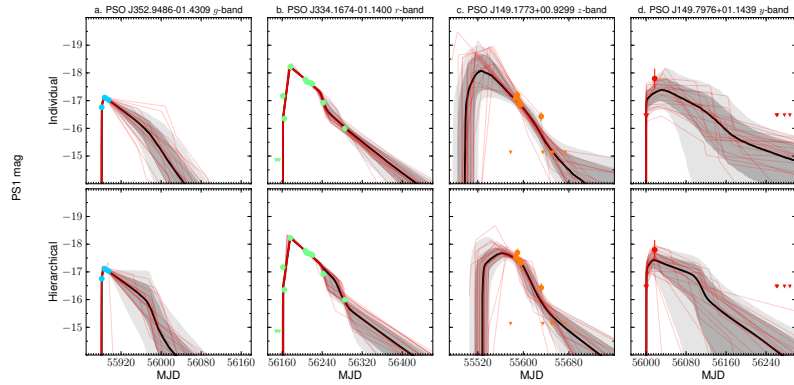


Figure 8.10.— Illustration of the advantages provided by the hierarchical model for fitting under different data coverage scenarios, relative to individual light curve fitting. Like Figure 8.9, but on the absolute magnitude scale and for a variety of PS1 SNe and photometric filters. The individual model fits are shown above, the with the corresponding hierarchical fits below. Triangles represent the locations of photometry that are not robust detections; they are plotted at the y -axis position of the limiting PS1 magnitude of the filter, though the actual flux and uncertainty of these points is used in the Bayesian likelihood calculation.

8.4.3 Population Parameter Distribution Characteristics

To further the investigation of SN IIP plateau durations from Sanders et al. (2014), in Figure 8.11 we compare the plateau duration inferences from that project to the duration distributions inferred from the hierarchical model. The plateau duration distribution hyperprior in the hierarchical model is a sum of the t_p and t_2 hyperpriors. The hyperpriors include both location (e.g. t_{hP}) and width (e.g. σt_{hP}) hyperparameters, so we visualize the posterior distribution of hyperpriors by showing multiple lognormal hyperpriors corresponding to random draws of the hyperparameters. We focus on the r -band durations here, and so include both the t_{hP} and t_{hF} hyperparameters.

The distribution of bottom-level plateau duration parameters for our hierarchical model agree well with the individual light curve fits from Sanders et al. (2014). Taking the median bottom level parameter from the MCMC chain, the distribution of values from the hierarchical model has a mean and standard deviation of 90 ± 6 days, compared to 92 ± 14 days for the individual model. Note that the variance in the hierarchical model distribution is significantly lower than from the individual fits, because partial pooling between objects constrains the bottom level posteriors.

By directly modeling the underlying population of transients, the hierarchical modeling framework allows us to overcome potential biases in transient search methodology. In particular, although long duration SNe IIP are less likely to be observed with full temporal coverage in ground based transient searches (Section 8.2), we can estimate the fraction of unseen, long-duration transients

in the population from the hierarchical model posterior. This product of the posterior distribution of the hierarchical model is constrained by both the observed characteristics of objects in the sample, and characteristics allowed by pre-explosion and late time non-detections from the transient search at the same location.

Our hyperparameter posterior distributions suggest there is a 60% probability that at least 10% of the underlying population of SNe IIP have r -band plateau durations longer than the bottom level parameter value for any individual object in the sample (> 112 days). The probability that at least 20% of objects fall above this value is 30%. Among the sampled hyperprior distributions, the median of the population standard deviation is 33 days. The standard deviation distribution has a strong tail at larger values, shown in Figure 8.11. These results emphasize and support the finding of Sanders et al. (2014), that the plateau duration distribution of SNe IIP has significant variance.

8.5 DISCUSSION

The multi-level model developed and applied in this paper points to a methodological framework for the interpretation of SN light curves from the next generation of wide-field transient searches, such as the Large Synoptic Survey Telescope (LSST; LSST Science Collaboration et al. 2009). In the coming era, the volume of available photometric data will increase dramatically, while the human and observational resources for follow-up of individual objects will not. In this regime, to capitalize on the larger SN sample sizes afforded by these

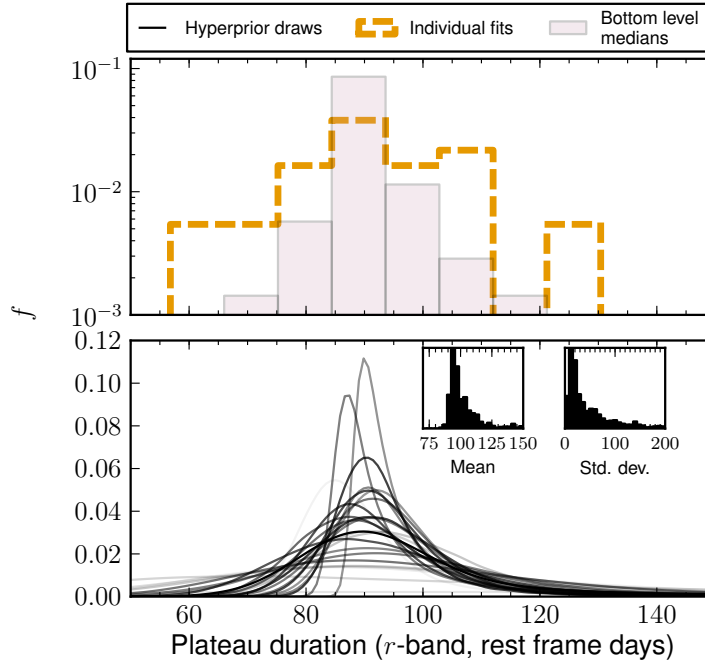


Figure 8.11.— Comparison of population level inferences on the SN IIP plateau duration distributions (in r -band) between the hierarchical and individual model fits. Top: The dashed line shows the histogram of plateau durations measured in Sanders et al. (2014) using the individual model (including only the objects with well constrained posteriors, as defined therein). The shaded area shows a histogram of the bottom level plateau duration parameters under the hierarchical model (for all objects in the sample). Bottom: The solid lines show draws of the plateau distribution hyperprior (a sum over the t_p and t_2 hyperpriors) from the hierarchical model fit, with the opacity scaled to the probability of the draw under the posterior. The inset plots show the marginalized posterior distributions for the mean and standard deviation of the summed hyperprior distributions (in rest frame days).

next generation searches, it will be critical to apply population level light curve modeling. To do this, it is necessary to apply analytical methods that are robust to data sparseness and posterior non-identifiability for individual objects, and computational methods that are capable of generating inferences from large datasets. The combination of hierarchical Bayesian methodology and Hamiltonian Monte Carlo methods explored in this work are natural methods for addressing both these concerns.

This work also suggests future paths for improvement of the Bayesian light curve modeling framework presented here. First, to permit applications to purely photometric datasets (where the SN classification and redshift are not known or poorly constrained), the model must be generalized. The redshift can trivially be added to the multi-level model as a vector of free parameters, but it will introduce significant posterior correlations and interactions that will need to be tested and may require the assertion of significant prior information to aid identifiability. Additional model components are needed to allow for application to multiple SN classes simultaneously. This could be accomplished through categorical mixture modeling with several different, physically-motivated SN light curve prescriptions for each SN type or by using a more generic, non-parametric, or continuously expanding light curve model to allow fitting of diverse SN types. Both of these solutions would support classification inferences, by assessment of the categorical simplex parameter posteriors directly, or by a clustering analysis of the continuous model expansion parameters, respectively. Applications to transient searches delving to significantly higher redshifts (and also the non-parametric modeling approach) may require full three-dimensional modeling of the SN spectral energy

distribution evolution, rather than two-dimensional light curve modeling in each filter, in order to permit K -corrections at all distances. Finally, incorporating host galaxy information will be critical to producing purely-photometric informative inferences across SN classes. This should include modeling of the distribution of host galaxy global properties per SN class to uncover and take advantage of differences in progenitor properties (see e.g. Kelly & Kirshner 2012; Sanders et al. 2012c; Foley & Mandel 2013; Lunnan et al. 2013a; McCrum et al. 2014), as well as the line-of-sight host galaxy extinction and reddening law (e.g. Mandel et al. 2011).

Finally, we look to Riemannian manifold Hamiltonian Monte Carlo (RMHMC; Betancourt 2013) techniques for permitting posterior characterization in the future, in the face of these additional modeling complexities. Compared to traditional, Euclidian Hamiltonian Monte Carlo (EHMC; as applied for this work), RHMC samplers efficiently explore highly correlated and high-dimensional posterior functions by automatically adapting the Hamiltonian integration step size to a value optimal for local conditions (Girolami & Calderhead 2011; Betancourt & Girolami 2013). This capability would permit unbiased sampling even amidst models with joint posterior distributions with higher curvature than the multi-level model examined here, such as a model including interactions between filter-level parameters or interactions between light curve parameter groups (e.g. t - r interactions). Our attempts to fit such a model with EHMC have not achieved convergence within reasonable integration times, with the high posterior curvature preventing the hyperparameters from moving at a sufficient rate to produce convergent chains. The addition of RHMC sampling capabilities

to *Stan* in the near future (Betancourt 2013) will make these techniques accessible to astronomers in the LSST era.

8.6 CONCLUSIONS

We have explored the use of Bayesian hierarchical modeling and Hamiltonian Monte Carlo (HMC) to enable population-level inference on multi-band transient light curves from comprehensive analysis of optical photometry from wide field transient searches. The primary conclusions of this work are:

- While computational limits still challenge the implementation of hierarchical models, due to the high curvature in their joint posterior distributions, sufficient convergence is achieved in the bottom level model parameters (Section 8.4.1) to enable their immediate application for transient light curve studies.
- Comparisons between light curve posterior predictive distributions from our hierarchical model fit to the individual light curve fits of Sanders et al. (2014) show strong agreement for well identified parameters, and show an advantage for hierarchical models among poorly identified parameters (Section 8.4.2). In particular, partial pooling of parameter information between transients supports improved regularization of light curve shapes, and supports model selection between partially degenerate light curve parameter scenarios.
- By directly modeling the underlying transient population, hierarchical

models permit inference on the occurrence of properties not observed within the dataset (Section 8.4.3). This feature is of particular value in overcoming observational biases induced by ground based transient searches, such as the under-representation of long duration transients like some SNe IIP.

We have concluded with a discussion of future directions for this modeling (Section 8.5), including applications to upcoming wide field transient searches, extensions to the hierarchical model structure developed here, and expanded capabilities to be enabled by the advent of Riemannian manifold Hamiltonian Monte Carlo.

8.7 Appendix A: Hierarchical Light Curve Stan Model

Below we reproduce the full hierarchical model for the 5 component piecewise SN IIP light curves in the *Stan* modeling language, as described in Section 8.2. The Stan model specification format is documented in the Stan Modeling Language Users Guide and Reference Manual (Stan Development Team 2014).

The model takes the following data as input: `N_obs`, the total number of photometric data points; `N_filt`, the number of photometric filters; `t`, a vector of MJD dates of the photometric observations; `fL`, a vector of luminosities corresponding to the photometric observations (with units as described in Sanders et al. 2014); `dfL` a corresponding vector of luminosity uncertainties; `z` the redshift; `t0_mean` an initial estimate of the explosion date (for initialization and for

centering the explosion date prior distribution); `J` a vector of integers specifying the filter ID of each photometric observation; `Kcor_N`, a matrix of pre-computed K -corrections for each filter, in magnitudes with spacing of 1 day; `fluxscale` the zero-point of the luminosity unit system (`fluxscale` = 10^7 in the system we have employed); and `duringseason`, a boolean value specifying whether the object exploded within or between observing seasons, for selection of the explosion date prior distribution parameters. The calculation of the model light curve flux and application of the K -correction values is performed in the `transformed parameters` section, and the prior and likelihood calculations are performed in the `model` section. Certain vector-valued prior distribution parameters are specified in the `transformed data` section for convenience. We note that the higher level parameters for the five different light curve rates and four different phase durations are grouped together in vectors (e.g. r_{hP} and t_{hP} for the top level, and r_{hF} and t_{hF} for the filter level, respectively) for convenience.

The *Stan* model is then compiled and run (Stan Development Team 2014) to yield MCMC samples from the posterior distribution of light curve parameters. We configured the *No-U-Turn Sampler* to use fixed 0 initialization of the parameter values, an adaptation phase of 30 steps, a maximum treedepth of 16, and otherwise employed the default sampler parameters. We have used CmdStan version 2.2.0³.

```
data {  
  int<lower=0> N_obs;  
  int<lower=0> N_SW;  
  int<lower=0> N_filt;
```

³<https://github.com/stan-dev/stan/releases/tag/v2.2.0>

```

vector[N_obs] t;
vector[N_obs] fL;
vector[N_obs] dfL;
vector[N_SN] z;
vector[N_SN] t0_mean;
int<lower=1,upper=N_filt> J[N_obs];
int<lower=1,upper=N_SN> SNid[N_obs];
int<lower=0> Kcor_N;
real Kcor[N_SN, N_filt,Kcor_N];
real<lower=0> fluxscale;
vector<lower=0,upper=1>[N_SN] duringseason;
}

transformed data {
vector[N_filt] prior_t_hF[4];
vector[N_filt] prior_t_hF_s[4];
vector[N_filt] prior_r_hF[5];
vector[N_filt] prior_r_hF_s[5];
for (i in 1:N_filt) {
  prior_t_hF[1,i] <- 0;
  prior_t_hF_s[1,i] <- 0.1;
}

prior_t_hF[2,1] <- -1;
prior_t_hF[2,2] <- -0.5;
prior_t_hF[2,3] <- 0;
prior_t_hF[2,4] <- 0.5;
prior_t_hF[2,5] <- 1;
for (i in 1:N_filt) {prior_t_hF_s[2,i] <- 0.1;}

for (i in 1:N_filt) {
  prior_t_hF[3,i] <- 0;
  prior_t_hF_s[3,i] <- 0.1;
}

for (i in 1:N_filt) {
  prior_t_hF[4,i] <- 0;
  prior_t_hF_s[4,i] <- 0.1;
}

for (i in 1:N_filt) {
  prior_r_hF[1,i] <- 0;
  prior_r_hF_s[1,i] <- 0.1;
}

prior_r_hF[2,1] <- 2;
prior_r_hF[2,2] <- 1;
prior_r_hF[2,3] <- 0;
prior_r_hF[2,4] <- -0.5;
prior_r_hF[2,5] <- -1;
for (i in 1:N_filt) {prior_r_hF_s[2,i] <- 0.1;}

prior_r_hF[3,1] <- 1;
prior_r_hF[3,2] <- 0.3;
prior_r_hF[3,3] <- 0;
prior_r_hF[3,4] <- -1;

```

```

prior_r_hF[3,5] <- -1;
for (i in 1:N_filt) {prior_r_hF_s[3,i] <- 0.1;}
for (i in 1:N_filt) {
  prior_r_hF[4,i] <- 0;
  prior_r_hF_s[4,i] <- 0.1;
}
for (i in 1:N_filt) {
  prior_r_hF[5,i] <- 0;
  prior_r_hF_s[5,i] <- 0.1;
}
}

parameters {
  vector[4] t_hP;
  vector<lower=0>[4] sig_t_hP;
  vector[N_filt] t_hF[4];
  vector<lower=0>[N_filt] sig_t_hF[4];
  vector[N_SN * N_filt] t_hSNF[4];
  vector<lower=0>[N_SN * N_filt] sig_t_hSNF[4];
  vector[5] r_hP;
  vector<lower=0>[5] sig_r_hP;
  vector[N_filt] r_hF[5];
  vector<lower=0>[5] sig_r_hF[5];
  vector[N_SN * N_filt] r_hSNF[5];
  vector<lower=0>[N_SN * N_filt] sig_r_hSNF[5];
  real M_h;
  real<lower=0> sig_M_h;
  vector[N_filt] M_hF;
  vector<lower=0>[N_filt] sig_M_hF;
  vector[N_SN * N_filt] M_hSNF;
  vector<lower=0>[N_SN * N_filt] sig_M_hSNF;
  real Y_h;
  real<lower=0> sig_Y_h;
  vector[N_SN * N_filt] Y_hSNF;
  vector<lower=0>[N_SN * N_filt] sig_Y_hSNF;
  real t0s_h;
  real<lower=0> sig_t0s_h;
  vector[N_SN] t0s_hSN;
  vector<lower=0>[N_SN] sig_t0s_hSN;
  real t01_h;
  real<lower=0> sig_t01_h;
  vector[N_SN] t01_hSN;
  vector<lower=0>[N_SN] sig_t01_hSN;
  real<lower=0> V_h;
  vector<lower=0>[N_filt] V_hF;
  vector<lower=0>[N_SN * N_filt] V_hSNF;
}

transformed parameters {
  vector[N_obs] mm;
  vector[N_obs] dm;

```



```

vector<upper=0>[N_SN] pt0;
matrix<lower=0>[N_SN, N_filt] t1;
matrix<lower=0>[N_SN, N_filt] t2;
matrix<lower=0>[N_SN, N_filt] td;
matrix<lower=0>[N_SN, N_filt] tp;
matrix[N_SN, N_filt] lalpha;
matrix[N_SN, N_filt] lbeta1;
matrix[N_SN, N_filt] lbeta2;
matrix[N_SN, N_filt] lbetadN;
matrix[N_SN, N_filt] lbetadC;
matrix[N_SN, N_filt] Mp;
matrix[N_SN, N_filt] Yb;
matrix<lower=0>[N_SN, N_filt] V;
matrix<lower=0>[N_SN, N_filt] M1;
matrix<lower=0>[N_SN, N_filt] M2;
matrix<lower=0>[N_SN, N_filt] Md;
for (l in 1:N_SN) {
  if (duringseason[l] == 1) {
    pt0[l] <- -exp( t0s_h + sig_t0s_h * ( t0s_hSN[l] .* sig_t0s_hSN[l] ));
  } else {
    pt0[l] <- -exp( t0l_h + sig_t0l_h * ( t0l_hSN[l] .* sig_t0l_hSN[l] ));
  }
}
for (i in 1:N_filt) {

  for (j in 1:N_SN) {

    t1[j,i] <- exp( log(1) + t_hP[1] + sig_t_hP[1] * (
      t_hF[1,i] * sig_t_hF[1,i]
      + sig_t_hSNF[1,(i-1)*N_SN+j] * t_hSNF[1,(i-1)*N_SN+j]
    ));

    tp[j,i] <- exp( log(10) + t_hP[2] + sig_t_hP[2] * (
      t_hF[2,i] * sig_t_hF[2,i]
      + sig_t_hSNF[2,(i-1)*N_SN+j] * t_hSNF[2,(i-1)*N_SN+j]
    ));

    t2[j,i] <- exp( log(100) + t_hP[3] + sig_t_hP[3] * (
      t_hF[3,i] * sig_t_hF[3,i]
      + sig_t_hSNF[3,(i-1)*N_SN+j] * t_hSNF[3,(i-1)*N_SN+j]
    ));

    td[j,i] <- exp( log(10) + t_hP[4] + sig_t_hP[4] * (
      t_hF[4,i] * sig_t_hF[4,i]
      + sig_t_hSNF[4,(i-1)*N_SN+j] * t_hSNF[4,(i-1)*N_SN+j]
    ));

    lalpha[j,i] <- -1 + ( r_hP[1] + sig_r_hP[1] * (
      r_hF[1,i] * sig_r_hF[1,i]
      + sig_r_hSNF[1,(i-1)*N_SN+j] * r_hSNF[1,(i-1)*N_SN+j]
    ));

    lbeta1[j,i] <- -4 + ( r_hP[2] + sig_r_hP[2] * (
      r_hF[2,i] * sig_r_hF[2,i]

```

```

        + sig_r_hSNF[2,(i-1)*N_SN+j] * r_hSNF[2,(i-1)*N_SN+j]
    ));
lbeta2[j,i] <- -4 + ( r_hP[3] + sig_r_hP[3] * (
    r_hF[3,i] * sig_r_hF[3,i]
    + sig_r_hSNF[3,(i-1)*N_SN+j] * r_hSNF[3,(i-1)*N_SN+j]
));
lbetaN[j,i] <- -3 + ( r_hP[4] + sig_r_hP[4] * (
    r_hF[4,i] * sig_r_hF[4,i]
    + sig_r_hSNF[4,(i-1)*N_SN+j] * r_hSNF[4,(i-1)*N_SN+j]
));
lbetaC[j,i] <- -5 + ( r_hP[5] + sig_r_hP[5] * (
    r_hF[5,i] * sig_r_hF[5,i]
    + sig_r_hSNF[5,(i-1)*N_SN+j] * r_hSNF[5,(i-1)*N_SN+j]
));
Mp[j,i] <- exp(M_h + sig_M_h * (
    M_hF[i] * sig_M_hF[i]
    + sig_M_hSNF[(i-1)*N_SN+j] * M_hSNF[(i-1)*N_SN+j]
));
Yb[j,i] <- Y_h + sig_Y_h * (Y_hSNF[(i-1)*N_SN+j] .* sig_Y_hSNF[(i-1)*N_SN+j]);
V[j,i] <- V_h * V_hF[i] * V_hSNF[(i-1)*N_SN+j];
}
}
M1 <- Mp ./ exp( exp(lbeta1) .* tp );
M2 <- Mp .* exp( -exp(lbeta2) .* t2 );
Md <- M2 .* exp( -exp(lbetadN) .* td );
for (n in 1:N_obs) {
    real N_SNC;
    int Kc_up;
    int Kc_down;
    real t_exp;
    int j;
    int k;
    real mm_1;
    real mm_2;
    real mm_3;
    real mm_4;
    real mm_5;
    real mm_6;
    j <- J[n];
    k <- SNid[n];
    t_exp <- ( t[n] - (t0_mean[k] + pt0[k]) ) / (1 + z[k]);
    if (t_exp>0) {
        mm_1 <- Yb[k,j];
    } else {
        mm_1 <- 0;
    }
}
if ((t_exp>=0) && (t_exp < t1[k,j])) {
    mm_2 <- Yb[k,j] + M1[k,j] * pow(t_exp / t1[k,j] , exp(lalpha[k,j]));
} else {

```

```

        mm_2 <- 0;
    }
    if ((t_exp >= t1[k,j]) && (t_exp < t1[k,j] + tp[k,j])) {
        mm_3 <- Yb[k,j] + M1[k,j] * exp(exp(lbeta1[k,j]) * (t_exp - t1[k,j]));
    } else {
        mm_3 <- 0;
    }
    if ((t_exp >= t1[k,j] + tp[k,j]) && (t_exp < t1[k,j] + tp[k,j] + t2[k,j])) {
        mm_4 <- Yb[k,j] + Mp[k,j] * exp(-exp(lbeta2[k,j]) * (t_exp - t1[k,j] - tp[k,j]));
    } else {
        mm_4 <- 0;
    }
    if ((t_exp >= t1[k,j] + tp[k,j] + t2[k,j]) && (t_exp < t1[k,j] + tp[k,j] + t2[k,j] + td[k,j])) {
        mm_5 <- Yb[k,j] + M2[k,j] * exp(-exp(lbetadN[k,j]) * (t_exp - t1[k,j] - tp[k,j] - t2[k,j]));
    } else {
        mm_5 <- 0;
    }
    if (t_exp >= t1[k,j] + tp[k,j] + t2[k,j] + td[k,j]) {
        mm_6 <- Yb[k,j] + Md[k,j] * exp(-exp(lbetadC[k,j]) * (t_exp - t1[k,j] - tp[k,j] - t2[k,j] - td[k,j]));
    } else {
        mm_6 <- 0;
    }
    dm[n] <- sqrt(pow(dfL[n],2) + pow(V[k,j],2));
    if (t_exp<0) {
        N_SNc <- 0;
    } else if (t_exp<Kcor_N-2){
        Kc_down <- 0;
        while ((Kc_down+1) < t_exp) {
Kc_down <- Kc_down + 1;
        }
        Kc_up <- Kc_down+1;
        N_SNc <- Kcor[k,j,Kc_down+1] + (t_exp - floor(t_exp)) * (Kcor[k,j,Kc_up+1]-Kcor[k,j,Kc_down+1]);
    } else {
        N_SNc <- Kcor[k,j,Kcor_N];
    }
    mm[n] <- (mm_1+mm_2+mm_3+mm_4+mm_5+mm_6) / (pow(10, N_SNc/(-2.5)));
}
}
model {
    t0s_h ~ normal(0, 0.5);
    sig_t0s_h ~ cauchy(0, 0.1);
    t01_h ~ normal(log(100), 1);
    sig_t01_h ~ cauchy(0, 0.1);
    V_h ~ cauchy(0, 0.001);
    Y_h ~ normal(0, 0.1);
    sig_Y_h ~ cauchy(0, 0.01);
    M_h ~ normal(0, 1);
    sig_M_h ~ cauchy(0, 0.1);
    t_hP ~ normal(0,0.1);

```

```

sig_t_hP ~ cauchy(0, 0.1);
for (i in 1:4) {
  t_hF[i] ~ normal(prior_t_hF[i], prior_t_hF_s[i]);
  sig_t_hF[i] ~ cauchy(0, 0.1);
  t_hSNF[i] ~ normal(0,1);
  sig_t_hSNF[i] ~ cauchy(0, 0.1);
}
r_hP ~ normal(0,1);
sig_r_hP ~ cauchy(0, 0.1);
for (i in 1:5) {
  r_hF[i] ~ normal(prior_r_hF[i], prior_r_hF_s[i]);
  sig_r_hF[i] ~ cauchy(0, 0.1);
  r_hSNF[i] ~ normal(0,1);
  sig_r_hSNF[i] ~ cauchy(0, 0.1);
}
M_hF ~ normal(0,1);
sig_M_hF ~ cauchy(0, 0.1);
M_hSNF ~ normal(0,1);
sig_M_hSNF ~ cauchy(0, 0.1);
Y_hSNF ~ normal(0,1);
sig_Y_hSNF ~ cauchy(0, 0.1);
V_hF ~ cauchy(0, 0.1);
V_hSNF ~ cauchy(0, 0.1);
t0s_hSN ~ normal(0,1);
sig_t0s_hSN ~ cauchy(0, 0.1);
t0l_hSN ~ normal(0,1);
sig_t0l_hSN ~ cauchy(0, 0.1);
fL ~ normal(mm,dm);
}

```

Chapter 9

Conclusions and Future

Directions

We have used optical observations from the wide field survey telescope Pan-STARRS1 (PS1) and other multiwavelength observational techniques, as well as a variety of statistical methods, to infer the progenitor properties of core-collapse supernovae (SNe). In Section 9.1, we summarize the results of the work presented in this thesis, organized according to the themes laid out in Chapter 1. We propose future directions for this work and for the field of supernova observation generally in Section 9.2.

9.1 Supernova progenitor insights from trail-blazing wide field transient searches

9.1.1 The role of metallicity in core-collapse supernovae

We have presented the first spectroscopic study of Type Ibc SN host environments using objects drawn exclusively from untargeted transient searches (Chapter 4). Our methodology obviates a persistent bias toward luminous, metal-rich galaxies that has affected past studies of this type. Our new sample more than doubled the corpus of published untargeted Type Ibc SN host galaxy spectroscopy in the literature, and we additionally performed a meta-analysis of all previously published spectroscopy. We determined that there is no evidence for an observational difference between the metallicity distributions of SN Ib and Ic host environments. This result challenges the role of metal line-driven winds as a stripping mechanism for their progenitor stars, and focuses attention on binary interaction to explain their atmospheric composition at the time of explosion. Moreover, echoing the concurrent results of Kelly & Kirshner (2012), we find that SN Ic-BL host environment metallicities are significantly lower than those of SN Ib and Ic. This result, and our complementary analysis of the young stellar population ages in these environments, suggests closer agreement between SN Ic-BL and long-duration gamma ray burst (GRB) host environments than recognized by previous studies.

Finally, we performed a comprehensive evaluation of the systematic effects afflicting studies of core-collapse SN host environment metallicities.

We determined that the bias introduced by galaxy-targeted SN searches is most significant, with the confounding effects of galaxy-nucleus spectroscopy and biases in spectroscopic follow-up of detected transients playing secondary roles. Additionally, we evaluated the uncertainty introduced by low-precision photometric metallicity calibrations, anticipating the results of Chapter 5.

Our analysis in Chapter 4 of the effects of spectroscopic localization for SN host environments relied on the results of Chapter 3, where we presented the largest spectroscopic study to date of individual emission nebulae in an external galaxy. We collected and analyzed MMT optical spectra of more than 250 HII regions and more than 400 planetary nebulae in M31 to determine their extinction, metallicities, and other nebular properties. Our investigation of the galactocentric metallicity gradient among HII regions in M31 reinforced the canonical results of Zaritsky et al. (1994) and Galarza et al. (1999) and explored several nuances in the metallicity profile: its dependence on the choice of abundance diagnostic, its variation as a function of other nebular properties (compactness), and its large intrinsic scatter. The latter property has significant implications for our SN host environment work, with the intrinsic scatter in M31's metallicity gradient being approximately 3 times the systematic observational uncertainty in the metallicity estimates. The complex and inhomogeneous nature of the interstellar medium of M31 illustrates the unresolved variance that underlies any extragalactic host environment metallicity measurement in the context of SN progenitor studies.

9.1.2 Characterizing the limits of the core-collapse mechanism

We have employed PS1 as a discovery engine for exotic core-collapse SN phenomenology, focusing on two particular events that have probed the extremities of the core-collapse explosion mechanism.

At the energetic extreme of core-collapse SNe, we have studied the Type Ic-BL SN 2010ay (Chapter 2). Many features of this supernova and its progenitor environment—its broad and high velocity spectroscopic features, its extreme peak luminosity, and its low-luminosity and metal-poor host galaxy—are characteristic of the SNe that have accompanied long-duration Gamma Ray Burst (GRB) explosions, like SN 2010bh. Yet non-detections from concurrent space-based gamma ray observations, as well as our strong upper limits on late-time radio emission from the JVLA, effectively rule out a GRB associated with SN 2010ay. We present SN 2010ay, together with SN 2009bb, as leading counter examples of the long-established paradigm for GRB-SN formation from low-metallicity progenitor stars (see e.g. MacFadyen & Woosley 1999). While SN 2010ay is a surprising case for its lack of relativistic outflow, the SN 2009bb represents an opposite case; a SN which exhibited relativistic ejecta properties despite its metal-rich host environment. Together, these events suggest that metallicity is not the key property which distinguishes SN explosions that proceed with and without relativistic outflows, pointing instead to another potential commonality such as binary interaction (echoing the results of Chapter 4).

At the extreme of core-collapse SN host environment properties, we have

explored the Type Ibn SN PS1-12sk, discovered by PS1 observations in the massive elliptical galaxy at the core of a galaxy cluster. As only the sixth discovered member of the rare SN Ibn class, this event has significant power in shaping our understanding of the progenitor properties of these unusual transients, marked by He-rich and dense circumstellar media. Using deep optical, X-ray, and radio observations of the host galaxy cluster, we rule out the presence of star formation in the host environment to sensitive limits. Using the exceptional temporal coverage of PS1, we place tight constraints on the time delay between the pre-explosion mass ejections and the SN. Together, these observations challenge the requirement for a very massive progenitor star for Type Ibn explosions, and we explore the potential for a non-core-collapse, white dwarf binary channel for this exotic class of transients.

9.1.3 21st century tools for supernova studies

We have proposed and characterized two new observational tools for the study of core-collapse SN populations that we believe will be increasingly important in the burgeoning era of wide field transient surveys: multi-band photometric calibrations for host galaxy metallicity estimation and Bayesian hierarchical modeling for inference on populations of SN light curves.

The first of these, a new photometric metallicity calibration for galaxies (Chapter 5), will facilitate next-generation studies of the kind presented in Chapter 4. In that study, we identified the fundamentally poor precision of single-band photometric metallicity estimation techniques as a primary barrier

to their use in host galaxy studies, requiring samples sizes approximately twice that needed by spectroscopic surveys to uncover a given difference in metallicity distributions. The new, multi-band technique we characterize in Chapter 5 (the “LZC relation”) alleviates this shortcoming, combining color information with luminosity measurements to break the degeneracy of galaxy metallicity with mass-to-light ratio and star formation rate. We achieve statistical uncertainties in galaxy metallicity estimation of $\lesssim 0.1$ dex, on par with spectroscopic techniques, and we show that this method additionally removes bias in metallicity estimation for blue compact galaxies like the hosts of SNe Ic-BL.

Second, we analyze the PS1 photometric observations of Type IIP supernovae (Chapter 7), a dataset consisting of 18,837 individual images of 76 SNe. We develop and apply a novel Bayesian light curve fitting methodology to homogeneously and robustly measure the light curve properties of every object in this sample, regardless of temporal coverage or data quality. We find no evidence of a slow-declining mode in the plateau phase decline rate distribution of this population, questioning the physical significance of the widely applied “Type IIL” classification. We do, however, find evidence for a significantly larger diversity among SN IIP light curve plateau durations than has been recognized in previous studies, and we identify a new relation between the peak magnitude and plateau phase decline rate among these objects. Taken together, these results support the conception of the death states of red supergiants as a single parameter family of explosions. We compare our light curve model parameters to theoretical hydrodynamic models, recovering estimates of progenitor properties such as initial stellar mass for some objects. However, we show that current models do

not fully encompass the diversity of light curve phenomenology observed among SNe IIP, arguing for continued hydrodynamic modeling over an expanded grid of progenitor parameters.

Finally, we have presented a new hierarchical Bayesian technique for comprehensively modeling and interpreting all photometric data from wide field transient searches (Chapter 8). In this framework, the underlying population of transients is modeled simultaneously with the light curves of individual objects. We have designed and presented such a model tailored for Type IIP SN light curves, and we apply this model to the PS1 observations of Chapter 7 as a test case. The model consists of 9,176 parameters, and we sample from this high dimensional posterior using an efficient Hamiltonian Monte Carlo technique. We compare the inferences derived from this hierarchical model to the individual light curve fits of Chapter 7, showing that partial pooling of information among all objects in the sample improves posterior constraints on individual light curve parameters. Moreover, we use the top level parameter posterior distributions of the hierarchical model to make direct inference on the underlying population of SNe IIP, allowing us to discuss the probability and occurrence rate of light curve characteristics unseen in the observed SN IIP sample. We conclude by discussing applications of this hierarchical method to future wide field transient searches, interpreting this approach as an unsupervised machine learning method for drawing robust inferences about transient light curve properties among large photometric datasets.

9.2 Future directions

The future of supernova astrophysics rests unambiguously in the realm of the Large Synoptic Survey Telescope (LSST) and other upcoming wide field transient searches. These searches will deliver SN discoveries at an unprecedented volume, far outpacing the community's capacity to perform detailed follow-up observations or spectroscopy, and revealing new, exotic classes of transients whose rarity or light curve properties have put them beyond the reach of contemporary surveys. The conclusions in each chapter of this thesis have the potential to influence, and to be influenced by, the discoveries awaiting in this new era.

Our understanding of the progenitor properties of SNe, as informed by observations of their host galaxies, should expand tremendously during this period. The identification and development of new photometric methods for inferring the host galaxy and stellar population properties of SN progenitors, like that presented in Chapter 5 and Kelly et al. (2014), will be crucial to enabling transient host galaxy science in the absence of a representative sample of follow-up host environment spectroscopy (i.e. the work of Chapter 4). We advocate for the development of an extension to the photometric galaxy metallicity calibration we presented in Chapter 5 to lower galaxy luminosities and higher redshifts. Ever more thorough spectroscopic galaxy surveys like the work of Zahid et al. (2013) and Amorín et al. (2014) will enable this extended calibration. Continued detailed study of the interstellar medium of individual galaxies, like the work of Chapter 3, is needed to robustly interpret these extragalactic host environment observations. Integral Field Unit spectroscopy suggests an exciting new means

for the investigation of the optical properties of the interstellar medium of nearby galaxies (Rosales-Ortega 2013), and is now being applied to SN host galaxies particularly (Stanishev et al. 2012).

Among the most exciting scientific questions to be answered by the availability of this future wide field survey data concern the universe's most rare and exotic transients, for which each additional object discovery can add significantly to our understanding. Chief among these questions is the relationship between SNe and long-duration gamma ray bursts. In Chapter 2, we used fortuitous PS1 optical observations, in combination with concurrent gamma ray observations and radio follow up, to place strong limits on the formation of relativistic ejecta within one explosion, SN 2010ay, that seemed ripe for gamma ray burst formation. A deep, high cadence, all sky survey like LSST would enable similar studies to be performed for all detected gamma ray bursts. In Chapter 4, we have discussed a photometric technique for the identification of of SN Ic-BL among optical transient survey data, capitalizing on the extreme properties of their host galaxies. We look to future discoveries of broad-lined Type Ic SNe discovered with and without associated radio and gamma ray emission, and the properties of their host galaxies, to unravel the link between these phenomenon.

Similarly, our PS1 discovery of the Type Ibn SN PS1-12sk has called into question the explosion mechanism for that transient class. We advocate for additional follow up observations of the host environment of PS1-12sk, using high resolution X-ray and/or deep ultraviolet observations to search for evidence of star formation. Such observations are needed to definitively confirm or refute the possibility of a highly massive stellar progenitor for this event. Additionally,

future discoveries of SNe Ibn by searches like LSST will enable statistical studies of their host environments, permitting inferences on their progenitor mass distribution.

Finally, we anticipated the overwhelming quantity of SN light curve data in the coming era, and advocate for the use of new statistical and computational techniques to take advantage of these riches. The old mode, treating optical surveys as a haystack in which to search for needles—bright, nearby, well sampled SN light curves—will not support the field in pushing past the existing boundaries of scientific discovery. Comprehensive and population level modeling techniques, like the Bayesian hierarchical framework delivered in Chapter 8, will permit observers to take full advantage of datasets like that to be provided by LSST.

To enable the application of these methods to datasets an order of magnitude and more larger than the PS1 sample we studied in Chapter 7, we advocate for several methodological and computational advancements. First, to enable purely photometric classification of transient light curves, machine learning methods like those explored in Kessler et al. (2010) and references therein must be further developed. Multi-band datasets from early generation wide field transient searches, like the PS1 SN II dataset (Chapter 7), provide crucial training sets for these algorithms. Additionally, improvements in galaxy photometric redshift estimation methods and incorporation of robust probabilistic treatment of redshift in hierarchical light curve models is needed. Second, yet more efficient computational techniques are needed to permit sampling from the posterior distributions of hierarchical models equally or more sophisticated than that presented in Chapter 8. The incorporation of Riemannian manifold Hamiltonian

Monte Carlo into general and accessible modeling packages, as is being pursued by Betancourt (2013), suggests a promising mechanism for order of magnitude gains in efficiency for sampling from high curvature posterior distributions.

The most exciting aspect of the nascent era of wide field transient searches is the potential for discovery of as yet unobserved transient classes, and the identification of new physics among these objects. PS1 alone has produced a number of unexpected discoveries (including PS1-12sk and the subjects of Chomiuk et al. 2011; Gezari et al. 2012; Chornock et al. 2013) stimulating new paths for theoretical work. Though we may not be able to anticipate their nature, it is certain that LSST and other future wide field survey will yield discoveries of equal or greater significance.

Appendix A

Supplemental Tables for Chapter 3

Abstract

This appendix includes tables supplemental to Chapter 3, recording the observational and modeled properties of HII regions and planetary nebulae in M31.

Table A.1. Basic data for M31 HII regions and PNe

ID	RA	DEC	R (kpc) ^a	Morph. Type ^b	SB ^c	ADC ^d	Velocity (km s ⁻¹)	M06 ^e	RBC ^f	AMB ^g
<i>HII regions</i>										
HII001	0:37:24.12	+40:17:56.2	23.0	s		2	n	-483.6		
HII002	0:37:29.91	+40:15:37.2	21.9	s		1	n	-517.5		
HII003	0:37:47.35	+39:51:30.8	23.7	s		1	n	-492.6		
HII004	0:37:59.17	+40:15:37.2	19.2	s		1	n	-476.2	M2372	
HII005	0:38:22.51	+40:10:52.8	18.4	s		2	n	-564.5		
HII006	0:38:39.79	+40:34:48.0	18.2	d		1	y	-469.3		HII9
HII007	0:38:41.29	+39:47:40.0	28.2	s		1	y	-526.8		
HII008	0:39:03.75	+39:53:28.9	26.9	s		1	y	-479.0		
HII009	0:39:07.69	+40:40:05.1	16.2	s		2	y	-486.1		HII1
HII010	0:39:13.09	+40:41:13.9	15.9	s		1	y	-488.5		HII1
HII011	0:39:13.60	+40:47:40.9	18.1	d		1	y	-463.1		HII1
HII012	0:39:14.70	+40:48:33.1	18.3	d		1	y	-406.4	M1975	HII1
HII013	0:39:16.48	+40:41:05.4	15.4	d		2	y	-484.5	M3197	DAO27 HII1
HII014	0:39:21.40	+40:21:25.1	15.2	s		1	y	-553.4		HII1
HII015	0:39:22.30	+40:45:14.7	16.0	d		1	y	-470.9		HII1
HII016	0:39:24.90	+40:24:51.7	14.3	s		1	n	-550.2		HII2
HII017	0:39:27.25	+40:29:03.5	13.5	s		1	y	-527.4	M2317	PN2
HII018	0:39:31.78	+40:04:57.8	23.0	s		2	n	-489.1	M2399	
HII019	0:39:37.85	+40:25:02.0	14.3	d		1	n	-549.1		HII2
HII020	0:39:41.53	+40:21:33.2	15.6	d		2	n	-524.5		HII2
HII021	0:39:45.49	+40:19:44.3	16.5	d		1	y	-518.8		HII3
HII022	0:39:51.84	+40:21:53.7	15.9	s		1	n	-498.4		HII4
HII023	0:39:55.42	+40:55:49.1	15.6	d		3	n	-424.1	M1806	
HII024	0:40:00.56	+40:39:12.4	11.0	d		2	n	-561.4	M2084	HII4
HII025	0:40:01.00	+40:54:56.5	14.4	s		1	y	-467.6	M1804	HII4
HII026	0:40:07.20	+40:44:25.8	10.6	s		1	y	-542.7		HII5
HII027	0:40:09.31	+40:24:03.2	15.9	d		1	y	-515.9		HII5
HII028	0:40:10.39	+41:01:24.2	16.0	d		1	y	-403.6		SK041B HII5
HII029	0:40:11.30	+40:41:45.9	10.3	d		2	y	-575.0	M3194	HII5
HII030	0:40:13.10	+40:48:42.4	10.7	s		1	y	-508.7		HII5
HII031	0:40:16.29	+40:43:23.5	9.9	s		1	y	-511.8	M1944	HII5
HII032	0:40:19.89	+40:47:58.9	9.9	d		1	y	-533.8		HII5
HII033	0:40:24.60	+40:30:23.4	13.7	d		1	y	-537.4		HII6
HII034	0:40:32.33	+40:55:27.1	10.2	d		2	y	...		HII7
HII035	0:40:33.70	+40:13:46.8	23.9	s		1	y	-298.2		
HII036	0:40:33.79	+40:43:28.9	9.2	s		1	y	-569.6		HII7

Table A.1—Continued

ID	RA	DEC	R (kpc) ^a	Morph. Type ^b	SB ^c	ADC ^d	Velocity (km s ⁻¹)	M06 ^e	RBC ^f	AMB ^g
HII037	0:40:34.29	+40:42:34.1	9.4	d	1	y	-573.9			HII7
HII038	0:40:35.30	+41:01:19.5	12.2	d	1	y	-416.9			HII7
HII039	0:40:35.80	+40:49:04.8	8.6	s	1	y	-552.3			HII7
HII040	0:40:36.25	+41:01:18.7	12.0	d	3	y	-411.4	M3162		HII7
HII041	0:40:38.40	+40:41:23.6	9.7	d	2	y	-561.3			HII8
HII042	0:40:40.20	+40:42:23.0	9.4	d	1	y	-561.2			HII8
HII043	0:40:40.48	+40:44:30.8	8.8	d	1	y	-548.2			HII8
HII044	0:40:42.26	+40:23:40.4	18.8	s	1	y	-358.8	M2238		
HII045	0:40:47.80	+40:59:06.0	9.5	d	3	y	-378.5	M2857		HII8
HII046	0:40:51.96	+40:36:02.8	12.7	d	2	y	-540.8			HII8
HII047	0:40:52.57	+41:19:07.6	19.3	s	1	y	-307.1			
HII048	0:40:58.16	+41:03:04.1	9.6	d	3	y	...	M1557		HII9
HII049	0:40:58.29	+40:27:28.0	18.2	s	1	y	-505.8			HII9
HII050	0:40:58.48	+40:46:05.1	8.5	d	2	y	-532.6			HII9
HII051	0:40:58.52	+41:03:44.7	9.9	d	1	y	...			HII1
HII052	0:40:58.53	+41:03:32.4	9.8	d	3	y	-456.5	M1560		HII1
HII053	0:40:59.40	+40:50:03.1	7.3	s	2	y	-521.3	M3266		HII1
HII054	0:41:00.40	+40:38:13.5	12.2	s	2	y	-523.7			HII1
HII055	0:41:01.86	+41:11:41.8	13.5	d	1	y	-374.8			HII1
HII056	0:41:02.01	+41:02:54.9	9.0	d	3	y	-452.3	M1555	V211	HII1
HII057	0:41:12.59	+41:06:10.6	8.9	d	2	y	-444.1			HII1
HII058	0:41:14.80	+41:09:23.4	10.2	d	3	y	-423.9	M3036	V226	HII1
HII059	0:41:16.60	+40:57:32.3	5.9	d	1	y	-522.4			HII1
HII060	0:41:17.11	+40:45:24.1	9.7	s	3	y	-491.5			HII1
HII061	0:41:19.44	+41:19:48.9	15.5	d	3	y	-321.6			HII1
HII062	0:41:20.79	+40:31:51.5	18.0	s	1	y	-520.9			HII1
HII063	0:41:21.60	+41:19:48.8	15.2	d	3	n	-317.3			HII1
HII064	0:41:21.67	+41:20:42.3	15.7	s	3	y	-321.9	M784		
HII065	0:41:22.02	+41:08:59.8	8.9	s	1	n	-416.5			
HII066	0:41:22.61	+41:11:01.5	9.9	s	3	y	-415.3			HII1
HII067	0:41:23.59	+41:18:32.3	14.1	s	1	y	-522.6			HII1
HII068	0:41:25.46	+41:11:54.3	9.9	s	3	y	-403.2	M1036		HII1
HII069	0:41:30.18	+41:05:01.9	5.9	d	3	y	-474.9			HII1
HII070	0:41:31.92	+41:13:32.1	9.8	s	3	n	-408.1	M1046		HII1
HII071	0:41:32.24	+41:07:30.1	6.6	s	1	y	-560.2	M1525		
HII072	0:41:33.98	+41:13:38.0	9.6	s	2	n	-398.9	M1047		HII1
HII073	0:41:40.26	+41:17:31.0	10.9	s	2	y	-375.4			HII1

Table A.1—Continued

ID	RA	DEC	R (kpc) ^a	Morph. Type ^b	SB ^c	ADC ^d	Velocity (km s ⁻¹)	M06 ^e	RBC ^f	AMB ^g
HII074	0:41:40.60	+41:11:02.7	7.1	s		2	y	-315.6		HII1
HII075	0:41:43.60	+40:45:24.4	12.2	d		1	y	-444.6		HII1
HII076	0:41:45.08	+40:40:41.4	15.4	s		1	n	-397.2		HII1
HII077	0:41:45.50	+41:09:11.5	5.4	d		2	y	-416.8		HII1
HII078	0:41:45.88	+41:17:03.0	9.7	d		2	y	-361.1		
HII079	0:41:46.48	+41:18:47.8	10.7	d		3	y	-338.2		HII1
HII080	0:41:46.74	+41:18:46.8	10.6	d		3	y	-337.8	M3253	HII1
HII081	0:41:47.49	+41:19:43.3	11.1	s		2	y	-376.1		HII1
HII082	0:41:48.02	+41:18:59.4	10.5	d		3	y	-377.4	M3254	HII1
HII083	0:41:48.19	+41:19:20.6	10.7	s		2	y	-379.4	M3111	HII1
HII084	0:41:51.68	+40:46:18.5	12.6	d		3	n	-443.2	M1891	HII1
HII085	0:41:54.74	+40:47:15.5	12.4	d		2	y	-430.5	SK089B	HII1
HII086	0:41:57.59	+40:55:11.3	7.8	d		1	n	-475.9		HII1
HII087	0:41:58.34	+40:59:33.6	5.3	s		2	n	-467.3		HII1
HII088	0:42:00.39	+40:47:46.0	12.7	d		3	y	-435.2	M1895 BH14	HII1
HII089	0:42:03.85	+40:49:07.1	12.3	d		3	n	-425.3	M1898	HII1
HII090	0:42:05.08	+41:06:22.3	2.7	s		1	y	-441.5		HII1
HII091	0:42:05.90	+41:12:07.9	3.8	s		1	y	-319.2	M1189	HII1
HII092	0:42:08.68	+41:24:10.0	10.6	d		3	y	-329.5	M769	HII1
HII093	0:42:08.81	+40:50:53.0	11.8	d		2	y	...	DAO52	HII1
HII094	0:42:09.43	+41:28:31.7	13.3	d		3	y	-274.0	G137	HII1
HII095	0:42:11.30	+41:04:33.6	3.7	d		1	y	-478.4		HII1
HII096	0:42:16.41	+41:00:05.9	6.8	s		2	n	-464.6	M1417	HII1
HII097	0:42:18.89	+40:53:58.7	11.1	s		1	n	-439.4		HII1
HII098	0:42:19.10	+41:27:32.3	11.2	s		2	y	-331.2		HII1
HII099	0:42:21.23	+41:27:12.4	10.7	s		2	n	-300.0		HII1
HII100	0:42:29.79	+40:51:57.1	13.8	d		1	n	-367.8		HII1
HII101	0:42:31.39	+41:30:07.1	11.1	d		2	y	-286.1		HII1
HII102	0:42:32.05	+40:52:26.8	13.8	s		1	n	-381.3	M3172	HII1
HII103	0:42:35.51	+41:32:25.1	12.0	s		3	y	-270.5		HII1
HII104	0:42:40.98	+40:59:10.7	10.7	d		2	n	-377.9	M3235	HII1
HII105	0:42:41.06	+41:35:04.9	12.9	s		2	y	-244.0		HII1
HII106	0:42:42.34	+41:03:03.2	8.3	d		1	n	-405.3		HII1
HII107	0:42:42.39	+41:31:54.6	10.7	s		3	y	-268.8	M574	HII1
HII108	0:42:44.18	+41:27:31.0	7.5	s		2	y	-286.8		HII1
HII109	0:42:44.52	+40:48:07.9	18.4	s		2	n	-197.2		HII1
HII110	0:42:46.80	+41:44:46.6	18.5	s		2	y	-252.1		HII1

Table A.1—Continued

ID	RA	DEC	R (kpc) ^a	Morph. Type ^b	SB ^c	ADC ^d	Velocity (km s ⁻¹)	M06 ^e	RBC ^f	AMB ^g
HII111	0:42:46.91	+41:25:31.2	5.8	d	1	y	-212.4			HII1
HII112	0:42:47.40	+41:01:14.1	10.2	d	1	y	-381.4			HII1
HII113	0:42:49.64	+40:47:34.0	19.5	s	1	y	-175.4			HII1
HII115	0:42:52.39	+41:34:38.6	11.1	d	3	y	-252.8			HII1
HII115	0:42:52.39	+41:44:31.9	17.6	s	1	y	-271.2			HII1
HII116	0:42:54.09	+41:45:52.5	18.2	s	2	y	-253.8			HII1
HII117	0:42:56.87	+40:49:05.1	19.6	d	1	y	-392.8			HII1
HII118	0:42:57.00	+41:37:41.1	12.4	d	2	y	-236.4			HII1
HII119	0:42:58.80	+41:37:40.7	12.2	d	2	y	-236.8			HII1
HII120	0:42:59.49	+41:43:30.7	15.9	d	1	y	-232.4			HII1
HII121	0:43:00.69	+41:50:15.0	20.2	d	1	y	-228.4			HII1
HII122	0:43:02.90	+41:48:09.0	18.5	d	2	y	-244.4	M184		HII1
HII123	0:43:02.99	+41:20:40.4	1.3	s	1	y	-137.3	M2756		
HII124	0:43:04.61	+41:32:45.8	8.2	s	2	n	-253.7			HII1
HII125	0:43:05.71	+41:43:06.9	14.8	d	2	y	-219.6	M374		HII1
HII126	0:43:07.54	+41:04:17.3	11.2	d	1	n	-368.8			HII1
HII127	0:43:12.25	+41:01:27.1	13.7	d	2	n	-335.9			HII2
HII128	0:43:12.91	+41:42:56.1	13.8	s	2	y	-216.2			HII2
HII129	0:43:13.64	+41:06:33.2	10.6	d	2	y	-338.2			HII2
HII130	0:43:14.52	+40:54:24.2	18.7	s	1	y	...			HII2
HII131	0:43:17.11	+41:45:39.9	15.0	d	1	y	-201.3			HII2
HII132	0:43:17.90	+41:02:53.5	13.6	s	2	y	-333.1	M1670		HII2
HII133	0:43:21.69	+41:29:36.5	4.4	s	1	y	-319.4	M560		HII2
HII134	0:43:21.79	+41:40:27.4	11.0	d	2	y	-186.3			HII2
HII135	0:43:24.52	+41:11:45.5	8.9	s	2	y	-321.2			HII2
HII136	0:43:25.60	+41:42:34.5	11.9	d	1	y	-201.6			HII2
HII137	0:43:26.21	+41:52:06.7	18.0	s	1	n	-204.5			
HII138	0:43:26.35	+41:05:09.4	13.4	d	3	y	-335.2	M1683		HII2
HII139	0:43:27.31	+41:51:21.2	17.4	s	2	y	-204.9			HII2
HII140	0:43:29.12	+41:48:48.1	15.5	s	3	y	-190.6	M2599		PN2
HII141	0:43:30.00	+41:47:02.4	14.3	d	2	y	-200.3			HII2
HII142	0:43:31.70	+41:42:37.4	11.2	s	2	y	-205.2			HII2
HII143	0:43:33.75	+41:20:44.1	5.1	s	2	y	-242.9			HII2
HII144	0:43:34.87	+41:09:55.3	11.7	d	3	y	-331.8	M1699		HII2
HII145	0:43:35.01	+41:43:58.2	11.7	s	2	y	-274.4	M381		PN2
HII146	0:43:36.79	+41:03:33.3	16.1	s	1	y	-267.5	M1672		
HII147	0:43:40.60	+41:39:15.4	8.2	s	1	y	-184.0	M370		HII2

Table A.1—Continued

ID	RA	DEC	R (kpc) ^a	Morph. Type ^b	SB ^c	ADC ^d	Velocity (km s ⁻¹)	M06 ^e	RBC ^f	AMB ^g
HII148	0:43:40.71	+41:14:25.1	9.8	s	1	y	-294.7			HII2
HII149	0:43:40.99	+41:19:32.5	6.8	s	1	y	-261.1	M885		
HII150	0:43:42.09	+41:48:00.7	13.4	d	1	y	-176.8			HII2
HII151	0:43:44.44	+41:14:32.3	10.3	s	1	y	-318.2			HII2
HII152	0:43:44.68	+41:26:21.1	4.3	s	1	y	-12.9			HII2
HII153	0:43:48.22	+41:56:40.6	18.2	d	1	y	-210.5	M72,73		HII2
HII154	0:43:49.00	+41:56:58.9	18.3	s	1	y	-217.4			HII2
HII155	0:43:49.39	+41:35:31.1	5.6	s	1	y	-144.8	M642		HII2
HII156	0:43:50.20	+41:47:01.3	11.9	d	1	y	-202.3			HII2
HII157	0:43:52.20	+41:57:56.5	18.6	d	1	y	-203.0			HII2
HII158	0:43:52.69	+41:58:11.3	18.7	d	2	y	-199.7	M2586		HII2
HII159	0:43:53.20	+41:52:15.9	14.9	s	2	y	-172.5			HII2
HII160	0:43:53.46	+41:57:48.2	18.3	d	2	n	-205.0			HII2
HII161	0:43:53.53	+41:25:41.7	5.7	d	2	y	-163.7	M948		HII2
HII162	0:43:54.99	+41:26:04.3	5.8	s	3	n	-151.0	M996		HII2
HII163	0:43:55.09	+41:14:32.8	12.0	s	2	n	-280.9			HII2
HII164	0:43:55.93	+41:26:33.7	5.7	d	3	y	-136.9	M1000		HII2
HII165	0:43:56.83	+41:48:29.7	12.1	d	3	y	-167.8	M208		HII2
HII166	0:43:58.18	+41:57:12.8	17.4	d	2	y	-186.3			HII2
HII167	0:43:59.29	+41:39:57.4	7.1	s	1	y	-28.2			HII2
HII168	0:44:00.40	+41:51:33.1	13.6	s	2	y	-153.6			HII2
HII169	0:44:03.04	+41:49:54.8	12.4	d	3	y	-156.6	M213		HII2
HII170	0:44:04.60	+42:01:22.7	19.3	d	1	y	-197.7			HII2
HII171	0:44:04.63	+41:21:08.0	9.6	d	1	n	-239.9			HII2
HII172	0:44:06.59	+41:52:07.8	13.3	s	2	y	-134.1			HII2
HII173	0:44:07.62	+41:21:08.4	10.1	d	3	y	-258.1	M972		HII2
HII174	0:44:10.29	+41:58:51.5	17.1	d	3	y	-165.1	M87		HII2
HII175	0:44:15.37	+41:58:52.6	16.5	d	1	y	-164.9			HII2
HII176	0:44:17.90	+41:24:55.8	9.6	s	3	y	-245.7			HII2
HII177	0:44:21.89	+41:51:25.6	11.5	s	1	y	-162.3			HII2
HII178	0:44:24.11	+41:49:18.4	10.2	d	3	n	-112.1	M232		HII2
HII179	0:44:24.40	+41:19:44.7	13.4	s	3	y	-283.1			HII2
HII180	0:44:24.96	+41:37:39.2	6.6	s	3	n	-65.9	M2664		HII2
HII181	0:44:25.22	+41:50:06.5	10.6	d	3	y	-112.0	M265		HII2
HII182	0:44:25.31	+41:49:34.6	10.3	d	3	y	-116.3	M233		HII2
HII183	0:44:27.50	+41:35:29.8	7.0	s	2	n	-69.6			HII2
HII184	0:44:28.47	+41:42:35.3	7.4	s	1	y	-144.6	M413		

Table A.1—Continued

ID	RA	DEC	R (kpc) ^a	Morph. Type ^b	SB ^c	ADC ^d	Velocity (km s ⁻¹)	M06 ^e	RBC ^f	AMB ^g
HII185	0:44:32.09	+41:19:40.7	14.7	s		2	n	-262.1		HII2
HII186	0:44:32.21	+41:26:55.8	10.7	s		1	n	-217.2		HII2
HII187	0:44:32.80	+41:25:21.0	11.6	d		2	y	-216.9		HII3
HII188	0:44:34.08	+41:57:15.9	13.8	d		2	y	-144.2	M84	HII3
HII189	0:44:34.95	+41:27:34.7	10.8	d		2	n	-196.0		HII3
HII190	0:44:35.13	+41:08:04.8	22.2	s		2	n	-320.8	M1704	
HII191	0:44:38.55	+41:25:11.0	12.6	d		3	y	-202.7	M999	SK153C HII3
HII192	0:44:39.13	+41:56:25.3	12.9	s		2	y	-98.5		HII3
HII193	0:44:40.49	+41:20:52.1	15.3	s		2	n	-225.9	M1005	PN3
HII194	0:44:41.93	+41:21:50.8	14.9	d		2	n	-252.4	M1019	HII3
HII195	0:44:43.45	+41:22:38.2	14.7	s		1	y	-202.6		HII3
HII196	0:44:45.70	+41:54:26.1	11.5	s		2	n	-104.6		HII3
HII197	0:44:47.37	+41:25:53.5	13.6	d		2	n	-197.0	M1020	SK180B HII3
HII198	0:44:47.40	+41:56:57.1	12.6	d		3	y	-91.0	M126	HII3
HII199	0:44:48.39	+41:22:54.6	15.3	s		2	n	-239.4	M1006	HII3
HII200	0:44:49.10	+41:30:34.3	11.5	d		2	y	-198.8		
HII201	0:44:50.30	+41:23:03.4	15.6	s		2	y	-237.1		HII3
HII202	0:44:51.28	+41:29:24.8	12.3	d		2	y	-162.8		HII3
HII203	0:44:51.94	+41:53:33.2	10.8	s		3	y	-104.8		HII3
HII204	0:44:52.70	+41:21:10.0	17.0	s		1	y	-258.7		HII3
HII205	0:44:53.33	+42:02:33.1	15.2	d		2	y	-120.7	M121	HII3
HII206	0:44:53.94	+41:34:05.5	10.6	s		1	y	-265.6	M705	PN3
HII207	0:44:58.94	+41:28:57.7	13.7	d		2	n	-198.3	M662	HII3
HII208	0:44:59.13	+41:32:33.9	12.0	d		3	y	-191.1	M690	HII3
HII209	0:45:00.65	+41:28:36.1	14.1	s		3	y	-209.9	M659	HII3
HII210	0:45:04.10	+41:19:55.2	19.5	s		1	y	-277.9		HII3
HII211	0:45:07.48	+41:32:24.0	13.3	d		2	y	-181.8		HII3
HII212	0:45:09.98	+41:50:09.2	9.8	s		1	y	-103.3	M281	PN3
HII213	0:45:10.28	+42:02:27.7	14.0	s		3	y	-76.2	M120	HII3
HII214	0:45:10.66	+41:49:26.1	9.7	s		1	y	-93.6	M277	
HII215	0:45:11.20	+41:34:59.5	12.7	d		1	y	-146.5		HII3
HII216	0:45:11.56	+42:01:31.0	13.4	s		3	y	-66.4		HII3
HII217	0:45:11.84	+41:37:12.7	11.8	d		3	y	-129.5	M2674	HII3
HII218	0:45:12.46	+41:37:16.8	11.9	d		3	y	-123.1	M2675,3225	HII3
HII219	0:45:18.00	+42:12:59.0	18.9	s		2	y	-107.7		HII3
HII220	0:45:18.48	+41:40:13.7	11.6	d		3	y	-125.8	M448	HII3
HII221	0:45:20.30	+41:47:13.5	10.3	s		2	y	-95.5		HII3

Table A.1—Continued

ID	RA	DEC	R (kpc) ^a	Morph. Type ^b	SB ^c	ADC ^d	Velocity (km s ⁻¹)	M06 ^e	RBC ^f	AMB ^g
HII222	0:45:21.55	+41:25:57.3	18.7	s	2	n	-141.0	M1016		
HII223	0:45:24.66	+41:38:02.8	13.2	s	2	n	-169.5			HII3
HII224	0:45:24.69	+41:43:38.6	11.4	d	1	y	-89.0			HII3
HII225	0:45:25.47	+42:14:10.7	19.0	s	1	y	-145.8	M42		
HII226	0:45:27.40	+41:46:21.3	11.1	d	1	y	-95.4			HII3
HII227	0:45:28.39	+41:50:15.3	10.8	d	2	y	-81.9			HII3
HII228	0:45:36.50	+41:51:35.2	11.3	d	3	y	-81.5			HII3
HII229	0:45:37.24	+41:51:07.1	11.4	d	3	n	-68.3	M285		HII3
HII230	0:45:38.63	+41:52:34.8	11.4	d	2	y	-68.1	M299		HII3
HII231	0:45:39.40	+41:43:47.9	13.1	d	2	y	-136.0			HII3
HII232	0:45:42.08	+42:13:51.1	17.7	d	1	y	...	M40		HII3
HII233	0:45:42.23	+41:55:45.9	11.7	d	3	y	-53.4	M2591		HII3
HII234	0:45:43.29	+41:45:40.6	13.0	s	2	y	-139.7			HII3
HII235	0:45:43.64	+41:42:35.8	14.0	s	3	y	-141.7	M494		HII3
HII236	0:45:43.99	+41:52:09.4	11.9	d	3	y	-80.1	M296		HII3
HII237	0:45:44.85	+41:24:29.7	23.1	s	1	y	-139.7	M1022		
HII238	0:45:46.80	+41:45:23.0	13.5	s	1	y	-129.0		M102	HII3
HII239	0:45:55.35	+41:53:21.2	12.7	s	1	y	-35.7	M2620		
HII240	0:46:22.13	+42:08:37.9	14.9	d	2	y	-54.7	M65		HII3
HII241	0:46:22.58	+41:42:00.2	19.7	s	1	y	-140.5	M2685		
HII242	0:46:27.38	+42:08:29.6	15.0	s	1	y	-71.8	M49		
HII243	0:46:29.23	+42:12:35.4	15.8	d	1	y	-57.5			HII3
HII244	0:46:30.10	+41:59:14.9	15.1	d	3	y	-82.4	M163		HII3
HII245	0:46:33.14	+41:57:03.5	15.8	d	3	y	-81.4	M147		HII3
HII246	0:46:33.18	+42:11:37.9	15.7	d	3	y	-57.7	M55		HII3
HII247	0:46:34.28	+42:11:42.7	15.7	d	3	y	-44.4	M57	B488	HII3
HII248	0:46:34.49	+42:11:24.3	15.7	d	3	y	-61.0			HII3
HII249	0:46:38.71	+41:41:06.3	22.4	s	1	y	-241.5			HII3
HII250	0:46:41.98	+42:15:45.9	16.7	d	2	y	-45.2	M2159	DAO88	HII3
HII251	0:46:54.51	+42:00:48.1	17.2	s	3	y	-117.7	M155	SK227B	HII3
HII252	0:46:55.19	+41:47:21.9	21.9	s	1	y	-169.1	M2206		
HII253	0:46:58.64	+41:50:20.2	21.1	s	3	y	-185.8			
<i>Planetary nebulae</i>										
PN001	0:38:44.18	+40:17:58.8	16.6	...	1	y	-465.4	M2364		PN7
PN002	0:39:02.52	+40:22:50.5	15.2	...	3	y	-529.4	M2964		PN9
PN003	0:39:05.33	+40:41:45.9	17.1	...	2	y	-387.9	M3198		
PN004	0:39:06.59	+40:14:59.7	17.1	...	3	y	-560.0	M2357		

Table A.1—Continued

ID	RA	DEC	R (kpc) ^a	Morph. Type ^b	SB ^c	ADC ^d	Velocity (km s ⁻¹)	M06 ^e	RBC ^f	AMB ^g
PN005	0:39:14.80	+40:24:28.5	14.6	...	1	y	-338.0	M2304		PN1
PN006	0:39:15.00	+40:26:34.5	14.3	...	3	y	-538.8	M2308		PN1
PN007	0:39:15.80	+40:12:38.4	18.3	...	2	y	-488.8	M2972		
PN008	0:39:16.29	+40:22:12.8	15.0	...	2	y	-551.0	M2960		PN1
PN009	0:39:18.51	+40:09:18.9	19.9	...	1	y	-379.4	M2404		
PN010	0:39:26.12	+40:44:25.9	15.2	...	1	y	-407.7	M1967		
PN011	0:39:29.51	+40:39:13.3	13.5	...	1	n	-396.4	M2086		PN2
PN012	0:39:31.39	+40:49:17.3	16.3	...	1	y	-424.9	M1981		HII2
PN013	0:39:36.65	+40:17:51.3	16.9	...	2	y	-523.9	M2345		PN2
PN014	0:39:40.38	+40:13:24.6	19.2	...	2	y	-462.0	M2970		
PN015	0:39:42.80	+40:22:49.1	15.1	...	3	y	-504.8	M2963		PN3
PN016	0:39:43.98	+40:35:42.0	12.1	...	1	y	-457.7	M2078		
PN017	0:39:44.64	+40:19:59.1	16.4	...	1	y	-498.1	M2346		PN3
PN018	0:39:44.79	+40:12:04.2	20.3	...	1	y	-480.6	M2411		
PN019	0:39:46.14	+40:11:01.7	20.9	...	3	y	-429.9	M2409		
PN020	0:39:49.61	+40:21:25.0	16.0	...	3	y	-416.7	M2352		HII3
PN021	0:39:52.56	+40:09:32.4	22.3	...	2	y	-490.8			
PN022	0:39:53.93	+40:31:56.4	12.3	...	2	y	-475.7	M2942		
PN023	0:39:54.50	+40:43:46.5	11.8	...	1	y	-591.3	M1945		HII4
PN024	0:39:54.90	+40:46:40.4	12.3	...	1	y	-474.8	M1954		HII4
PN025	0:39:58.69	+40:49:44.7	12.7	...	1	y	-513.7			HII4
PN026	0:40:00.85	+41:04:09.4	18.8	...	3	y	-319.8	M1583		HII4
PN027	0:40:01.29	+41:04:41.5	19.1	...	2	y	-371.6	M1586		HII4
PN028	0:40:01.80	+40:37:28.6	11.1	...	3	y	-562.7	M2079		
PN029	0:40:04.60	+40:42:23.7	10.7	...	1	y	-533.4			HII4
PN030	0:40:07.65	+40:28:34.1	13.7	...	3	y	-471.9	M2286		PN4
PN031	0:40:12.02	+40:54:25.8	12.6	...	2	y	-562.1	M2882		
PN032	0:40:12.82	+40:13:02.4	22.2	...	2	y	-394.7	M2334		
PN033	0:40:13.56	+40:55:32.3	12.8	...	3	y	-431.3	M2885		HII5
PN034	0:40:13.96	+40:10:26.3	23.8	...	3	y	-518.3			
PN035	0:40:14.23	+40:23:23.9	16.5	...	3	y	-148.6	M2267		PN5
PN036	0:40:15.29	+40:24:13.6	16.2	...	1	y	-487.5	M2270		PN5
PN037	0:40:16.72	+41:04:28.8	16.6	...	3	y	-352.0	M1585		
PN038	0:40:17.22	+40:59:45.8	14.1	...	3	y	-551.1	M2858		
PN039	0:40:20.84	+40:28:08.9	14.6	...	2	y	-519.0	M2283		PN6
PN040	0:40:21.09	+40:46:41.1	9.6	...	1	y	-438.7	M1953		HII5
PN041	0:40:22.60	+40:29:04.9	14.2	...	1	y	-506.7			HII5

Table A.1—Continued

ID	RA	DEC	R (kpc) ^a	Morph. Type ^b	SB ^c	ADC ^d	Velocity (km s ⁻¹)	M06 ^e	RBC ^f	AMB ^g
PN042	0:40:24.73	+40:58:02.8	12.3	...	2	y	-359.4	M1795		
PN043	0:40:26.59	+41:04:19.5	15.0	...	1	y	-293.1	M1584		HII6
PN044	0:40:26.60	+40:27:59.3	15.1	...	2	y	-500.8			HII6
PN045	0:40:30.07	+41:01:20.4	13.0	...	2	y	-451.1	M1581		
PN046	0:40:30.79	+40:36:54.4	11.2	...	3	y	-489.8	M2049		
PN047	0:40:33.50	+40:24:07.3	17.7	...	3	n	-440.9	M2268		HII7
PN048	0:40:33.88	+41:08:34.6	16.1	...	3	y	-575.6	M3264		
PN049	0:40:36.00	+40:38:11.4	10.8	...	1	y	-562.5			HII7
PN050	0:40:36.96	+41:01:05.3	11.8	...	3	y	-375.4	M3160		HII7
PN051	0:40:39.03	+41:14:39.0	18.7	...	2	y	-336.5	M1072		
PN052	0:40:39.92	+40:43:37.5	9.1	...	2	y	-448.0	M1909		
PN053	0:40:40.34	+40:58:48.2	10.4	...	1	y	-450.2	M1799		
PN054	0:40:40.93	+41:07:29.6	14.4	...	1	y	-307.3	M1573		
PN055	0:40:42.49	+41:02:07.4	11.5	...	1	y	-396.6	M1552		
PN056	0:40:44.01	+40:25:08.6	18.2	...	2	y	-485.6	M2241		PN8
PN057	0:40:44.24	+40:27:11.1	17.0	...	2	y	-500.7	M2248		
PN058	0:40:45.32	+40:41:30.2	9.8	...	3	y	-533.1	M3190		PN8
PN059	0:40:46.09	+41:06:38.3	13.2	...	1	y	-523.7	M1569		PN8
PN060	0:40:47.30	+40:28:25.6	16.6	...	1	y	-490.2	M2253		PN9
PN061	0:40:51.12	+40:58:48.2	8.9	...	3	y	-366.8	M1797		PN9
PN062	0:40:52.39	+40:28:27.7	17.0	...	2	y	-589.8	M2254		PN9
PN063	0:40:52.57	+40:59:42.6	9.0	...	3	y	-326.7	M2854		PN9
PN064	0:40:53.26	+41:07:47.4	12.7	...	1	y	-280.8	M1574		
PN065	0:40:53.30	+41:16:38.0	17.7	...	2	y	-285.6	M1073		
PN066	0:40:54.26	+41:08:39.2	13.0	...	3	y	-406.8	M3041		PN1
PN067	0:40:56.41	+40:53:53.8	7.2	...	2	y	-611.8	M1778		PN1
PN068	0:40:57.31	+40:50:39.2	7.3	...	1	y	-531.9	M3076		
PN069	0:40:57.57	+41:00:02.0	8.5	...	2	y	-263.3	M2855		
PN070	0:40:58.48	+41:09:07.2	12.6	...	3	y	-343.3	M3255		
PN071	0:41:00.28	+40:28:50.0	17.6	...	2	y	-439.7	M2256		PN1
PN072	0:41:01.86	+40:24:20.3	20.5	...	3	y	-405.9	M2240		HII1
PN073	0:41:03.77	+40:48:50.6	7.6	...	3	y	-356.7	M1935		
PN074	0:41:05.71	+40:48:11.5	7.9	...	2	y	-286.3	M1930		
PN075	0:41:05.77	+40:28:13.3	18.6	...	1	y	-509.3	M2251		PN1
PN076	0:41:09.67	+40:27:17.4	19.6	...	1	y	-535.0	M2246		
PN077	0:41:09.79	+41:20:45.7	17.6	...	1	y	-266.5	M785		
PN078	0:41:10.56	+41:01:02.7	7.1	...	1	y	-462.2	M1548		

Table A.1—Continued

ID	RA	DEC	R (kpc) ^a	Morph. Type ^b	SB ^c	ADC ^d	Velocity (km s ⁻¹)	M06 ^e	RBC ^f	AMB ^g
PN079	0:41:12.74	+40:58:27.0	6.3	...	3	y	-556.4	M1755		HII1
PN080	0:41:13.37	+41:11:35.1	11.6	...	2	y	-387.1	M1033		PN1
PN081	0:41:14.70	+40:44:33.0	10.0	...	1	y	-493.6	M1910		PN1
PN082	0:41:14.87	+40:53:20.4	6.4	...	1	y	-408.3	M1719		HII1
PN083	0:41:15.07	+41:07:26.8	9.2	...	1	y	-330.5	M1571		
PN084	0:41:16.70	+40:47:46.6	8.5	...	1	y	-560.6			HII1
PN085	0:41:17.21	+41:16:01.8	13.6	...	3	y	-445.8	M1053		PN1
PN086	0:41:17.50	+41:12:06.5	11.3	...	1	y	-352.5	M1039		PN1
PN087	0:41:17.63	+40:58:45.0	5.9	...	2	y	-451.3	M1760		PN1
PN088	0:41:17.63	+41:18:45.5	15.1	...	2	y	-390.1	M2732		
PN089	0:41:18.05	+40:53:36.0	6.3	...	2	y	-534.6	M1721		HII1
PN090	0:41:19.06	+40:53:42.0	6.3	...	2	y	-499.7	M1722		
PN091	0:41:19.32	+40:52:20.7	6.7	...	3	y	-423.1	M1714		
PN092	0:41:19.91	+40:44:58.2	10.1	...	2	y	-441.2	M1912		
PN093	0:41:20.66	+41:10:17.1	9.8	...	3	y	-284.0	M1029		PN1
PN094	0:41:20.80	+40:55:00.8	5.9	...	2	y	-564.3	M1729		PN1
PN095	0:41:23.42	+41:14:28.0	11.7	...	3	y	-390.7	M1051		
PN096	0:41:25.24	+40:56:02.5	5.6	...	3	y	-539.1	M1737		
PN097	0:41:26.48	+40:32:45.3	18.1	...	3	y	-410.6	M3200		
PN098	0:41:27.00	+40:58:06.4	5.2	...	2	y	-419.8	M1750		
PN099	0:41:28.78	+41:26:47.9	18.4	...	2	y	-270.4	M780		
PN100	0:41:31.08	+41:09:35.9	7.8	...	3	y	-420.2	M2787		
PN101	0:41:31.18	+41:01:11.2	4.9	...	3	y	-431.8	M1425		
PN102	0:41:32.23	+41:00:12.0	4.8	...	2	y	-530.3	M3054		
PN103	0:41:32.52	+40:54:27.4	6.3	...	3	y	-556.0	M1726		PN1
PN104	0:41:33.70	+41:12:56.5	9.2	...	3	y	-384.8	M1044		
PN105	0:41:34.36	+40:59:45.0	4.7	...	3	y	-484.8	M3046		HII1
PN106	0:41:37.11	+41:00:04.8	4.6	...	3	n	-494.0	M3052		PN1
PN107	0:41:37.50	+41:15:10.7	9.9	...	1	y	-345.4	M1052		
PN108	0:41:37.60	+41:11:41.9	7.9	...	1	y	-320.6	M1032		HII1
PN109	0:41:39.06	+41:04:45.3	4.7	...	1	y	-485.9	M1476		
PN110	0:41:39.17	+40:42:22.0	13.6	...	3	n	-306.7	M1874		PN1
PN111	0:41:39.19	+40:57:49.8	5.2	...	2	y	-584.8	M1747		HII1
PN112	0:41:39.43	+41:07:18.5	5.5	...	1	y	-466.2	M1520		
PN113	0:41:40.16	+41:01:02.8	4.4	...	1	y	-499.5	M1423		PN1
PN114	0:41:40.89	+41:09:39.9	6.4	...	2	y	-410.7	M3130		HII1
PN115	0:41:41.14	+40:52:47.0	7.6	...	3	y	-459.9	M1716		

Table A.1—Continued

ID	RA	DEC	R (kpc) ^a	Morph. Type ^b	SB ^c	ADC ^d	Velocity (km s ⁻¹)	M06 ^e	RBC ^f	AMB ^g
PN116	0:41:42.57	+41:18:05.9	10.8	...	2	n	-341.6	M2728		PN1
PN117	0:41:42.94	+41:16:36.8	9.9	...	3	y	-331.6	M1056		
PN118	0:41:44.36	+41:02:11.2	4.1	...	2	y	-455.9	M1436		PN1
PN119	0:41:44.66	+40:48:11.2	10.6	...	1	y	-412.4	M1896		PN1
PN120	0:41:44.91	+41:08:07.3	5.1	...	1	y	-543.6	M1533		
PN121	0:41:45.41	+41:20:36.5	11.9	...	3	y	-307.2	M760		
PN122	0:41:45.44	+40:58:36.3	5.0	...	1	y	-459.5	M1754		
PN123	0:41:45.85	+41:10:36.6	6.1	...	1	y	-397.0	M1030		
PN124	0:41:45.87	+41:26:34.5	15.6	...	3	y	-432.7	M779		
PN125	0:41:46.24	+41:00:34.5	4.3	...	3	y	-503.7	M3057		
PN126	0:41:46.30	+40:53:21.1	7.7	...	2	y	-508.7	M1718		HII1
PN127	0:41:46.91	+41:00:21.3	4.4	...	1	y	-534.1	M3055		PN1
PN128	0:41:48.71	+41:25:19.0	14.4	...	2	y	-170.8	M775		
PN129	0:41:48.99	+41:04:25.8	3.7	...	2	y	-353.8	M1470		PN1
PN130	0:41:49.44	+41:28:14.2	16.1	...	3	y	-342.0	M3281		HII1
PN131	0:41:50.14	+41:07:33.9	4.2	...	3	y	-334.2	M1524		
PN132	0:41:51.78	+40:37:33.1	18.2	...	1	y	-525.6	M2123		
PN133	0:41:52.09	+41:24:18.6	13.2	...	3	y	-454.7	M773		
PN134	0:41:52.32	+41:25:32.4	14.0	...	3	y	-220.5	M776		
PN135	0:41:52.33	+41:15:42.5	7.9	...	2	y	-385.0	M1154		PN1
PN136	0:41:53.64	+41:13:23.7	6.4	...	2	y	-426.1	M1128		
PN137	0:41:54.44	+41:19:56.4	10.1	...	3	y	-338.9	M758		HII1
PN138	0:41:54.53	+41:13:24.9	6.2	...	2	y	-436.2	M1126		HII1
PN139	0:41:54.66	+40:56:09.5	6.9	...	2	y	-466.2	M1830		PN1
PN140	0:41:54.96	+40:40:22.8	16.8	...	1	y	-511.4	M3188		
PN141	0:41:57.69	+41:09:43.3	3.9	...	1	y	-433.9	M1088		HII1
PN142	0:41:57.93	+41:16:14.8	7.3	...	1	y	-285.6	M1157		
PN143	0:41:58.00	+41:12:08.6	5.0	...	2	y	-409.8			HII1
PN144	0:41:58.12	+41:08:10.0	3.4	...	2	y	-488.7	M3147		HII1
PN145	0:41:58.20	+41:03:57.9	3.4	...	1	y	-570.3	M1459		HII1
PN146	0:42:00.54	+41:02:06.2	4.2	...	2	y	-581.3	M1433		
PN147	0:42:01.50	+41:24:20.9	11.8	...	3	y	-240.5	M772		
PN148	0:42:01.60	+41:07:19.5	2.9	...	2	y	-536.0	M1518		HII1
PN149	0:42:01.84	+40:53:22.6	9.3	...	2	y	-470.9	M1826		
PN150	0:42:01.86	+41:07:54.2	2.9	...	1	y	-557.4	M1528		
PN151	0:42:03.00	+41:33:53.6	17.7	...	1	y	-277.3	M547		HII1
PN152	0:42:04.97	+40:58:36.2	6.5	...	2	y	-505.1	M1838		PN1

Table A.1—Continued

ID	RA	DEC	R (kpc) ^a	Morph. Type ^b	SB ^c	ADC ^d	Velocity (km s ⁻¹)	M06 ^e	RBC ^f	AMB ^g
PN153	0:42:06.20	+41:14:23.5	5.0	...	3	y	-112.7	M1136		
PN154	0:42:08.29	+41:19:29.3	7.7	...	3	y	-411.1	M756		
PN155	0:42:08.49	+41:07:35.3	2.4	...	2	y	-372.0	M1522		HII1
PN156	0:42:09.41	+40:57:11.7	7.8	...	2	y	-280.6	M1831		PN1
PN157	0:42:09.90	+41:35:39.6	17.8	...	3	y	-327.7	M551		
PN158	0:42:10.18	+41:07:18.6	2.5	...	2	y	-450.2	M1517		HII1
PN159	0:42:10.30	+41:12:37.2	3.4	...	3	y	-404.7	M1116		
PN160	0:42:10.38	+41:20:45.0	8.2	...	2	y	-446.5	M761		
PN161	0:42:11.88	+40:49:08.1	13.3	...	2	y	-398.6	M3187		
PN162	0:42:12.60	+41:13:24.9	3.4	...	2	y	-379.9	M1124		
PN163	0:42:13.52	+40:59:42.9	6.7	...	2	y	-597.2	M3284		PN1
PN164	0:42:13.60	+40:50:29.0	12.6	...	2	y	-395.5	M3298		
PN165	0:42:14.49	+40:52:22.4	11.5	...	3	y	-476.4	M1822		PN1
PN166	0:42:14.95	+40:58:45.5	7.5	...	2	y	-123.2	M1839		PN1
PN167	0:42:15.70	+41:03:38.8	4.6	...	1	y	-439.0	M3060		HII1
PN168	0:42:19.12	+40:57:08.9	9.0	...	3	y	-277.1	M3179		
PN169	0:42:20.78	+41:16:53.2	4.2	...	2	y	-171.1	M1186		
PN170	0:42:21.17	+41:00:53.7	6.9	...	3	n	-504.3	M1603		PN1
PN171	0:42:22.00	+41:33:44.6	14.8	...	3	y	-213.6	M546		HII1
PN172	0:42:22.13	+41:11:25.6	1.5	...	3	y	-576.9	M1102		
PN173	0:42:22.82	+40:43:06.5	18.7	...	1	y	-506.5	M1994		
PN174	0:42:23.00	+41:23:06.3	7.7	...	3	y	-320.9			HII1
PN175	0:42:23.19	+41:13:36.8	2.0	...	3	y	-372.8	M1130		
PN176	0:42:23.23	+40:46:28.7	16.5	...	3	y	-190.6	M2927		HII1
PN177	0:42:23.88	+41:08:30.3	2.5	...	2	y	-483.3	M2820		
PN178	0:42:24.44	+41:12:11.0	1.4	...	3	y	-382.7	M1110		
PN179	0:42:28.91	+40:44:38.9	18.5	...	1	y	-161.5	M1997		
PN180	0:42:28.94	+41:07:11.9	3.8	...	3	y	-504.9	M1643		
PN181	0:42:28.99	+41:11:36.6	1.3	...	1	y	-276.0	M1104		
PN182	0:42:29.50	+41:10:49.4	1.7	...	2	y	-129.9	M1095		
PN183	0:42:29.57	+41:03:37.9	6.2	...	3	n	-324.6	M1618		PN1
PN184	0:42:29.75	+41:03:30.4	6.3	...	3	y	-460.4	M1616		
PN185	0:42:31.03	+40:53:04.7	13.3	...	2	y	-402.5	M3175		
PN186	0:42:31.34	+41:07:46.3	3.7	...	2	y	-310.3	M1650		PN1
PN187	0:42:33.96	+41:10:08.7	2.5	...	1	y	-456.3	M1090		
PN188	0:42:35.88	+40:53:00.7	14.0	...	3	y	-202.9	M3174		PN2
PN189	0:42:36.38	+41:16:57.1	1.8	...	1	y	-302.8	M2819		

Table A.1—Continued

ID	RA	DEC	R (kpc) ^a	Morph. Type ^b	SB ^c	ADC ^d	Velocity (km s ⁻¹)	M06 ^e	RBC ^f	AMB ^g
PN190	0:42:37.21	+41:04:19.4	6.8	...	2	y	-457.2	M1622		PN2
PN191	0:42:37.63	+41:25:47.3	7.3	...	2	y	-262.5	M863		HII1
PN192	0:42:39.60	+40:52:40.3	14.7	...	3	y	-238.7	M3276		
PN193	0:42:39.68	+41:15:49.3	0.6	...	2	y	-483.5	M2825		
PN194	0:42:40.10	+40:49:41.5	16.8	...	1	y	-160.8	M3243		HII1
PN195	0:42:40.36	+40:52:43.8	14.8	...	3	y	-187.8	M3277		
PN196	0:42:40.57	+41:35:48.3	13.5	...	2	y	-230.8	M3014		HII1
PN197	0:42:41.52	+41:09:58.4	3.6	...	1	y	-589.7	M1331		
PN198	0:42:42.86	+41:09:46.6	4.0	...	2	y	-357.4	M2837		
PN199	0:42:43.86	+41:10:46.2	3.4	...	2	y	-236.8	M1214		
PN200	0:42:43.90	+41:09:00.4	4.6	...	1	y	-367.8	M2831		
PN201	0:42:45.19	+41:15:23.4	0.6	...	1	y	-529.1	M1266		
PN202	0:42:45.59	+40:59:21.6	11.2	...	2	y	-320.3	M2861		
PN203	0:42:45.87	+41:23:33.8	4.7	...	3	y	-215.0	M852		HII1
PN204	0:42:46.68	+40:55:04.9	14.2	...	1	y	-369.4	M2904		PN2
PN205	0:42:47.29	+41:16:28.6	0.3	...	3	y	-229.4	M1312		
PN206	0:42:48.19	+40:54:13.3	14.9	...	3	y	-188.0	M2901		PN2
PN207	0:42:49.45	+41:08:22.9	5.8	...	2	y	-503.9	M2841		PN2
PN208	0:42:49.45	+41:22:09.9	3.3	...	1	y	-308.2	M836		
PN209	0:42:49.83	+40:51:10.5	17.2	...	1	y	-499.9	M3242		
PN210	0:42:51.45	+41:08:55.9	5.7	...	1	y	-320.4	M2829		
PN211	0:42:52.04	+41:36:43.0	12.5	...	3	y	-115.8	M3003		HII1
PN212	0:42:52.68	+40:55:53.1	14.5	...	1	y	-138.5	M2908		PN2
PN213	0:42:53.43	+41:08:57.8	6.0	...	2	y	-390.7	M2830		
PN214	0:42:53.66	+41:34:45.2	11.0	...	2	y	-118.2	M580		
PN215	0:42:55.94	+41:30:07.3	7.6	...	2	y	-184.0	M564		PN2
PN216	0:42:56.30	+41:37:38.6	12.5	...	3	y	-255.3	M3004		
PN217	0:42:57.43	+41:23:05.1	2.9	...	3	y	-301.0	M849		
PN218	0:42:57.53	+41:24:33.1	3.8	...	3	y	-223.3	M861		HII1
PN219	0:42:58.07	+41:34:37.3	10.3	...	1	y	-252.0	M579		
PN220	0:42:58.29	+41:46:36.1	18.1	...	2	y	-246.6			HII1
PN221	0:42:58.30	+41:25:10.4	4.1	...	1	y	-387.8	M865		
PN222	0:42:58.82	+41:22:13.2	2.2	...	1	y	-138.2	M835		
PN223	0:42:59.75	+41:28:08.1	5.8	...	1	y	-189.3	M2700		PN2
PN224	0:43:02.29	+41:28:15.1	5.6	...	1	y	-172.6	M3260		
PN225	0:43:02.89	+41:26:10.4	4.2	...	2	y	-84.2	M2760		
PN226	0:43:03.15	+40:57:18.5	15.1	...	2	y	-368.4	M2910		HII1

Table A.1—Continued

ID	RA	DEC	R (kpc) ^a	Morph. Type ^b	SB ^c	ADC ^d	Velocity (km s ⁻¹)	M06 ^e	RBC ^f	AMB ^g
PN227	0:43:05.22	+41:17:38.9	2.4	...	1	y	-209.5	M2778		
PN228	0:43:05.26	+40:53:34.1	17.8	...	1	y	-524.3	M2899		HII1
PN229	0:43:05.93	+41:19:16.9	1.7	...	3	y	-250.0	M883		
PN230	0:43:06.16	+41:10:55.9	6.6	...	1	y	-339.7	M1215		PN2
PN231	0:43:06.44	+41:07:22.8	9.0	...	2	y	-83.4	M1694		HII1
PN232	0:43:06.65	+41:18:38.6	2.1	...	1	y	-70.5	M2771		
PN233	0:43:07.34	+41:19:23.0	1.9	...	1	y	-336.1	M886		
PN234	0:43:09.45	+41:04:53.1	11.1	...	2	y	-525.6	M1678		HII2
PN235	0:43:09.50	+41:15:53.5	4.0	...	1	y	-203.9	M1304		
PN236	0:43:10.80	+41:19:54.8	2.1	...	2	y	-99.7	M895		
PN237	0:43:11.40	+41:29:05.6	5.1	...	2	y	-154.5			HII2
PN238	0:43:12.38	+41:12:44.0	6.4	...	2	y	-334.6	M1230		
PN239	0:43:14.17	+41:35:27.5	8.8	...	2	y	-129.8	M582		HII2
PN240	0:43:14.39	+41:21:59.9	2.0	...	1	y	-340.8	M916		
PN241	0:43:14.68	+41:30:33.2	5.6	...	2	y	-105.4	M568		PN2
PN242	0:43:15.19	+41:04:21.5	12.3	...	2	y	-374.4	M1675		
PN243	0:43:17.98	+41:45:46.5	15.0	...	3	y	-221.9	M2603		
PN244	0:43:18.18	+41:19:36.1	3.3	...	3	y	-276.6	M891		
PN245	0:43:18.99	+40:58:02.1	17.0	...	2	y	-449.4	M1849		PN2
PN246	0:43:19.18	+41:12:13.4	7.8	...	3	y	-293.9	M1223		
PN247	0:43:19.84	+41:02:34.0	14.1	...	2	y	-422.4	M1669		
PN248	0:43:19.93	+41:35:31.6	8.1	...	1	y	-60.9	M2702		
PN249	0:43:20.89	+41:17:52.7	4.7	...	3	y	-315.5	M2764		
PN250	0:43:21.64	+40:59:12.7	16.6	...	1	y	-348.4	M2871		
PN251	0:43:22.98	+41:10:50.9	9.3	...	3	y	-322.6	M1210		PN2
PN252	0:43:23.20	+41:46:21.7	14.7	...	1	y	-216.3	M2999		HII2
PN253	0:43:23.26	+41:21:56.9	3.0	...	2	y	-266.0	M960		PN2
PN254	0:43:23.40	+41:23:51.4	2.6	...	2	y	-301.3	M938		
PN255	0:43:23.50	+41:53:36.3	19.4	...	2	y	-287.9	M196		
PN256	0:43:23.68	+41:50:18.8	17.2	...	3	y	-197.4	M188		
PN257	0:43:24.29	+41:23:16.0	2.8	...	1	y	-84.3	M928		
PN258	0:43:24.92	+41:09:56.8	10.1	...	3	y	-360.1	M3152		PN2
PN259	0:43:26.41	+41:06:42.4	12.4	...	2	y	-345.8	M1690		
PN260	0:43:27.05	+41:10:28.5	10.1	...	3	y	-256.4	M2838		
PN261	0:43:32.74	+41:18:33.3	6.1	...	3	y	-425.9	M2767		HII2
PN262	0:43:32.79	+41:54:10.1	18.5	...	3	y	-320.3	M222		
PN263	0:43:34.34	+41:19:35.6	5.8	...	2	y	-250.1	M889		HII2

Table A.1—Continued

ID	RA	DEC	R (kpc) ^a	Morph. Type ^b	SB ^c	ADC ^d	Velocity (km s ⁻¹)	M06 ^e	RBC ^f	AMB ^g
PN264	0:43:34.61	+41:30:43.5	4.2	...	1	y	-90.5	M608		
PN265	0:43:35.40	+41:22:29.7	4.5	...	2	y	-82.9	M919		
PN266	0:43:36.09	+41:30:52.1	4.2	...	3	n	-86.1	M609		HII2
PN267	0:43:36.30	+41:42:57.1	10.9	...	1	y	-117.7	M372		
PN268	0:43:36.96	+41:15:09.8	8.8	...	3	y	-226.4	M1383		PN2
PN269	0:43:37.79	+41:27:38.1	3.5	...	2	y	-106.3	M2707		
PN270	0:43:37.86	+41:32:00.8	4.6	...	3	n	-209.4	M624		HII2
PN271	0:43:39.27	+41:54:47.9	18.1	...	2	y	-183.3	M227		
PN272	0:43:39.69	+41:29:18.2	3.8	...	2	y	-263.2	M599	SK070A	HII2
PN273	0:43:39.72	+41:08:55.6	13.1	...	2	y	-329.0	M3154		PN2
PN274	0:43:40.16	+41:36:01.4	6.4	...	1	y	-75.4	M647		HII2
PN275	0:43:41.31	+41:18:12.3	7.6	...	3	y	-271.3	M2765		
PN276	0:43:43.25	+41:09:31.0	13.2	...	2	y	-336.9	M3157		
PN277	0:43:43.51	+41:14:53.6	9.9	...	3	n	-174.3	M1382		PN2
PN278	0:43:43.60	+41:19:13.8	7.4	...	3	y	-131.1	M880		PN2
PN279	0:43:46.03	+41:58:20.9	19.6	...	1	y	-185.4	M76		
PN280	0:43:49.74	+41:22:42.1	6.5	...	3	y	-179.9	M965		PN2
PN281	0:43:51.02	+41:58:24.9	19.0	...	2	y	-56.3	M2991		
PN282	0:43:52.29	+41:39:29.1	7.4	...	3	n	-54.4	M3099		HII2
PN283	0:43:54.80	+41:22:05.0	7.6	...	2	y	-136.2	M2780		PN2
PN284	0:43:55.60	+41:22:20.8	7.6	...	3	n	-266.5	M980		PN2
PN285	0:43:56.70	+41:42:01.3	8.4	...	2	y	-180.4	M410		PN3
PN286	0:43:57.69	+41:32:34.7	4.9	...	1	y	-141.1			HII2
PN287	0:43:58.58	+41:19:23.6	9.6	...	1	y	-301.2	M967		PN3
PN288	0:43:58.84	+41:11:30.3	14.4	...	2	y	-256.4	M1369		
PN289	0:43:59.43	+41:16:47.6	11.3	...	1	y	-27.0	M1389		
PN290	0:43:59.93	+41:50:57.0	13.3	...	3	y	-34.3	M215		
PN291	0:44:01.68	+41:19:39.3	10.0	...	2	y	-291.3	M968		PN3
PN292	0:44:02.14	+41:44:16.0	9.2	...	1	y	-184.9	M424		
PN293	0:44:04.65	+41:12:08.9	14.9	...	3	y	-298.3	M1374		PN3
PN294	0:44:04.94	+41:09:18.6	16.7	...	2	y	-206.0	M2843		PN3
PN295	0:44:05.08	+41:45:14.7	9.5	...	1	y	-154.8	M427		
PN296	0:44:05.68	+41:18:03.0	11.5	...	3	y	-215.6	M2782		PN3
PN297	0:44:07.49	+41:10:09.7	16.6	...	3	y	-264.4	M1365		
PN298	0:44:10.78	+41:18:14.1	12.2	...	2	y	-177.2	M3124		PN3
PN299	0:44:11.91	+41:14:00.0	14.9	...	2	y	-229.8	M1380		
PN300	0:44:11.98	+41:35:56.2	5.8	...	1	y	-87.8	M644		

Table A.1—Continued

ID	RA	DEC	R (kpc) ^a	Morph. Type ^b	SB ^c	ADC ^d	Velocity (km s ⁻¹)	M06 ^e	RBC ^f	AMB ^g
PN301	0:44:12.10	+41:39:49.0	6.6	...	2	y	-639.7	M429		
PN302	0:44:15.16	+41:29:06.4	7.3	...	2	n	-74.9	M2710		HII2
PN303	0:44:15.87	+41:22:10.4	10.8	...	3	y	-248.2	M976		PN3
PN304	0:44:16.21	+41:18:53.1	12.7	...	3	y	-185.9	M3296		HII2
PN305	0:44:16.23	+41:57:03.2	15.3	...	3	y	-222.5	M83		
PN306	0:44:17.73	+41:18:51.7	12.9	...	2	y	-245.6			
PN307	0:44:19.33	+41:46:09.2	9.0	...	2	y	-69.3	M3215		
PN308	0:44:21.04	+41:15:41.1	15.3	...	3	y	-282.9	M1400		
PN309	0:44:23.32	+41:29:33.0	8.3	...	2	y	-431.4	M669		PN3
PN310	0:44:25.61	+41:27:03.6	9.7	...	3	n	-175.4	M653		HII2
PN311	0:44:25.75	+41:59:57.1	16.1	...	3	y	-154.0	M88		
PN312	0:44:30.51	+42:00:35.2	16.0	...	3	y	-171.9	M89		PN3
PN313	0:44:32.46	+41:46:37.9	8.7	...	3	y	-1.6	M2613		
PN314	0:44:35.59	+41:56:07.2	13.0	...	3	n	-94.5	M2587		
PN315	0:44:36.75	+41:49:52.9	9.8	...	3	y	-241.0	M235		PN3
PN316	0:44:38.27	+41:43:54.0	7.8	...	1	y	-127.5	M419		
PN317	0:44:40.97	+41:37:06.7	8.1	...	2	y	-171.5	M3224		
PN318	0:44:41.75	+41:43:02.3	7.8	...	1	y	-165.2	M3007		PN3
PN319	0:44:44.18	+41:44:04.8	8.0	...	3	y	-116.1	M2666		PN3
PN320	0:44:44.59	+41:44:12.8	8.1	...	1	y	-138.6	M478		HII3
PN321	0:44:44.61	+41:47:05.7	8.7	...	3	y	-374.6	M264		
PN322	0:44:47.34	+42:02:59.4	15.9	...	3	y	-180.1	M122		PN3
PN323	0:44:47.99	+42:11:54.3	21.1	...	1	y	-84.2	M22		
PN324	0:44:48.91	+41:28:16.7	12.6	...	1	y	-183.8			
PN325	0:44:49.53	+41:47:16.6	8.7	...	3	y	-163.8	M228		PN3
PN326	0:44:50.19	+41:31:07.8	11.4	...	3	y	-109.7	M677		
PN327	0:44:50.88	+42:05:06.2	16.8	...	3	y	-160.4	M2571		HII3
PN328	0:44:52.98	+42:03:35.3	15.8	...	2	y	-96.5	M123		
PN329	0:44:54.71	+41:53:05.4	10.5	...	2	y	24.0	M252		
PN330	0:44:55.48	+42:13:46.0	21.5	...	1	y	-203.9	M24		
PN331	0:44:56.30	+41:20:25.4	18.0	...	3	y	-291.1	M1004		
PN332	0:44:59.88	+42:07:44.7	17.5	...	2	y	-186.9	M17		
PN333	0:45:00.19	+41:36:43.1	10.5	...	3	y	-98.8	M2670		HII3
PN334	0:45:00.99	+42:08:44.8	18.0	...	1	y	-65.4	M18		
PN335	0:45:03.02	+41:59:23.0	12.9	...	1	y	-95.8	M110		
PN336	0:45:09.55	+41:33:37.8	13.0	...	1	y	-127.1	M726		
PN337	0:45:15.09	+42:05:58.5	15.4	...	3	y	-1.3	M2574		

Table A.1—Continued

ID	RA	DEC	R (kpc) ^a	Morph. Type ^b	SB ^c	ADC ^d	Velocity (km s ⁻¹)	M06 ^e	RBC ^f	AMB ^g
PN338	0:45:16.10	+41:33:05.2	14.2	...	1	y	-115.8	M722		
PN339	0:45:17.39	+41:39:33.0	11.7	...	3	y	-117.1		M077	
PN340	0:45:21.06	+41:52:07.7	10.4	...	1	y	-40.8	M297		HII3
PN341	0:45:21.80	+41:46:50.4	10.5	...	2	y	-36.3	M2619		PN3
PN342	0:45:22.99	+42:00:38.7	12.6	...	2	y	-141.5	M115		
PN343	0:45:23.18	+42:15:26.4	19.9	...	1	y	-103.7			
PN344	0:45:24.27	+41:52:00.0	10.6	...	2	y	-60.9	M294		
PN345	0:45:24.82	+41:47:31.4	10.7	...	3	y	-85.0	M271		
PN346	0:45:26.02	+41:36:31.6	14.1	...	1	y	-187.0	M2667		
PN347	0:45:27.45	+42:04:42.6	14.1	...	2	y	-60.7	M2573		
PN348	0:45:31.55	+42:08:38.5	15.7	...	2	y	-271.6	M31		
PN349	0:45:37.83	+41:51:17.4	11.4	...	1	y	-164.6	M289		PN3
PN350	0:45:38.43	+42:00:24.3	12.4	...	1	y	-115.3	M134		
PN351	0:45:43.83	+41:59:33.1	12.3	...	1	y	-483.3	M130		
PN352	0:45:44.67	+41:52:40.9	11.9	...	1	y	-56.7	M300		HII3
PN353	0:45:46.03	+42:03:33.6	13.3	...	2	y	-112.8	M137		
PN354	0:45:47.33	+41:35:12.9	17.8	...	1	y	-152.3	M732		
PN355	0:45:49.17	+41:36:44.2	17.3	...	1	y	-152.1	M2682		
PN356	0:45:50.78	+42:06:49.2	14.3	...	1	y	7.9	M29		HII3
PN357	0:45:52.14	+42:04:05.1	13.4	...	1	y	-6.7	M138		
PN358	0:45:52.24	+41:37:08.3	17.6	...	1	y	-197.8	M2684		
PN359	0:45:52.50	+42:00:10.2	12.6	...	1	y	-227.7	M133		
PN360	0:45:53.36	+42:08:50.2	15.0	...	1	y	-60.5	M32		
PN361	0:45:53.85	+41:39:55.8	16.5	...	1	y	-192.5	M488		
PN362	0:45:59.86	+41:52:26.3	13.3	...	1	y	-172.0	M328		
PN363	0:46:02.14	+42:07:38.6	14.4	...	1	y	-202.6	M46		
PN364	0:46:06.21	+42:07:00.7	14.3	...	2	y	-69.9	M45		
PN365	0:46:07.05	+41:52:04.7	14.1	...	1	y	-23.7	M325		
PN366	0:46:08.40	+42:11:31.5	15.6	...	3	y	-82.3	M56		HII3
PN367	0:46:09.32	+41:55:44.3	13.7	...	3	y	-39.9	M2590		
PN368	0:46:13.62	+41:49:30.0	15.5	...	3	y	-130.4	M319		PN3
PN369	0:46:17.34	+41:43:28.7	18.3	...	1	y	-320.3	M499		
PN370	0:46:17.56	+41:51:58.2	15.3	...	3	y	-107.9	M324		HII3
PN371	0:46:18.54	+42:03:07.9	14.1	...	1	y	-171.7	M136		PN3
PN372	0:46:26.24	+41:55:39.1	15.3	...	2	y	-124.3			
PN373	0:46:28.86	+42:03:10.3	14.7	...	1	y	-134.2	M161		
PN374	0:46:29.27	+41:47:29.4	18.3	...	1	y	-147.3	M315		

Table A.1—Continued

ID	RA	DEC	R (kpc) ^a	Morph. Type ^b	SB ^c	ADC ^d	Velocity (km s ⁻¹)	M06 ^e	RBC ^f	AMB ^g
PN375	0:46:40.30	+41:45:46.2	20.5	...	1	y	-130.8	M3095		
PN376	0:46:44.68	+41:53:20.6	18.1	...	1	y	-265.8	M331		
PN377	0:46:54.62	+42:00:43.5	17.3	...	1	y	...			III3
PN378	0:47:04.91	+41:56:38.7	19.6	...	1	y	-164.7	M141		
PN379	0:47:09.30	+41:56:13.1	20.3	...	1	y	-90.0	M140		
<i>Planetary nebulae (halo population)</i>										
PNh0010:35:50.74	+42:21:04.4	104.8	...	2	y	-296.8	M2543			
PNh0020:36:27.15	+42:06:21.8	89.9	...	1	y	-15.2	M2549			
PNh0030:37:09.28	+42:38:18.9	103.6	...	1	y	-245.0	M2542			
PNh0040:37:28.34	+42:10:57.6	83.3	...	1	y	-231.0	M2544			
PNh0050:37:54.37	+42:14:49.3	81.7	...	1	y	-334.2	M7			
PNh0060:38:48.46	+41:39:37.3	51.2	...	2	y	-195.4	M352			
PNh0070:38:56.63	+39:47:14.1	29.7	...	2	y	-417.0				
PNh0080:39:01.08	+41:51:11.2	56.5	...	3	y	-216.0	M174			
PNh0090:39:21.16	+42:25:16.3	75.2	...	1	y	-331.8				
PNh0100:39:31.59	+42:11:56.7	65.0	...	1	y	-343.5	M5			
PNh0110:39:34.85	+41:23:44.5	34.2	...	1	y	-250.8	M800			
PNh0120:39:49.21	+41:24:09.7	32.2	...	3	y	-255.3	M798			
PNh0130:39:50.65	+41:30:42.9	36.0	...	1	y	-259.8	M524			
PNh0140:39:54.23	+39:50:59.9	33.4	...	2	y	-479.7				
PNh0150:40:15.77	+41:28:23.1	30.7	...	1	y	-312.7	M2692			
PNh0160:40:16.20	+40:09:59.7	24.3	...	1	y	-461.2				
PNh0170:40:35.35	+42:10:32.0	54.5	...	3	y	-142.9	M2			
PNh0180:40:37.96	+40:13:35.5	24.5	...	3	y	-589.3				
PNh0190:40:38.06	+41:16:48.2	20.2	...	2	y	-447.9	M1074			
PNh0200:40:56.88	+40:20:09.0	22.6	...	3	y	-575.2				III9
PNh0210:40:58.73	+41:29:32.3	24.7	...	3	y	-281.4	M2690			
PNh0220:41:15.69	+41:27:19.9	20.7	...	1	y	-313.9	M793			
PNh0230:41:19.07	+41:51:46.6	35.9	...	1	y	-273.0	M168			
PNh0240:41:19.74	+41:41:10.0	28.9	...	1	y	-349.0	M346			
PNh0250:41:25.37	+41:28:22.4	19.9	...	1	y	-284.7	M2687			
PNh0260:41:33.67	+40:20:39.5	26.8	...	2	y	-409.0				
PNh0270:41:41.02	+41:38:14.7	23.8	...	3	y	8.7	M337			
PNh0280:41:41.75	+41:34:03.5	21.0	...	2	y	-316.7	M515			
PNh0290:41:54.52	+41:36:16.6	20.5	...	3	y	-133.3	M553			
PNh0300:42:03.33	+40:31:39.7	23.5	...	2	y	-553.9	M2108			
PNh0310:42:04.07	+40:29:37.6	25.0	...	1	y	-511.1				

Table A.1—Continued

ID	RA	DEC	R (kpc) ^a	Morph. Type ^b	SB ^c	ADC ^d	Velocity (km s ⁻¹)	M06 ^e	RBC ^f	AMB ^g
PNh0320:42:21.19	+40:33:49.9	24.5	...	3	y	-391.2	M2112		PN1	
PNh0330:42:32.17	+40:33:58.8	26.0	...	3	n	231.2	M2113			
PNh0340:42:32.34	+40:42:26.2	20.4	...	1	y	-373.1	M1992		PN1	
PNh0350:42:41.96	+41:56:56.4	27.2	...	3	y	-100.1	M68			
PNh0360:42:44.48	+40:17:30.9	38.6	...	1	y	-472.8	M2493			
PNh0370:42:46.59	+40:26:15.2	33.1	...	2	y	-478.8	M2488			
PNh0380:42:50.60	+40:45:28.4	21.0	...	2	y	-177.7	M2000			
PNh0390:42:51.64	+41:54:23.5	24.2	...	1	y	-223.9	M200			
PNh0400:42:52.05	+40:29:03.1	32.1	...	1	y	-294.2	M2489			
PNh0410:42:54.34	+40:41:58.0	23.9	...	2	n	-258.1			HII1	
PNh0420:42:56.18	+40:35:40.3	28.3	...	1	y	-531.4	M2129			
PNh0430:42:59.08	+42:02:14.1	28.3	...	3	y	-319.9	M71			
PNh0440:43:00.48	+41:58:56.0	25.9	...	2	y	-270.2	M70			
PNh0450:43:02.01	+40:49:30.4	20.0	...	2	y	-152.5	M3245			
PNh0460:43:05.16	+41:55:52.7	23.3	...	3	y	-283.4	M3213			
PNh0470:43:11.17	+42:20:45.6	38.9	...	1	y	-261.3	M2471			
PNh0480:43:11.55	+42:07:12.9	29.9	...	1	y	-199.7	M8			
PNh0490:43:11.82	+41:55:46.5	22.3	...	2	y	-48.9	M2585			
PNh0500:43:15.17	+40:51:12.6	20.8	...	1	y	-515.4	M2893		PN2	
PNh0510:43:17.24	+41:59:04.7	23.8	...	1	y	-194.4	M78			
PNh0520:43:20.61	+40:55:32.4	18.8	...	3	y	-304.3	M1845			
PNh0530:43:27.18	+42:04:45.6	26.2	...	3	y	-189.0	M3212			
PNh0540:43:28.31	+40:51:19.8	22.7	...	1	y	-483.9	M3240			
PNh0550:43:32.32	+41:58:42.6	21.5	...	3	y	-600.1	M77			
PNh0560:43:36.80	+40:37:38.5	33.0	...	1	y	-311.0	M2131			
PNh0570:43:42.52	+42:22:35.6	35.9	...	1	y	-220.5	M2475			
PNh0580:43:44.51	+40:59:59.6	19.5	...	3	y	-271.4	M2869			
PNh0590:44:02.33	+42:17:16.6	29.8	...	3	y	-254.8	M2472			
PNh0600:44:03.12	+42:27:46.5	36.6	...	1	y	-215.6				
PNh0610:44:11.42	+41:01:02.1	23.0	...	2	y	-350.3	M1701			
PNh0620:44:25.98	+40:15:45.7	54.7	...	3	y	-345.4	M2496			
PNh0630:44:35.27	+42:15:31.3	24.8	...	1	y	-215.7				
PNh0640:44:37.91	+41:14:14.4	18.8	...	2	y	-225.9	M1394			
PNh0650:44:42.22	+41:08:01.8	23.3	...	3	y	-246.9	M3167			
PNh0660:44:42.77	+40:40:05.7	41.3	...	2	y	-376.7	M2132			
PNh0670:44:43.80	+41:14:28.0	19.6	...	1	y	-311.6	M1396			
PNh0680:44:46.95	+41:15:28.7	19.5	...	2	y	-594.7	M1408			

Table A.1—Continued

ID	RA	DEC	R (kpc) ^a	Morph. Type ^b	SB ^c	ADC ^d	Velocity (km s ⁻¹)	M06 ^e	RBC ^f	AMB ^g
PNh0690:44:50.69	+41:17:22.3	18.9	3	y	-282.6	M1404		
PNh0700:44:54.43	+40:52:45.3	34.9	3	y	-453.8	M1869		
PNh0710:44:54.98	+41:09:53.2	24.1	3	y	-322.8	M2844		
PNh0720:45:05.05	+41:12:52.5	23.9	2	y	-208.0	M2845		
PNh0730:45:07.13	+40:39:33.4	45.4	1	y	-276.8	M2948		
PNh0740:45:16.24	+41:18:14.4	22.4	1	y	-279.6	M2784		
PNh0750:45:28.36	+41:04:54.2	32.4	1	y	-394.9	M1706		
PNh0760:45:35.31	+40:59:57.1	36.6	2	y	-215.5	M2874		
PNh0770:45:38.13	+40:59:19.5	37.4	2	y	-289.4	M2872		
PNh0780:45:43.98	+41:22:40.5	24.1	3	y	-317.6	M1021		
PNh0790:46:18.30	+41:31:10.0	24.5	3	y	-168.3	M746		
PNh0800:47:00.98	+40:49:23.3	56.6	1	y	-337.8	M2567		
PNh0810:48:24.78	+41:08:11.1	57.7	2	y	-355.5	M2564		
<i>Unclassified</i>										
X001	0:39:06.10	+40:37:22.8	15.7	s	1	y	-512.5			HII1
X002	0:39:07.30	+40:36:25.5	15.4	s	1	y	-513.9			HII1
X003	0:39:08.89	+40:24:11.5	14.8	s	1	y	-534.1			HII1
X004	0:39:09.40	+40:29:16.0	14.4	s	1	y	-542.2			HII1
X005	0:39:12.90	+40:50:59.6	19.7	s	1	y	-408.2			HII1
X006	0:39:16.09	+40:43:55.5	16.4	s	1	y	-530.5			HII1
X007	0:39:16.90	+40:20:55.5	15.4	s	1	n	-560.4			HII1
X008	0:39:24.30	+40:48:07.5	16.8	s	1	y	-469.8			HII2
X009	0:39:34.80	+40:49:59.5	16.1	s	1	y	-446.3			HII2
X010	0:40:10.29	+40:45:19.0	10.4	s	1	y	-533.0			HII5
X011	0:40:37.20	+40:50:36.9	8.6	s	1	y	-560.4			HII7
X012	0:40:46.80	+40:41:30.1	9.9	s	1	y	-537.7			HII8
X013	0:40:52.00	+40:43:10.9	9.4	d	1	y	-525.4			HII9
X014	0:41:24.40	+40:42:12.9	12.1	d	1	y	-467.9			HII1
X015	0:41:28.10	+41:04:37.5	6.0	d	1	y	-467.9			HII1
X016	0:41:42.69	+41:16:10.5	9.7	s	1	y	-458.5			HII1
X017	0:42:13.80	+40:51:50.0	11.8	s	1	y	-412.7			HII1
X018	0:42:28.80	+41:28:47.6	10.6	s	1	y	-289.4			HII1
X019	0:43:48.83	+41:44:27.0	10.5	s	1	y	...			
X020	0:43:54.00	+41:29:24.3	4.7	s	1	y	-191.5			HII2
X021	0:44:18.11	+41:34:12.0	6.3	s	1	y	...			
X022	0:44:22.20	+41:49:51.6	10.7	s	1	y	-123.0			HII2
X023	0:44:26.59	+41:27:29.8	9.6	s	1	y	-202.9			HII2

Table A.1—Continued

ID	RA	DEC	R (kpc) ^a	Morph. Type ^b	SB ^c	ADC ^d	Velocity (km s ⁻¹)	M06 ^e	RBC ^f	AMB ^g
X024	0:44:40.21	+41:28:33.0	11.1	s	1	y	-219.6			HII3
X025	0:45:05.55	+41:38:54.8	10.4	d	1	y	...			

Note. — The table is divided into sections based on the spectroscopic classification of the object as either an HII region (HII), planetary nebula (PN), PN in the halo population (PNh), or unclassified (X). This classification is based on line ratio diagnostics, as described in Section 3.2.2.

^aThe galactocentric radius of the object, calculated as described in Section 3.2.3.

^bThe morphological classification of the object based on LGGs H α imaging, as described in Section 3.2.2.

^cThe surface brightness class of the object as defined in Section 3.2.4 based on the H α flux.

^dThe status of the atmospheric dispersion compensator during the observation of this object: “y” indicates that it was functioning, “n” indicates that it was not.

^eThe ID number of the object from the PNe catalog of Merrett et al. (2006).

^fThe name of the object from version 3.5 of the Revised Bologna Catalog, Galleti et al. (2007).

^gThe ID number of the object from the HII region catalog of Azimlu et al. (2011).

APPENDIX A. SUPPLEMENTAL TABLES FOR CHAPTER 3

Table A.2. Measured line fluxes for M31 HII regions and PNe, relative to $H\beta$

ID	[O II] λ 3727	[O III] λ 4363	[O III] λ 4959	[O III] λ 5007	[N II] λ 6548	H α λ 6562	[N II] λ 6584	[S II] λ 6717	[S II] λ 6731
<i>HII regions</i>									
HII001	50 ± 20	48 ± 3	442 ± 5	150 ± 3	57 ± 4	45 ± 5
HII002	54 ± 6	255 ± 4	151 ± 5
HII003	26 ± 6	264 ± 6	76 ± 7	22 ± 4	20 ± 4
HII004	40 ± 10	100 ± 10	...	252 ± 8	70 ± 8
HII005	87 ± 9	409 ± 9	270 ± 10
HII006	430 ± 40	110 ± 20	...	340 ± 20
HII007	299 ± 6	852 ± 9	...	213 ± 6
HII008	...	15 ± 4	286 ± 5	830 ± 10	...	221 ± 5
HII009	50 ± 10	...	606 ± 10
HII010	270 ± 10	27 ± 6	306 ± 6	82 ± 6	43 ± 6	33 ± 6
HII011	310 ± 20	38 ± 9	390 ± 10	110 ± 10	60 ± 10	50 ± 10
HII012	380 ± 10	60 ± 10	...	340 ± 10	74 ± 8	36 ± 9	...
HII013	287 ± 3	...	54 ± 2	160 ± 2	20.4 ± 0.8	329 ± 3	63 ± 1	24 ± 1	16.4 ± 0.9
HII014	360 ± 40	340 ± 20	110 ± 20
HII015	260 ± 10	37 ± 8	340 ± 10	109 ± 8	50 ± 10	40 ± 10
HII016	80 ± 20	360 ± 20	220 ± 20
HII017	180 ± 10	490 ± 10	...	326 ± 10
HII018	30 ± 5	...	26 ± 2	79 ± 2	71 ± 2	324 ± 3	213 ± 2	...	8 ± 2
HII019	190 ± 30	40 ± 10	319 ± 10	100 ± 10	40 ± 10	...
HII020	44 ± 9	...	98 ± 3	295 ± 4	18 ± 2	598 ± 8	55 ± 2	24 ± 2	17 ± 2
HII021	230 ± 30	340 ± 20	100 ± 20
HII022	60 ± 10	...	518 ± 7
HII023	146 ± 2	...	11.8 ± 0.7	36.5 ± 0.7	48.5 ± 0.7	437 ± 5	145 ± 2	39.8 ± 0.6	28.5 ± 0.7
HII024	190 ± 20	...	18 ± 3	51 ± 3	46 ± 4	419 ± 5	141 ± 3	25 ± 3	15 ± 4
HII025	...	70 ± 20	140 ± 20	420 ± 20	...	530 ± 10
HII026	220 ± 20	50 ± 10	430 ± 10	140 ± 10	50 ± 10	40 ± 10
HII027	340 ± 20	40 ± 10	350 ± 10	100 ± 10	40 ± 10	...
HII028	230 ± 20	40 ± 10	40 ± 10	387 ± 9	100 ± 10	40 ± 10	...
HII029	198 ± 9	...	25 ± 2	73 ± 3	31 ± 2	376 ± 3	93 ± 2	28 ± 2	20 ± 2
HII030	140 ± 20	...	390 ± 10	130 ± 10
HII031	280 ± 30	820 ± 30	...	560 ± 30
HII032	520 ± 50	52 ± 8	325 ± 10	155 ± 9	60 ± 10	40 ± 10
HII033	350 ± 20	40 ± 10	340 ± 10	120 ± 10	50 ± 10	...
HII034	340 ± 30	70 ± 20	640 ± 20	190 ± 20	70 ± 10	...
HII035	290 ± 10	860 ± 10	...	290 ± 9
HII036	530 ± 20	120 ± 20	60 ± 20	...

Table A.2—Continued

ID	[O II] λ 3727	[O III] λ 4363	[O III] λ 4959	[O III] λ 5007	[N II] λ 6548	H α λ 6562	[N II] λ 6584	[S II] λ 6717	[S II] λ 6731
HII037	220 ± 20	50 ± 20	380 ± 10	140 ± 10	70 ± 10	50 ± 20
HII038	250 ± 50	440 ± 20	170 ± 20	110 ± 20	70 ± 20
HII039	70 ± 20	...	350 ± 10	90 ± 10	40 ± 10	...
HII040	155 ± 1	...	38.2 ± 0.7	116 ± 1	45.0 ± 0.4	492 ± 5	134 ± 1	37.6 ± 0.4	27.3 ± 0.5
HII041	120 ± 30	80 ± 20	710 ± 20	230 ± 10	90 ± 20	50 ± 20
HII042	60 ± 10	...	500 ± 20	140 ± 20	47 ± 10	...
HII043	260 ± 20	70 ± 10	440 ± 10	200 ± 20	90 ± 20	60 ± 20
HII044	210 ± 20	590 ± 10	...	230 ± 20
HII045	138 ± 1	1.4 ± 0.1	106 ± 1	317 ± 3	13.2 ± 0.1	338 ± 4	37.0 ± 0.4	11.7 ± 0.1	8.71 ± 0.09
HII046	198 ± 5	...	23 ± 3	70 ± 4	33 ± 2	360 ± 4	99 ± 3	26 ± 2	18 ± 3
HII047	180 ± 10	90 ± 5	275 ± 5	271 ± 5
HII048	145 ± 1	...	47.8 ± 0.4	142 ± 2	17.2 ± 0.2	314 ± 3	51.0 ± 0.5	12.8 ± 0.2	9.5 ± 0.2
HII049	340 ± 40	400 ± 20	110 ± 30
HII050	80 ± 10	690 ± 10	240 ± 10	80 ± 20	50 ± 10
HII051	90 ± 30	...	400 ± 20
HII052	116 ± 1	...	51.2 ± 0.6	157 ± 2	65.3 ± 0.6	721 ± 8	204 ± 2	48.4 ± 0.5	40.2 ± 0.4
HII053	90 ± 10	...	570 ± 10
HII054	150 ± 30	60 ± 20	630 ± 20	200 ± 20	90 ± 20	70 ± 20
HII055	190 ± 10	50 ± 4	339 ± 5	124 ± 4	59 ± 4	41 ± 4
HII056	229 ± 2	...	36.7 ± 0.3	110 ± 1	33.2 ± 0.4	337 ± 3	99 ± 1	24.9 ± 0.2	19.8 ± 0.2
HII057	50 ± 10	550 ± 10	160 ± 10	50 ± 8	37 ± 7
HII058	93.5 ± 0.8	...	54.9 ± 0.6	168 ± 2	50.7 ± 0.5	713 ± 8	156 ± 1	33.4 ± 0.4	27.0 ± 0.3
HII059	320 ± 10	80 ± 10
HII060	...	19 ± 7	27 ± 5	78 ± 5	...	850 ± 10
HII061	135 ± 1	...	76.8 ± 0.8	233 ± 2	24.9 ± 0.3	483 ± 5	72.4 ± 0.7	21.5 ± 0.2	16.3 ± 0.2
HII062	160 ± 10	69 ± 9	314 ± 9	199 ± 9
HII063	134 ± 2	...	89.9 ± 1.0	270 ± 3	11.9 ± 0.7	429 ± 5	35.5 ± 0.7	10.4 ± 0.7	7.7 ± 0.8
HII064	258 ± 7	2.6 ± 0.8	46.3 ± 0.7	142 ± 1	29.9 ± 0.7	400 ± 5	89.4 ± 0.9	29.3 ± 0.7	21.1 ± 0.6
HII065	160 ± 10	47 ± 8	407 ± 8	135 ± 8	60 ± 7	41 ± 8
HII066	180 ± 10	16 ± 4	93 ± 5	657 ± 6	272 ± 4	90 ± 4	68 ± 4
HII067	300 ± 40	200 ± 10	120 ± 20
HII068	177 ± 3	...	32 ± 1	93 ± 1	45.9 ± 0.9	524 ± 5	140 ± 1	39 ± 1	28.9 ± 0.7
HII069	131 ± 1	...	11.4 ± 0.2	34.5 ± 0.4	68.2 ± 0.8	472 ± 5	210 ± 2	63.5 ± 0.6	53.7 ± 0.5
HII070	106 ± 2	...	36 ± 1	113 ± 1	64 ± 2	646 ± 6	192 ± 2	49 ± 1	39 ± 1
HII071	300 ± 20	880 ± 20	...	340 ± 20
HII072	85 ± 8	...	27 ± 5	86 ± 5	58 ± 4	704 ± 7	168 ± 5	54 ± 5	40 ± 4
HII073	46 ± 7	581 ± 8	140 ± 7	82 ± 4	57 ± 4

Table A.2—Continued

ID	[O II] λ 3727	[O III] λ 4363	[O III] λ 4959	[O III] λ 5007	[N II] λ 6548	H α λ 6562	[N II] λ 6584	[S II] λ 6717	[S II] λ 6731
HII074	90 ± 20	80 ± 20	60 ± 10	580 ± 10	190 ± 10
HII075	230 ± 20	420 ± 20	160 ± 20	60 ± 20	...
HII076	190 ± 20	380 ± 20	120 ± 10	50 ± 10	50 ± 10
HII077	90 ± 20	65 ± 8	603 ± 6	190 ± 9	71 ± 7	47 ± 8
HII078	250 ± 40	50 ± 10	50 ± 10	577 ± 9	158 ± 9	57 ± 9	30 ± 10
HII079	126 ± 3	...	21 ± 1	62 ± 1	33.7 ± 0.7	414 ± 4	97.6 ± 1.0	26.2 ± 0.7	19.2 ± 0.7
HII080	108.2 ± 0.9	...	29.8 ± 0.7	88.2 ± 1.0	41.1 ± 0.5	539 ± 6	123 ± 1	29.1 ± 0.3	20.7 ± 0.3
HII081	180 ± 10	100 ± 10	600 ± 10	280 ± 10	99 ± 8	76 ± 7
HII082	115 ± 6	...	26 ± 2	76 ± 2	47 ± 2	611 ± 7	140 ± 2	37 ± 2	27 ± 2
HII083	187 ± 5	...	13 ± 4	37 ± 3	58 ± 3	490 ± 4	174 ± 3	58 ± 2	43 ± 2
HII084	174 ± 2	...	17.2 ± 0.8	51.5 ± 0.5	46.4 ± 0.7	455 ± 4	139 ± 1	36.1 ± 0.6	26.8 ± 0.6
HII085	210 ± 20	...	20 ± 5	58 ± 5	69 ± 5	531 ± 6	208 ± 4	61 ± 5	44 ± 5
HII086	100 ± 10	40 ± 10	400 ± 10	130 ± 10	46 ± 6	38 ± 5
HII087	51 ± 10	116 ± 4	390 ± 4	351 ± 4	...	16 ± 4
HII088	191 ± 2	...	27.3 ± 0.7	81.9 ± 0.9	38.4 ± 0.5	403 ± 5	113 ± 1	33.6 ± 0.5	24.6 ± 0.4
HII089	94 ± 2	...	81.3 ± 0.8	248 ± 2	47.1 ± 0.4	657 ± 6	140 ± 1	22.9 ± 0.5	24.4 ± 0.5
HII090	120 ± 20	360 ± 20	380 ± 20
HII091	252 ± 6	...	26 ± 4	87 ± 5	54 ± 4	312 ± 5	174 ± 5
HII092	153 ± 3	...	23 ± 1	67 ± 1	32.1 ± 0.8	413 ± 5	94.5 ± 0.8	27.4 ± 0.9	19.3 ± 0.8
HII093	175 ± 7	53 ± 4	439 ± 4	154 ± 4	59 ± 2	44 ± 2
HII094	58 ± 2	...	114 ± 1	338 ± 4	5.7 ± 0.2	349 ± 4	15.8 ± 0.2	5.2 ± 0.1	4.1 ± 0.1
HII095	110 ± 50	450 ± 30	370 ± 40
HII096	62 ± 5	...	11 ± 2	29 ± 3	95 ± 3	361 ± 4	290 ± 3	...	9 ± 2
HII097	131 ± 9	26 ± 6	38 ± 4	362 ± 5	123 ± 5	43 ± 5	27 ± 4
HII098	90 ± 20	810 ± 20	300 ± 20	150 ± 10	100 ± 10
HII099	112 ± 7	12 ± 3	68 ± 3	527 ± 5	198 ± 3	55 ± 3	39 ± 3
HII100	200 ± 20	360 ± 10	120 ± 10	50 ± 10	...
HII101	160 ± 20	70 ± 10	680 ± 10	210 ± 10	100 ± 10	80 ± 10
HII102	284 ± 9	...	59 ± 4	168 ± 5	37 ± 4	334 ± 4	106 ± 4	41 ± 4	27 ± 4
HII103	60 ± 10	96 ± 3	690 ± 7	294 ± 4	108 ± 3	80 ± 3
HII104	45 ± 7	...	68 ± 5	206 ± 4	71 ± 3	1160 ± 10	209 ± 4	59 ± 3	44 ± 3
HII105	253 ± 4	...	11 ± 2	24 ± 2	57 ± 1	437 ± 5	175 ± 2	39 ± 2	32 ± 1
HII106	730 ± 20
HII107	121 ± 1	...	50.4 ± 0.5	152 ± 2	37.9 ± 0.4	486 ± 4	116 ± 1	25.5 ± 0.3	19.3 ± 0.2
HII108	540 ± 30	220 ± 30
HII109	55 ± 4	98 ± 2	310 ± 3	303 ± 4	8 ± 2	18 ± 3
HII110	430 ± 40	510 ± 20	140 ± 20	94 ± 6	68 ± 7

Table A.2—Continued

ID	[O II] λ 3727	[O III] λ 4363	[O III] λ 4959	[O III] λ 5007	[N II] λ 6548	H α λ 6562	[N II] λ 6584	[S II] λ 6717	[S II] λ 6731
HII111	110 ± 9	35 ± 3	334 ± 3	97 ± 3	33 ± 3	25 ± 3
HII112	540 ± 30	110 ± 20	100 ± 20	500 ± 10	270 ± 20	230 ± 20	160 ± 10
HII113	107 ± 10	370 ± 9	359 ± 9
HII115	170 ± 50	101 ± 7	870 ± 10	327 ± 8	102 ± 8	64 ± 9
HII115	120 ± 30	24 ± 6	102 ± 7	355 ± 7	321 ± 8
HII116	220 ± 70	540 ± 10	130 ± 20	110 ± 10	50 ± 10
HII117	280 ± 30	140 ± 30	...	420 ± 10	80 ± 10	40 ± 10	...
HII118	190 ± 20	37 ± 4	65 ± 6	476 ± 7	199 ± 7	113 ± 3	76 ± 5
HII119	110 ± 20	21 ± 5	33 ± 6	387 ± 5	100 ± 5	59 ± 4	40 ± 4
HII120	470 ± 20	14 ± 4	41 ± 3	345 ± 3	143 ± 3	68 ± 3	48 ± 3
HII121	514 ± 8	...	54 ± 2	153 ± 2	15 ± 2	283 ± 3	43 ± 2	19 ± 2	13 ± 2
HII122	370 ± 20	...	26 ± 2	81 ± 2	27 ± 4	338 ± 4	76 ± 4	30 ± 2	20 ± 2
HII123	250 ± 20	670 ± 20	...	350 ± 10
HII124	147 ± 5	...	8 ± 2	23 ± 2	71 ± 2	531 ± 5	213 ± 2	55 ± 2	43 ± 2
HII125	303 ± 3	...	21.3 ± 0.8	66.7 ± 0.7	26.7 ± 0.6	321 ± 2	77.2 ± 0.8	30.6 ± 0.8	21.5 ± 0.6
HII126	140 ± 30	43 ± 9	410 ± 8	133 ± 9	53 ± 10	38 ± 9
HII127	113 ± 3	...	82 ± 2	241 ± 2	14 ± 2	441 ± 4	41 ± 1	12 ± 1	8 ± 2
HII128	272 ± 9	35 ± 4	321 ± 5	108 ± 5	51 ± 2	31 ± 2
HII129	140 ± 10	80 ± 10	65 ± 7	654 ± 8	183 ± 7	63 ± 6	42 ± 7
HII130	460 ± 90	520 ± 20	140 ± 20	70 ± 20	...
HII131	380 ± 30	50 ± 10	60 ± 10	350 ± 10	150 ± 10	100 ± 10	70 ± 10
HII132	240 ± 10	62 ± 10	67 ± 9	641 ± 8	200 ± 10	61 ± 5	53 ± 5
HII133	225 ± 8	644 ± 8	...	295 ± 7
HII134	240 ± 30	27 ± 6	71 ± 6	567 ± 6	225 ± 7	88 ± 7	65 ± 7
HII135	50 ± 10	670 ± 10	140 ± 10	70 ± 20	50 ± 10
HII136	390 ± 10	...	51 ± 4	154 ± 4	13 ± 2	307 ± 3	45 ± 2	17 ± 2	12 ± 2
HII137	110 ± 20	47 ± 8	463 ± 7	131 ± 7	65 ± 6	45 ± 6
HII138	163 ± 2	...	79.6 ± 0.9	242 ± 2	28.8 ± 0.4	490 ± 5	85.4 ± 1.0	25.9 ± 0.4	19.8 ± 0.4
HII139	310 ± 10	37 ± 2	384 ± 4	122 ± 2	64 ± 2	46 ± 2
HII140	80 ± 4	252 ± 4	47 ± 4	692 ± 9	126 ± 4	18 ± 3	21 ± 4
HII141	320 ± 30	37 ± 6	465 ± 6	136 ± 7	51 ± 7	35 ± 6
HII142	130 ± 20	610 ± 20	180 ± 20	100 ± 10	70 ± 10
HII143	760 ± 20	170 ± 20	100 ± 20	80 ± 20
HII144	185 ± 2	...	29.3 ± 0.3	87.1 ± 0.8	36.5 ± 0.4	373 ± 4	111 ± 1	31.2 ± 0.4	23.6 ± 0.2
HII145	...	34 ± 9	44 ± 6	141 ± 7	...	430 ± 10
HII146	260 ± 20	770 ± 20	...	220 ± 20
HII147	220 ± 20	...	27 ± 6	82 ± 6	82 ± 5	353 ± 4	251 ± 4

Table A.2—Continued

ID	[O II] λ 3727	[O III] λ 4363	[O III] λ 4959	[O III] λ 5007	[N II] λ 6548	H α λ 6562	[N II] λ 6584	[S II] λ 6717	[S II] λ 6731
HII148	60 ± 10	420 ± 10	150 ± 10	62 ± 10	40 ± 10
HII149	280 ± 10	830 ± 10	...	310 ± 10
HII150	170 ± 30	55 ± 9	484 ± 9	164 ± 8	58 ± 8	43 ± 8
HII151	100 ± 10	80 ± 5	319 ± 5	234 ± 5
HII152	100 ± 10	95 ± 5	306 ± 5	302 ± 6	...	21 ± 4
HII153	160 ± 40	...	111 ± 10	290 ± 10	...	295 ± 4	28 ± 4	19 ± 4	12 ± 4
HII154	340 ± 30	31 ± 6	354 ± 7	104 ± 7	75 ± 6	56 ± 6
HII155	270 ± 10	800 ± 10	...	290 ± 10
HII156	540 ± 30	330 ± 10	110 ± 10	116 ± 7	69 ± 7
HII157	380 ± 40	34 ± 8	362 ± 8	120 ± 10	126 ± 6	94 ± 6
HII158	279 ± 5	...	43 ± 2	129 ± 3	22 ± 1	311 ± 3	64 ± 1	25 ± 2	18 ± 2
HII159	260 ± 20	57 ± 7	480 ± 6	163 ± 7	80 ± 5	62 ± 6
HII160	270 ± 10	...	76 ± 3	213 ± 4	26 ± 3	332 ± 3	73 ± 3	24 ± 3	18 ± 3
HII161	102 ± 6	...	59 ± 2	174 ± 2	20 ± 2	307 ± 4	62 ± 2	27 ± 2	20 ± 2
HII162	77 ± 1	...	24.8 ± 0.4	75.4 ± 0.6	71.2 ± 0.7	584 ± 5	212 ± 3	39.1 ± 0.4	30.0 ± 0.3
HII163	114 ± 5	...	25 ± 2	69 ± 3	73 ± 2	547 ± 5	221 ± 3	44 ± 2	42 ± 2
HII164	71 ± 1	...	20 ± 1	58 ± 1	33.8 ± 0.5	458 ± 5	101 ± 1	23.0 ± 0.5	16.7 ± 0.5
HII165	18 ± 1	52 ± 1	62.6 ± 0.9	581 ± 6	189 ± 2	49.9 ± 0.8	38.3 ± 1.0
HII166	8 ± 2	37 ± 2	379 ± 4	114 ± 2	47 ± 2	35 ± 1
HII167	128 ± 6	375 ± 6	397 ± 5	...	21 ± 5
HII168	170 ± 20	72 ± 4	568 ± 5	215 ± 4	87 ± 4	67 ± 4
HII169	53 ± 4	...	38 ± 2	119 ± 1	80 ± 2	1020 ± 10	246 ± 2	48 ± 1	40 ± 1
HII170	570 ± 70	29 ± 6	354 ± 7	110 ± 5	57 ± 6	40 ± 6
HII171	90 ± 10	42 ± 4	370 ± 5	118 ± 4	44 ± 5	27 ± 5
HII172	180 ± 20	730 ± 20	560 ± 20
HII173	122 ± 2	...	16.0 ± 0.7	46.1 ± 0.9	58.1 ± 0.6	498 ± 5	176 ± 2	45.5 ± 0.7	32.2 ± 0.6
HII174	251 ± 3	...	63 ± 2	185 ± 2	16.7 ± 0.7	333 ± 3	49.1 ± 0.9	15.1 ± 0.5	10.9 ± 0.5
HII175	42 ± 9	319 ± 10	93 ± 10	38 ± 8	29 ± 8
HII176	220 ± 20	40 ± 7	82 ± 6	675 ± 6	259 ± 8	83 ± 5	61 ± 4
HII177	...	40 ± 4	41 ± 4	117 ± 4
HII178	38 ± 1	...	41.5 ± 1.0	127 ± 2	29.8 ± 0.6	552 ± 5	87.5 ± 0.7	19.3 ± 0.6	14.8 ± 0.5
HII179	390 ± 40	100 ± 10	940 ± 10	360 ± 10	100 ± 10	90 ± 10
HII180	30 ± 2	...	40.5 ± 0.9	125 ± 1	97 ± 1	933 ± 9	288 ± 3	55.3 ± 0.8	45.2 ± 0.7
HII181	109 ± 1	...	28.8 ± 0.7	88.0 ± 1.0	30.9 ± 0.5	434 ± 5	95.3 ± 1.0	24.7 ± 0.5	18.2 ± 0.6
HII182	19 ± 5	51 ± 3	58 ± 2	575 ± 5	173 ± 2	45 ± 2	30 ± 2
HII183	70 ± 6	19 ± 4	86 ± 2	603 ± 5	259 ± 2	92 ± 2	65 ± 3
HII184	320 ± 30	840 ± 30	...	360 ± 20

Table A.2—Continued

ID	[O II] λ 3727	[O III] λ 4363	[O III] λ 4959	[O III] λ 5007	[N II] λ 6548	H α λ 6562	[N II] λ 6584	[S II] λ 6717	[S II] λ 6731
HII185	...	47 ± 7	79 ± 5	235 ± 6	...	514 ± 6	36 ± 5
HII186	150 ± 10	59 ± 6	523 ± 6	164 ± 6	64 ± 7	39 ± 6
HII187	174 ± 2	13 ± 2	38.3 ± 1.0	331 ± 3	113 ± 1	37.4 ± 0.7	26.4 ± 0.8
HII188	13 ± 2	31 ± 3	33 ± 1	359 ± 3	99 ± 1	38 ± 1	26 ± 1
HII189	106 ± 8	49 ± 2	410 ± 4	143 ± 2	62 ± 2	44 ± 2
HII190	52 ± 6	...	27 ± 2	76 ± 2	17 ± 2	252 ± 3	48 ± 2
HII191	213 ± 2	...	10.9 ± 0.5	29.8 ± 0.6	52.0 ± 0.6	453 ± 5	160 ± 1	42.1 ± 0.5	30.5 ± 0.3
HII192	40 ± 3	459 ± 4	118 ± 3	65 ± 4	49 ± 3
HII193	...	65 ± 2	103 ± 2	306 ± 3	...	373 ± 4	14 ± 2
HII194	290 ± 10	...	32 ± 5	87 ± 6	29 ± 5	396 ± 5	80 ± 4	27 ± 5	21 ± 4
HII195	84 ± 5	349 ± 4	276 ± 5	...	19 ± 4
HII196	60 ± 5	9 ± 2	87 ± 2	574 ± 4	261 ± 2	81 ± 2	59 ± 2
HII197	166 ± 4	...	57 ± 2	167 ± 3	47 ± 2	554 ± 6	138 ± 2	41 ± 1	29 ± 1
HII198	211 ± 3	...	76.9 ± 0.8	230 ± 2	16.1 ± 0.2	339 ± 4	49.3 ± 0.5	16.8 ± 0.2	12.9 ± 0.2
HII199	247 ± 5	...	25 ± 3	76 ± 3	41 ± 2	447 ± 5	121 ± 1	41 ± 1	31 ± 1
HII200	140 ± 20	120 ± 20	50 ± 10	700 ± 10	160 ± 10	100 ± 10	70 ± 10
HII201	300 ± 20	29 ± 7	48 ± 7	491 ± 7	150 ± 7	62 ± 5	47 ± 5
HII202	194 ± 4	...	12 ± 2	35 ± 2	44.9 ± 0.9	379 ± 4	136 ± 1	49 ± 1	33.8 ± 0.8
HII203	30 ± 10	131 ± 10	1110 ± 10	400 ± 9	117 ± 7	95 ± 8
HII204	340 ± 20	36 ± 10	350 ± 10	110 ± 10	58 ± 4	37 ± 5
HII205	108 ± 2	...	117 ± 2	354 ± 3	8.9 ± 0.6	361 ± 4	26.3 ± 0.6	8.8 ± 0.6	7.1 ± 0.6
HII206	...	40 ± 10	170 ± 10	485 ± 10	...	360 ± 8
HII207	100 ± 30	...	56 ± 4	170 ± 4	34 ± 3	526 ± 4	98 ± 3	35 ± 3	24 ± 3
HII208	76 ± 1	234 ± 3	64 ± 1	960 ± 10	196 ± 2	57 ± 1	45 ± 1
HII209	134 ± 2	0.6 ± 0.1	71.0 ± 0.7	213 ± 2	32.4 ± 0.4	469 ± 5	101 ± 1	21.4 ± 0.2	18.1 ± 0.2
HII210	120 ± 8	58 ± 2	299 ± 3	181 ± 2	...	5 ± 2
HII211	23 ± 7	55 ± 5	64 ± 6	570 ± 6	191 ± 6	59 ± 5	49 ± 5
HII212	65 ± 7	201 ± 7	38 ± 5	286 ± 6	90 ± 7
HII213	157 ± 3	...	79.5 ± 0.8	244 ± 3	22.5 ± 0.3	499 ± 5	68.0 ± 0.6	23.1 ± 0.3	16.3 ± 0.3
HII214	270 ± 20	770 ± 20	...	260 ± 20
HII215	230 ± 10	23 ± 4	40 ± 3	312 ± 4	110 ± 3	48 ± 3	30 ± 3
HII216	150 ± 40	105 ± 9	900 ± 9	329 ± 6	133 ± 8	92 ± 7
HII217	137 ± 1	...	35.1 ± 0.3	107 ± 1	30.6 ± 0.3	378 ± 4	92.2 ± 0.9	23.9 ± 0.2	17.6 ± 0.2
HII218	119 ± 4	...	43.5 ± 0.9	131 ± 2	29.4 ± 0.5	435 ± 4	91.3 ± 0.8	32.6 ± 0.6	23.5 ± 0.6
HII219	160 ± 8	59 ± 2	303 ± 3	186 ± 2
HII220	56 ± 1	171 ± 1	40.7 ± 0.9	581 ± 6	122 ± 1	28.9 ± 0.8	24.1 ± 0.7
HII221	170 ± 20	70 ± 4	458 ± 5	213 ± 4	69 ± 3	51 ± 4

Table A.2—Continued

ID	[O II] λ 3727	[O III] λ 4363	[O III] λ 4959	[O III] λ 5007	[N II] λ 6548	H α λ 6562	[N II] λ 6584	[S II] λ 6717	[S II] λ 6731
HII222	...	35 ± 2	85 ± 3	251 ± 3	13 ± 2	631 ± 7	30 ± 3
HII223	25 ± 7	67 ± 6	120 ± 6	1110 ± 10	378 ± 5	96 ± 6	74 ± 7
HII224	680 ± 40	...	34 ± 10	110 ± 10	80 ± 20	380 ± 10	240 ± 10	207 ± 8	144 ± 9
HII225	260 ± 20	710 ± 20	...	310 ± 30
HII226	270 ± 50	36 ± 9	397 ± 10	140 ± 10	80 ± 10	47 ± 9
HII227	190 ± 10	37 ± 7	40 ± 4	397 ± 4	126 ± 4	35 ± 2	27 ± 2
HII228	230 ± 30	67 ± 7	678 ± 7	230 ± 6	86 ± 6	56 ± 6
HII229	108 ± 1	...	28.3 ± 0.3	87.0 ± 0.8	44.3 ± 0.5	520 ± 5	134 ± 1	35.3 ± 0.4	25.8 ± 0.3
HII230	41 ± 2	122 ± 2	20 ± 2	352 ± 4	57 ± 2	8 ± 2	6 ± 2
HII231	300 ± 20	42 ± 8	36 ± 8	435 ± 10	120 ± 10	36 ± 8	33 ± 6
HII232	233 ± 6	...	44 ± 5	147 ± 6	17 ± 3	299 ± 3	53 ± 4	21 ± 3	15 ± 3
HII233	36 ± 2	125 ± 2	27.9 ± 1.0	420 ± 4	78.1 ± 0.8	22 ± 1	14.8 ± 0.9
HII234	240 ± 30	58 ± 7	490 ± 8	170 ± 8	88 ± 6	65 ± 8
HII235	191 ± 2	...	29.3 ± 0.8	88.4 ± 0.9	47.4 ± 0.8	501 ± 5	142 ± 1	44.6 ± 1.0	31.7 ± 0.8
HII236	258 ± 4	...	43 ± 1	126 ± 1	30.7 ± 0.9	458 ± 4	96.3 ± 1.0	37.4 ± 0.9	26.5 ± 0.8
HII237	270 ± 10	820 ± 20	...	290 ± 10
HII238	240 ± 50	...	34 ± 8	80 ± 8	32 ± 5	383 ± 5	98 ± 5	56 ± 5	41 ± 6
HII239	190 ± 20	510 ± 20	...	220 ± 20
HII240	55 ± 2	166 ± 2	21 ± 2	367 ± 3	62 ± 2	26 ± 2	17 ± 2
HII241	300 ± 10	850 ± 10	...	280 ± 10
HII242	320 ± 20	820 ± 30	...	180 ± 20
HII243	260 ± 30	27 ± 5	25 ± 5	393 ± 6	89 ± 6	49 ± 6	34 ± 5
HII244	188 ± 4	...	55 ± 3	166 ± 4	31 ± 1	448 ± 6	96 ± 1	26 ± 1	17 ± 1
HII245	216 ± 3	...	15.5 ± 1.0	42 ± 1	49.5 ± 1.0	416 ± 4	146 ± 1	49 ± 1	35 ± 1
HII246	193 ± 2	...	53.5 ± 0.5	163 ± 2	28.7 ± 0.3	442 ± 5	88.5 ± 1.0	28.9 ± 0.3	21.0 ± 0.2
HII247	132 ± 1	1.3 ± 0.1	101.7 ± 0.8	303 ± 3	12.5 ± 0.1	341 ± 4	37.6 ± 0.4	9.65 ± 0.08	7.87 ± 0.08
HII248	167 ± 9	...	81 ± 2	241 ± 2	10.5 ± 0.8	355 ± 4	33.7 ± 1.0	6.8 ± 0.6	4.2 ± 0.6
HII249	120 ± 10	57 ± 3	300 ± 3	178 ± 3
HII250	248 ± 3	...	4 ± 1	12 ± 1	48 ± 1	432 ± 4	145 ± 2	53 ± 1	38.2 ± 0.9
HII251	189 ± 2	0.9 ± 0.1	82.3 ± 0.8	250 ± 3	21.7 ± 0.2	418 ± 5	65.0 ± 0.7	20.7 ± 0.2	15.5 ± 0.2
HII252	160 ± 30	...	54 ± 6	156 ± 4	42 ± 4	297 ± 5	136 ± 5
HII253	180 ± 10	...	82 ± 2	251 ± 2	26 ± 2	579 ± 6	80 ± 2	29 ± 2	25 ± 1
<i>Planetary Nebulae</i>									
PN001	383 ± 5	1115 ± 10	...	247 ± 9
PN002	462 ± 5	1360 ± 10	29 ± 3	411 ± 5	75 ± 3
PN003	149 ± 4	442 ± 4	...	312 ± 5	23 ± 6
PN004	34 ± 3	13 ± 1	440 ± 4	1300 ± 10	16 ± 2	292 ± 3	47 ± 2

Table A.2—Continued

ID	[O II] λ 3727	[O III] λ 4363	[O III] λ 4959	[O III] λ 5007	[N II] λ 6548	H α λ 6562	[N II] λ 6584	[S II] λ 6717	[S II] λ 6731
PN005	470 ± 10	1410 ± 10	...	320 ± 10
PN006	70 ± 20	...	312 ± 5	930 ± 10	50 ± 6	443 ± 6	146 ± 6
PN007	110 ± 20	...	191 ± 3	562 ± 6	39 ± 8	322 ± 8	113 ± 8
PN008	80 ± 10	...	381 ± 5	1160 ± 10	27 ± 7	342 ± 8	73 ± 8	18 ± 6	...
PN009	31 ± 5	100 ± 5
PN010	100 ± 20	...	220 ± 10	650 ± 10	...	224 ± 5	27 ± 6
PN011	81 ± 10	...	100 ± 6
PN012	210 ± 20	660 ± 20	...	350 ± 20	120 ± 10
PN013	...	14 ± 3	458 ± 4	1340 ± 10	...	283 ± 3	16 ± 2
PN014	442 ± 4	1300 ± 10	8 ± 2	287 ± 3	12 ± 2
PN015	510 ± 10	1540 ± 10	110 ± 20	470 ± 10	340 ± 20	24 ± 8	42 ± 8
PN016	390 ± 20	1160 ± 30	...	320 ± 20
PN017	80 ± 20	...	364 ± 7	1078 ± 9	...	321 ± 10	50 ± 10	25 ± 7	...
PN018	140 ± 40	...	460 ± 20	1390 ± 20	...	280 ± 20	100 ± 20
PN019	225 ± 5	677 ± 8	32 ± 3	334 ± 3	93 ± 3
PN020	115 ± 6	18 ± 5	229 ± 6	687 ± 8	66 ± 4	510 ± 5	190 ± 6	22 ± 3	26 ± 3
PN021	60 ± 20	...	214 ± 3	631 ± 6	12 ± 3	295 ± 3	32 ± 3
PN022	460 ± 10	1360 ± 20	...	387 ± 7	49 ± 9
PN023	510 ± 30	1530 ± 30	...	460 ± 20
PN024	510 ± 30	1500 ± 30	...	400 ± 20
PN025	110 ± 30	...	100 ± 20
PN026	60 ± 20	15 ± 3	481 ± 5	1450 ± 20	18 ± 2	276 ± 3	51 ± 2
PN027	52 ± 7	...	188 ± 4	560 ± 6	20 ± 4	306 ± 4	58 ± 4
PN028	40 ± 10	8 ± 2	440 ± 4	1300 ± 10	27 ± 2	308 ± 3	84 ± 2
PN029	240 ± 50	330 ± 30	...	370 ± 30	160 ± 30
PN030	49 ± 9	...	380 ± 7	1140 ± 10	33 ± 6	426 ± 7	85 ± 8	14 ± 3	11 ± 3
PN031	420 ± 10	1270 ± 10	...	440 ± 30
PN032	372 ± 4	1170 ± 10	...	297 ± 3
PN033	90 ± 30	...	507 ± 8	1500 ± 10	113 ± 6	411 ± 7	335 ± 6	28 ± 8	38 ± 8
PN034	25 ± 7	14 ± 3	418 ± 5	1250 ± 10	14 ± 2	311 ± 3	46 ± 2
PN035	242 ± 3	699 ± 8	14 ± 3	329 ± 3	34 ± 3
PN036	530 ± 10	1580 ± 20	60 ± 10	380 ± 10	170 ± 10
PN037	40 ± 10	21 ± 3	508 ± 6	1490 ± 20	11 ± 3	314 ± 3	32 ± 3
PN038	495 ± 6	1510 ± 10	...	393 ± 8	80 ± 10
PN039	60 ± 20	16 ± 4	439 ± 5	1280 ± 10	19 ± 5	286 ± 6	48 ± 5
PN040	190 ± 20	130 ± 20	80 ± 10	300 ± 10	240 ± 20
PN041	300 ± 20	70 ± 20	...	100 ± 10	50 ± 10	40 ± 10	...

Table A.2—Continued

ID	[O II]	[O III]	[O III]	[O III]	[N II]	H α	[N II]	[S II]	[S II]
	λ 3727	λ 4363	λ 4959	λ 5007	λ 6548	λ 6562	λ 6584	λ 6717	λ 6731
PN042	60 \pm 10	...	299 \pm 4	895 \pm 9	38 \pm 4	260 \pm 5	111 \pm 5	...	14 \pm 4
PN043	70 \pm 20	...	100 \pm 10
PN044	170 \pm 40	480 \pm 40	...	600 \pm 20	140 \pm 30	70 \pm 20	...
PN045	444 \pm 5	1290 \pm 10	...	315 \pm 4	19 \pm 4
PN046	...	18 \pm 2	396 \pm 4	1180 \pm 10	11 \pm 1	327 \pm 3	40 \pm 2
PN047	40 \pm 10	...	22 \pm 4	65 \pm 4	142 \pm 3	318 \pm 4	427 \pm 5	14 \pm 3	25 \pm 4
PN048	365 \pm 5	1100 \pm 10	17 \pm 4	407 \pm 4	38 \pm 3
PN049	270 \pm 20	...	230 \pm 10	680 \pm 10	...	370 \pm 20	150 \pm 20	66 \pm 10	50 \pm 10
PN050	68 \pm 8	22 \pm 3	430 \pm 4	1270 \pm 10	43 \pm 4	310 \pm 3	119 \pm 4
PN051	40 \pm 8	20 \pm 4	517 \pm 6	1530 \pm 20	16 \pm 3	309 \pm 3	49 \pm 3
PN052	90 \pm 10	...	427 \pm 4	1250 \pm 10	18 \pm 2	283 \pm 3	55 \pm 2
PN053	410 \pm 40	...	130 \pm 20	380 \pm 10	...	330 \pm 20	130 \pm 30	60 \pm 10	...
PN054	372 \pm 7	1130 \pm 10	...	280 \pm 8	24 \pm 6
PN055	...	30 \pm 9	110 \pm 7	328 \pm 7	...	100 \pm 10
PN056	...	33 \pm 8	424 \pm 7	1260 \pm 10	24 \pm 4	350 \pm 4	56 \pm 5
PN057	330 \pm 50	34 \pm 9	417 \pm 7	1260 \pm 10	120 \pm 20	350 \pm 10	320 \pm 20	43 \pm 7	47 \pm 8
PN058	541 \pm 4	1590 \pm 20	25 \pm 5	378 \pm 5	74 \pm 6
PN059	308 \pm 7	899 \pm 10	...	296 \pm 6
PN060	270 \pm 70	40 \pm 10	390 \pm 20	1170 \pm 20	110 \pm 20	340 \pm 20	360 \pm 20	...	50 \pm 20
PN061	38 \pm 5	10 \pm 3	420 \pm 4	1250 \pm 10	21 \pm 3	300 \pm 3	62 \pm 3
PN062	311 \pm 7	921 \pm 9	...	294 \pm 4	12 \pm 6
PN063	27 \pm 6	14 \pm 2	572 \pm 5	1710 \pm 20	29 \pm 2	361 \pm 4	81 \pm 2	...	8 \pm 2
PN064	340 \pm 30	970 \pm 30	...	310 \pm 30	100 \pm 30
PN065	117 \pm 7	...	99 \pm 2	286 \pm 3	33 \pm 3	253 \pm 3	97 \pm 4
PN066	22 \pm 7	...	367 \pm 3	1110 \pm 10	23 \pm 3	407 \pm 4	63 \pm 3
PN067	29 \pm 8	...	284 \pm 7	859 \pm 8	22 \pm 3	326 \pm 4	67 \pm 3
PN068	270 \pm 10	820 \pm 10	40 \pm 10	280 \pm 10	40 \pm 10
PN069	502 \pm 7	1520 \pm 10	73 \pm 7	401 \pm 8	196 \pm 6
PN070	208 \pm 3	614 \pm 6	53 \pm 2	418 \pm 4	155 \pm 3	...	12 \pm 4
PN071	120 \pm 30	...	474 \pm 7	1380 \pm 20	38 \pm 5	292 \pm 4	107 \pm 4	16 \pm 5	19 \pm 5
PN072	50 \pm 10	30 \pm 4	560 \pm 6	1670 \pm 20	36 \pm 2	349 \pm 4	100 \pm 2
PN073	34 \pm 9	...	288 \pm 5	863 \pm 9	72 \pm 4	410 \pm 5	221 \pm 5
PN074	38 \pm 6	...	293 \pm 4	862 \pm 8	...	282 \pm 3	21 \pm 3
PN075	370 \pm 10	1056 \pm 10	...	310 \pm 10
PN076	120 \pm 10	33 \pm 9	513 \pm 5	1510 \pm 20	28 \pm 5	285 \pm 5	80 \pm 5
PN077	420 \pm 20	1260 \pm 10	...	300 \pm 20
PN078	330 \pm 20	970 \pm 20	...	260 \pm 20

Table A.2—Continued

ID	[O II] λ 3727	[O III] λ 4363	[O III] λ 4959	[O III] λ 5007	[N II] λ 6548	H α λ 6562	[N II] λ 6584	[S II] λ 6717	[S II] λ 6731
PN079	41 ± 5	14 ± 2	557 ± 7	1640 ± 20	27 ± 2	298 ± 3	75 ± 2	...	7 ± 2
PN080	443 ± 9	1270 ± 20	...	356 ± 10	52 ± 9
PN081	190 ± 20	...	400 ± 10	1180 ± 10	40 ± 7	303 ± 7	117 ± 8
PN082	330 ± 20	1000 ± 20	...	350 ± 10
PN083	...	29 ± 8	486 ± 8	1290 ± 10	...	298 ± 7
PN084	220 ± 10	58 ± 9	112 ± 8	359 ± 9	351 ± 8
PN085	400 ± 4	1200 ± 10	13 ± 2	386 ± 4	31 ± 3
PN086	340 ± 20	...	543 ± 8	1590 ± 20	175 ± 9	311 ± 9	532 ± 8	51 ± 9	45 ± 10
PN087	210 ± 10	...	525 ± 6	1540 ± 20	94 ± 5	331 ± 4	290 ± 5	24 ± 5	34 ± 5
PN088	329 ± 7	989 ± 9	...	350 ± 7
PN089	377 ± 5	1110 ± 10	...	329 ± 10
PN090	630 ± 10	1820 ± 20	30 ± 6	406 ± 8	73 ± 7
PN091	50 ± 10	...	434 ± 8	1280 ± 10	32 ± 5	449 ± 6	89 ± 5
PN092	100 ± 20	...	339 ± 7	993 ± 9	31 ± 5	308 ± 5	105 ± 4
PN093	40 ± 10	...	356 ± 5	1070 ± 10	50 ± 6	353 ± 5	145 ± 7	14 ± 4	17 ± 4
PN094	540 ± 5	1610 ± 10	35 ± 8	334 ± 9	111 ± 8
PN095	27 ± 4	10 ± 2	545 ± 6	1450 ± 10	46 ± 1	389 ± 4	124 ± 2	8 ± 1	8 ± 2
PN096	22 ± 6	...	462 ± 4	1360 ± 20	18 ± 2	298 ± 3	32 ± 2
PN097	213 ± 3	624 ± 5	19 ± 4	338 ± 3	53 ± 3
PN098	36 ± 7	...	480 ± 5	1430 ± 20	23 ± 3	304 ± 3	61 ± 4
PN099	620 ± 20	1840 ± 20	70 ± 20	460 ± 20	230 ± 20
PN100	94 ± 5	15 ± 2	461 ± 5	1370 ± 10	91 ± 2	340 ± 3	275 ± 2	11 ± 2	19 ± 2
PN101	322 ± 5	970 ± 10	57 ± 5	416 ± 5	161 ± 5
PN102	366 ± 4	1076 ± 10	35 ± 3	326 ± 4	101 ± 4
PN103	37 ± 5	17 ± 3	467 ± 5	1410 ± 10	...	278 ± 3	15 ± 4
PN104	92 ± 6	20 ± 3	564 ± 6	1660 ± 20	47 ± 3	307 ± 3	141 ± 3
PN105	50 ± 10	18 ± 4	472 ± 5	1490 ± 10	22 ± 6	334 ± 7	65 ± 6
PN106	66 ± 4	...	100 ± 2	306 ± 3	79 ± 2	356 ± 4	233 ± 3	...	8 ± 2
PN107	476 ± 8	1400 ± 10	...	327 ± 8
PN108	190 ± 10	600 ± 20	...	330 ± 20	70 ± 20
PN109	460 ± 20	1390 ± 20	...	370 ± 30
PN110	230 ± 10	...	89 ± 2	260 ± 3	42 ± 1	235 ± 2	127 ± 2
PN111	434 ± 6	1300 ± 10	22 ± 6	313 ± 6	66 ± 6
PN112	41 ± 4	127 ± 4	...	100 ± 3	15 ± 3
PN113	403 ± 8	1170 ± 10	...	310 ± 20
PN114	70 ± 9	211 ± 9	111 ± 7	414 ± 6	337 ± 8
PN115	410 ± 10	1230 ± 10	97 ± 10	575 ± 8	278 ± 9

Table A.2—Continued

ID	[O II] λ 3727	[O III] λ 4363	[O III] λ 4959	[O III] λ 5007	[N II] λ 6548	H α λ 6562	[N II] λ 6584	[S II] λ 6717	[S II] λ 6731
PN116	200 ± 10	...	79 ± 5	237 ± 5	57 ± 6	407 ± 6	176 ± 7	68 ± 4	50 ± 5
PN117	82 ± 6	...	330 ± 4	960 ± 10	23 ± 3	297 ± 4	69 ± 3	...	4 ± 1
PN118	52 ± 8	...	501 ± 5	1480 ± 10	29 ± 3	302 ± 3	85 ± 3
PN119	170 ± 20	...	440 ± 20	1280 ± 30	60 ± 10	302 ± 9	190 ± 10	50 ± 10	40 ± 20
PN120	550 ± 30	1660 ± 30	...	320 ± 30
PN121	40 ± 10	6 ± 2	434 ± 4	1300 ± 10	36 ± 2	406 ± 4	99 ± 2
PN122	640 ± 10	1910 ± 20	...	310 ± 10	50 ± 10
PN123	383 ± 6	1130 ± 10	...	284 ± 9
PN124	60 ± 20	27 ± 8	565 ± 7	1670 ± 20	51 ± 7	422 ± 7	145 ± 9
PN125	28 ± 4	...	404 ± 4	1200 ± 10	18 ± 2	330 ± 3	56 ± 2
PN126	560 ± 20	1620 ± 20	150 ± 20	460 ± 20	500 ± 20
PN127	340 ± 10	1002 ± 10	...	260 ± 10
PN128	389 ± 7	1130 ± 10	...	350 ± 10
PN129	93 ± 10	...	123 ± 2	347 ± 3	40 ± 3	255 ± 3	112 ± 3
PN130	38 ± 3	11 ± 1	469 ± 5	1390 ± 10	14 ± 1	282 ± 3	44 ± 2	3.1 ± 0.9	5.5 ± 0.8
PN131	502 ± 10	1490 ± 20	64 ± 6	471 ± 7	208 ± 6
PN132	710 ± 30	2100 ± 30	...	390 ± 20
PN133	...	29 ± 9	209 ± 7	634 ± 6	...	480 ± 10	40 ± 10
PN134	98 ± 5	...	234 ± 3	712 ± 7	93 ± 4	412 ± 4	294 ± 4	8 ± 2	17 ± 2
PN135	...	13 ± 3	348 ± 6	1049 ± 10	13 ± 2	281 ± 3	30 ± 3
PN136	420 ± 10	1260 ± 20	...	342 ± 9
PN137	201 ± 9	26 ± 5	418 ± 5	1260 ± 10	445 ± 5	339 ± 4	1360 ± 10	73 ± 3	90 ± 4
PN138	37 ± 6	...	307 ± 5	920 ± 10	17 ± 3	332 ± 4	56 ± 3
PN139	35 ± 8	...	370 ± 4	1090 ± 10	...	270 ± 3	12 ± 3
PN140	470 ± 20	1430 ± 20	...	310 ± 20
PN141	270 ± 30	820 ± 30	...	100 ± 20
PN142	460 ± 20	1350 ± 20	...	310 ± 10
PN143	90 ± 30	330 ± 30	80 ± 20	530 ± 20	210 ± 20
PN144	33 ± 7	18 ± 3	497 ± 5	1460 ± 10	11 ± 3	288 ± 3	27 ± 2
PN145	190 ± 40	...	130 ± 30	390 ± 40	...	360 ± 20	100 ± 20
PN146	336 ± 4	1010 ± 10	23 ± 4	302 ± 4	70 ± 3
PN147	60 ± 20	15 ± 3	493 ± 5	1450 ± 10	18 ± 2	282 ± 3	49 ± 2	...	8 ± 2
PN148	130 ± 10	...	540 ± 10	1600 ± 20	90 ± 10	330 ± 10	255 ± 10	20 ± 5	33 ± 5
PN149	75 ± 9	35 ± 4	395 ± 4	1180 ± 10	115 ± 5	315 ± 4	342 ± 5	10 ± 3	21 ± 4
PN150	486 ± 7	1440 ± 10	...	293 ± 5
PN151	130 ± 20	340 ± 20	...	100 ± 20
PN152	130 ± 20	...	468 ± 7	1390 ± 10	44 ± 7	327 ± 9	141 ± 10

Table A.2—Continued

ID	[O II]	[O III]	[O III]	[O III]	[N II]	H α	[N II]	[S II]	[S II]
	λ 3727	λ 4363	λ 4959	λ 5007	λ 6548	λ 6562	λ 6584	λ 6717	λ 6731
PN153	26 \pm 6	...	291 \pm 3	869 \pm 8	25 \pm 2	387 \pm 4	69 \pm 2
PN154	440 \pm 30	1380 \pm 30	90 \pm 10	500 \pm 10	270 \pm 10
PN155	233 \pm 5	692 \pm 7	68 \pm 5	331 \pm 5	192 \pm 4	...	19 \pm 4
PN156	170 \pm 20	...	201 \pm 5	610 \pm 8	...	305 \pm 4	82 \pm 4	23 \pm 6	21 \pm 6
PN157	36 \pm 9	...	321 \pm 3	950 \pm 10	19 \pm 3	329 \pm 3	57 \pm 3
PN158	33 \pm 9	...	194 \pm 4	588 \pm 6	24 \pm 3	288 \pm 4	72 \pm 3
PN159	15 \pm 5	...	435 \pm 4	1290 \pm 10	11 \pm 2	319 \pm 3	31 \pm 1
PN160	198 \pm 8	611 \pm 7	60 \pm 20	360 \pm 20	180 \pm 20
PN161	518 \pm 6	1540 \pm 10	...	324 \pm 4	27 \pm 4
PN162	374 \pm 6	1100 \pm 10	...	306 \pm 4	30 \pm 5
PN163	60 \pm 20	...	323 \pm 4	948 \pm 9	45 \pm 2	309 \pm 3	130 \pm 3
PN164	240 \pm 20	...	214 \pm 8	646 \pm 8	36 \pm 8	424 \pm 7	111 \pm 7	58 \pm 7	46 \pm 9
PN165	55 \pm 5	19 \pm 2	575 \pm 7	1680 \pm 10	20 \pm 1	289 \pm 3	58 \pm 1	5 \pm 1	7 \pm 1
PN166	37 \pm 6	14 \pm 5	453 \pm 5	1330 \pm 10	...	271 \pm 4	35 \pm 4
PN167	...	30 \pm 10	489 \pm 7	1420 \pm 10	...	287 \pm 5	20 \pm 5
PN168	...	18 \pm 5	517 \pm 5	1540 \pm 20	37 \pm 4	415 \pm 4	107 \pm 5
PN169	458 \pm 4	1360 \pm 10	...	305 \pm 4
PN170	120 \pm 4	...	116 \pm 2	341 \pm 4	47 \pm 1	317 \pm 3	141 \pm 2	...	7 \pm 2
PN171	611 \pm 7	1850 \pm 20	...	415 \pm 7
PN172	100 \pm 20	...	395 \pm 4	1180 \pm 10	39 \pm 3	292 \pm 3	119 \pm 3	11 \pm 3	12 \pm 3
PN173	550 \pm 20	1620 \pm 20	...	280 \pm 20
PN174	16 \pm 3	9 \pm 2	353 \pm 4	1040 \pm 10	15 \pm 1	320 \pm 3	40 \pm 1
PN175	43 \pm 8	...	245 \pm 8	751 \pm 8	33 \pm 4	351 \pm 4	95 \pm 3
PN176	100 \pm 10	...	240 \pm 5	716 \pm 8	36 \pm 5	390 \pm 5	94 \pm 6
PN177	443 \pm 5	1310 \pm 20	21 \pm 5	312 \pm 4	66 \pm 5
PN178	40 \pm 4	...	300 \pm 4	889 \pm 8	6 \pm 2	309 \pm 3	20 \pm 2
PN179	382 \pm 8	1138 \pm 10	...	262 \pm 8
PN180	37 \pm 7	...	480 \pm 5	1430 \pm 10	41 \pm 4	367 \pm 4	124 \pm 5	...	10 \pm 3
PN181	580 \pm 10	1740 \pm 20	...	300 \pm 100
PN182	41 \pm 5	...	454 \pm 5	1340 \pm 20	...	318 \pm 4	28 \pm 3
PN183	55 \pm 9	...	83 \pm 3	248 \pm 3	98 \pm 2	417 \pm 4	289 \pm 3	...	13 \pm 3
PN184	67 \pm 6	16 \pm 3	522 \pm 5	1540 \pm 20	31 \pm 2	346 \pm 4	92 \pm 3	...	8 \pm 3
PN185	70 \pm 10	22 \pm 6	587 \pm 6	1740 \pm 20	19 \pm 4	306 \pm 4	59 \pm 4
PN186	357 \pm 6	1054 \pm 10	...	304 \pm 3
PN187	131 \pm 9	413 \pm 7	20 \pm 6	267 \pm 6	60 \pm 6
PN188	95 \pm 6	8 \pm 3	324 \pm 4	964 \pm 9	86 \pm 2	311 \pm 4	257 \pm 3	13 \pm 2	20 \pm 2
PN189	380 \pm 20	1200 \pm 20	...	260 \pm 10	50 \pm 10

Table A.2—Continued

ID	[O II] λ 3727	[O III] λ 4363	[O III] λ 4959	[O III] λ 5007	[N II] λ 6548	H α λ 6562	[N II] λ 6584	[S II] λ 6717	[S II] λ 6731
PN190	496 ± 6	1460 ± 20	...	313 ± 5	33 ± 5
PN191	30 ± 10	...	190 ± 3	556 ± 5	13 ± 3	307 ± 3	32 ± 3
PN192	43 ± 8	...	475 ± 6	1390 ± 10	40 ± 3	324 ± 4	116 ± 3	...	13 ± 3
PN193	540 ± 10	1550 ± 10	45 ± 6	254 ± 7	106 ± 7
PN194	400 ± 40	1200 ± 40	...	300 ± 20
PN195	90 ± 10	55 ± 6	850 ± 10	2560 ± 20	25 ± 6	427 ± 4	85 ± 6
PN196	130 ± 20	14 ± 5	492 ± 4	1460 ± 10	75 ± 5	309 ± 5	229 ± 7	13 ± 2	19 ± 2
PN197	490 ± 20	1460 ± 20	...	290 ± 10	40 ± 10
PN198	50 ± 10	...	458 ± 9	1350 ± 10	...	289 ± 5	25 ± 6
PN199	...	20 ± 6	682 ± 7	1990 ± 20	12 ± 4	289 ± 3	26 ± 3
PN200	473 ± 8	1390 ± 10	...	300 ± 7	38 ± 7
PN201	390 ± 20	1220 ± 20	...	260 ± 20	70 ± 20
PN202	35 ± 6	...	422 ± 4	1250 ± 10	14 ± 3	297 ± 3	34 ± 3
PN203	475 ± 8	1370 ± 10	48 ± 4	369 ± 4	144 ± 4
PN204	250 ± 30	...	260 ± 10	800 ± 10	80 ± 10	220 ± 10	270 ± 10	...	50 ± 10
PN205	230 ± 40	...	275 ± 9	790 ± 10	96 ± 8	342 ± 9	299 ± 9	113 ± 9	95 ± 9
PN206	33 ± 5	...	261 ± 3	766 ± 9	6 ± 2	276 ± 3	12 ± 2
PN207	33 ± 8	...	274 ± 4	808 ± 9	25 ± 4	277 ± 4	74 ± 5
PN208	530 ± 50	...	420 ± 30	1330 ± 30	90 ± 10	280 ± 20	320 ± 20
PN209	40 ± 10	100 ± 10
PN210	60 ± 10	...	170 ± 10	530 ± 10	...	100 ± 9	60 ± 10
PN211	50 ± 10	12 ± 3	479 ± 5	1440 ± 20	23 ± 2	340 ± 3	64 ± 2	...	8 ± 2
PN212	530 ± 20	1480 ± 30	...	380 ± 20	160 ± 20
PN213	570 ± 10	1770 ± 20	...	401 ± 9	50 ± 20
PN214	390 ± 10	1190 ± 10	...	366 ± 9
PN215	145 ± 6	424 ± 7	30 ± 7	340 ± 7	75 ± 6
PN216	142 ± 3	...	93 ± 2	276 ± 3	50 ± 2	326 ± 3	146 ± 2
PN217	29 ± 9	...	344 ± 3	1007 ± 9	46 ± 3	329 ± 3	142 ± 4	...	9 ± 3
PN218	417 ± 8	1280 ± 10	...	427 ± 6	30 ± 8
PN219	410 ± 20	1090 ± 20	...	330 ± 20
PN220	584 ± 10	...	83 ± 4	252 ± 4	30 ± 6	277 ± 6	93 ± 7	44 ± 2	33 ± 3
PN221	542 ± 7	1600 ± 20	...	282 ± 6
PN222	40 ± 10	...	500 ± 5	1480 ± 10	...	255 ± 5	35 ± 5
PN223	380 ± 20	1160 ± 20	...	320 ± 10
PN224	540 ± 10	1570 ± 20	...	380 ± 20
PN225	600 ± 20	1850 ± 30	...	400 ± 10
PN226	310 ± 10	930 ± 10	...	355 ± 7	31 ± 8

Table A.2—Continued

ID	[O II] λ 3727	[O III] λ 4363	[O III] λ 4959	[O III] λ 5007	[N II] λ 6548	H α λ 6562	[N II] λ 6584	[S II] λ 6717	[S II] λ 6731
PN227	110 ± 10	288 ± 9	...	100 ± 10
PN228	304 ± 6	876 ± 8	13 ± 4	265 ± 4	24 ± 4
PN229	57 ± 5	...	198 ± 4	583 ± 6	77 ± 2	352 ± 3	231 ± 2	...	10 ± 2
PN230	492 ± 5	1430 ± 10	...	243 ± 5	19 ± 5
PN231	395 ± 6	1130 ± 10	...	292 ± 7
PN232	120 ± 30	...	260 ± 20	650 ± 20	...	100 ± 10
PN233	340 ± 10	1080 ± 20	...	270 ± 10	60 ± 10
PN234	435 ± 4	1290 ± 10	...	317 ± 6	...	11 ± 3	...
PN235	640 ± 10	1880 ± 20	...	316 ± 9	62 ± 8
PN236	260 ± 10	...	880 ± 20	2640 ± 30	39 ± 8	380 ± 8	138 ± 9
PN237	1230 ± 30	...	80 ± 10	250 ± 10	112 ± 8	324 ± 8	351 ± 7	210 ± 8	148 ± 7
PN238	...	57 ± 7	489 ± 5	1430 ± 10	...	280 ± 5
PN239	591 ± 7	1750 ± 20	...	341 ± 5	28 ± 7
PN240	500 ± 20	1500 ± 20	...	284 ± 9	35 ± 9
PN241	437 ± 4	1300 ± 10	...	288 ± 4
PN242	56 ± 8	14 ± 3	549 ± 5	1620 ± 20	40 ± 4	310 ± 4	118 ± 4
PN243	...	18 ± 3	547 ± 6	1630 ± 10	...	301 ± 3	19 ± 3
PN244	740 ± 20	2360 ± 20	62 ± 7	640 ± 8	190 ± 10
PN245	70 ± 10	...	343 ± 4	1000 ± 10	18 ± 4	244 ± 4	31 ± 4
PN246	357 ± 8	1043 ± 10	38 ± 7	445 ± 9	105 ± 8
PN247	404 ± 6	15 ± 3	523 ± 6	1530 ± 20	97 ± 2	260 ± 2	290 ± 3	19 ± 2	25 ± 2
PN248	370 ± 20	1130 ± 30	...	350 ± 20
PN249	33 ± 3	...	280 ± 3	836 ± 9	65 ± 2	355 ± 3	189 ± 2	...	6 ± 2
PN250	340 ± 20	1000 ± 20	...	280 ± 20
PN251	38 ± 3	8 ± 2	188 ± 2	553 ± 5	11 ± 2	313 ± 3	33 ± 2
PN252	540 ± 20	1570 ± 20	80 ± 10	380 ± 10	250 ± 10
PN253	262 ± 5	760 ± 6	...	330 ± 6	35 ± 6
PN254	610 ± 20	1720 ± 20	...	370 ± 20	60 ± 20
PN255	463 ± 5	1370 ± 20	15 ± 5	338 ± 5	35 ± 5
PN256	210 ± 20	...	453 ± 7	1360 ± 10	169 ± 9	421 ± 7	500 ± 10	21 ± 6	37 ± 6
PN257	460 ± 20	1260 ± 20	...	290 ± 20
PN258	163 ± 7	...	453 ± 8	1370 ± 10	102 ± 7	465 ± 5	310 ± 6	...	27 ± 5
PN259	580 ± 20	1740 ± 20	60 ± 10	460 ± 20	160 ± 20
PN260	153 ± 3	12 ± 1	457 ± 5	1360 ± 10	82 ± 1	293 ± 3	247 ± 2	10 ± 1	18 ± 2
PN261	71 ± 9	15 ± 5	306 ± 4	909 ± 8	18 ± 6	339 ± 5	24 ± 4
PN262	39 ± 7	...	406 ± 4	1210 ± 10	9 ± 2	352 ± 4	28 ± 3
PN263	74 ± 9	...	400 ± 9	1190 ± 10	46 ± 6	373 ± 6	147 ± 6

Table A.2—Continued

ID	[O II] λ 3727	[O III] λ 4363	[O III] λ 4959	[O III] λ 5007	[N II] λ 6548	H α λ 6562	[N II] λ 6584	[S II] λ 6717	[S II] λ 6731
PN264	490 ± 30	1400 ± 30	...	370 ± 20
PN265	570 ± 9	1700 ± 20	...	309 ± 6	34 ± 7
PN266	65 ± 5	...	53 ± 3	151 ± 2	94 ± 2	377 ± 4	279 ± 3	...	9 ± 2
PN267	...	100 ± 30	460 ± 30	1360 ± 30	...	430 ± 30
PN268	56 ± 6	...	187 ± 3	553 ± 6	16 ± 2	257 ± 2	52 ± 1
PN269	255 ± 7	765 ± 7	...	312 ± 5	26 ± 6
PN270	40 ± 3	...	88 ± 1	266 ± 2	70 ± 1	358 ± 4	213 ± 2	...	5 ± 2
PN271	170 ± 10	...	340 ± 7	1010 ± 10	153 ± 6	375 ± 7	453 ± 6	23 ± 6	21 ± 8
PN272	190 ± 40	...	560 ± 10	1680 ± 20	106 ± 7	391 ± 9	319 ± 10	23 ± 7	27 ± 6
PN273	103 ± 3	...	285 ± 3	839 ± 10	27 ± 2	289 ± 3	82 ± 2
PN274	390 ± 20	1190 ± 20	...	350 ± 10	60 ± 10
PN275	321 ± 8	954 ± 9	37 ± 4	383 ± 4	110 ± 4
PN276	24 ± 4	9 ± 3	217 ± 3	645 ± 6	15 ± 2	279 ± 3	45 ± 3
PN277	132 ± 3	401 ± 4	23 ± 4	353 ± 4	68 ± 4
PN278	17 ± 5	12 ± 4	298 ± 3	888 ± 10	17 ± 2	354 ± 3	47 ± 2
PN279	340 ± 30	...	130 ± 10	390 ± 10	...	271 ± 8	70 ± 10	40 ± 10	...
PN280	50 ± 10	...	387 ± 6	1169 ± 10	100 ± 3	380 ± 4	289 ± 5	...	14 ± 4
PN281	70 ± 20	...	248 ± 4	733 ± 8	43 ± 4	350 ± 5	134 ± 4
PN282	67 ± 6	...	34 ± 3	103 ± 3	111 ± 3	378 ± 4	334 ± 3	...	10 ± 2
PN283	180 ± 20	...	578 ± 10	1680 ± 20	50 ± 10	324 ± 9	147 ± 10
PN284	98 ± 4	...	99 ± 2	310 ± 3	45 ± 2	322 ± 3	129 ± 2
PN285	155 ± 9	460 ± 10	...	352 ± 9	43 ± 9
PN286	140 ± 30	70 ± 10	99 ± 6	306 ± 6	306 ± 6
PN287	110 ± 20	...	476 ± 7	1410 ± 10	25 ± 8	320 ± 8	68 ± 6
PN288	99 ± 9	22 ± 5	250 ± 6	744 ± 9	209 ± 4	363 ± 5	633 ± 5	38 ± 5	47 ± 6
PN289	227 ± 9	28 ± 6	540 ± 7	1590 ± 20	28 ± 4	280 ± 5	87 ± 4	...	17 ± 5
PN290	541 ± 6	1650 ± 20	33 ± 5	493 ± 6	108 ± 5
PN291	120 ± 3	...	264 ± 3	779 ± 9	31 ± 2	297 ± 3	91 ± 2	...	8 ± 3
PN292	370 ± 10	1100 ± 20	...	310 ± 10
PN293	36 ± 6	...	282 ± 3	839 ± 9	30 ± 2	338 ± 4	89 ± 2	...	6 ± 2
PN294	433 ± 4	1280 ± 10	...	283 ± 3
PN295	380 ± 20	1090 ± 30	...	410 ± 20
PN296	90 ± 10	...	499 ± 6	1560 ± 20	82 ± 4	443 ± 5	252 ± 4	17 ± 4	29 ± 4
PN297	37 ± 7	...	289 ± 2	854 ± 8	18 ± 2	302 ± 4	51 ± 2
PN298	330 ± 5	969 ± 9	...	307 ± 3	27 ± 4
PN299	501 ± 8	1470 ± 10	...	291 ± 4	16 ± 4
PN300	110 ± 10	360 ± 10	...	100 ± 10

Table A.2—Continued

ID	[O II] λ 3727	[O III] λ 4363	[O III] λ 4959	[O III] λ 5007	[N II] λ 6548	H α λ 6562	[N II] λ 6584	[S II] λ 6717	[S II] λ 6731
PN301	220 ± 20	27 ± 7	452 ± 6	1340 ± 10	...	300 ± 10	100 ± 10	...	19 ± 6
PN302	59 ± 8	...	105 ± 4	306 ± 4	24 ± 5	304 ± 4	65 ± 4
PN303	386 ± 4	1140 ± 10	48 ± 3	462 ± 5	144 ± 3	...	10 ± 3
PN304	51 ± 3	...	263 ± 3	774 ± 8	12 ± 1	292 ± 3	33 ± 2	6 ± 1	4.8 ± 1.0
PN305	31 ± 6	11 ± 2	357 ± 4	1060 ± 10	24 ± 2	336 ± 3	71 ± 2
PN306	473 ± 7	1380 ± 10	27 ± 6	329 ± 6	79 ± 6	43 ± 4	31 ± 5
PN307	130 ± 10	40 ± 10	444 ± 6	1320 ± 10	87 ± 4	336 ± 5	260 ± 6	17 ± 5	23 ± 5
PN308	33 ± 5	10 ± 2	471 ± 5	1390 ± 20	11 ± 1	310 ± 3	27 ± 1
PN309	330 ± 10	970 ± 20	...	320 ± 20
PN310	54 ± 8	...	49 ± 6	153 ± 5	131 ± 4	511 ± 6	390 ± 4
PN311	459 ± 4	1360 ± 10	27 ± 4	355 ± 3	77 ± 4
PN312	510 ± 6	1500 ± 20	22 ± 2	350 ± 3	63 ± 3	...	10 ± 3
PN313	634 ± 8	1900 ± 20	65 ± 5	440 ± 6	200 ± 6
PN314	97 ± 4	300 ± 4	180 ± 4	1290 ± 20	567 ± 6	15 ± 5	21 ± 4
PN315	21 ± 8	...	376 ± 3	1105 ± 9	...	329 ± 4	27 ± 3
PN316	350 ± 10	960 ± 10	50 ± 10	308 ± 9	130 ± 10
PN317	300 ± 20	880 ± 20	...	410 ± 20
PN318	150 ± 40	...	80 ± 20	230 ± 20	40 ± 10	100 ± 10	130 ± 20
PN319	40 ± 10	...	123 ± 4	365 ± 6	37 ± 3	386 ± 4	112 ± 4
PN320	340 ± 10	1000 ± 10	...	300 ± 10
PN321	220 ± 4	656 ± 7	18 ± 6	410 ± 5	40 ± 5
PN322	208 ± 6	579 ± 6	18 ± 6	461 ± 6	60 ± 5
PN323	420 ± 10	1220 ± 20	...	330 ± 10
PN324	37 ± 7	23 ± 7	...	100 ± 6	35 ± 7	27 ± 4	16 ± 4
PN325	35 ± 8	...	476 ± 5	1380 ± 20	24 ± 3	311 ± 3	61 ± 3
PN326	...	21 ± 3	571 ± 5	1690 ± 20	28 ± 3	311 ± 3	84 ± 3
PN327	499 ± 9	1510 ± 20	40 ± 7	581 ± 5	107 ± 7
PN328	560 ± 30	1760 ± 30	160 ± 30	510 ± 20	430 ± 30
PN329	330 ± 10	1020 ± 20	...	380 ± 10
PN330	330 ± 20	960 ± 20	...	280 ± 20
PN331	...	9 ± 3	423 ± 4	1250 ± 10	60 ± 2	309 ± 3	187 ± 2	10 ± 2	16 ± 3
PN332	569 ± 10	1660 ± 20	20 ± 6	379 ± 6	50 ± 5
PN333	218 ± 4	640 ± 7	12 ± 3	341 ± 3	28 ± 3
PN334	170 ± 20	500 ± 20	...	100 ± 20
PN335	85 ± 5	255 ± 4	11 ± 3	100 ± 4	40 ± 3
PN336	430 ± 30	1210 ± 30	...	400 ± 20
PN337	60 ± 20	...	331 ± 6	991 ± 10	24 ± 6	444 ± 7	76 ± 6	20 ± 6	...

Table A.2—Continued

ID	[O II] λ 3727	[O III] λ 4363	[O III] λ 4959	[O III] λ 5007	[N II] λ 6548	H α λ 6562	[N II] λ 6584	[S II] λ 6717	[S II] λ 6731
PN338	240 \pm 10	610 \pm 10	...	100 \pm 10	70 \pm 10
PN339	620 \pm 30	...	110 \pm 20	290 \pm 20	80 \pm 10	590 \pm 10	300 \pm 10	157 \pm 10	110 \pm 10
PN340	80 \pm 20	...	350 \pm 10	1020 \pm 10	...	340 \pm 10	50 \pm 10
PN341	330 \pm 20	1000 \pm 20	70 \pm 20	490 \pm 20	210 \pm 20
PN342	580 \pm 20	1680 \pm 20	80 \pm 20	460 \pm 20	240 \pm 20
PN343	34 \pm 6	100 \pm 5
PN344	390 \pm 20	1160 \pm 20	...	432 \pm 9	60 \pm 10
PN345	306 \pm 3	900 \pm 10	...	321 \pm 3	18 \pm 3
PN346	290 \pm 10	870 \pm 20	...	340 \pm 10
PN347	480 \pm 20	1500 \pm 20	70 \pm 10	510 \pm 20	190 \pm 20
PN348	463 \pm 5	1370 \pm 10	...	300 \pm 10
PN349	35 \pm 1	100 \pm 1	8 \pm 1	...	17 \pm 1
PN350	370 \pm 20	1090 \pm 20	...	330 \pm 20	90 \pm 20
PN351	150 \pm 20	400 \pm 20	...	100 \pm 9
PN352	310 \pm 10	910 \pm 10	...	370 \pm 10
PN353	256 \pm 7	765 \pm 7	58 \pm 8	383 \pm 7	175 \pm 10	27 \pm 7	24 \pm 7
PN354	130 \pm 10	380 \pm 10	...	100 \pm 10
PN355	410 \pm 10	1170 \pm 10	...	300 \pm 20
PN356	90 \pm 10	260 \pm 10	50 \pm 10	100 \pm 10	110 \pm 10
PN357	320 \pm 10	910 \pm 10	...	340 \pm 10
PN358	110 \pm 20	310 \pm 20	...	100 \pm 10	110 \pm 20
PN359	128 \pm 10	368 \pm 10	...	100 \pm 7
PN360	470 \pm 20	1360 \pm 20	...	360 \pm 10
PN361	140 \pm 10	400 \pm 10	60 \pm 20	100 \pm 20	160 \pm 20
PN362	150 \pm 50	...	110 \pm 20	330 \pm 20	...	100 \pm 20	130 \pm 20
PN363	110 \pm 10	328 \pm 10	...	100 \pm 9
PN364	...	33 \pm 10	520 \pm 10	1550 \pm 20	...	385 \pm 7	37 \pm 7
PN365	440 \pm 20	1170 \pm 20	...	340 \pm 20
PN366	129 \pm 2	...	136 \pm 1	422 \pm 5	45.0 \pm 0.6	899 \pm 9	137 \pm 1	38.9 \pm 0.6	34.8 \pm 0.6
PN367	222 \pm 3	664 \pm 6	10 \pm 3	329 \pm 3	27 \pm 3
PN368	46 \pm 6	9 \pm 3	471 \pm 5	1400 \pm 20	25 \pm 2	310 \pm 3	74 \pm 2
PN369	340 \pm 10	990 \pm 10	...	320 \pm 10
PN370	119 \pm 1	1.2 \pm 0.1	126 \pm 1	381 \pm 4	21.1 \pm 0.2	483 \pm 5	64.3 \pm 0.6	14.2 \pm 0.2	13.1 \pm 0.1
PN371	310 \pm 10	890 \pm 10	...	335 \pm 9
PN372	419 \pm 7	1240 \pm 10	...	331 \pm 5
PN373	80 \pm 10	230 \pm 10	...	100 \pm 6
PN374	370 \pm 90	...	220 \pm 20	680 \pm 20	100 \pm 10	280 \pm 10	310 \pm 20	40 \pm 20	...

Table A.2—Continued

ID	[O II] λ 3727	[O III] λ 4363	[O III] λ 4959	[O III] λ 5007	[N II] λ 6548	H α λ 6562	[N II] λ 6584	[S II] λ 6717	[S II] λ 6731
PN375	330 ± 30	1010 ± 50	...	260 ± 20
PN376	384 ± 8	1110 ± 10	...	316 ± 9	40 ± 10
PN377	40 ± 10	70 ± 10	...	100 ± 10
PN378	120 ± 20	340 ± 10	...	100 ± 20	130 ± 30
PN379	318 ± 8	942 ± 9	289 ± 9	234 ± 9	873 ± 9
<i>Planetary nebulae (halo population)</i>									
PNh001	414 ± 6	1240 ± 10	9 ± 3	294 ± 3	25 ± 3
PNh002	...	18 ± 5	421 ± 7	1240 ± 10	...	259 ± 4	22 ± 5
PNh003	470 ± 10	1380 ± 10	...	310 ± 10	40 ± 10
PNh004	380 ± 20	1090 ± 20	...	260 ± 20
PNh005	120 ± 10	360 ± 20	...	100 ± 30
PNh006	90 ± 20	...	360 ± 5	1062 ± 9	...	291 ± 6	52 ± 6	...	14 ± 4
PNh007	107 ± 6	...	120 ± 2	345 ± 3	59 ± 4	264 ± 5	164 ± 5
PNh008	48 ± 6	5 ± 1	337 ± 3	989 ± 9	12.2 ± 0.9	284 ± 2	41 ± 1
PNh009	130 ± 10	380 ± 10	...	100 ± 20
PNh010	140 ± 20	420 ± 10	...	100 ± 20
PNh011	340 ± 20	1020 ± 20	...	240 ± 20
PNh012	66 ± 3	...	136 ± 2	400 ± 4	25.0 ± 0.9	299 ± 3	75 ± 1
PNh013	370 ± 10	1070 ± 10	...	269 ± 5
PNh014	476 ± 4	1400 ± 10	...	255 ± 8
PNh015	430 ± 50	...	280 ± 20	780 ± 20	90 ± 30	310 ± 20	250 ± 20
PNh016	420 ± 10	1230 ± 10	...	310 ± 10
PNh017	42 ± 4	...	243 ± 3	707 ± 7	13 ± 1	287 ± 3	35.4 ± 1.0
PNh018	168 ± 6	...	174 ± 2	507 ± 5	47 ± 2	301 ± 3	147 ± 2
PNh019	...	19 ± 3	462 ± 4	1390 ± 10	10 ± 2	286 ± 3	20 ± 2
PNh020	41 ± 7	13 ± 2	488 ± 5	1450 ± 20	21 ± 2	303 ± 3	61 ± 2
PNh021	30 ± 3	10 ± 1	419 ± 4	1240 ± 10	8.0 ± 0.8	278 ± 3	22.2 ± 0.8
PNh022	160 ± 20	...	601 ± 7	1770 ± 20	24 ± 7	278 ± 7	64 ± 7
PNh023	210 ± 10	610 ± 10	...	227 ± 7
PNh024	372 ± 7	1096 ± 10	...	266 ± 5
PNh025	444 ± 10	1290 ± 10	...	296 ± 7
PNh026	59 ± 10	...	354 ± 4	1040 ± 10	...	293 ± 4	36 ± 4
PNh027	50 ± 4	9.2 ± 0.9	452 ± 5	1330 ± 10	24.2 ± 1.0	291 ± 3	73 ± 1	...	2.9 ± 0.5
PNh028	120 ± 10	...	356 ± 4	1060 ± 10	74 ± 9	318 ± 8	231 ± 9	19 ± 3	26 ± 4
PNh029	60 ± 3	14 ± 1	468 ± 5	1370 ± 10	20 ± 1	279 ± 3	58 ± 1	...	3.5 ± 0.8
PNh030	50 ± 10	...	438 ± 5	1280 ± 10	22 ± 7	302 ± 7	63 ± 7
PNh031	420 ± 20	1250 ± 20	...	280 ± 20

Table A.2—Continued

ID	[O II] λ 3727	[O III] λ 4363	[O III] λ 4959	[O III] λ 5007	[N II] λ 6548	H α λ 6562	[N II] λ 6584	[S II] λ 6717	[S II] λ 6731
PNh032	44 ± 6	...	189 ± 4	553 ± 5	30 ± 2	309 ± 4	87 ± 2
PNh033	128 ± 2	4 ± 1	74 ± 2	219 ± 2	...	304 ± 3	8.0 ± 1.0	11 ± 1	8 ± 1
PNh034	320 ± 20	950 ± 20	...	290 ± 10
PNh035	28 ± 9	32 ± 2	63 ± 2	178 ± 2	...	425 ± 4	21 ± 2
PNh036	40 ± 10	16 ± 6	492 ± 8	1450 ± 10	...	283 ± 9
PNh037	40 ± 10	18 ± 5	474 ± 5	1390 ± 10	...	299 ± 6
PNh038	80 ± 10	8 ± 2	218 ± 2	642 ± 6	11 ± 2	281 ± 3	28 ± 2
PNh039	400 ± 10	1170 ± 20	...	302 ± 9
PNh040	130 ± 30	...	480 ± 10	1360 ± 10	...	265 ± 9	50 ± 10
PNh041	61 ± 7	84 ± 3	308 ± 3	260 ± 3	21 ± 3	39 ± 3
PNh042	310 ± 20	890 ± 10	...	300 ± 20	70 ± 20
PNh043	425 ± 5	1250 ± 10	19 ± 2	294 ± 3	52 ± 2
PNh044	27 ± 4	11 ± 2	322 ± 3	948 ± 10	13 ± 2	304 ± 4	36 ± 3
PNh045	90 ± 20	...	430 ± 10	1250 ± 10	61 ± 4	338 ± 5	195 ± 5	16 ± 4	24 ± 4
PNh046	...	16 ± 3	463 ± 4	1390 ± 10	23 ± 2	310 ± 3	64 ± 2	...	8 ± 2
PNh047	487 ± 5	1440 ± 10	...	253 ± 5	45 ± 6
PNh048	310 ± 20	26 ± 6	393 ± 7	1174 ± 9	77 ± 6	269 ± 5	249 ± 6	28 ± 6	30 ± 7
PNh049	82 ± 9	...	225 ± 3	678 ± 7	16 ± 3	314 ± 3	47 ± 3
PNh050	359 ± 5	1090 ± 10	...	277 ± 5
PNh051	250 ± 7	713 ± 7	...	306 ± 8	25 ± 9
PNh052	157 ± 2	...	55 ± 1	160 ± 2	79.0 ± 0.6	292 ± 3	236 ± 2	4.3 ± 0.6	7.1 ± 0.6
PNh053	170 ± 10	...	51 ± 1	148 ± 2	49 ± 1	299 ± 3	152 ± 2
PNh054	33 ± 3	100 ± 2
PNh055	64 ± 8	...	329 ± 3	976 ± 9	21 ± 2	331 ± 3	64 ± 2	6 ± 2	7 ± 2
PNh056	220 ± 10	660 ± 10	...	233 ± 7
PNh057	430 ± 10	1260 ± 20	...	240 ± 10
PNh058	49 ± 6	13 ± 2	428 ± 5	1270 ± 10	8 ± 2	290 ± 3	20 ± 2
PNh059	57 ± 3	6 ± 1	417 ± 4	1230 ± 10	21 ± 1	307 ± 3	64 ± 2
PNh060	403 ± 10	1180 ± 10	...	270 ± 10
PNh061	231 ± 5	24 ± 2	500 ± 5	1460 ± 10	53 ± 2	265 ± 3	153 ± 2	12 ± 2	20 ± 2
PNh062	...	17 ± 1	432 ± 4	1270 ± 10	...	312 ± 3	18 ± 3
PNh063	380 ± 20	1090 ± 20	450 ± 20	290 ± 20	1420 ± 20	...	70 ± 20
PNh064	120 ± 20	...	216 ± 5	639 ± 6	30 ± 4	306 ± 4	81 ± 4
PNh065	67 ± 3	13 ± 1	420 ± 5	1240 ± 10	19 ± 2	279 ± 3	56 ± 2
PNh066	428 ± 6	1240 ± 10	...	269 ± 3
PNh067	392 ± 7	1150 ± 10	...	274 ± 6	51 ± 5
PNh068	...	12 ± 4	477 ± 5	1390 ± 10	...	273 ± 3	12 ± 3

Table A.2—Continued

ID	[O II]	[O III]	[O III]	[O III]	[N II]	H α	[N II]	[S II]	[S II]
	λ 3727	λ 4363	λ 4959	λ 5007	λ 6548	λ 6562	λ 6584	λ 6717	λ 6731
PNh069	417 \pm 4	1230 \pm 10	17 \pm 3	308 \pm 3	62 \pm 4
PNh070	74 \pm 8	...	179 \pm 2	534 \pm 5	34 \pm 2	305 \pm 3	104 \pm 2
PNh071	37 \pm 5	6 \pm 2	350 \pm 4	1030 \pm 10	11 \pm 1	292 \pm 3	35 \pm 2
PNh072	142 \pm 8	...	129 \pm 2	376 \pm 4	27 \pm 2	292 \pm 4	82 \pm 2
PNh073	...	18 \pm 5	322 \pm 4	940 \pm 10	...	252 \pm 4	15 \pm 4
PNh074	80 \pm 20	...	123 \pm 7	371 \pm 7	...	281 \pm 6	46 \pm 5
PNh075	365 \pm 8	1100 \pm 10	...	290 \pm 10
PNh076	336 \pm 6	970 \pm 10	10 \pm 3	282 \pm 3	32 \pm 3
PNh077	80 \pm 30	...	204 \pm 7	621 \pm 8	31 \pm 4	310 \pm 4	88 \pm 4	17 \pm 4	17 \pm 5
PNh078	69 \pm 9	...	183 \pm 3	545 \pm 5	...	315 \pm 5	25 \pm 5
PNh079	...	13 \pm 2	507 \pm 5	1490 \pm 20	19 \pm 2	290 \pm 3	51 \pm 2
PNh080	100 \pm 30	...	487 \pm 5	1440 \pm 10	43 \pm 6	295 \pm 6	130 \pm 7	...	17 \pm 5
PNh081	37 \pm 8	17 \pm 3	332 \pm 4	913 \pm 8	20 \pm 2	247 \pm 3	53 \pm 2
<i>Unclassified</i>									
X001	100 \pm 6	28 \pm 6	20 \pm 6	...
X002	60 \pm 10	100 \pm 10	...	22 \pm 7	...
X003	100 \pm 20
X004	100 \pm 10
X005	100 \pm 7	25 \pm 8
X006	100 \pm 10	70 \pm 10
X007	100 \pm 4	30 \pm 3	16 \pm 4	13 \pm 4
X008	60 \pm 10	100 \pm 6	41 \pm 5
X009	100 \pm 10
X010	100 \pm 10
X011	100 \pm 9	60 \pm 8
X012	100 \pm 8	69 \pm 8
X013	100 \pm 6	24 \pm 9
X014	100 \pm 5	37 \pm 6	13 \pm 4	...
X015	100 \pm 8	40 \pm 7
X016	40 \pm 10	100 \pm 9	100 \pm 10
X017	100 \pm 8	51 \pm 10
X018	31 \pm 8	100 \pm 7	43 \pm 7	21 \pm 5	15 \pm 4
X019	100 \pm 7	40 \pm 9
X020	100 \pm 6
X021	100 \pm 8	60 \pm 10	35 \pm 8	...
X022	100 \pm 3	28 \pm 4	13 \pm 4	...
X023	100 \pm 6	47 \pm 7

Table A.2—Continued

ID	[O II] λ 3727	[O III] λ 4363	[O III] λ 4959	[O III] λ 5007	[N II] λ 6548	H α λ 6562	[N II] λ 6584	[S II] λ 6717	[S II] λ 6731
X024	9 ± 2	100 ± 2	36 ± 2	13 ± 2	12 ± 2
X025	54 ± 8	100 ± 4	31 ± 5	23 ± 5	18 ± 5

Note. — This table is organized into sections similarly to Table A.1. Extinction correction has not been applied. Line fluxes are reported relative to H β =100; however, line flux ratios for lines with large wavelength separations are unreliable for spectra where the ADC was not functioning (see Table A.1). For objects where H β is not detected, fluxes are instead normalized relative to another line whose flux is given as 100.

Table A.3. Derived quantities for M31 HII regions

ID	A_V (mag)	Direct	Z94	KD02	N06 N2	N06 O3N2	PT05	PVT ONS (log(N/H)+12)
HII001	9.06 ± 0.03
HII002
HII003	8.90 ± 0.08
HII004	8.87 ± 0.09
HII005
HII006	0.6 ± 0.8
HII007
HII008
HII009	2.6 ± 0.4
HII010	0.2 ± 0.3	8.85 ± 0.05	8.83 ± 0.06
HII011	1.1 ± 0.4	8.76 ± 0.08	8.89 ± 0.09
HII012	0.6 ± 0.5	8.68 ± 0.09	8.70 ± 0.07	8.86 ± 0.05
HII013	0.49 ± 0.07	...	8.72 ± 0.02	8.74 ± 0.01	8.63 ± 0.01	8.63	8.23 ± 0.02	7.36 ± 0.02
HII014	0.7 ± 0.8	8.8 ± 0.1	9.0 ± 0.2
HII015	0.6 ± 0.4	8.87 ± 0.07	9.01 ± 0.09
HII016
HII017	0.5 ± 0.6
HII018
HII019	9.0 ± 0.1
HII020	8.35 ± 0.01
HII021	1 ± 1	8.9 ± 0.1	8.9 ± 0.2
HII022
HII023	9.03 ± 0.01
HII024	9.05 ± 0.03
HII025	2.1 ± 0.6
HII026	1.4 ± 0.8	8.8 ± 0.1	8.99 ± 0.10
HII027	0.7 ± 0.4	8.76 ± 0.08	8.85 ± 0.09
HII028	1.1 ± 0.5	8.81 ± 0.09	8.79 ± 0.09	8.93 ± 0.07
HII029	0.97 ± 0.09	...	8.94 ± 0.02	8.85 ± 0.02	8.78 ± 0.02	8.83 ± 0.01	8.29 ± 0.04	7.46 ± 0.03
HII030	1.1 ± 0.5	9.1 ± 0.1	8.77 ± 0.05
HII031	2 ± 1
HII032	0.4 ± 0.4	8.82 ± 0.06
HII033	0.6 ± 0.5	8.82 ± 0.07	9.1 ± 0.1
HII034	2.8 ± 0.8	8.6 ± 0.2	8.91 ± 0.07
HII035	0.1 ± 0.2
HII036	2.2 ± 0.7	8.73 ± 0.09
HII037	1.0 ± 0.7	8.9 ± 0.1	9.1 ± 0.1

Table A.3—Continued

ID	A_V (mag)	Direct	Z94	KD02	N06 N2	N06 O3N2	PT05	PVT ONS (log(N/H)+12)
HII038	1.4 ± 1.0	8.9 ± 0.1	9.2 ± 0.2
HII039	0.7 ± 0.5	8.82 ± 0.09	8.85 ± 0.07
HII040	1.87 ± 0.05	...	8.86	8.84	8.85 ± 0.01	8.76	8.30 ± 0.01	7.47 ± 0.01
HII041	3.1 ± 0.7	8.8 ± 0.1	8.99 ± 0.07
HII042	2.0 ± 0.4	8.8 ± 0.1	8.88 ± 0.05
HII043	1.5 ± 0.9	8.9 ± 0.1
HII044
HII045	0.59 ± 0.05	8.33 ± 0.04	8.68 ± 0.01	8.77	8.40	8.39	8.46	7.39 ± 0.02
HII046	0.8 ± 0.2	...	8.96 ± 0.04	8.88 ± 0.03	8.86 ± 0.02	8.86 ± 0.01	8.32 ± 0.06	7.53 ± 0.05
HII047	0.0	9.18 ± 0.01
HII048	0.33 ± 0.04	...	8.96	8.87	8.55	8.62	8.56	7.57 ± 0.01
HII049	1.2 ± 1.0	8.7 ± 0.2	8.8 ± 0.2
HII050	3.0 ± 0.6	9.10 ± 0.07
HII051	1.1 ± 0.7
HII052	3.18 ± 0.05	...	8.74 ± 0.01	8.81	8.88 ± 0.01	8.71	8.21 ± 0.02	7.40 ± 0.02
HII053	2.4 ± 0.5
HII054	2.7 ± 0.8	8.8 ± 0.2	8.98 ± 0.10
HII055	0.6 ± 0.2	8.97 ± 0.03	9.15 ± 0.04
HII056	0.57 ± 0.05	...	8.88 ± 0.01	8.89	8.92 ± 0.01	8.78	8.33 ± 0.02	7.54 ± 0.02
HII057	2.3 ± 0.3	8.89 ± 0.06
HII058	3.14 ± 0.05	...	8.82 ± 0.01	8.80	8.70	8.65	8.35 ± 0.01	7.51 ± 0.01
HII059	0.4 ± 0.5	8.8 ± 0.1
HII060	3.8 ± 0.2
HII061	1.81 ± 0.05	...	8.74	8.74	8.52	8.51	8.38	7.37 ± 0.01
HII062	0.3 ± 0.3	9.12 ± 0.04
HII063	8.32
HII064	1.16 ± 0.06	...	8.71 ± 0.02	8.74 ± 0.01	8.71 ± 0.01	8.68	8.15 ± 0.02	...
HII065	9.04 ± 0.05
HII066	2.9 ± 0.2	8.82 ± 0.03	9.31 ± 0.02	9.25 ± 0.07
HII067	8.95 ± 0.05
HII068	2.08 ± 0.06	...	8.81 ± 0.02	8.79 ± 0.01	8.84 ± 0.01	8.80	8.15 ± 0.02	7.36 ± 0.02
HII069	1.73 ± 0.06	...	9.04	9.00	9.41 ± 0.02	9.10	8.27 ± 0.01	7.73 ± 0.02
HII070	8.93 ± 0.01
HII071	0.6 ± 0.6
HII072	8.76 ± 0.02
HII073	2.4 ± 0.2	8.76 ± 0.03
HII074	2.4 ± 0.5	8.99 ± 0.09	9.06 ± 0.07	8.89 ± 0.07

Table A.3—Continued

ID	A_V (mag)	Direct	Z94	KD02	N06 N2	N06 O3N2	PT05	PVT ONS (log(N/H)+12)
HII075	1.4 ± 0.7	8.9 ± 0.1	9.2 ± 0.2
HII076	9.0 ± 0.1
HII077	2.6 ± 0.3	8.94 ± 0.06	8.98 ± 0.04
HII078	2.4 ± 0.4	8.67 ± 0.09	8.86 ± 0.05	8.92 ± 0.04
HII079	1.27 ± 0.05	...	9.05	8.91	8.75	8.85	8.44 ± 0.01	7.59 ± 0.02
HII080	2.20 ± 0.06	...	8.97 ± 0.01	8.86	8.72	8.78	8.40 ± 0.02	7.50 ± 0.02
HII081	2.6 ± 0.3	8.88 ± 0.05
HII082	2.60 ± 0.08	...	8.93 ± 0.02	8.81 ± 0.02	8.73	8.81	8.28 ± 0.04	7.41 ± 0.03
HII083	1.86 ± 0.09	...	8.90 ± 0.03	8.86 ± 0.02	9.10 ± 0.02	9.04 ± 0.02	...	7.48 ± 0.03
HII084	8.95 ± 0.01
HII085	2.1 ± 0.2	...	8.76 ± 0.08	8.83 ± 0.03	9.23 ± 0.03	8.97 ± 0.02	...	7.41 ± 0.06
HII086	9.01 ± 0.10
HII087
HII088	1.19 ± 0.06	...	8.91 ± 0.01	8.86	8.88 ± 0.01	8.83	8.28 ± 0.02	7.50 ± 0.02
HII089	8.69
HII090	0.9 ± 0.7
HII091	0.3 ± 0.1	...	8.91 ± 0.03	9.01 ± 0.02	...	8.96 ± 0.01	8.30 ± 0.04	...
HII092	1.28 ± 0.06	...	8.99 ± 0.01	8.86 ± 0.01	8.73	8.83	8.36 ± 0.02	7.49 ± 0.02
HII093	1.5 ± 0.1	8.91 ± 0.02	9.10 ± 0.03
HII094	0.69 ± 0.05	...	8.77	8.76 ± 0.01	8.12	8.20	8.57	7.27 ± 0.02
HII095	2 ± 1
HII096
HII097	9.06 ± 0.05
HII098	3.6 ± 0.7	9.17 ± 0.08
HII099	9.18 ± 0.02
HII100	9.0 ± 0.1
HII101	3.0 ± 0.6	8.78 ± 0.10	8.98 ± 0.07
HII102	8.99 ± 0.04
HII103	3.0 ± 0.1	9.05 ± 0.05	9.35 ± 0.02
HII104	8.60
HII105	1.47 ± 0.06	...	8.84 ± 0.02	8.86	9.25 ± 0.02	9.15 ± 0.02	...	7.46 ± 0.02
HII106
HII107	1.83 ± 0.05	...	8.89	8.88	8.76	8.68	8.44 ± 0.01	7.55 ± 0.01
HII108	2.2 ± 0.7	9.2 ± 0.2
HII109
HII110	2.0 ± 0.4	8.55 ± 0.09	8.87 ± 0.09
HII111	0.6 ± 0.1	9.03 ± 0.02	8.90 ± 0.03

Table A.3—Continued

ID	A_V (mag)	Direct	Z94	KD02	N06 N2	N06 O3N2	PT05	PVT ONS (log(N/H)+12)
HII112	2.0 ± 0.5	8.7 ± 0.1	...	8.91 ± 0.04
HII113	0.9 ± 0.4
HII115	3.8 ± 0.4	8.73 ± 0.09	9.18 ± 0.03
HII115	0.8 ± 0.3	9.19 ± 0.04	...	9.33 ± 0.06
HII116	2.2 ± 0.6	8.7 ± 0.1	8.75 ± 0.08
HII117	1.4 ± 0.9	8.7 ± 0.2	8.62 ± 0.07	8.66 ± 0.07
HII118	1.7 ± 0.2	8.91 ± 0.03	9.33 ± 0.07	9.08 ± 0.03
HII119	1.0 ± 0.2	8.97 ± 0.05	8.81 ± 0.03	9.09 ± 0.05
HII120	0.7 ± 0.1	8.79 ± 0.02	9.30 ± 0.04	9.28 ± 0.06
HII121	0.0	...	8.52 ± 0.03	8.52 ± 0.03	8.52 ± 0.02	8.59 ± 0.01	...	7.07 ± 0.03
HII122	0.6 ± 0.1	...	8.71 ± 0.05	8.70 ± 0.03	8.72 ± 0.03	8.79 ± 0.01
HII123	0.7 ± 0.6
HII124	9.26 ± 0.02
HII125	0.41 ± 0.04	...	8.86 ± 0.01	8.79	8.76	8.84	8.14 ± 0.02	7.36 ± 0.01
HII126	9.00 ± 0.07
HII127	8.35 ± 0.01
HII128	0.42 ± 0.10	8.89 ± 0.02	9.05 ± 0.05
HII129	2.8 ± 0.2	8.79 ± 0.05	8.87 ± 0.03	8.84 ± 0.04
HII130	2 ± 1	8.9 ± 0.1
HII131	0.7 ± 0.4	8.86 ± 0.06	9.41 ± 0.08	9.01 ± 0.05
HII132	2.8 ± 0.2	8.68 ± 0.05	8.98 ± 0.05	8.92 ± 0.03
HII133	0.1 ± 0.2
HII134	2.4 ± 0.3	8.79 ± 0.06	9.25 ± 0.04	9.13 ± 0.06
HII135	2.9 ± 0.6	8.68 ± 0.06
HII136	0.3 ± 0.1	...	8.63 ± 0.04	8.59 ± 0.03	8.51 ± 0.02	8.58 ± 0.01	...	7.11 ± 0.03
HII137	8.88 ± 0.05
HII138	1.86 ± 0.05	...	8.65 ± 0.01	8.72 ± 0.01	8.58	8.53	8.28 ± 0.02	7.37 ± 0.01
HII139	1.0 ± 0.1	8.79 ± 0.02	8.99 ± 0.02
HII140	3.0 ± 0.1	8.60 ± 0.01	8.54 ± 0.01
HII141	1.7 ± 0.3	8.71 ± 0.06	8.91 ± 0.05
HII142	2.6 ± 0.7	8.85 ± 0.09	8.9 ± 0.1
HII143	3.4 ± 0.6	8.73 ± 0.08
HII144	0.92 ± 0.04	...	8.94	8.90	8.93 ± 0.01	8.83	8.35 ± 0.01	7.57 ± 0.01
HII145	1.4 ± 0.2
HII146	0.0
HII147	0.7 ± 0.2	...	8.91 ± 0.07	9.05 ± 0.04	...	9.02 ± 0.02	8.28 ± 0.09	...
HII148	1.4 ± 0.8	9.14 ± 0.08

Table A.3—Continued

ID	A_V (mag)	Direct	Z94	KD02	N06 N2	N06 O3N2	PT05	PVT ONS (log(N/H)+12)
HII149	0.4 ± 0.6
HII150	1.8 ± 0.4	8.87 ± 0.07	9.05 ± 0.06
HII151	0.4 ± 0.3	9.21 ± 0.03
HII152	0.3 ± 0.2	9.25 ± 0.02
HII153	0.2 ± 0.2	...	8.71 ± 0.07	8.73 ± 0.08	8.36 ± 0.04	8.38 ± 0.03	8.47 ± 0.07	...
HII154	0.8 ± 0.3	8.79 ± 0.05	8.92 ± 0.07
HII155	0.1 ± 0.2
HII156	0.5 ± 0.3	8.72 ± 0.07	9.1 ± 0.1
HII157	0.8 ± 0.3	8.76 ± 0.07	8.99 ± 0.08
HII158	0.30 ± 0.07	...	8.81 ± 0.02	8.78 ± 0.01	8.67 ± 0.01	8.68	8.28 ± 0.02	7.41 ± 0.02
HII159	1.8 ± 0.2	8.78 ± 0.04	9.06 ± 0.05
HII160	8.71 ± 0.03
HII161	0.26 ± 0.08	...	8.97 ± 0.01	9.00 ± 0.01	8.65 ± 0.01	8.62	8.64 ± 0.01	...
HII162	9.13 ± 0.02
HII163	9.28 ± 0.02
HII164	1.62 ± 0.05	...	9.14	8.99	8.71	8.86	8.61	...
HII165	2.44 ± 0.05	9.01 ± 0.02	8.96
HII166	0.98 ± 0.10	8.94 ± 0.02	9.34 ± 0.07
HII167	0.9 ± 0.2
HII168	2.4 ± 0.2	8.85 ± 0.04	9.19 ± 0.03
HII169	4.38 ± 0.06	...	8.93 ± 0.02	8.85 ± 0.02	8.76 ± 0.01	8.74	8.40 ± 0.04	7.51 ± 0.05
HII170	0.8 ± 0.3	8.64 ± 0.07	8.97 ± 0.05
HII171	8.99 ± 0.04
HII172	3.2 ± 0.6
HII173	1.92 ± 0.05	...	9.03 ± 0.01	8.95	9.10 ± 0.02	9.00	8.31 ± 0.02	7.65 ± 0.02
HII174	0.52 ± 0.05	...	8.73 ± 0.01	8.70 ± 0.01	8.51	8.55	8.31 ± 0.01	7.30 ± 0.02
HII175	0.4 ± 0.4	8.91 ± 0.10
HII176	2.9 ± 0.2	8.75 ± 0.04	9.20 ± 0.04	9.04 ± 0.04
HII177
HII178	8.54
HII179	4.1 ± 0.5	9.18 ± 0.06
HII180	8.96 ± 0.01
HII181	1.44 ± 0.05	...	9.03	8.91	8.70	8.77	8.51 ± 0.01	7.62 ± 0.01
HII182	2.40 ± 0.09	8.94 ± 0.01	8.94 ± 0.02
HII183	9.36 ± 0.02
HII184	0.7 ± 0.9
HII185	8.27 ± 0.04

Table A.3—Continued

ID	A_V (mag)	Direct	Z94	KD02	N06 N2	N06 O3N2	PT05	PVT ONS (log(N/H)+12)
HII186	8.98 ± 0.04
HII187	0.52 ± 0.05	8.98	9.06 ± 0.02	9.26 ± 0.03
HII188	0.8 ± 0.1	8.87 ± 0.01	9.02 ± 0.02
HII189	9.09 ± 0.02
HII190	8.63 ± 0.02
HII191	1.59 ± 0.05	...	8.90 ± 0.01	8.86	9.10 ± 0.02	9.09	...	7.47 ± 0.01
HII192	1.6 ± 0.1	8.81 ± 0.02
HII193	8.06 ± 0.04
HII194	8.65 ± 0.03
HII195	0.7 ± 0.2
HII196	9.45 ± 0.02
HII197	8.79 ± 0.01
HII198	0.60 ± 0.05	...	8.71 ± 0.01	8.73	8.50	8.51	8.37 ± 0.01	7.34 ± 0.01
HII199	8.85 ± 0.01
HII200	3.1 ± 0.4	8.73 ± 0.08	8.75 ± 0.04	8.73 ± 0.04
HII201	1.9 ± 0.2	8.71 ± 0.05	8.96 ± 0.04	9.07 ± 0.05
HII202	0.98 ± 0.08	...	9.00 ± 0.02	8.93 ± 0.01	9.13 ± 0.02	9.06 ± 0.01	8.21 ± 0.03	7.61 ± 0.02
HII203	4.7 ± 0.4	9.13 ± 0.03	9.08 ± 0.06
HII204	0.6 ± 0.2	8.80 ± 0.05	8.9 ± 0.1
HII205	0.82 ± 0.07	...	8.67 ± 0.01	8.71 ± 0.02	8.28	8.29	8.47	7.23 ± 0.03
HII206	0.8 ± 0.4
HII207	8.61 ± 0.02
HII208	4.18 ± 0.07	8.66	8.57
HII209	1.70 ± 0.06	8.41 ± 0.08	8.78 ± 0.01	8.84	8.69	8.60	8.41 ± 0.01	7.59 ± 0.01
HII210	0.16 ± 0.08	9.17 ± 0.01
HII211	2.4 ± 0.3	9.04 ± 0.04	8.95 ± 0.03
HII212	0.0 ± 0.2	8.98 ± 0.08	8.67 ± 0.02
HII213	1.92 ± 0.05	...	8.66 ± 0.02	8.66 ± 0.01	8.48	8.49	8.29 ± 0.02	7.23 ± 0.01
HII214	0.0
HII215	0.3 ± 0.2	8.95 ± 0.03	9.10 ± 0.03	9.14 ± 0.04
HII216	4.0 ± 0.4	8.7 ± 0.1	9.14 ± 0.03
HII217	0.97 ± 0.06	...	8.99	8.92	8.77	8.75	8.50 ± 0.01	7.63 ± 0.02
HII218	1.45 ± 0.05	...	8.95	8.88	8.67	8.68	8.50 ± 0.01	7.58 ± 0.01
HII219	0.21 ± 0.07	9.12 ± 0.01
HII220	2.43 ± 0.06	8.68	8.64
HII221	1.6 ± 0.2	8.96 ± 0.03
HII222	8.14 ± 0.04

Table A.3—Continued

ID	A_V (mag)	Direct	Z94	KD02	N06 N2	N06 O3N2	PT05	PVT ONS (log(N/H)+12)
HII223	9.07 ± 0.02
HII224	1.0 ± 0.4	8.78 ± 0.07	...	8.94 ± 0.03
HII225	0.2 ± 0.6
HII226	1.1 ± 0.5	8.86 ± 0.09	9.11 ± 0.10
HII227	1.1 ± 0.1	8.89 ± 0.02	8.99 ± 0.03	9.02 ± 0.04
HII228	3.0 ± 0.3	8.69 ± 0.06	9.06 ± 0.03
HII229	8.81 ± 0.01
HII230	0.71 ± 0.08	8.54 ± 0.01	8.65
HII231	1.5 ± 0.3	8.71 ± 0.07	8.83 ± 0.07	8.95 ± 0.04
HII232	0.16 ± 0.10	...	8.86 ± 0.02	8.80 ± 0.02	8.59 ± 0.03	8.63 ± 0.02	8.40 ± 0.03	7.44 ± 0.04
HII233	1.33 ± 0.06	8.61	8.67
HII234	1.9 ± 0.3	8.81 ± 0.06	9.09 ± 0.05
HII235	1.94 ± 0.05	...	8.81 ± 0.01	8.80	8.89 ± 0.01	8.82	8.13 ± 0.02	7.38 ± 0.01
HII236	1.63 ± 0.05	...	8.65 ± 0.02	8.67 ± 0.01	8.68	8.69	...	7.26 ± 0.02
HII237	0.1 ± 0.4
HII238	1.0 ± 0.2	...	8.86 ± 0.10	8.81 ± 0.05	8.80 ± 0.04	8.82 ± 0.03	...	7.41 ± 0.08
HII239	0.0
HII240	0.86 ± 0.09	8.56 ± 0.01	8.60
HII241	0.0
HII242
HII243	1.1 ± 0.2	8.75 ± 0.04	8.72 ± 0.05	9.02 ± 0.04
HII244	1.55 ± 0.07	...	8.75 ± 0.02	8.77 ± 0.01	8.69	8.64	8.27 ± 0.02	7.46 ± 0.03
HII245	1.31 ± 0.08	...	8.91 ± 0.02	8.87 ± 0.01	9.10 ± 0.01	9.01	...	7.50 ± 0.02
HII246	1.50 ± 0.05	...	8.75 ± 0.01	8.75 ± 0.01	8.65	8.63	8.27 ± 0.02	7.40 ± 0.01
HII247	0.61 ± 0.04	8.35 ± 0.04	8.72	8.78	8.41	8.40	8.48	7.41 ± 0.01
HII248	0.75 ± 0.07	...	8.75 ± 0.02	8.66 ± 0.02	8.36	8.42	8.43 ± 0.02	7.22 ± 0.03
HII249	0.2 ± 0.1	9.16 ± 0.02
HII250	1.42 ± 0.06	...	8.88 ± 0.02	8.82	9.04 ± 0.01	9.28 ± 0.02	...	7.43 ± 0.02
HII251	1.31 ± 0.05	8.40 ± 0.06	8.65 ± 0.01	8.71 ± 0.01	8.53	8.51	8.30 ± 0.01	7.33 ± 0.02
HII252	0.1 ± 0.2	...	8.92 ± 0.04	9.07 ± 0.03	...	8.80 ± 0.01	8.54 ± 0.05	...
HII253	2.43 ± 0.08	...	8.53 ± 0.05	8.56 ± 0.03	8.48	8.48	...	7.11 ± 0.04

Note. — The abundance diagnostics applied in this table are described in Section 3.2.7; all quantities are $(\log(\text{O}/\text{H}) + 12)$ unless otherwise noted. The reported uncertainties are derived by propagation of the line flux uncertainties, as described in Section 3.2.7 and does not include other systematic effects. When this “statistical” uncertainty is less than 0.01 dex, we do not report it.

Table A.4. Derived quantities for M31 planetary nebulae

ID	A_V	$\log(\text{O}/\text{H})+12$
PN001
PN002	1.3 ± 0.1	...
PN003	0.3 ± 0.2	...
PN004	0.09 ± 0.05	8.51 ± 0.04
PN005	0.4 ± 0.5	...
PN006	1.5 ± 0.3	...
PN007	0.4 ± 0.2	...
PN008	0.6 ± 0.3	...
PN009
PN010
PN011
PN012	0.7 ± 0.5	...
PN013	0.0	...
PN014	0.01 ± 0.09	...
PN015	1.8 ± 0.3	...
PN016	0.5 ± 0.7	...
PN017	0.4 ± 0.4	...
PN018	0.0 ± 0.4	...
PN019	0.6 ± 0.2	...
PN020	2.0 ± 0.1	7.6 ± 0.2
PN021	0.1 ± 0.1	...
PN022	1.0 ± 0.4	...
PN023	2 ± 1	...
PN024	1.1 ± 0.9	...
PN025
PN026	...	8.57 ± 0.09
PN027	0.2 ± 0.2	...
PN028	0.27 ± 0.07	8.7 ± 0.1
PN029	1 ± 1	...
PN030	1.4 ± 0.2	...
PN031	1.6 ± 0.5	...
PN032	0.1 ± 0.1	...
PN033	1.3 ± 0.3	...
PN034	0.30 ± 0.07	8.4 ± 0.1
PN035	0.49 ± 0.10	...
PN036	0.9 ± 0.4	...
PN037	0.3 ± 0.1	8.39 ± 0.08
PN038	1.1 ± 0.2	...

Table A.4—Continued

ID	A_V	$\log(\text{O}/\text{H})+12$
PN039	0.0	8.42 ± 0.10
PN040	0.2 ± 0.4	...
PN041
PN042
PN043
PN044	3 ± 1	...
PN045	0.4 ± 0.2	...
PN046	0.47 ± 0.08	...
PN047
PN048	1.2 ± 0.1	...
PN049	0.9 ± 0.5	...
PN050	0.29 ± 0.10	8.25 ± 0.06
PN051	0.3 ± 0.1	8.42 ± 0.10
PN052	0.0	...
PN053	0.6 ± 0.6	...
PN054	0.0	...
PN055
PN056	0.7 ± 0.4	...
PN057	0.7 ± 0.4	8.0 ± 0.2
PN058	1.0 ± 0.2	...
PN059	0.1 ± 0.2	...
PN060	0.6 ± 0.5	7.9 ± 0.2
PN061	0.2 ± 0.1	8.6 ± 0.1
PN062	0.1 ± 0.2	...
PN063	0.81 ± 0.09	8.62 ± 0.08
PN064	0.3 ± 1.0	...
PN065
PN066	1.21 ± 0.10	...
PN067	0.5 ± 0.2	...
PN068	0.0	...
PN069	1.2 ± 0.3	...
PN070	1.3 ± 0.1	...
PN071	0.1 ± 0.2	...
PN072	0.7 ± 0.1	8.26 ± 0.06
PN073	1.2 ± 0.2	...
PN074	0.0	...
PN075	0.3 ± 0.4	...
PN076	0.0	8.3 ± 0.2

Table A.4—Continued

ID	A_V	$\log(\text{O}/\text{H})+12$
PN077	0.2 ± 0.4	...
PN078	0.0	...
PN079	0.15 ± 0.08	8.66 ± 0.07
PN080	0.8 ± 0.4	...
PN081	0.2 ± 0.3	...
PN082	0.7 ± 0.7	...
PN083	0.1 ± 0.2	...
PN084	0.8 ± 0.4	...
PN085	1.0 ± 0.1	...
PN086	0.3 ± 0.3	...
PN087	0.5 ± 0.2	...
PN088	0.7 ± 0.3	...
PN089	0.5 ± 0.2	...
PN090	1.2 ± 0.3	...
PN091	1.6 ± 0.4	...
PN092	0.2 ± 0.3	...
PN093	0.7 ± 0.2	...
PN094	0.5 ± 0.2	...
PN095	1.07 ± 0.06	8.61 ± 0.07
PN096	0.14 ± 0.09	...
PN097	0.6 ± 0.1	...
PN098	0.2 ± 0.1	...
PN099	1.6 ± 0.5	...
PN100	0.6 ± 0.1	8.44 ± 0.07
PN101	1.3 ± 0.2	...
PN102	0.5 ± 0.2	...
PN103	0.0	8.46 ± 0.09
PN104	0.24 ± 0.08	8.55 ± 0.08
PN105	0.5 ± 0.2	8.4 ± 0.1
PN106
PN107	0.5 ± 0.3	...
PN108	0.4 ± 0.4	...
PN109	0.9 ± 0.9	...
PN110
PN111	0.3 ± 0.2	...
PN112
PN113	0.3 ± 0.3	...
PN114	1.3 ± 0.4	...

Table A.4—Continued

ID	A_V	$\log(\text{O}/\text{H})+12$
PN115	2.4 ± 0.4	...
PN116
PN117	0.14 ± 0.08	...
PN118	0.2 ± 0.1	...
PN119	0.2 ± 0.3	...
PN120	0.3 ± 0.9	...
PN121	1.22 ± 0.08	8.7 ± 0.2
PN122	0.3 ± 0.3	...
PN123	0.0	...
PN124	1.3 ± 0.3	8.3 ± 0.2
PN125	0.51 ± 0.10	...
PN126	1.6 ± 0.5	...
PN127	0.0	...
PN128	0.7 ± 0.3	...
PN129
PN130	0.0	8.61 ± 0.05
PN131	1.7 ± 0.2	...
PN132	1.1 ± 0.9	...
PN133	1.8 ± 0.2	...
PN134	1.3 ± 0.1	...
PN135	0.0	...
PN136	0.6 ± 0.4	...
PN137	0.6 ± 0.2	8.1 ± 0.1
PN138	0.5 ± 0.1	...
PN139
PN140	0.3 ± 0.4	...
PN141
PN142	0.3 ± 0.5	...
PN143	2.0 ± 0.9	...
PN144	0.05 ± 0.08	8.45 ± 0.08
PN145	1 ± 1	...
PN146	0.2 ± 0.2	...
PN147	0.0	8.55 ± 0.10
PN148	0.5 ± 0.3	...
PN149	0.3 ± 0.1	...
PN150	0.1 ± 0.2	...
PN151
PN152	0.5 ± 0.3	...

Table A.4—Continued

ID	A_V	$\log(\text{O}/\text{H})+12$
PN153	1.1 ± 0.1	...
PN154	1.9 ± 0.5	...
PN155	0.5 ± 0.2	...
PN156	0.2 ± 0.2	...
PN157	0.5 ± 0.1	...
PN158	0.02 ± 0.09	...
PN159	0.4 ± 0.1	...
PN160	0.8 ± 0.3	...
PN161	0.4 ± 0.1	...
PN162	0.2 ± 0.2	...
PN163	0.3 ± 0.1	...
PN164	1.4 ± 0.3	...
PN165	0.04 ± 0.07	8.54 ± 0.05
PN166	...	8.5 ± 0.2
PN167	0.0 ± 0.1	...
PN168	1.3 ± 0.2	...
PN169	0.2 ± 0.2	...
PN170
PN171	1.3 ± 0.3	...
PN172	0.1 ± 0.1	...
PN173	0.0	...
PN174	0.40 ± 0.04	8.44 ± 0.09
PN175	0.7 ± 0.2	...
PN176	1.1 ± 0.3	...
PN177	0.3 ± 0.2	...
PN178	0.28 ± 0.10	...
PN179	0.0	...
PN180	0.9 ± 0.1	...
PN181	0.3 ± 0.7	...
PN182	0.4 ± 0.2	...
PN183
PN184	0.66 ± 0.10	8.53 ± 0.08
PN185	0.2 ± 0.2	8.5 ± 0.1
PN186	0.2 ± 0.1	...
PN187	0.0	...
PN188	0.30 ± 0.10	8.5 ± 0.2
PN189	0.0	...
PN190	0.3 ± 0.2	...

Table A.4—Continued

ID	A_V	$\log(\text{O}/\text{H})+12$
PN191	0.3 ± 0.1	...
PN192	0.4 ± 0.1	...
PN193
PN194	0.2 ± 0.7	...
PN195	1.4 ± 0.2	8.31 ± 0.06
PN196	0.3 ± 0.1	8.6 ± 0.1
PN197	0.0 ± 0.3	...
PN198	0.06 ± 0.10	...
PN199	0.04 ± 0.10	...
PN200	0.2 ± 0.2	...
PN201	0.0	...
PN202	0.1 ± 0.1	...
PN203	0.9 ± 0.1	...
PN204
PN205	0.6 ± 0.4	...
PN206
PN207	0.0	...
PN208	0.0	...
PN209
PN210
PN211	0.60 ± 0.08	8.6 ± 0.1
PN212	1.0 ± 0.8	...
PN213	1.2 ± 0.4	...
PN214	0.8 ± 0.4	...
PN215	0.6 ± 0.2	...
PN216	0.46 ± 0.05	...
PN217	0.5 ± 0.2	...
PN218	1.3 ± 0.3	...
PN219	0.5 ± 0.7	...
PN220	0.0	...
PN221	0.0 ± 0.1	...
PN222
PN223	0.4 ± 0.4	...
PN224	1.0 ± 0.7	...
PN225	1.2 ± 0.6	...
PN226	0.8 ± 0.3	...
PN227
PN228

Table A.4—Continued

ID	A_V	$\log(\text{O}/\text{H})+12$
PN229	0.7 ± 0.1	...
PN230
PN231	0.1 ± 0.2	...
PN232
PN233	0.0	...
PN234	0.4 ± 0.1	...
PN235	0.4 ± 0.3	...
PN236	1.0 ± 0.2	...
PN237	0.5 ± 0.3	...
PN238	0.0	...
PN239	0.6 ± 0.2	...
PN240	0.0	...
PN241	0.0 ± 0.1	...
PN242	0.3 ± 0.1	8.67 ± 0.09
PN243	0.19 ± 0.08	...
PN244	2.8 ± 0.3	...
PN245
PN246	1.5 ± 0.3	...
PN247	...	8.7 ± 0.1
PN248	0.7 ± 0.9	...
PN249	0.75 ± 0.09	...
PN250	0.0	...
PN251	0.32 ± 0.10	8.0 ± 0.1
PN252	1.0 ± 0.6	...
PN253	0.5 ± 0.3	...
PN254	0.9 ± 0.5	...
PN255	0.6 ± 0.1	...
PN256	1.3 ± 0.2	...
PN257	0.1 ± 0.5	...
PN258	1.7 ± 0.2	...
PN259	1.6 ± 0.6	...
PN260	0.09 ± 0.07	8.62 ± 0.08
PN261	0.6 ± 0.2	8.1 ± 0.2
PN262	0.75 ± 0.10	...
PN263	0.9 ± 0.2	...
PN264	1 ± 1	...
PN265	0.3 ± 0.3	...
PN266

Table A.4—Continued

ID	A_V	$\log(\text{O}/\text{H})+12$
PN267	1 ± 1	...
PN268
PN269	0.3 ± 0.3	...
PN270
PN271	0.9 ± 0.3	...
PN272	1.1 ± 0.3	...
PN273	0.05 ± 0.08	...
PN274	0.7 ± 0.5	...
PN275	1.0 ± 0.2	...
PN276	0.0	8.1 ± 0.2
PN277
PN278	0.73 ± 0.09	8.1 ± 0.2
PN279	0.0	...
PN280	1.0 ± 0.2	...
PN281	0.7 ± 0.2	...
PN282
PN283	0.4 ± 0.4	...
PN284
PN285	0.7 ± 0.4	...
PN286	0.2 ± 0.3	...
PN287	0.4 ± 0.3	...
PN288	0.8 ± 0.2	7.7 ± 0.1
PN289	0.0	8.4 ± 0.1
PN290	1.9 ± 0.2	...
PN291	0.1 ± 0.1	...
PN292	0.3 ± 0.4	...
PN293	0.59 ± 0.09	...
PN294	0.0	...
PN295	1.4 ± 0.9	...
PN296	1.5 ± 0.2	...
PN297	0.19 ± 0.07	...
PN298	0.3 ± 0.1	...
PN299	0.1 ± 0.1	...
PN300
PN301	0.2 ± 0.2	8.3 ± 0.1
PN302
PN303	1.7 ± 0.1	...
PN304	0.10 ± 0.06	...

Table A.4—Continued

ID	A_V	$\log(\text{O}/\text{H})+12$
PN305	0.56 ± 0.09	8.4 ± 0.1
PN306	0.5 ± 0.2	...
PN307	0.6 ± 0.2	7.9 ± 0.1
PN308	0.28 ± 0.08	8.69 ± 0.09
PN309	0.4 ± 0.3	...
PN310
PN311	0.8 ± 0.2	...
PN312	0.7 ± 0.1	...
PN313	1.5 ± 0.3	...
PN314
PN315	0.5 ± 0.1	...
PN316	0.2 ± 0.3	...
PN317	1.2 ± 0.7	...
PN318
PN319	1.1 ± 0.1	...
PN320	0.1 ± 0.4	...
PN321	1.3 ± 0.2	...
PN322	1.7 ± 0.3	...
PN323	0.5 ± 0.6	...
PN324
PN325	0.3 ± 0.1	...
PN326	0.3 ± 0.1	...
PN327	2.4 ± 0.3	...
PN328	2 ± 1	...
PN329	1.0 ± 0.7	...
PN330	0.0	...
PN331	0.27 ± 0.09	...
PN332	1.0 ± 0.3	...
PN333	0.6 ± 0.2	...
PN334
PN335
PN336	1.2 ± 0.9	...
PN337	1.5 ± 0.3	...
PN338
PN339	2.5 ± 0.5	...
PN340	0.6 ± 0.4	...
PN341	1.9 ± 0.8	...
PN342	1.7 ± 0.7	...

Table A.4—Continued

ID	A_V	$\log(\text{O}/\text{H})+12$
PN343
PN344	1.4 ± 0.4	...
PN345	0.4 ± 0.1	...
PN346	0.6 ± 0.5	...
PN347	2.0 ± 0.6	...
PN348	0.2 ± 0.2	...
PN349
PN350	0.4 ± 0.8	...
PN351
PN352	0.9 ± 0.5	...
PN353	1.0 ± 0.3	...
PN354
PN355	0.1 ± 0.3	...
PN356
PN357	0.6 ± 0.5	...
PN358
PN359
PN360	0.8 ± 0.5	...
PN361
PN362
PN363
PN364	1.0 ± 0.3	...
PN365	0.7 ± 0.8	...
PN366	3.95 ± 0.05	...
PN367	0.49 ± 0.10	...
PN368	0.3 ± 0.1	8.7 ± 0.1
PN369	0.4 ± 0.4	...
PN370	1.81 ± 0.05	8.47 ± 0.04
PN371	0.6 ± 0.5	...
PN372	0.5 ± 0.2	...
PN373
PN374	0.0	...
PN375	0.0	...
PN376	0.3 ± 0.4	...
PN377
PN378
PN379
PNh001	0.1 ± 0.1	...

Table A.4—Continued

ID	A_V	$\log(\text{O}/\text{H})+12$
PNh002
PNh003	0.2 ± 0.4	...
PNh004	0.0	...
PNh005
PNh006	0.1 ± 0.2	...
PNh007
PNh008	0.0	8.7 ± 0.1
PNh009
PNh010
PNh011	0.0	...
PNh012	0.17 ± 0.07	...
PNh013	0.0	...
PNh014
PNh015	0.3 ± 0.4	...
PNh016	0.3 ± 0.3	...
PNh017	0.01 ± 0.03	...
PNh018	0.2 ± 0.1	...
PNh019	0.02 ± 0.06	...
PNh020	0.22 ± 0.10	8.61 ± 0.07
PNh021	...	8.62 ± 0.05
PNh022	0.0	...
PNh023
PNh024
PNh025	0.1 ± 0.2	...
PNh026	0.1 ± 0.1	...
PNh027	0.07 ± 0.05	8.70 ± 0.04
PNh028	0.4 ± 0.2	...
PNh029	...	8.56 ± 0.03
PNh030	0.2 ± 0.1	...
PNh031	0.0	...
PNh032	0.3 ± 0.1	...
PNh033
PNh034	0.1 ± 0.4	...
PNh035	1.36 ± 0.06	8.04 ± 0.07
PNh036	0.0	8.5 ± 0.2
PNh037	0.2 ± 0.2	8.4 ± 0.1
PNh038	0.0	8.2 ± 0.1
PNh039	0.2 ± 0.3	...

Table A.4—Continued

ID	A_V	$\log(\text{O}/\text{H})+12$
PNh040	0.0	...
PNh041
PNh042	0.2 ± 0.3	...
PNh043	0.11 ± 0.09	...
PNh044	0.22 ± 0.08	8.3 ± 0.1
PNh045	0.6 ± 0.2	...
PNh046	0.29 ± 0.09	...
PNh047
PNh048	0.0	8.2 ± 0.1
PNh049	0.3 ± 0.1	...
PNh050	0.0	...
PNh051	0.2 ± 0.3	...
PNh052	0.09 ± 0.06	...
PNh053	0.17 ± 0.06	...
PNh054
PNh055	0.51 ± 0.07	...
PNh056
PNh057
PNh058	0.05 ± 0.07	8.51 ± 0.07
PNh059	0.26 ± 0.06	8.80 ± 0.10
PNh060	0.0	...
PNh061	...	8.39 ± 0.05
PNh062	0.32 ± 0.06	...
PNh063	0.1 ± 0.5	...
PNh064	0.2 ± 0.2	...
PNh065	...	8.50 ± 0.05
PNh066
PNh067	0.0	...
PNh068
PNh069	0.3 ± 0.1	...
PNh070	0.24 ± 0.07	...
PNh071	0.08 ± 0.08	8.6 ± 0.1
PNh072	0.1 ± 0.1	...
PNh073
PNh074	0.0	...
PNh075	0.1 ± 0.2	...
PNh076	0.0	...
PNh077	0.3 ± 0.2	...

Table A.4—Continued

ID	A_V	$\log(\text{O}/\text{H})+12$
PNh078	0.3 ± 0.2	...
PNh079	0.05 ± 0.06	...
PNh080	0.1 ± 0.1	...
PNh081	...	8.09 ± 0.08

Note. — See caption for Table A.3.

Table A.5. Fitted parameters for the abundance profiles of M31 HII regions and PNe

	N	Bootstrap		Spearman	
		Central (dex)	Slope (dex kpc ⁻¹)	ρ	p
<i>HII regions — All</i>					
A_V	199	2.31 ± 0.26	-0.0690 ± 0.0168	-0.31	8×10^{-06}
$\log([\text{N II}]/\text{H}\alpha)$	223	-0.42 ± 0.06	-0.0087 ± 0.0048	-0.17	0.01
R_{23}	61	0.43 ± 0.06	0.0169 ± 0.0044	0.54	8×10^{-06}
P	61	0.26 ± 0.08	0.0077 ± 0.0061	0.18	0.18
$\log(\text{O}/\text{H})+12$ (Z94)	60	9.10 ± 0.06	-0.0208 ± 0.0048	-0.57	2×10^{-06}
$\log(\text{O}/\text{H})+12$ (KD02)	136	8.96 ± 0.06	-0.0096 ± 0.0049	-0.33	1×10^{-04}
$\log(\text{O}/\text{H})+12$ (N06 N2)	192	9.13 ± 0.07	-0.0195 ± 0.0055	-0.26	3×10^{-04}
$\log(\text{O}/\text{H})+12$ (N06 O3N2)	100	8.98 ± 0.08	-0.0130 ± 0.0068	-0.19	0.06
$\log(\text{O}/\text{H})+12$ (PT05)	48	8.42 ± 0.09	-0.0054 ± 0.0064	-0.08	0.60
$\log(\text{N}/\text{H})+12$ (PVT ONS)	52	7.83 ± 0.07	-0.0303 ± 0.0049	-0.53	5×10^{-05}
<i>HII regions — Stellar</i>					
A_V	92	2.20 ± 0.36	-0.0555 ± 0.0231	-0.27	0.01
$\log([\text{N II}]/\text{H}\alpha)$	98	-0.34 ± 0.07	-0.0080 ± 0.0056	-0.14	0.18
R_{23}	14	0.54 ± 0.12	0.0107 ± 0.0096	0.52	0.06
P	14	0.04 ± 0.11	0.0218 ± 0.0068	0.55	0.04
$\log(\text{O}/\text{H})+12$ (Z94)	14	9.00 ± 0.16	-0.0152 ± 0.0133	-0.52	0.06
$\log(\text{O}/\text{H})+12$ (KD02)	47	8.92 ± 0.12	-0.0037 ± 0.0092	-0.16	0.27
$\log(\text{O}/\text{H})+12$ (N06 N2)	72	9.24 ± 0.11	-0.0224 ± 0.0082	-0.39	6×10^{-04}
$\log(\text{O}/\text{H})+12$ (N06 O3N2)	25	9.10 ± 0.13	-0.0191 ± 0.0110	-0.33	0.10
$\log(\text{O}/\text{H})+12$ (PT05)	10	8.18 ± 0.19	0.0077 ± 0.0141	0.33	0.35
$\log(\text{N}/\text{H})+12$ (PVT ONS)	10	7.80 ± 0.16	-0.0283 ± 0.0112	-0.42	0.23
<i>HII regions — Diffuse</i>					
A_V	107	2.75 ± 0.37	-0.1066 ± 0.0261	-0.40	2×10^{-05}
$\log([\text{N II}]/\text{H}\alpha)$	125	-0.37 ± 0.06	-0.0177 ± 0.0049	-0.26	4×10^{-03}
R_{23}	47	0.38 ± 0.07	0.0210 ± 0.0044	0.52	2×10^{-04}
P	47	0.33 ± 0.11	0.0033 ± 0.0089	0.08	0.60
$\log(\text{O}/\text{H})+12$ (Z94)	46	9.16 ± 0.07	-0.0248 ± 0.0048	-0.56	6×10^{-05}
$\log(\text{O}/\text{H})+12$ (KD02)	89	9.01 ± 0.04	-0.0160 ± 0.0031	-0.43	2×10^{-05}
$\log(\text{O}/\text{H})+12$ (N06 N2)	120	9.09 ± 0.09	-0.0195 ± 0.0070	-0.20	0.03
$\log(\text{O}/\text{H})+12$ (N06 O3N2)	75	8.93 ± 0.11	-0.0102 ± 0.0095	-0.11	0.35
$\log(\text{O}/\text{H})+12$ (PT05)	38	8.51 ± 0.09	-0.0113 ± 0.0065	-0.16	0.33
$\log(\text{N}/\text{H})+12$ (PVT ONS)	42	7.83 ± 0.08	-0.0300 ± 0.0058	-0.54	2×10^{-04}
<i>PNe — Disk</i>					
A_V	333	0.58 ± 0.08	0.0070 ± 0.0071	0.04	0.51
$\log([\text{N II}]/\text{H}\alpha)$	277	-0.57 ± 0.05	-0.0023 ± 0.0044	-0.05	0.38

Table A.5—Continued

	N	Bootstrap		Spearman	
		Central (dex)	Slope (dex kpc ⁻¹)	ρ	p
R_{23}	148	1.20 ± 0.03	-0.0016 ± 0.0027	-0.07	0.42
P	148	0.93 ± 0.02	-0.0027 ± 0.0020	-0.17	0.04
log(O/H)+12 (direct)	51	8.47 ± 0.09	-0.0056 ± 0.0076	-0.11	0.45

Note. — The bootstrap fitting reported in this table is described in Section 3.3.2. The central value and slope define the best-fit line to the data with respect to the de-projected radius in M31.

Appendix B

Preparing Undergraduates for Research Careers

"Preparing Undergraduates for Research Careers: Using Astrobites in the Classroom," N. E. Sanders, S. Kohler, E. Newton 2012, *Astronomy Education Review*

Abstract

Because undergraduate participation in research is a longstanding and increasingly important aspect of the career path for future scientists, students can benefit from additional resources to introduce them to the culture and process of research.

We suggest the adoption of the web resource Astrobites as a classroom tool to increase the preparation of undergraduate physics and astronomy students for careers in research. We describe the content and development of the website,

discuss previous university courses that have made use of Astrobites, and suggest additional strategies for using Astrobites in the classroom.

B.1 Introduction

Research experience is a vital aspect of undergraduate education in the physical sciences, as well as an increasingly-critical qualification for graduate admissions (Crowe and Brakke 2008, Russell et al. 2007, DeHaan 2005, Wilkerson 2007). However, many developmental barriers stand in the way of undergraduate students successful participation in research, even for those with strong conceptual and technical backgrounds from coursework. Comprehension of the specialized jargon and idioms of the field, understanding of research practices and technical methods, and familiarity with the technical literature are useful knowledge that students new to research lack. The challenge of obtaining this background can be particularly intimidating to undergraduates working with more senior researchers who acquired a more complete command of these faculties through a decade or more of undergraduate, graduate, and post-doctoral study.

Immersion in scientific discourse through activities such as seminar attendance and interaction with senior researchers has been a leading pathway for undergraduates to attain literacy in research, similar to the widely-applied philosophy for education in foreign language (Johnson and Swain 1997). However, the time available for such direct interaction is necessarily limited, and can vary substantially depending on the size of the host department at the students institution. To supplement these important real-world interactions, virtual tools

can be used to increase student immersion (Price 2007, Chang et al. 2012).

In this commentary, we suggest the use of the web resource Astrobites as a learning tool in undergraduate astronomy courses. We describe the content and goals of the Astrobites website and its authorship, discuss previous uses of Astrobites in formal academic settings, and suggest novel applications of its content to prepare undergraduates for careers in research.

B.2 Describing Astrobites

The Astrobites website (<http://astrobites.com>), founded in December 2010, is an online readers digest for the astrophysics preprint server astro-ph.¹ As illustrated in Figure 1, the website publishes succinct (47 paragraph) summaries of the methods, results, conclusions, and context of new research papers in astrophysics posted to astro-ph. The summaries are designed for undergraduates who have taken coursework in the physical sciences. Knowledge of basic physical concepts (e.g. energy conservation or blackbody radiation) is assumed, but relevant terminology and research methods are defined and links are provided to detailed references. Astrobites articles incorporate figures from the original sources, guiding readers to understand the visual presentation of key results from the paper. About 400 of these summaries have been posted to date, with a current publication rate of one per day. Additionally, Astrobites also periodically publishes pieces with career advice for young researchers, notices of professional opportunities available to undergraduate students (such as Research Experiences for Undergraduates, REU, programs), and other supplementary content at a rate

The screenshot shows the Astrobites website interface. At the top left is the 'astrobites' logo with the tagline 'THE ASTRO-PH READER'S DIGEST'. A search bar is located at the top right. Below the logo is a navigation menu with links for HOME, ABOUT, GLOSSARIES, MEET THE AUTHORS, YOUR RESEARCH, and ASTRO-PH. A 'SUBSCRIBE TO RSS' button is also present. The main content area features a large image of a star field. Below the image, the article title 'How to Make "A Star that Should Not Exist"' is displayed, along with the author 'ANNA ROSEN' and the date 'APRIL 24, 2012'. The article is categorized under 'DUST, LOW-MASS STARS, POPULATION III STARS, STAR FORMATION, SUPERNOVAE'. A summary of the article is provided, mentioning the discovery of a metal-poor halo star and the authors' reconstruction of its birth environment. A figure is included, showing a comparison of observed element abundance ratios for star J102915+172927 against models for progenitor masses of 20, 35, and 50 solar masses. The figure consists of three panels, each showing a plot of [X/Fe] versus atomic number for various elements. The right sidebar contains sections for 'EMAIL SUBSCRIPTION', 'POST CATEGORIES' (including Career navigation, Current Events, Daily paper summaries, Personal experiences, Quick notes, Topic Overview, and Undergraduate Research), 'ARCHIVES' (with a 'Select Month' dropdown), and 'POPULAR TOPICS' (including AGN, astronomical methods, astronomy, astrophysics, black holes, cosmology, dark matter, exoplanets, galaxies, galaxy clusters, galaxy evolution, instrumentation, interstellar medium, Kepler observations, planetary science, simulations, and exoplanets).

Figure B.1.— Screenshot of the Astrobites website, featuring the summary of Schneider et al. (2012). Accessed 2012 April 30.

of about twice per week.

Astrobit.es was created and is developed and maintained by graduate students in astrophysical sciences from throughout the United States and Europe (including the authors of this commentary). A regular rotation of 30 authors each write 1 Astrobit.es post per month and an additional set of 10 graduate students provide supplemental contributions.² The motivation for drawing on graduate students to prepare content for Astrobit.es is two-fold: 1) researchers at this stage of their career are sufficiently expert in the content of the research papers to prepare summaries, but are also aware of the level of familiarity to expect from the undergraduate target audience, and 2) the graduate students benefit from the pedagogical exercise of synthesizing research papers into an accessible format. Astrobit.es currently receives 300 regular readers per day, as measured by returning visitors tracked by Google Analytics. In addition, an informal September 2011 reader survey (for which there were 125 respondents) indicated that 2/3 of our readers do not visit our website, but instead subscribe to our RSS feed. The survey also showed that 20% of the respondents were undergraduate students. The remainder of the readership is approximately evenly divided between graduate students in astronomy, researchers who have already earned the PhD, and non-professional astronomy enthusiasts. We therefore estimate that Astrobit.es daily readership already includes ~150 students in our target demographic of undergraduates in a physical science field. In the same reader survey, ~80% of undergraduate respondents listed their career goal as researcher in astrophysics or a related field.

B.3 Astrobites in the Classroom

B.3.1 Past uses of Astrobites

To assess the usage of Astrobites in undergraduate classrooms to date, we performed a survey targeted at both students and educators in our readership that have used Astrobites in the classroom.³ We received responses from 4 students and 6 educators that indicated that they had used Astrobites in a class. From among these responses, we present two anecdotes regarding the use of Astrobites in undergraduate classrooms:

Astronomy 20, Basic Astronomy & the Galaxy, California Institute of Technology, Fall 2012, Prof. John Johnson

In this inquiry-based introductory astronomy course, students were instructed to maintain their own blogs.⁴ Students used the blogs to record problem-solving techniques learned in the class, as well as to produce original content including interviews with astronomers and summaries of modern research topics. Astrobites was presented to the students as a model for a blog of this type.

Astronomy 61, Current Problems in Astronomy and Astrophysics, Swarthmore College, Spring 2012, Prof. Eric Jensen

In this journal-club-style discussion course for advanced undergraduates, students were responsible for selecting and summarizing research papers for the weeks seminar on a rotating basis. Astrobites was offered to students as a resource

for selecting interesting papers and as a source for background information and context. These anecdotes illustrate a subset of the possibilities for incorporating Astrobites into a formal educational settings to increase student engagement outside the classroom.

B.3.2 Suggested uses of Astrobites

To supplement the existing examples of Astrobites usage in the classroom described in the previous section, here we present suggestions for novel applications of Astrobites in undergraduate curricula.

Reading assignments: Students are asked to read Astrobites throughout the semester, to increase immersion in astronomy outside the classroom and to reinforce concepts learned in lectures. Astrobites would therefore be used in a manner similar to web-based multimedia learning modules as pre-lecture assignments to supplement textbook materials (Stelzer et al. 2009, Sadaghiani 2012). Student participation could be evaluated during in-class discussions of current research, or by asking students to formulate follow-up questions based on the reading. These questions could be submitted for class discussion, or could be posted directly on the Astrobites website (see 4 below).

Written summaries Students are asked to write their own summaries of research papers in astronomy, modeled on the format of Astrobites. These research summaries could be assigned periodically throughout the semester, or as a single term project where the students are asked to review several

topical papers. The Astrobites website provides a convenient archive of brief, informative, and accessible summaries of recent research in astrophysics and can therefore serve as a resource to help students identify specific studies or topics that have methodology and results that interest them. This obviates the need for students to become sufficiently expert in the full range of astrophysics research to select a recent paper from a general bibliography of publications. If student writing is posted online, in a blog format, it may facilitate peer discussion and encourage students to make high-order connections between scientific topics discussed in the classroom and research methods (Daniels 2010).

In-class presentations Students are asked to describe a research paper in astrophysics to their peers via an in-class presentation. As in #2 above, the Astrobites website provides an archive of summaries which students can use to select interesting papers or topics. Moreover, if students plan to present on a paper that was already discussed on Astrobites, their classmates can read the Astrobites summary to rapidly familiarize themselves with the subject matter so they may come prepared to start a discussion. In this way, students can engage in a collaborative argumentation learning environment where they can debate the merits of the scientific ideas presented in the papers, as well as the assumptions that the ideas rely on (Bell and Linn 2000).

Discussion forum Students are asked to use the commenting feature of the Astrobites website to hold a discussion forum on a given research topic. By holding this discussion on the website rather than in the classroom,

students have the opportunity to formulate their responses after doing background research into the topics as necessary and to cite relevant materials. Furthermore, because Astrobites authors and researchers from throughout the world (including, often, the authors of the paper in discussion) read Astrobites, the discussion may broaden to include a wide range of perspectives and expertise.

B.4 Conclusions

In this commentary, we have presented Astrobites as a web resource that can be integrated into formal classroom education to improve undergraduate preparation for careers in research. We have described previous applications of Astrobites to the undergraduate curriculum and suggested novel uses for the website in future curricula. In the sense that Astrobites is written by and for students in astronomy, and because many of the strategies we have suggested involve classroom discussions and peer-teaching, the usage of Astrobites in the classroom is a form of peer-assisted learning (see e.g. Parkinson 2009). If the adoption of Astrobites as a mechanism for this type of instruction becomes more widespread, it could facilitate the use of statistically-validated studies on the educational impact of Astrobites or other web-based pedagogy tools in the classroom.

Appendix C

Interactive Modules for Science Education

”A New Approach to Developing Interactive Software Modules through Graduate Education,” N. E. Sanders, C. Faesi, A. A. Goodman 2013, *Journal of Science Education and Technology*

Abstract

Educational technology has attained significant importance as a mechanism for supporting experiential learning of science concepts. However, the growth of this mechanism is limited by the significant time and technical expertise needed to develop such products, particularly in specialized fields of science. We sought to test whether interactive, educational, online software modules can be developed effectively by students as a curriculum component of an advanced science course.

We discuss a set of fifteen such modules developed by Harvard University graduate students to demonstrate various concepts related to astronomy and physics. Their successful development of these modules demonstrates that online software tools for education and outreach on specialized topics can be produced while simultaneously fulfilling project-based learning objectives. We describe a set of technologies suitable for module development and present in detail four examples of modules developed by the students. We offer recommendations for incorporating educational software development within a graduate curriculum and conclude by discussing the relevance of this novel approach to new online learning environments like edX.

C.1 Introduction

Instructor demand for and utilization of educational technology to enable experiential learning is well documented (see e.g. Bell et al. 2008 and Campbell et al. 2010). Providing interactive software tools and manipulable simulations in addition to traditional printed textbooks can enhance the classroom and out-of-classroom learning experience for some students (see Vogel et al. 2006 for a meta-analysis and review). Modern educational resources include software modules for desktop (Sadler et al. 1999; Härtel 2000; Monaghan & Clement 2000; Gazit et al. 2005; Kumar & Sherwood 2007; Lamb & Annetta 2012) and mobile (Cheng & Tsai 2013; Powell & Mason 2013; van der Kolk et al. 2013) devices and programs or web sites that enable distributed research or “citizen science” (Shell et al. 2011; Friedrich 2013) or bring results from academic research journals into

the classroom (Sanders et al. 2012b).

However, instructors typically lack the time and/or engineering expertise to develop software or online content of this type, and software developers often lack the content knowledge and/or interest to develop modules with significant educational value for advanced students. This has historically limited the availability of such software modules to only the most broadly salient topics, or content areas with significant associated industrial or academic research investment.

We set out to test a novel approach to the development of specialized software modules, utilizing a set of experts with the pre-requisite programming experience and content knowledge: graduate students. The module development task was integrated into a graduate course curriculum. Our motivations for enlisting graduate students in this effort are as follows.

First, the software development exercise is intended to fulfill the same educational objectives as other long-term project-based learning initiatives. These objectives include achieving student engagement and self-motivation, promoting conceptual understanding through problem solving and decision making in complex tasks, and appreciation for the application of scientific principles to realistic problems (Blumenfeld et al. 1991; Thomas 2000). Such projects may promote specialized learning through incorporated literature reviews and writing assignments. If instructors encourage interaction through in-class presentations or collaboration, the projects may also facilitate peer-learning.

Second, the product of the students' work is a publicly accessible and

reusable educational tool. Such software modules are often not available for specialized topics frequently encountered by astrophysics educators at the advanced undergraduate and graduate levels. Graduate students in astronomy can produce modules from their position as content experts, via their direct research experience and/or concurrent coursework. The student products have the potential to enhance learning on their target topics, as they may be the first interactive educational tools available for the subject. For topics with appeal to the broader public, the software products may serve an additional public outreach purpose. After a course ends, students, faculty, and technical professionals can collaborate to incorporate robust versions of relevant modules into formal “massive” online learning systems, currently represented by systems like edX.

Here we present the results of our test, a new software modules developed by graduate students in the Harvard University Department of Astronomy in the Spring of 2013 as a term project for the AY201b graduate course, “The Interstellar Medium and Star Formation.” Each of the fifteen enrolled students was required to produce a software module, amounting to a significant percentage of the total course grade. Project oversight was provided by the course Professor (A. Goodman) and graduate teaching fellows (N.E. Sanders and C. Faesi). In Section C.2 we discuss and compare the set of software technologies which the students used to develop their modules. We present a description of four example modules in Section C.3. We conclude with a set of recommendations for instructors seeking to implement a similar module development class requirement (Section C.4) and a discussion of how modules can be used in the context of massive online learning platforms (Section C.5).

C.2 Technologies for Module Development

Various software technologies provide convenient frameworks for students to develop online interactive modules. The key features desired in these technologies are ease of use (approachable learning curve for graduate students with research computing, but not software development, backgrounds), support (availability of sufficient tutorial material), suitability (pre-existing capability to display astronomical imagery, interactive plotting, or other scientific data visualization), and accessibility to users (online playback in web browsers on common platforms).

We have identified four technologies from the current software development landscape which best meet these criteria. Table C.1 summarizes these technologies. In the following sub-sections we describe each technology and provide web links to support resources for students developing modules.

C.2.1 WorldWide Telescope

(WWT) is an interactive scientific data visualization and aggregation package developed by Microsoft Research. WWT includes a comprehensive variety of all-sky and high resolution astronomical imagery from across the electromagnetic spectrum, as well as a 3D Universe visualization that can be zoomed from Earth to the solar system (animated with physically realistic orbital mechanics) to the large scale structure of the universe (visualizing 3D galaxy positions from the Sloan Digital Sky Survey). Users can import their own catalog data or imagery in a wide variety of standard formats, including ASCII, VOTable, and Excel for





	WorldWide Telescope 	JavaScript/d3 	Wolfram CDF 	Python 
Free to use authoring software	Y	Y	N	Y
Likelihood of graduate student prior familiarity	Low	Low	Medium	Medium
Technical experience required for module development	Low	High	Medium	High
Authoring software platform	Windows	Windows, Mac, Linux and Unix variants	Windows, Mac, Linux	Windows, Mac, Linux and Unix variants
Software installation requirements for module user	Low	Low	Medium	High
Technical requirements for distribution	Low	High	Low	Medium

Table C.1: Summary comparison of suitability and technical requirements for authors and users for module development technologies discussed in this article.

tables, and JPEG and FITS for images.

A key feature of WWT is the ability to author interactive narrated tours. The tours are built from a series of “slides” consisting of static or animated views of astronomical imagery. A tour proceeds by transitioning between these views, and it is typically accompanied by explanatory narration from the tour author. Users can pause the tour at any time during playback and manipulate the imagery displayed by the client (e.g. turning on overlays of observations in different wavelengths or rotating a 3D view of the solar system), and tours can include hyperlinks to web resources with additional information.

The flagship client software for WWT is a free Microsoft Windows desktop software package. WWT web clients have also been developed for both the Microsoft Silverlight plugin (already released) and for HTML5-enabled browsers (currently available as an application programming interface, API). At present, tours can only be authored in the desktop client, but tours can be played back in the desktop or web clients.

Developing a tour in WWT requires the least technical/programming experience of any of the technologies described here. WWT has extensive online documentation, video tutorials, as well as an active community of WWT outreach experts, the WWT Ambassadors program (WWTA), led by A. Goodman and collaborators in association with Microsoft Research, available as resources. The WWTA website can provide hosting of and distribution of tours free of charge to authors, enabling tours to reach a large audience assuming it has passed the quality requirements imposed by the WWTA program.

WWT offers extensive capabilities to display imagery, but relatively little functionality to display other data types interactively. The remaining technologies in our survey offer more flexibility, but developing advanced visualizations requires significantly more technical expertise from authors.

C.2.2 Javascript / d3

JavaScript is an interpreted programming (scripting) language. JavaScript is commonly used in so-called “Web 2.0” platforms such as Google Gmail and to perform smaller interactive functions in a vast number of pages on the web. JavaScript’s functionality will be familiar to users of other scripting languages popular among graduate student researchers, such as Python. Several JavaScript programming tutorials are available online (see for example CodeAcademy)

Many libraries have been developed and distributed to extend the core functionality of JavaScript. A popular JavaScript library for data visualization is d3.js, standing for “Data Driven Documents.” d3 allows for the display of scientific data in a wide variety of formats, including line plots and bar charts and extending to network graph browsers and map projections.

Scores of example pages produced in d3 are available on the project web page, complete with full source code and data files. These examples can serve as templates for student module development. Additionally, web pages are available that allow users to experiment with modifications to JavaScript and d3 code while watching the results appear in real time within a web browser window (see for example this page).

A pre-requisite for students intending to develop modules using JavaScript is familiarity with other web technologies, including HTML for web page development, and access to a web server for hosting (as many university departments provide).

C.2.3 Wolfram Computable Documents

The Computable Document Format (CDF), designed by Wolfram Research, takes interactive code written in Wolfram’s Mathematica software and renders it graphically in either a standalone player or via a browser plugin. Mathematica is a high-level computing language that is commonly used for a wide range of scientific and mathematical applications such as equation solving, numerical integration, two- and three-dimensional plotting, and data analysis. It will already be familiar to many graduate students through use in coursework and/or research, and has a shallow learning curve and thorough tutorials and documentation. Mathematica is proprietary software that must be purchased, although institutional licenses are common, and a student (discounted) version is also available.

CDF relies on the Mathematica “manipulate” command, which allows plot inputs to be customized by the user via interactive elements such as sliders, radio buttons, and menus. Plotting is updated dynamically. Code is written directly in the Mathematica language and formatted appropriately for CDF viewing. Text can be incorporated to provide topical background and orient the user with the module. Importantly, the user need only have the CDF player to view the document, which is available as a free download.

The CDF platform has been utilized by Wolfram to launch the new Wolfram Demonstrations Project, a central repository of user-created modules in science, engineering, mathematics, and economics. Demonstration source codes are available for download and can serve as templates or examples. Student modules are ideally suited for submission to the Demonstrations Project, and one of our students, Lauren Woolsey, has already had her module on the Zeeman effect accepted to the Project. The increased visibility possible through such promotion is an additional beneficial side effect of using the Wolfram CDF technology for module implementation.

C.2.4 Python

Like JavaScript, Python is an interpreted programming language. However, it is typically used for desktop application development or for server-side scripting rather than in web applications run in the browser. A disadvantage of Python as a module development technology is therefore that it requires users to download and manually run software on their computers, and users must have already installed the Python framework. However, software developed in Python does not necessarily need to be installed by end users, and can be run as a standalone ASCII script file (depending on what associated data files and libraries are needed). The software can be hosted using any web space or file hosting service. And, (soon) when “hosted” web-ready Python installations come to Massive Online Open Course (“MOOC”) platforms like edX, then learners using modules installed on those MOOC platforms will not need a desktop Python installation.

The advantage for module authors is that many graduate students are already familiar with Python and its associated scientific data analysis and visualization modules (numpy, and matplotlib) from their research experience. Like JavaScript, many online programming tutorials are available for learning Python (e.g. CodeAcademy).

The matplotlib library allows for the creation of sophisticated data visualizations using Python. Any matplotlib visualization can be made animated and/or interactive using an object oriented programming interface for adding customizable buttons, switches, sliders, and other interface objects. As in the case of d3, code for plots from a library of examples can be used as templates for student projects.

C.3 Examples of Student Modules

Here we describe in detail four of the fifteen modules created by graduate students in the Spring 2013 semester Harvard AY201b course. These modules have been selected to showcase the diversity of subject matter, software technologies, and target audiences addressed by the student projects. Summaries of and web links for all the modules can be found at the AY201b course website.

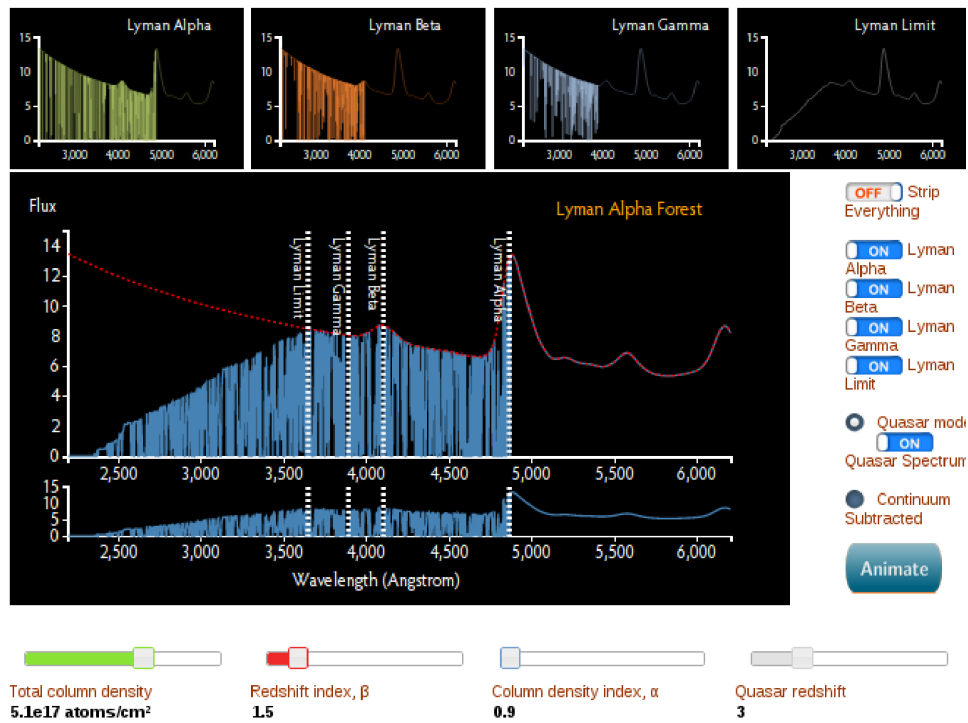


Figure C.1.— Screenshot of the Lyman Alpha forest JavaScript module developed by Yuan-Sen Ting

C.3.1 Simulating the Lyman Alpha Forest (Yuan-Sen Ting)

This module demonstrates the physical origin of the Lyman Alpha forest absorption features seen in the optical spectra of high-redshift quasars, one of the most important observational probes of the early universe (see e.g. Rauch 1998 for a review). The primary feature of the module is a physically realistic and fully-interactive visualization of the formation and observable spectrum of the Lyman Alpha forest, created using d3 and shown in Figure C.1. Interactive scalers and switches allow users to adjust the physical parameters of the simulated system, the properties of the displayed spectrum, and to animate the appearance of absorption features as a function of light travel time. Hovering over the interactive buttons yields pop-up boxes with descriptions of their functions.

The module is written in JavaScript and has several interactive features in addition to the simulation shown in Figure C.1. First, two versions of the detailed explanatory text (addressing of relevant topics in cosmology and spectroscopic line formation) are available for different audiences, 1) the general public and 2) undergraduate and graduate students in astronomy. A series of animated figures from the astrophysical literature accompany the advanced versions. Second, an additional interactive simulation (also made using d3) illustrates the formation of different spectroscopic line profiles as a function of physical conditions and the associated position on the curve of growth.

Ting's work exemplifies a full-featured interactive module suitable for use by several different audiences. The module supports inquiry-based exploration by

individual students, who can use the simulation to test and visualize hypotheses for the effects of changes to physical parameters that they generate based on descriptions they have read of Lyman Alpha forest formation in textbooks or Ting's own explanatory text. Classroom discussion at the undergraduate and graduate level can be facilitated by exploring similar hypotheses in a group setting, replacing the display of static plots or schematic chalkboard illustrations. Finally, as the simulation is scientifically accurate, it can be applied by research astronomers working in related fields to generate animations to accompany scientific presentations.

C.3.2 Landmarks of the Interstellar Medium (Meredith MacGregor)

Meredith MacGregor's WorldWide Telescope Tour "Landmarks of the ISM" guides viewers through the broad range of phenomenology in the interstellar medium (ISM) of the Milky Way, stopping at specific well-known objects (landmarks) and discussing relevant physical processes. This includes a multi-wavelength view of Kepler's supernova remnant, an infrared window into newly formed stars in NGC 2264, and a description of ionization in the IC 1396A ("Elephant's trunk") emission nebula.

Developed using the WWT Windows desktop client, the tour is available as a 16 megabyte standalone file (hosted on the module web site; see Figure C.2). The file includes the tour slides and playback program, audio narration recorded by the author and music, and images not already available through the WWT

interface. The tour can be viewed by importing this file into the Windows desktop client or cross-platform web clients.

The tour and its narration are designed for the general public, particularly for viewers with exposure to science at approximately a high school level. The tour includes hyperlinks to pages (hosted on the module web site) with additional details on topics discussed in the narration, including more advanced information and literature citations for learners at the undergraduate or graduate level.

C.3.3 The Effects of Clumpiness in Giant Molecular Clouds (George Miller)

In combination with its accompanying web site, this module enables users to simulate the observational signature of clumpiness in the structure of giant molecular clouds, the sites of star formation within galaxies (see e.g. Wolfire et al. 1993). Users can vary physical parameters including the clump size and filling factor, the width of the radio telescope beam, and the velocity dispersion of the clumps. Figures on the module interface visualize the clump geometry and velocity distribution, and a button allows users to simulate the observed line profile for their desired configuration (see Figure C.3).

The module was developed by George Miller using Python and the matplotlib library. The total codebase, including both simulation backend and user interface, consists of only about 300 lines of Python code distributed as a single script file. Users on any platform with Python installed can launch the code with a single command, with no installation necessary, as documented on the module web site.

The accompanying explanatory material on the module web site is appropriate for upper-level undergraduate or graduate students. Students at that level can use the module to explore the effects of different cloud parameters on the radio spectrum, and build intuition needed to interpret observations. The module could be used to facilitate in-class discussions of structure in the interstellar medium, or as a resource to accompany laboratory exercises involving radio telescopes.

C.3.4 Magnetohydrodynamic Shocks (Philip Mocz)

Philip Mocz's module provides an introduction to one-dimensional hydrodynamic shocks. The module allows users to explore the implications of the shock discontinuity for the fluid variables density, velocity, pressure, and magnetic field. Both the inviscid (zero viscosity) and magnetohydrodynamic (MHD) cases are included. The website includes a thorough introduction to the theory behind shocks (particularly the Riemann problem, e.g. Menikoff & Plohr 1989) as well as background material describing how more complex and realistic three-dimensional problems can be solved using numerical methods.

In the module itself, the user is invited to adjust the values of the fluid variables on either side of the shock discontinuity and observe the effects on the structure of the shock through dynamically updating plots (see Figure C.4). The website also includes a helpful list of suggested adjustments for the user to try when first using the module. This provides a natural connection between the theory and the demonstration, and gives the user context and guidance in exploring the visualization.

This module is written in Mathematica and viewed in a Computable Document Format (CDF) player embedded directly in the website. The interactive portion is seamlessly integrated with the supplementary content. The user need only download the free CDF player in order to access the full set of online materials.

As with several other modules produced for AY201b, Mocz's work is suitable for upper-level undergraduate or graduate students. The background material is thorough in introducing the shock-specific information, but assumes some understanding of advanced mathematics. Liberal use of schematics and figures aids intuition, and the interactive module itself builds nicely upon the theory. Since shocks are ubiquitous in many areas of astronomy as well as in physics, this website could serve as supplementary material for a range of courses, from fluid dynamics to the interstellar medium to high-energy astrophysics.

C.4 Recommendations for Instructors

Here we provide a set of recommendations for instructors who wish to implement a module development project as we have described in a graduate curriculum. These recommendations reflect our experience in teaching the Harvard AY201b course and are intended to provide support to the graduate student module developers and to improve the final products made available to users.

First, we recommend beginning the module development project by providing students with brief in-class tutorials of the software technologies to expose them

to relevant choices and functionality. In our case, we spent a total of two hours, spread over two class periods, on live tutorials, led by the Teaching Fellows. Section C.2 of this article includes links to a variety of online tutorial programs and sample/template codes. The modules now available on the AY201b website can serve as further examples. For classes of students with limited past experience in computation, we recommend that instructors focus on using the module technologies identified as having lower technical experience requirements in our Table 1 (Worldwide Telescope and Wolfram CDF). Additionally, instructors should identify technologies relevant to the subject matter of their course with which their students may have prior familiarity. This may include field-specific technologies beyond those we present here in the context of astrophysics.

Second, we recommend regular consultations between students and the teaching staff to monitor the progression of module development. An initial proposal should be submitted by students for instructors to evaluate the intended scope of the project. Requiring students to give in-class presentations of their module well before the final due date can serve the dual purpose of peer-teaching (with the presentation including substantive description of the science topic the module targets), and providing instructors with a snapshot of development progress so they may return feedback. Additional lecture discussion of the modules science target by instructors can ensure that the course's curriculum goals are met. For about half of the fifteen modules created in AY201b, substantial revisions to a student's module scheme were made after consultations and/or in-class presentations.

Some common difficulties may be experienced by students during module

development. Technical barriers may halt progress; instructors may wish to encourage affected students to focus on the scientific content of the module, and meanwhile help students find workarounds or contact other experts to troubleshoot technical issues. As well, students may have difficulty focusing their piece for a well-defined audience. If students have produced material too specialized or advanced for the intended target audience, this can be separated into a distinct online web page (as in the Ting module) or, in the case of a WWT tour, a second version (a “Director’s Cut”) can be made that includes additional details. This second version can easily be produced in the WWT authoring tool as an alternate audio narration track.

Third, it is critical for end users that the software modules be accompanied by written explanatory material. This should serve as an instruction manual for the software, as well as a pedagogical exercise for the students in documenting the scientific concepts their modules seeks to illustrate. Developing this text will play an important role in fulfilling the teaching objectives of the project, as students investigate their specialized topics in great detail and synthesize information as they would in a traditional term paper assignment. This material can be easily hosted online using a free service such as Wordpress.com, which Ting and MacGregor have done (see Section C.3).

Finally, we strongly recommend making a narrated video tour of the software available on an associated web page. This video will ideally show users the key functionality of the software module, and also discuss the most important scientific concepts it illustrates. As an example of such a narrated video tour, see the video produced by Ting for his Lyman Alpha forest module. Such tours are

particularly valuable for modules made using technologies not native to the web (e.g. Python)

C.5 Evaluation and Reuse of Modules in cMOOC Environments

We conclude with a discussion of the importance of these student-developed modules in the broader context of the growing landscape of online course materials, and a path forward for evaluating the effectiveness of the modules as educational tools. The students who created the AY201b modules were exceptionally motivated and worked intensely on their projects. The key motivator for the students was the idea that the work they were doing on a term project would be of legitimate use to others trying to learn the material they sought to explain.

Student writing and software products from the AY201b course have been made publicly available online through several means. Students in both the 2011 and 2013 versions of the biennial course contributed web-page style content on specific topics as their term projects. The AY201b WordPress site that incorporated the student content receives a surprisingly large number of views (> 10,000 per year) given the specialized nature of its content. Moreover, the 2013 AY201b graduate students were aware that their online modules would all be linked from the WordPress site, and that some modules would also be selected for incorporation into edX, the Massive Online Open Course (MOOC) environment

founded by MIT and Harvard in 2012. The selection of which modules went to edX would be (and now is being) made based on a combination of how relevant the modules subject matter is to advanced undergraduate courses, the usability of the module (user experience), and how adaptable the modules technology is to a web-based platform (see Table 1).

edX, at present, is offering primarily lecture-based courses, in their entirety, online. That form of MOOC, where an end-to-end replica of an in-person course is made available online, is known as an “xMOOC.” An alternative form of MOOC is known as a “cMOOC,” where the “c” stands for “connectivist”. One key goal of the AY201b module experiment was to see if graduate students could create material suitable for inclusion in a cMOOC-like environment. Now that the answer appears to be “yes,” our team is working with the edX staff at Harvard (HarvardX) to pair students whose modules are most suitable for a broad audience with technical professionals within the HarvardX organization, so that they can re-cast the modules into forms that will withstand high user demand online. It is likely that the three WWT-based modules developed will be put online first, thanks to WWT’s visual appeal and the relatively introductory-level nature of the modules made using it.

Interest in expanding HarvardX to include cMOOC-like modular content has been brewing ever since edX was announced, and it appears that the AY201b modules will be the first cMOOC-style content added to edX. The intent is two-fold: 1) learners seeking to know more about the specific topics covered will discover the modules on their own, much as they would otherwise discover a whole course on a broader topic; and 2) teachers at all levels seeking multimedia

content, to incorporate into both live courses and online ones, will find these modules and use them in much the same way they would have used articles or videos discovered in libraries or online in the past.

An important ancillary benefit of the inclusion of these modules in a cMOOC environment is the potential to use data from this system for evaluation. The edX platform allows for detailed monitoring of who uses what material and how, including the data needed to search for correlations between usage of each module and individual student performance across all courses throughout the edX environment. By exploring this data, we will be able to evaluate the educational impact of these modules using a large sample of online student users. We plan to report these usage and evaluation results in a follow-up publication after sufficient data has been collected, as well as to evaluate the impact of integrating these modules into future classroom versions of the Harvard AY201b course.

The interactive student-generated content we discuss here could easily be implemented in graduate-level courses across the sciences. While assignments of this type may be most easily implemented in fields where knowledge of computer programming is pre-requisite, they may hold even more educational value for students in fields where it is not. The finished online modules can serve as useful educational tools for all disciplines.

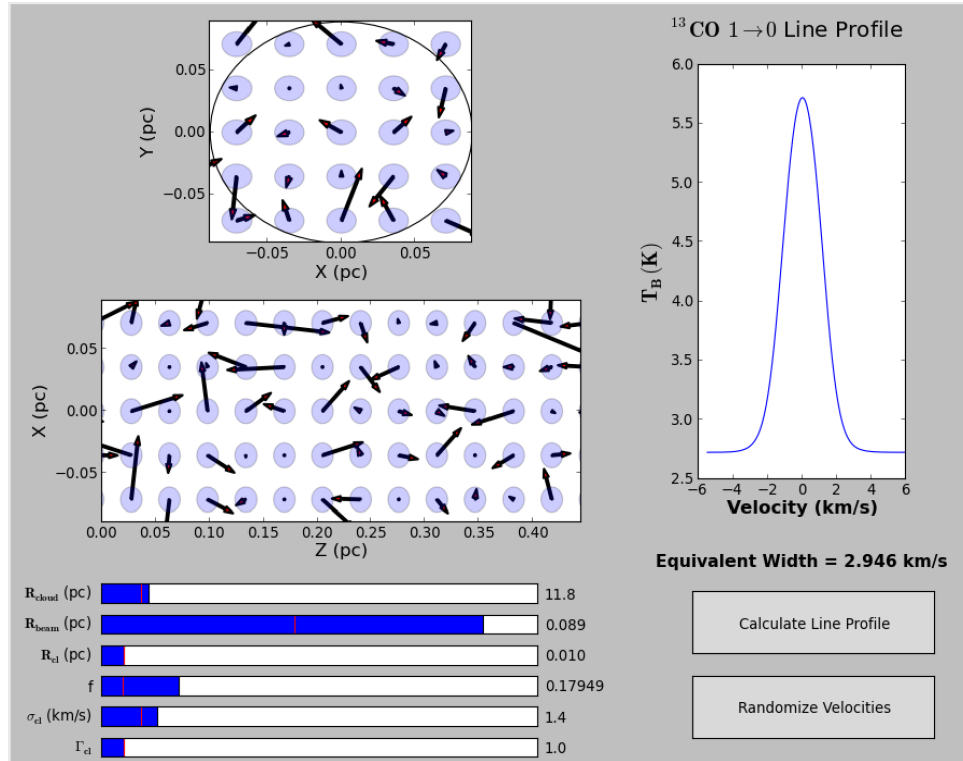


Figure C.3.— Screenshot of the interactive module visualizing the effect of clumpiness on the observed line profiles of molecular clouds, developed by George Miller

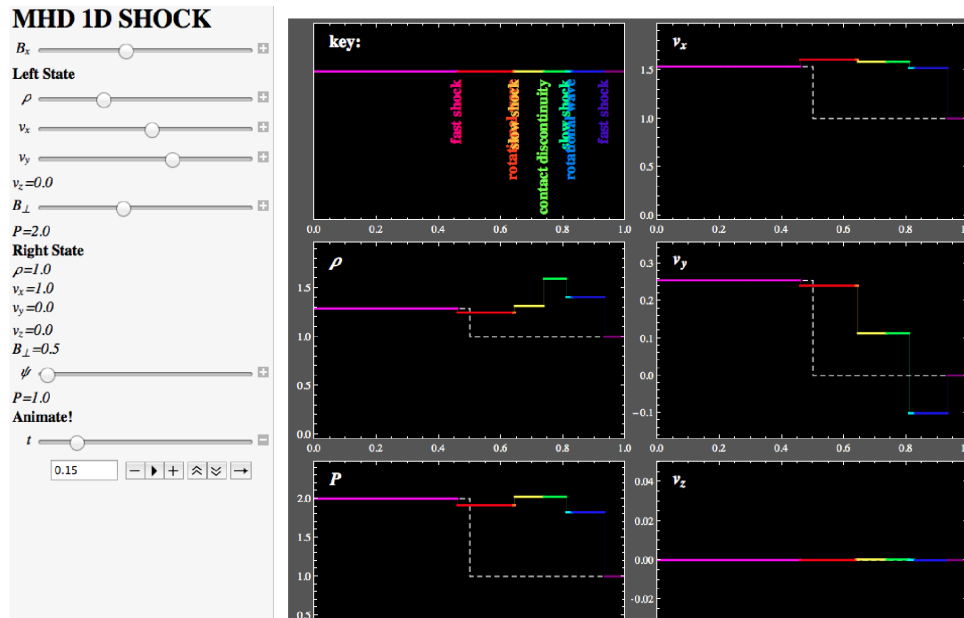


Figure C.4.— Screenshot of the Mathematica-based module on one-dimensional magnetohydrodynamic (MHD) shocks developed by Philip Mocz

Appendix D

Public Awareness, Policy, &

Science: A Mystic River Case

Study

While scientific research is a critical input to the decision making of public policymakers, few scientists (particularly in the physical sciences) have the opportunity to engage in the legislative or other political processes. The Rappaport Institute of Greater Boston at the Harvard Kennedy School of Government provides this opportunity through a fellowship program to approximately 10 advanced degree candidates from all fields, at universities throughout the Greater Boston area.

I served as a Rappaport Institute Public Policy Fellow in the summer of 2013, working as a Legislative Fellow in the offices of Senator Pat Jehlen

(D-Somerville) Representative Denise Provost (D-Somerville). My work focused on applying my background in the interpretation and analysis of scientific research to navigating the state-level legislative structure supporting clean water policy. In particular, our goal was to improve the water quality of the Mystic River, which flows through the Representative and Senators' districts, for the benefit of its recreational uses and ecological function. Through collaborations with other Mystic Watershed legislators, local community organizations like the Mystic River Watershed Association, and state agencies such as the Department of Environmental Protection, we developed a legislative strategy and agenda for first improving public awareness of the environmental issues facing Mystic communities and support for combating these issues, and second to effect change through infrastructure enhancement and regulation.

Many Mystic River Watershed municipalities have been designated Environmental Justice communities in recognition of their historically high burden of environmental pollution, including surface water discharges, and historically low levels of public spending and oversight to limit this burden. Combined Sewer Overflows (CSOs), purposeful discharges of raw or treated sewage from combined sewer systems (primarily during stormwater surge events), pose a particular danger to the Mystic River Watershed, contributing to high levels of bacterial contamination, low levels of dissolved oxygen, and high levels of floatable detritus. CSO discharges afflict many Massachusetts rivers due to our Commonwealth's aging water infrastructure system. Our legislative strategy aims to support renewal of the Mystic specifically, while providing equal benefits to all Massachusetts freshwater ecosystems. To that end, I applied scientific data

analysis, Geographic Information Systems, and interactive visualization tools (e.g. Section C) to develop print and online maps showing the scope and spread of the sewage discharge problem within Massachusetts (e.g. Figure D.1).

The primary outcomes of this experience were the drafting and filing by Sen. Jehlen and Rep. Provost of a bill (MA SD1867; Section D.1), with more than twenty co-sponsors, that would require agencies discharging sewage into MA rivers and streams to report those discharges to the state, so that citizens can be made aware of when public waterways are safe to recreate in, and when they are unsafe. This includes provisions for a Department of Environmental Protection-operated website, that would provide email notifications and a historical record of discharges, annual aggregate reporting, and the installation of signage at public access points.

I found the Rappaport Fellowship term provided invaluable exposure to not only the legislative process, but also exposure to the methods of communication, explication, and argumentation that are effective in influencing decision making beyond introspective scientific disciplines. These skills are complimentary to the communication skills exercised in academic scientific discourse, and necessary for scientists seeking to extend the impacts of their work beyond their field of study. Our Communicating Science (ComSciCon) Workshop series similarly aims to expose young scientists and engineers to the skills needed to communicate complex and technical concepts to broad and diverse audiences.

APPENDIX D. PUBLIC AWARENESS, POLICY, & SCIENCE: A MYSTIC RIVER CASE STUDY

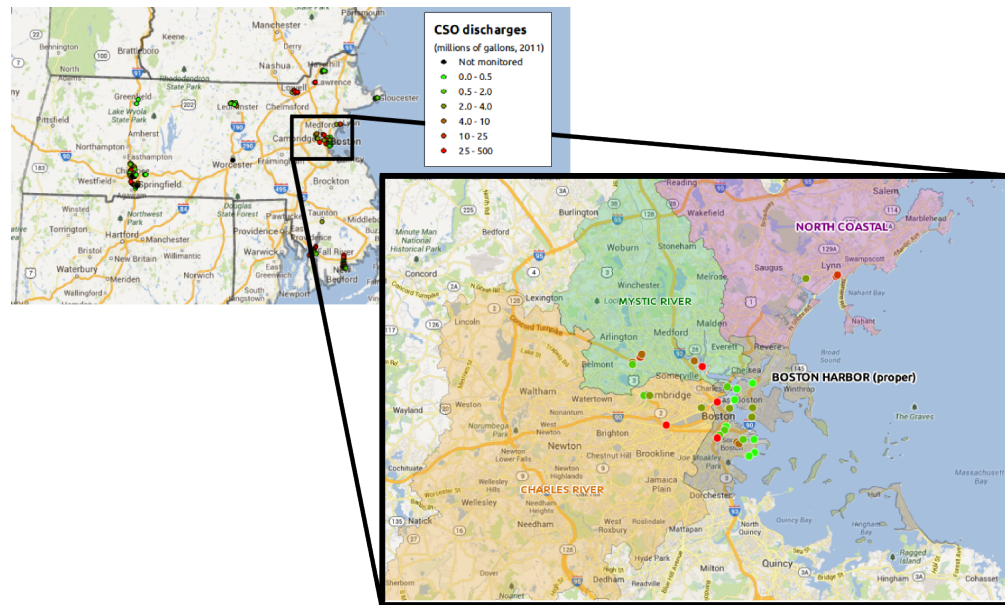


Figure D.1.— Overview of annual combined sewer overflow discharges into Boston-area watersheds. The color coding indicates the 2011 discharge volume for each outfall, and the shading on the inset plot displays the watershed hydrological boundaries.

APPENDIX D. PUBLIC AWARENESS, POLICY, & SCIENCE: A MYSTIC RIVER CASE STUDY

Table D.1. CSO discharges in Massachusetts by Senate district (2011)

District	Senator	Volume discharged (10 ⁶ gallons)	Number of discharges
First Bristol and Plymouth	Michael J. Rodrigues (D)	870.2	958
Hampden	James T. Welch (D)	599.7	999
First Suffolk and Middlesex	Anthony W. Petrucci (D)	422.4	46
Second Bristol and Plymouth	Mark C. Montigny (D)	366.5	647
First Middlesex	Eileen M. Donoghue (D)	290.0	186
Second Hampden and Hampshire	Michael R. Knapik (R)	180.3	710
Second Middlesex	Patricia D. Jehlen (D)	114.4	42
Middlesex, Suffolk, and Essex	Sal N. DiDomenico (D)	52.4	12
Third Essex and Middlesex	Thomas M. McGee (D)	46.0	61
Second Essex and Middlesex	Barry R. Finegold (D)	42.2	10
Second Suffolk	Sonia Chang-Diaz (D)	39.5	22
First Essex	Steven A. Baddour (D)	36.4	133
Worcester and Middlesex	Jennifer L. Flanagan (D)	29.4	137
Second Suffolk and Middlesex	Steven A. Tolman (D)	27.5	48
First Suffolk	John A. Hart Jr. (D)	18.7	66
First Plymouth and Bristol	Marc R. Pacheco (D)	3.7	2
First Essex and Middlesex	Bruce E. Tarr (R)	2.6	31
First Hampden and Hampshire	Gale D. Candaras (D)	1.6	31
Hampshire and Franklin	Stanley C. Rosenberg (D)	0.5	18
Second Worcester	Michael O. Moore (D)	0.0	0

Note. — This table is based on data compiled by D. Struck, New England Center for Investigative Journalism.

D.1 An Act Promoting Awareness of Safe Recreation in Public Waterways

SECTION 1. Section 26A of chapter 21 of the General Laws, as appearing in the 2012 Official Edition, is hereby amended by inserting the following definitions:-

CSO discharge, a discharge of treated, untreated, or incompletely treated sewage, industrial waste, or other waste into, directly or indirectly, a public waterway from a combined sewer system that has exceeded its maximum capacity.

CSO outfall, a location at which a combined sewer system is designed to produce a CSO discharge.

”Combined sewer system”, a system so designed or constructed as to allow surface runoff to enter the conduit carrying sewage, industrial waste, or other waste.

Discharge flow data, measurements consisting of the date and daily flow rate of CSO discharge collected using meters at CSO outfalls and the daily rainfall measured at a proximate location in the same watershed as the outfall.

Discharge notifications, reports written in plain language and delivered to registered members of the public by electronic mail to notify them of all CSO discharges that occurred in a watershed in the past 24 hours. The notification shall state (1) the volume of all CSO discharges, (2) the location of all discharging outfalls and their operating authority, (3) the approximate time and date when each CSO discharge began and ended, (4) the level of treatment of each CSO

discharge, and (5) the geographic area that may be affected by its flow or by potential flooding. Furthermore, the notification shall include the following general information, (1) a list of common primary and secondary contact activities which the department of environmental protection has identified that the waterway can support in dry conditions, (2) information about the public health implications of CSO discharges and what recreational activities are impaired under these circumstances, (3) widely applicable precautionary measures that recreational users can take to avoid health risk including, but not limited to, advisories against primary or secondary contact activities within a certain time period of rainfall or CSO discharge events, and (4) a list of all authorities that operate outfalls in the watershed. Registered notification recipients shall include the two largest circulation newspapers as identified by the department of environmental protection in each watershed containing a CSO outfall, all boards of health as defined in Section 1 of Chapter 111 operated by municipalities in the watershed, and the department of public health.

Level of treatment, a description in plain language of the measures taken to remove contaminants from sewage before its discharge at a CSO outfall. This description should include, but not be limited to, disinfectant procedures undertaken to remove bacteria, filtration to remove solids, and any nutrient removal procedures.

Watersheds, the geographic area and natural basin from within which water drains or in natural course would drain into a major water of the commonwealth, as determined by the department of environmental protection.

SECTION 2. Section 43 of chapter 21 of the General Laws, as appearing in the 2012 Official Edition, is hereby amended by inserting after paragraph (10) the following paragraph:-

(11) Permits or variances granted under this section for any CSO outfalls emptying into public waterways shall include the following requirements:

(a) The permittee shall install and maintain metering equipment at the outfall to collect discharge flow data. This data shall be collected and made available to the department of environmental protection electronically on a daily basis. The department of environmental protection shall promulgate all necessary regulations to enable the accessibility and prompt collection of this data.

(b) Signage shall be installed at a clearly visible site adjacent to the CSO outfall and any public access point to the waterway which the department of environmental protection determines to be affected by CSO discharges at the CSO outfall. The department of environmental protection shall promulgate rules and regulations for the content, placement, and maintenance of CSO outfall signage. This content shall include, but not be limited to, descriptions of the existence of the CSO outfall, associated health risks due to bacterial and chemical contamination following CSO discharges, and appropriate precautions the public should take to ensure safe recreation in and around the waterway. Furthermore, the signage shall use plain language and include pictographic figures clearly communicating these factors to non-English speakers. The department of environmental protection shall coordinate with the department of conservation and recreation to administer placement of signage on department of conservation

and recreation lands.

SECTION 3. Chapter 21 of the General Laws is hereby amended by inserting after Section 43 the following section:-

Section 43A. (a) The department of environmental protection shall establish and maintain a website for reporting to the public any CSO discharges, using the discharge flow data collected under Subsection 11 of Section 43 of this chapter.

The website shall have features including, but not limited to, (1) a report of all discharge flow data collected from each CSO outfall permitted under Section 43, updated within 24 hours of receipt of the data from the permittee, (2) past daily CSO discharge monitoring data maintained for a period not less than ten years, (3) an application by which any member of the public may receive discharge notifications by electronic mail related to any particular outfall or set of outfalls, to be delivered at the same time the discharge commences, (4) a record of all past discharge notifications.

(b) The department of environmental protection shall issue an annual watershed CSO discharge report by April 15th of each year to the registered recipients of discharge notifications, which shall include an annual summary report of the previous years CSO discharge volumes and frequencies, the operating authorities of all CSO outfalls in the watershed, and the general information included in the discharge notifications.

(c) The department of environmental protection shall have the authority to post any available discharge flow data collected prior to the adoption of the permit requirement to this website.

References

- Abazajian, K. N., et al. 2009, *ApJS*, 182, 543
- Aihara, H., et al. 2011, *ApJS*, 193, 29
- Alard, C. 2000, *A&AS*, 144, 363
- Aldering, G., et al. 2002, in *Society of Photo-Optical Instrumentation Engineers (SPIE) Conference Series*, Vol. 4836, *Society of Photo-Optical Instrumentation Engineers (SPIE) Conference Series*, ed. J. A. Tyson & S. Wolff, 61–72
- Aldering, G., et al. 2006, *ApJ*, 650, 510
- Allen, D. A., Wright, A. E., & Goss, W. M. 1976, *MNRAS*, 177, 91
- Amorín, R., et al. 2014, *ArXiv e-prints*, 1403.3692
- Anderson, J. P., Covarrubias, R. A., James, P. A., Hamuy, M., & Haberman, S. M. 2010, *MNRAS*, 407, 2660
- Anderson, J. P., et al. 2014, *ArXiv e-prints*, 1403.7091
- Anderson, J. P., & James, P. A. 2009, *MNRAS*, 399, 559
- Andrews, B. H., & Martini, P. 2013, *ApJ*, 765, 140
- Anupama, G. C., Sahu, D. K., Gurugubelli, U. K., Prabhu, T. P., Tominaga, N., Tanaka, M., & Nomoto, K. 2009, *MNRAS*, 392, 894
- Arcavi, I., et al. 2012, *ApJ*, 756, L30
- . 2010, *ApJ*, 721, 777
- Arnett, W. D. 1980, *ApJ*, 237, 541
- . 1982, *ApJ*, 253, 785

REFERENCES

- Arp, H., & Brueckel, F. 1973, *ApJ*, 179, 445
- Asplund, M., Grevesse, N., & Sauval, A. J. 2005, in *Astronomical Society of the Pacific Conference Series*, Vol. 336, *Cosmic Abundances as Records of Stellar Evolution and Nucleosynthesis*, ed. T. G. Barnes III & F. N. Bash, 25–+
- Azimlu, M., Marciniak, R., & Barmby, P. 2011, *AJ*, 142, 139
- Baade, W., & Arp, H. 1964, *ApJ*, 139, 1027
- Baldwin, J. A., Phillips, M. M., & Terlevich, R. 1981, *PASP*, 93, 5
- Ball, N. M., Brunner, R. J., Myers, A. D., Strand, N. E., Alberts, S. L., & Tchong, D. 2008, *ApJ*, 683, 12
- Barbon, R., Ciatti, F., & Rosino, L. 1979, *A&A*, 72, 287
- Baron, E., Nugent, P. E., Branch, D., & Hauschildt, P. H. 2004, *ApJ*, 616, L91
- Barthelmy, S. D., et al. 2005, *Space Sci. Rev.*, 120, 143
- Bell, E. F., & de Jong, R. S. 2001, *ApJ*, 550, 212
- Bell, R., Gess-Newsome, J., & Luft, J. 2008, *Technology in the secondary science classroom* (NSTA Press)
- Benetti, S., Branch, D., Turatto, M., Cappellaro, E., Baron, E., Zampieri, L., Della Valle, M., & Pastorello, A. 2002, *MNRAS*, 336, 91
- Berger, E., et al. 2012, *ApJ*, 755, L29
- Berger, E., Fox, D. B., Kulkarni, S. R., Frail, D. A., & Djorgovski, S. G. 2007, *ApJ*, 660, 504
- Berger, E., Kulkarni, S. R., Frail, D. A., & Soderberg, A. M. 2003a, *ApJ*, 599, 408
- Berger, E., et al. 2003b, *Nature*, 426, 154
- Bersten, M. C., & Hamuy, M. 2009, *ApJ*, 701, 200
- Bertin, E., & Arnouts, S. 1996, *A&AS*, 117, 393
- Betancourt, M. J. 2013, *arXiv*, 1304

REFERENCES

- Betancourt, M. J., & Girolami, M. 2013, ArXiv e-prints, 1312.0906
- Bildsten, L., Shen, K. J., Weinberg, N. N., & Nelemans, G. 2007, *ApJ*, 662, L95
- Blair, W. P., Kirshner, R. P., & Chevalier, R. A. 1982, *ApJ*, 254, 50
- Blanton, M. R., & Roweis, S. 2007, *AJ*, 133, 734
- Blanton, M. R., et al. 2005, *AJ*, 129, 2562
- Blondin, S., et al. 2006a, *AJ*, 131, 1648
- Blondin, S., Modjaz, M., Kirshner, R., Challis, P., & Calkins, M. 2006b, *Central Bureau Electronic Telegrams*, 699, 1
- Blondin, S., & Tonry, J. L. 2007, *ApJ*, 666, 1024
- Bloom, J. S., Starr, D. L., Blake, C. H., Skrutskie, M. F., & Falco, E. E. 2006, in *Astronomical Society of the Pacific Conference Series*, Vol. 351, *Astronomical Data Analysis Software and Systems XV*, ed. C. Gabriel, C. Arviset, D. Ponz, & S. Enrique, 751
- Blumenfeld, P. C., Soloway, E., Marx, R. W., Krajcik, J. S., Guzdial, M., & Palincsar, A. 1991, *Educational Psychologist*, 26, 369
- Böhringer, H., et al. 2000, *ApJS*, 129, 435
- Boissier, S., & Prantzos, N. 2009, *A&A*, 503, 137
- Botticella, M. T., et al. 2010, *ApJ*, 717, L52
- Bresolin, F. 2011, *ApJ*, 730, 129
- Bresolin, F., Gieren, W., Kudritzki, R.-P., Pietrzyński, G., Urbaneja, M. A., & Carraro, G. 2009, *ApJ*, 700, 309
- Bresolin, F., Stasińska, G., Vílchez, J. M., Simon, J. D., & Rosolowsky, E. 2010, *MNRAS*, 404, 1679
- Brinchmann, J., Charlot, S., White, S. D. M., Tremonti, C., Kauffmann, G., Heckman, T., & Brinkmann, J. 2004, *MNRAS*, 351, 1151
- Brown, P. J., et al. 2009, *AJ*, 137, 4517
- Burrows, D. N., et al. 2005, *Space Sci. Rev.*, 120, 165

REFERENCES

- Caldwell, N., Harding, P., Morrison, H., Rose, J. A., Schiavon, R., & Kriessler, J. 2009, *AJ*, 137, 94
- Campana, S., et al. 2006, *Nature*, 442, 1008
- Campbell, T., Wang, S. K., Hsu, H.-Y., Duffy, A. M., & Wolf, P. G. 2010, *Journal of Science Education and Technology*, 19, 505
- Cano, Z., et al. 2011a, *ApJ*, 740, 41
- . 2011b, *MNRAS*, 413, 669
- Cardelli, J. A., Clayton, G. C., & Mathis, J. S. 1989, *ApJ*, 345, 245
- Carigi, L., & Peimbert, M. 2010, *ArXiv e-prints*, 1004.0756
- Cenko, S. B., Cobb, B. E., Kleiser, I. K., & Filippenko, A. V. 2010, *Central Bureau Electronic Telegrams*, 2208, 2
- Challis, P., Blondin, S., Matheson, T., Foley, R., Rodney, S., Leibundgut, B., & Spyromilio, J. 2007, *Central Bureau Electronic Telegrams*, 830, 1
- Chambers, K. C, *et al.* in preparation
- Chatzopoulos, E., Wheeler, J. C., & Vinko, J. 2009, *ApJ*, 704, 1251
- Cheng, K.-H., & Tsai, C.-C. 2013, *Journal of Science Education and Technology*, 22, 449
- Chevalier, R. A. 1982, *ApJ*, 258, 790
- . 1998, *ApJ*, 499, 810
- Chevalier, R. A., & Fransson, C. 2006, *ApJ*, 651, 381
- Chevalier, R. A., & Irwin, C. M. 2011, *ApJ*, 729, L6+
- Chevalier, R. A., & Soderberg, A. M. 2010, *ApJ*, 711, L40
- Chiboucas, K., et al. 2011, *ApJ*, 737, 86
- Chieffi, A., Domínguez, I., Höflich, P., Limongi, M., & Straniero, O. 2003, *MNRAS*, 345, 111
- Chilingarian, I. V., Melchior, A.-L., & Zolotukhin, I. Y. 2010, *MNRAS*, 405, 1409

REFERENCES

- Chomiuk, L., et al. 2011, ArXiv e-prints, 1107.3552
- Chornock, R., et al. 2010, ArXiv e-prints, 1004.2262
- . 2013, ArXiv e-prints, 1302.0009
- Christensen, L., Vreeswijk, P. M., Sollerman, J., Thöne, C. C., Le Floch, E., & Wiersema, K. 2008, *A&A*, 490, 45
- Chugai, N. N. 2009, *MNRAS*, 400, 866
- Chugai, N. N., & Utrobin, V. P. 2000, *A&A*, 354, 557
- Ciabattari, F., Mazzoni, E., Koff, R. A., Tomasella, L., Pastorello, A., Valenti, S., & Benetti, S. 2011, *Central Bureau Electronic Telegrams*, 2938, 1
- Clark, D. H., McCrea, W. H., & Stephenson, F. R. 1977, *Nature*, 265, 318
- Clayton, G. C., et al. 2011, *ApJ*, 743, 44
- Clocchiatti, A., Wheeler, J. C., Benetti, S., & Frueh, M. 1996, *ApJ*, 459, 547
- Condon, J. J., Cotton, W. D., Greisen, E. W., Yin, Q. F., Perley, R. A., Taylor, G. B., & Broderick, J. J. 1998, *AJ*, 115, 1693
- Conley, A., et al. 2006, *AJ*, 132, 1707
- Corsi, A., et al. 2011, *ApJ*, 741, 76
- . 2012, *ApJ*, 747, L5
- Cresci, G., Mannucci, F., Sommariva, V., Maiolino, R., Marconi, A., & Brusa, M. 2012, *MNRAS*, 421, 262
- Crowther, P. A. 2012, ArXiv e-prints, 1210.1126
- Csabai, I., Dobos, L., Trencsényi, M., Herczegh, G., Józsa, P., Purger, N., Budavári, T., & Szalay, A. S. 2007, *Astronomische Nachrichten*, 328, 852
- Cutri, R. M., et al. 2003, 2MASS All Sky Catalog of point sources.
- Dan, M., Rosswog, S., Guillochon, J., & Ramirez-Ruiz, E. 2011, *ApJ*, 737, 89
- D’Andrea, C. B., et al. 2010, *ApJ*, 708, 661

REFERENCES

- Delahaye, F., & Pinsonneault, M. H. 2006, *ApJ*, 649, 529
- Denisenko, V., Gerke, V., Novichonok, A., Korotkiy, S., Tomasella, L., Pastorello, A., Valenti, S., & Benetti, S. 2011, *Central Bureau Electronic Telegrams*, 2932, 1
- Dennefeld, M., & Kunth, D. 1981, *AJ*, 86, 989
- Dessart, L., & Hillier, D. J. 2011, *MNRAS*, 410, 1739
- Dessart, L., Hillier, D. J., Li, C., & Woosley, S. 2012, *ArXiv e-prints*, 1205.5349
- Dessart, L., Hillier, D. J., Livne, E., Yoon, S.-C., Woosley, S., Waldman, R., & Langer, N. 2011, *MNRAS*, 414, 2985
- Dessart, L., Hillier, D. J., Waldman, R., & Livne, E. 2013, *MNRAS*, 433, 1745
- Di Carlo, E., et al. 2008, *ApJ*, 684, 471
- Dilday, B., et al. 2012, *Science*, 337, 942
- Dimai, A. 2008, *Central Bureau Electronic Telegrams*, 1269, 1
- Dintinjana, B., et al. 2011, *Central Bureau Electronic Telegrams*, 2906, 1
- Drake, A. J., et al. 2009a, *ApJ*, 696, 870
- . 2010, *Central Bureau Electronic Telegrams*, 2224, 1
- . 2011a, *Central Bureau Electronic Telegrams*, 2645, 1
- . 2011b, *Central Bureau Electronic Telegrams*, 2733, 2
- Drake, A. J., Djorgovski, S. G., Williams, R., Mahabal, A., Graham, M. J., Catelan, M., Beshore, E. C., & Larson, S. M. 2009b, *Central Bureau Electronic Telegrams*, 1681, 1
- Dressler, A., Hare, T., Bigelow, B. C., & Osip, D. J. 2006, in *Society of Photo-Optical Instrumentation Engineers (SPIE) Conference Series*, Vol. 6269, *Society of Photo-Optical Instrumentation Engineers (SPIE) Conference Series*
- Driebe, T., Schoenberner, D., Bloeker, T., & Herwig, F. 1998, *A&A*, 339, 123

REFERENCES

- Drout, M. R., et al. 2011, *ApJ*, 741, 97
- Dwarkadas, V. V. 2014, *ArXiv e-prints*, 1402.5150
- Ekström, S., et al. 2012, *A&A*, 537, A146
- Eldridge, J. J., Izzard, R. G., & Tout, C. A. 2008, *MNRAS*, 384, 1109
- Eldridge, J. J., Langer, N., & Tout, C. A. 2011, *MNRAS*, 414, 3501
- Elias, J. H., Matthews, K., Neugebauer, G., & Persson, S. E. 1985, *ApJ*, 296, 379
- Elias-Rosa, N., et al. 2011, *ApJ*, 742, 6
- Fabbiano, G., et al. 2004, *ApJ*, 605, L21
- Fabricant, D., et al. 2005, *PASP*, 117, 1411
- Fabricant, D. G., Kurtz, M. J., Geller, M. J., Caldwell, N., Woods, D., & Dell'Antonio, I. 2008, *PASP*, 120, 1222
- Falk, S. W., & Arnett, W. D. 1977, *ApJS*, 33, 515
- Faran, T., et al. 2014, *ArXiv e-prints*, 1404.0378
- Faraway, J., Mahabal, A., Sun, J., Wang, X., Yi, Wang, & Zhang, L. 2014, *ArXiv e-prints*, 1401.3211
- Fassia, A., et al. 2000, *MNRAS*, 318, 1093
- Filippenko, A. V. 1997, *ARA&A*, 35, 309
- Filippenko, A. V., & Chornock, R. 2003, *IAU Circ.*, 8158, 4
- Filippenko, A. V., & Sargent, W. L. W. 1985, *Nature*, 316, 407
- Filippenko, A. V., Silverman, J. M., Kleiser, I. K. W., & Morton, A. J. L. 2010, *Central Bureau Electronic Telegrams*, 2224, 3
- Folatelli, G., & Stritzinger, M. 2010, *Central Bureau Electronic Telegrams*, 2279, 1
- Foley, R. J., Berger, E., Fox, O., Levesque, E. M., Challis, P. J., Ivans, I. I., Rhoads, J. E., & Soderberg, A. M. 2011a, *ApJ*, 732, 32
- Foley, R. J., et al. 2009a, *AJ*, 138, 376

REFERENCES

- Foley, R. J., & Mandel, K. 2013, *ApJ*, 778, 167
- Foley, R. J., et al. 2009b, *AJ*, 137, 3731
- Foley, R. J., Sanders, N. E., & Kirshner, R. P. 2011b, *ApJ*, 742, 89
- Foley, R. J., Smith, N., Ganeshalingam, M., Li, W., Chornock, R., & Filippenko, A. V. 2007, *ApJ*, 657, L105
- Foreman-Mackey, D., Hogg, D. W., Lang, D., & Goodman, J. 2012, *ArXiv e-prints*, 1202.3665
- Fox, O. D., et al. 2011, *ApJ*, 741, 7
- Frail, D. A., Soderberg, A. M., Kulkarni, S. R., Berger, E., Yost, S., Fox, D. W., & Harrison, F. A. 2005, *ApJ*, 619, 994
- Frail, D. A., Waxman, E., & Kulkarni, S. R. 2000, *ApJ*, 537, 191
- Fraser, M., et al. 2010, *ApJ*, 714, L280
- Freedman, W. L., & Madore, B. F. 1990, *ApJ*, 365, 186
- Friedrich, J. 2013, *Journal of Science Education and Technology*, 1
- Frieman, J. A., et al. 2008, *AJ*, 135, 338
- Fruchter, A. S., et al. 2006, *Nature*, 441, 463
- Fryer, C. L. 1999, *ApJ*, 522, 413
- Fryer, C. L., & Heger, A. 2005, *ApJ*, 623, 302
- Fryer, C. L., et al. 2007, *PASP*, 119, 1211
- Fukugita, M., Ichikawa, T., Gunn, J. E., Doi, M., Shimasaku, K., & Schneider, D. P. 1996, *AJ*, 111, 1748
- Fynbo, J. P. U., et al. 2003, *A&A*, 406, L63
- Gal-Yam, A., & Leonard, D. C. 2009, *Nature*, 458, 865
- Gal-Yam, A., et al. 2007, *ApJ*, 656, 372
- Gal-Yam, A., Maoz, D., Guhathakurta, P., & Filippenko, A. V. 2003, *AJ*, 125, 1087
- Gal-Yam, A., Maoz, D., & Sharon, K. 2002a, *MNRAS*, 332, 37

REFERENCES

- Gal-Yam, A., et al. 2009, *Nature*, 462, 624
- Gal-Yam, A., Ofek, E. O., & Shemmer, O. 2002b, *MNRAS*, 332, L73
- Galama, T. J., et al. 1998, *Nature*, 395, 670
- Galarza, V. C., Walterbos, R. A. M., & Braun, R. 1999, *AJ*, 118, 2775
- Galleti, S., Bellazzini, M., Federici, L., Buzzoni, A., & Fusi Pecci, F. 2007, *A&A*, 471, 127
- Garg, A., et al. 2007, *AJ*, 133, 403
- Garland, C. A., Pisano, D. J., Williams, J. P., Guzmán, R., & Castander, F. J. 2004, *ApJ*, 615, 689
- Garnett, D. R. 1992, *AJ*, 103, 1330
- Garnett, D. R., & Shields, G. A. 1987, *ApJ*, 317, 82
- Gazit, E., Yair, Y., & Chen, D. 2005, *Journal of Science Education and Technology*, 14, 459
- Gehrels, N., et al. 2004, *ApJ*, 611, 1005
- Gelman, A., Carlin, J., Stern, H., Dunson, D., Vehtari, A., & Rubin, D. 2013, *Bayesian Data Analysis, Third Edition*, Chapman & Hall/CRC Texts in Statistical Science (Taylor & Francis)
- Gelman, A., Jakulin, A., Pittau, M. G., & Su, Y.-S. 2008, *The Annals of Applied Statistics*, 2, 1360
- Geogy, C., et al. 2013, *A&A*, 558, A103
- Geogy, C., Ekström, S., Meynet, G., Massey, P., Levesque, E. M., Hirschi, R., Eggenberger, P., & Maeder, A. 2012, *ArXiv e-prints*, 1203.5243
- Gezari, S., et al. 2012, *Nature*, 485, 217
- . 2010, *ApJ*, 720, L77
- Gilliland, R. L., Nugent, P. E., & Phillips, M. M. 1999, *ApJ*, 521, 30
- Girolami, M., & Calderhead, B. 2011, *Journal of the Royal Statistical Society: Series B (Statistical Methodology)*, 73, 123

REFERENCES

- Gjergo, E., Duggan, J., Cunningham, J. D., Kuhlmann, S., Biswas, R., Kovacs, E., Bernstein, J. P., & Spinka, H. 2012, ArXiv e-prints, 1205.1480
- Gong, Y., Cooray, A., & Chen, X. 2010, ApJ, 709, 1420
- Graham, J. F., Fruchter, A. S., Kewley, L. J., Levesque, E. M., Levan, A. J., Tanvir, N. R., Reichart, D. E., & Nysewander, M. 2009, in American Institute of Physics Conference Series, Vol. 1133, American Institute of Physics Conference Series, ed. C. Meegan, C. Kouveliotou, & N. Gehrels, 269–272
- Graham, M. L., et al. 2012, ArXiv e-prints, 1205.0015
- Grieco, V., Matteucci, F., Meynet, G., Longo, F., Della Valle, M., & Salvaterra, R. 2012, ArXiv e-prints, 1204.2417
- Groh, J. H., Meynet, G., & Ekström, S. 2013a, A&A, 550, L7
- Groh, J. H., Meynet, G., Georgy, C., & Ekström, S. 2013b, A&A, 558, A131
- Guerrero, J., García-Berro, E., & Isern, J. 2004, A&A, 413, 257
- Habergham, S. M., James, P. A., & Anderson, J. P. 2012, eprint arXiv:1205.6732
- Hachinger, S., Mazzali, P. A., Taubenberger, S., Hillebrandt, W., Nomoto, K., & Sauer, D. N. 2012, ArXiv e-prints, 1201.1506
- Hadjiyska, E. I., Rabinowitz, D., Baltay, C., Zinn, R., Coppi, P., Ellman, N., & Miller, L. R. 2011, in Bulletin of the American Astronomical Society, Vol. 43, American Astronomical Society Meeting Abstracts 217, 433.18
- Hakobyan, A. A., Adibekyan, V. Z., Aramyan, L. S., Petrosian, A. R., Gomes, J. M., Mamon, G. A., Kunth, D., & Turatto, M. 2012, A&A, 544, A81
- Hakobyan, A. A., Petrosian, A. R., McLean, B., Kunth, D., Allen, R. J., Turatto, M., & Barbon, R. 2008, A&A, 488, 523
- Halliday, C., et al. 2006, MNRAS, 369, 97
- Hamuy, M. 2003a, ApJ, 582, 905
- . 2003b, ArXiv Astrophysics e-prints
- Hamuy, M., Phillips, M., & Maza, J. 2003, IAU Circ., 8059, 3

REFERENCES

- Hamuy, M., Phillips, M. M., Suntzeff, N. B., Schommer, R. A., Maza, J., & Aviles, R. 1996, *AJ*, 112, 2391
- Hamuy, M., & Pinto, P. A. 2002, *ApJ*, 566, L63
- Hamuy, M., Roth, M., & Morrell, N. 2002, *IAU Circ.*, 8037, 2
- Han, X. H., Hammer, F., Liang, Y. C., Flores, H., Rodrigues, M., Hou, J. L., & Wei, J. Y. 2010, *A&A*, 514, A24+
- Härtel, H. 2000, *Journal of Science Education and Technology*, 9, 175
- Haud, U. 1981, *Ap&SS*, 76, 477
- Heger, A., Fryer, C. L., Woosley, S. E., Langer, N., & Hartmann, D. H. 2003, *ApJ*, 591, 288
- Heger, A., & Woosley, S. E. 2002, *ApJ*, 567, 532
- Henry, R. B. C., Kwitter, K. B., Jaskot, A. E., Balick, B., Morrison, M. A., & Milingo, J. B. 2010, *ApJ*, 724, 748
- Henry, R. B. C., & Worthey, G. 1999, *PASP*, 111, 919
- Hernandez-Martinez, L., Peña, M., Carigi, L., & Garcia-Rojas, J. 2009, *ArXiv e-prints*, 0906.4402
- Hjorth, J., et al. 2003, *Nature*, 423, 847
- Hodapp, K. W., Siegmund, W. A., Kaiser, N., Chambers, K. C., Laux, U., Morgan, J., & Mannery, E. 2004, in *Society of Photo-Optical Instrumentation Engineers (SPIE) Conference Series*, Vol. 5489, *Society of Photo-Optical Instrumentation Engineers (SPIE) Conference Series*, ed. J. M. Oschmann Jr., 667–678
- Hoffman, M. D., & Gelman, A. 2013, *Journal of Machine Learning Research*, in press
- Hogg, D. W., Baldry, I. K., Blanton, M. R., & Eisenstein, D. J. 2002, *ArXiv Astrophysics e-prints*
- Hogg, D. W., Bovy, J., & Lang, D. 2010, *ArXiv e-prints*, 1008.4686
- Hoogerwerf, R., de Bruijne, J. H. J., & de Zeeuw, P. T. 2001, *A&A*, 365, 49

REFERENCES

- Hook, I. M., Jørgensen, I., Allington-Smith, J. R., Davies, R. L., Metcalfe, N., Murowinski, R. G., & Crampton, D. 2004, *PASP*, 116, 425
- Hu, J. Y., et al. 1997, *IAU Circ.*, 6783, 1
- Hudson, D. S., Mittal, R., Reiprich, T. H., Nulsen, P. E. J., Andernach, H., & Sarazin, C. L. 2010, *A&A*, 513, A37
- Hurley, K., et al. 2010, in *American Institute of Physics Conference Series*, Vol. 1279, *American Institute of Physics Conference Series*, ed. N. Kawai & S. Nagataki, 330–333
- Iben, Jr., I., & Tutukov, A. V. 1989, *ApJ*, 342, 430
- Immler, S., et al. 2008, *ApJ*, 674, L85
- Itagaki, K., et al. 2006, *IAU Circ.*, 8762, 1
- Iwamoto, K., et al. 1998, *Nature*, 395, 672
- Izzard, R. G., Ramirez-Ruiz, E., & Tout, C. A. 2004, *MNRAS*, 348, 1215
- Jacoby, G. H., & Ford, H. C. 1986, *ApJ*, 304, 490
- Jeltema, T. E., Mulchaey, J. S., Lubin, L. M., Rosati, P., & Böhringer, H. 2006, *ApJ*, 649, 649
- Jerkstrand, A., Smartt, S. J., Fraser, M., Fransson, C., Sollerman, J., Taddia, F., & Kotak, R. 2013, *ArXiv e-prints*, 1311.2031
- Kaiser, N., et al. 2002, in *Society of Photo-Optical Instrumentation Engineers (SPIE) Conference Series*, Vol. 4836, *Society of Photo-Optical Instrumentation Engineers (SPIE) Conference Series*, ed. J. A. Tyson & S. Wolff, 154–164
- Kalberla, P. M. W., Burton, W. B., Hartmann, D., Arnal, E. M., Bajaja, E., Morras, R., & Pöppel, W. G. L. 2005, *A&A*, 440, 775
- Kasen, D., & Woosley, S. E. 2009, *ApJ*, 703, 2205
- Kasliwal, M. M., et al. 2012, *ApJ*, 755, 161
- Kauffmann, G., et al. 2003a, *MNRAS*, 346, 1055
- . 2003b, *MNRAS*, 341, 33

REFERENCES

- Kaufman, M., Bash, F. N., Kennicutt, Jr., R. C., & Hodge, P. W. 1987, *ApJ*, 319, 61
- Kelly, P. L., Filippenko, A. V., Modjaz, M., & Kocevski, D. 2014, *ArXiv e-prints*, 1401.0729
- Kelly, P. L., & Kirshner, R. P. 2012, *ApJ*, 759, 107
- Kelly, P. L., Kirshner, R. P., & Pahre, M. 2008, *ApJ*, 687, 1201
- Kennicutt, Jr., R. C. 1998, *ARA&A*, 36, 189
- Kessler, R., et al. 2010, *PASP*, 122, 1415
- Kewley, L. J., & Dopita, M. A. 2002, *ApJS*, 142, 35
- Kewley, L. J., & Ellison, S. L. 2008, *ApJ*, 681, 1183
- Kewley, L. J., Groves, B., Kauffmann, G., & Heckman, T. 2006, *MNRAS*, 372, 961
- Kewley, L. J., Jansen, R. A., & Geller, M. J. 2005, *PASP*, 117, 227
- Kinugasa, K., et al. 2002, *ApJ*, 577, L97
- Kniazev, A. Y., Grebel, E. K., Zucker, D. B., Bell, E. F., Rix, H.-W., Martínez-Delgado, D., & Harris, H. C. 2005, in *American Institute of Physics Conference Series*, Vol. 804, *Planetary Nebulae as Astronomical Tools*, ed. R. Szczerba, G. Stasińska, & S. K. Gorny, 15–19
- Kniazev, A. Y., Pustilnik, S. A., & Zucker, D. B. 2008, *MNRAS*, 384, 1045
- Kobulnicky, H. A., & Fryer, C. L. 2007, *ApJ*, 670, 747
- Kobulnicky, H. A., Kennicutt, Jr., R. C., & Pizagno, J. L. 1999, *ApJ*, 514, 544
- Kobulnicky, H. A., & Kewley, L. J. 2004, *ApJ*, 617, 240
- Kocevski, D., & West, A. A. 2011, *ApJ*, 735, L8+
- Kocevski, D., West, A. A., & Modjaz, M. 2009, *ApJ*, 702, 377
- Kochanek, C. S., Szczygiel, D. M., & Stanek, K. Z. 2011, *ApJ*, 737, 76
- Kohoutek, L. 2001, *A&A*, 378, 843

REFERENCES

- Kong, X., & Cheng, F. Z. 2002, *A&A*, 389, 845
- Kotak, R., Meikle, W. P. S., Adamson, A., & Leggett, S. K. 2004, *MNRAS*, 354, L13
- Kouwenhoven, M. B. N., Brown, A. G. A., Portegies Zwart, S. F., & Kaper, L. 2007, *A&A*, 474, 77
- Kromer, M., Sim, S. A., Fink, M., Röpke, F. K., Seitenzahl, I. R., & Hillebrandt, W. 2010, *ApJ*, 719, 1067
- Kudritzki, R. P., Pauldrach, A., & Puls, J. 1987, *A&A*, 173, 293
- Kulkarni, S. R., et al. 1998, *Nature*, 395, 663
- Kumar, C. K. 1979, *ApJ*, 230, 386
- Kumar, D. D., & Sherwood, R. D. 2007, *Journal of Science Education and Technology*, 16, 239
- Kunth, D., & Östlin, G. 2000, *A&A Rev.*, 10, 1
- Kunth, D., & Sargent, W. L. W. 1981, *A&A*, 101, L5
- Kwitter, K. B., Lehman, E. M. M., Balick, B., & Henry, R. B. C. 2012, *ArXiv e-prints*, 1202.4933
- Lamb, R. L., & Annetta, L. 2012, *Journal of Science Education and Technology*
- Lara-López, M. A., et al. 2010, *A&A*, 521, L53+
- Lauberts, A., & Valentijn, E. A. 1989, *The surface photometry catalogue of the ESO-Uppsala galaxies*
- Law, N. M., et al. 2009, *PASP*, 121, 1395
- Leaman, J., Li, W., Chornock, R., & Filippenko, A. V. 2011, *MNRAS*, 412, 1419
- Lee, J. C., et al. 2009, *ApJ*, 706, 599
- Leibundgut, B., Kirshner, R., Huchra, J., & Daugherty, D. 1991, *IAU Circ.*, 5237, 2
- Leitherer, C., Robert, C., & Drissen, L. 1992, *ApJ*, 401, 596

REFERENCES

- Leitherer, C., et al. 1999, *ApJS*, 123, 3
- Leloudas, G., et al. 2011, *A&A*, 530, A95+
- Leonard, D. C. 2010, *The Astronomer's Telegram*, 2750, 1
- Leonard, D. C., et al. 2002, *PASP*, 114, 35
- Lequeux, J., Peimbert, M., Rayo, J. F., Serrano, A., & Torres-Peimbert, S. 1979, *A&A*, 80, 155
- Levesque, E. M., Berger, E., Kewley, L. J., & Bagley, M. M. 2010a, *AJ*, 139, 694
- Levesque, E. M., Berger, E., Soderberg, A. M., & Chornock, R. 2011, *ApJ*, 739, 23
- Levesque, E. M., Kewley, L. J., Berger, E., & Zahid, H. J. 2010b, *AJ*, 140, 1557
- Levesque, E. M., Kewley, L. J., Graham, J. F., & Fruchter, A. S. 2010c, *ApJ*, 712, L26
- Levesque, E. M., et al. 2010d, *ApJ*, 709, L26
- Levesque, E. M., Soderberg, A. M., Kewley, L. J., & Berger, E. 2010e, *ApJ*, 725, 1337
- Li, W., et al. 2011, *MNRAS*, 412, 1441
- Li, W., Wang, X., Van Dyk, S. D., Cuillandre, J.-C., Foley, R. J., & Filippenko, A. V. 2007, *ApJ*, 661, 1013
- Li, Z.-Y., & Chevalier, R. A. 1999, *ApJ*, 526, 716
- Lineweaver, C. H., Fenner, Y., & Gibson, B. K. 2004, *Science*, 303, 59
- Lintott, C., et al. 2011, *MNRAS*, 410, 166
- Litvinova, I. Y., & Nadezhin, D. K. 1985, *Soviet Astronomy Letters*, 11, 145
- Lopez-Sanchez, A. R., Dopita, M. A., Kewley, L. J., Zahid, H. J., Nicholls, D. C., & Scharwachter, J. 2012, *ArXiv e-prints*, 1203.5021
- López-Sánchez, Á. R., & Esteban, C. 2010a, *A&A*, 516, A104
- . 2010b, *A&A*, 517, A85+

REFERENCES

- López-Sánchez, Á. R., Esteban, C., & García-Rojas, J. 2006, *A&A*, 449, 997
- LSST Science Collaboration, et al. 2009, ArXiv e-prints, 0912.0201
- Lunnan, R., et al. 2013a, ArXiv e-prints, 1311.0026
- . 2013b, ArXiv e-prints, 1303.1531
- Lynden-Bell, D. 1975, *Vistas in Astronomy*, 19, 299
- MacFadyen, A. I., & Woosley, S. E. 1999, *ApJ*, 524, 262
- MacFadyen, A. I., Woosley, S. E., & Heger, A. 2001, *ApJ*, 550, 410
- Maciel, W. J., Lago, L. G., & Costa, R. D. D. 2005, *A&A*, 433, 127
- Maeda, K., Mazzali, P. A., Deng, J., Nomoto, K., Yoshii, Y., Tomita, H., & Kobayashi, Y. 2003, *ApJ*, 593, 931
- Magill, L., Kotak, R., & Nielsen, M. B. 2011, *Central Bureau Electronic Telegrams*, 2853, 1
- Magnier, E. 2006, in *The Advanced Maui Optical and Space Surveillance Technologies Conference*
- Magnier, E. A., Liu, M., Monet, D. G., & Chambers, K. C. 2008, in *IAU Symposium, Vol. 248, IAU Symposium*, ed. W. J. Jin, I. Platais, & M. A. C. Perryman, 553–559
- Magnier, E. A., et al. 2013, *ApJS*, 205, 20
- Magrini, L., & Gonçalves, D. R. 2009, *MNRAS*, 398, 280
- Magrini, L., Stanghellini, L., Corbelli, E., Galli, D., & Villaver, E. 2010, *A&A*, 512, A63
- Magrini, L., Stanghellini, L., & Villaver, E. 2009, *ApJ*, 696, 729
- Maguire, K., et al. 2010, *MNRAS*, 404, 981
- . 2012, *MNRAS*, 420, 3451
- Maiolino, R., et al. 2008, *A&A*, 488, 463
- Mandel, K. S., Narayan, G., & Kirshner, R. P. 2011, *ApJ*, 731, 120

REFERENCES

- Mandel, K. S., Wood-Vasey, W. M., Friedman, A. S., & Kirshner, R. P. 2009, *ApJ*, 704, 629
- Mannucci, F., Cresci, G., Maiolino, R., Marconi, A., & Gnerucci, A. 2010, *MNRAS*, 408, 2115
- Mannucci, F., Maoz, D., Sharon, K., Botticella, M. T., Della Valle, M., Gal-Yam, A., & Panagia, N. 2008, *MNRAS*, 383, 1121
- Mannucci, F., Salvaterra, R., & Campisi, M. A. 2011, *MNRAS*, 439
- Maoz, D., & Gal-Yam, A. 2004, *MNRAS*, 347, 951
- Maoz, D., Sharon, K., & Gal-Yam, A. 2010, *ApJ*, 722, 1879
- Margutti, R, *et al.* in preparation
- Marion, G. H., Challis, P., & Berlind, P. 2011, *Central Bureau Electronic Telegrams*, 2627, 2
- Marion, G. H., Vinko, J., Wheeler, J. C., & Shetrone, M. 2010, *Central Bureau Electronic Telegrams*, 2270, 1
- Martin, D. C., et al. 2005, *ApJ*, 619, L1
- Massey, P., & Johnson, O. 1998, *ApJ*, 505, 793
- Massey, P., McNeill, R. T., Olsen, K. A. G., Hodge, P. W., Blaha, C., Jacoby, G. H., Smith, R. C., & Strong, S. B. 2007, *AJ*, 134, 2474
- Matheson, T., Filippenko, A. V., Chornock, R., Leonard, D. C., & Li, W. 2000, *AJ*, 119, 2303
- Mattila, S., et al. 2012, eprint arXiv:1206.1314
- . 2008, *MNRAS*, 389, 141
- Mauerhan, J. C., et al. 2012, *ArXiv e-prints*, 1209.6320
- Mazzali, P. A., et al. 2006, *ApJ*, 645, 1323
- . 2003, *ApJ*, 599, L95
- Mazzali, P. A., Iwamoto, K., & Nomoto, K. 2000, *ApJ*, 545, 407
- McCall, M. L., Rybski, P. M., & Shields, G. A. 1985, *ApJS*, 57, 1

REFERENCES

- McCrum, M., et al. 2014, ArXiv e-prints, 1402.1631
- McDonald, M., & Veilleux, S. 2009, ApJ, 703, L172
- McDonald, M., Veilleux, S., Rupke, D. S. N., Mushotzky, R., & Reynolds, C. 2011, ApJ, 734, 95
- McGaugh, S. S. 1991, ApJ, 380, 140
- McNaught, R. H., & McKenzie, P. 1991, IAU Circ., 5237, 2
- Menikoff, R., & Plohr, B. J. 1989, Reviews of Modern Physics, 61, 75
- Merrett, H. R., et al. 2006, MNRAS, 369, 120
- Metzger, B. D., Piro, A. L., & Quataert, E. 2009, MNRAS, 396, 1659
- Meynet, G., Eggenberger, P., Ekstrom, S., Georgy, C., Groh, J., Maeder, A., Saio, H., & Moriya, T. 2013, ArXiv e-prints, 1308.5797
- Meynet, G., Maeder, A., Schaller, G., Schaerer, D., & Charbonnel, C. 1994, A&AS, 103, 97
- Miknaitis, G., et al. 2007, ApJ, 666, 674
- Milisavljevic, D., et al. 2012, ArXiv e-prints, 1207.2152
- . 2013, ApJ, 767, 71
- Milisavljevic, D., Parrent, J., & Fesen, R. 2011, Central Bureau Electronic Telegrams, 2650, 2
- Minkowski, R. 1946, PASP, 58, 305
- Modjaz, M., Filippenko, A. V., Silverman, J. M., Kleiser, I. K. W., & Morton, A. J. L. 2010, The Astronomer's Telegram, 2503, 1
- Modjaz, M., Kewley, L., Bloom, J. S., Filippenko, A. V., Perley, D., & Silverman, J. M. 2011a, ApJ, 731, L4+
- . 2011b, ApJ, 731, L4+
- Modjaz, M., et al. 2008, AJ, 135, 1136
- . 2006, ApJ, 645, L21
- Mollá, M., & Díaz, A. I. 2005, MNRAS, 358, 521

REFERENCES

- Monaghan, J. M., & Clement, K. J. 2000, *Journal of Science Education and Technology*, 9, 311
- Moran, S. M., et al. 2012, *ApJ*, 745, 66
- Nadyozhin, D. K. 2003, *MNRAS*, 346, 97
- Nagao, T., Maiolino, R., & Marconi, A. 2006, *A&A*, 459, 85
- Nakar, E., & Sari, R. 2010, *ApJ*, 725, 904
- Narayan, G., et al. 2011, *ApJ*, 731, L11
- Narla, A., et al. 2011, *Central Bureau Electronic Telegrams*, 2627, 1
- Nolthenius, R., & Ford, H. C. 1987, *ApJ*, 317, 62
- Nomoto, K., Kobayashi, C., & Tominaga, N. 2013, *ARA&A*, 51, 457
- Nomoto, K., Tominaga, N., Umeda, H., Kobayashi, C., & Maeda, K. 2006, *Nuclear Physics A*, 777, 424
- Nomoto, K. I., Iwamoto, K., & Suzuki, T. 1995, *Phys. Rep.*, 256, 173
- Nozawa, T., et al. 2008, *ApJ*, 684, 1343
- Nugent, P., et al. 2006, *ApJ*, 645, 841
- O’Dea, C. P., et al. 2008, *ApJ*, 681, 1035
- Odewahn, S. C., & Terrazas, E. 2007, *Central Bureau Electronic Telegrams*, 953, 1
- Oksanen, A. 2008, *Central Bureau Electronic Telegrams*, 1635, 1
- Olivares, F. 2008, *ArXiv e-prints*, 0810.5518
- Osterbrock, D. E., & Ferland, G. J. 2006, *Astrophysics of gaseous nebulae and active galactic nuclei*, ed. Osterbrock, D. E. & Ferland, G. J.
- Pacifici, C., Charlot, S., Blaizot, J., & Brinchmann, J. 2012, *MNRAS*, 421, 2002
- Padmanabhan, N., et al. 2008, *ApJ*, 674, 1217
- Panagia, N. 1978, in *IAU Symposium, Vol. 76, Planetary Nebulae*, ed. Y. Terzian, 315–321

REFERENCES

- Panei, J. A., Althaus, L. G., Chen, X., & Han, Z. 2007, *MNRAS*, 382, 779
- Papaspiliopoulos, O., Roberts, G. O., & Skld, M. 2007, *Statistical Science*, 22, 59
- Parrent, J. T., et al. 2011, *ApJ*, 732, 30
- Pastorello, A., et al. 2012, *ArXiv e-prints*, 1210.3568
- . 2008a, *MNRAS*, 389, 113
- . 2008b, *MNRAS*, 389, 131
- . 2010, *ApJ*, 724, L16
- . 2007, *Nature*, 447, 829
- . 2004, *MNRAS*, 347, 74
- Patat, F., Barbon, R., Cappellaro, E., & Turatto, M. 1993, *A&AS*, 98, 443
- . 1994, *A&A*, 282, 731
- Patat, F., et al. 2001, *ApJ*, 555, 900
- Patil, A., Huard, D., & Fonnesbeck, C. 2010, *Journal of Statistical Software*, 35, 1
- Pedregosa, F., et al. 2011, *Journal of Machine Learning Research*, 12, 2825
- Peeples, M. S., & Shankar, F. 2011, *MNRAS*, 417, 2962
- Pellegrini, E. W., Baldwin, J. A., & Ferland, G. J. 2010, *ApJS*, 191, 160
- Pellet, A., Astier, N., Viale, A., Courtes, G., Maucherat, A., Monnet, G., & Simien, F. 1978, *A&AS*, 31, 439
- Peng, C. Y., Ho, L. C., Impey, C. D., & Rix, H.-W. 2002, *AJ*, 124, 266
- . 2010, *AJ*, 139, 2097
- Perets, H. B., et al. 2010, *Nature*, 465, 322
- Pérez-Montero, E., & Contini, T. 2009, *MNRAS*, 398, 949
- Perez-Montero, E., et al. 2012, *ArXiv e-prints*, 1210.0334
- Perley, R., et al. 2009, *IEEE Proceedings*, 97, 1448

REFERENCES

- Pettini, M., & Pagel, B. E. J. 2004, MNRAS, 348, L59
- Phillips, M. M., Lira, P., Suntzeff, N. B., Schommer, R. A., Hamuy, M., & Maza, J. 1999, AJ, 118, 1766
- Pian, E., et al. 2000, ApJ, 536, 778
- . 2006, Nature, 442, 1011
- Pignata, G., et al. 2009, in American Institute of Physics Conference Series, Vol. 1111, American Institute of Physics Conference Series, ed. G. Giobbi, A. Tornambe, G. Raimondo, M. Limongi, L. A. Antonelli, N. Menci, & E. Brocato, 551–554, 0812.4923
- Pignata, G., et al. 2011, ApJ, 728, 14
- Pilyugin, L. S. 2001a, A&A, 369, 594
- . 2001b, A&A, 374, 412
- Pilyugin, L. S., & Thuan, T. X. 2005, ApJ, 631, 231
- Pilyugin, L. S., Vílchez, J. M., & Thuan, T. X. 2010, ApJ, 720, 1738
- Piro, A. L., & Kulkarni, S. R. 2012, ArXiv e-prints, 1211.0547
- Podsiadlowski, P., Joss, P. C., & Hsu, J. J. L. 1992, ApJ, 391, 246
- Podsiadlowski, P., Mazzali, P. A., Nomoto, K., Lazzati, D., & Cappellaro, E. 2004, ApJ, 607, L17
- Poole, T. S., et al. 2008, MNRAS, 383, 627
- Pottasch, S. R., & Bernard-Salas, J. 2006, A&A, 457, 189
- Powell, C., & Mason, D. 2013, Journal of Science Education and Technology, 22, 148
- Poznanski, D. 2013, MNRAS
- Poznanski, D., et al. 2009, ApJ, 694, 1067
- Prantzos, N., & Boissier, S. 2003, A&A, 406, 259
- Prieto, J. 2010, Central Bureau Electronic Telegrams, 2224, 3
- Prieto, J. L. 2011, Central Bureau Electronic Telegrams, 2704, 2

REFERENCES

- Prieto, J. L., Stanek, K. Z., & Beacom, J. F. 2008, *ApJ*, 673, 999
- Prochaska, J. X., et al. 2004, *ApJ*, 611, 200
- Puget, P., et al. 2004, in *Society of Photo-Optical Instrumentation Engineers (SPIE) Conference Series*, Vol. 5492, *Society of Photo-Optical Instrumentation Engineers (SPIE) Conference Series*, ed. A. F. M. Moorwood & M. Iye, 978–987
- Quimby, R., Mondol, P., Castro, F., Roman, B., & Rostopchin, S. 2006, *IAU Circ.*, 8657, 1
- Quimby, R., Odewahn, S. C., Terrazas, E., Rau, A., & Ofek, E. O. 2007, *Central Bureau Electronic Telegrams*, 953, 1
- Quimby, R. M., et al. 2011, *Nature*, 474, 487
- Rabinak, I., & Waxman, E. 2011, *ApJ*, 728, 63
- Rauch, M. 1998, *ARA&A*, 36, 267
- Reiprich, T. H., & Böhringer, H. 2002, *ApJ*, 567, 716
- Rest, A., et al. 2013, *ArXiv e-prints*, 1310.3828
- . 2005, *ApJ*, 634, 1103
- Richardson, D., Branch, D., & Baron, E. 2006, *AJ*, 131, 2233
- Richardson, D., Jenkins, III, R. L., Wright, J., & Maddox, L. 2014, *ArXiv e-prints*, 1403.5755
- Richer, M. G., & McCall, M. L. 2007, *ApJ*, 658, 328
- Richer, M. G., Stasińska, G., & McCall, M. L. 1999, *A&AS*, 135, 203
- Riello, M., et al. 2004a, *IAU Circ.*, 8296, 3
- Riello, M., Benetti, S., Cappellaro, E., Patat, F., Botticella, M. T., Turatto, M., & Valenti, S. 2004b, *IAU Circ.*, 8352, 2
- Rodríguez, M., & Delgado-Inglada, G. 2011, *ApJ*, 733, L50+
- Roming, P. W. A., et al. 2005, *Space Sci. Rev.*, 120, 95
- Rosales-Ortega, F. F. 2013, *Advances in Astronomy*, 2013

REFERENCES

- Rosolowsky, E., & Simon, J. D. 2008, *ApJ*, 675, 1213
- Sadler, P. M., Whitney, C. A., Shore, L., & Deutsch, F. 1999, *Journal of Science Education and Technology*, 8, 197
- Saglia, R. P., et al. 2012, *ApJ*, 746, 128
- Sahu, D. K., Gurugubelli, U. K., Anupama, G. C., & Nomoto, K. 2011, *MNRAS*, 413, 2583
- Sahu, D. K., Tanaka, M., Anupama, G. C., Gurugubelli, U. K., & Nomoto, K. 2009, *ApJ*, 697, 676
- Sako, M., et al. 2008, *AJ*, 135, 348
- Sakon, I., et al. 2009, *ApJ*, 692, 546
- Salim, S., et al. 2007, *ApJS*, 173, 267
- Sana, H., et al. 2012, *Science*, 337, 444
- Sand, D., et al. 2009, *Central Bureau Electronic Telegrams*, 1894, 1
- Sand, D. J., et al. 2011, *ApJ*, 729, 142
- . 2012, *ApJ*, 746, 163
- Sanders, N. E., Caldwell, N., McDowell, J., & Harding, P. 2012a, *ApJ*, 758, 133
- Sanders, N. E., Kohler, S., Newton, E., & Astrobites Collaboration. 2012b, *Astronomy Education Review*, 11, 010201
- Sanders, N. E., Levesque, E. M., & Soderberg, A. M. 2013, *ApJ*, 775, 125
- Sanders, N. E., et al. 2014, *ArXiv e-prints*, 1404.2004
- . 2012c, *ApJ*, 758, 132
- . 2012d, *ApJ*, 756, 184
- Sarazin, C. L. 1976, *ApJ*, 208, 323
- Sari, R., Piran, T., & Narayan, R. 1998, *ApJ*, 497, L17+
- Savaglio, S., Glazebrook, K., & Le Borgne, D. 2009, *ApJ*, 691, 182
- Sazonov, S. Y., Lutovinov, A. A., & Sunyaev, R. A. 2004, *Nature*, 430, 646

REFERENCES

- Scannapieco, C., Tissera, P. B., White, S. D. M., & Springel, V. 2008, *MNRAS*, 389, 1137
- Schaerer, D., Contini, T., & Pindao, M. 1999, *A&AS*, 136, 35
- Schaerer, D., & Vacca, W. D. 1998, *ApJ*, 497, 618
- Schlafly, E. F., & Finkbeiner, D. P. 2011, *ApJ*, 737, 103
- Schlafly, E. F., et al. 2012, *ApJ*, 756, 158
- Schlegel, D. J., Finkbeiner, D. P., & Davis, M. 1998, *ApJ*, 500, 525
- Schmidt, G. D., Weymann, R. J., & Foltz, C. B. 1989a, *PASP*, 101, 713
- . 1989b, *PASP*, 101, 713
- Schoenberner, D. 1975, *A&A*, 44, 383
- Schwab, J., Shen, K. J., Quataert, E., Dan, M., & Rosswog, S. 2012, *MNRAS*, 427, 190
- Scolnic, D., et al. 2013, *ArXiv e-prints*, 1310.3824
- Scott, D. 1992, *Multivariate Density Estimation: Theory, Practice, and Visualization*, A Wiley-interscience publication (Wiley)
- SDSS-III Collaboration, et al. 2012, *ArXiv e-prints*, 1207.7137
- Sharon, K., Gal-Yam, A., Maoz, D., Filippenko, A. V., & Guhathakurta, P. 2007, *ApJ*, 660, 1165
- Shaver, P. A., McGee, R. X., Newton, L. M., Danks, A. C., & Pottasch, S. R. 1983, *MNRAS*, 204, 53
- Shaw, R. A., & Dufour, R. J. 1994, in *Astronomical Society of the Pacific Conference Series*, Vol. 61, *Astronomical Data Analysis Software and Systems III*, ed. D. R. Crabtree, R. J. Hanisch, & J. Barnes, 327–+
- Shell, D. F., Snow, G. R., & Claes, D. R. 2011, *Journal of Science Education and Technology*, 20, 161
- Shen, K. J., & Bildsten, L. 2009a, *ApJ*, 692, 324
- . 2009b, *ApJ*, 699, 1365
- Shen, K. J., Bildsten, L., Kasen, D., & Quataert, E. 2012, *ApJ*, 748, 35

REFERENCES

- Shi, F., Kong, X., & Cheng, F. Z. 2006, *A&A*, 453, 487
- Shields, G. A. 1990, *ARA&A*, 28, 525
- Shields, G. A., & Searle, L. 1978, *ApJ*, 222, 821
- Silverman, J. M., Chornock, R., & Filippenko, A. V. 2007, *Central Bureau Electronic Telegrams*, 909, 1
- Silverman, J. M., Kandrashoff, M. T., & Filippenko, A. V. 2010, *Central Bureau Electronic Telegrams*, 2272, 1
- Silverman, J. M., Modjaz, M., George, M. R., & Filippenko, A. V. 2008, *Central Bureau Electronic Telegrams*, 1503, 1
- Simien, F., Pellet, A., Monnet, G., Athanassoula, E., Maucherat, A., & Courtes, G. 1978, *A&A*, 67, 73
- Skvarc, J., & Mikuz, H. 2008, *Central Bureau Electronic Telegrams*, 1493, 1
- Smartt, S. J. 2009, *ARA&A*, 47, 63
- Smartt, S. J., Eldridge, J. J., Crockett, R. M., & Maund, J. R. 2009, *MNRAS*, 395, 1409
- Smith, N., Chornock, R., Silverman, J. M., Filippenko, A. V., & Foley, R. J. 2010, *ApJ*, 709, 856
- Smith, N., Foley, R. J., & Filippenko, A. V. 2008, *ApJ*, 680, 568
- Smith, N., Li, W., Filippenko, A. V., & Chornock, R. 2011a, *MNRAS*, 412, 1522
- Smith, N., et al. 2011b, *ApJ*, 732, 63
- Smith, N., Mauerhan, J. C., Silverman, J. M., Ganeshalingam, M., Filippenko, A. V., Cenko, S. B., Clubb, K. I., & Kandrashoff, M. 2012, *ArXiv e-prints*, 1204.0043
- Soderberg, A. 2006, *The Astronomer's Telegram*, 917, 1
- Soderberg, A. M. 2007, *Caltech PhD Thesis*
- Soderberg, A. M., et al. 2010, *Nature*, 463, 513
- Soderberg, A. M., Kulkarni, S. R., Berger, E., Chevalier, R. A., Frail, D. A., Fox, D. B., & Walker, R. C. 2005, *ApJ*, 621, 908

REFERENCES

- Soderberg, A. M., et al. 2004a, *ApJ*, 606, 994
- . 2004b, *Nature*, 430, 648
- . 2006a, *Nature*, 442, 1014
- . 2006b, *ApJ*, 636, 391
- Soderberg, A. M., Nakar, E., Berger, E., & Kulkarni, S. R. 2006c, *ApJ*, 638, 930
- Sofue, Y., & Kato, T. 1981, *PASJ*, 33, 449
- Solheim, J.-E. 2010, *PASP*, 122, 1133
- Sollerman, J., Östlin, G., Fynbo, J. P. U., Hjorth, J., Fruchter, A., & Pedersen, K. 2005, *New A*, 11, 103
- Stan Development Team. 2013, *Stan: A C++ Library for Probability and Sampling*, Version 1.3
- . 2014, *Stan Modeling Language Users Guide and Reference Manual*, Version 2.2
- Stanek, K. Z., et al. 2006, *Acta Astron.*, 56, 333
- Stanghellini, L., Shaw, R. A., & Villaver, E. 2008, *ApJ*, 689, 194
- Stanishev, V., Rodrigues, M., Mourão, A., & Flores, H. 2012, *A&A*, 545, A58
- Starling, R. L. C., et al. 2011, *MNRAS*, 411, 2792
- Stasińska, G. 2002, *ArXiv Astrophysics e-prints*
- Stasińska, G., & Leitherer, C. 1996, *ApJS*, 107, 661
- Steele, T. N., Silverman, J. M., Ganeshalingam, M., Lee, N., Li, W., & Filippenko, A. V. 2008, *Central Bureau Electronic Telegrams*, 1275, 1
- Stilp, A. M., Dalcanton, J. J., Warren, S. R., Weisz, D. R., Skillman, E., Ott, J., Williams, B. F., & Dolphin, A. E. 2013, *ApJ*, 772, 124
- Stoll, R., Prieto, J. L., Stanek, K. Z., & Pogge, R. W. 2012, *ArXiv e-prints*, 1205.2338
- Stoughton, C., et al. 2002, *AJ*, 123, 485

REFERENCES

- Stritzinger, M., Folatelli, G., Pignata, G., Forster, F., & Hamuy, M. 2008a, Central Bureau Electronic Telegrams, 1540, 1
- Stritzinger, M., Lira, P., & Pignata, G. 2008b, Central Bureau Electronic Telegrams, 1629, 2
- Stubbs, C. W., Doherty, P., Cramer, C., Narayan, G., Brown, Y. J., Lykke, K. R., Woodward, J. T., & Tonry, J. L. 2010, ApJS, 191, 376
- Suh, H., Yoon, S.-c., Jeong, H., & Yi, S. K. 2011, ApJ, 730, 110
- Sullivan, M., et al. 2006, ApJ, 648, 868
- Sun, M. 2009, ApJ, 704, 1586
- Swartz, D. A., Wheeler, J. C., & Harkness, R. P. 1991, ApJ, 374, 266
- Takáts, K., et al. 2013, ArXiv e-prints, 1311.2525
- Tanaka, M., et al. 2008, ApJ, 677, 448
- Taubenberger, S., et al. 2006, MNRAS, 371, 1459
- Tempel, E., Tago, E., & Liivamägi, L. J. 2012, A&A, 540, A106
- Thomas, J. W. 2000, A Review of Research on Project-Based Learning
- Timmes, F. X., Woosley, S. E., & Weaver, T. A. 1995, ApJS, 98, 617
- Tominaga, N., et al. 2008, ApJ, 687, 1208
- Tonry, J., & Onaka, P. 2009, in Advanced Maui Optical and Space Surveillance Technologies Conference,
- Tonry, J. L., et al. 2012, ApJ, 750, 99
- Townsley, D. M., & Bildsten, L. 2004, ApJ, 600, 390
- Tremblay, G. R., et al. 2012, MNRAS, 424, 1042
- Tremonti, C. A., et al. 2004, ApJ, 613, 898
- Trundle, C., Dufton, P. L., Lennon, D. J., Smartt, S. J., & Urbaneja, M. A. 2002, A&A, 395, 519
- Uomoto, A., & Kirshner, R. P. 1985, A&A, 149, L7
- Urbaneja, M. A., et al. 2005, ApJ, 622, 862

REFERENCES

- Utrobin, V. P., & Chugai, N. N. 2008, *A&A*, 491, 507
- Valenti, S., et al. 2008, *MNRAS*, 383, 1485
- . 2011, *MNRAS*, 416, 3138
- . 2009, *Nature*, 459, 674
- . 2012, *ArXiv e-prints*, 1203.1933
- van der Hulst, J. M., Kennicutt, R. C., Crane, P. C., & Rots, A. H. 1988, *A&A*, 195, 38
- van der Kolk, K., Hartog, R., Beldman, G., & Gruppen, H. 2013, *Journal of Science Education and Technology*, 1
- van Eerten, H., Zhang, W., & MacFadyen, A. 2010, *ApJ*, 722, 235
- van Eerten, H. J., & MacFadyen, A. I. 2011, *ApJ*, 733, L37
- Viallefond, F., & Goss, W. M. 1986, *A&A*, 154, 357
- Vink, J. S., & de Koter, A. 2005, *A&A*, 442, 587
- Vogel, J. J., Vogel, D. S., Cannon-Bowers, J., Bowes, C. A., Muse, K., & Wright, M. 2006, *Journal of Educational Computing Research*, 34, 3
- Walmswell, J. J., & Eldridge, J. J. 2012, *MNRAS*, 419, 2054
- Walterbos, R. A. M., & Braun, R. 1992, *A&AS*, 92, 625
- Waxman, E. 2004, *ApJ*, 602, 886
- Wheeler, J. C., & Levreault, R. 1985, *ApJ*, 294, L17
- Wiersema, K., et al. 2007, *A&A*, 464, 529
- Windhorst, R. A., et al. 1991, *ApJ*, 380, 362
- Wolfire, M. G., Hollenbach, D., & Tielens, A. G. G. M. 1993, *ApJ*, 402, 195
- Wood-Vasey, W. M., et al. 2008, *ApJ*, 689, 377
- Wosley, S. E., & Bloom, J. S. 2006, *ARA&A*, 44, 507
- Wosley, S. E., & Heger, A. 2006, *ApJ*, 637, 914

REFERENCES

- Woosley, S. E., Heger, A., & Weaver, T. A. 2002, *Reviews of Modern Physics*, 74, 1015
- Woosley, S. E., & Kasen, D. 2011, *ApJ*, 734, 38
- Woosley, S. E., Langer, N., & Weaver, T. A. 1995, *ApJ*, 448, 315
- Worthey, G., España, A., MacArthur, L. A., & Courteau, S. 2005, *ApJ*, 631, 820
- Yang, X., Mo, H. J., van den Bosch, F. C., Pasquali, A., Li, C., & Barden, M. 2007, *ApJ*, 671, 153
- Yates, R. M., Kauffmann, G., & Guo, Q. 2012, *MNRAS*, 422, 215
- Yoon, S.-C., Woosley, S. E., & Langer, N. 2010, *ApJ*, 725, 940
- York, D. G., et al. 2000, *AJ*, 120, 1579
- Young, D. R., Smartt, S. J., Mattila, S., Tanvir, N. R., Bersier, D., Chambers, K. C., Kaiser, N., & Tonry, J. L. 2008, *A&A*, 489, 359
- Young, D. R., et al. 2010, *A&A*, 512, A70+
- Young, T. R. 2004, *ApJ*, 617, 1233
- Zahid, H. J., Geller, M. J., Kewley, L. J., Hwang, H. S., Fabricant, D. G., & Kurtz, M. J. 2013, *ApJ*, 771, L19
- Zaritsky, D., Kennicutt, Jr., R. C., & Huchra, J. P. 1994, *ApJ*, 420, 87